

AUGUST 2019

AJNR

VOLUME 40 • PP 1251-1436

AJNR

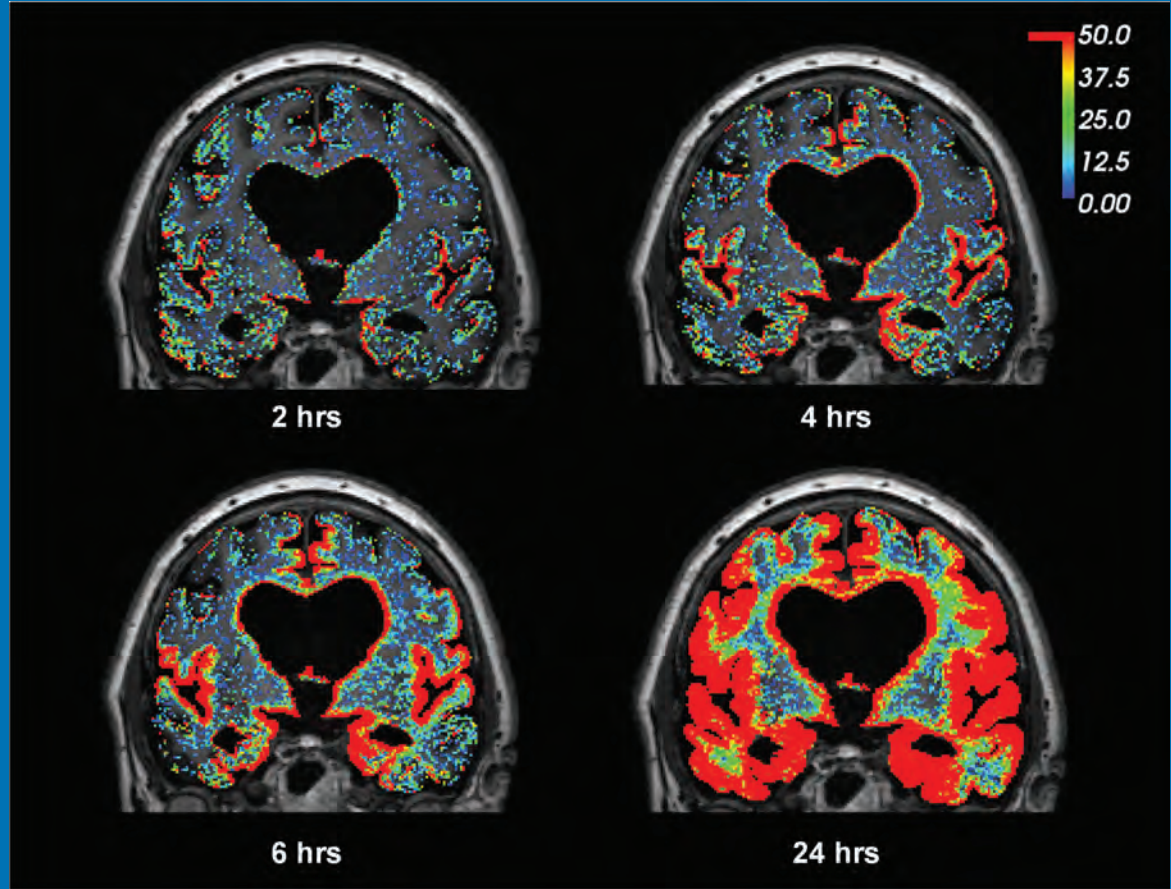
AMERICAN JOURNAL OF NEURORADIOLOGY

AUGUST 2019
VOLUME 40
NUMBER 8
WWW.AJNR.ORG

THE JOURNAL OF DIAGNOSTIC AND
INTERVENTIONAL NEURORADIOLOGY

Glymphatic imaging of the brain
Automated FLAIR lesion segmentation with CNN
Same room flat panel detector CT perfusion and thrombectomy
for large-vessel occlusion

Official Journal ASNR • ASFNR • ASHNR • ASPNR • ASSR





ONE AND DONE

INDICATIONS FOR USE:

The WEB Aneurysm Embolization System is indicated for use at the middle cerebral artery (MCA) bifurcation, internal carotid artery (ICA) terminus, anterior communicating artery (AComm) complex, or basilar artery apex for the endovascular treatment of adult patients with saccular, wide neck bifurcation intracranial aneurysms with dome diameter from 3 mm to 10 mm and either neck size 4 mm or greater or the dome-to-neck ratio is greater than 1 and less than 2.

The WEB Aneurysm Embolization System is contraindicated for patients with known bacterial infection that may interfere with or negatively affect the implantation procedure and patients with known hypersensitivity to nickel. For complete indications, contraindications, potential complications, warnings, precautions, and instructions, see instructions for use (IFU provided with the device).

The VIA® Catheter is intended for the introduction of non-liquid interventional devices (such as stents/_ow diverters) and infusion of diagnostic (such as contrast media) or non-liquid therapeutic agents into the neuro, peripheral, and coronary vasculature. The VIA Catheter is contraindicated for use with liquid embolic materials, such as n-butyl 2-cyanoacrylate or ethylene vinyl alcohol & DMSO (dimethyl sulfoxide). The VIA Catheter is contraindicated for use in the pediatric population (<22 yrs of age).

Caution: Federal law restricts these devices to sale by or on the order of a physician.

WEB[®]

Aneurysm Embolization System

MicroVention[®] delivers the first intrasaccular solution for wide neck bifurcation aneurysms.

The **world leader**
and **first**
PMA - approved
device in an
important new
category of
intrasaccular
flow disruptors.

The WEB[®] System is a safe
and effective single-device
solution for treating wide
neck bifurcation aneurysms.



SL Device



SLS Device

Contact a MicroVention sales associate to learn more about integrating the WEB[®] device into your practice.



**MicroVention Worldwide
Innovation Center**

35 Enterprise
Aliso Viejo, CA 92656 USA

MicroVention UK Limited

MicroVention Europe, S.A.R.L.

MicroVention Deutschland GmbH

microvention.com

PH +1.714.247.8000

PH +44 (0) 191 258 6777

PH +33 (1) 39 21 77 46

PH +49 211 210 798-0

ASNR 58th Annual Meeting & The Foundation of the ASNR Symposium 2020

CALL FOR ABSTRACTS

Join us May 30-June 4, 2020 at Caesars Palace in Las Vegas to present the best scientific research in Neuroradiology.

Submission Deadline: Friday, November 1, 2019 (8:00PM EST)

Submit online at [ASNR.org/AnnualMeeting](https://www.asnr.org/AnnualMeeting)

Acceptance notifications will be sent on or before January 15, 2020 upon conclusion of peer review.

Submit an abstract for the ASNR 58th Annual Meeting (May 30 - June 4, 2020, Las Vegas, NV) in one of the following presentation categories:

- | | |
|-------------------------------------|---|
| • Scientific Paper Oral | • Electronic Scientific Poster Electronic |
| • Excerpta Oral | • Electronic Educational Exhibit Electronic |
| • Scientific Poster Print | • Educational Exhibit Poster Print |

Abstract Submissions Information and Criteria

1. Abstracts should describe the learning objectives of the presentation.
2. The *American Journal of Neuroradiology (AJNR)* encourages presenters to submit manuscripts based on their work to *AJNR* before considering other journals.
3. Presenters of accepted abstracts **must register** for the ASNR 58th Annual Meeting and/or the Foundation of the ASNR Symposium 2020.
4. Published or previously presented works should NOT be submitted.
5. Submission topic areas include: **Adult Brain, Spine, Head and Neck, Pediatrics, Functional/Advanced Imaging, Interventional, Health Policy, AI/ Informatics, and Professional Development.**
6. Submit each abstract in **one** category only.
7. Format abstract text using headings required for submission category.
8. Maximum length: **2,500 characters**, not including title, authors, images, figures.
9. Submission site allows uploading of files into the system.
10. Changes can be made to the abstract until the deadline.

Questions?

Contact the ASNR Education Department at ekruse@asnr.org.

Neuroform Atlas® Stent System

RX ONLY

See package insert for complete indications, contraindications, warnings and instructions for use.

Indications for use

The Neuroform Atlas Stent System is indicated for use with neurovascular embolization coils in the anterior circulation of the neurovasculature for the endovascular treatment of patients ≥ 18 years of age with sacular wide-necked (neck width ≥ 4 mm or a dome-to-neck ratio of < 2) intracranial aneurysms arising from a parent vessel with a diameter of ≥ 2.0 mm and ≤ 4.5 mm.

Contraindications

- Patients in whom the parent vessel size does not fall within the indicated range.
- Patients in whom antiplatelet and/or anticoagulation therapy (e.g., aspirin and clopidogrel) is contraindicated.
- Patients who have not received anti-platelet agents prior to stent implantation.
- Patients with an active bacterial infection.
- Patients in whom angiography demonstrates the anatomy is not appropriate for endovascular treatment due to conditions such as:
 - Severe intracranial vessel tortuosity or stenosis;
 - Intracranial vasospasm not responsive to medical therapy.
- Patients in whom a pre-existing stent is in place in the parent artery at the target intracranial aneurysm location.

Potential adverse events

The potential adverse events listed below, as well as others, may be associated with the use of the Neuroform Atlas Stent System or with the procedure:

- Aphasia
- Allergic reaction to Nitinol metal and medications
- Aneurysm perforation/rupture, leak or contrast extravasation
- Blindness
- Cardiac arrhythmia
- Coil herniation through stent into parent vessel
- Cranial neuropathy
- Death
- Embolus
- Headache
- Hemiplegia
- Hemorrhage (i.e., intracerebral, subarachnoid, retroperitoneal, or in other locations)
- Hydrocephalus
- In-stent stenosis
- Infection
- Ischemia

Stryker or its affiliated entities own, use, or have applied for the following trademarks or service marks:

Neuroform Atlas, Stryker. All other trademarks are trademarks of their respective owners or holders. The absence of a product, feature, or service name, or logo from this list does not constitute a waiver of Stryker's trademark or other intellectual property rights concerning that name or logo.

Copyright © 2019 Stryker
AF002547 v2.0 | Page 2 of 2

AXS Vecta Aspiration System

RX ONLY

CAUTION: Federal Law (USA) restricts this device to sale by or on the order of a physician.

See package insert for complete indications, contraindications, warnings and instructions for use.

Intended use/indications for use

The AXS Vecta Aspiration Catheter, as part of the AXS Vecta Aspiration System is indicated in the revascularization of patients with acute ischemic stroke secondary to intracranial large vessel occlusive disease (within the internal carotid, middle cerebral – M1 and M2 segments, basilar, and vertebral arteries) within 8 hours of symptom onset.

Patients who are ineligible for intravenous tissue plasminogen activator (IV t-PA) or who failed IV t-PA therapy are candidates for treatment.

Device description

The AXS Vecta Aspiration System is composed of the following components:

- AXS Vecta 71 or 74 Aspiration Catheter
- Medela Dominant Flex Pump
- AXS Universal Aspiration Tubing
- AXS Universal Liner Set.

The AXS Vecta Aspiration Catheter delivers aspiration from the Medela Dominant Flex Pump directly to the site of the occlusion to remove the clot. The AXS Vecta Aspiration Catheter is a single lumen, flexible, variable stiffness catheter. It has a radiopaque marker band on the distal end and a Luer hub at the proximal end. The AXS Vecta Aspiration Catheter shaft has a lubricious hydrophilic coating at the distal end (distal 25cm) to reduce friction during use. It is packaged with one Scout Introducer, one hemostasis valve, and two peel-away introducers.

The Scout Introducer may be used in conjunction with the AXS Vecta Aspiration Catheter to facilitate in the introduction of the AXS Vecta Aspiration Catheter into distal vasculature and aid in navigation to distal anatomy. The Scout Introducer has a lubricious hydrophilic coating at the distal end to reduce friction during use. The inner lumen of the AXS Vecta Aspiration Catheter is compatible with the Scout Introducer, guide wires and microcatheters. The inner lumen of the Scout Introducer is compatible with guide wires and microcatheters of an outer diameter of less than 0.044in.

The AXS Universal Aspiration Tubing serves as a conduit to supply vacuum from the Medela Dominant Flex Pump to the distal tip of the AXS Vecta Aspiration Catheter. The AXS Universal Aspiration Tubing provides a connection between the sterile and non-sterile environments. The proximal end of the AXS Universal Aspiration Tubing is connected to the AXS Universal Liner Set (outside of the sterile environment) while the distal end of the AXS Universal Aspiration Tubing is connected to the AXS Vecta Aspiration Catheter (inside the sterile environment). The AXS Universal Liner Set is connected to the Medela Dominant Flex Pump (also outside of the sterile environment).

The Medela Dominant Flex Pump is designed to generate vacuum for the AXS Vecta Aspiration System. When used as part of the AXS Vecta Aspiration System, the AXS Vecta Aspiration Catheter requires a minimum vacuum pressure of -68 kPa (-20.08 in Hg) from the Medela Dominant Flex Pump. The Medela Dominant Flex Pump is reusable, non-sterile, and intended to be utilized outside of the sterile environment.

The AXS Universal Liner Set is provided non-sterile and consists of an individually packaged canister liner and a ClotFinder specimen cup. The AXS Universal Liner Set is offered with and without a desiccant. The AXS Universal Liner Set is single-use and the repository for aspirated material.

Dimensions of the AXS Vecta Aspiration Catheter and Scout Introducer are included on the individual device label. The AXS Vecta Aspiration Catheters are available in 3 different lengths, the device configurations including the length of the Scout packaged with each catheter and the recommended Microcatheter length is presented in the table 1.0 below.

Stryker or its affiliated entities own, use, or have applied for the following trademarks or service marks: AXS Universal, AXS Vecta, ClotFinder, Stryker.

Scout is a registered trademark of InNeuroCo, Inc. All other trademarks are trademarks of their respective owners or holders.

The absence of a product, feature, or service name, or logo from this list does not constitute a waiver of Stryker's trademark or other intellectual property rights concerning that name or logo.

Copyright © 2019 Stryker
AF002595 v2.0 | Page 2 of 2

- Mass effect
- Myocardial infarction
- Neurological deficit/intracranial sequele
- Pseudoaneurysm
- Reaction to radiation exposure (i.e., alopecia, burns ranging in severity from skin reddening to ulcers, cataracts, or delayed neoplasia)
- Reactions to anti-platelet/anti-coagulant agents
- Renal failure
- Seizure
- Stent fracture, migration/embolization, or misplacement
- Stent thrombosis
- Stroke
- Transient ischemic attack
- Vasospasm
- Vessel occlusion or closure including parent vessel or non-target side-branches
- Vessel perforation/rupture, dissection, trauma or damage
- Vessel thrombosis
- Visual impairment
- Other procedural complications including but not limited to anesthetic and contrast media risks, hypotension, hypertension, access site complications (including pain, hematoma, local bleeding, local infection, and injury to the artery (i.e. dissection), vein, or adjacent nerves)
- Unplanned intervention

Warnings

Contents supplied STERILE using an ethylene oxide (EO) process. Do not use if sterile barrier is damaged. If damage is found, call your Stryker Neurovascular representative.

For single use only. Do not reuse, reprocess or resterilize. Reuse, reprocessing or resterilization may compromise the structural integrity of the device and/or lead to device failure which, in turn, may result in patient injury, illness or death. Reuse, reprocessing or resterilization may also create a risk of contamination of the device and/or cause patient infection or cross-infection, including, but not limited to, the transmission of infectious disease(s) from one patient to another. Contamination of the device may lead to injury, illness or death of the patient.

After use, dispose of product and packaging in accordance with hospital, administrative and/or local government policy.

- This device should only be used by physicians who have received appropriate training in interventional neuroradiology or interventional radiology and preclinical training on the use of this device as established by Stryker Neurovascular.
- Persons allergic to nickel titanium (Nitinol) may suffer an allergic response to this stent implant.
- Higher adverse event rates may be experienced for distal aneurysms located in the anterior and middle cerebral arteries.
- Do not use device to treat patients with ruptured intracranial aneurysms within a minimum of 30 days from the aneurysm rupture.

Catheter part number	INC-11129	INC-11129	INC-11129	INC-11129	INC-11597	INC-11597
Catheter inner diameter (in)	0.071	0.071	0.071	0.074	0.074	0.074
Distal catheter outer diameter (in)	0.082	0.082	0.082	0.083	0.083	0.083
Catheter working length (cm)	115	125	132	115	125	132
Scout Introducer length (cm)	133	143	150	133	143	150
Recommended compatible microcatheter length (cm)	150	160	160	150	160	160
Recommended compatible microcatheter outer diameter (in)	0.044	0.044	0.044	0.044	0.044	0.044
Recommended compatible guidewire outer diameter (in)	0.038	0.038	0.038	0.038	0.038	0.038

The AXS Vecta Aspiration System is recommended for use in the following vessel size ranges based on non-clinical testing. Refer to Table 2.0 below.

AXS Vecta Aspiration Catheter	Catheter part number	Vessel size in mm (Vessel size in inches)
AXS Vecta 71	INC-11129-115	2.1-4 mm (0.083in – 0.157in)
	INC-11129-125	2.1-4 mm (0.083in – 0.157in)
	INC-11129-132	2.1-4 mm (0.083in – 0.157in)
AXS Vecta 74	INC-11597-115	2.2-4 mm (0.087in – 0.157in)
	INC-11597-125	2.2-4 mm (0.087in – 0.157in)
	INC-11597-132	2.2-4 mm (0.087in – 0.157in)

Contraindications

The AXS Vecta Aspiration Catheter has not been evaluated for use in the coronary vasculature.

Do not use automated high-pressure contrast injection equipment with the AXS Vecta Aspiration Catheter because it may damage the device.

Adverse events

Potential adverse events associated with the use of catheters or with the endovascular procedures include, but are not limited to:

- Acute Vessel Occlusion
- Air Embolism
- Allergic reaction and anaphylaxis from contrast media
- Arteriovenous fistula
- Death
- Device malfunction
- Distal Embolization
- Emboli
- False Aneurysm Formation
- Hematoma or Hemorrhage at the puncture site
- Inability to completely remove thrombus
- Infection
- Intracranial Hemorrhage
- Ischemia
- Kidney damage from contrast media
- Neurological Deficit including Stroke
- Risks Associated with angiographic and fluoroscopic radiation including but not limited to: Alopecia, burns ranging in severity from skin reddening to ulcers, cataracts, and delayed neoplasia
- Sterile inflammation or granulomas at the access site
- Tissue necrosis
- Vessel Spasm, Thrombosis, Dissection or Perforation

Warnings

Contents supplied STERILE using an ethylene oxide (EO) process. Do not use if sterile barrier is damaged. If damage is found, call your Stryker Neurovascular representative.

For single use only. Do not reuse, reprocess or resterilize.

Cautions / precautions

- Take all necessary precautions to limit X-ray radiation doses to clinical operators by using sufficient shielding, reducing fluoroscopy times, and modifying X-ray technical factors whenever possible.
- The Neuroform Atlas stent may create local field inhomogeneity and susceptibility artifacts during magnetic resonance angiography (MRA), which may degrade the diagnostic quality to assess effective intracranial aneurysm occlusion.
- Safety and effectiveness of the Neuroform Atlas Stent System in patients below the age of 18 has not been established.
- The benefits may not outweigh the risks of device use in patients with small and medium asymptomatic extracranial intracranial aneurysms, including those located in the cavernous internal carotid artery.
- Carefully weigh the benefits vs. risks of device treatment for each individual patient based on their medical health status and risk factors for intracranial aneurysm rupture during their expected life time such as age, comorbidities, history of smoking, intracranial aneurysm size, location, and morphology, family history, history of prior asymptomatic subarachnoid hemorrhage (aSAH), documented growth of intracranial aneurysm on serial imaging, presence of multiple intracranial aneurysms, and presence of concurrent pathology. The benefits may not outweigh the risks associated with device use in certain patients; therefore, judicious patient selection is recommended based on clinical practice guidelines or tools to assess the life time risk of intracranial aneurysm rupture.

Safety Information Magnetic Resonance Conditional

Non-clinical testing and analysis have demonstrated that the Neuroform Atlas Stent is MR Conditional alone, or when overlapped with a second stent, and adjacent to a Stryker Neurovascular coil mass. A patient with the Neuroform Atlas Stent can be safely scanned immediately after placement of this implant, under the following conditions:

- Static magnetic field of 1.5 and 3.0 Tesla
- Maximum spatial gradient field up to 2500 Gauss/cm (25 Tesla/m)
- Maximum MR system reported whole body averaged specific absorption rate of 2 W/kg (Normal Operating Mode) and head averaged specific absorption rate of 3.2 W/kg.

Under the scan conditions defined above, the Neuroform Atlas Stent is expected to produce a maximum temperature rise of 4 °C after 15 minutes of continuous scanning. The Neuroform Atlas Stent should not migrate in this MRI environment.

In non-clinical testing, the image artifact caused by the device extends approximately 2 mm from the Neuroform Atlas Stent when imaged with a spin echo pulse sequence and 3 Tesla MRI system. The artifact may obscure the device lumen and may be necessary to optimize MR imaging parameters for the presence of this implant. See additional precaution related to the image artifact from the implant in the "Precautions" section of this labeling.



Stryker Neurovascular
47900 Bayside Parkway
Fremont, CA 94538

strykerneurovascular.com

Date of Release: MAY/2019

EX_EN_US

Reuse, reprocessing or resterilization may compromise the structural integrity of the device and/or lead to device failure which, in turn, may result in patient injury, illness or death. Reuse, reprocessing or resterilization may also create a risk of contamination of the device and/or cause patient infection or cross-infection, including, but not limited to, the transmission of infectious disease(s) from one patient to another. Contamination of the device may lead to injury, illness or death of the patient.

After use, dispose of product and packaging in accordance with hospital, administrative and/or local government policy.

Warnings

- The AXS Vecta Aspiration Catheter has not been evaluated for more than one (1) clot retrieval attempt.
- This product is intended for single use only, do not re-sterilize or reuse. Re-sterilization and/or reuse may result in cross contamination and/or reduced performance.
- When the catheter is exposed to the vascular system, it should be manipulated while under high-quality fluoroscopic observation. Do not advance or retract the catheter if resistance is encountered during manipulation; determine the cause of the resistance before proceeding.
- Operators should take all necessary precautions to limit X-Radiation doses to patients and themselves by using sufficient shielding, reducing fluoroscopy times, and modifying X-Ray technical factors where possible.
- This device is coated with a hydrophilic coating at the distal end of the device for a length of 25 cm. Please refer to the Device Preparation Section for further information on how to prepare and use this device to ensure it performs as intended. Failure to abide by the warnings in this labeling might result in damage to the device coating, which may necessitate intervention or result in serious adverse events.

Precautions

- Do not use kinked, damaged, or opened devices.
- Use the device prior to the "Use By" date specified on the package.
- Exposure to temperatures above 54°C (130°F) may damage device. Do not autoclave.
- Torquing or moving the device against resistance may result in damage to the vessel or device.
- Maintain a constant infusion of appropriate flush solution.
- If flow through the device becomes restricted, do not attempt to clear the lumen by infusion. Remove and replace the device.
- Examine the device to verify functionality and to ensure that its size and shape are suitable for the specific procedure for which it is to be used.
- The AXS Vecta Aspiration System should be used only by physicians trained in percutaneous procedures and/or interventional techniques.
- The Scout Introducer should be used with a guidewire and Microcatheter inserted when in vasculature.
- If using the AXS Vecta Aspiration System for Thrombectomy, monitor the canister fluid level and replace the canister if the fill level reaches 75% of the canister volume.
- Administration of anticoagulants and antiplatelets should be suspended until 24 hours post-treatment. Medical management and acute post stroke care should follow the ASA guidelines.
- Any neurological determination should be evaluated by urgent CT scan and other evaluations as indicated according to investigator/hospital best practice.
- As in all surgical interventions, monitoring of intra-procedural blood loss is recommended so that appropriate management may be instituted.
- Limit the usage of the AXS Vecta Aspiration Catheter to arteries greater than the catheter's outer diameter.
- Excessive aspiration with the distal tip of the AXS Vecta Aspiration Catheter covered by the vessel wall may cause vessel injury. Carefully investigate location of the distal tip under fluoroscopy prior to aspiration.
- There is an inherent risk with the use of angiography and fluoroscopy.
- When transporting the Medela Dominant Flex Pump, utilize the pump handle.



Stryker Neurovascular
47900 Bayside Parkway
Fremont, CA 94538

strykerneurovascular.com

Date of Release: JUN/2019

EX_EN_US

Ingest more.



Empowering first pass retrieval
with AXS Vecta 71 Aspiration
Catheter **now powered by** the
Dual Action Aspiration of Medela
Dominant Flex.

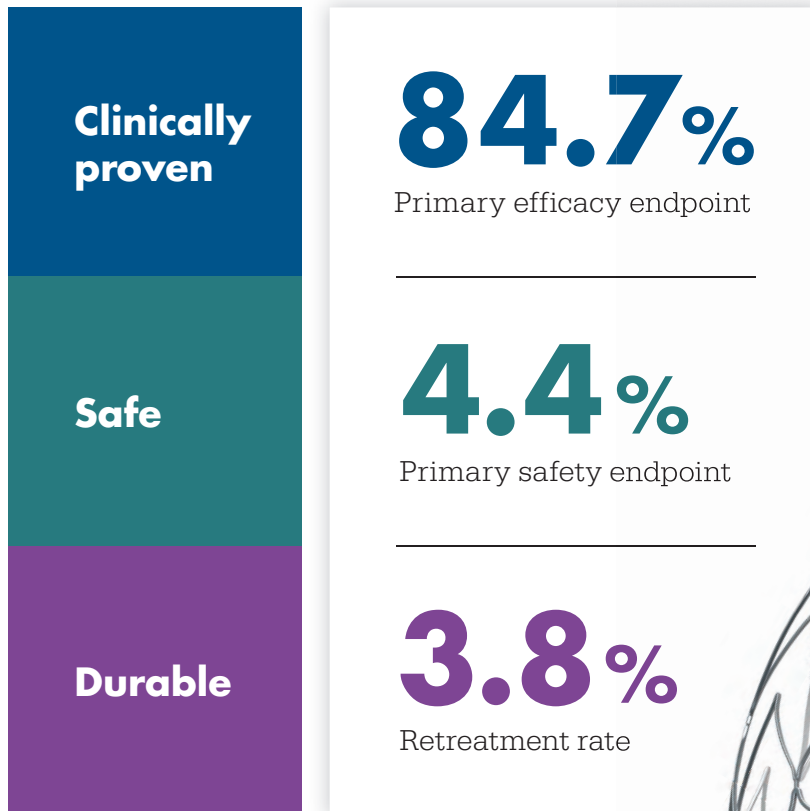
AXS Vecta™ 71 Aspiration Catheter

Testing completed by Stryker. Data on file at Stryker.

The AXS Vecta 71 Aspiration Catheter has a larger lumen compared to the AXS Catalyst 6 Distal Access Catheter, which is cleared for use with the Dominant Flex, sold as the AXS Universal Aspiration System. A larger lumen provides more aspiration power and more room for clot ingestion.

The results say it all

Now **PMA** approved



The ATLAS IDE Study is the largest of its class with **182 patients treated.**

Neuroform Atlas[®]
Stent System

AJNR

AMERICAN JOURNAL OF NEURORADIOLOGY

AUGUST 2019
VOLUME 40
NUMBER 8
WWW.AJNR.ORG

Publication Preview at www.ajnr.org features articles released in advance of print. Visit www.ajnrblog.org to comment on AJNR content and chat with colleagues and AJNR's News Digest at <http://ajnrdigest.org> to read the stories behind the latest research in neuroimaging.

1251 **PERSPECTIVES** *B. Thomas*

PRACTICE PERSPECTIVES

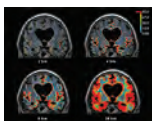
 1252 **Risk Factors for Perceptual-versus-Interpretative Errors in Diagnostic Neuroradiology** *S.H. Patel, et al.*

GENERAL CONTENTS

-  1257 **Intrathecal Use of Gadobutrol for Glymphatic MR Imaging: Prospective Safety Study of 100 Patients** *C.S. Edelev, et al.* **PATIENT SAFETY**
-   1265 **Gadolinium Retention in the Brain: An MRI Relaxometry Study of Linear and Macrocyclic Gadolinium-Based Contrast Agents in Multiple Sclerosis** *Y. Forslin, et al.* **ADULT BRAIN PATIENT SAFETY**
-  1274 **Signal Hyperintensity on Unenhanced T1-Weighted Brain and Cervical Spinal Cord MR Images after Multiple Doses of Linear Gadolinium-Based Contrast Agent** *G. Barisano, et al.* **ADULT BRAIN PATIENT SAFETY**
-     1282 **Convolutional Neural Network for Automated FLAIR Lesion Segmentation on Clinical Brain MR Imaging** *M.T. Duong, et al.* **ADULT BRAIN FUNCTIONAL**
-    1291 **White Matter Lesion Penumbra Shows Abnormalities on Structural and Physiologic MRIs in the Coronary Artery Risk Development in Young Adults Cohort** *I.M. Nasrallah, et al.* **ADULT BRAIN**
-  1299 **The Interpeduncular Angle: A Practical and Objective Marker for the Detection and Diagnosis of Intracranial Hypotension on Brain MRI** *D.J. Wang, et al.* **ADULT BRAIN**
- 1304 **Cytotoxic Lesions of the Corpus Callosum Caused by Thermogenic Dietary Supplements** *J.A. Galnares-Olalde, et al.* **ADULT BRAIN**
-   1309 **Manganese-Enhanced MRI of the Brain in Healthy Volunteers** *D.M. Sudarshana, et al.* **ADULT BRAIN**
-    1317 **The Association between FLAIR Vascular Hyperintensity and Stroke Outcome Varies with Time from Onset** *W.J. Shang, et al.* **ADULT BRAIN**
-    1323 **Leukoaraiosis May Confound the Interpretation of CT Perfusion in Patients Treated with Mechanical Thrombectomy for Acute Ischemic Stroke** *S. Rudilosso, et al.* **ADULT BRAIN INTERVENTIONAL**
-    1330 **One-Stop Management with Perfusion for Transfer Patients with Stroke due to a Large-Vessel Occlusion: Feasibility and Effects on In-Hospital Times** *A. Brehm, et al.* **ADULT BRAIN INTERVENTIONAL**

AJNR (Am J Neuroradiol ISSN 0195-6108) is a journal published monthly, owned and published by the American Society of Neuroradiology (ASNR), 800 Enterprise Drive, Suite 205, Oak Brook, IL 60523. Annual dues for the ASNR include \$170.00 for journal subscription. The journal is printed by Cadmus Journal Services, 5457 Twin Knolls Road, Suite 200, Columbia, MD 21045; Periodicals postage paid at Oak Brook, IL and additional mailing offices. Printed in the U.S.A. POSTMASTER: Please send address changes to American Journal of Neuroradiology, P.O. Box 3000, Denville, NJ 07834, U.S.A. Subscription rates: nonmember \$410 (\$480 foreign) print and online, \$320 online only; institutions \$470 (\$540 foreign) print and basic online, \$935 (\$1000 foreign) print and extended online, \$380 online only (basic), extended online \$825; single copies are \$35 each (\$40 foreign). Indexed by PubMed/Medline, BIOSIS Previews, Current Contents (Clinical Medicine and Life Sciences), EMBASE, Google Scholar, HighWire Press, Q-Sensei, RefSeek, Science Citation Index, SCI Expanded, Meta/CZI and ReadCube. Copyright © American Society of Neuroradiology.

- 1335 **A Standardized Aspiration-First Approach for Thrombectomy to Increase Speed and Improve Recanalization Rates** *D. O'Neill, et al.* **INTERVENTIONAL**
-  1342 **Distal Balloon Angioplasty of Cerebral Vasospasm Decreases the Risk of Delayed Cerebral Infarction** *M.-A. Labeyrie, et al.* **INTERVENTIONAL**
- 1349 **Pretreatment Anterior Choroidal Artery Infarction Predicts Poor Outcome after Thrombectomy in Intracranial ICA Occlusion** *B.H. Baek, et al.* **INTERVENTIONAL**
- 1356 **GUide sheath Advancement and aspiRation in the Distal petrocavernous internal carotid artery (GUARD) Technique during Thrombectomy Improves Reperfusion and Clinical Outcomes** *S.A. Ansari, et al.* **INTERVENTIONAL**
-  1363 **Posterior Fossa Dural Arteriovenous Fistulas with Subarachnoid Venous Drainage: Outcomes of Endovascular Treatment** *L. Détraz, et al.* **INTERVENTIONAL**
- 1369 **Carotid Artery Stiffness Accurately Predicts White Matter Hyperintensity Volume 20 Years Later: A Secondary Analysis of the Atherosclerosis Risk in the Community Study** *A. de Havenon, et al.* **EXTRACRANIAL VASCULAR ADULT BRAIN**
- 1374 **Carotid CTA at the Lowest Tube Voltage (70 kV) in Comparison with Automated Tube Voltage Adaption** *A. Eller, et al.* **EXTRACRANIAL VASCULAR**
-  1383 **Standardization of Temporal Bone CT Planes across a Multisite Academic Institution** *J.P. Guenette, et al.* **HEAD & NECK**
- 1388 **Prolapse of Orbital Fat through the Inferior Orbital Fissure: Description, Prevalence, and Assessment of Possible Pathologic Associations** *P.M. Bunch, et al.* **HEAD & NECK**
-   1392 **Detection of Local Recurrence in Patients with Head and Neck Squamous Cell Carcinoma Using Voxel-Based Color Maps of Initial and Final Area under the Curve Values Derived from DCE-MRI** *J.Y. Lee, et al.* **HEAD & NECK**
- 1402 **Prevalence of Spontaneous Asymptomatic Facial Nerve Canal Meningoceles: A Retrospective Review** *J.C. Benson, et al.* **HEAD & NECK**
-  1406 **Evaluating Tissue Contrast and Detecting White Matter Injury in the Infant Brain: A Comparison Study of Synthetic Phase-Sensitive Inversion Recovery** *D.Y. Kim, et al.* **PEDIATRICS**
- 1413 **Comparison of CSF and MRI Findings among Neonates and Infants with *E coli* or Group B Streptococcal Meningitis** *S.F. Kralik, et al.* **PEDIATRICS**
-  1418 **Human Parechovirus Meningoencephalitis: Neuroimaging in the Era of Polymerase Chain Reaction-Based Testing** *A. Sarma, et al.* **PEDIATRICS**
- 1422 **The Complex Spine in Children with Spinal Muscular Atrophy: The Transforaminal Approach—A Transformative Technique** *R. Towbin, et al.* **PEDIATRICS SPINE**
-  1427 **MRI Predictors of Recurrence and Outcome after Acute Transverse Myelitis of Unidentified Etiology** *E. Bulut, et al.* **SPINE**
-  1433 **CT-Guided Block and Radiofrequency Ablation of the C2 Dorsal Root Ganglion for Cervicogenic Headache** *J.L. Chazen, et al.* **SPINE**



Serial glymphatic MRI in a subject with iNPH following intrathecal gadobutrol (0.05 mmol) at 2, 4, 6, and 24 hours, shows enrichment of the CSF tracer as a percentage change in the T1 signal unit ratio. Contrast enhancement of the brain occurred in a centripetal pattern and primarily in regions of the brain adjacent to large artery trunks at the surface. The periventricular tracer enhancement reflects reflux of tracer into the ventricular system.

ONLINE FEATURES

LETTERS

- E40 **Epidural Spinal Injections in Spinal Stenosis due to Lipomatosis: With or without Steroids?** *J. Gossner*
- E41 **Blood-Brain Barrier Permeability in Patients with Systemic Lupus Erythematosus** *A. Lecler, et al.*
- E42 **Reply** *J.M. Chi, et al.*

BOOK REVIEWS

R.M. Quencer, Section Editor

Please visit www.ajnrblog.org to read and comment on Book Reviews.



Indicates Editor's Choices selection



Indicates Fellows' Journal Club selection



Indicates open access to non-subscribers at www.ajnr.org



Indicates article with supplemental on-line table



Indicates article with supplemental on-line photo



Indicates article with supplemental on-line video



Evidence-Based Medicine Level 1



Evidence-Based Medicine Level 2

Official Journal:

American Society of Neuroradiology
 American Society of Functional Neuroradiology
 American Society of Head and Neck Radiology
 American Society of Pediatric Neuroradiology
 American Society of Spine Radiology

EDITOR-IN-CHIEF

Jeffrey S. Ross, MD

Professor of Radiology, Department of Radiology,
 Mayo Clinic College of Medicine, Phoenix, AZ

SENIOR EDITORS

Harry J. Cloft, MD, PhD

Professor of Radiology and Neurosurgery,
 Department of Radiology, Mayo Clinic College of
 Medicine, Rochester, MN

Thierry A.G.M. Huisman, MD

Radiologist-in-Chief, Texas Children's Hospital,
 Houston, TX

Yvonne W. Lui, MD

Associate Professor of Radiology,
 Chief of Neuroradiology,
 New York University School of Medicine,
 New York, NY

C.D. Phillips, MD, FACR

Professor of Radiology, Weill Cornell Medical
 College, Director of Head and Neck Imaging,
 New York-Presbyterian Hospital, New York, NY

Lubdhra M. Shah, MD

Associate Professor of Radiology and Director of
 Spine Imaging, University of Utah Department of
 Radiology and Imaging Sciences, Salt Lake City, UT

Charles M. Strother, MD

Professor of Radiology, Emeritus, University of
 Wisconsin, Madison, WI

STATISTICAL SENIOR EDITOR

Bryan A. Comstock, MS

Senior Biostatistician,
 Department of Biostatistics,
 University of Washington, Seattle, WA

ARTIFICIAL INTELLIGENCE DEPUTY EDITOR

Christopher G. Filippi, MD

Professor and Vice Chair of Biomedical and
 Translational Science,
 Donald and Barbara Zucker School of Medicine at
 Hofstra/Northwell,
 Lenox Hill Hospital and Greenwich Village
 Healthplex, New York, NY

EDITORIAL BOARD

Ashley H. Aiken, Atlanta, GA
 Lea M. Alhilali, Phoenix, AZ
 Kubilay Aydin, Istanbul, Turkey
 John D. Barr, Dallas, TX
 Ari Blitz, Baltimore, MD
 Barton F. Branstetter IV, Pittsburgh, PA
 Jonathan L. Brisman, Lake Success, NY
 Keith Cauley, Danville, PA
 James Y. Chen, San Diego, CA
 Asim F. Choudhri, Memphis, TN
 Daniel Chow, Irvine, CA
 J. Matthew Debnam, Houston, TX
 Seena Dehkharghani, New York, NY
 Yonghong Ding, Rochester, MN
 Clifford J. Eskey, Hanover, NH
 Saeed Fakhran, Phoenix, AZ
 Massimo Filippi, Milan, Italy
 Reza Forghani, Montreal, Quebec, Canada
 Nils D. Forkert, Calgary, Alberta, Canada
 Wende N. Gibbs, Phoenix, AZ
 Christine M. Glastonbury, San Francisco, CA
 John L. Go, Los Angeles, CA
 Philipp Göllitz, Erlangen, Germany
 Allison Grayev, Madison, WI
 Brent Griffith, Detroit, MI
 Ajay Gupta, New York, NY
 Rakesh Kumar Gupta, Haryana, India
 Lotfi Hacein-Bey, Sacramento, CA
 Christopher P. Hess, San Francisco, CA
 Andrei Holodny, New York, NY
 Benjamin Huang, Chapel Hill, NC
 Mahesh V. Jayaraman, Providence, RI
 Valerie Jewells, Chapel Hill, NC
 Christof Karmonik, Houston, TX
 Timothy J. Kaufmann, Rochester, MN
 Hillary R. Kelly, Boston, MA
 Toshibumi Kinoshita, Akita, Japan
 Kenneth F. Layton, Dallas, TX
 Alexander Lerner, Los Angeles, CA
 Michael Lev, Boston, MA
 Karl-Olof Lovblad, Geneva, Switzerland
 Franklin A. Marden, Chicago, IL
 Joseph C. McGowan, Merion Station, PA
 Stephan Meckel, Freiburg, Germany
 Christopher J. Moran, St. Louis, MO
 Takahisa Mori, Kamakura City, Japan
 Suresh Mukherji, Ann Arbor, MI
 Alexander J. Nemeth, Chicago, IL
 Renato Hoffmann Nunes, Sao Paulo, Brazil
 Sasan Partovi, Cleveland, OH
 Laurent Pierot, Reims, France
 Jay J. Pillai, Baltimore, MD
 Whitney B. Pope, Los Angeles, CA
 Joana Ramalho, Lisbon, Portugal
 Otto Rapalino, Boston, MA

Álex Rovira-Cañellas, Barcelona, Spain
 Paul M. Ruggieri, Cleveland, OH
 Amit M. Saindane, Atlanta, GA
 Maksim Shapiro, New York, NY
 Timothy Shepherd, New York, NY
 Mark S. Shiroishi, Los Angeles, CA
 Bruno P. Soares, Baltimore, MD
 Maria Vittoria Spampinato, Charleston, SC
 Khin Khin Tha, Sapporo, Hokkaido, Japan
 Krishnamoorthy Thamburaj, Hershey, PA
 Cheng Hong Toh, Taipei, Taiwan
 Aquilla S. Turk, Greenville, SC
 Anja G. van der Kolk, Utrecht, the Netherlands
 Willem Jan van Rooij, Tilburg, Netherlands
 Arastoo Vossough, Philadelphia, PA
 Elysa Widjaja, Toronto, Ontario, Canada
 Max Wintermark, Stanford, CA
 Ronald L. Wolf, Philadelphia, PA
 Kei Yamada, Kyoto, Japan
 Carlos Zamora, Chapel Hill, NC
 Vahe M. Zohrabian, New Haven, CT

EDITORIAL FELLOW

Hediyeh Baradaran, Salt Lake City, UT

SPECIAL CONSULTANTS TO THE EDITOR

AJNR Blog Editor

Neil Lall, Denver, CO

Case of the Month Editor

Nicholas Stence, Aurora, CO

Case of the Week Editors

Juan Pablo Cruz, Santiago, Chile
 Sapna Rawal, Toronto, Ontario, Canada

Classic Case Editor

Sandy Cheng-Yu Chen, Taipei, Taiwan

Health Care and Socioeconomics Editor

Pina C. Sanelli, New York, NY

Physics Editor

Greg Zaharchuk, Stanford, CA

Podcast Editor

Wende N. Gibbs, Phoenix, AZ

Twitter Editor

Jennifer McCarty, Houston, TX

Founding Editor
 Juan M. Taveras

Editors Emeriti
 Mauricio Castillo, Robert I. Grossman,
 Michael S. Huckman, Robert M. Quencer

Managing Editor
 Karen Halm

Assistant Managing Editor
 Laura Wilhelm

Communications Coordinator
 Rebecca Artz

Executive Director, ASNR
 Mary Beth Hepp



Title: Refugees. Watercolor on paper, painted using color-soaked threads and brushes. The human outlines in the painting were done with the thread work.
Bejoy Thomas, MD, DNB, PDCC, Trivandrum, Kerala, India

Risk Factors for Perceptual-versus-Interpretative Errors in Diagnostic Neuroradiology

 S.H. Patel,  C.L. Stanton,  S.G. Miller,  J.T. Patrie,  J.N. Itri, and  T.M. Shepherd



ABSTRACT

BACKGROUND AND PURPOSE: Diagnostic errors in radiology are classified as perception or interpretation errors. This study determined whether specific conditions differed when perception or interpretation errors occurred during neuroradiology image interpretation.

MATERIALS AND METHODS: In a sample of 254 clinical error cases in diagnostic neuroradiology, we classified errors as perception or interpretation errors, then characterized imaging technique, interpreting radiologist's experience, anatomic location of the abnormality, disease etiology, time of day, and day of the week. Interpretation and perception errors were compared with hours worked per shift, cases read per shift, average cases read per shift hour, and the order of case during the shift when the error occurred.

RESULTS: Perception and interpretation errors were 74.8% ($n = 190$) and 25.2% ($n = 64$) of errors, respectively. Logistic regression analyses showed that the odds of an interpretation error were 2 times greater (OR, 2.09; 95% CI, 1.05–4.15; $P = .04$) for neuroradiology attending physicians with ≤ 5 years of experience. Interpretation errors were more likely with MR imaging compared with CT (OR, 2.10; 95% CI, 1.09–4.01; $P = .03$). Infectious/inflammatory/autoimmune diseases were more frequently associated with interpretation errors ($P = .04$). Perception errors were associated with faster reading rates (6.01 versus 5.03 cases read per hour; $P = .004$) and occurred later during the shift (24th-versus-18th case; $P = .04$).

CONCLUSIONS: Among diagnostic neuroradiology error cases, interpretation-versus-perception errors are affected by the neuroradiologist's experience, technique, and the volume and rate of cases read. Recognition of these risk factors may help guide programs for error reduction in clinical neuroradiology services.

Medical errors are a substantial cause source of patient morbidity and mortality.¹ Given the important role that diagnostic imaging plays in patient management, errors in diagnostic imaging interpretation likely contribute to this burden of medical error.² To improve patient care, radiologists should analyze errors to identify conditions that may alter the risk of future errors. Such analysis may uncover contributory factors that can inform appro-

appropriate systematic corrective steps and improve the overall quality of patient care.³⁻⁵

Errors in diagnostic radiology take 2 broad forms: errors of perception and errors of interpretation. A perception error occurs when a radiologist fails to identify an abnormality that is clearly present to most readers on a diagnostic image (false-negative errors). An interpretation error occurs when a radiologist identifies a finding on a diagnostic image but misinterprets its significance or meaning. Interpretation errors may take several forms such as attributing the wrong diagnosis to a finding, misjudging the severity of a finding, interpreting a normal finding as an abnormality, or interpreting an abnormal finding as a normal finding.

Prior studies of errors in radiology demonstrated that errors of perception compose most radiologic errors (60%–80%).⁶⁻⁸ Little is known about potential risk factors that might predispose radiologists to perceptual-versus-interpretive errors. We hypothesized that the imaging technique, specific imaging finding, underlying diagnosis, radiologist's experience, and environmental conditions would influence the type of error made by neuroradiologists. Our study characterized whether case-specific metrics differed between perception and interpretation errors among a

Received March 21, 2019; accepted after revision June 9.

From the Departments of Radiology and Medical Imaging (S.H.P.) and Public Health Sciences (J.T.P.), University of Virginia Health System, Charlottesville, Virginia; Department of Radiology (C.L.S., S.G.M., T.M.S.), New York University Langone Medical Center, New York, New York; Department of Radiology (J.N.I.), Wake Forest Baptist Health, Winston-Salem, North Carolina; and Center for Advanced Imaging Innovation and Research (T.M.S.), New York, New York.

Paper previously presented, in part, at: Annual Meeting of the American Society of Neuroradiology and the Foundation of the ASNR Symposium, April 22–27, 2017; Long Beach, California.

Please address correspondence to Sohil H. Patel, MD, Department of Radiology and Medical Imaging, University of Virginia Health System, PO Box 800170, Charlottesville, VA 22908; e-mail: shp4k@virginia.edu

 Indicates article with supplemental on-line Table.

<http://dx.doi.org/10.3174/ajnr.A6125>

cohort of recognized neuroradiology error cases from a large academic medical center.

MATERIALS AND METHODS

Case Selection and Categorization

This study was Health Insurance Portability and Accountability Act-compliant and was approved by the local institutional review board.

Cases of diagnostic errors were collected by staff and trainees in the neuroradiology division at a large tertiary care medical center as part of an ongoing practice-quality-improvement initiative. Each attending physician, fellow, and rotating resident in the neuroradiology division was instructed to place any error case they identified during clinical practice into a specified digital folder in our PACS. This requires a single-click drag-and-drop function facilitating addition of relevant cases to the cohort. A monthly divisional “M&M” conference was held where error cases were presented in a confidential manner, and the error was adjudicated by consensus among board-certified staff neuroradiologists.

Cases for this study accrued from July 2014 to January 2016 (19 months) during which time 75,804 CT and MR imaging neuroradiology examinations were interpreted at our institution. The cases and radiologist reports were retrospectively reviewed by a neuroradiology fellow and 2 board-certified attending neuroradi-

ologists (with 5 and 7 years of experience, respectively) confirming that an error had occurred by consensus, with incorporation of any relevant clinical information available in the electronic medical record or PACS before and subsequent to the case in question. Errors were defined as findings or interpretations that both neuroradiologists thought should have been in the impression of the radiology report and that both neuroradiologists agreed would potentially change clinical management (eg, missed aneurysm, but not inflammatory maxillary sinus changes in an immunocompetent patient). Because not all cases have criterion standard final diagnoses (such as surgical pathology distinguishing meningioma from schwannoma), for interpretation errors, we emphasized missing differential diagnoses that both neuroradiologists thought should have been included in the radiology report. A total of 254 errors were discovered. Each error was categorized as either a perception error (the relevant finding was not identified) or an interpretation error (the relevant finding was identified, but not interpreted correctly) (Figs 1 and 2).

Each error case was categorized by the imaging technique (CT, MR imaging, radiograph), anatomic location of the relevant finding (cerebral gray matter, cerebral white matter, infratentorial brain, vasculature, meninges/ventricles, calvaria/scalp, face/skull base, neck or spine/paraspinal), and etiology (neoplastic, vascular/ischemic, congenital, trauma, degenerative, infection/inflammation/autoimmune, or other). The diagnoses were tabulated for each case. The experience level of the radiologist who made the error was noted (trainee; non-neuroradiology attending physician; attending neuroradiologist with ≤ 5 years, 6–10 years, 11–20 years, or > 20 years of experience). There were 12 attending neuroradiologists who made at least 5 errors included in this study, and each attending neuroradiologist experience level comprised exactly 3 such attending neuroradiologists. The remaining attending neuroradiologists who made < 5 errors included in our study were part-time or per diem neuroradiologists, neuroradiologists who previously worked at our institution but have since left, and community neuroradiologists affiliated with our institution. Trainee errors were only included if the trainee created and signed a “preliminary report” that was available in the electronic medical record for viewing by the referring clinicians. The cases were classified as those reported during regular week-

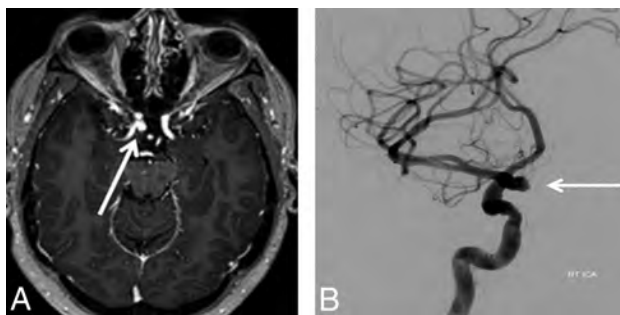


FIG 1. Perception error. A 55-year-old woman undergoing brain MR imaging for multiple sclerosis. A, Contrast-enhanced T1WI (using a 3D magnetization prepared rapid acquisition of gradient echo sequence) reveals an incidental aneurysm of the right internal carotid artery (arrow), which was not identified on this examination. It was detected on subsequent MR imaging. B, A cerebral angiogram confirms the aneurysm (arrow).

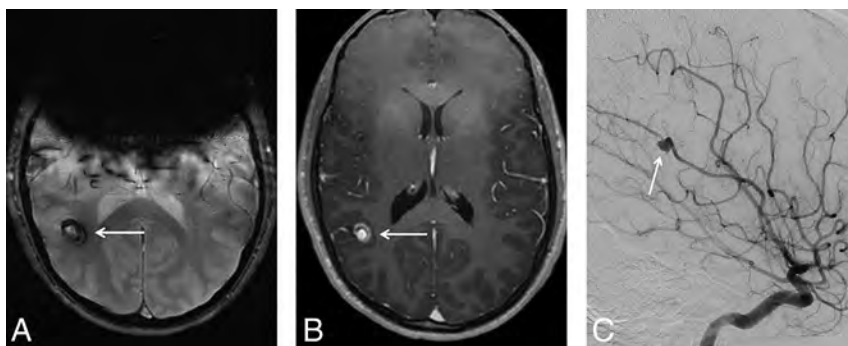


FIG 2. Interpretation error. A 17-year-old adolescent boy undergoing brain MR imaging for headache. A round mass (arrows) was identified in the right parietal lobe, demonstrating peripheral hypointense “blooming” on the T2*WI (A) and both central and peripheral contrast enhancement on the contrast-enhanced T1WI (B). The MR imaging finding was detected but incorrectly interpreted as representing a cavernous malformation. C, A subsequent angiogram revealed that this was, in fact, a partially thrombosed aneurysm arising from the right middle cerebral artery (arrow). (In A and B, there are artifacts from the patient’s braces).

day hours (Monday through Friday, 8 AM to 5 PM) and those reported at all other times (ie, on-call situations). Characteristics of the specific radiologist’s work shift when the error occurred were available in a subset ($n = 217$) of the cohort and included the number of cases read during the total shift, the shift length (in hours), and the average number of cases read per hour during that shift. Finally, the sequence in which the error case occurred during the shift was recorded (ie, was it the fifth case of the day or the 30th?).

Statistical Analysis

Perception errors and interpretation errors were summarized by frequencies and percentages. Logistic regression was used to examine whether interpretation-

versus-perception errors were systematically related to the neuro-radiologist's experience, imaging technique, anatomic location, disease etiology, day of the week, and time of day. The logistic regression outcome variables were binary variables that were assigned the value 1 if the diagnostic error was classified as an interpretation error and value 0 if the diagnostic error was classified as a perception error. We tested the null hypothesis that there was no systematic relationship between the categories of the predictor variable and the log-odds of cognitive error. The Wald statistic served as the pivotal quantity of the null hypothesis test, with $P < .05$ defined a priori as a statistically significant difference. The confidence interval was based on the Wald large-sample approximation method. Additionally, 2-tailed t tests at the $P < .05$ significance level were performed to compare the hours worked per shift, cases read per shift, cases read per shift hour, and the order of the error case during the shift, between perception and interpretation errors.

RESULTS

A total of 254 recognized diagnostic neuroradiology errors were included. During the same time as error collection, approximately 75,000 diagnostic neuroradiology CT and MR imaging studies were performed at our institution. There were a total of 190 perception errors (74.8%) and 64 interpretation errors (25.2%). The On-line Table lists the errors by various categories. The most common diagnoses among the errors were the following: metastasis ($n = 23$), infarction ($n = 20$), vascular thrombus ($n = 14$), intracranial aneurysm ($n = 14$), and malformation of cortical development ($n = 11$).

There was no association among the 3 radiologist subgroups, trainees, non-neuroradiology attending physicians, and attending neuroradiologists for interpretation-versus-perception errors ($P = .57$). We note that during the shifts when errors occurred, the trainees (versus attending physicians) worked slightly longer hours per shift (9.0; 95% CI, 7.14–10.86 versus 7.3; 95% CI, 6.92–7.68; $P = .04$) and read fewer cases per shift hour (3.83; 95% CI, 2.91–4.74 versus 5.88; 95% CI, 5.53–6.24; $P < .001$). However, we found no significant difference in the average total cases read per shift (33.5 versus 41.3; $P = .22$) and sequential error occurrence during the shift (14th case versus 23rd case; $P = .08$) between trainees and attending physicians.

Examining only attending neuroradiologists did not reveal a statistical association between attending physician experience and interpretation-versus-perception error, when attending physician experience was categorized as 1–5 years, 6–10 years, 11–20 years, and >20 years of experience ($P = .18$). However, a post hoc comparison did reveal that the errors made by those with ≤ 5 years of experience were more likely to be interpretation errors (OR, 2.09; 95% CI, 1.05–4.15; $P = .04$) compared with the errors made by those with >5 years of experience.

There were 161 MR imaging cases (including 20 MRA/MRV), 89 CT cases (including 9 CTA/CTV), and 4 plain film cases. Errors associated with MRI examinations were more likely to be interpretation errors (OR, 2.10 [1.09, 4.01], $P = 0.03$) compared to errors associated with CT examinations. There was a significant association between interpretation-versus-perception error and disease etiology ($P = .04$), driven by the infectious/inflammatory/

autoimmune category of which interpretation errors represented 52% of the errors (for all other disease categories, interpretation errors represented <30% of total errors).

There was no significant association between interpretation-versus-perception errors and the anatomic location of the relevant imaging findings ($P = .48$). There was no association between the type of error and the time of the week when the case was read (comparing routine weekday hours with all other times, $P = .92$).

Perception errors were associated with a 16% higher mean number of cases read per shift (42.5; 95% CI, 39.0–46.0 versus 36.7; 95% CI, 32.0–41.3; $P = .05$) and a 19% higher mean number of cases read per shift hour (6.01; 95% CI, 5.6–6.4 versus 5.03; 95% CI, 4.5–5.5; $P = .004$). There was no difference in the mean total hours per shift between the occurrence of perception errors or interpretation errors (7.3; 95% CI, 6.9–7.7 versus 7.6; 95% CI, 6.8–8.5; $P = .45$); however, perception errors did occur sequentially later during the shift (23.5; 95% CI, 20.8–26.2 versus 17.9; 95% CI, 13.7–22.0 previous cases read; $P = .04$).

DISCUSSION

We characterized the relative proportion of perceptual and interpretive errors and the underlying conditions associated with these errors among a cohort of known, recognized error cases interpreted predominantly by academic subspecialty-trained neuroradiologists. To our knowledge, this is a novel approach to studying diagnostic error. Prior studies of diagnostic errors in neuroradiology have focused on determining the rate and significance of errors when interpreting emergency imaging studies^{9–21} or discrepancy rates between general practice radiologists and academic subspecialists.^{22–25} Discrepancy rates can be misleading because the incidence can be confounded by discovery or recall bias and were not the focus of this study.

Our results identified certain specific case, neuroradiologist, and reading situation features that were associated with interpretative or perception errors in neuroradiology practice. Less experienced neuroradiologists made a higher proportion of interpretation errors, while more experienced neuroradiologists made a higher proportion of perception errors. Errors were more likely to be perceptual with CT studies and interpretative with MR imaging studies. Errors were more likely to be interpretative during evaluation of patients with infectious, inflammatory, or autoimmune diseases. Perception errors were associated with a higher case volume, faster reading rates, and later parts of a work shift compared with interpretation errors.

Our results regarding imaging technique should be intuitive to most radiologists. Compared with CT, MR imaging is known to produce far greater sensitivity for many common pathologic processes seen on neuroimaging studies (eg, acute infarcts,²⁶ cerebral neoplasms,²⁷ demyelinating disease²⁸), which should decrease the number of perception errors among MR imaging cases. Conversely, MR imaging has more artifacts, there are more MR imaging sequences per study to evaluate, and the greater complexity inherent to MR imaging findings relative to CT all might have contributed to the relatively higher proportion of interpretation errors among MR imaging-versus-CT cases.

Prior research in medical imaging perception might help to

explain our results concerning the radiologist's experience level. Studies using eye-tracking technology indicate that more experienced radiologists have shorter image-viewing times, fewer visual fixations, fewer visual fixations on nondiagnostic areas of the image, and less dwell time per visual fixation when evaluating diagnostic imaging studies.²⁹ Although such tendencies correlate with greater efficiency in image search, they might also explain the higher proportion of perceptual-type errors (ie, not seeing a pertinent imaging finding) among more experienced neuroradiologists. We stress, however, that while the proportion of errors among more experienced neuroradiologists compared with less experienced neuroradiologists was more heavily weighted toward perceptual errors, our results have not established that more experienced radiologists have a higher overall rate of perceptual errors.

Gaining an appreciation for predisposing conditions toward error type (interpretive-versus-perceptual) might aid future efforts towards error reduction in diagnostic neuroimaging. Perceptual errors (ie, nonidentification of a relevant imaging finding) might be reduced when radiologists use consistent search patterns or checklists during image evaluation,³⁰ have improved accessibility to an accurate clinical indication,³¹ and read studies from state-of-the-art imaging systems.³² Clinical coverage schedules can be tailored to avoid overly long work shifts that may predispose to fatigue-related perceptual errors.^{33,34} Specific practice measures can also be implemented to reduce interpretation errors (ie, misinterpretation of a detected imaging finding), though such measures are less well-established in the literature. In theory, these practices may include multidisciplinary case discussion,^{35,36} selective second reading of studies associated with a higher risk for error,^{37,38} and application of a "slow-thinking" metacognition approach to avoid heuristic pitfalls when interpreting imaging abnormalities.³⁹

This study has limitations. We collected 254 errors during a time when 75,000 CT and MR imaging studies were performed at our institution. This discovered error rate (<0.5%) is lower than previous clinically significant error rates reported from similar academic radiology practices.⁴⁰ This finding likely reflects differences in the discovery mechanism and/or differences in what was considered a clinically significant error and does not indicate differences in interpretation accuracy between institutions. The subsequent study analysis implicitly assumes that error discovery was random and the subset used was a true representation of all errors that occurred. Error detection depended on a second radiologist's review of the images or a follow-up study; diagnostic errors that occur in outpatients without follow-up or image review during multidisciplinary conferences may be under-represented in our sample. Yet, our error-collection mechanism appeared to provide an externally valid representative cohort of cases; the percentage of perceptual errors and interpretive errors (74.8% and 25.2%, respectively) here is similar to that in previous reports.⁶⁻⁸ Moreover, prior studies have shown that neoplastic and vascular etiologies are the most common neuroradiology error cases,^{25,40} concordant with our dataset (On-line Table). It would also be helpful in a future study to match error cases to similar cases that were interpreted correctly (ie, controls) to better resolve specific factors that contribute to errors. Such a measure may allow determina-

tion of differences in the error rate based on case-specific, work shift-specific, or radiologist-specific metrics and would be important for future study of this topic. The 2 neuroradiologists who adjudicated errors for this study would be considered less experienced in the above analytic framework, but these readers each had 5+ years reading only neuroradiology studies at an academic institution, adjudicated the studies by consensus (after prior group discussion), and had access to the full medical record (including subsequent clinical data).

Finally, we chose a simple, binary, and mutually exclusive scheme for classifying the error cases (ie, each case was either a perception or an interpretation error). Although this form of radiologic error categorization is commonly accepted in the literature,³⁰ errors can take far more specific or overlapping forms than simply errors of perception or interpretation. For instance, research on medical imaging perception using eye-tracking technology indicates that perceptual errors broadly take 3 forms: 1) search error: the lesion is never fixated on; 2) recognition error: the lesion is fixated on, but below the threshold necessary for recognition; and 3) decision error: the lesion is fixated on for long periods, but its features are not fully appreciated and/or are dismissed.⁴¹ Interpretation errors also may vary, for instance, depending on whether a specific heuristic bias was involved in a given misinterpretation or a whether lack of sufficient knowledge contributed to the error.^{42,43} Understanding error trends at these higher levels of nuance is an important challenge for future research efforts.

CONCLUSIONS

Among diagnostic neuroradiology error cases, interpretation-versus-perception errors are associated with neuroradiology attending physician experience, imaging technique, disease etiology, case volume, reading rate, and case order. Our results highlight differences between error types that may inform future situation-specific effort toward error reduction in clinical neuro-radiology services.

Disclosures: Sohil H. Patel—UNRELATED: Expert Testimony: medicolegal work*; Grants/Grants Pending: Radiological Society of North America Research Scholar Grant (RSCH1819)*. Jason N. Itri—UNRELATED: Expert Testimony: medicolegal work; Grants/Grants Pending: Coverys Community Healthcare Foundation. Comments: grant entitled, "Strategies to reduce diagnostic errors in imaging."* Timothy M. Shepherd—UNRELATED: Expert Testimony: medicolegal work; Grants/Grants Pending: National Institutes of Health, National Institute on Aging K23-AG048622; Stock/Stock Options: MICroStructure Imaging (MICS), Inc. Comments: start-up focused on advanced MRI processing and applications. *Money paid to the institution.

REFERENCES

1. Makary MA, Daniel M. **Medical error—the third leading cause of death in the US.** *BMJ* 2016;353:i2139 [CrossRef Medline](#)
2. Bruno MA, Walker EA, Abujudeh HH. **Understanding and confronting our mistakes: the epidemiology of error in radiology and strategies for error reduction.** *Radiographics* 2015;35:1668–76 [CrossRef Medline](#)
3. Brook OR, O'Connell AM, Thornton E, et al. **Quality initiatives: anatomy and pathophysiology of errors occurring in clinical radiology practice.** *Radiographics* 2010;30:1401–10 [CrossRef Medline](#)
4. Fitzgerald R. **Error in radiology.** *Clin Radiol* 2001;56:938–46 [CrossRef Medline](#)
5. Itri JN, Tappouni RR, McEachern RO, et al. **Fundamentals of diag-**

- nostic error in imaging. *Radiographics* 2018;38:1845–65 CrossRef Medline
6. Donald JJ, Barnard SA. **Common patterns in 558 diagnostic radiology errors.** *J Med Imaging Radiat Oncol* 2012;56:173–78 CrossRef Medline
 7. Kabadi SJ, Krishnaraj A. **Strategies for improving the value of the radiology report: a retrospective analysis of errors in formally over-read studies.** *J Am Coll Radiol* 2017;14:459–66 CrossRef Medline
 8. Renfrew DL, Franken EA Jr, Berbaum KS, et al. **Error in radiology: classification and lessons in 182 cases presented at a problem case conference.** *Radiology* 1992;183:145–50 CrossRef Medline
 9. Cooper VF, Goodhartz LA, Nemcek AA Jr, et al. **Radiology resident interpretations of on-call imaging studies: the incidence of major discrepancies.** *Acad Radiol* 2008;15:1198–204 CrossRef Medline
 10. Erly WK, Berger WG, Krupinski E, et al. **Radiology resident evaluation of head CT scan orders in the emergency department.** *AJNR Am J Neuroradiol* 2002;23:103–07 Medline
 11. Filippi CG, Schneider B, Burbank HN, et al. **Discrepancy rates of radiology resident interpretations of on-call neuroradiology MR imaging studies.** *Radiology* 2008;249:972–79 CrossRef Medline
 12. Funaki B, Szymiski GX, Rosenblum JD. **Significant on-call misses by radiology residents interpreting computed tomographic studies: perception versus cognition.** *Emerg Radiol* 1997;4:290–94 CrossRef Medline
 13. Goradia D, Blackmore CC, Talner LB, et al. **Predicting radiology resident errors in diagnosis of cervical spine fractures.** *Acad Radiol* 2005;12:888–93 CrossRef Medline
 14. Guimaraes CV, Leach JL, Jones BV. **Trainee misinterpretations on pediatric neuroimaging studies: classification, imaging analysis, and outcome assessment.** *AJNR Am J Neuroradiol* 2011;32:1591–99 CrossRef Medline
 15. Hillier JC, Tattersall DJ, and Gleeson FV. **Trainee reporting of computed tomography examinations: do they make mistakes and does it matter?** *Clin Radiol* 2004;59:159–62, discussion 157–58 Medline
 16. Lal NR, Murray UM, Eldevik OP, et al. **Clinical consequences of misinterpretations of neuroradiologic CT scans by on-call radiology residents.** *AJNR Am J Neuroradiol* 2000;21:124–29 Medline
 17. Meyer RE, Nickerson JP, Burbank HN, et al. **Discrepancy rates of on-call radiology residents' interpretations of CT angiography studies of the neck and circle of Willis.** *AJR Am J Roentgenol* 2009;193:527–32 CrossRef Medline
 18. Miyakoshi A, Nguyen QT, Cohen WA, et al. **Accuracy of preliminary interpretation of neurologic CT examinations by on-call radiology residents and assessment of patient outcomes at a level I trauma center.** *J Am Coll Radiol* 2009;6:864–70 CrossRef Medline
 19. Strub WM, Leach JL, Tomsick T, et al. **Overnight preliminary head CT interpretations provided by residents: locations of misidentified intracranial hemorrhage.** *AJNR Am J Neuroradiol* 2007;28:1679–82 CrossRef Medline
 20. Walls J, Hunter N, Brasher PM, et al. **The DePICTORS Study: discrepancies in preliminary interpretation of CT scans between on-call residents and staff.** *Emerg Radiol* 2009;16:303–08 CrossRef Medline
 21. Wysoki MG, Nassar CJ, Koenigsberg RA, et al. **Head trauma: CT scan interpretation by radiology residents versus staff radiologists.** *Radiology* 1998;208:125–28 CrossRef Medline
 22. Erly WK, Ashdown BC, Lucio RW 2nd, et al. **Evaluation of emergency CT scans of the head: is there a community standard?** *AJR Am J Roentgenol* 2003;180:1727–30 CrossRef Medline
 23. Jordan MJ, Lightfoote JB, Jordan JE. **Quality outcomes of reinterpretation of brain CT imaging studies by subspecialty experts in neuroradiology.** *J Natl Med Assoc* 2006;98:1326–28 Medline
 24. Loevner LA, Sonners AI, Schulman BJ, et al. **Reinterpretation of cross-sectional images in patients with head and neck cancer in the setting of a multidisciplinary cancer center.** *AJNR Am J Neuroradiol* 2002;23:1622–26 Medline
 25. Zan E, Yousem DM, Carone M, et al. **Second-opinion consultations in neuroradiology.** *Radiology* 2010;255:135–41 CrossRef Medline
 26. González RG, Schwamm LH. **Imaging acute ischemic stroke.** *Handb Clin Neurol* 2016;135:293–315 CrossRef Medline
 27. Higer HP, Pedrosa P, Schuth M. **MR imaging of cerebral tumors: state of the art and work in progress.** *Neurosurg Rev* 1989;12:91–106 CrossRef Medline
 28. Young IR, Hall AS, Pallis CA, et al. **Nuclear magnetic resonance imaging of the brain in multiple sclerosis.** *Lancet* 1981;2:1063–66 Medline
 29. Krupinski EA. **The role of perception in imaging: past and future.** *Semin Nucl Med* 2011;41:392–400 CrossRef Medline
 30. Bahrami S, Yim CM. **Quality initiatives: blind spots at brain imaging.** *Radiographics* 2009;29:1877–96 CrossRef Medline
 31. Mullins ME, Lev MH, Schellingerhout D, et al. **Influence of availability of clinical history on detection of early stroke using unenhanced CT and diffusion-weighted MR imaging.** *AJR Am J Roentgenol* 2002;179:223–28 CrossRef Medline
 32. Knake S, Triantafyllou C, Wald LL, et al. **3T phased array MRI improves the presurgical evaluation in focal epilepsies: a prospective study.** *Neurology* 2005;65:1026–31 CrossRef Medline
 33. Krupinski EA, Berbaum KS, Caldwell RT, et al. **Long radiology workdays reduce detection and accommodation accuracy.** *J Am Coll Radiol* 2010;7:698–704 CrossRef Medline
 34. Krupinski EA, Berbaum KS, Caldwell RT, et al. **Do long radiology workdays affect nodule detection in dynamic CT interpretation?** *J Am Coll Radiol* 2012;9:191–98 CrossRef Medline
 35. Maldonado MD, Batchala P, Ornan D, et al. **Features of diffuse gliomas that are misdiagnosed on initial neuroimaging: a case control study.** *J Neurooncol* 2018;140:107–13 CrossRef Medline
 36. Lee CS, Nagy PG, Weaver SJ, et al. **Cognitive and system factors contributing to diagnostic errors in radiology.** *AJR Am J Roentgenol* 2013;201:611–17 CrossRef Medline
 37. Lauritzen PM, Andersen JG, Stokke MV, et al. **Radiologist-initiated double reading of abdominal CT: retrospective analysis of the clinical importance of changes to radiology reports.** *BMJ Qual Saf* 2016;25:595–603 CrossRef Medline
 38. Lauritzen PM, Stavem K, Andersen JG, et al. **Double reading of current chest CT examinations: clinical importance of changes to radiology reports.** *Eur J Radiol* 2016;85:199–204 CrossRef Medline
 39. Busby LP, Courtier JL, Glastonbury CM. **Bias in radiology: the how and why of misses and misinterpretations.** *Radiographics* 2018;38:236–47 CrossRef Medline
 40. Babiarz LS, Yousem DM. **Quality control in neuroradiology: discrepancies in image interpretation among academic neuroradiologists.** *AJNR Am J Neuroradiol* 2012;33:37–42 CrossRef Medline
 41. Krupinski EA. **Current perspectives in medical image perception.** *Atten Percept Psychophys* 2010;72:1205–17 CrossRef Medline
 42. Itri JN, Patel SH. **Heuristics and cognitive error in medical imaging.** *AJR Am J Roentgenol* 2018;210:1097–105 CrossRef Medline
 43. Patel SH, Ambrosino MM, McGuinness G. **The challenging case conference: initial observations and feedback.** *J Am Coll Radiol* 2012;9:666–68 CrossRef Medline

Intrathecal Use of Gadobutrol for Glymphatic MR Imaging: Prospective Safety Study of 100 Patients

C.S. Edeklev, M. Halvorsen, G. Løvland, S.A.S. Vatnehol, Ø. Gjertsen, B. Nedregaard, R. Sletteberg, G. Ringstad, and P.K. Eide



ABSTRACT

BACKGROUND AND PURPOSE: Intrathecal contrast-enhanced glymphatic MR imaging has shown promise in assessing glymphatic function in patients with dementia. The purpose of this study was to determine the safety profile and feasibility of this new MR imaging technique.

MATERIALS AND METHODS: A prospective safety and feasibility study was performed in 100 consecutive patients (58 women and 42 men, 51 ± 19 years of age) undergoing glymphatic MR imaging from September 2015 to August 2018. Short- and long-term serious and nonserious adverse events were registered clinically and by interview after intrathecal administration of 0.5 mL of gadobutrol (1.0 mmol/mL) along with 3 mL of iodixanol (270 mg I/mL). Adverse events are presented as numbers and percentages.

RESULTS: One serious adverse event (anaphylaxis) occurred in a patient with known allergy to iodine-containing contrast agents (1%). The main nonserious adverse events during the first 1–3 days after contrast injection included severe headache (28%) and severe nausea (34%), though the frequency depended heavily on the diagnosis. After 4 weeks, adverse events had resolved.

CONCLUSIONS: Intrathecal administration of gadobutrol in conjunction with iodixanol for glymphatic MR imaging is safe and feasible. We cannot conclude whether short-duration symptoms such as headache and nausea were caused by gadobutrol, iodixanol, the lumbar puncture, or the diagnosis. The safety profile closely resembles that of iodixanol alone.

ABBREVIATIONS: gMRI = glymphatic MR imaging; iNPH = idiopathic normal pressure hydrocephalus

The glia-lymphatic (or glymphatic) system was described in 2012, providing experimental evidence for direct communication between the CSF of the subarachnoid space and the perivascular spaces of the mouse brain.¹ The glymphatic pathways were suggested to be dependent on aquaporin-4 water channels at astrocytic end-feet and are fundamental for the transport and clearance of waste solutes such as amyloid- β and τ protein, which may accumulate in the brain and thereby cause neurodegenerative disease.² Furthermore, it was suggested that intrathecal contrast-enhanced MR imaging might be used for imaging of the glymphatic circulation in man,^{3,4} and such studies have recently

confirmed communication between the subarachnoid space and the extravascular compartment of all brain regions, thereby extending previous animal data (Fig 1).

The human glymphatic system differs from that in rodents in several ways, first by being much slower.^{5,6} Moreover, human studies have shown delayed clearance of CSF tracer from all brain regions in individuals with idiopathic normal pressure hydrocephalus (iNPH),⁵ and particularly from the entorhinal cortex, where volume loss precedes hippocampal atrophy in Alzheimer disease.⁷ After the discovery of meningeal brain lymphatic vessels in 2015,^{8,9} observations from human glymphatic MR imaging (gMRI) have suggested a functional link between glymphatic and lymphatic pathways because peak CSF tracer enhancement coincided in time in both the brain and extracranial lymph nodes.¹⁰

The risk of gadolinium retention within the human brain after repeat intravenous administrations has been extensively debated.¹¹⁻¹³ It has recently been acknowledged that gadolinium-containing MR imaging contrast agents leak from blood to the CSF,¹⁴ even in patients without blood-brain barrier dysfunction,¹⁵ and probably in substantial amounts through the choroid plexus.¹⁶ In principle, an intravenous dosage of contrast agent to

Received April 1, 2019; accepted after revision June 15.

From the Department of Neurosurgery (C.S.E., M.H., P.K.E.), Interventional Centre (G.L., S.A.S.V.), and Department of Radiology and Nuclear Medicine (Ø.G., B.N. R.S., G.R.), Oslo University Hospital, Rikshospitalet, Oslo, Norway; and Institute of Clinical Medicine (P.K.E.), Faculty of Medicine, University of Oslo, Oslo, Norway.

Camilla S. Edeklev and Merete Halvorsen contributed equally to this work.

Please address correspondence to Per Kristian Eide, MD, PhD, Department of Neurosurgery, Oslo University Hospital, Rikshospitalet, Postboks 4950 Nydalen, 0424 Oslo, Norway; e-mail: p.k.eide@medisin.uio.no

<http://dx.doi.org/10.3174/ajnr.A6136>

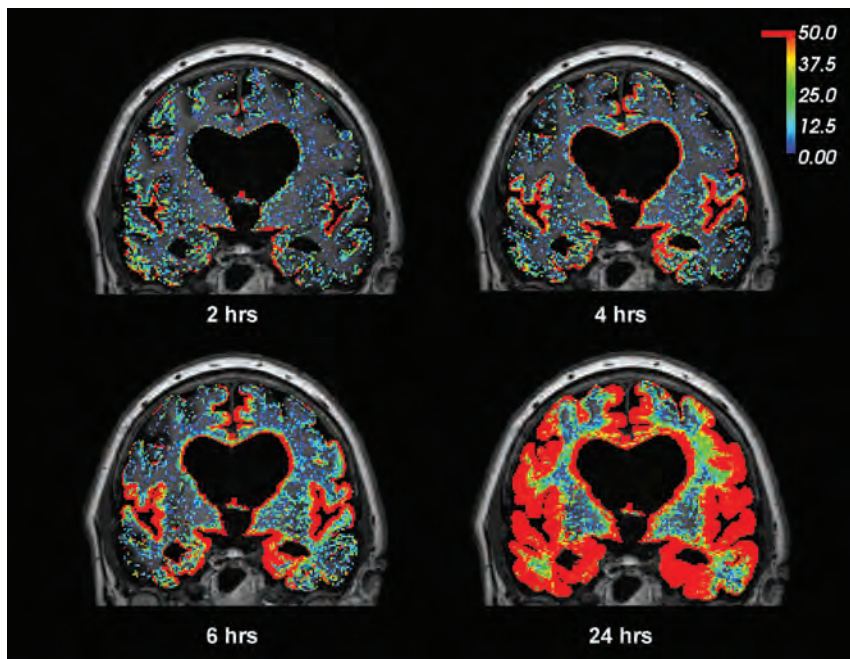


FIG 1. gMRI in a subject with iNPH. Intrathecal gadobutrol (0.05 mmol) used as a CSF tracer, followed by MR imaging acquisitions after 2, 4, 6, and 24 hours, shows enrichment of the CSF tracer as a percentage change in the T1 signal unit ratio. The color scale shows a contrast agent-dependent percentage increase in the T1 signal unit ratio (for more detailed description see Ringstad et al⁵). Note that contrast enhancement of the brain occurred in a centripetal pattern and primarily in regions of the brain adjacent to large artery trunks at the surface—that is, the anterior, middle, and posterior cerebral arteries. The periventricular tracer enhancement is due to reflux of tracer into the ventricular system, which is a typical feature of iNPH.

venous blood therefore also represents a dosage of contrast agent to the CSF.

With this background, exploring the safety profile of intrathecal MR imaging contrast agent administration is highly warranted. We performed a prospective safety and feasibility study of 100 individuals undergoing gMRI following intrathecal injection of 0.5 mL of gadobutrol (Gadovist, 1.0 mmol/mL; Bayer Schering Pharma, Berlin, Germany), in conjunction with 3 mL of iodixanol (Visipaque, 270 mg I/mL; GE Healthcare, Piscataway, New Jersey), and recorded immediate, short-term, and long-term adverse events.

MATERIALS AND METHODS

Approvals

The institutional review board (2015/1868), regional ethics committee (2015/96), and the National Medicines Agency (15/04932–7) approved the study. Inclusion was by written and oral informed consent.

Experimental Design and Patients

This observational and prospective study included consecutive patients admitted to the Department of Neurosurgery, Oslo University Hospital, Rikshospitalet, for management of tentative CSF circulation disorders during September 2015 to August 2018 (Table 1).

We used the following exclusion criteria: history of hypersensitivity reactions to contrast agents, history of severe allergy reactions in general, evidence of renal dysfunction, pregnant or breastfeeding women, and age younger than 18 years or older than 80 years.

MR Imaging Protocol

Sagittal T1-weighted spoiled gradient-echo volume scans were obtained using a 3T Ingenia MR imaging scanner (Philips Healthcare, Best, the Netherlands), with equal imaging sequence parameters at all time points. The main imaging parameters were the following: TR = shortest (typically 5.1 ms), TE = shortest (typically 2.3 ms), flip angle = 8°, FOV = 256 × 256 cm, matrix = 256 × 256 pixels (reconstructed to 512 × 512). We sampled 184 overcontiguous slices with 1-mm thickness that were automatically reconstructed to 368 slices with a thickness of 0.5 mm. Each image acquisition lasted 6 minutes 29 seconds.

Intrathecal Administration of Gadobutrol

After precontrast MR imaging (approximately 8 AM), the patient was transported on a mobile table to an adjacent neurosurgery operating room, where an interventional neuroradiologist performed x-ray-guided lumbar puncture. The level that provided the best access to the spinal canal was determined by the neuroradiologist on an individual basis, most typically at level L2/L3 or L3/L4, and, in some cases, at level L4/5. Correct placement of a spinal syringe tip in the subarachnoid space at the lower lumbar level was verified in terms of CSF backflow from the puncture needle (22 ga × 3.5 inches). Subsequently, a mixture of 2–3 mL of 270 mg I/mL of iodixanol (Visipaque) and 0.5 mL of 1.0 mmol/mL gadobutrol (Gadovist) was injected guided by fluoroscopy, to confirm unrestricted distribution of radiopaque contrast agent in the lumbar subarachnoid space. After needle removal, the patients were instructed to rotate around the long axis of the body once before transportation back to the MR imaging suite, to keep the patient in the supine position.

Postcontrast MR Imaging Acquisitions and Image Analysis

Assessment of contrast agent entry at the level of the craniocervical junction (spinal transit time) by means of MR imaging was initiated as soon as possible after intrathecal gadobutrol administration (typically with an approximately 5- to 10-minute delay). Consecutive and identical MR imaging acquisitions covering the cranial compartment and upper neck region with the previously outlined MR imaging protocol parameters were initiated and performed approximately every 10 minutes during the first hour after contrast agent injection. The patients were thereafter instructed to remain supine in bed. Repeat, identical MR imaging acquisitions were then performed approximately every 2 hours after intrathecal gadobutrol administration until afternoon (about 4 PM). Transfer of patients between the neurosurgical department and the MR imaging suite and between the bed and the MR imaging table was performed by the hospital staff to help the

Table 1: Patient material^a

	Total Material
No.	100
Mean age (yr)	51 ± 19
Sex (female/male)	58:42
BMI (kg/m ²)	27 ± 5
Comorbidity	
Hypertension	18 (18%)
Diabetes	4 (4%)
Diagnosis	
iNPH	35 (35%)
SIH	14 (14%)
AC	18 (18%)
PC	22 (22%)
IIH	6 (6%)
cHC	5 (5%)

Note:—SIH indicates spontaneous intracranial hypotension; AC, arachnoid cyst; PC, pineal cyst; IIH, idiopathic intracranial hypertension; cHC, communicating hydrocephalus; BMI, body mass index.

^aData are No. (percentage in parentheses) and means.

patient remain in the supine position. Beginning in the afternoon, the patients could move freely; new MR imaging acquisitions were repeated after 24 and 48 hours.

The first appearance of any MR imaging contrast agent at the level of the foramen magnum was assessed visually by an experienced neuroradiologist (G.R.) on the sagittal T1-weighted volume scans in the hospital PACS.

Assessment of Serious and Nonserious Adverse Events

Serious and nonserious adverse events were recorded systematically by study nurses not otherwise involved in management of patients. Serious adverse events were defined as any untoward medical occurrence that, at any dose, results in the following: death, an immediately life-threatening situation, inpatient hospitalization or prolongation of existing hospitalization, persistent or significant disability or incapacity, or an important medical event that may jeopardize the subject or may require medical intervention to prevent one of the outcomes listed here. Adverse events not having these consequences were considered nonserious.

Assessment of adverse events was performed prospectively during days 1–3 after intrathecal contrast agent administration, after 4 weeks, and finally after about 12 months. The patients were specifically queried for the presence of a defined set of symptoms presenting or being aggravated after intrathecal contrast administration and MR imaging and for symptom duration. These symptoms were chosen according to adverse effects most commonly observed after intrathecal iohexanol: headache (mild/moderate/severe), nausea (mild/moderate/severe), dizziness (mild/moderate/severe), itch, warm feeling, paresthesia, visual problems, cognitive difficulties, muscular spasms, discomfort at the injection site, and tremor. Other symptoms than those specifically requested were listed independent of possible causes. All patients who still reported symptoms at 4 weeks were phoned by the study nurses at a later time, ranging from a few months to up to 12 months, for a final assessment. Report of symptoms at any other contact after 4 weeks was also registered and categorized as “late.”

RESULTS

Patients

Table 1 presents demographic information about the 100 consecutive patients who were included in the study. The cohort included 58 female and 42 male patients, with a mean of 51 ± 19 years of age. Comorbidity was common.

Verified Intracranial Distribution of Gadobutrol

Gadobutrol enhancement in cranial CSF spaces was verified in all individuals (Fig 2). Contrast was still visible intracranially after 24 and 48 hours. The gMRI of 1 patient with iNPH is shown in Fig 3.

The mean time from intrathecal administration of gadobutrol until the first visual detection of the contrast agent at the foramen magnum (spinal transit time) was 20 ± 23 minutes (median, 13 minutes; range, 6–150 minutes). As illustrated in Fig 4, there was some interindividual variation concerning spinal transit time. There were no significant differences in spinal transit time across the patient groups (data not shown). In all patients, scans obtained until 4 PM were assessed visually to ensure the expected magnitude of enhancement in the intracranial CSF spaces, which could be confirmed. Prolonged spinal transit time was, therefore, less likely to be attributed to extradural injection of contrast agent at the lumbar level.

Serious Adverse Effects

No patients without a history of prior adverse events experienced serious adverse reactions likely related to intrathecal gadobutrol administration. One woman with established allergy to iodinated radiocontrast agents was, by error, included in the study, even after interaction with the referring doctor, study nurse, the neurologist who managed hospital admittance, and an anesthesiologist. This individual experienced an immediate anaphylactic reaction consisting of skin rash, dyspnea, and a fall in blood pressure, symptoms that were comparable with a previous reaction to iodinated radiocontrast agent (Table 2). Fortunately, after receiving intravenous Ringer-acetate (1000 mL) and surveillance within the intensive care unit for a few hours, no further actions were required. After a few hours, the patient was able to undergo MR imaging, though estimation of spinal transit time was not possible in this individual.

One 80-year-old man with iNPH had a pulmonary embolism, which was attributed to a long train journey and reduced mobility a few days before.

Nonserious Adverse Events

The nonserious adverse events within 3 days, at 4 weeks, and at 12 months, respectively, are presented in Table 2.

Nonserious adverse events within the first 1–3 days (delayed) after intrathecal gadobutrol were rather frequent and usually occurred after 10–20 minutes or in the afternoon about 3 PM. Adverse events rarely occurred at days 2 or 3. Twenty-two of 100 individuals reported no symptoms, while 78/100 individuals had symptoms of variable degrees (Table 2). About one-third of individuals experienced the combination of severe headache and nausea. These symptoms were managed conservatively. Whether the high frequency of headache and nausea was caused by the under-

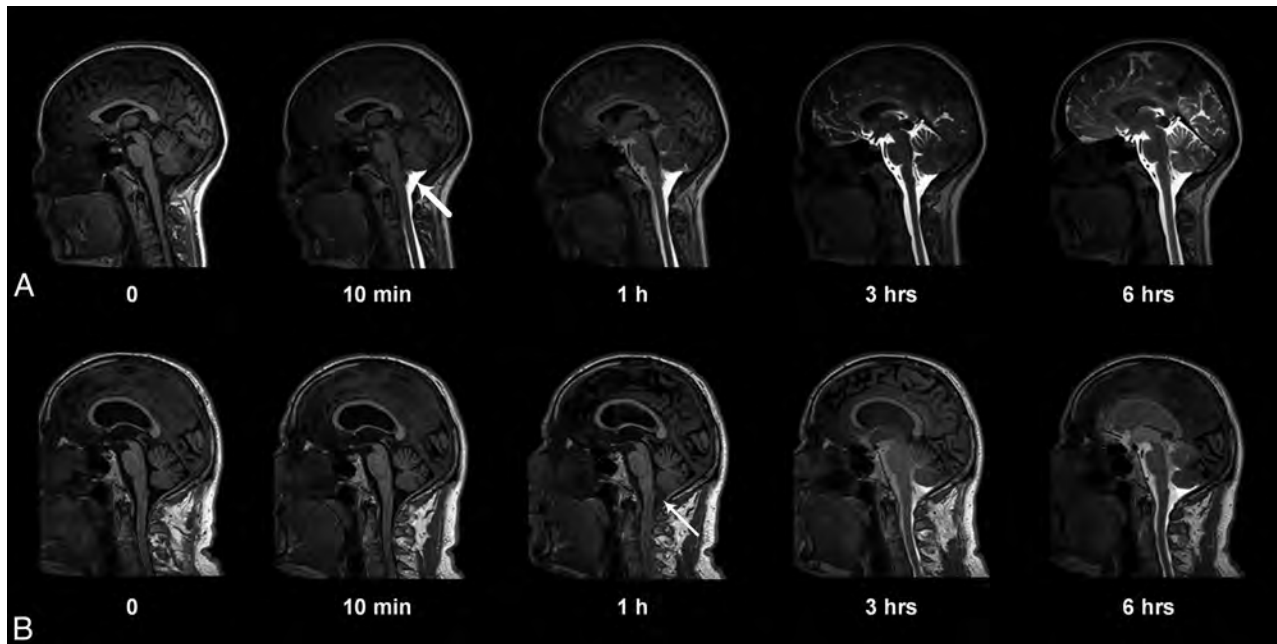


FIG 2. Entry of gadobutrol into the CSF within the intracranial compartment at consecutive MR imaging of a patient with a pineal gland cyst (A) and iNPH (B). Intrathecal administration of 0.5 mL (1.0 mmol/mL) of gadobutrol at the lower lumbar level was preceded by unenhanced, T1-weighted MR imaging (time point zero). After the correct needle position had been verified at fluoroscopy by injection of 3 mL of iohexanol (270 mg I/mL), the patient was transported in the supine position to the MR imaging suite next door, and acquisition of identical, consecutive T1 scans was initiated immediately and performed continuously within the first hour. Typically, the contrast agent had reached the cisterna magna at the first postcontrast scan obtained after approximately 10 minutes (A, *thick arrow*). In some patients, however, enhancement occurred much later, as in B, where slight enhancement was first depicted at 1 hour (*thin arrow*). At 6-hour scans, gadobutrol is distributed widely in the CSF of both patients, but less prominently in B, where ventricular reflux can also be noted.

lying disease, the gadobutrol or iohexanol per se, or the spinal puncture could not be determined with certainty.

After 4 weeks, 88 individuals reported no symptoms, while 12 had various symptoms (Table 2). One individual with iNPH reported an itch. In 5 patients with either pineal or arachnoid cysts, 3 had variable degrees of headache, 1 had nausea, and 1 reported dizziness. Three patients reported discomfort at the injection site or in the lumbar region and/or paresthesia, which most likely was related to the lumbar puncture itself.

After 12 months, 1 patient with a pineal cyst had mild headache and dizziness, but these symptoms were the same as she experienced before MR imaging (Table 2).

Table 3 presents nonserious adverse events recorded during days 1–3 according to the diagnosis category. The data show that symptoms like headache, nausea, and dizziness particularly depend on the diagnosis. For example, 15/22 (68%) patients with pineal cysts reported severe headache and nausea, while severe headache and nausea were reported by 2/35 (6%) and 10/35 (29%) patients with iNPH, respectively. Moreover, while no symptoms were reported by 12/35 (34%) patients with iNPH, they were reported by 0/22 (0%) patients with pineal cysts. Notably, the high frequency of symptoms such as headache, nausea, and dizziness reported by patients with pineal gland cysts closely resembles the frequency and character of symptoms they had experienced previously and that represented the main reason for their referral to our hospital in the first place.

DISCUSSION

The main observation of this prospective study is that administration of 0.5 mL of gadobutrol (1.0 mmol/mL) is safe in patients with no history of allergic reactions to contrast agents.

Nonserious adverse events were rather frequent; however, the occurrence depended heavily on the diagnosis. Among individuals with a pineal cyst, 15/22 (68%) reported severe headache and nausea during days 1–3. We previously reported a high frequency of these symptoms in this patient group in general.¹⁷ Headache is a predominant symptom in individuals with symptomatic arachnoid cysts.¹⁸ We cannot with certainty know whether nonserious adverse events such as headache, nausea, and dizziness after 1–3 days or after 4 weeks were caused by any of the contrast agents or related to the diagnosis itself. Inclusion of other patient categories, such as those with iNPH, most likely would provide other frequencies of reported symptoms.

Because gadobutrol was given in conjunction with iohexanol, to what extent these adverse effects can be attributed to gadobutrol alone remains unanswered.

The study reports prospective data from 100 patients to whom intrathecal gadobutrol was given off-label after special permission from the National Medicines Agency of Norway. Intrathecal doses of MR imaging contrast agents in similar amounts have, however, been used off-label on a clinical basis for years to visualize CSF leakage in individuals with spontaneous intracranial hypotension, as previously reported by others.^{19,20} Intrathecal MR imaging contrast agents were also found to benefit assessment

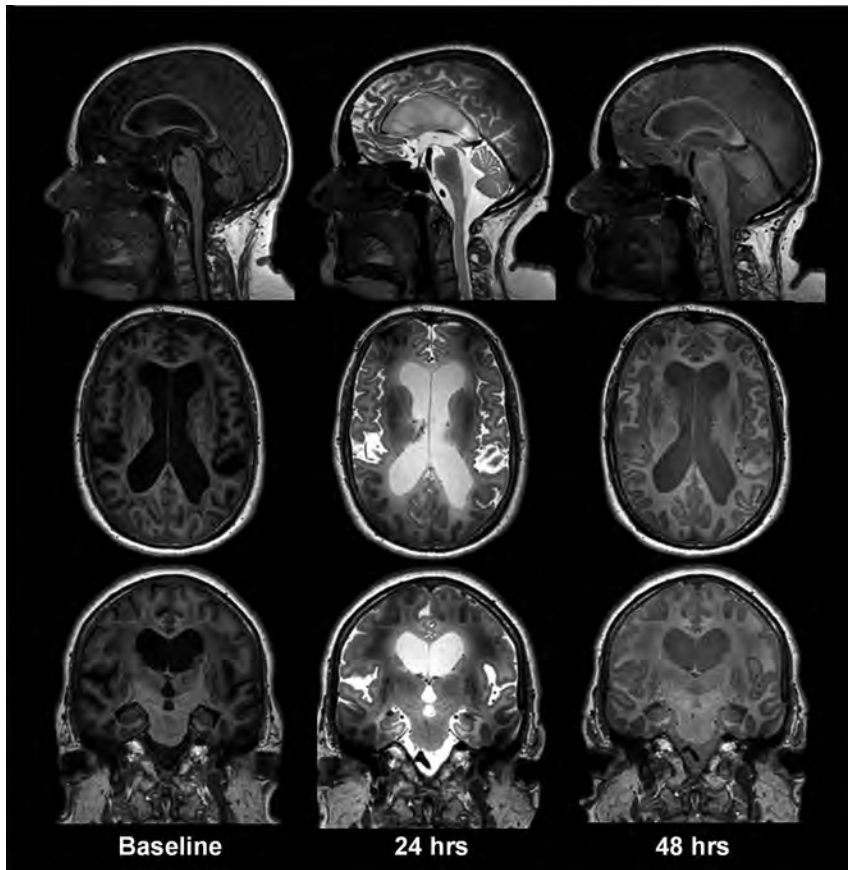


FIG 3. gMRI shown as standardized T1 acquisitions before and 24 and 48 hours after intrathecal gadobutrol in a subject with iNPH, including midsagittal, midaxial, and midcoronal images. In iNPH, gadobutrol clearance from the CSF is delayed compared with reference patients at 24 and 48 hours, respectively. Other typical features of iNPH are early ventricular reflux and subsequent periventricular enhancement of contrast agent, typically most prominent at 24 hours.

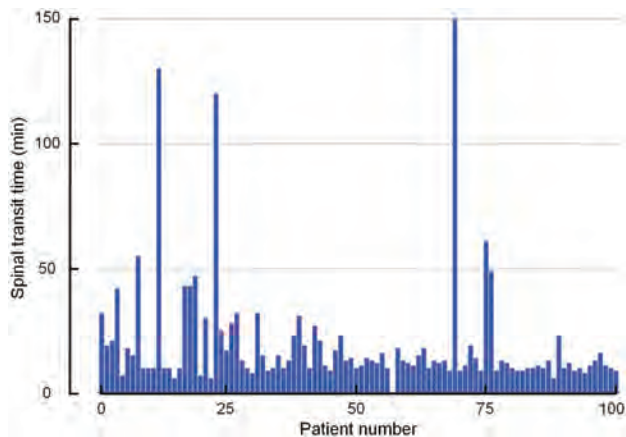


FIG 4. The time from intrathecal administration of gadobutrol until the first enhancement of the contrast agent within subarachnoid space of the foramen magnum (spinal transit time) for the 100 patients included in the study. The mean \pm SD spinal transit time was 20 ± 23 minutes.

of arachnoid cysts²¹ and iNPH,²² and in diagnosing the cause of otorrhorrhea.²³

We verified that gadobutrol reached the intracranial CSF compartment in all subjects (except the one with an anaphylactic reaction). The mean spinal transit time was 20 ± 23 minutes (median, 13 minutes; range, 6–150 minutes; Fig 4).

In terms of safety with intrathecal gadolinium injections, the linear contrast agents have been more investigated than the macrocyclic ones. Gadopentetic acid in a dose 0.5–1.0 mmol was well-tolerated in animal studies^{20,21,24–27} and was found to have a low risk when given in low doses (0.5–1.0 mmol) to patients.^{19,24–26,28,29} Headache has been the most dominating adverse effect, which also might be related to the spinal puncture. Neurotoxic effects on animal brains were seen when gadopentetic acid was given intraventricularly in a dose of 5.0 $\mu\text{mol/g}$ brain but was not observed when the dose was $<3.3\text{-}\mu\text{mol/g}$ brain.³⁰ Previous studies in patients showed that overdose of gadopentetic acid (6–20 times the normal dose) can be neurotoxic.^{31,32} Hence, 1 patient who, by accident, received 20 mL of gadopentetic acid (7.0 $\mu\text{mol/g}$ brain) developed neurologic deficits (speech problems, visual impairment, fatigue, and psychotic symptoms) lasting 2 weeks, but symptoms had disappeared after 2 months.³³ Moreover, following intrathecal administration of 2.0 mL of gadobutrol, 1 individual reported spastic pain of the lower extremities.³⁴

In an adult brain weighing 1400 g, gadobutrol in a dose of 0.5 mmol corresponds to 500- $\mu\text{mol}/1400\text{-g}$ brain (0.36- $\mu\text{mol/g}$ brain). Thus, the dose of gadobutrol in this study was on the order of one-tenth of previously appreciated toxic levels. Nevertheless, nonserious adverse events within 1–3 days postcontrast were seen rather frequently, in particular headache and nausea. Intrathecal gadopentetic acid was previously reported to cause headache in 10/36 (27%) patients with iNPH²² and in 6/20 (30%) patients with arachnoid cysts.²⁹

Iodixanol was given intrathecally to verify the correct needle position, which is part of the spinal puncture routine. The safety profile of iodixanol³⁵ closely resembles that of gadobutrol in combination with iodixanol in this current study. Thus, intrathecal iodixanol caused nonserious adverse events in a comparable proportion of patients as reported here.³⁵

While MR imaging contrast agents are approved for intravenous administration only, gadolinium has recently been depicted in CSF samples obtained from individuals even with normal renal function and an intact blood-brain barrier.^{14,15} Given that the concentration of MR imaging contrast agent in CSF exceeded that of blood 4.5 hours after intravenous administration,¹⁶ a typical intravenous dose (0.1 mmol/kg in a 80-kg patient = 8 mmol, half-time in blood is approximately 2 hours) may cause significant passage of contrast agent to the CSF. Except from our previous reports using gMRI,^{5–7,10} time-dependent quantification of gadobutrol in human CSF after a typical intravenous dose, for

example using T1 maps, has been reported in a case study.³⁶ Four weeks after 1 single intrathecal administration, gadolinium is not detectable by MR imaging in any brain region, including the basal ganglia.⁵

The potential risk inherent in the use of any contrast agent should always be weighed against its potential benefits. After intrathecal contrast-enhanced MR imaging of humans was first proposed,^{3,4} gMRI has been demonstrated to be a promising clinical tool in the assessment of CSF circulation disorders.⁵⁻⁷ In particular, delayed glymphatic clearance of gadobutrol, which is anticipated to be cleared through the same pathways as amyloid- β

and τ , has been proved in a dementia cohort.⁵ Contrast enhancement of the entire brain extravascular space is expected to have a large potential for better characterization of disease within the brain and spinal cord but remains yet unexplored.

Limitations

While the present study addressed the safety profile of intrathecal gadobutrol, the major limitation is that we cannot determine with certainty which adverse events solely relate to the MR imaging contrast agent. The nonserious effects we observed might, as well, be caused by the accompanied administration of iodixanol, the spinal puncture, a heavy load of repeat MR imaging, and repeat transport to and from the MR imaging lab.

To what extent the nonserious adverse events are related to the dose of intrathecal gadobutrol remains to be determined. Another study²³ using 0.5 mL of Gd-DTPA or Magnevist (Bayer HealthCare Pharmaceuticals, Wayne, New Jersey), which corresponds to half the dose of gadobutrol used in the present study, seemed to give a better profile concerning nonserious adverse events, though having a high sensitivity in diagnosing the cause of otorrhorrhea. Hence, a lower dose of gadobutrol than used in the present study might give fewer adverse effects. However, because gadobutrol distributes to both the CSF and the entire extravascular compartment, it remains to be determined whether such low doses are sufficient to demonstrate contrast enhancement in deep brain regions, where we have experienced it to be quite marginal.⁵ In fu-

Table 2: Occurrence of adverse events following intrathecal MRI contrast agent administration^a

	Immediate	Delayed (Days 1–3)	4 Weeks	Late
Serious adverse events				
Allergy reaction	1 (1%)	0	0	0
Pulmonary embolism	0	1 (1%)	0	0
Nonserious adverse events				
Headache				
Mild		3 (3%)	1 (1%)	1 (1%)
Moderate		13 (13%)	2 (2%)	0
Severe		28 (28%)	1 (1%)	0
Nausea				
Mild		17 (17%)	0	0
Moderate		5 (5%)	0	0
Severe		34 (34%)	1 (1%)	0
Dizziness				
Mild		10 (10%)	0	1 (1%)
Moderate		11 (11%)	1 (1%)	0
Severe		17 (17%)	0	0
Itch		3 (3%)	1 (1%)	0
Warm feeling		7 (7%)	1 (1%)	0
Paresthesia		12 (12%)	2 (2%)	0
Vision problems		0	0	0
Cognitive difficulties		0	0	0
Discomfort at injection site and/or lumbar region		13 (13%)	2 (2%)	0
Tremor		0	0	0

^aData are No. of individuals (percentage in parentheses).

Table 3: Occurrence of nonserious adverse events within days 1–3, depending on diagnosis^a

Nonserious Adverse Events	iNPH (n = 35)	SIH (n = 14)	AC (n = 18)	PC (n = 22)	IIH (n = 6)	cHC (n = 5)
Headache						
Mild	1 (3%)	2 (14%)	0	0	0	0
Moderate	2 (6%)	3 (21%)	2 (11%)	4 (18%)	0	2 (40%)
Severe	2 (6%)	2 (14%)	6 (33%)	15 (68%)	1 (17%)	2 (40%)
Nausea						
Mild	6 (17%)	2 (14%)	4 (22%)	4 (18%)	0	2 (40%)
Moderate	1 (3%)	1 (7%)	1 (6%)	1 (5%)	1 (17%)	0
Severe	10 (29%)	2 (14%)	5 (28%)	15 (68%)	1 (17%)	1 (20%)
Dizziness						
Mild	4 (11%)	2 (14%)	2 (11%)	2 (9%)	0	0
Moderate	1 (3%)	1 (7%)	3 (17%)	6 (27%)	0	0
Severe	0	0	5 (28%)	9 (41%)	2 (33%)	1 (20%)
Itch	1 (3%)	0	1 (6%)	0	0	1 (20%)
Warm feeling	3 (9%)	1 (7%)	1 (6%)	2 (9%)	0	0
Paresthesia	1 (3%)	2 (14%)	3 (17%)	6 (27%)	0	0
Vision problems	0	0	0	0	0	0
Cognitive difficulties	0	0	0	0	0	0
Discomfort at injection site and/or lumbar region	0	2 (14%)	2 (11%)	7 (32%)	2 (33%)	1 (20%)
Tremor	0	0	0	0	0	0
No adverse events	12 (34%)	3 (21%)	4 (22%)	0	2 (33%)	1 (20%)

Note:—SIH indicates spontaneous intracranial hypotension; AC, arachnoid cyst; PC, pineal cyst; IIH, idiopathic intracranial hypertension; cHC, communicating hydrocephalus.

^aData are presented as No. of individuals (percentage in parentheses).

ture studies, the effects of lower doses of gadobutrol should be explored. Additionally, other gadolinium-based contrast agents might be examined.

Another limitation is that the study included a high proportion of individuals with symptoms similar those reported after intrathecal gadobutrol. The patient selection most likely affected the symptom profile we also registered at time points after intrathecal injections.

CONCLUSIONS

This study showed intrathecal administration of gadobutrol for gMRI to be safe and feasible. We cannot, with certainty, conclude whether nonserious adverse effects such as headache and nausea were caused by gadobutrol, iohexanol, the lumbar puncture, or the diagnosis.

Disclosures: Svein Are Sirirud Vatnehol—UNRELATED: Payment for Lectures Including Service on Speakers Bureaus: Norwegian Medical Association, Comments: MRI safety lecture for radiologists in training.

REFERENCES

1. Iliff JJ, Wang M, Liao Y, et al. **A paravascular pathway facilitates CSF flow through the brain parenchyma and the clearance of interstitial solutes, including amyloid β .** *Sci Transl Med* 2012;4:147ra111 CrossRef Medline
2. Rasmussen MK, Mestre H, Nedergaard M. **The glymphatic pathway in neurological disorders.** *Lancet Neurol* 2018;17:1016–24 CrossRef Medline
3. Iliff JJ, Lee H, Yu M, et al. **Brain-wide pathway for waste clearance captured by contrast-enhanced MRI.** *J Clin Invest* 2013;123:1299–309 CrossRef Medline
4. Yang L, Kress BT, Weber HJ, et al. **Evaluating glymphatic pathway function utilizing clinically relevant intrathecal infusion of CSF tracer.** *J Transl Med* 2013;11:107 CrossRef Medline
5. Ringstad G, Valnes LM, Dale AM, et al. **Brain-wide glymphatic enhancement and clearance in humans assessed with MRI.** *JCI Insight* 2018;3 CrossRef Medline
6. Ringstad G, Vatnehol SA, Eide PK. **Glymphatic MRI in idiopathic normal pressure hydrocephalus.** *Brain* 2017;140:2691–705 CrossRef Medline
7. Eide PK, Ringstad G. **Delayed clearance of cerebrospinal fluid tracer from entorhinal cortex in idiopathic normal pressure hydrocephalus: a glymphatic magnetic resonance imaging study.** *J Cereb Blood Flow Metab* 2018 Feb 27:271678X18760974. [Epub ahead of print] CrossRef Medline
8. Louveau A, Smirnov I, Keyes TJ, et al. **Structural and functional features of central nervous system lymphatic vessels.** *Nature* 2015; 523:337–41 CrossRef Medline
9. Aspelund A, Antila S, Proulx ST, et al. **A dural lymphatic vascular system that drains brain interstitial fluid and macromolecules.** *J Exp Med* 2015;212:991–99 CrossRef Medline
10. Eide PK, Vatnehol SA, Emblem KE, et al. **Magnetic resonance imaging provides evidence of glymphatic drainage from human brain to cervical lymph nodes.** *Sci Rep* 2018;8:7194 CrossRef Medline
11. Kanda T, Ishii K, Kawaguchi H, et al. **High signal intensity in the dentate nucleus and globus pallidus on unenhanced T1-weighted MR images: relationship with increasing cumulative dose of a gadolinium-based contrast material.** *Radiology* 2014;270:834–41 CrossRef Medline
12. Gulani V, Calamante F, Shellock FG, et al; International Society for Magnetic Resonance in Medicine. **Gadolinium deposition in the brain: summary of evidence and recommendations.** *Lancet Neurol* 2017;16:564–70 CrossRef Medline
13. Radbruch A, Haase R, Kieslich PJ, et al. **No signal intensity increase in the dentate nucleus on unenhanced T1-weighted MR images after more than 20 serial injections of macrocyclic gadolinium-based contrast agents.** *Radiology* 2017;282:699–707 CrossRef Medline
14. Berger F, Kubik-Huch RA, Niemann T, et al. **Gadolinium distribution in cerebrospinal fluid after administration of a gadolinium-based MR contrast agent in humans.** *Radiology* 2018;288:703–09 CrossRef Medline
15. Nehra AK, McDonald RJ, Bluhm AM, et al. **Accumulation of gadolinium in human cerebrospinal fluid after gadobutrol-enhanced MR imaging: a prospective observational cohort study.** *Radiology* 2018;288:416–23 CrossRef Medline
16. Jost G, Frenzel T, Lohrke J, et al. **Penetration and distribution of gadolinium-based contrast agents into the cerebrospinal fluid in healthy rats: a potential pathway of entry into the brain tissue.** *Eur Radiol* 2017;27:2877–85 CrossRef Medline
17. Eide PK, Pripp AH, Ringstad GA. **Magnetic resonance imaging biomarkers indicate a central venous hypertension syndrome in patients with symptomatic pineal cysts.** *J Neurol Sci* 2016;363:207–16 CrossRef Medline
18. Pradilla G, Jallo G. **Arachnoid cysts: case series and review of the literature.** *Neurosurg Focus* 2007;22:E7 Medline
19. Akbar JJ, Luetmer PH, Schwartz KM, et al. **The role of MR myelography with intrathecal gadolinium in localization of spinal CSF leaks in patients with spontaneous intracranial hypotension.** *AJNR Am J Neuroradiol* 2012;33:535–40 CrossRef Medline
20. Selcuk H, Albayram S, Ozer H, et al. **Intrathecal gadolinium-enhanced MR cisternography in the evaluation of CSF leakage.** *AJNR Am J Neuroradiol* 2010;31:71–75 CrossRef Medline
21. Tali ET, Ercan N, Kaymaz M, et al. **Intrathecal gadolinium (gadopentetate dimeglumine)-enhanced MR cisternography used to determine potential communication between the cerebrospinal fluid pathways and intracranial arachnoid cysts.** *Neuroradiology* 2004;46: 744–54 CrossRef Medline
22. Algin O, Hakyemez B, Ocakoğlu G, et al. **MR cisternography: is it useful in the diagnosis of normal-pressure hydrocephalus and the selection of “good shunt responders”?** *Diagn Interv Radiol* 2011;17: 105–11 CrossRef Medline
23. Nacar Dogan S, Kizilkilic O, Kocak B, et al. **Intrathecal gadolinium-enhanced MR cisternography in patients with otorrhorrhea: 10-year experience of a tertiary referral center.** *Neuroradiology* 2018;60: 471–77 CrossRef Medline
24. Aydin K, Guven K, Sencer S, et al. **MRI cisternography with gadolinium-containing contrast medium: its role, advantages and limitations in the investigation of rhinorrhoea.** *Neuroradiology* 2004;46: 75–80 CrossRef Medline
25. Aydin K, Terzibasoglu E, Sencer S, et al. **Localization of cerebrospinal fluid leaks by gadolinium-enhanced magnetic resonance cisternography: a 5-year single-center experience.** *Neurosurgery* 2008;62:584–89; discussion 584–89 CrossRef Medline
26. Reiche W, Komenda Y, Schick B, et al. **MR cisternography after intrathecal Gd-DTPA application.** *Eur Radiol* 2002;12:2943–49 Medline
27. Skälpe IO, Tang GJ. **Magnetic resonance imaging contrast media in the subarachnoid space: a comparison between gadodiamide injection and gadopentetate dimeglumine in an experimental study in pigs.** *Invest Radiol* 1997;32:140–48 CrossRef Medline
28. Jinkins JR, Rudwan M, Krumina G, et al. **Intrathecal gadolinium-enhanced MR cisternography in the evaluation of clinically suspected cerebrospinal fluid rhinorrhea in humans: early experience.** *Radiology* 2002;222:555–59 CrossRef Medline
29. Tali ET, Ercan N, Krumina G, et al. **Intrathecal gadolinium (gadopentetate dimeglumine) enhanced magnetic resonance myelography and cisternography: results of a multicenter study.** *Invest Radiol* 2002;37:152–59 CrossRef Medline
30. Ray DE, Cavanagh JB, Nolan CC, et al. **Neurotoxic effects of gadopentetate dimeglumine: behavioral disturbance and morphology after intracerebroventricular injection in rats.** *AJNR Am J Neuroradiol* 1996;17:365–73 Medline
31. Li L, Gao FQ, Zhang B, et al. **Overdosage of intrathecal gadolinium**

- and neurological response.** *Clin Radiol* 2008;63:1063–68 CrossRef Medline
32. Park KW, Im SB, Kim BT, et al. **Neurotoxic manifestations of an overdose intrathecal injection of gadopentetate dimeglumine.** *J Korean Med Sci* 2010;25:505–08 CrossRef Medline
33. Arlt S, Cepek L, Rustenbeck HH, et al. **Gadolinium encephalopathy due to accidental intrathecal administration of gadopentetate dimeglumine.** *J Neurol* 2007;254:810–12 CrossRef Medline
34. Reeves C, Galang E, Padalia R, et al. **Intrathecal injection of gadobutrol: a tale of caution.** *J Pain Palliat Care Pharmacother* 2017; 31:139–43 CrossRef Medline
35. Palmers Y, Kuhn FP, Petersen D, et al. **Comparison in myelography between iodixanol 270 and 320 mgI/ml and iotrolan 300 mgI/ml: a multicentre, randomised, parallel-group, double-blind, phase III trial.** *Eur Radiol* 2002;12:686–91 CrossRef Medline
36. Watts R, Steinklein JM, Waldman L, et al. **Measuring glymphatic flow in man using quantitative contrast-enhanced MRI.** *AJNR Am J Neuroradiol* 2019;40:648–51 CrossRef Medline

Gadolinium Retention in the Brain: An MRI Relaxometry Study of Linear and Macrocyclic Gadolinium-Based Contrast Agents in Multiple Sclerosis

Y. Forslin, J. Martola, Å. Bergendal, S. Fredrikson, M.K. Wiberg, and T. Granberg



ABSTRACT

BACKGROUND AND PURPOSE: Brain gadolinium retention is consistently reported for linear gadolinium-based contrast agents, while the results for macrocyclics are contradictory and potential clinical manifestations remain controversial. Furthermore, most previous studies are based on conventional T1-weighted MR imaging. We therefore aimed to quantitatively investigate longitudinal and transversal relaxation in the brain in relation to previous gadolinium-based contrast agent administration and explore associations with disability in multiple sclerosis.

MATERIALS AND METHODS: Eighty-five patients with MS and 21 healthy controls underwent longitudinal and transverse relaxation rate (R_1 and R_2) relaxometry. Patients were divided into linear, mixed, and macrocyclic groups based on previous gadolinium-based contrast agent administration. Neuropsychological testing was performed in 53 patients. The dentate nucleus, globus pallidus, caudate nucleus, and thalamus were manually segmented. Repeatability measures were also performed.

RESULTS: The relaxometry was robust (2.0% scan-rescan difference) and detected higher R_1 (dentate nucleus, globus pallidus, caudate nucleus, thalamus) and R_2 (globus pallidus, caudate nucleus) in patients receiving linear gadolinium-based contrast agents compared with controls. The number of linear gadolinium-based contrast agent administrations was associated with higher R_1 and R_2 in all regions (except R_2 in the thalamus). No similar differences and associations were found for the macrocyclic group. Higher relaxation was associated with lower information-processing speed (dentate nucleus, thalamus) and verbal fluency (caudate nucleus, thalamus). No associations were found with physical disability or fatigue.

CONCLUSIONS: Previous linear, but not macrocyclic, gadolinium-based contrast agent administration is associated with higher relaxation rates in a dose-dependent manner. Higher relaxation in some regions is associated with cognitive impairment but not physical disability or fatigue in MS. The findings should be interpreted with care but encourage studies into gadolinium retention and cognition.

ABBREVIATIONS: CN = caudate nucleus; DN = dentate nucleus; EDSS = Expanded Disability Status Scale; GBCA = gadolinium-based contrast agent; GP = globus pallidus; R_1 = longitudinal relaxation rate; R_2 = transverse relaxation rate; SDMT = Symbol Digit Modalities Test

Brain gadolinium retention after administration of gadolinium-based contrast agents (GBCAs) has been demonstrated, mainly for linear GBCAs in the dentate nucleus (DN) and globus pallidus (GP), by several studies since the initial report in 2014.¹ Studies of macrocyclic GBCAs, however, remain contradictory, with several studies showing no lasting T1 hyperintensities,²⁻⁴

while a few retrospective studies had positive findings,⁵⁻⁷ though there has been criticism regarding some of these results.⁸ Animal studies have, however, found brain gadolinium retention after multiple administrations of macrocyclic GBCAs, though to a lesser extent than for linear GBCAs.² This finding suggests that detecting T1 alterations after macrocyclic GBCAs may require more sensitive methods than conventional MR imaging. Furthermore, the semiquantitative approach of signal intensity ratios based on T1-weighted imaging may also be flawed by the need for scaling the arbitrary signal intensities with a reference region. Histopathologic studies have shown that gadolinium retention is widespread and also occurs in brain regions that are often used as

Received March 19, 2019; accepted after revision May 20.

From the Department of Clinical Neuroscience (Y.F., J.M., Å.B., S.F., M.K.W., T.G.), Karolinska Institutet, Stockholm, Sweden; Departments of Radiology (Y.F., J.M., M.K.W., T.G.) and Neurology (S.F.), Karolinska University Hospital, Stockholm, Sweden; and Department of Medical and Health Sciences (M.K.W.), Division of Radiological Sciences, Linköping University, Linköping, Sweden.

This research was supported by Karolinska Institutet and the Stockholm County Council through an ALF grant.

Please address correspondence to Yngve Forslin, MD, Department of Radiology, CI-46, Karolinska University Hospital, 141 86 Stockholm, Sweden; e-mail: yngve.forslin@ki.se

 Indicates article with supplemental on-line tables.

 Indicates article with supplemental on-line photos.

<http://dx.doi.org/10.3174/ajnr.A6112>

Table 1: Demographics of the study population and the number of GBCA administrations

	Healthy Controls	Linear MS Group	Mixed MS Group	Macrocytic MS Group
Participants (No.)	21	11	59	15
Male/female ratio	10:11	3:8	18:41	4:11
Age (mean) (yr)	35.9 ± 13.8	51.0 ± 10.7	43.8 ± 10.3	37.4 ± 13.7
MS duration (mean) (yr)	NA	19.8 ± 9.3	12.9 ± 8.1	5.1 ± 6.0
MS subtype, RR/SP/PP	NA	5/6/0	39/17/3	14/1/0
EDSS score (median) (range)	NA	2.5 (0–6); n = 11	2 (0.5); n = 54	2 (1–4); n = 13
SDMT score (median) (range)	NA	−0.19 (−1.47–0.84); n = 5	−1.1 (−3.9–1.4); n = 36	−1.3 (−4.3–0.51); n = 12
Verbal fluency test score (median) (range)	NA	0.74 (−1.82–.36); n = 4	−0.24 (−2.47–2.17); n = 17	−1.32 (−2.94–.04); n = 6
MS lesion volume (median ± interquartile range) (mL)	NA	5.1 ± 10.1	3.1 ± 9.2	2.4 ± 4.2
Brain parenchymal fraction (%)	88.0 ± 2.4	79.6 ± 4.9	82.7 ± 5.9	84.6 ± 5.0
Linear GBCA administrations (No.) (median) (range)	0	3 (1–7)	4 (1–19)	0 (0)
Macrocytic GBCA administrations (No.) (median) (range)	0	0	2 (1–4)	3 (1–6)
Time since last GBCA administration (median) (range) (mo)	NA	52 (24–172)	12 (3–91)	7 (3–14)

Note:—PP indicates primary-progressive; RR, relapsing-remitting; SP, secondary-progressive; NA, not applicable.

^aNumbers are given as means unless otherwise specified.

a reference, such as the thalami.⁹ Relaxometry provides the means to study gadolinium retention quantitatively without the need for a reference region, but so far, there are only a few T1-relaxometry studies in the context of gadolinium retention,^{10,11} and no T2-relaxometry studies. While chelated GBCAs lead to a shortening of T1, they also cause a shortening of T2.¹²

The clinical significance of the retained gadolinium is debated, but medical authorities have used the precaution of moderating the use of mainly the linear GBCAs.^{13,14} A large retrospective study of patients undergoing contrast-enhanced MR imaging without a neurologic indication did not find any increased incidence of Parkinsonism in the exposed patients.¹⁵ Furthermore, a preliminary report from an aging cohort did not show any cognitive decline or worsened motor performance in those who were exposed to GBCAs during the study.¹⁶ However, in a small retrospective long-term follow-up study in multiple sclerosis, there were associations between T1 signal intensity ratio increases and impaired cognitive function, prompting further studies on the subject.¹⁷

We aimed to apply a new robust method for simultaneous T1 and T2 relaxometry in a prospective cohort of patients with MS and healthy controls to investigate associations between both longitudinal and transverse relaxation rates in the DN, GP, caudate nucleus (CN), and thalamus with exposure to linear and macrocytic GBCAs. We also aimed to study possible associations between longitudinal and transverse relaxation rate (R_1 and R_2) values and cognitive and physical disability scores in MS.

MATERIALS AND METHODS

Study Population

This prospective cross-sectional cohort study was approved by the local ethics review board, and written informed consent was obtained from all participants. We consecutively recruited patients with MS referred for brain MR imaging between January and June 2015 at Karolinska University Hospital in Huddinge, Stockholm, Sweden. The only inclusion criterion was an MS diagnosis according to the concurrent 2010 McDonald criteria for patients. Exclusion

criteria were neurologic diseases (other than MS for patients), traumatic brain injury, or imaging artifacts. Additionally, 23 age- and sex-matched healthy controls without exposure to GBCAs were recruited. In total, 88 patients with MS consented to participate, but 2 were excluded due to previous brain trauma and 1 due to movement artifacts. Among the controls, 2 were excluded due to widespread white matter hyperintensities and a cerebellar cardiovascular lesion in 1 of the 2 excluded controls. In total, 85 patients with MS and 21 healthy controls were found eligible and were enrolled in the study. The demographics of the study population is detailed in Table 1.

The 85 patients with MS were divided into 3 groups depending on which type of GBCA they had received. The linear group consisted of 11 patients who had previously received only linear GBCAs, nonionic gadodiamide (Omniscan; GE Healthcare, Piscataway, New Jersey), and/or linear ionic gadopentetate dimeglumine (Magnevist; Bayer HealthCare Pharmaceuticals, Wayne, New Jersey). The mixed group consisted of 59 patients who had received linear nonionic gadodiamide (Omniscan) and/or linear ionic gadopentetate dimeglumine (Magnevist) as well as macrocytic gadoterate meglumine (Dotarem; Guerbet, Aulnay-sous-Bois, France). The macrocytic group consisted of 15 patients who had received only gadoterate meglumine (Dotarem). None of the 21 healthy controls had received any GBCAs.

To evaluate the repeatability of the relaxometry MR imaging scans, 14 patients with MS and 17 healthy controls also underwent a second MR imaging acquisition with repositioning immediately after the first scan. The demographics of the repeatability cohort is presented in On-line Table 1.

Image Acquisition

All imaging was performed on the same 3T Magnetom Trio MR imaging scanner (Siemens, Erlangen, Germany) with a 12-channel head coil. In addition to the national Swedish brain MR imaging protocol for MS,¹⁸ a quantitative MR imaging sequence for simultaneous T1 and T2 relaxometry was applied without administration of any GBCA. The quantitative sequence consisted of a saturation-recovery TSE sequence with 2 TEs and 4 TRs, for

which the acquisition order was changed with each repetition, resulting in 4 different TIs. Both the phase and magnitude data were saved, providing a total of 16 images per voxel. A least squares fit was applied to the data to obtain the R_1 and R_2 ($R_1 = 1/T_1$ and $R_2 = 1/T_2$, with a unit of second^{-1}) in the SyMRI software 11.0 Beta 4 for Mac (Synthetic MR, Linköping, Sweden).¹⁹ The technique has been validated as having good accuracy for T1 and T2 quantifications.²⁰ The quantitative maps were also used to synthesize T1- and T2-weighted images on the basis of the default settings in the same software. SyMRI was further used to measure the brain parenchymal fraction (brain parenchymal volume normalized to the intracranial volume) as a measure of brain atrophy, which has been shown to be a robust atrophy measure in MS.^{21,22} For the patients with MS, the lesion-probability algorithm in the Lesion Segmentation Toolbox 2.0.12 (Technische Universität München, Munich, Germany) for SPM12 (<http://www.fil.ion.ucl.ac.uk/spm/software/spm12>)^{23,24} was used to automatically segment MS lesions on the basis of a 3D-FLAIR acquisition. The lesion masks were manually corrected by a resident in radiology (T.G.) to obtain the MS lesion volumes. The MR imaging parameters are detailed in On-line Table 2.

Radiologic Evaluation

On the basis of previous publications,^{3,9,25} the DN, GP, head of the CN, and thalamus were a priori selected as ROIs. The segmentations were performed by a resident in radiology (Y.F.) in ITK-SNAP, Version 3.4.0 (www.itksnap.org)²⁶ on the synthetic T1- and T2-weighted images. As exemplified in On-line Fig 1, synthetic T2-weighted images were chosen to easily identify the DN, and synthetic T1-weighted images, to identify the CN, GP, and thalamus. The outer edges of the structures were not included in the segmentations to mitigate partial volume effects. Furthermore, lesioned voxels were excluded from the ROI. On-line Fig 2 illustrates how lacunar infarcts within the caudate nucleus were avoided. The segmentations were applied to the inherently aligned R_1 and R_2 maps using FMRIB Software Library tools, Version 6.0 (<http://fsl.fmrib.ox.ac.uk/fsl>) to extract the relaxation values for each structure.²⁷

Clinical Information

The radiologic and clinical charts of the patients with MS were reviewed to obtain information on the number and type of previous GBCA administrations, MS disease duration, MS subtype, and disease-modifying therapy. Charts were also used to extract disability scores from the Expanded Disability Status Scale (EDSS), Fatigue Severity Scale, Symbol Digit Modalities Test (SDMT), and verbal fluency test. The cognitive test scores were normalized to z scores by adjusting for age, educational level, and sex on the basis of normative data. Only results within 6 months from the MR imaging examination were accepted for the study.

Statistics

SPSS, Version 24.0 (IBM, Armonk, New York) was used for the statistical analyses. Measures of the relaxation values from the paired right and left anatomic structures were averaged. The Shapiro-Wilk test was used to determine whether the data were

normally distributed. The R_1 and R_2 values were normally distributed, except for the R_2 values in the GP for the macrocyclic group that were positively skewed. After exclusion of 1 extreme outlier (>3 interquartile ranges of the data), normal distribution was achieved for all relaxation values. The ordinal EDSS data were, as expected, positively skewed, and normal distribution was achieved after a logarithmic transformation. The scores of SDMT, verbal fluency, and the Fatigue Severity Scale were all normally distributed.

Group comparisons were performed with 1-way ANOVA, followed by the Hochberg post hoc test for pair-wise comparisons among the groups. Multiple linear regression analyses were used to investigate associations between the number of received GBCA administrations (independent variable) and the R_1 and R_2 values (dependent variable). The healthy controls were included as a baseline reference in the regression analyses for each group. To increase the generalizability of the results, we excluded 1 patient with a high (0.45) leverage value (who had received 19 GBCA administrations) from the linear regression analyses.

Associations between cognitive and physical disability scores (dependent variable) and R_1 and R_2 values (independent variable) were evaluated with multiple linear regression. To correct for the MS disease severity, we additionally performed these regression analyses with the disease duration, lesion volume, and brain parenchymal fraction added as covariates.

The scan-rescan repeatability was assessed by calculating the relative change in relaxation values between the 2 measurements by dividing the absolute difference by their mean: $|\text{Scan 1} - \text{Scan 2}| / \text{Mean}(\text{Scan 1} + \text{Scan 2})$.

An α level of .05 was used to determine statistical significance, which was adjusted to .023 for the regression and ANOVA analyses after correction for the false discovery rate.²⁸

RESULTS

Repeatability

The median scan-rescan difference of the R_1 and R_2 measurements among all regions was 2.0%. The difference ranged between 0.8% and 2.1% for the DN, thalamus, and CN, while the GP had a median difference of 4.1% and 4.2%, respectively, for the R_1 and R_2 measurements. On-line Table 3 details the repeatability for R_1 and R_2 in all ROIs.

Group Differences

There were overall differences in R_1 and R_2 ($P < .001-.031$) among the 4 groups (linear, mixed, macrocyclic, and controls) in all ROIs in the 1-way ANOVA, except the R_2 values in the DN ($P = .05$) and thalamus ($P = .66$). The Hochberg post hoc test was used to explore between-group differences, as further detailed in Table 2. The R_1 was higher in the DN, GP, and CN in both the linear and mixed groups compared with the healthy controls. The R_1 was higher in the thalamus, and R_2 was higher in both the GP and CN in the mixed group compared with the healthy controls.

Associations of GBCA Administrations with R_1 Values

Table 3 details all regression analysis results between the number of GBCA administrations and relaxation rates. In the linear group, a higher number of GBCA administrations was associated

Table 2: Group comparisons of the relaxation rates^a

	Dentate Nucleus		Globus Pallidus		Caudate Nucleus		Thalamus	
	R ₁	R ₂	R ₁	R ₂	R ₁	R ₂	R ₁	R ₂
Linear	1.28 ± 0.05	16.74 ± 1.96	1.31 ± 0.05	20.52 ± 1.74	0.96 ± 0.03	14.44 ± 0.62	1.14 ± 0.05	14.45 ± 0.54
Mix	1.29 ± 0.05	16.59 ± 1.21	1.29 ± 0.06	20.89 ± 1.47	0.95 ± 0.04	14.75 ± 0.83	1.15 ± 0.05	14.64 ± 0.50
Macrocytic	1.26 ± 0.04	15.87 ± 1.14	1.27 ± 0.04	20.50 ± 1.101	0.93 ± 0.02	14.18 ± 0.74	1.15 ± 0.03	14.55 ± 0.48
Controls	1.23 ± 0.05	15.86 ± 0.96	1.24 ± 0.06	19.63 ± 1.24	0.91 ± 0.03	13.88 ± 0.50	1.12 ± 0.04	14.64 ± 0.47
Linear vs controls	.026	.32	.012 ^b	.52	.006 ^b	.28	.41	.87
Mix vs controls	>.001 ^b	.14	.004 ^b	.004 ^b	<.001 ^b	<.001 ^b	.020 ^b	1.0
Macrocytic vs controls	.13	1.0	.55	.41	.69	.82	.25	1.0
Linear vs mix	.99	.99	.89	.97	1.0	.79	1.0	.82
Linear vs Macrocytic	.98	.44	.42	1.0	.27	.95	1.0	1.0
Mix vs macrocytic	.64	.32	.77	.93	.18	.07	1.0	.99

^a The upper 4 rows report the R₁ and R₂ values in seconds⁻¹ as the means. The lower 6 rows report the *P* values for the group comparisons performed with 1-way ANOVA and the Hochberg post hoc test.

^b *P* < .023.

Table 3: Associations between the number of GBCA administrations and relaxation rates^a

	Linear		Mixed		Macrocytic	
	Uncorrected	Corrected ^b	Uncorrected	Corrected ^c	Uncorrected	Corrected ^b
DN R ₁	0.52, <i>P</i> = .002 ^d	0.50, <i>P</i> = .005 ^d	0.57, <i>P</i> < .001 ^d	0.54, <i>P</i> < .001 ^d	0.23, <i>P</i> = .19	0.24, <i>P</i> = .16
DN R ₂	0.14, <i>P</i> = .45	0.04, <i>P</i> = .83	0.30, <i>P</i> = .006 ^d	0.17, <i>P</i> = .14	0.04, <i>P</i> = .82	0.07, <i>P</i> = .64
GP R ₁	0.51, <i>P</i> = .004 ^d	0.50, <i>P</i> = .009 ^d	0.43, <i>P</i> < .001 ^d	0.37, <i>P</i> = .002 ^d	0.16, <i>P</i> = .36	0.17, <i>P</i> = .33
GP R ₂	0.28, <i>P</i> = .14	0.26, <i>P</i> = .19	0.43, <i>P</i> < .001 ^d	0.42, <i>P</i> < .001 ^d	0.29, <i>P</i> = .10	0.29, <i>P</i> = .10
CN R ₁	0.41, <i>P</i> = .020 ^d	0.33, <i>P</i> = .07	0.45, <i>P</i> < .001 ^d	0.39, <i>P</i> = .001 ^d	0.24, <i>P</i> = .16	0.27, <i>P</i> = .11
CN R ₂	0.21, <i>P</i> = .25	0.06, <i>P</i> = .72	0.50, <i>P</i> < .001 ^d	0.36, <i>P</i> < .001 ^d	0.36, <i>P</i> = .032	0.40, <i>P</i> = .006 ^d
Thalamus R ₁	0.23, <i>P</i> = .21	0.24, <i>P</i> = .22	0.39, <i>P</i> = .001 ^d	0.41, <i>P</i> < .001 ^d	0.28, <i>P</i> = .10	0.27, <i>P</i> = .12
Thalamus R ₂	-0.2, <i>P</i> = .26	0.15, <i>P</i> = .44	0.11, <i>P</i> = .32	0.16, <i>P</i> = .17	0.10, <i>P</i> = .59	0.08, <i>P</i> = .65

^a All association results are given as β coefficients. The healthy controls (GBCA administrations: *n* = 0) are included in regression analyses for each group.

^b Corrected for age.

^c Corrected for age and number of macrocytic GBCA administrations.

^d *P* < .023.

with a higher R₁ in the DN, GP, and CN. The results for the DN and GP remained significant after correcting for the patient's age. In the mixed group, the number of linear GBCA administrations was associated with higher R₁ in all ROIs, and the results remained significant after correction for the patient's age and the number of macrocytic GBCA administrations. In the macrocytic group, no significant associations were found between the number of macrocytic GBCA administrations and R₁. The associations of GBCA administrations with relaxation values are shown in Fig 1.

Associations of GBCA Administrations with R₂ Values

In the linear group, no associations were found between the number of GBCA administrations and R₂. In the mixed group, a higher number of linear GBCA administrations was associated with higher R₂ in the DN, GP, and CN. The results for the GP and CN remained significant after correcting for the patient's age and the number of macrocytic GBCA administrations. In the macrocytic group, there was a trend toward higher R₂ in the CN, which became significant after correction for the patient's age. For the other ROIs, no significant associations were found.

Associations with Cognitive and Physical Disabilities

In terms of information-processing speed (SDMT), there were few patients with data in the linear group, explaining why only the mixed and macrocytic groups were studied. A detailed presentation of all regression results with cognitive tests for the mixed group can be found in Table 4. In the mixed group, there were several significant results and trends between higher relaxation rates and lower information-processing speed. Most notably,

higher R₁ and R₂ in the thalamus were associated lower processing speeds both before and after correction for the MS disease duration, lesion volume, and brain parenchymal fraction. Higher R₂ in the DN was also associated with lower SDMT scores before and after these corrections. In the macrocytic group, no associations were found between R₁ and R₂ values and information-processing speed (*P* = .14–.94).

In terms of verbal fluency, there were few patients with data in the linear (*n* = 4) and macrocytic (*n* = 6) groups, explaining why only the mixed group was studied. In the mixed group, higher R₁ in the CN and thalamus was associated with lower verbal fluency both before and after correction for MS disease duration, lesion volume, and brain parenchymal fraction. A similar trend was found for R₂ in the CN and GP, which, after corrections, became statistically significant. No association was found between verbal fluency and relaxation values in the other brain structures. Figure 2 illustrates the associations of R₁ and R₂ with information-processing speed and verbal fluency in the mixed group.

No significant associations were found between fatigue or EDSS scores and R₁ and R₂ values for any structure (data not shown).

DISCUSSION

In this study, we applied multiparametric MR imaging in patients with MS and healthy controls to quantitatively study changes in relaxation values and their association with GBCA administration. We have shown that our method has good repeatability and was able to detect relaxation abnormalities associated with GBCA

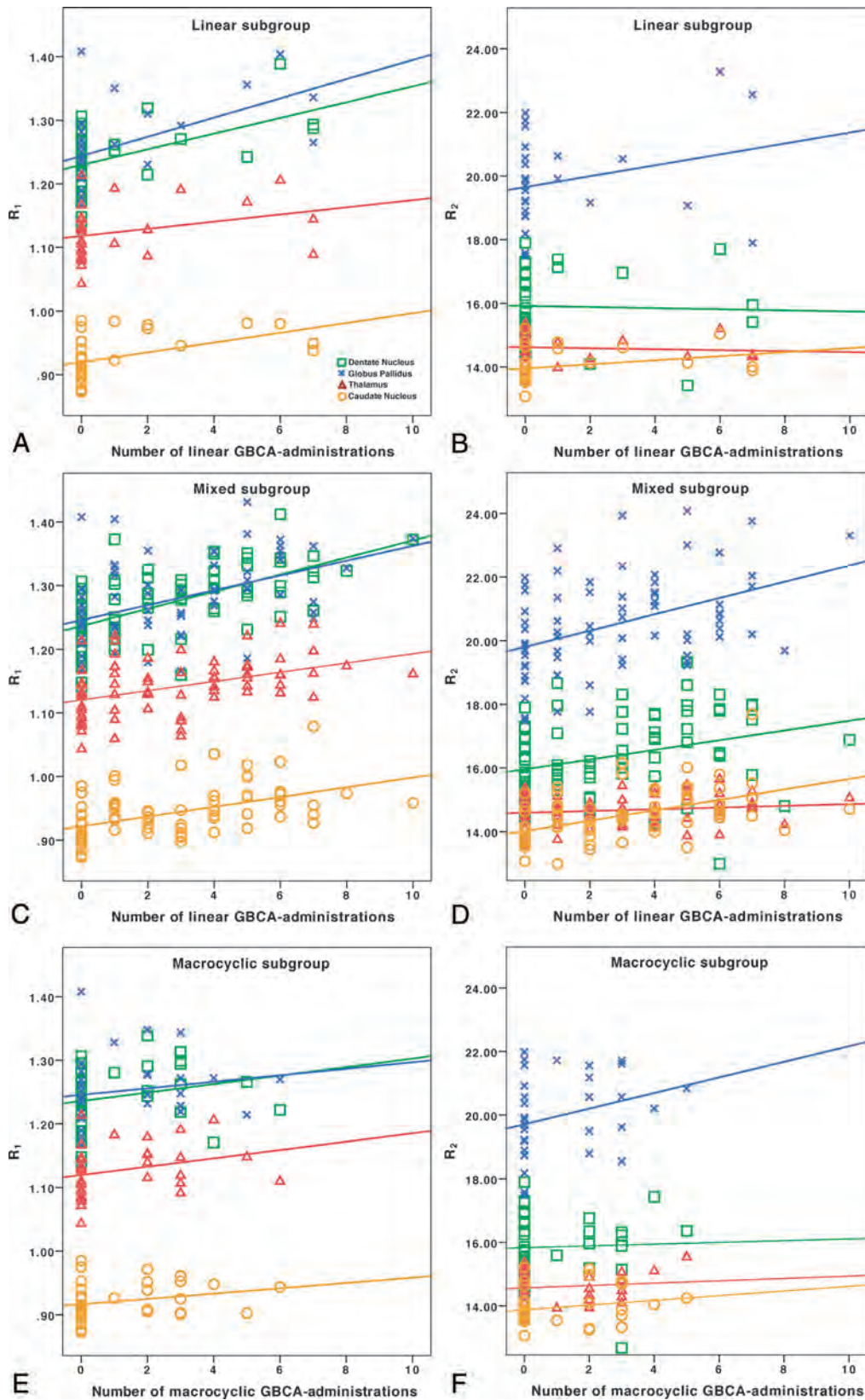


FIG 1. Associations of R_1 and R_2 with the number of GBCA administrations. In the linear group, the number of linear GBCA administrations was associated with higher R_1 (A), but not R_2 (B). In the mixed group, the number of linear GBCA administrations was associated with both higher R_1 (C) and R_2 (D). The healthy controls, who had not received any GBCA administrations, are represented in each group and included in the regression analyses. The full regression analysis results are reported in Table 3. In the macrocytic group, no significant associations were found with the number of macrocytic GBCA administrations (E and F). The dentate nucleus is represented by *green squares*; the globus pallidus, by *blue x's*; the caudate nucleus, by *orange circles*; and the thalamus, by *red triangles* with corresponding linear regression lines. The y-axis presents the relaxation rates (R_1 and R_2) in seconds⁻¹.

Table 4: Associations between relaxation rates and cognitive tests for the mixed group^a

	SDMT (n = 36)		Verbal Fluency Test (n = 17)	
	Uncorrected	Corrected ^b	Uncorrected	Corrected ^b
DN R ₁	-0.34, P = .04	-0.35, P = .028	-0.38, P = .18	-0.36, P = .13
DN R ₂	-0.41, P = .012 ^c	-0.37, P = .014 ^c	-0.06, P = .82	-0.04, P = .87
GP R ₁	-0.32, P = .07	-0.29, P = .13	-0.43, P = .16	-0.31, P = .26
GP R ₂	-0.18, P = .32	-0.12, P = .51	-0.37, P = .23	-0.64, P = .003 ^c
CN R ₁	-0.46, P = .005 ^c	-0.34, P = .05	-0.63, P = .009 ^c	-0.68, P = .003 ^c
CN R ₂	-0.39, P = .018 ^c	-0.21, P = .29	-0.52, P = .04	-0.89, P = .006 ^c
Thalamus R ₁	-0.45, P = .005 ^c	-0.38, P = .014 ^c	-0.59, P = .017 ^c	-0.50, P = .020 ^c
Thalamus R ₂	-0.42, P = .011 ^c	-0.45, P = .002 ^c	-0.44, P = .09	-0.34, P = .10

^a All association results are given as β coefficients.

^b Corrected for disease duration, lesion volume, and brain parenchymal fraction.

^c $P < .023$.

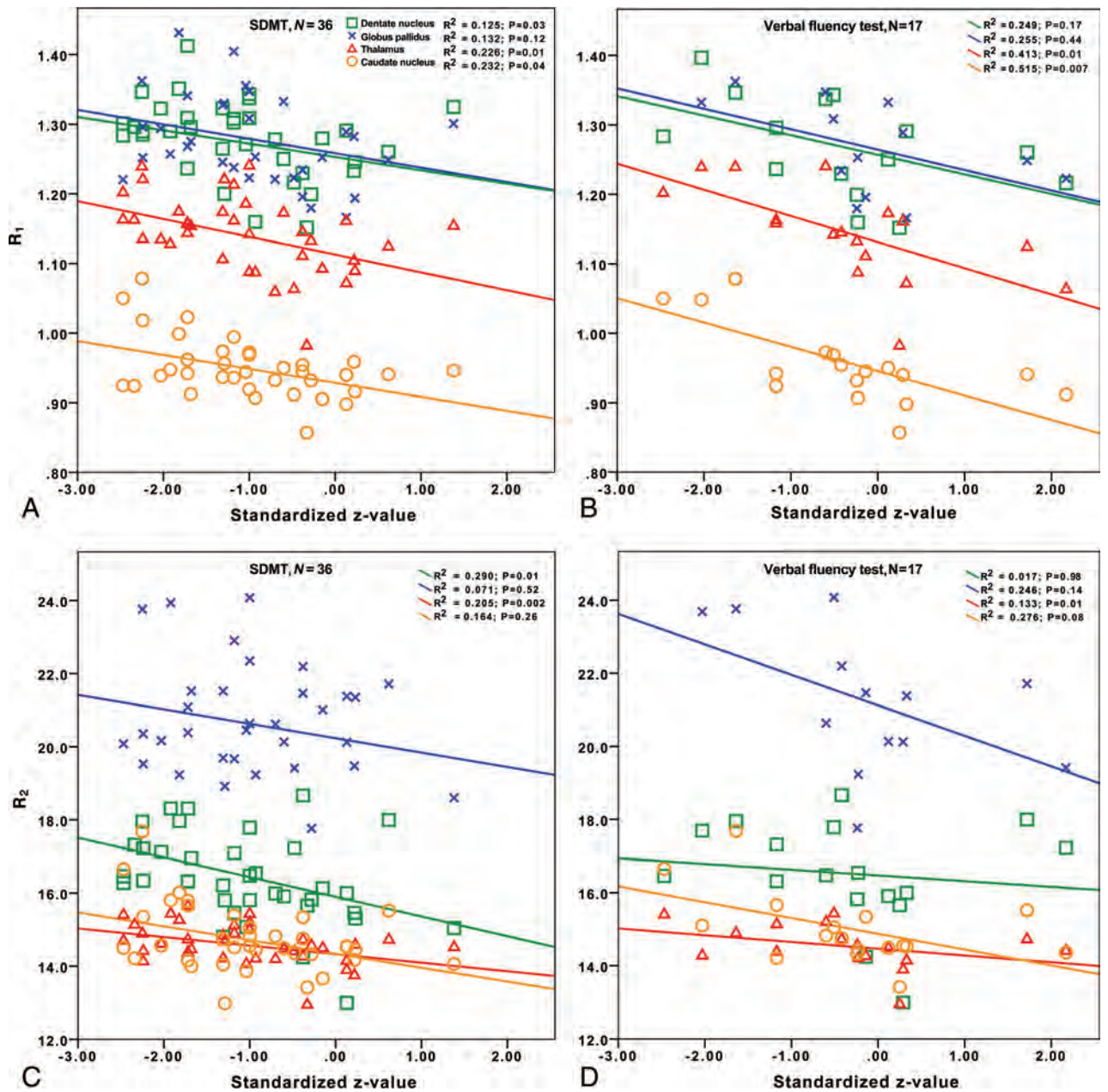


FIG 2. Associations of R₁ (A and B) and R₂ (C and D) with information-processing speed and verbal fluency in the mixed group. Please refer to Table 4 for the regression analyses corresponding to this figure.

administrations not only in R_1 but also in R_2 . We have also provided tentative results regarding associations between relaxation values and cognitive performance in MS.

We found that patients with MS receiving linear GBCAs had higher R_1 in the DN, GP, and CN (and in the mixed MS group, also the thalamus) compared with healthy controls and that the number of administrations of linear, but not macrocyclic, GBCAs was associated with higher R_1 in all studied brain regions, suggesting a dose-dependent association. With regard to the high R_1 in at least the DN, increased T1 signal in the DN has previously been associated with MS progression²⁹ and could thus be partly due to iron deposits related to neurodegeneration.³⁰

Furthermore, the R_2 in the GP and CN was also higher in the mixed group than in healthy controls, a finding indicating that T2 relaxation is also affected by gadolinium retention. It is also known that chelates that bind to macromolecules cause higher relaxivity.¹² It is, however, unclear how much the transversal relaxation is affected by retained gadolinium that is bound to different macromolecules or retained in other species (rather than chelated in GBCAs).¹² This problem highlights the need to also study T2 effects in the context of gadolinium retention.

The European Medicines Agency has recently decided to suspend the use of several linear types of GBCA, while the US Food and Drug Administration instead merely recommended more precautionary use, particularly of linear GBCAs.^{13,14} In line with the results of most previous studies, we found no associations between the number of administrations of the macrocyclic agent gadoterate meglumine (Dotarem) and the relaxation rates. Macrocyclic agents have histopathologically been shown to be retained to a lower degree than linear GBCAs and have previously shown weaker or no associations in imaging studies.^{2,3,11,31,32} However, the lack of significant associations within the macrocyclic group might also be caused by the small number of patients ($n = 15$) and the relatively few administrations of macrocyclic GBCAs (median, 3) in the current study. Meanwhile, significant associations were found in the linear group, which was even smaller ($n = 11$), illustrating that the methodology used in this study is sensitive in picking up signal changes related to previous GBCA administrations and that the lack of significant results in the macrocyclic group may indeed reflect differences in the degree of retention between linear and macrocyclic GBCAs.

A few industry-sponsored studies on rodents have shown that retained gadolinium from gadodiamide has a time-dependent partial clearance from the brain of healthy rats, which leads to a decrease in T1 intensity, especially during the first month after the GBCA administration.^{2,33} One of these animal studies also showed, by using histopathologic measurements in the DN, a higher degree of gadolinium clearance for gadoterate meglumine compared with gadodiamide.² However, the current finding of remaining gadolinium retention after the initial washout period is in line with a previous study in which high T1 hyperintensities on conventional MR imaging remained even 9 years after the last administrations of linear GBCA.¹⁷ If there is a continued clearance of gadolinium with time, it would have been unfavorable to the macrocyclic GBCAs in our study because there was a shorter time since the last GBCA administration in the macrocyclic group

(median, 8 months) in comparison with the mixed (median, 12 months) and linear groups (median, 52 months).

In line with a previous study in which a separate cohort of patients with MS was studied retrospectively with semiquantitative T1-weighted intensity ratios,¹⁷ significant associations were found in the current study between detected MR imaging changes and lower verbal fluency performance. Furthermore, in this study, we also found associations between lower information-processing speed and higher relaxation rates in the DN and thalamus, with similar tendencies also in the GP and CN. Nevertheless, the associations between relaxation rates and cognitive functioning must be interpreted with caution because the MS pathology may confound the results, and although we corrected for the MS disease progression, brain parenchymal fraction, and lesion volume it might not have been sufficient to counteract such confounds. For example, MS is a disease with varying lesion topography (including cortical lesions), numerous treatment regimens, and differences in cognitive reserves among patients, which might also need to be taken into account.^{34,35}

Information-processing speed is also one of the most affected cognitive domains in MS, making it even harder to conclude any causality to GBCA exposure.³⁴ Designing prospective studies exploring such associations should, therefore, focus on other patient groups exposed to multiple GBCA administrations, with fewer confounders related to the clinical outcome variables, such as in a previous study performed in patients with Crohn disease.³⁶ In line with a recent study,³⁷ we did not find any association between gadolinium exposure and physical disability in MS. This suggests that future studies should continue to focus on cognitive aspects.

Limitations of the study are mainly related to the results of the MS cohort possibly being confounded by MS itself. The investigative possibilities of the study are also limited by its cross-sectional and noninterventional design, in which the stratification of the groups (based on the type of administered GBCA) is not randomized. There were also relatively few patients who had undergone neuropsychological testing. There are, however, also strengths to the study. By applying a quantitative approach with the same MR imaging scanner, we avoided methodologic limitations of many previous studies with reliance on conventional MR imaging and semiquantitative signal intensity ratios, which may have been due to several risks for confounders such as the diversity of MR imaging parameters and equipment as well as the need for a reference region, which may, in itself, be affected by gadolinium retention.⁹

CONCLUSIONS

T1 and T2 relaxometry can be used to robustly and quantitatively study MR imaging changes related to administration of GBCAs, removing the need for a reference region that may, in itself, be confounded by retained gadolinium. The number of linear, but not macrocyclic, GBCA administrations was associated with high R_1 in all investigated brain structures and R_2 in the GP and CN in MS. Higher relaxivity in patients with MS receiving linear GBCAs was associated with a lower information-processing speed and verbal fluency in some brain regions, but not with motor function or fatigue. These findings must, however, be interpreted with care because they may be confounded by cognitive decline caused by

MS. The findings do, however, encourage future studies to further explore possible negative clinical effects of retained gadolinium, especially in regard to cognitive domains and exposure to linear GBCAs.

Disclosures: Yngve Forslin—RELATED: Grant: Karolinska Institutet and Stockholm County Council ALF grant.* Juha Martola—UNRELATED: Payment for Lecture: Santen. Sten Fredrikson—UNRELATED: Payment for Lectures Including Service on Speakers Bureaus: Merck, Novartis, Roche, Sanofi. Tobias Granberg—RELATED: Grant: ALF grant from Stockholm City Council and postdoctoral research fellowship from Swedish Society for Medical Research*; UNRELATED: Employment: Karolinska University Hospital. *Money paid to institution.

REFERENCES

1. Kanda T, Ishii K, Kawaguchi H, et al. **High signal intensity in the dentate nucleus and globus pallidus on unenhanced T1-weighted MR images: relationship with increasing cumulative dose of a gadolinium-based contrast material.** *Radiology* 2014;270:834–41 CrossRef Medline
2. Robert P, Fingerhut S, Factor C, et al. **One-year retention of gadolinium in the brain: comparison of gadodiamide and gadoterate meglumine in a rodent model.** *Radiology* 2018;288:424–33 CrossRef Medline
3. Radbruch A, Weberling LD, Kieslich PJ, et al. **Gadolinium retention in the dentate nucleus and globus pallidus is dependent on the class of contrast agent.** *Radiology* 2015;275:783–91 CrossRef Medline
4. Jaulent P, Hannoun S, Kocevar G, et al. **Weekly enhanced T1-weighted MRI with gadobutrol injections in patients with MS: is there a signal intensity increase in the dentate nucleus and the globus pallidus?** *Eur J Radiol* 2018;105:204–08 CrossRef Medline
5. Bjørnerud A, Vatnehol SA, Larsson C, et al. **Signal enhancement of the dentate nucleus at unenhanced MR imaging after very high cumulative doses of the macrocyclic gadolinium-based contrast agent gadobutrol: an observational study.** *Radiology* 2017;285:434–44 CrossRef Medline
6. Rossi Espagnet MC, Bernardi B, Pasquini L, et al. **Signal intensity at unenhanced T1-weighted magnetic resonance in the globus pallidus and dentate nucleus after serial administrations of a macrocyclic gadolinium-based contrast agent in children.** *Pediatr Radiol* 2017;47:1345–52 CrossRef Medline
7. Splendiani A, Perri M, Marsecano C, et al. **Effects of serial macrocyclic-based contrast materials gadoterate meglumine and gadobutrol administrations on gadolinium-related dentate nuclei signal increases in unenhanced T1-weighted brain: a retrospective study in 158 multiple sclerosis (MS) patients.** *Radiol Med* 2018;123:125–34 CrossRef Medline
8. Radbruch A, Quattrocchi CC. **Interpreting signal-intensity ratios without visible T1 hyperintensities in clinical gadolinium retention studies.** *Pediatr Radiol* 2017;47:1688–89 CrossRef Medline
9. McDonald RJ, McDonald JS, Kallmes DF, et al. **Intracranial gadolinium deposition after contrast-enhanced MR imaging.** *Radiology* 2015;275:772–82 CrossRef Medline
10. Tedeschi E, Palma G, Canna A, et al. **In vivo dentate nucleus MRI relaxometry correlates with previous administration of gadolinium-based contrast agents.** *Eur Radiol* 2016;26:4577–84 CrossRef Medline
11. Müller A, Jurcoane A, Mädler B, et al. **Brain relaxometry after macrocyclic Gd-based contrast agent.** *Clin Neuroradiol* 2017;27:459–68 CrossRef Medline
12. Rohrer M, Bauer H, Mintorovitch J, et al. **Comparison of magnetic properties of MRI contrast media solutions at different magnetic field strengths.** *Invest Radiol* 2005;40:715–24 CrossRef Medline
13. European Medicines Agency. EMA's final opinion confirms restrictions on use of linear gadolinium agents in body scans. 625317. July 21, 2017. <https://www.ema.europa.eu/en/news/emas-final-opinion-confirms-restrictions-use-linear-gadolinium-agents-body-scans>. Accessed January 29, 2019
14. US Food and Drug Administration. **FDA Drug Safety Communication: FDA warns that gadolinium-based contrast agents (GBCAs) are retained in the body; requires new class warnings.** 2017. <https://www.fda.gov/drugs/drug-safety-and-availability/fda-drug-safety-communication-fda-warns-gadolinium-based-contrast-agents-gbcas-are-retained-body>. Accessed February 15, 2019
15. Welk B, McArthur E, Morrow SA, et al. **Association between gadolinium contrast exposure and the risk of parkinsonism.** *JAMA* 2016;316:96–98 CrossRef Medline
16. McDonald RJ. **No evidence gadolinium causes neurologic harm.** *RSNA 2017 Daily Bulletin*. December 1, 2017. <https://rsna2017.rsna.org/dailybulletin/index.cfm?pg=17fri10>. Accessed September 5, 2018
17. Forslin Y, Shams S, Hashim F, et al. **Retention of gadolinium-based contrast agents in multiple sclerosis: retrospective analysis of an 18-year longitudinal study.** *AJNR Am J Neuroradiol* 2017;38:1311–16 CrossRef Medline
18. Vågberg M, Axelsson M, Birgander R, et al. **Guidelines for the use of magnetic resonance imaging in diagnosing and monitoring the treatment of multiple sclerosis: recommendations of the Swedish Multiple Sclerosis Association and the Swedish Neuroradiological Society.** *Acta Neurol Scand* 2017;135:17–24 CrossRef Medline
19. Warntjes JB, Leinhard OD, West J, et al. **Rapid magnetic resonance quantification on the brain: optimization for clinical usage.** *Magn Reson Med* 2008;60:320–29 CrossRef Medline
20. Mängeat G, Ouellette R, Warntjes JBM, et al. **Accuracy and precision of Synthetic MRI.** In: *Proceedings of the Joint Meeting of the International Society for Magnetic Resonance in Medicine and the European Society for Magnetic Resonance in Medicine and Biology*, Paris, France. June 16–21, 2018
21. Vågberg M, Lindqvist T, Ambarki K, et al. **Automated determination of brain parenchymal fraction in multiple sclerosis.** *AJNR Am J Neuroradiol* 2013;34:498–504 CrossRef Medline
22. Granberg T, Uppman M, Hashim F, et al. **Clinical feasibility of Synthetic MRI in multiple sclerosis: a diagnostic and volumetric validation study.** *AJNR Am J Neuroradiol* 2016;37:1023–29 CrossRef Medline
23. Schmidt P, Gaser C, Arsic M, et al. **An automated tool for detection of FLAIR-hyperintense white-matter lesions in multiple sclerosis.** *Neuroimage* 2012;59:3774–83 CrossRef Medline
24. Ashburner J, Friston KJ. **Unified segmentation.** *Neuroimage* 2005;26:839–51 CrossRef Medline
25. Errante Y, Cirimele V, Mallio CA, et al. **Progressive increase of T1 signal intensity of the dentate nucleus on unenhanced magnetic resonance images is associated with cumulative doses of intravenously administered gadodiamide in patients with normal renal function, suggesting dechelation.** *Invest Radiol* 2014;49:685–90 CrossRef Medline
26. Yushkevich PA, Piven J, Hazlett HC, et al. **User-guided 3D active contour segmentation of anatomical structures: significantly improved efficiency and reliability.** *Neuroimage* 2006;31:1116–28 CrossRef Medline
27. Jenkinson M, Beckmann CF, Behrens TE, et al. **FSL.** *Neuroimage* 2012;62:782–90 CrossRef Medline
28. Benjamini Y, Hochberg Y. **Controlling the false discovery rate: a practical and powerful approach to multiple testing.** *Journal of the Royal Statistical Society. Series B: Methodological* 1995;57:289–300 CrossRef
29. Roccatagliata L, Vuolo L, Bonzano L, et al. **Multiple sclerosis: hyperintense dentate nucleus on unenhanced T1-weighted MR images is associated with the secondary progressive subtype.** *Radiology* 2009;251:503–10 CrossRef Medline
30. Bond KM, Brinjikji W, Eckel LJ, et al. **Dentate update: imaging features of entities that affect the dentate nucleus.** *AJNR Am J Neuroradiol* 2017;38:1467–74 CrossRef Medline
31. Robert P, Lehericy S, Grand S, et al. **T1-weighted hypersignal in the deep cerebellar nuclei after repeated administrations of gadolinium-based contrast agents in healthy rats: difference between linear**

- and macrocyclic agents. *Invest Radiol* 2015;50:473–80 CrossRef Medline
32. Jost G, Frenzel T, Boyken J, et al. **Long-term excretion of gadolinium-based contrast agents: linear versus macrocyclic agents in an experimental rat model.** *Radiology* 2019;290:340–48 CrossRef Medline
33. Smith AP, Marino M, Roberts J, et al. **Clearance of gadolinium from the brain with no pathologic effect after repeated administration of gadodiamide in healthy rats: an analytical and histologic study.** *Radiology* 2017;282:743–51 CrossRef Medline
34. Chiaravalloti ND, DeLuca J. **Cognitive impairment in multiple sclerosis.** *Lancet Neurol* 2008;7:1139–51 CrossRef Medline
35. Thompson AJ, Banwell BL, Barkhof F, et al. **Diagnosis of multiple sclerosis: 2017 revisions of the McDonald criteria.** *Lancet Neurol* 2018;17:162–73 CrossRef Medline
36. Mallio CA, Piervincenzi C, Gianolio E, et al. **Absence of dentate nucleus resting-state functional connectivity changes in nonneurological patients with gadolinium-related hyperintensity on T1-weighted images.** *J Magn Reson Imaging* 2019 Jan 25. [Epub ahead of print] CrossRef Medline
37. Coccozza S, Pontillo G, Lanzillo R, et al. **MRI features suggestive of gadolinium retention do not correlate with Expanded Disability Status Scale worsening in multiple sclerosis.** *Neuroradiology* 2019; 61:155–62 CrossRef Medline

Signal Hyperintensity on Unenhanced T1-Weighted Brain and Cervical Spinal Cord MR Images after Multiple Doses of Linear Gadolinium-Based Contrast Agent

G. Barisano, B. Bigjahan, S. Metting, S. Cen, L. Amezcua, A. Lerner, A.W. Toga, and M. Law



ABSTRACT

BACKGROUND AND PURPOSE: The clinical implications of gadolinium deposition in the CNS are not fully understood, and it is still not known whether gadolinium tends to be retained more in the brain compared with the spinal cord. In this study, we assessed the effects of linear gadolinium-based contrast agents on the T1 signal intensity of 3 cerebral areas (dentate nucleus, globus pallidus, and the less studied substantia nigra) and the cervical spinal cord in a population of patients with MS.

MATERIALS AND METHODS: A single-center population of 100 patients with MS was analyzed. Patients underwent 2–16 contrast-enhanced MRIs. Fifty patients received ≤ 5 linear gadolinium injections, and 50 patients had ≥ 6 injections: Fifty-two patients had both Gd-DTPA and gadobenate dimeglumine injections, and 48 patients received only gadobenate dimeglumine. A quantitative analysis of signal intensity changes was independently performed by 2 readers on the first and last MR imaging scan. The globus pallidus-to-thalamus, substantia nigra-to-midbrain, dentate nucleus-to-middle cerebellar peduncle, and the cervical spinal cord-to-pons signal intensity ratios were calculated.

RESULTS: An increase of globus pallidus-to-thalamus (mean, $+0.0251 \pm 0.0432$; $P < .001$), dentate nucleus-to-middle cerebellar peduncle (mean, $+0.0266 \pm 0.0841$; $P = .002$), and substantia nigra-to-midbrain (mean, $+0.0262 \pm 0.0673$; $P < .001$) signal intensity ratios after multiple administrations of linear gadolinium-based contrast agents was observed. These changes were significantly higher in patients who received ≥ 6 injections ($P < .001$) and positively correlated with the number of injections and the accumulated dose of contrast. No significant changes were detected in the spinal cord (mean, $+0.0008 \pm 0.0089$; $P = .400$).

CONCLUSIONS: Patients with MS receiving ≥ 6 linear gadolinium-based contrast agent injections showed a significant increase in the signal intensity of the globus pallidus, dentate nucleus, and substantia nigra; no detectable changes were observed in the cervical spinal cord.

ABBREVIATIONS: CP = middle cerebellar peduncle; CS = cervical spinal cord; DN = dentate nucleus; EDSS = Expanded Disability Status Scale; GBCA = gadolinium-based contrast agent; Gd-BOPTA = gadobenate dimeglumine; GP = globus pallidus; L-GBCA = linear gadolinium-based contrast agent; SI = signal intensity; SN = substantia nigra

In the past 4 years, a number of publications have demonstrated a dose-dependent relationship between the administration of gadolinium-based contrast agents (GBCAs) and high signal intensity (SI) on unenhanced T1-weighted images in the dentate

nucleus (DN) and globus pallidus (GP).^{1–4} Initially, 2 research groups proposed that these hyperintensities were a consequence of cerebral irradiation⁵ or the development of the secondary-progressive subtype of MS,⁶ but GBCA administration was not considered in either investigation.^{5,6} Further postmortem studies verified the presence of retained gadolinium not only in the DN and GP but also in other regions such as CSF, bone, and skin.^{7–10} However, the clinical implications of gadolinium retention and the possibility of gadolinium deposition in other human body areas remain unclear. Additionally, the mechanisms responsible for the gadolinium deposition in the CNS are not fully understood, and it is still not known whether gadolinium tends to be retained more in the brain compared with the spinal cord.¹¹

In this retrospective study including a large cohort of patients with MS with normal renal function who underwent multiple

Received March 22, 2019; accepted after revision June 6.

From the Department of Radiology (G.B., B.B., S.M., S.C., A.L., M.L.), Stevens Neuroimaging and Informatics Institute (G.B., B.B., A.W.T., M.L.), and Department of Neurology (L.A.), Keck School of Medicine, University of Southern California, Los Angeles, California.

Giuseppe Barisano and Bavrina Bigjahan contributed equally as co-first authors.

Please address correspondence to Giuseppe Barisano, MD, Laboratory of Neuro Imaging, Stevens Neuroimaging and Informatics Institute, Keck School of Medicine, University of Southern California, 2025 Zonal Ave, Los Angeles, CA 90033; e-mail: giuseppe.barisano@loni.usc.edu; @g_barisano; @USCneurorads; @USCLONI

Indicates article with supplemental on-line photos.

<http://dx.doi.org/10.3174/ajnr.A6148>

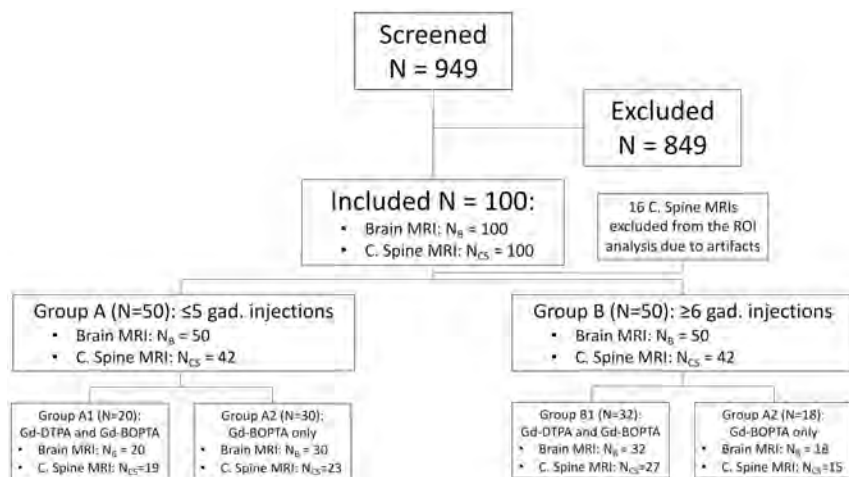


FIG 1. Flow diagram of patients screened and included in the study. N indicates number of patients.

contrast-enhanced MRIs with linear gadolinium-based contrast agent (L-GBCA), we analyzed SI changes not only in the DN and GP, which have been extensively studied in previous investigations, but also in the substantia nigra (SN) and cervical spinal cord (CS), 2 CNS structures in which potential gadolinium deposits in patients with MS have not been investigated. Clinical factors have been integrated in the analysis as well.

MATERIALS AND METHODS

Study Population

This retrospective Health Insurance Portability and Accountability Act–compliant study was approved by our institutional review board with a waiver of informed consent.

The clinical charts of patients with MS treated between October 2005 and April 2018 were reviewed; collected information included age, sex, race, symptoms of MS, Expanded Disability Status Scale (EDSS) assessed by a qualified MS neurologist, comorbidities, medications and disease-modifying therapy, the interval between each contrast-enhanced MR imaging, L-GBCA type, and the number of injections and the dose (milliliters) administered between the first and last scan. Because the ROIs were placed on precontrast T1-weighted images, the injections performed during the last MR imaging session were not counted for the analysis.

Inclusion criteria were the following: 1) a relapsing-remitting MS diagnosis according to the McDonald criteria; 2) first and last contrast-enhanced MR imaging scans of the brain and the cervical spine performed at our institution; and 3) injections of exclusively L-GBCA.

Exclusion criteria included a history of the following: 1) brain irradiation/chemotherapy; 2) brain hemorrhage/stroke; 3) intracranial infection, edema, tumor, or other diseases affecting cerebellum, pons, midbrain, basal ganglia, thalamus, or CS; 4) abnormal renal function (ie, an estimated glomerular filtration rate of <60 mL/min/1.73 m²); 5) abnormal hepatic function (ie, a total bilirubin level of >2 mg/dL); 6) conditions associated with iron deposition in the brain and/or T1-weighted hyperintensity in the deep gray nuclei; and 7) the presence of lesions in the C1–C5 level of the CS on the sagittal midline plane.

After the analysis of 949 medical charts, clinical and radiologic data of 100 patients with relapsing-remitting MS (67 women and 33 men; mean age, 41.6 ± 11.8 years) conforming to eligibility criteria were collected. The population was divided in 2 groups (Fig 1): The population of group A had ≤ 5 L-GBCA injections; group B had ≥ 6 . In each group, we defined 2 subgroups: subgroups A1 and B1 included patients who had both Gd-DTPA and gadobenate dimeglumine (Gd-BOPTA) injections; patients in subgroups A2 and B2 received only Gd-BOPTA. Demographic and clinical data for each group and subgroup are reported in Table 1

MR Imaging Protocol

MR images were obtained on the same 3T scanner (Signa HD; GE Healthcare, Milwaukee, Wisconsin). Unenhanced T1-weighted turbo spin-echo sequences of the brain and cervical spine were performed (TR = 500–650 ms; TE = 9–11 ms; section thickness = 3 mm; matrix size = 192×256). Standard dosing of 0.1 mmol/kg of body weight was targeted for GBCA intravenous administration.

Imaging Data Analysis

The first and last brain and cervical spine MR imaging scans were analyzed on ImageJ software (National Institutes of Health, Bethesda, Maryland). ROIs were manually drawn to measure the SI on unenhanced T1-weighted images. After coregistration of the first and last MR imaging scans, the ROI size and coordinates of the first scan were correspondingly transposed on the last one, to minimize the possibility of detecting SI changes related to the placement of ROIs in different areas. Additionally, all the measurements were independently performed by 2 readers, twice, with a 4-month interval between the 2 analyses: therefore, each ROI was measured 4 times, and the concordance between each measure was computed. Readers were blinded to the clinical data.

The ROIs in the brain included the GP and thalami (same axial slice), SN and midbrain (same axial slice), DN and middle cerebellar peduncles (CP) (same axial slice). When the detection of the GP, SN, and DN was inconclusive, the equivalent slice on T2WI was used for the correct ROI placement. The average SI of the bilateral structures (GP, thalamus, SN, DN, and CP) was computed; the obtained values were used in the successive calculations of GP-to-thalamus, SN-to-midbrain, and DN-to-CP SI ratios.

Regarding the spinal cord, rectangular ROIs covering the whole midline section of the spinal cord were placed at the C1, C2, C3, C4, and C5 levels on the unenhanced T1-weighted sagittal midline plane. The C6 and C7 levels were excluded from the analysis due to frequent artifacts in the lower CS. On the same slice, another ROI was placed on the pons. The CS-to-pons SI ratio was

Table 1: Demographic and clinical data in the study population

Parameters	Group A (≤ 5 CE-MRI)		Group B (≥ 6 CE-MRI)	
	Subg. A1 (Gd-DTPA+Gd-BOPTA)	Subg. A2 (Gd-BOPTA)	Subg. B1 (Gd-DTPA+Gd-BOPTA)	Subg. B2 (Gd-BOPTA)
No. of patients	50		50	
Age (mean) (yr)	20	30	32	18
	42.8 \pm 11.35	43.7 \pm 12.6	40.3 \pm 12.12	39.9 \pm 12.3
Sex (M/F)	41.6 \pm 9.34	17/33	40.5 \pm 12.2	16/34
EDSS first MRI (mean/median)	8/12	9/21	9/23	7/11
	1.8/1	1.6/1	1.6/1	1.6/1
EDSS last MRI (mean/median)	2.2/0.5	1.6/1	1.5/1	1.6/1
	1.9/1	1.6/1	1.9/1.5	2.2/1.5
DMT	2.3/1.5	43	42	2.7/2.3
Mean interval between GBCA administrations (mo)	15	28	26	16
	11.8 \pm 6.28	11.2 \pm 5.25	9.2 \pm 2.22	9.6 \pm 2.33
No. injections of L-GBCA (mean) (median) (range)	12.6 \pm 7.64	3.6 \pm 1.43, 4, 1–5	9.0 \pm 2.17	8.2 \pm 2.25, 7, 6–15
	3.4 \pm 1.50, 4, 1–5	3.7 \pm 1.39, 4, 1–5	8.9 \pm 2.41, 9, 6–15	7 \pm 1.24, 7, 6–10
Accumulated dose of L-GBCA (mean) (mL)	52.0 \pm 22.76	52.5 \pm 21.63	121.4 \pm 38.69	102.5 \pm 25.16

Note:—CE indicates contrast-enhanced; Subg., subgroup; DMT, disease-modifying therapy.

calculated by dividing the average signal of the 5 ROIs located in the CS by the signal of the pons.

Statistical Analysis

Analyses were conducted using the Statistical Package for the Social Sciences, Version 24.0 (IBM, Armonk, New York). Statistical significance was defined as $P \leq .05$, after adjustments according to the Benjamini-Hochberg procedure.

The Lin concordance was used to test the interobserver agreement between the 2 readers' measurements.¹²

A 1-sample t test was performed to assess whether the differences of EDSS, GP-to-thalamus, SN-to-midbrain, DN-to-CP, and CS-to-pons SI ratios between the first and last scan as well as the differences of all SI ratios between the first and second quantitative analyses were significantly different from zero.

Independent-samples t tests were used to evaluate whether differences of EDSS, GP-to-thalamus, SN-to-midbrain, DN-to-CP, and CS-to-pons SI ratios between the groups and subgroups were statistically significant. SI ratios of the first and second quantitative analyses were tested as well.

The following clinical factors were tested with multiple linear regression analyses using the changes of SI ratios between the first and last MR imaging scans as the predictive variable: age, sex, race, EDSS, disease-modifying therapy, mean interval between each contrast-enhanced MR imaging, type of L-GBCA, and the number of injections. Finally, correlation analyses were performed to test which variables had a significant influence on the SI differences.

RESULTS

Clinical Analysis

The mean and median EDSS scores were 1.7 and 1.0 at the first MR imaging examination, and 2.0 and 1.0 at the last (mean age, 46.4 \pm 11.8 years), respectively. Thirteen patients had worsening of EDSS scores at the last contrast-enhanced MR imaging compared with the first one, while EDSS scores remained stable in 87 patients. The difference of EDSS scores between the first and last MR imaging was not significant in patients receiving only Gd-BOPTA compared with patients who had been injected with both

Gd-BOPTA and Gd-DTPA ($P = .983$). The interval between the first and last contrast-enhanced MR imaging, the number of injections, the accumulated dose of L-GBCA, and the increase in SI in the DN showed a significant positive correlation with EDSS worsening (Spearman $\rho = 0.276$, $P = .005$; Spearman $\rho = 0.258$, $P = .010$; Spearman $\rho = 0.299$, $P = .003$; and Spearman $\rho = 0.196$, $P = .050$, respectively). The type of L-GBCA was not significantly associated with the increased EDSS score (Spearman $\rho = 0.062$, $P = .540$). At the time of the first MR imaging, 85 patients were being treated with disease-modifying therapy. In most cases, glatiramer acetate and natalizumab were prescribed (27 and 25 cases, respectively); other disease-modifying therapies in our cohort included teriflunomide, alemtuzumab, fingolimod, interferon β -1a, interferon β -1b, and dimethyl fumarate. In 48 patients, the disease-modifying therapy was not switched during the interval between the first and last MR imaging scans.

Patients underwent 2–16 contrast-enhanced MRIs (mean, 6.9; median, 6.5). The mean and median follow-ups between the first and last MR imaging examinations were at 58 and 56 months, respectively. The mean and median intervals between each contrast-enhanced MR imaging scan were 10.5 and 9.5 months, respectively.

The total number of injections was 588 (Gd-BOPTA in 488 cases, Gd-DTPA in 100 cases). The average number of injections per patient was 6 (median, 5.5; range, 1–15), with means of 72.29 mL of Gd-BOPTA and 14.64 mL of Gd-DTPA injected from the first to the last scan.

Radiologic Analysis: Brain

Interobserver agreement was substantial for all structures evaluated (Lin concordance correlation coefficient, 0.974; 95% CI, 0.972–0.976).

The GP-to-thalamus, SN-to-midbrain, and DN-to-CP SI ratio differences between the first and last MR imaging scans in our population were significantly higher than 0 ($P < .001$, $P < .001$, and $P = .002$, respectively), with mean values of $+0.0251 \pm 0.0432$ (95% CI, 0.0165–0.0336), $+0.0262 \pm 0.0673$ (95% CI, 0.0128–0.0395), and $+0.0266 \pm 0.0841$

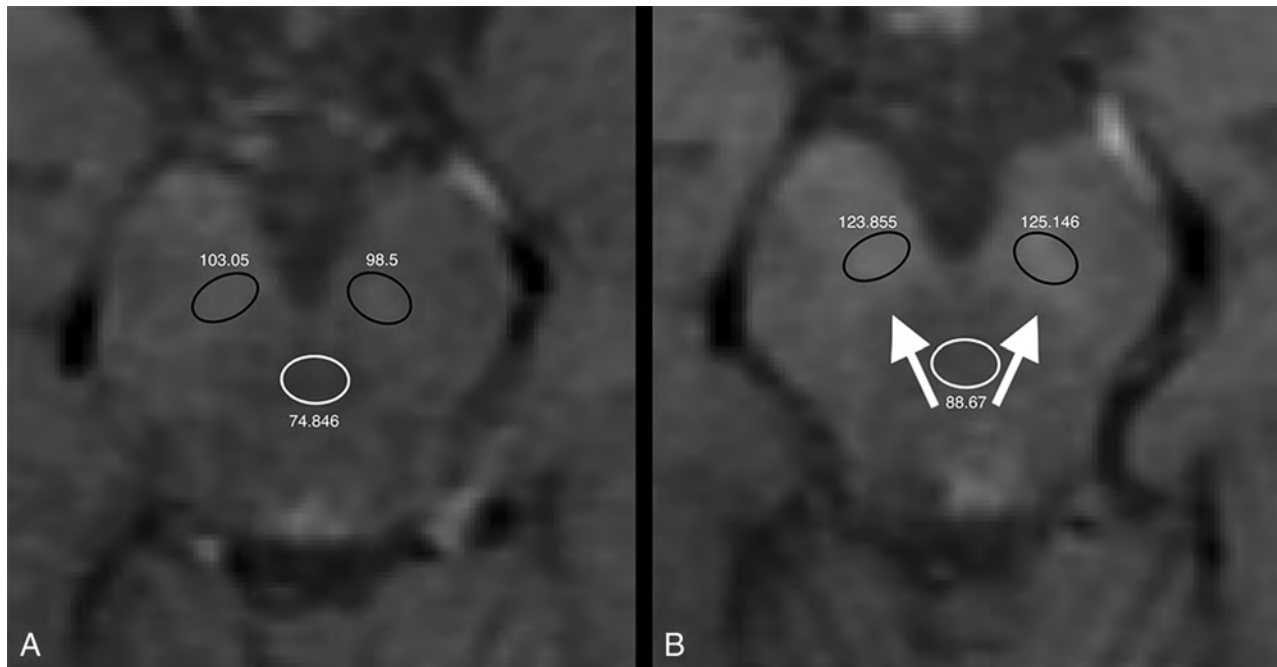


FIG 2. Unenhanced axial T1-weighted images at the first (A) and seventh (B) contrast-enhanced MR imaging of a 26-year-old man with relapsing-remitting multiple sclerosis treated with glatiramer acetate. Absolute numbers of signal intensity measurements are reported for each ROI (black circles indicate the substantia nigra ROIs; white circles, the midbrain ROIs). Increased signal intensity in the substantia nigra at the last MR imaging scan is shown (white arrows). TR = 500 ms; TE = 9 ms; section thickness = 3 mm; matrix = 192 × 256.

(95% CI, 0.0099–0.0432), respectively (Fig 2 and On-line Figs 1–3).

In patients who had ≥ 6 L-GBCA injections, the difference in SI ratios between the first and last MR imaging scans was statistically significant for the GP ($P < .001$), SN ($P < .001$), and DN ($P = .001$), but it was not significant in patients with ≤ 5 injections ($P = .059$, $P = .572$, and $P = .821$, respectively) (Fig 3). These differences were also significantly higher in patients who had ≥ 6 injections compared with patients with ≤ 5 injections ($P < .001$, $P < .001$, and $P < .001$, respectively).

Patients who were injected with only Gd-BOPTA (subgroups A2 + B2, $n = 48$) from the first to the last scan had a significantly lower increase of the SN-to-midbrain SI ratio (mean increase, $+0.0103 \pm 0.0512$; $P = .023$), compared with patients who had both Gd-DTPA and Gd-BOPTA injections (subgroups A1 + B1, $n = 52$; mean increase, $+0.0408 \pm 0.0769$). However, in a separate analysis of groups A and B, the differences in GP-to-thalamus, SN-to-midbrain, and DN-to-CP SI ratios between the 2 subgroups were not significant (A1 compared with A2, $P = .62$, $P = .58$, and $P = .65$, respectively; B1 compared with B2, $P = .33$, $P = .17$, and $P = .47$, respectively).

Three different multiple linear regression analyses were performed to test the relationship between clinical data and changes in the GP-to-thalamus, SN-to-midbrain, and DN-to-CP SI ratios. The results are summarized in Table 2.

The number of injections showed the highest significance level to predict GP-to-thalamus changes ($P = .001$), SN-to-midbrain changes ($P = .002$), and DN-to-CP changes ($P = .049$).

In separate correlation analyses, there was a significant positive correlation with the changes of GP-to-thalamus, SN-to-midbrain, and DN-to-CP SI for the total number of injections (Spear-

man $\rho = 0.423$, $P < .001$; Spearman $\rho = 0.453$, $P < .001$; and Spearman $\rho = 0.310$, $P = .002$, respectively; Fig 4) and the accumulated dose of L-GBCA (Spearman $\rho = 0.359$, $P < .001$; Spearman $\rho = 0.455$, $P < .001$; and Spearman $\rho = 0.273$, $P = .006$, respectively), while the mean interval between contrast-enhanced MR imaging showed a significant negative correlation with the SN-to-midbrain and DN-to-CP SI changes (Spearman $\rho = -0.259$, $P = .009$; Spearman $\rho = -0.241$, $P = .016$, respectively).

Radiologic Analysis: Cervical Spinal Cord

Sixteen cases (8 in each group) were discarded from the analysis due to artifacts involving ≥ 1 ROI and therefore potentially affecting the SI analysis.

The CS-to-pons SI changes were found to be not significantly different from 0 ($P = .400$), with a mean value of $+0.0008 \pm 0.0089$ (95% CI, -0.0011 – 0.0027) (Fig 5). The difference in the CS-to-pons SI between the first and last scan was not statistically significant in patients who had ≥ 6 injections compared with patients who had ≤ 5 injections ($P = .565$) (Fig 3). Furthermore, in both groups, the CS-to-pons SI changes were not significantly different between patients who received only Gd-BOPTA from the first to last scan compared with patients who had both Gd-BOPTA and Gd-DTPA injections (group A, $P = .738$; Group B, $P = .906$).

DISCUSSION

Our results showed an increase in the T1-weighted SI of the GP, SN, and DN after multiple administrations of L-GBCAs in patients with relapsing-remitting MS, whereas no changes were detected in the CS. Several studies have established a high T1-

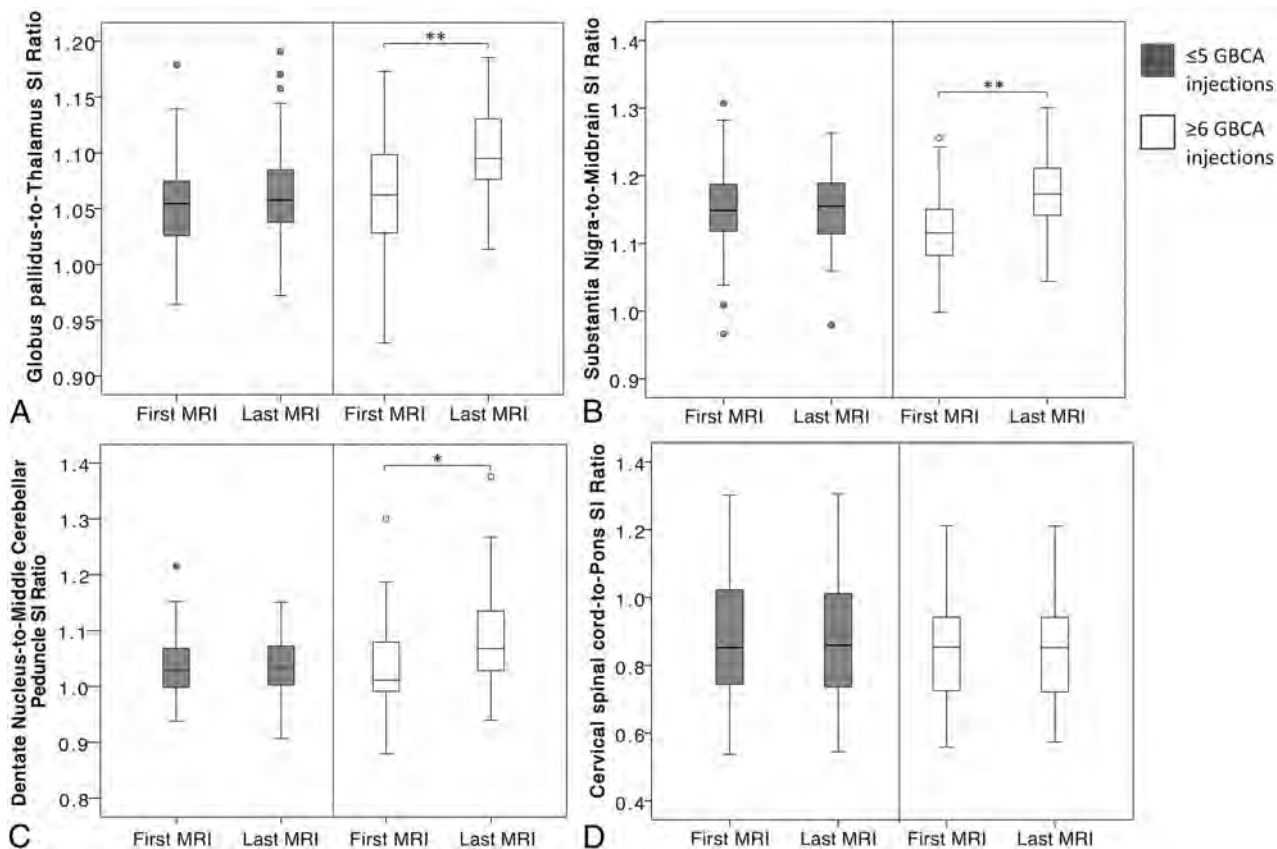


FIG 3. Boxplots representing the distribution of globus pallidus-to-thalamus (A), substantia nigra-to-midbrain (B), dentate nucleus-to-middle cerebellar peduncle (C), and cervical spinal cord-to-pons (D) SI ratios at the first and last MR imaging examinations, stratified by patients who received ≤ 5 (gray boxes on the left side of each plot) and ≥ 6 linear GBCA injections (white boxes on the right side of each plot). One hundred pairs of scans (first and last brain MR imaging scans) were analyzed in A, B, and C (50 per each group); 84 pairs of scans (first and last cervical spine MR imaging scans) were analyzed in D (42 per each group). The asterisk indicates P value $\leq .05$; double asterisks, P value $< .001$.

Table 2: Results of multiple linear regression analysis

Parameter	Regression Coefficient	95% CI	Standardized Regression Coefficient	P Value
Globus pallidus-to-thalamus SI ratio changes				
Age	-0.0001	(-0.001-0.001)	-0.019	.853
Sex	0.003	(-0.015-0.021)	0.033	.734
Race	-0.007	(-0.019-0.005)	-0.115	.257
EDSS	-0.002	(-0.006-0.002)	-0.120	.235
DMT	0.002	(-0.002-0.005)	0.104	.298
Interval between CE-MRIs	<0.001	(-0.002-0.002)	0.002	.986
GBCA type	0.001	(-0.016-0.018)	0.012	.907
No. of injections	0.005	(0.002-0.008)	0.373	.001
Substantia nigra-to-midbrain SI ratio changes				
Age	0.001	(0.000-0.002)	0.144	.136
Sex	0.030	(0.004-0.056)	0.211	.023
Race	0.006	(-0.012-0.023)	0.064	.500
EDSS	-0.003	(-0.009-0.003)	-0.088	.352
DMT	-0.004	(-0.009-0.001)	-0.157	.096
Interval between CE-MRIs	-0.001	(-0.004-0.001)	-0.106	.271
GBCA type	0.022	(-0.003-0.047)	0.166	.079
No. of injections	0.007	(0.003-0.011)	0.315	.002
Dentate nucleus-to-middle cerebellar peduncle SI ratio changes				
Age	0.0001	(-0.001-0.002)	0.023	.828
Sex	-0.015	(-0.050-0.020)	-0.085	.394
Race	-0.011	(-0.035-0.012)	-0.096	.351
EDSS	-0.004	(-0.012-0.004)	-0.113	.272
DMT	-0.004	(-0.011-0.002)	-0.129	.205
Interval between CE-MRIs	-0.003	(-0.006-0.001)	-0.156	.139
GBCA type	-0.002	(-0.036-0.032)	-0.012	.909
No. of injections	0.006	(0.000-0.012)	0.216	.049

Note:—CE indicates contrast-enhanced; DMT, disease-modifying therapy.

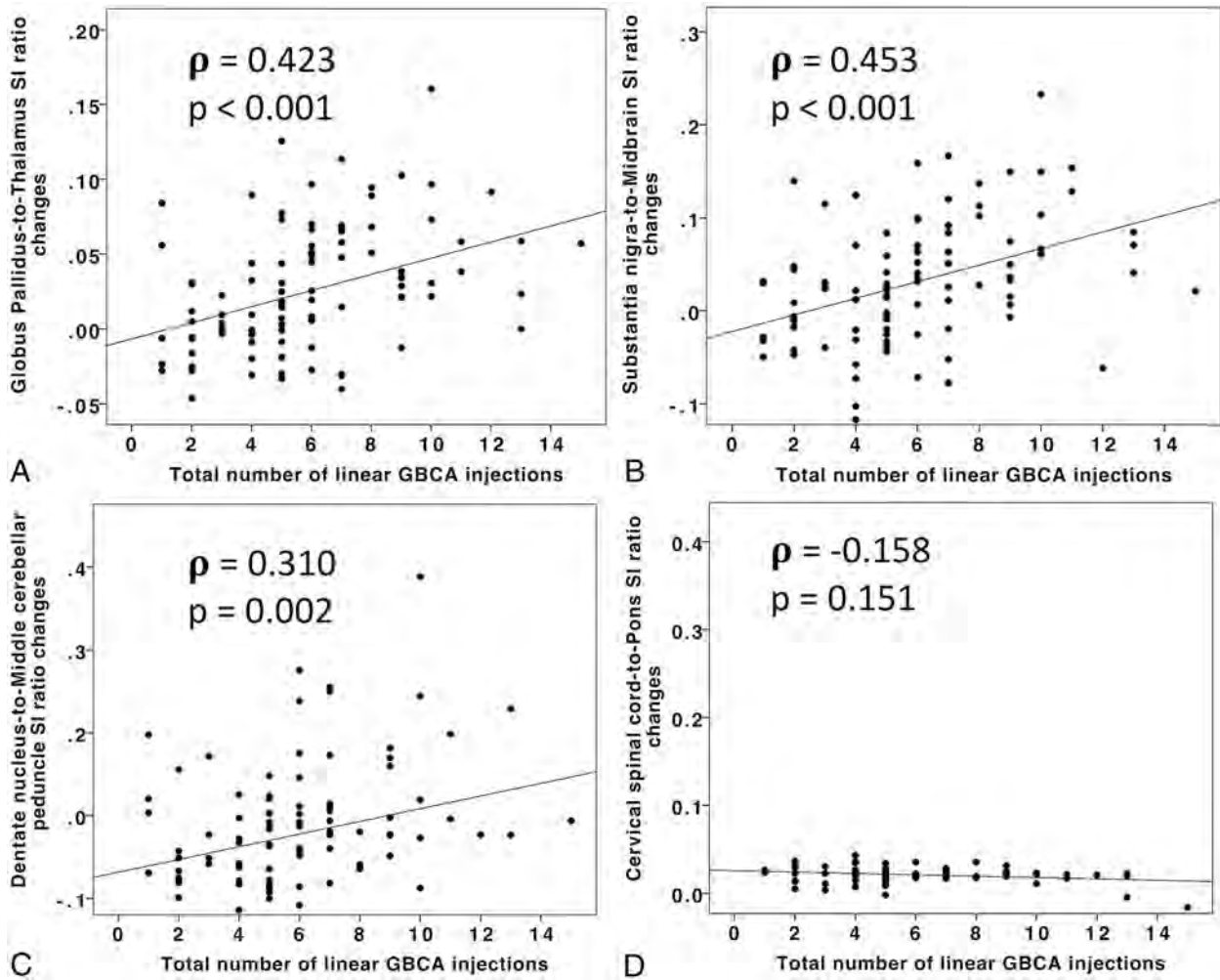


FIG 4. Scatterplots representing the SI ratio changes of the globus pallidus-to-thalamus (A), substantia nigra-to-midbrain (B), dentate nucleus-to-middle cerebellar peduncle (C), and cervical spinal cord-to-pons (D) according to the total number of linear GBCA injections. The Spearman rank correlation coefficient (ρ) and associated P value (P) are reported.

weighted SI as an indirect sign of gadolinium deposition in the setting of numerous administrations of GBCA.^{1-4,8-10,13-15}

SI changes after >35 injections of L-GBCA in the SN were previously investigated in a small cohort of patients with brain tumors¹⁶: All patients had increased SI in the SN. The authors hypothesized that the SN might also be accumulating GBCAs, but in smaller amounts that could be detected only after a large number of injections.¹⁶ According to our analysis, we found significant SI changes in the SN after ≥ 6 L-GBCA injections. The SN was not specifically studied in previous studies investigating gadolinium deposition on histologic analysis.⁸⁻¹⁰ Gadolinium ions could bind to citrates chelated to the endogenous neuromelanin pigment in the SN.¹⁷ Neuromelanin chelates iron as well; this feature might explain an increase in the SI on unenhanced T1WI.¹⁸ However, our results show significant SI changes only in patients who had ≥ 6 injections, suggesting that these changes are related to the use of gadolinium.

Gadolinium deposits have also been demonstrated in organs other than the brain,¹⁰ yet there are no studies investigating the accumulation of gadolinium in the spinal cord. We found no evidence of SI changes in the C1–C5 level of the spinal cord, suggesting no or very little gadolinium retention. Recently, the glym-

phatic system has been proposed to be important in both CSF and CNS gadolinium biodistributions.^{7,19,20} According to Nehra et al,⁷ the intravenous administration of a macrocyclic GBCA resulted in gadolinium accumulation within the CSF, even in the setting of normal renal function and no blood-brain dysfunction. The aquaporin-4 water channel in astrocytes enables the passive transport of low-molecular-weight materials from the CSF into the brain parenchyma and spinal cord. Our findings might be supported by the different expression of glymphatic aquaporin-4 water channels in the spinal cord compared with the brain²¹ and their selective loss found in inflammatory demyelinating diseases (including MS), which have a different pattern in the brain and spinal cord.^{22,23}

In the first study investigating gadolinium deposition, specifically in patients with MS, potential confounding factors (eg, age, sex, immunotherapy and disability status) were not addressed.⁶ More recently, a retrospective analysis investigated the relationship of multiple L-GBCAs injections to the SI Index in the DN and GP and any associations with cognitive function in patients with MS.²⁴ In our study, we included multiple clinical factors and focused on physical disability (EDSS), but extensive neuropsychological testing was not collected. Although we found a positive

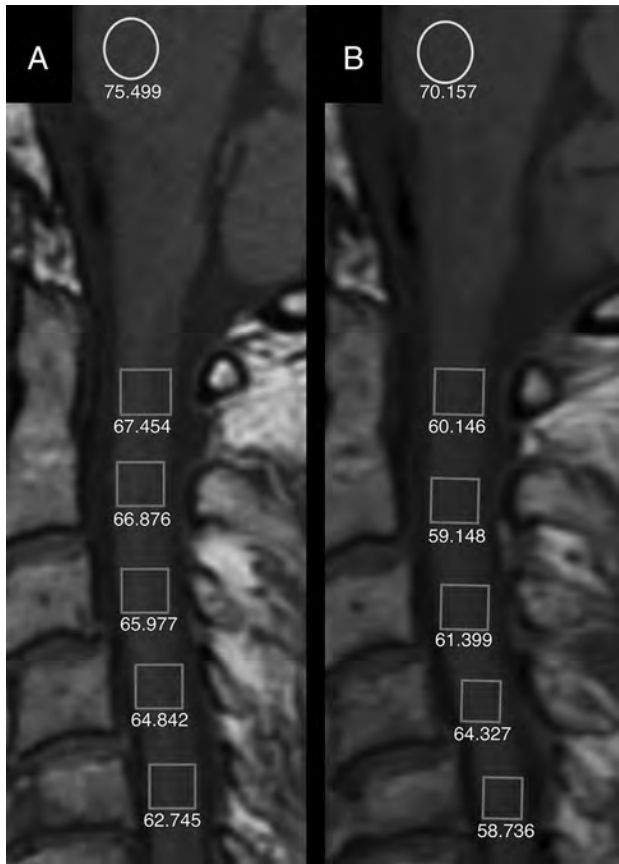


FIG 5. Unenhanced sagittal T1-weighted images at the first (A) and the ninth (B) contrast-enhanced MR imaging of a 57-year-old woman with relapsing-remitting multiple sclerosis treated with natalizumab. *Rectangles* are the ROIs placed from the C1 to C5 level. *Circles* are the ROIs in the pons. Absolute numbers of signal intensity measurements are reported for each ROI. The changes of the cervical spinal cord-to-pons signal intensity ratio between the first and the last MR imaging scans are not statistically different. TR = 650 ms; TE = 10 ms; section thickness = 3 mm; matrix = 192 × 256.

correlation between L-GBCA injections and EDSS worsening, the causal relationship cannot be established on the basis of our results. We believe this is more likely the effect of the pathophysiologic progression of MS associated with chronic neurodegeneration and a gradual increase in disability.

Limitations of our study include its retrospective nature and the absence of pathologic correlation with neuroimaging findings. Moreover, as with most published articles investigating gadolinium deposition, any GBCA injections in addition to the ones reported in clinical records could not be excluded in the study population. However, patients conforming to eligibility criteria were asked about GBCA injections not performed in our institution to limit this potential confounder.

The lack of a control group does not exclude the possibility of SI changes due to MS.

The slight variation of imaging-acquisition parameters ($\pm 13\%$ for TR and $\pm 1\%$ for TE) could potentially affect the SI measurements. Nevertheless, we decided to accept a limited variation because previous studies have shown that SI analysis should not be crucially affected when the variation of TR and TE is small.^{3,13} This allowed us to include a large number of patients in the study, increasing the statistical power of the results. Further-

more, in our study, most of the variation occurred among different patients, while the parameters did not remarkably change between the first and the last scan in each patient.

It was not possible to compare Gd-DTPA with Gd-BOPTA. The statistical power of the results concerning the subgroup analysis is lower than that of the group analysis, due to the lower number of patients included in each subgroup. Although the number of Gd-DTPA injections was only 17% of the total, the inclusion of both Gd-DTPA and Gd-BOPTA represents a potential bias because Gd-BOPTA has been shown to be potentially more stable than other GBCAs.¹¹

Concerning the CS, it was not possible to include the whole spinal cord in the ROI analysis; however, the unenhanced T1-weighted sequences were assessed entirely visually as well; no visible SI increase was detected.

Despite these limitations, this is the first study to systematically investigate SI changes of the SN and CS after multiple L-GBCAs injections. To the best of our knowledge, this study represents the largest MS series on the topic. Additionally, multiple clinical factors were included in the analyses to strengthen our results and limit other confounders.

CONCLUSIONS

In this study, we demonstrated that patients with MS receiving ≥ 6 L-GBCA injections showed a significant increase of the SI in the GP, DN, and SN, while no detectable signal changes were observed in the CS. This finding is relevant for future studies investigating the clinical implications of gadolinium retention and the mechanisms that contribute to it.

Disclosures: Alexander Lerner—UNRELATED: Board Membership: Guerbet, Comments: Advisory Board member; Grants/Grants Pending: Bracco Diagnostics, Philips Healthcare, Comments: research grants.* Arthur W. Toga—UNRELATED: Grant: National Institutes of Health, Michael J. Fox Foundation, Alzheimer's Association, CHDI Foundation, Department of Defense*; Support for Travel to Meetings for the Study or Other Purposes: International Organization of Psychophysiology, Michael J. Fox Foundation, Ontario Brain Institute, Gates Ventures, National Institutes of Health, Medical Research Council UK, Institute of Electrical and Electronics Engineers, Forschungszentrum Jülich GmbH. Meng Law—UNRELATED: Board Membership: Guerbet; Consultancy: GE Healthcare; Grants/Grants Pending: National Institutes of Health, Bracco Diagnostics.* Lilyana Amezcua—UNRELATED: Consultancy: Sanofi Genzyme, Biogen; Grants/Grants Pending: National Multiple Sclerosis Society, National Institutes of Health—National Institute of Neurological Disorders and Stroke, Biogen. *Money paid to institution.

REFERENCES

1. Kanda T, Ishii K, Kawaguchi H, et al. **High signal intensity in the dentate nucleus and globus pallidus on unenhanced T1-weighted MR images: relationship with increasing cumulative dose of a gadolinium-based contrast material.** *Radiology* 2014;270:834–41 CrossRef Medline
2. Errante Y, Cirimele V, Mallio CA, et al. **Progressive increase of T1 signal intensity of the dentate nucleus on unenhanced magnetic resonance images is associated with cumulative doses of intravenously administered gadodiamide in patients with normal renal function, suggesting dechelation.** *Invest Radiol* 2014;49:685–90 CrossRef Medline
3. Radbruch A, Weberling LD, Kieslich PJ, et al. **High-signal intensity in the dentate nucleus and globus pallidus on unenhanced T1-weighted images: evaluation of the macrocyclic gadolinium-based contrast agent gadobutrol.** *Invest Radiol* 2015;50:805–10 CrossRef Medline
4. Weberling LD, Kieslich PJ, Kickingeder P, et al. **Increased signal intensity in the dentate nucleus on unenhanced T1-weighted im-**

- ages after gadobenate dimeglumine administration. *Invest Radiol* 2015;50:743–48 CrossRef Medline
5. Kasahara S, Miki Y, Kanagaki M, et al. **Hyperintense dentate nucleus on unenhanced T1-weighted MR images is associated with a history of brain irradiation.** *Radiology* 2011;258:222–28 CrossRef Medline
 6. Roccatagliata L, Vuolo L, Bonzano L, et al. **Multiple sclerosis: hyperintense dentate nucleus on unenhanced T1-weighted MR images is associated with the secondary progressive subtype.** *Radiology* 2009;251:503–10 CrossRef Medline
 7. Nehra AK, McDonald RJ, Bluhm AM, et al. **Accumulation of gadolinium in human cerebrospinal fluid after gadobutrol-enhanced MR imaging: a prospective observational cohort study.** *Radiology* 2018;288:416–43 CrossRef Medline
 8. McDonald RJ, McDonald JS, Kallmes DF, et al. **Intracranial gadolinium deposition after contrast-enhanced MR imaging.** *Radiology* 2015;275:772–82 CrossRef Medline
 9. Kanda T, Fukusato T, Matsuda M, et al. **Gadolinium-based contrast agent accumulates in the brain even in subjects without severe renal dysfunction: evaluation of autopsy brain specimens with inductively coupled plasma mass spectroscopy.** *Radiology* 2015;276:228–32 CrossRef Medline
 10. Murata N, Gonzalez-Cuyar LF, Murata K, et al. **Macrocyclic and other non-group 1 gadolinium contrast agents deposit low levels of gadolinium in brain and bone tissue: preliminary results from 9 patients with normal renal function.** *Invest Radiol* 2016;51:447–53 CrossRef Medline
 11. Ramalho J, Semelka RC, Ramalho M, et al. **Gadolinium-based contrast agent accumulation and toxicity: an update.** *AJNR Am J Neuroradiol* 2016;37:1192–98 CrossRef Medline
 12. Lin LI. **A concordance correlation coefficient to evaluate reproducibility.** *Biometrics* 1989;45:255–68 CrossRef Medline
 13. Radbruch A, Weberling LD, Kieslich PJ, et al. **Gadolinium retention in the dentate nucleus and globus pallidus is dependent on the class of contrast agent.** *Radiology* 2015;275:783–91 CrossRef Medline
 14. Tedeschi E, Palma G, Canna A, et al. **In vivo dentate nucleus MRI relaxometry correlates with previous administration of gadolinium-based contrast agents.** *Eur Radiol* 2016;26:4577–84 CrossRef Medline
 15. Stojanov DA, Aracki-Trenkic A, Vojinovic S, et al. **Increasing signal intensity within the dentate nucleus and globus pallidus on unenhanced T1W magnetic resonance images in patients with relapsing-remitting multiple sclerosis: correlation with cumulative dose of a macrocyclic gadolinium-based contrast agent, gadobutrol.** *Eur Radiol* 2016;26:807–15 CrossRef Medline
 16. Zhang Y, Cao Y, Shih GL, et al. **Extent of signal hyperintensity on unenhanced T1-weighted brain MR images after more than 35 administrations of linear gadolinium-based contrast agents.** *Radiology* 2017;282:516–25 CrossRef Medline
 17. Cao Y, Huang DQ, Shih G, et al. **Signal change in the dentate nucleus on T1-weighted MR images after multiple administrations of gadopentetate dimeglumine versus gadobutrol.** *AJR Am J Roentgenol* 2016;206:414–19 CrossRef Medline
 18. Schwarz ST, Rittman T, Gontu V, et al. **T1-weighted MRI shows stage-dependent substantia nigra signal loss in Parkinson's disease.** *Mov Disord* 2011;26:1633–38 CrossRef Medline
 19. Naganawa S, Nakane T, Kawai H, et al. **Gd-based contrast enhancement of the perivascular spaces in the basal ganglia.** *Magn Reson Med Sci* 2017;16:61–65 CrossRef Medline
 20. Öner AY, Barutcu B, Aykol Ş, et al. **Intrathecal contrast-enhanced magnetic resonance imaging-related brain signal changes: residual gadolinium deposition?** *Invest Radiol* 2017;52:195–97 CrossRef Medline
 21. Oklinski MK, Skowronski MT, Skowronska A, et al. **Aquaporins in the spinal cord.** *Int J Mol Sci* 2016;17:1–18 CrossRef Medline
 22. Matsuoka T, Suzuki SO, Suenaga T, et al. **Reappraisal of aquaporin-4 astrocytopathy in Asian neuromyelitis optica and multiple sclerosis patients.** *Brain Pathol* 2011;21:516–32 CrossRef Medline
 23. Sharma R, Fischer MT, Bauer J, et al. **Inflammation induced by innate immunity in the central nervous system leads to primary astrocyte dysfunction followed by demyelination.** *Acta Neuropathol* 2010;120:223–36 CrossRef Medline
 24. Forslin XY, Shams XS, Hashim XF, et al. **Retention of gadolinium-based contrast agents in multiple sclerosis: retrospective analysis of an 18-year longitudinal study.** *AJNR Am J Neuroradiol* 2017;38:1311–16 CrossRef Medline

Convolutional Neural Network for Automated FLAIR Lesion Segmentation on Clinical Brain MR Imaging

 M.T. Duong,  J.D. Rudie,  J. Wang,  L. Xie,  S. Mohan,  J.C. Gee, and  A.M. Rauschecker



ABSTRACT

BACKGROUND AND PURPOSE: Most brain lesions are characterized by hyperintense signal on FLAIR. We sought to develop an automated deep learning–based method for segmentation of abnormalities on FLAIR and volumetric quantification on clinical brain MRIs across many pathologic entities and scanning parameters. We evaluated the performance of the algorithm compared with manual segmentation and existing automated methods.

MATERIALS AND METHODS: We adapted a U-Net convolutional neural network architecture for brain MRIs using 3D volumes. This network was retrospectively trained on 295 brain MRIs to perform automated FLAIR lesion segmentation. Performance was evaluated on 92 validation cases using Dice scores and voxelwise sensitivity and specificity, compared with radiologists' manual segmentations. The algorithm was also evaluated on measuring total lesion volume.

RESULTS: Our model demonstrated accurate FLAIR lesion segmentation performance (median Dice score, 0.79) on the validation dataset across a large range of lesion characteristics. Across 19 neurologic diseases, performance was significantly higher than existing methods (Dice, 0.56 and 0.41) and approached human performance (Dice, 0.81). There was a strong correlation between the predictions of lesion volume of the algorithm compared with true lesion volume ($\rho = 0.99$). Lesion segmentations were accurate across a large range of image-acquisition parameters on >30 different MR imaging scanners.

CONCLUSIONS: A 3D convolutional neural network adapted from a U-Net architecture can achieve high automated FLAIR segmentation performance on clinical brain MR imaging across a variety of underlying pathologies and image acquisition parameters. The method provides accurate volumetric lesion data that can be incorporated into assessments of disease burden or into radiologic reports.

ABBREVIATIONS: BIANCA = Brain Intensity Abnormality Classification Algorithm; CNN = convolutional neural network; FDR = false discovery rate; LST = lesion segmentation tool; RMdSPE = root median squared percentage error; RMSPE = root mean squared percentage error; SVID = small-vessel ischemic disease

Approximately 36 million MR imaging studies are performed annually in the United States, and this number is rising.¹ Approximately 65% of these MRIs are used to assess the central nervous system. The FLAIR sequence is universally used to identify and characterize imaging abnormalities in terms of location, size, and extent, due to its broad utility across many pathologies and lesion appearances. Specific applications of FLAIR include, among numerous others, primary and metastatic brain tumors;

demyelinating, autoimmune, infectious, and inflammatory conditions; and ischemia.^{2–4} Because of its general utility, FLAIR is acquired on nearly every clinical brain MRI. There is a growing need to develop fully automated, rapid, precise, quantitative assessments of FLAIR abnormalities to standardize quantitative descriptions of pathology.

A quantitative lesion-burden assessment has the potential to reduce errors from interobserver variability, 2D measurements, “satisfaction of search,” and confirmation bias, promising to improve workflow efficiency and diagnostic accuracy, eventually translating

Received January 28, 2019; accepted after revision June 17.

From the Department of Radiology, Hospital of the University of Pennsylvania, Philadelphia, Pennsylvania.

Michael Tran Duong and Jeffrey D. Rudie contributed equally to this work and are co-first authors.

A.M. Rauschecker was supported by a Radiological Society of North America Resident Grant (RR1778). A.M. Rauschecker and Jeffrey D. Rudie were supported by a National Institutes of Health T-32 Training Grant from Penn Radiology for the duration of the project (T32-EB004311-10). A.M. Rauschecker was also supported by a National Institutes of Health T-32 Training Grant from the University of California, San Francisco, Radiology, for a portion of the project (T32-EB001631-14).

Please address correspondence to Andreas M. Rauschecker, MD, PhD, Department of Radiology & Biomedical Imaging, University of California, San Francisco, 513 Parnassus Ave, Room 5-261, Box 0628, San Francisco, CA 94143-0628; e-mail: andreas.rauschecker@gmail.com; @DrDreMDPhD

 Indicates open access to non-subscribers at www.ajnr.org

 Indicates article with supplemental on-line appendix.

 Indicates article with supplemental on-line photos.

<http://dx.doi.org/10.3174/ajnr.A6138>

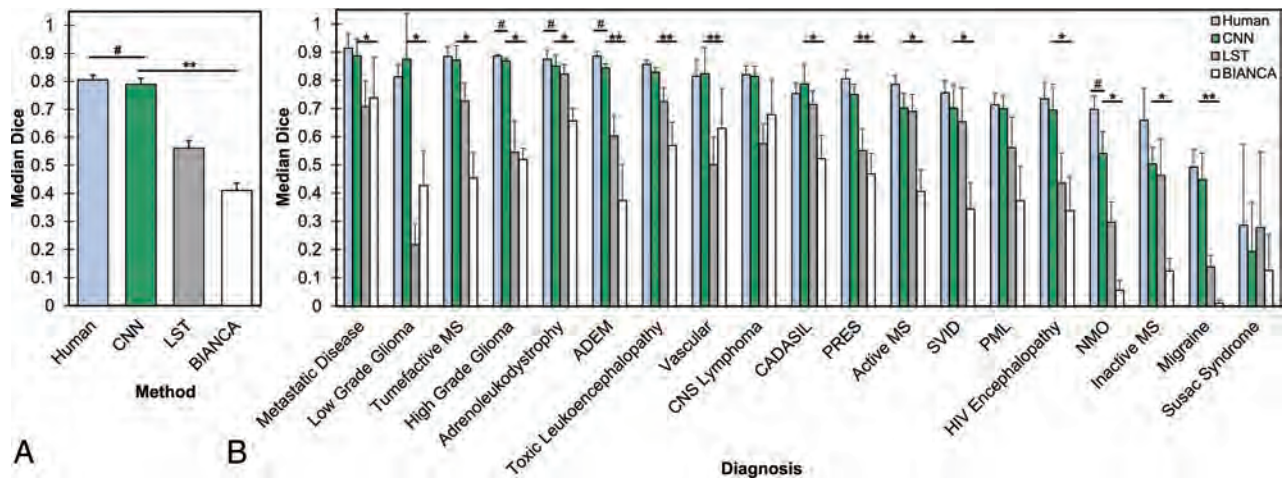


FIG 1. Performance of the CNN compared with human manual segmentation and other automated FLAIR segmentation methods. **A**, Median Dice scores across all validation cases. The asterisks denotes $P < .05$ for paired 2-tailed t tests compared with the CNN. The hashtag denotes $P < .05$ for human performance compared with the CNN. **B**, Median Dice scores across validation cases separated by underlying diagnosis. The asterisk denotes $P < .05$ (FDR-corrected for multiple comparisons) for the CNN compared with 1 method, and double asterisks denote $P < .05$ (FDR-corrected for multiple comparisons) for CNN compared with both methods using paired 2-tailed t tests. The hashtag separately denotes $P < .05$ (FDR-corrected for multiple comparisons) for human performance compared with the CNN. Error bars represent 1 standard error of the mean across cases. ADEM indicates acute disseminated encephalomyelitis; PRES, posterior reversible encephalopathy syndrome; PML, progressive multifocal leukoencephalopathy; NMO, neuromyelitis optica.

to better patient outcomes.^{5,6} To this aim, machine learning methods have been used for identifying FLAIR lesions in specific diseases, such as gliomas,^{7,8} multiple sclerosis,⁹⁻¹¹ acute infarcts,^{12,13} traumatic brain injury,¹⁴ and white matter hyperintensities related to small-vessel ischemic disease and Alzheimer disease.¹⁵⁻¹⁷ These methods represent specialized tools for distinct research purposes.¹⁸

No methods currently exist to identify FLAIR lesions independent of the underlying etiology in a clinical environment. Many brain MRIs are obtained before a known diagnosis. Furthermore, existing algorithms often assume specific requirements for image acquisition, further decreasing clinical utility. In the clinical setting, brain MRIs and their FLAIR sequences may be acquired with differing image-acquisition parameters and resolutions, which are often suboptimal for automated algorithms. To be clinically applicable across most brain MRIs, a lesion segmentation method must operate well, despite this high degree of image and lesion heterogeneity.

Deep learning-based approaches have recently demonstrated success with a variety of other image-segmentation tasks, including intracranial hemorrhage segmentation on CT,¹⁹ structural neuroanatomy classification on brain MR imaging,²⁰ cartilage segmentation on knee MR imaging,²¹ and left ventricular volume on cardiac MR imaging.²² The winner of the 20th International Conference on Medical Image Computing and Computer Assisted Intervention (MICCAI) 2017 challenge for white matter hyperintensity segmentation²³ was based on a U-Net.²⁴ Therefore, we adopted a deep learning approach, adapting a U-Net convolutional neural network (CNN) architecture for 3D imaging for the task of disease-invariant FLAIR lesion segmentation. Our study was designed to test this automated FLAIR lesion-segmentation algorithm on 19 different brain pathologies producing a wide range of lesion appearances and to compare CNN-based automated segmentations with those of manual lesion segmentations and existing automated tools.

MATERIALS AND METHODS

Subjects and Data

This retrospective study was approved by the institutional review board of the University of Pennsylvania, with a waiver for consent. A total of 387 study subjects (218 females and 169 males; age range, 14–95 years; median age, 53 years) were included, with 1 MRI (2 sequences: T1-weighted and FLAIR) per subject. Subjects were identified by searching the radiology archives of our tertiary care university hospital (Hospital of the University of Pennsylvania) for 19 prespecified diagnoses, confirmed using the electronic medical record and procedures detailed in the On-line Appendix.

Diseases and Training/Validation Assignment

The 19 diseases included in the validation sample are listed in the On-line Appendix (see also Fig 1). These diseases encompass a large range that cause FLAIR abnormalities on brain MR imaging. They were also specifically chosen to represent a very heterogeneous sample, including wide ranges of individual lesion and total lesion volumes and heterogeneity in lesion shape and internal signal characteristics.

In assigning cases to training and validation samples, we randomly selected 5 cases of each of the 19 unique diseases to be part of the validation sample. When diagnoses were rare enough that <5 exemplars of the disease existed in the PACS of our institution (which was only the case with Susac syndrome), then all cases of that disease were included in the validation set (none in the training set). The remainder of the cases were assigned to the training set. The training set was also supplemented with 20 age-matched healthy brains (without abnormality on FLAIR) to further boost specificity; more healthy cases were unnecessary given that the remainder of the training cases already included many individual regions without abnormality on FLAIR.

Assignments resulted in 295 training cases and 92 validation cases. Because no hyperparameter optimization was performed (see

Table 1: Heterogeneous scanning parameters used for FLAIR sequences in training and validation samples, showing the number of study subjects in each category^a

Summary	Training (n = 295)	Validation (n = 92)
Field strength		
1.5T	230 (78.0%)	57 (62.0%)
3T	65 (22.0%)	35 (38.0%)
Dimension		
2D	287 (97.3%)	81 (88.0%)
3D	8 (2.7%)	11 (12.0%)
Manufacturer/model		
GE Healthcare ^b		
Discovery MR750w	4 (1.4%)	3 (3.3%)
Genesis Signa	20 (6.8%)	6 (6.5%)
Optima MR450w	15 (5.1%)	1 (1.1%)
Signa Excite	20 (6.8%)	7 (7.6%)
Signa HDxt	14 (4.7%)	7 (7.6%)
Phillips ^c		
Intera	2 (0.7%)	1 (1.1%)
Siemens ^d		
Magnetom Aera	15 (5.1%)	2 (2.2%)
Avanto	39 (13.2%)	8 (8.7%)
Magnetom Espree	83 (28.1%)	19 (20.1%)
Magnetom Essenza	9 (3.1%)	1 (1.1%)
Magnetom Skyra	8 (2.7%)	8 (8.7%)
Magnetom Symphony	4 (1.4%)	3 (3.3%)
Magnetom Symphony Tim	5 (1.7%)	1 (1.1%)
Tim Trio	37 (12.5%)	11 (20.0%)
Magnetom Verio	16 (5.4%)	13 (14.1%)
Toshiba ^e		
Titan	4 (1.4%)	1 (1.1%)
TE (ms)		
Minimum	86	82
Median	136	136
Maximum	396	398
TR (ms)		
Minimum	5000	5000
Median	9000	9000
Maximum	12,000	12,000

^a The percentage of the total training or validation sample is in parentheses.

^b Milwaukee, Wisconsin.

^c Best, the Netherlands.

^d Erlangen, Germany.

^e Toshiba Medical Systems, Tokyo, Japan.

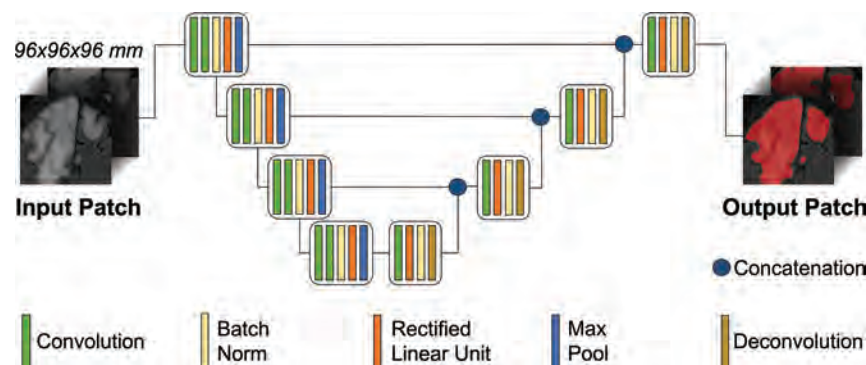


FIG 2. Schematic of the CNN U-net architecture. The architecture uses a 3D region-based approach for training and validation. The sample MR FLAIR images are from a patient with progressive multifocal leukoencephalopathy. Max indicates maximum.

“CNN Model Architecture [U-Net]” below), this study did not require separate test and validation sets. The model was trained with only the training dataset and was separately tested on the validation dataset.

MR Imaging Parameters and Ground Truth Segmentations

Imaging data stemmed from a wide range of imaging parameters (Table 1), typical of clinical imaging studies. Moreover, imaging was performed on >30 different MR imaging scanners and 16 different scanner models across all study subjects. Image-acquisition parameters for the training sample were similar to those on the validation sample (randomly assigned).

Criterion standard lesion segmentations were based on manual segmentations by a radiologist using ITK-SNAP (www.itksnap.org),²⁵ further described in the On-line Appendix.

Image Preprocessing

Skull stripping of T1-weighted images was performed with Advanced Normalization Tools (ANTs; <http://neuro.debian.net/pkgs/ants.html>), which were then registered and applied to FLAIR images.²⁶ Images were normalized by the mean and SD signal intensity to zero mean and unit SDs. Images were resampled to 1-mm³ isotropic resolution via linear interpolation. Despite most MR imaging acquisitions being 2D (Table 1), all 2D and 3D acquisitions were treated with the same preprocessing steps to produce common resolution 1-mm³ volumes suitable for use in a 3D-CNN architecture. Elastic transformations²⁷ were applied to the images for data augmentation, which included small random rotations, translations, scaling, and free-form deformations. We split the full-resolution augmented imaging volume into 96-mm³ cubes (3D patches) as the network input to fit within graphic memory constraints. Note that these 3D regions encompass a large portion of the full-resolution imaging volume (Fig 2) and are created only to address memory constraints. The large patches, in comparison with the size of any lesion, ensure that the lesion transition zones are included within the patches. During training, the cubes were randomly sampled across the full-brain volumes. To prevent sample imbalance, we sampled the same number of patches that included lesion voxels as those that excluded lesions during training. A total of 80 patches were extracted from each training case, with 3 random augmentations per

case, resulting in 240 patches per case or a total of 70,800 training patches. During testing, the brain volume was densely sampled with the cubes using a step size of 32 mm in each direction, resulting in a 64-mm overlap between cubes. The overlapped segmentation predictions were averaged.

CNN Model Architecture (U-Net)

We used a fine-tuned 3D U-Net^{28,29} to predict lesion segmentations on the FLAIR images because of the ability of the U-Net to provide pixelwise/voxelwise predictions, ideal for voxelwise segmentation problems. The network consists of 4 consecutive down-sampled

blocks followed by 4 consecutive up-sampled blocks. We used the rectified linear unit for nonlinearity. For down-sampling, we used a stride-2 convolution; for up-sampling, we used a stride-2 deconvolution. We used the kernel size 3 × 3 × 3 across the net-

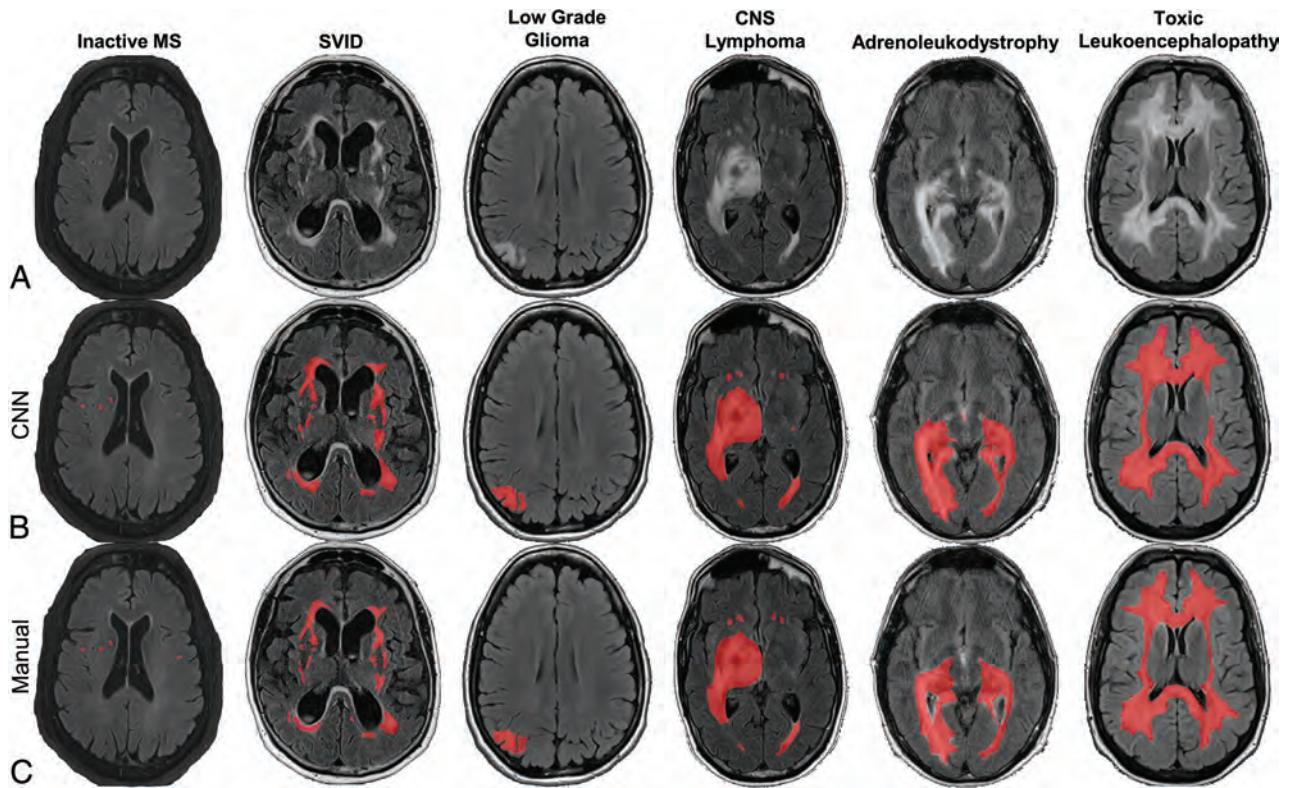


FIG 3. Representative slices from validation samples of FLAIR MR brain images (A) with CNN-based (B) and manual lesion segmentations (C), with predicted or ground truth lesion segmentations overlaid in red. The CNN performs well on a variety of different neurologic disorders, here shown in cases of multiple sclerosis, SVID, low grade-glioma, primary CNS lymphoma, adrenoleukodystrophy, and toxic leukoencephalopathy.

work. We applied a dilation factor of 2 in all convolutional layers. Other than the standard cross-link between corresponding up-sampling and down-sampling blocks, we also added a residual connection between subsequent layers, with a number of features matched by a plain $1 \times 1 \times 1$ convolution. After the final up-sampling block, 3 additional convolutional, rectified linear unit, batched-normalized layers were added before the final normalized exponential (softmax) head function (Fig 2). A batch consisted of six 3D patches.

We used standard cross-entropy loss²⁹ and an Adam optimizer with a learning rate of 10^{-5} . The network was trained for 50 epochs. The network was implemented using TensorFlow (<https://www.tensorflow.org/>),³⁰ a deep learning module within the Python programming language. Implementation was on a Titan Xp GPU (NVIDIA, Santa Clara, California).

Comparison Algorithms

We compared CNN performance against that of previously published automated algorithms designed for FLAIR lesion identification: lesion segmentation tool (LST; <https://www.applied-statistics.de/lst.html>)³¹ and Brain Intensity Abnormality Classification Algorithm (BIANCA; <https://fsl.fmrib.ox.ac.uk/fsl/fslwiki/BIANCA>).³² We also compared the performance with a second independent radiologist's manual segmentations, which we refer to as "human performance." These methods were all applied to the same validation dataset. Refer to the On-line Appendix for additional information on comparison methods.

Statistical Analysis

The performance of our U-Net architecture neural network was validated against the manual-segmentation criterion standard on 92 cases (ie, FLAIR volumes) representing 19 different diseases, after being trained on 295 FLAIR volumes. Although acquisition parameters included 2D and 3D methods (Table 1), we refer to all cases as FLAIR volumes, given that we resampled all images to a 1-mm^3 resolution (ie, a 3D volume) for CNN training and validation, before resampling back into native space for comparison with native space manual segmentations. All analyses were performed in subject native space. Segmentation performance of all methods was compared using Dice coefficients,³³ the most commonly used similarity measure for evaluating segmentation performance, with manual lesion segmentations as the ground truth. Voxelwise performance measures compared with manual segmentation were also calculated. Comparisons of performance across methods was accomplished using paired 2-tailed *t* tests. Additional statistical comparisons are discussed in the On-line Appendix.

RESULTS

CNN-Based FLAIR Lesion Segmentation Accuracy

The CNN segments brain MR lesions qualitatively with a high degree of accuracy. Representative comparisons of CNN-based automatic segmentations and criterion standard manual segmentations are shown in Fig 3 (see also On-line Fig 2 and the On-line Appendix).

We quantified CNN segmentation performance across all val-

Table 2: Summary measures of accuracy (Dice, voxelwise sensitivity, specificity, FDR, PPV/NPV) and comparisons of true and predicted lesion volumes by forecasting RMdSPE and Spearman correlation r of methods^a

	Human	CNN	LST	BIANCA
Dice				
Median	0.805	0.789	0.562	0.410
SEM	0.017	0.022	0.026	0.027
Sensitivity (1-FNR)				
Median	0.800	0.767	0.599	0.556
SEM	0.017	0.025	0.026	0.020
Specificity (1-FPR)				
Median	0.999	0.999	0.999	0.997
SEM	0.000	0.000	0.000	0.000
PPV				
Median	0.824	0.769	0.690	0.335
SEM	0.018	0.018	0.030	0.034
NPV				
Median	0.999	0.999	0.999	0.999
SEM	0.000	0.000	0.001	0.001
RMdSPE	0.97%	1.38%	3.80%	6.56%
Spearman r	0.991	0.985	0.862	0.655

Note:—PPV indicates positive predictive value; NPV, negative predictive value; FNR, false negative rate; FPR, false positive rate; SEM, standard error of the mean.

^a Methods: Human, CNN, LST, and BIANCA.

validation cases using Dice scores, and we compared its performance with existing state-of-the-art automated FLAIR segmentation methods, LST and BIANCA^{31,32} and with a second independent radiologist. Across the validation sample, the CNN demonstrated a median Dice score of 0.789 (mean, 0.699 ± 0.022), which approached human performance (Fig 1A). This performance was significantly higher than the Dice scores of LST (median, 0.562; mean, 0.533 ± 0.026) and BIANCA (median, 0.410; mean, 0.395 ± 0.027) (ANOVA and paired 2-tailed t tests compared with CNN; $P < .001$). Similarly, among the algorithms tested, other voxelwise measures of performance were highest for the CNN (Table 2). Human performance (median Dice, 0.805; mean, 0.759 ± 0.017) was very slightly-but-consistently better than CNN performance ($P < .01$, paired 2-tailed t test).

Effect of Disease Pathology

Next, we examined how segmentation performance varies as a function of underlying disease pathology. The CNN had significantly higher mean Dice scores than at least 1 of the other methods in 16/19 diagnoses and significantly higher than those in both other methods in 5/19 diagnoses (paired 2-tailed t tests, $P < .05$; false discovery rate [FDR]-corrected for multiple comparisons). Segmentation performance was not statistically different from the performance of the independent radiologist's manual segmentations in 15/19 diagnoses. Note that low sample sizes within each diagnosis group limit statistical power, but the median Dice was numerically higher for the CNN than the other methods in all diseases except Susac syndrome (Fig 1B). Even for those diseases for which LST and BIANCA were specifically designed (multiple sclerosis and small-vessel ischemic disease [SVI], respectively), the CNN produced segmentations that were better than those for SVI ($P < .05$, paired t test comparing CNN and BIANCA) or not significantly different from those for MS ($P > .05$, paired t test comparing CNN and LST), the comparison algorithms. Performance was consistently low for Susac syndrome across all methods, likely due to a combination of factors, including the follow-

ing: a large amount of noise and imaging artifacts, only 2 cases total available (none in the training data), and very small and limited extent of lesions in these 2 cases. Note the low performance of the independent radiologist for these cases as well. Heterogeneity of FLAIR signal within a lesion did not prove a barrier to accurate segmentation; performance on 16 validation cases with heterogeneous FLAIR lesions was excellent, with a median Dice score of 0.87 (range, 0.80–0.92; On-line Fig 2).

Lesion Volume Quantification

We found that the CNN performs well in estimating total lesion volume, with a Spearman correlation $\rho = 0.985$ and a best fit line slope $\beta = 0.958$ when comparing predicted with true total lesion volume across all cases, indicating a very high degree of fidelity between the predicted and true total lesion volumes on an individual subject basis (Fig 4A). The comparison methods, meanwhile, had lower Spearman correlations (LST $\rho = 0.862$, BIANCA $\rho = 0.655$) and lower best fit line slopes (LST $\beta = 0.490$, BIANCA $\beta = 0.277$), with both methods tending to overestimate smaller lesion volumes and underestimate larger lesion volumes. We also analyzed the degree of error in the predicted lesion volume on a subject-specific basis using the root median squared percentage error (RMdSPE) and the root mean squared percentage error (RMSPE), which measure the average percentage error from true lesion volume. The CNN generated lesion volumes with lower errors (RMdSPE = 1.4%, RMSPE = 4.8%) compared with LST (RMdSPE = 3.8%, RMSPE = 72.3%) and BIANCA (RMdSPE = 6.6%, RMSPE = 433.8%) (Table 2).

Effect of Lesion Volume

We investigated how each method performed as a function of lesion volume (Fig 4B). As expected, all methods performed better with larger total lesion volumes, which is partially inherent in the Dice similarity index^{33,34} and was also true of the independent radiologist's performance. However, the CNN performed the best of the 3 automated methods at all lesion volumes (ANOVA and paired 2-sample t tests compared with CNN $P < .01$), and performance did not degrade even at the highest lesion volumes ($>100 \text{ cm}^3$), whereas performance did degrade slightly at the highest lesion volumes for the other methods (Fig 4B). Even at very low total lesion volumes, the CNN produced reasonable estimates, with Dice scores of ~ 0.55 and accurate estimates of lesion volume (Fig 3, inactive case of MS, as an example), whereas the other methods performed poorly in these cases. Similarly, false-positive voxels were most common for all methods in cases with low lesion volumes, but this effect was much less pronounced with the CNN and with a second radiologist (Fig 4C).

When we categorized diseases by median CNN Dice and true lesion volume, no apparent clusters arose on the basis of etiology (Fig 4D), noting that the lowest Dice scores were for diseases in which the total lesion volume and individual lesion sizes tend to be small (migraine, multiple sclerosis, neuromyelitis optica, and Susac syndrome). Indeed, Dice scores for all methods including human segmentation depend on individual lesion sizes, with poorer performance in cases with small lesions (Fig 4E) due to a higher number of false-positive and false-negative voxels in these cases (On-line Fig 1). In summary, Dice scores within each disease

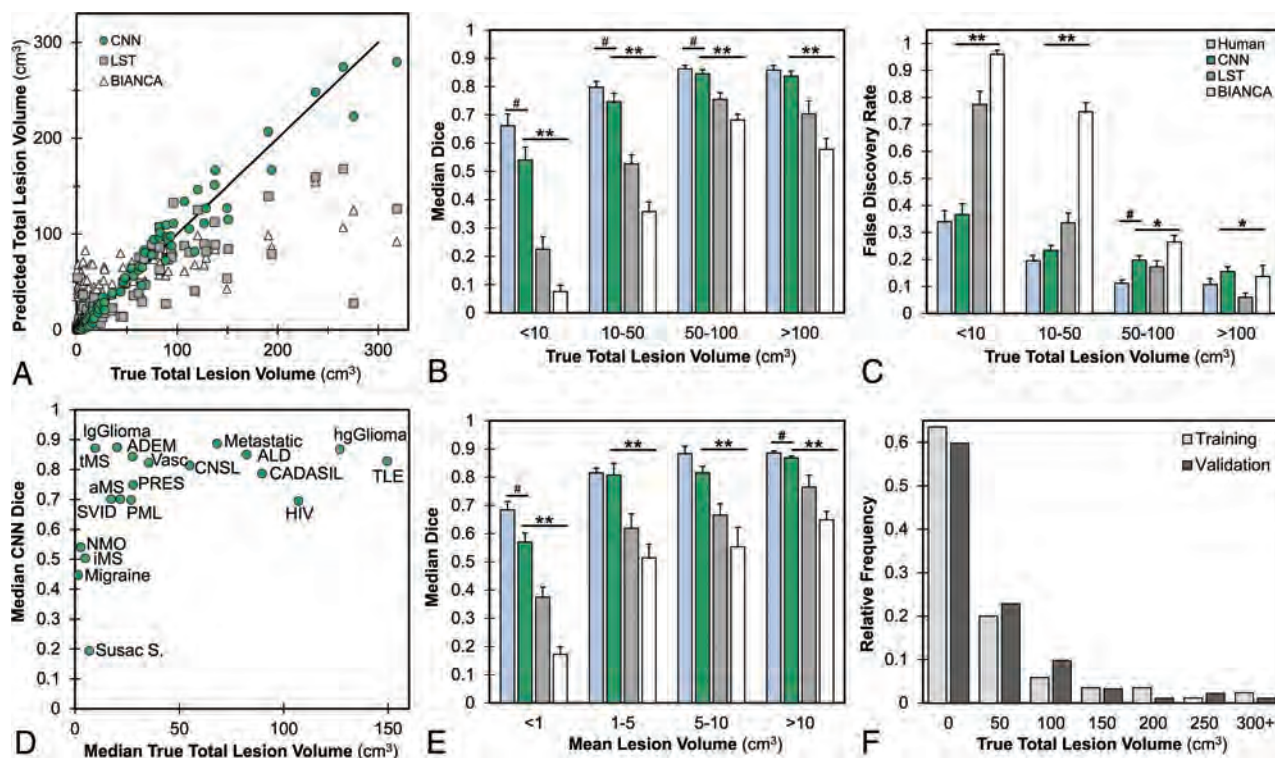


FIG 4. Performance of segmentation methods according to lesion characteristics. A, Scatterplot of predicted-versus-true total lesion volume with CNN (green circle) (Spearman correlation $\rho = 0.985$, best fit line slope $\beta = 0.958$), LST (gray square) $\rho = 0.862$, $\beta = 0.490$, and BIANCA (white triangle) ($\rho = 0.655$, $\beta = 0.277$) with the $y = x$ line. Note clustering of CNN points along the $y = x$ line, representing low deviation of CNN-based volume estimates from manual lesion volumes. B, Median Dice scores of cases stratified by total lesion volume. C, False discovery rate stratified by total lesion volume. D, Scatterplot of median CNN Dice score versus median true total lesion volume per diagnostic group. E, Median Dice scores of cases grouped by mean individual lesion volume. F, Histogram of lesion volumes in training and validation datasets. Error bars in all panels represent ± 1 standard error of the mean across cases. The asterisk denotes $P < .01$ for the CNN compared with 1 method, and double asterisks denote $P < .01$ for CNN compared with both methods using 1-way group ANOVA and paired 2-tailed t tests. The hashtag separately denotes $P < .05$ for human performance compared with the CNN. ADEM indicates acute disseminated encephalomyelitis; ALD, adrenoleukodystrophy; TLE, toxic leukoencephalopathy; aMS, active MS; TMS, tumefactive MS; PRES, posterior reversible encephalopathy syndrome; iMS, inactive MS; NMO, neuromyelitis optica; Vasc, Vascular disease (ischemia); CNSL, CNS lymphoma; Susac S, Susac syndrome; lg, low-grade; hg, high-grade; PML, progressive multifocal leukoencephalopathy.

are driven mainly by lesion size/volume but are otherwise independent of pathology, demonstrating the broad utility of the CNN for a range of diseases.

Effect of Technical Factors

We investigated whether CNN performance depends on technical acquisition factors such as MR imaging scanner models or acquisition parameters (Fig 5). We found no significant differences in CNN performance with respect to different scanner models (1-way ANOVA of Dice across 16 scanner types, $F = 0.65$, $P = .84$) or manufacturers (1-way ANOVA across 4 manufacturers, $F = 0.61$, $P = .61$). We also found no correlation between the number of training cases and validation performance across scanner types ($r^2 = 0.015$, $P = .65$, Fig 5B). Thus, the CNN generalizes well across scanner types. Similarly, there was no effect of field strength on performance (2-sample t test, $P = 0.22$). There was a trend toward better performance with 2D acquisition sequences ($P = .06$), noting an inherent bias in that patients with small lesions (in particular those with MS) more commonly undergo 3D acquisitions at our institution. Finally, we tested whether performance decreased when the CNN is applied to imaging from outside hospitals. In contrast, we found slightly better Dice scores on those scans obtained at outside hospitals than at our home institution

($P < .05$), but with no significant difference after accounting for mean lesion size ($P = .85$), which was overall larger in cases from outside hospitals.

Inference Time

One advantage of automated methods over manual lesion segmentation is processing speed. The mean inference time of the CNN on a single FLAIR volume is 28.2 ± 1.48 seconds, which includes all preprocessing steps (brain extraction, interpolation, patches, and so forth), model loading, and model application. The average inference of BIANCA for a single subject was fastest at 4.6 ± 1.35 seconds, also including relevant preprocessing steps. LST was the slowest, with a mean inference time of 1.8 minutes \pm 34.0 seconds. All of these times compare favorably with those of manual lesion segmentations, which take, on average, approximately 15–20 minutes for a single FLAIR volume by an experienced individual.

DISCUSSION

This study is the first demonstration of a quantitative, automated FLAIR lesion evaluation algorithm that applies to a multitude of clinically distinct and radiologically unique pathologies. The CNN, specifically a U-Net,²⁸ functions on clinical-grade images from

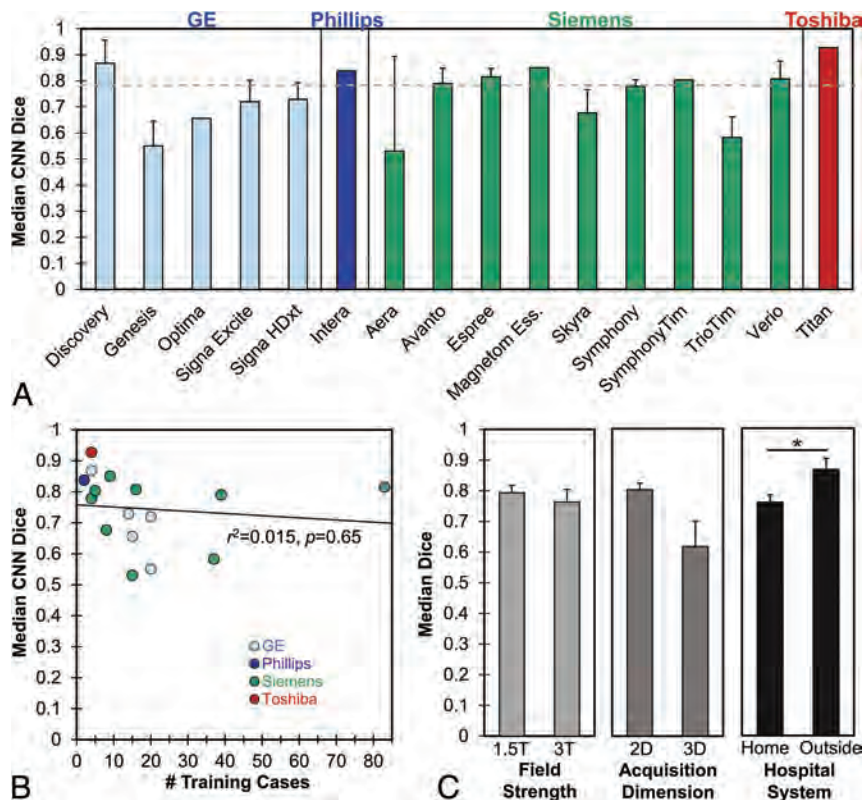


FIG 5. Performance of the CNN segmentation method according to technical characteristics. *A*, Median Dice scores on validation cases across different scanner models, grouped by MR imaging manufacturer. The *dashed line* indicates overall mean Dice score. There was no significant difference in Dice scores according to scanner model or manufacturer ($P > .05$ by 1-way ANOVA, see Results). *B*, Median Dice scores according to the number of training cases from that scanner model, with the best fit line. There is no significant correlation between the number of training cases and Dice scores ($P > .05$). *C*, Median Dice scores on validation cases grouped by field strength (*left panel*), acquisition dimension (*middle panel*), and hospital system where images were acquired (*right panel*). Error bars in all panels represent ± 1 standard error of the mean across cases. The asterisk denotes $P < .05$ for the 2-tailed *t* test among groups. See Table 1 for manufacturers' information. Ess indicates Essenza.

a PACS. We demonstrate that this CNN performs high-quality lesion segmentations despite a number of heterogeneous scanners, image acquisition parameters, lesion sizes, and underlying diagnoses, even with modest training data (≤ 5 cases per diagnosis).

The CNN performs well at FLAIR lesion segmentation across these variables because of the basic commonality that all these disease pathologies share: hyperintense FLAIR signal. Our 3D-U-Net method is specifically designed for and trained on noisy real-world clinical images to identify hyperintense FLAIR signal while avoiding artifacts. The utility of an algorithm that is broadly trained on hyperintense FLAIR signal, as opposed to specific diseases, is that it can be used in clinical situations even when the diagnosis is unknown. Thus, the CNN can provide accurate lesion-volume estimates on any disease with hyperintense FLAIR signal without being extensively trained with any particular pathology, noting that specific training with 1 disease may boost performance for that disease at the detriment of others. In contrast to using disease-specific methods, we also intentionally avoided inclusion of other MR images beyond FLAIR, such as T1,²⁴ in the training model because those sequences do not consistently show abnormalities across the wide range of pathologies included in the study or in neuroimaging generally.

As a result, the CNN estimates true total lesion volumes with very high fidelity across a range of 19 diseases tested here, thereby making the algorithm clinically applicable to quantitatively measuring lesion volume. The CNN outperforms current state-of-the-art algorithms in brain FLAIR lesion segmentation, as measured by Dice overlap coefficients, false-positives, false-negatives, and predictions of lesion volume. On clinical imaging, it outperforms or is equivalent to these algorithms both on those diseases for which those algorithms are designed (MS for LST and SVID for BIANCA), as well as for diseases (eg, adrenoleukodystrophy) for which no algorithms currently exist. For high-grade glioma whole-tumor segmentation, it functions at a level comparable with the winning algorithms from the Brain Tumor Image Segmentation (BraTS 2017) challenge.³⁵⁻³⁷ Overall, it functions nearly at the level of a human expert.

Another strength of the current method is that it generates accurate lesion segmentations despite a very heterogeneous array of imaging-acquisition parameters. This particular feature allows the methodology to be easily integrated into the clinical workflow because it has no specific requirements for FLAIR image acquisition. In addition to supporting the clinical workflow, the method has strong potential to be applied retrospectively in extracting quantitative lesion data from the massive amount of clinical data available in PACS storage across radiology departments. When used in combination with natural language processing on radiology reports or other diagnostic data from electronic medical records, these measures may support the association of quantitative lesion characteristics with various neurologic diseases on a large scale.

There is room for further improvement in the methodology. From a technical standpoint, we found that the most difficult cases for the CNN, as with any method, are cases with a small extent of lesions and small lesion sizes. Further developments in the neural network model architecture and training, including hyperparameter optimization, additional training cases, and/or the use of specialized techniques such as a second object localization network,¹⁹ may continue to boost performance in such situations. Specific training methods have been developed for avoiding false-positives, such as fine-tuning the network with more representative baseline lesion distributions or using the Dice score as the loss function.²⁸

Furthermore, while the current results are promising, there are limitations to the conclusions we can draw from this cross-sectional retrospective study. Prospective use of the technology may encounter a different typical range of lesion appearances than in our study. However, we expect the CNN to iteratively improve in such situations, further learning from the cases at an institution. The algorithm already appears to generalize well across multiple MR imaging scanners, even from outside institutions. Finally, a critically important test of the system for future clinical implementation will be to test the longitudinal precision of the methodology, to evaluate changes in lesion volume with time. Current studies are underway to address these important questions.

CONCLUSIONS

Our findings indicate that a fully-automated deep learning algorithm can achieve high performance on brain MR imaging (FLAIR) lesion segmentation across an array of different diseases and image acquisitions. It outperforms current state-of-the-art FLAIR lesion segmentation algorithms in detecting lesions and quantifying their volume, and it approaches near-human performance. We anticipate that such a system may be useful for descriptions of brain lesions in the clinical setting, replacing subjective, qualitative assessments with objective quantitative metrics, an essential component of a modern and efficient neuroradiologic workflow.

Disclosures: Jeffrey D. Rudie—*RELATED: Grant:* National Institutes of Health T32-EB004311-10 (Research Track Radiology Residency), Radiological Society of North America Resident Research Grant (RR1778)*; *UNRELATED: Grants/Grants Pending:* American Society for Neuroradiology, Radiological Society of North America, *Comments:* I have applied for additional grants to fund related work.* Suyash Mohan—*UNRELATED: Grants/Grants Pending:* Galileo Clinical Decision Support, *Comments:* research grant.* Andreas M. Rauschecker—*RELATED: Grant:* Radiological Society of North America Resident Research and Education Foundation, *Comments:* Resident Research Grant RR1778*; *Other:* National Institutes of Health, *Comments:* T32 Training Grants: T32-EB004311-10, T32-EB001631-14*; *UNRELATED: Support for Travel to Meetings for the Study or Other Purposes:* American College of Radiology—Association of University Radiologists Research Scholar Program, *Comments:* \$1000 to support travel to and presentation at the Association of University Radiologists 2018 on this work.* James C. Gee—*RELATED: Grant:* National Institutes of Health, *Comments:* National Institutes of Health grants supported the contribution and participation of me and my lab members with respect to development, evaluation, and application of methods for neuroimage processing and analysis*; *UNRELATED: Employment:* University of Electronic Science and Technology of China, *Comments:* I receive effort support for my role as Director of Center for Health Innovation at University of Pennsylvania—University of Electronic Science and Technology of China; *Stock/Stock Options:* mutual funds, *Comments:* as part of general retirement investment portfolio; *Travel/Accommodations/Meeting Expenses Unrelated To Activities Listed:* various scientific societies and academic institutions, *Comments:* for invited scientific lectures and presentations. *Money paid to the institution.

ACKNOWLEDGMENTS

We graciously acknowledge NVIDIA for the donation of 2 Titan Xp GPUs, through their GPU Grant Program, that were used for this research.

REFERENCES

1. OECD. **Health at a glance 2017: OECD indicators.** October 2018 https://doi.org/10.1787/health_glance-2017-en. Accessed December 24, 2018
2. Bydder GM, Young IR. **MR imaging: clinical use of the inversion recovery sequence.** *J Comput Assist Tomogr* 1985;9:659–75 CrossRef Medline
3. Bakshi R, Ariyaratana S, Benedict RH, et al. **Fluid-attenuated inversion recovery magnetic resonance imaging detects cortical and juxtacortical multiple sclerosis lesions.** *Arch Neurol* 2001;58:742–48 CrossRef Medline
4. Villanueva-Meyer JE, Mabray MC, Cha S. **Current clinical brain tumor imaging.** *Neurosurgery* 2017;81:397–415 CrossRef Medline
5. Busby LP, Courtier JL, Glastonbury CM. **Bias in radiology: the how and why of misses and misinterpretations.** *Radiographics* 2018;38:236–47 CrossRef Medline
6. Lee CS, Nagy PG, Weaver SJ, et al. **Cognitive and system factors contributing to diagnostic errors in radiology.** *AJR Am J Roentgenol* 2013;201:611–17 CrossRef Medline
7. Korfiatis P, Kline TL, Erickson BJ. **Automated segmentation of hyperintense regions in FLAIR MRI using deep learning.** *Tomography* 2016;2:334–40 CrossRef Medline
8. Artzi M, Liberman G, Naday G, et al. **Differentiation between treatment-related changes and progressive disease in patients with high grade brain tumors using support vector machine classification based on DCE MRI.** *J Neurooncol* 2016;127:515–24 CrossRef Medline
9. Yoo Y, Tang LY, Brosch T, et al. **Deep learning of joint myelin and T1w MRI features in normal-appearing brain tissue to distinguish between multiple sclerosis patients and healthy controls.** *Neuroimage Clin* 2018;17:169–78 CrossRef Medline
10. Fartaria MJ, Bonnier G, Roche A, et al. **Automated detection of white matter and cortical lesions in early stages of multiple sclerosis.** *J Magn Res Imaging* 2016;43:1445–64 CrossRef Medline
11. Lao Z, Shen D, Liu D, et al. **Computer-assisted segmentation of white matter lesions in 3D MR images using support vector machine.** *Acad Radiol* 2008;15:300–13 CrossRef Medline
12. Guerrero R, Qin C, Oktay O, et al. **White matter hyperintensity and stroke lesion segmentation and differentiation using convolutional neural networks.** *Neuroimage Clin* 2018;17:918–34 CrossRef Medline
13. Tsai JZ, Peng SJ, Chen YW, et al. **Automated segmentation and quantification of white matter hyperintensities in acute ischemic stroke patients with cerebral infarction.** *PLoS One* 2014;9:e104011 CrossRef Medline
14. Stone JR, Wilde EA, Taylor BA, et al. **Supervised learning technique for the automated identification of white matter hyperintensities in traumatic brain injury.** *Brain Inj* 2016;30:1458–68 CrossRef Medline
15. Rachmadi MF, Valdés-Hernández MD, Agan ML, et al. **Segmentation of white matter hyperintensities using convolutional neural networks with global spatial information in routine clinical brain MRI with none or mild vascular pathology.** *Comp Med Imaging Graph* 2018;66:28–43 CrossRef Medline
16. Habes M, Erus G, Toledo JB, et al. **White matter hyperintensities and imaging patterns of brain ageing in the general population.** *Brain* 2016;139:1164–79 CrossRef Medline
17. Bilello M, Doshi J, Nabavizadeh SA, et al. **Correlating cognitive decline with white matter lesion and brain atrophy: magnetic resonance imaging measurements in Alzheimer's disease.** *J Alzheimers Dis* 2015;48:987–94 CrossRef Medline
18. Viera S, Pinaya WH, Mechelli A. **Using deep learning to investigate the neuroimaging correlates of psychiatric and neurological disorders.** *Neurosci Biobehav Rev* 2017;74:58–75 CrossRef Medline
19. Chang PD, Kuoy E, Grinband J, et al. **Hybrid 3D/2D convolutional neural network for hemorrhage evaluation on head CT.** *AJNR Am J Neuroradiol* 2018;39:1609–16 CrossRef Medline
20. Wachinger C, Reuter M, Klein T. **DeepNAT: deep convolutional neural network for segmenting neuroanatomy.** *Neuroimage* 2018;170:434–45 CrossRef Medline
21. Norman B, Padoia V, Majumdar S. **Use of 2D U-Net convolutional neural networks for automated cartilage and meniscus segmentation of knee MR imaging data to determine relaxometry and morphometry.** *Radiology* 2018;288:177–85 CrossRef Medline

22. Tao Q, Yan W, Wang Y, et al. **Deep learning–based method for fully automatic quantification of left ventricle function from cine MR images: a multivendor, multicenter study.** *Radiology* 2019;290:81–88 CrossRef Medline
23. Kuijf HJ, Biesbroek JM, de Bresser J, et al. **Standardized assessment of automatic segmentation of white matter hyperintensities: results of the WMH segmentation challenge.** *IEEE Trans Med Imaging* 2019 Mar 19. [Epub ahead of print] CrossRef Medline
24. Li H, Jiang G, Zhang J, et al. **Fully convolutional network ensembles for white matter hyperintensities segmentation in MR images.** *Neuroimage* 2018;183:650–65 CrossRef Medline
25. Yushkevich PA, Piven J, Hazlett HC, et al. **User-guided 3D active contour segmentation of anatomical structures: significantly improved efficiency and reliability.** *Neuroimage* 2006;31:1116–28 CrossRef Medline
26. Avants BB, Epstein CL, Grossman M, et al. **Symmetric diffeomorphic image registration with cross-correlation: evaluating automated labeling of elderly and neurodegenerative brain.** *Med Image Anal* 2008;12:26–41 CrossRef Medline
27. Simard PY, Steinkraus D, Platt JC. **Best practices for convolutional neural networks applied to visual document analysis.** Institute of Electrical and Electronic Engineers 2003;958. <https://www.microsoft.com/en-us/research/publication/best-practices-for-convolutional-neural-networks-applied-to-visual-document-analysis/>. Accessed April 15, 2018
28. Ronneberger O, Fischer P, Brox T. **U-net: convolutional networks for biomedical image segmentation.** In: Navab N, Wells WM, Hornegger S, et al. *Medical Imaging Computing and Computer Assisted Intervention—MICCAI*. New York: Springer; 2015;234–41
29. Milletari F, Navab N, Ahmadi SA. **V-net: fully convolutional neural networks for volumetric medical image segmentation.** In: Stanford University. *3D Vision, 2016 Fourth International Conference, Institute of Electrical and Electronic Engineers*. Los Alamitos: Conference Publishing Services, IEEE Computer Society, 2016;565–71
30. Abadi M, Agarwal A, Barham P, et al. **TensorFlow: large-scale machine learning on heterogeneous systems.** *arXiv* 2016;1603.04467v2. <https://arxiv.org/abs/1603.04467>. Accessed April 15, 2018
31. Schmidt P, Gaser C, Arsic M, et al. **An automated tool for detection of FLAIR-hyperintense white-matter lesions in multiple sclerosis.** *Neuroimage* 2012;59:3774–83 CrossRef Medline
32. Griffanti L, Zamboni G, Khan A, et al. **BIANCA (Brain Intensity AbNormality Classification Algorithm): a new tool for automated segmentation of white matter hyperintensities.** *Neuroimage* 2016; 141:191–205 Medline
33. Dice LR. **Measures of the amount of ecologic association between species.** *Ecology* 1945;26:297–302 CrossRef
34. Taha AA, Hanbury A. **Metrics for evaluating 3D medical image segmentation: analysis, selection, and tool.** *BMC Med Imaging* 2015; 15:29 CrossRef Medline
35. Wang G, Li W, Ourselin S, et al. **Automatic brain tumor segmentation using cascaded anisotropic convolutional neural networks.** *arXiv:1709.00382*. <https://arxiv.org/abs/1709.00382>, Accessed June 15, 2018
36. Kamnitsas K, Bai W, Ferrante E, et al. **Ensembles of multiple models and architectures for robust brain tumour segmentation.** *arXiv: 1711.01468*. <https://arxiv.org/abs/1711.01468>. Accessed June 15, 2018
37. Isensee F, Kickingereder P, Wick W, et al. **Brain tumor segmentation and radiomics survival prediction: contribution to the BraTS 2017 challenge.** February 2018. https://www.researchgate.net/publication/323471060_Brain_Tumor_Segmentation_and_Radiomics_Survival_Prediction_Contribution_to_the_BrATS_2017_Challenge. Accessed April 15, 2018

White Matter Lesion Penumbra Shows Abnormalities on Structural and Physiologic MRIs in the Coronary Artery Risk Development in Young Adults Cohort

I.M. Nasrallah, M.-K. Hsieh, G. Erus, H. Battapady, S. Dolui, J.A. Detre, L.J. Launer, D.R. Jacobs, C. Davatzikos, and R.N. Bryan



ABSTRACT

BACKGROUND AND PURPOSE: White matter lesions are 1 age-related manifestation of cerebrovascular disease, but subthreshold abnormalities have been identified in nonlesional WM. We hypothesized that structural and physiologic MR imaging findings of early cerebrovascular disease can be measured in middle-aged subjects in tissue adjacent to WM lesions, termed “penumbra.”

MATERIALS AND METHODS: WM lesions were defined using automated segmentation in 463 subjects, 43–56 years of age, from the Coronary Artery Risk Development in Young Adults (CARDIA) longitudinal observational cohort study. We described 0- to 2-mm and 2- to 4-mm-thick spatially defined penumbral WM tissue ROIs as rings surrounding WM lesions. The remaining WM was defined as distant normal-appearing WM. Mean signal intensities were measured for FLAIR, T1-, and T2-weighted images, and from fractional anisotropy, mean diffusivity, CBF, and vascular reactivity maps. Group comparisons were made using Kruskal-Wallis and pair-wise *t* tests.

RESULTS: Lesion volumes averaged $0.738 \pm 0.842 \text{ cm}^3$ (range, 0.005–7.27 cm^3). Mean signal intensity for FLAIR, T2, and mean diffusivity was increased, while T1, fractional anisotropy, and CBF were decreased in white matter lesions versus distant normal-appearing WM, with penumbral tissues showing graded intermediate values (corrected $P < .001$ for all group/parameter comparisons). Vascular reactivity was significantly elevated in white matter lesions and penumbral tissue compared with distant normal-appearing white matter (corrected $P \leq .001$).

CONCLUSIONS: Even in relatively healthy 43- to 56-year-old subjects with small white matter lesion burden, structural and functional MR imaging in penumbral tissue reveals significant signal abnormalities versus white matter lesions and other normal WM. Findings suggest that the onset of WM injury starts by middle age and involves substantially more tissue than evident from focal white matter lesions visualized on structural imaging.

ABBREVIATIONS: BMI = body mass index; BOLD = blood oxygen level–dependent; dNAWM = distant normal-appearing white matter; FA = fractional anisotropy; MD = mean diffusivity; NAWM = normal-appearing white matter; RF_{score} = risk factor score; VR = vascular reactivity; WML = white matter lesion

Cerebral white matter lesions (WMLs), or leukoaraiosis, are common age-related MR imaging findings but may be pres-

ent in younger individuals.¹ WMLs are associated with cognitive decline,^{2–4} future infarction, depression,⁵ and poor clinical prognosis.⁶ WMLs commonly affect terminal vascular territories and their burden progresses⁷ by expansion of existing lesions and development of new lesions.

Pathologically, WMLs demonstrate capillary loss, arterial tortuosity, gliosis,⁸ demyelination, and ischemia.⁹ Imaging has shown physiologic abnormalities in WMLs, including decreased cerebral blood flow^{10,11} and vascular reactivity (VR),¹² and in-

Received February 7, 2019; accepted after revision June 6.

From the Department of Radiology (I.M.N., R.N.B.), Center for Biomedical Image Computing and Analytics (I.M.N., M.-K.H., G.E., H.B., C.D.), and Department of Neurology (S.D., J.A.D.), University of Pennsylvania, Philadelphia, Pennsylvania; National Institute on Aging (L.J.L.), National Institutes of Health, Bethesda, Maryland; and Division of Epidemiology (D.R.J.), School of Public Health, University of Minnesota, Minneapolis, Minnesota.

The Coronary Artery Risk Development in Young Adults Study (CARDIA) is conducted and supported by the National Heart, Lung, and Blood Institute in collaboration with the University of Alabama at Birmingham (HHSN2682018000051, HHSN2682018000071), Northwestern University (HHSN2682018000031), University of Minnesota (HHSN2682018000061), and the Kaiser Foundation Research Institute (HHSN2682018000041). CARDIA is also partially supported by the Intramural Research Program of the National Institute on Aging and an intra-agency agreement between National Institute on Aging and National Heart, Lung, and Blood Institute (AG0005). This article has been reviewed by CARDIA for scientific content. Data processing and analysis was supported by NIH grants S10OD023495, P41 EB015893, P30 AG010124, and R01 NS111115.

Paper previously presented, in part, at: American Society of Neuroradiology Annual Meeting and the Foundation of the ASNR Symposium, May 21–26, 2016; Washington DC.

Please address correspondence to Ilya M. Nasrallah, MD, PhD, Department of Radiology, University of Pennsylvania, 3400 Spruce St, Philadelphia, PA 19104; e-mail: ilya.nasrallah@penmedicine.upenn.edu

Indicates open access to non-subscribers at www.ajnr.org

Indicates article with supplemental online tables.

Indicates article with supplemental online photos.

<http://dx.doi.org/10.3174/ajnr.A6119>

Table 1: Demographic and risk factor data of the subjects from CARDIA with MRI included in this study

	Total	KPDR	UMN	P Value
No.	463	213	250	NA
Mean age (yr)	50.5 ± 3.4	50.5 ± 3.4	50.5 ± 3.3	.98
Race				
Black	36%	38%	34%	.48
White	64%	62%	66%	
Sex				
Male	47%	47%	46%	.98
Female	53%	53%	54%	
Mean BMI	28.3 ± 5.3	27.6 ± 5.4	28.9 ± 5.2	.009
Mean systolic/diastolic blood pressure (mm Hg)	118 ± 15/74 ± 12	118 ± 14/74 ± 11	119 ± 16/73 ± 12	.58/.66
Diabetic (%)	7.6%	6.9%	8.2%	.61
Smoking history				.005
Never	60%	67%	53%	
Former	25%	22%	28%	
Current	15%	11%	19%	
Sedentary behavior (>75th percentile)	19%	18%	20%	.55
Hypercholesterolemia	69%	71%	68%	.38
Mean risk factor score (range, 0–6)	2.1 ± 1.3	1.9 ± 1.2	2.2 ± 1.3	.06

Note:—KPDR indicates Kaiser-Permanente Division of Research; UMN, University of Minnesota; NA, not applicable.

creased blood-brain barrier permeability¹³; other studies have established that age, hypertension, and smoking are important risk factors for WMLs.¹⁴ These observations lead to the hypothesis that cardiovascular risk factors result in chronic vascular impairment that causes tissue damage visualized as WMLs, though there is also evidence for progression through acute injury.¹⁵ Together, these injuries likely interfere with axonal function and connectivity, contributing to clinical deficits, including cognitive decline.

Many methods exist to automatically segment WMLs from MR imaging, usually relying on structural MR imaging signal intensity characteristics. Because WMLs are usually progressive, MR imaging techniques sensitive to early pathologic changes may identify at-risk tissue in normal-appearing white matter (NAWM). Indeed, MR imaging studies, mostly in elderly populations,^{7,16,17} have demonstrated abnormalities in several measurements of NAWM on conventional MR imaging. NAWM near WMLs is most likely to show abnormality.¹⁷ One large study evaluating signal abnormalities in NAWM found increased FLAIR signal, increased mean diffusivity (MD), and decreased fractional anisotropy (FA) in tissue that ultimately developed into WMLs,⁷ while a smaller study showed similar findings for low CBF.¹⁸ White matter integrity metrics from diffusion tensor imaging, like FA and MD, are also abnormal in NAWM in individuals with WMLs.^{19–21} However, many previous studies are limited by small sample sizes and ROI image-analysis techniques that do not broadly evaluate WMLs and NAWM. Furthermore, structural, diffusion, and physiologic parameters have not been simultaneously evaluated in WMLs versus NAWM to allow evaluation of correlations among MR imaging parameters, which might be redundant due to measurement of similar physiology or for technical reasons.

We hypothesized that even in the relatively healthy Coronary Artery Risk Development in Young Adults (CARDIA) cohort, 43–56 years of age, visible WMLs under-represent total white matter abnormality. Evidence of more widespread injury may

suggest that antihypertensive therapy and other therapies to control vascular risk factors may benefit brain health starting in middle age. We investigated tissue immediately surrounding WMLs, termed WML penumbra, which was likely exposed to similar vascular stressors, predicting that the imaging correlates of injury would be intermediate between WMLs and distant NAWM. We simultaneously characterized structural abnormalities, measures of white matter integrity, and vascular physiologic parameters to determine the characteristics of WML penumbral tissue using MR imaging.

MATERIALS AND METHODS

Study Sample

The CARDIA study is a prospective, longitudinal cohort study evaluating the development of vascular risk factors in healthy young adults who provided informed consent to participate. The original cohort consisted of 5115 healthy black and white participants, 18–30 years of age.²² In the 25th year of follow-up, at a mean of 50 years of age, brain MR imaging was performed between August 19, 2010, and August 31, 2011, in 719 randomly selected subjects in the CARDIA study who had no contraindications to MR imaging. Structural (T1, T2, FLAIR), diffusion (MD, FA), and physiologic data (arterial spin-labeling perfusion, breath-hold fMRI) were acquired, and complete, analyzable datasets were obtained in 463 subjects (On-line Fig 1) from 2 sites: the University of Minnesota ($n = 250$) and Kaiser-Permanente Division of Research ($n = 213$), both using 3T Tim Trio scanners (Siemens, Erlangen, Germany). Demographic composition of this subgroup is shown in the Table 1; these subjects are similar to the overall CARDIA 25th year of follow-up MR imaging cohort,¹ and there was no significant difference on the basis of site except for body mass index (BMI) and smoking history.

MR Imaging and Analysis

This study was a retrospective analysis of prospectively acquired data, approved by the institutional review board of the University of Pennsylvania. The CARDIA brain MR imaging protocol has been published previously¹; briefly, it included T1 (TR = 1900 ms, TE = 2.89 ms, FOV = 250 mm, thickness = 1 mm, slices = 176, native resolution = 1 mm isotropic), T2 (TR = 3200 ms, TE = 409 ms, FOV = 250 mm, thickness = 1 mm, slices = 176, native resolution = 1 mm isotropic), FLAIR (TR = 6000 ms, TE = 285 ms, FOV = 258 mm, thickness = 1 mm, slices = 160, native resolution = 1 mm isotropic), 30-direction diffusion tensor imaging (TR = 7400 ms, TE = 82 ms, FOV = 246 mm, thickness = 2.2 mm, slices = 64, native resolution = 2.2 mm isotropic), pseudocontinuous arterial spin-labeling perfusion (TR = 4000 ms, TE = 11 ms, FOV = 220 mm, thickness = 5 mm, slices = 20, native resolution = 3.4 × 3.4 × 6 mm), and breath-hold blood oxygen level-dependent (BOLD) fMRI (TR = 2000

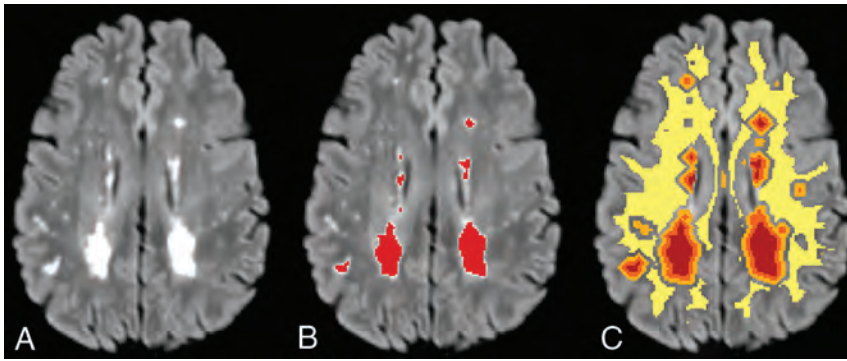


FIG 1. Sample FLAIR image showing WML (A); WML segmentation in red (B); and WML (red), 0–2 mm (orange) and 2–4 mm (light orange) penumbra, and dNAWM (yellow) (C). dNAWM is eroded from GM to eliminate partial volume effects among these tissue types.

ms, TE = 25 ms, FOV = 224 mm, thickness = 3.5 mm, slices = 35, native resolution = 3.5 mm isotropic). Scanner performance was monitored with quarterly Alzheimer’s Disease Neuroimaging Initiative and fBIRN phantom acquisitions (EZfMRI, Chicago, Illinois), with the scanners showing stability of phantom measurements throughout the study.

Processing of structural MR imaging sequences first involved histogram normalization and bias field correction of raw image data, which improve comparability of the uncalibrated, ordinal data, followed by template registration²³ and semiautomated tissue segmentation.²⁴ WML segmentation was performed using a previously validated supervised learning-based multimodal segmentation method.^{24,25} This support vector machine classifier was originally trained on multimodal MR imaging data from a separate training set with expert human manual segmentation of WMLs. It provides segmentation based on structural MR imaging (T1, T2, FLAIR) that strongly correlates with a definition of WMLs in the training set of a human observer. The model was applied on subjects in the CARDIA study to calculate binary WML masks and has been used in prior analyses of CARDIA imaging data. WML masks were morphologically dilated to define 2-mm rims of adjacent penumbral tissue (0–2 and 2–4 mm) within tissue classified as NAWM. These 2-mm ROIs were selected on the basis of a compromise between the intrinsic spatial resolution of the acquired data and the relatively narrow expected transition from WMLs to normal tissue. Voxels within these penumbral ROIs are more likely to have been exposed to similar vascular injury compared with those in WMLs and therefore are more likely to be abnormal; however, there is no a priori standard for subclassifying these voxels. Distant normal-appearing white matter (dNAWM) was defined by eroding the white matter segmentation mask from the GM and WML/penumbra ROIs by 2 mm to avoid partial volume effects.

From DTI, we calculated FA and MD scalar maps. CBF maps were calculated from pseudocontinuous arterial spin-labeling.²⁶ Maps of VR as measured by the percentage signal change in BOLD fMRI between breath-hold and rest states were generated using a method similar to that of Murphy et al.²⁷ To summarize, breath-holding was used to elevate blood CO₂ and thereby induce cerebral vasodilation to effect changes in BOLD signal. During acquisition of BOLD fMRI, subjects were cued to follow four 16-second breath-holds using E-Prime (Psychology Software Tools, Sharpsburg, Pennsylvania). Using FSL (<http://www.fmrib.ox.ac.uk/fsl>), we mo-

tion-corrected the resulting images and smoothed them, and a whole-brain generalized linear model analysis was performed using a 9-second delay to account for hemodynamic lag. We excluded subjects without activation of the superior sagittal sinus, a marker of breath-hold compliance, measured as a *z* score within the superior sagittal sinus of <2.3. VR *z* score maps were thresholded at *z* > 2.3, and percentage activation was calculated relative to the median *z* score in the superior sagittal sinus. Only voxels with activation above this threshold were included for analysis. Maps for FA, MD, CBF, and VR were registered to T1 space and inter-

polated to 1-mm isotropic resolution.

3D volumes and imaging maps were aligned using FSL. In each of the 4 ROIs—WML, 0- to 2-mm penumbra, 2- to 4-mm penumbra, and dNAWM (Fig 1)—mean intensity was extracted from each of the acquired sequences, resulting in mean intensity values for each of the 4 regions for FLAIR, T1, T2, FA, MD, CBF, and VR. For VR, to evaluate the possible contributions of noise from subjects with few activated voxels, we repeated the analyses after exclusion of subjects with the lowest quartile of activated voxels for each ROI as a secondary analysis.

Statistics

Statistical analysis was performed using Python 2.7 (<https://www.python.org/download/releases/2.7/>). Mean values for each parameter were compared between groups using Kruskal-Wallis and Wilcoxon signed rank pair-wise *t* tests. Regression analysis of median intensity across regions was performed by applying a generalized estimating equation to *z* score–normalized intensity measures. Correlation matrices using Pearson product-moment correlation coefficients were computed for intensities of each parameter. The Holm-Bonferroni correction was used to adjust for multiple comparisons in pair-wise *t* tests and correlation matrices. Recursive feature elimination with stratified 10-fold cross-validation was performed to determine the optimal set of parameters that best predicted assignment to WML, 0- to 2-mm penumbra, 2- to 4-mm penumbra, and NAWM ROIs for each voxel. This method initially used all parameters to train the estimator; then, features with the lowest weights were recursively eliminated until further feature removal reduced classification accuracy. We investigated the associations of imaging parameters in WMLs and penumbras with clinical risk factors of systolic blood pressure, BMI, smoking status, and sedentary behavior, as previously defined,¹ controlling for imaging site and demographic factors of age, sex, and race using ordinary least-squares linear regression modeling with *z* score–transformed data, adjusting for age, sex, race, and site. Similarly, we evaluated overall cardiovascular risk using a derived risk factor score (RF_{score} range, 0–6) that was generated for each participant as a count of which of the following 6 risk factors were present: hypertension (systolic blood pressure > 140 mm Hg or on antihypertensive medication), hypercholesterolemia (total serum cholesterol level > 100 mg/dL or

Table 2: Regional volumes and mean intensity values for MRI parameters^a

	WML	Penumbra (0–2 mm)	Penumbra (2–4 mm)	dNAWM	Regression Coefficient
Mean volume (cm ³)	0.738 (0.842) [0.661–0.815]	2.78 (2.26) [2.57–2.99]	5.81 (4.21) [5.43–6.19]	219 (3.68) [186–253]	NA
FLAIR intensity	136 (10.1) [135–137]	98.9 (3.50) [98.6–99.2]	79.4 (3.71) [79.1–79.7]	70.8 (2.58) [70.6–71.0]	–0.854
T1 intensity	116 (6.43) [115–117]	132 (5.80) [132–133]	142 (4.50) [142–142]	156 (1.31) [156–156]	0.824
T2 intensity	115 (8.62) [114–115]	88.3 (6.82) [87.7–88.9]	74.1 (4.75) [73.7–74.5]	60.6 (1.02) [60.5–60.7]	–0.734
FA	0.279 (0.0554) [0.273–0.284]	0.328 (0.0411) [0.324–0.331]	0.374 (0.0380) [0.371–0.377]	0.384 (0.0254) [0.382–0.386]	0.630
MD (10 ^{–3})	3.68 (0.662) [3.62–3.73]	3.23 (0.445) [3.19–3.27]	2.97 (0.344) [2.93–3.00]	2.33 (0.112) [2.32–2.34]	–0.578
CBF (mL/100 g/min)	25.2 (10.3) [24.3–26.1]	26.9 (9.37) [26.1–27.7]	28.8 (9.06) [28.0–29.6]	34.4 (8.56) [33.6–35.2]	0.306
VR (Mean % change)	0.776 (0.493) [0.731–0.821]	0.779 (0.379) [0.745–0.813]	0.790 (0.328) [0.760–0.820]	0.681 (0.377) [0.647–0.715]	0.192

Note:—NA indicates not applicable.

^a SD is in parentheses, and 95% confidence intervals for intensity parameters are in brackets. Kruskal-Wallis tests were significant for all parameters, and pair-wise comparisons had $P < .001$ except that the WML and penumbral ROIs did not show significant differences in VR. The slope of linear regression across the 4 regions for intensity variables using a median value is shown in the last column; regression analyses were all statistically significant with $P < .001$.

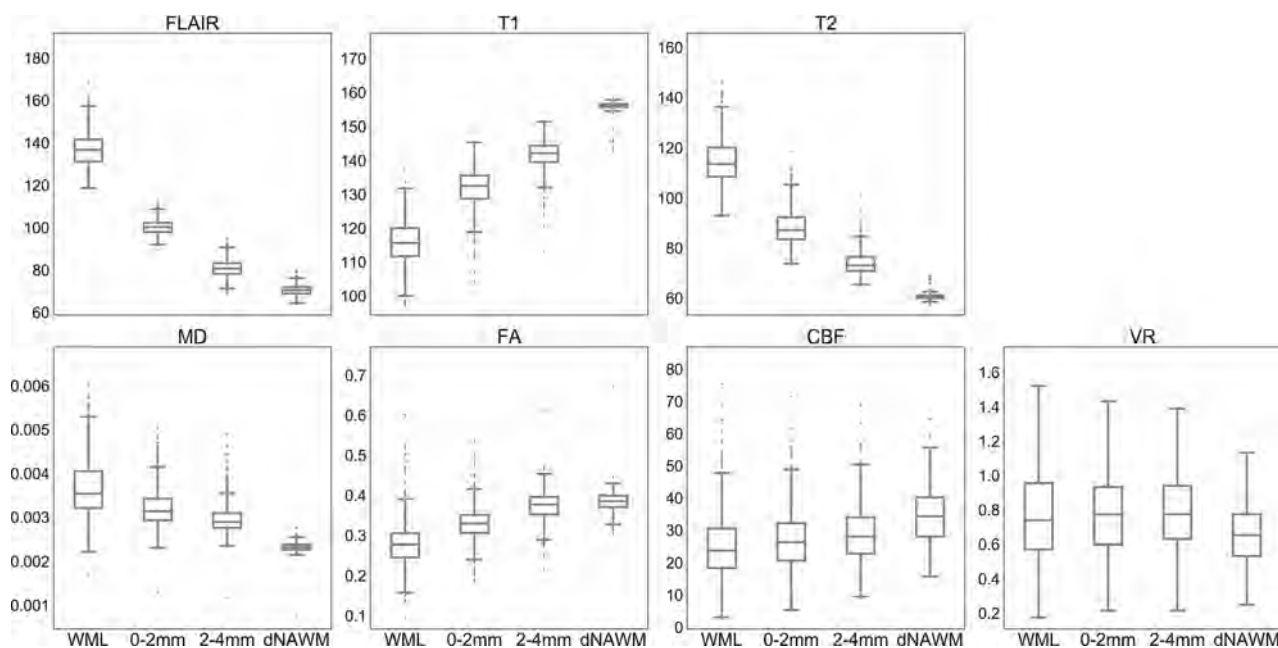


FIG 2. Boxplots of mean intensity values for each region. CBF is measured in cubic millimeters/100 g/min, and VR shows the mean percentage signal change. For vascular reactivity, outliers are excluded (comprising ~10% of the sample) to better demonstrate differences among means. A graph with outliers is available (On-line Fig 2). For each parameter, mean values are significantly different among all pair-wise comparisons between ROIs with corrected $P < .001$, except for VR in which comparison of WML and dNAWM shows corrected $P = .001$, and there is no significant difference among WMLs and the 2 penumbra regions ($P > .4$).

on cholesterol-lowering medication), sedentary behavior (>75th percentile, equivalent to >8.5 hours of sedentary behavior per day), diabetes (if present), BMI (if ≥ 30), or history of smoking (current and former smokers).

RESULTS

WML volumes averaged 0.738 ± 0.842 cm³ (range, 0.005–7.27 cm³) in the 463 subjects from the CARDIA 25th year of follow-up cohort included in this study. Derived volumes of 0- to 2-mm penumbra, 2- to 4-mm penumbra, and dNAWM measured at 2.78 ± 2.26 , 5.81 ± 4.21 , and 219 ± 36.8 cm³, respectively.

We found significant differences for most parameters across ROIs (Table 2 and Fig 2). Mean FLAIR intensity, T2, and MD were higher in WMLs than in dNAWM, while mean T1 intensity, FA, and CBF were lower (all $P < .001$). For all these parameters, penumbral tissue showed intermediate values that were significantly different from each other and from both WMLs and dNAWM ($P < .001$ for all pair-wise t tests). Regression analysis by group demonstrated a strong effect of tissue type on signal intensities for FLAIR, T1, T2, MD, and FA, all statistically significant ($P < .001$), with the strongest effects seen for structural parameters (Table 2); these correlations were not materially affected by adjusting for

study. The CARDIA Brain MRI cohort has a much lower mean age and WML volume compared with most other studies that have evaluated WMLs and penumbra; for comparison, the study of de Groot et al⁷ had a mean age of 67 years with a median WML volume of 3.4 cm³. The Women's Health Initiative Memory Study, which used the same WML classifier method as in the current study, had a mean age of 78.5 years and mean WML volume of 4.3 cm³,³¹ and the study of Promjunyakul et al¹⁶ had a mean age of 85 years, with a mean WML volume of 11.2 cm³. Most CARDIA MRI participants were normotensive (57%), with 11% prehypertensive and 32% hypertensive.¹

Despite the low lesion burden, we found statistically significant abnormalities in all measured structural, diffusion, and physiologic MR imaging parameters in penumbral tissue, encompassing, on average, more than 10-fold larger volume than WMLs (Fig 2 and Table 2). Signal abnormalities in WML and penumbral regions were worsened when vascular risk factors were present, specifically with relationships between systolic blood pressure and FLAIR intensity and between systolic blood pressure and BMI and CBF. These findings indicate that as in the elderly, WM damage is more extensive in middle age than represented by the typical low WML volume, suggesting that early intervention for reversible cardiovascular risk factors may yield benefit in slowing progression of this damage. Recent results from the Systolic Blood Pressure Intervention Trial (SPRINT) have shown that aggressive blood pressure control may slow progression of WML volume,³² and it is possible that such an intervention would also affect penumbral tissue. Most interesting, we did not find an association between regional signal intensities and age, which has been shown to be the strongest risk factor for WMLs in prior studies. It is possible that at the younger age of this cohort, lesions are primarily the consequence of hypertension; therefore, growth could potentially be prevented with adequate antihypertensive therapy. Overall, we found limited associations between cardiovascular risk factors and regional intensity values; however, effects were shown in multivariate analyses between a cumulative risk factor score and, individually, with sedentary behavior, smoking history, and BMI. These associations require further investigation, particularly as the exposure lengthens with aging.

The physiologic MR imaging variables, CBF and VR, have been less extensively studied in WMLs and penumbra. Our study confirms prior reports showing decreased CBF in WMLs^{10,11} and penumbra compared with NAWM.¹⁶ Unlike the other imaging parameters, which probably measure sequelae from injury, CBF and VR may more directly measure etiologic abnormalities for WMLs; most interesting, CBF was the only variable significantly associated with the number of cardiovascular risk factors. Regional differences were less pronounced in the physiologic CBF and VR data, partially related to lower signal to noise and resolution and greater biologic variability. Compared with VR, CBF is more technologically mature with greater potential for widespread implementation.

The few studies that have evaluated VR in WMLs mostly evaluated global VR, which is dominated by GM, and more often used transcranial Doppler sonography rather than MR imaging. Hypertension and vascular risk factors have been associated with

decreased VR; some but not all studies showed adverse associations of global cerebral VR with WMLs.³³⁻³⁵ Studies in elderly subjects measuring BOLD VR with a more reproducible CO₂ inhalation method showed a 50%–60% decreased VR in WML versus NAWM.^{12,28} In our study, the mean VR was unexpectedly higher in WMLs and penumbra than in dNAWM; if validated, this finding might suggest a difference in physiology in WMLs and at-risk tissue in younger or subjects with low-WML volume compared with elderly or subjects with high-WML volume. Increased VR may indicate a compensatory, possibly protective, vasoreactivity versus an indication of intrinsic, possibly harmful, abnormality of the vessels.

The mechanisms behind WML propagation are unknown. Vascular compromise may spread from extant WMLs, or independent events may accumulate in vulnerable territory. We found that adjacent tissue, including that 2–4 mm removed from WMLs, showed detectable abnormalities on structural imaging, measures of white matter integrity, and physiologic parameters. For all parameters except VR, penumbra showed intermediate values transitioning between WMLs and dNAWM, suggesting lesser injury. Longitudinal evaluation comparing regions that develop into lesions versus those that do not will likely identify heterogeneity within penumbral tissue and show whether these parameters can predict lesion growth. Unfortunately, prospective prediction of lesion development has not yet been successful. Scoring each voxel based on a combination of MR imaging parameters may provide a means to identify at-risk regions. We found that a combination of FLAIR, T1, and T2 provided optimal, nonredundant classification of voxels into the WML, penumbral, and dNAWM ROIs; however, it remains to be seen whether longitudinal change in WMLs is better predicted by baseline structural or physiologic measures or a combination.

There are several limitations of this study. Due to lower resolution of diffusion and functional sequences compared with structural imaging, partial volume effects likely affect calculation of mean intensities. However, significant differences were seen between WMLs and the 2- to 4-mm penumbra, which would be less affected by partial volume effects from WMLs. The WML segmentation classifier used to identify WMLs is conservative, and as a result, some tiny WMLs may be included in other regions, which should decrease statistical differences by increasing variability. Using two, 2-mm concentric penumbral rings was a compromise between the need to evaluate a relatively narrow band of tissue around WMLs and the need to reduce partial volume effects. Others have shown similar graded changes extending even further around WMLs.¹⁶ The morphologic dilation used to generate the penumbral ROI overlooks the expected heterogeneity of penumbral tissue; however, mixing tissues with varying levels of injury in concentric ROIs is expected to decrease the power of this study.

T1, T2, and FLAIR intensities vary depending on scanner and imaging parameters. Our data were acquired on the same scanner model with the same imaging parameters, and normalization techniques were implemented to harmonize the data; however, these features affect generalizability to other sites. We made no correction for the mild, normal regional variations of signal intensity in the brain, which has been previously performed.⁷ Nor-

mal signal variations may accentuate some regional differences; for example, FLAIR is normally slightly increased in periventricular regions most commonly affected by WMLs relative to NAWM. FA, however, shows significant decreases in regions that normally have higher FA, suggesting that applying regional intensity corrections might result in even greater differences.

CONCLUSIONS

Even in relatively healthy, middle-aged adults with low total WML burden, WMLs have a substantial penumbra of tissue with abnormalities quantifiable by structural and physiologic MR imaging parameters, in some individuals involving volumes >10 times larger than WMLs visible on FLAIR. Furthermore, the gradation of signal abnormalities in penumbral tissue suggests early/milder injury, compatible with the hypothesis that injury expands from established lesions; this penumbral tissue may be a target for therapeutic intervention to prevent worsening of WMLs. Multimodal MR imaging may better define injured white matter than methods that use only structural data. Further investigation is needed to determine the optimal combination of parameters to prospectively identify the full extent of abnormal white matter and the effects of these abnormalities on neural circuits and cognition. An epidemiologic priority is to examine whether the volume and characteristics of these expanded injury regions predict future lesions and risk of brain-related disease.

ACKNOWLEDGMENTS

The authors thank Raymond Pomponio for statistical assistance.

Disclosures: Ilya M. Nasrallah—*RELATED: Grant:* National Institutes of Health*; *Support for Travel to Meetings for the Study or Other Purposes:* National Institutes of Health*; *UNRELATED: Grants/Grants Pending:* National Institutes of Health.* Guray Erus—*RELATED: Grant:* National Institutes of Health.* John A. Detre—*RELATED: Grant:* National Institutes of Health*; *UNRELATED: Consultancy:* Blackfynn, CHDI Foundation, Dana Foundation, National Institutes of Health, *Comments:* I have provided expert advice on neuroimaging to the University of Pennsylvania spinoff startup company Blackfynn. I have received stock options. I have provided consulting to the CHDI Foundation, a private foundation involved in Huntington disease research, but none in the last year. I am compensated as a grant reviewer for the Dana Foundation and the National Institutes of Health, total approximately \$2000 per year; *Grants/Grants Pending:* National Institutes of Health*; *Payment for Manuscript Preparation:* Dana Foundation, *Comments:* I received \$10,000 from the Dana Foundation for assisting with a Web article on neuroimaging; *Patents (Planned, Pending or Issued):* University of Pennsylvania, *Comments:* I am listed as a coinventor on 2 University of Pennsylvania patents for optical monitoring of cerebral blood flow. Neither has been licensed. Lenore J. Launer—*UNRELATED: Employment:* National Institutes of Health. Robert N. Bryan—*RELATED: Grant:* National Institutes of Health*; *UNRELATED: Board Membership:* Galileo CDS, *Comments:* no cash transaction or value; *Grants/Grants Pending:* National Institutes of Health; *Patents (Planned, Pending or Issued):* University of Pennsylvania patent license to Galileo CDS; *Stock/Stock Options:* Galileo CDS. *Money paid to the institution.

REFERENCES

- Launer LJ, Lewis CE, Schreiner PJ, et al. **Vascular factors and multiple measures of early brain health: CARDIA Brain MRI Study.** *PLoS One* 2015;10:e0122138 CrossRef Medline
- Jokinen H, Kalska H, Ylikoski R, et al; LADIS group. **Longitudinal cognitive decline in subcortical ischemic vascular disease: the LADIS study.** *Cerebrovasc Dis* 2009;27:384–91 CrossRef Medline
- Verdelho A, Madureira S, Moleiro C, et al; LADIS Study. **White matter changes and diabetes predict cognitive decline in the elderly: the LADIS study.** *Neurology* 2010;75:160–67 CrossRef Medline
- Debette S, Markus HS. **The clinical importance of white matter hyperintensities on brain magnetic resonance imaging: systematic review and meta-analysis.** *BMJ* 2010;341:c3666 CrossRef Medline
- Teodorczuk A, Firbank MJ, Pantoni L, et al; LADIS Group. **Relationship between baseline white-matter changes and development of late-life depressive symptoms: 3-year results from the LADIS study.** *Psychol Med* 2010;40:603–10 CrossRef Medline
- Inzitari D, Pracucci G, Poggesi A, et al; LADIS Study Group. **Changes in white matter as determinant of global functional decline in older independent outpatients: three-year follow-up of LADIS (leukoaraiosis and disability) study cohort.** *BMJ* 2009;339:b2477 CrossRef Medline
- de Groot M, Verhaaren BF, de Boer R, et al. **Changes in normal-appearing white matter precede development of white matter lesions.** *Stroke* 2013;44:1037–42 CrossRef Medline
- Brown WR, Thore CR. **Review: cerebral microvascular pathology in ageing and neurodegeneration.** *Neuropathol Appl Neurobiol* 2011; 37:56–74 CrossRef Medline
- Fazekas F, Kleinert R, Offenbacher H, et al. **Pathologic correlates of incidental MRI white matter signal hyperintensities.** *Neurology* 1993;43:1683–89 CrossRef Medline
- O'Sullivan M, Lythgoe DJ, Pereira AC, et al. **Patterns of cerebral blood flow reduction in patients with ischemic leukoaraiosis.** *Neurology* 2002;59:321–26 CrossRef Medline
- Brickman AM, Zahra A, Muraskin J, et al. **Reduction in cerebral blood flow in areas appearing as white matter hyperintensities on magnetic resonance imaging.** *Psychiatry Res* 2009;172:117–20 CrossRef Medline
- Sam K, Crawley AP, Poulblanc J, et al. **Vascular dysfunction in leukoaraiosis.** *AJNR Am J Neuroradiol* 2016;37:2258–64 CrossRef Medline
- Topakian R, Barrick TR, Howe FA, et al. **Blood-brain barrier permeability is increased in normal-appearing white matter in patients with lacunar stroke and leukoaraiosis.** *J Neurol Neurosurg Psychiatry* 2010;81:192–97 CrossRef Medline
- Grueter BE, Schulz UG. **Age-related cerebral white matter disease (leukoaraiosis): a review.** *Postgrad Med J* 2012;88:79–87 CrossRef Medline
- Conklin J, Silver FL, Mikulis DJ, et al. **Are acute infarcts the cause of leukoaraiosis? Brain mapping for 16 consecutive weeks.** *Ann Neurol* 2014;76:899–904 CrossRef Medline
- Promjunyakul N, Lahna D, Kaye JA, et al. **Characterizing the white matter hyperintensity penumbra with cerebral blood flow measures.** *Neuroimage Clin* 2015;8:224–29 CrossRef Medline
- Maniega SM, Valdés Hernandez MC, Clayden JD, et al. **White matter hyperintensities and normal-appearing white matter integrity in the aging brain.** *Neurobiol Aging* 2015;36:909–18 CrossRef Medline
- Bernbaum M, Menon BK, Fick G, et al. **Reduced blood flow in normal white matter predicts development of leukoaraiosis.** *J Cereb Blood Flow Metab* 2015;35:1610–15 CrossRef Medline
- Schmidt R, Ropele S, Ferro J, et al; LADIS study group. **Diffusion-weighted imaging and cognition in the leukoaraiosis and disability in the elderly study.** *Stroke* 2010;41:e402–08 CrossRef Medline
- Pelletier A, Periot O, Dilharreguy B, et al. **Age-related modifications of diffusion tensor imaging parameters and white matter hyperintensities as inter-dependent processes.** *Front Aging Neurosci* 2016;7: 255 CrossRef Medline
- Maillard P, Carmichael O, Harvey D, et al. **FLAIR and diffusion MRI signals are independent predictors of white matter hyperintensities.** *AJNR Am J Neuroradiol* 2013;34:54–61 CrossRef Medline
- Friedman GD, Cutter GR, Donahue RP, et al. **CARDIA: study design, recruitment, and some characteristics of the examined subjects.** *J Clin Epidemiol* 1988;41:1105–16 CrossRef Medline
- Shen D, Davatzikos C. **HAMMER: hierarchical attribute matching mechanism for elastic registration.** *IEEE Trans Med Imaging* 2002; 21:1421–39 CrossRef Medline
- Zacharaki EI, Kanterakis S, Bryan RN, et al. **Measuring brain lesion progression with a supervised tissue classification system.** *Med Image Comput Comput Assist Interv* 2008;11:620–27 Medline

25. Lao Z, Shen D, Liu D, et al. **Computer-assisted segmentation of white matter lesions in 3D MR images using support vector machine.** *Acad Radiol* 2008;15:300–13 [CrossRef Medline](#)
26. Wang Z, Aguirre GK, Rao H, et al. **Empirical optimization of ASL data analysis using an ASL data processing toolbox: ASLtbx.** *Magn Reson Imaging* 2008;26:261–69 [CrossRef Medline](#)
27. Murphy K, Harris AD, Wise RG. **Robustly measuring vascular reactivity differences with breath-hold: normalising stimulus-evoked and resting state BOLD fMRI data.** *Neuroimage* 2011;54:369–79 [CrossRef Medline](#)
28. Uh J, Yezhuvath U, Cheng Y, et al. **In vivo vascular hallmarks of diffuse leukoaraiosis.** *J Magn Reson Imaging* 2010;32:184–90 [CrossRef Medline](#)
29. Reich T, Rusinek H. **Cerebral cortical and white matter reactivity to carbon dioxide.** *Stroke* 1989;20:453–57 [CrossRef Medline](#)
30. Guyon I, Weston J, Barnhill S, et al. **Gene selection for cancer classification using support vector machines.** *Machine Learning* 2002;46:389–422 [CrossRef](#)
31. Kuller LH, Margolis KL, Gaussoin SA, et al; Women's Health Initiative Memory Study Research Group. **Relationship of hypertension, blood pressure, and blood pressure control with white matter abnormalities in the Women's Health Initiative Memory Study (WHIMS)-MRI trial.** *J Clin Hypertens (Greenwich)* 2010;12:203–12 [CrossRef Medline](#)
32. Nasrallah IM; Alzheimer's Association International Conference. **A Randomized Trial of Intensive Versus Standard Systolic Blood Pressure Control and Brain Structure: SPRINT MIND MRI.** Chicago, IL; July 25, 2018
33. Matsushita K, Kuriyama Y, Nagatsuka K, et al. **Periventricular white matter lucency and cerebral blood flow autoregulation in hypertensive patients.** *Hypertension* 1994;23:565–68 [CrossRef Medline](#)
34. Bakker SL, de Leeuw FE, de Groot JC, et al. **Cerebral vasomotor reactivity and cerebral white matter lesions in the elderly.** *Neurology* 1999;52:578–83 [CrossRef Medline](#)
35. Birns J, Jarosz J, Markus HS, et al. **Cerebrovascular reactivity and dynamic autoregulation in ischaemic subcortical white matter disease.** *J Neurol Neurosurg Psychiatry* 2009;80:1093–98 [CrossRef Medline](#)

The Interpeduncular Angle: A Practical and Objective Marker for the Detection and Diagnosis of Intracranial Hypotension on Brain MRI

D.J. Wang, S.K. Pandey, D.H. Lee, and M. Sharma



ABSTRACT

BACKGROUND AND PURPOSE: Classic findings of intracranial hypotension on MR imaging, such as brain stem slumping, can be variably present and, at times, subjective, potentially making the diagnosis difficult. We hypothesize that the angle between the cerebral peduncles correlates with the volume of interpeduncular cistern fluid and is decreased in cases of intracranial hypotension. We aimed to investigate its use as an objective assessment for intracranial hypotension.

MATERIALS AND METHODS: Brain MRIs of 30 patients with intracranial hypotension and 30 age-matched controls were evaluated by 2 fellowship-trained neuroradiologists for classic findings of intracranial hypotension and the interpeduncular angle. Group analysis was performed with a Student *t* test, and receiver operating characteristic analysis was used to identify an ideal angle threshold to maximize sensitivity and specificity. Interobserver reliability was assessed for classic findings of intracranial hypotension using the Cohen κ value, and the interpeduncular angle, using the intraclass correlation.

RESULTS: The interpeduncular angle had excellent interobserver reliability (intraclass correlation coefficient value = 0.833) and was significantly lower in the intracranial hypotension group compared with the control group (25.3° versus 56.3°; $P < .001$). There was significant correlation between the interpeduncular angle and the presence of brain stem slumping ($P < .001$) and in cases with ≥ 3 classic features of intracranial hypotension ($P = .01$). With a threshold of 40.5°, sensitivity and specificity were 80% and 96.7%, respectively.

CONCLUSIONS: The interpeduncular angle is a sensitive and specific measure of intracranial hypotension and is a reliably reproducible parameter on routine clinical MR imaging.

Intracranial hypotension is a neurologic syndrome with various etiologies that share a common final pathway of decreased CSF volume and pressure. The classic clinical presentation is orthostatic headache with associated nonspecific symptoms such as nausea and vertigo.¹ In severe cases, the disease can progress to cranial nerve palsies and even coma.²⁻⁴ The nonspecific nature of the clinical presentation can result in considerable delays in work-up, mimicking entities with drastically different treatments such as migraine, meningitis, or psychogenic disorders.⁵ The diagnosis is made clinically, based on the International Classification of Headache Disorders, 3rd edition, which requires a headache that develops in temporal relation with one of either low CSF pressure

(< 60 mm of CSF) or imaging features demonstrating or suggestive of CSF leak.⁶ Currently, no criterion standard diagnostic test exists; the site of CSF leak in the spine is not always identified on imaging and a wide range of CSF opening pressures has been observed. For various clinical and practical considerations, contrast-enhanced MR imaging of the head is frequently the first-line investigation to confirm the diagnosis and rule out other mimics. However, even classically described imaging features are not always present and, at times, can be challenging to objectively report.⁷⁻¹² For example, the most sensitive MR imaging finding for intracranial hypotension is pachymeningeal enhancement, but this can also be seen routinely in postoperative or post-lumbar puncture cases.^{7,8} Brain stem slumping has shown reasonable specificity for the syndrome, but the finding is only present in approximately 51% of cases and can be subjective.⁸⁻¹² These issues have led to attempts to develop more objective criteria in determining low CSF volume.¹¹⁻¹³ We propose a quantitative marker, the interpeduncular angle, to support the diagnosis of intracranial hypotension on MR imaging as a quick and repro-

Received April 2, 2019; accepted after revision June 6.

From the Department of Medical Imaging (D.J.W.), Western University, London, Ontario, Canada; and Department of Medical Imaging (D.J.W., S.K.P., D.H.L., M.S.), London Health Sciences Centre, University Hospital, London, Ontario, Canada.

Please address correspondence to Manas Sharma, MD, Department of Medical Imaging, London Health Sciences Centre, University Hospital, 339 Windermere Rd, London, Ontario, Canada, N6A5A5; e-mail: manas.sharma@lhsc.on.ca

<http://dx.doi.org/10.3174/ajnr.A6120>

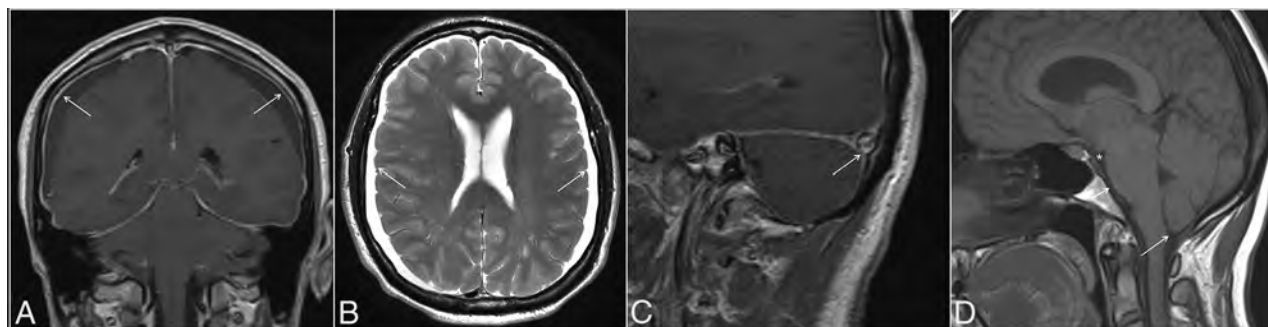


FIG 1. Classic MR imaging features of intracranial hypotension (arrows), including diffuse pachymeningeal enhancement (A), bilateral subdural collections (B), the venous distension sign (C), defined as a convex inferior margin of the dominant transverse sinus, and brain stem slumping (D), characterized by effacement of the interpeduncular cistern (asterisk), flattening of the anterior surface of the pons (short arrow), and tonsillar herniation (long arrow).

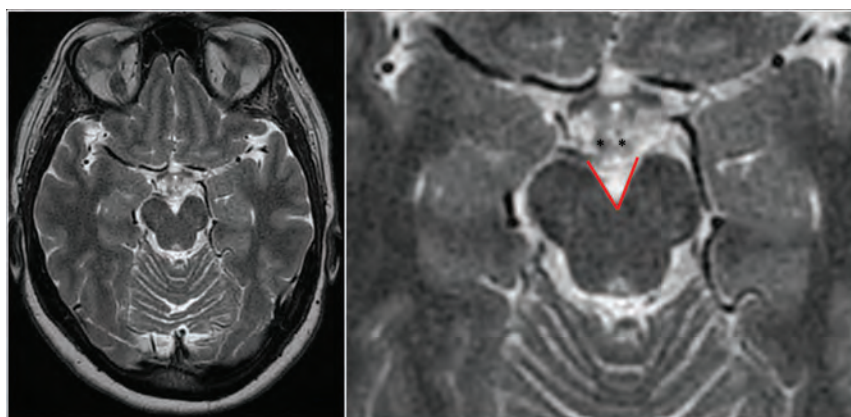


FIG 2. Full FOV (left) and magnified (right) axial T2WI depicting the interpeduncular angle (red lines) measured at the level of the mammillary bodies (asterisks) in a control patient.

ducible measure. We aimed to investigate the relationship between this angle and the diagnosis of intracranial hypotension as well as its correlation to classically described imaging findings.

MATERIALS AND METHODS

Approval from the Western University institutional ethics committee review board was obtained. A retrospective search of the PACS between January 2008 and December 2017 with the keywords “intracranial hypotension” was performed. Inclusion criteria were patients older than 17 years of age with a clinical diagnosis of intracranial hypotension and a brain MR imaging examination. Exclusion criteria included patients with tumor, hydrocephalus, leptomenigeal disease, subdural empyema, congenital Chiari malformation, and intracranial hypertension. Age-matched controls were selected from the same time period. Most of the controls were evaluated for headache, with a minority assessed for nonspecific symptoms, and none had a final clinical diagnosis of intracranial hypotension.

Two fellowship-trained neuroradiologists with combined 10 years of practice experience reviewed the MR imaging studies in a binary fashion for the following qualitative parameters of intracranial hypotension: pachymeningeal enhancement (or thickening in cases with no gadolinium), subdural collections, venous engorgement, and brain stem slumping (Fig 1). Venous engorgement was defined as a convex inferior border of the middle third of the dominant transverse sinus on a T1-weighted sagittal image, termed the “venous dis-

ension sign,” as described previously.¹³ Brain stem slumping was evaluated subjectively but was based on prior described findings such as a downward shift of the mammillary bodies with or without associated deformity of the tuber cinereum, a downward shift of the splenium of the corpus callosum, flattening of the anterior surface of the pons, and tonsillar herniation. In cases of discrepancy, a third fellowship-trained neuroradiologist with >30 years of experience reviewed the images and made a final decision.

The radiologists also evaluated the MR images in both groups for the interpeduncular angle, defined as the angle

formed by the posterior half of the cerebral peduncles obtained on an axial T2-weighted image at the level of the mammillary bodies or the slice immediately below it, whichever yields a lesser value (Fig 2). The angle was measured by both radiologists, and an average was taken as the true value.

Statistical Analysis

All statistical analysis was performed with SPSS statistical software, Version 25 (IBM, Armonk, New York). Intergroup analysis for continuous variables was performed with the Student *t* test. All data were analyzed using 2-tailed tests, with a *P* value < .05 considered significant. Receiver operating characteristic (ROC) curves were used to estimate a threshold angle for optimal sensitivity and specificity. Interobserver correlation was assessed using a weighted Cohen κ coefficient for categorical items and the intraclass correlation coefficient for continuous items. The strength of agreement based on coefficient values was defined as follows: 0, poor agreement; 0.01–0.20, slight agreement; 0.21–0.40, fair agreement; 0.41–0.60, moderate agreement; 0.61–0.80, good agreement; and 0.81–1.0, excellent agreement.

RESULTS

Thirty patients with intracranial hypotension and 30 controls were evaluated (Table). The average age of the intracranial hypotension group was 50.3 years (range, 24–81 years), while that of

Population demographics

	Intracranial Hypotension (n = 30)	Control (n = 30)	Significance (P < .05)
Age (range) (mean) (yr)	24–81, 50.3	17–78, 49.6	.88
Sex (female) (No.) (%)	13 (43%)	22 (73%)	.02 ^a
Headache	87%	73%	.49
Treatment (EBP)	19/30 (14 responded)		

Note:—EBP indicates epidural blood patch.

^aStatistical significance reached.

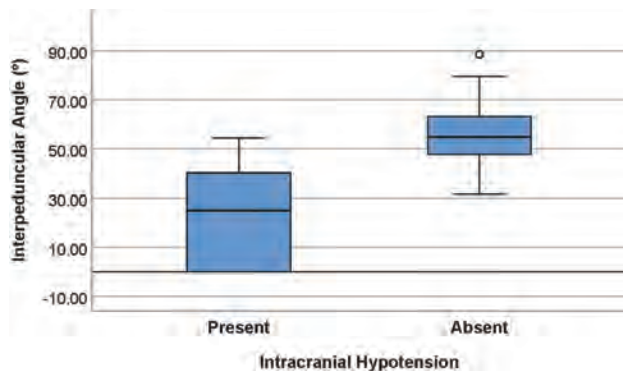


FIG 3. Boxplots showing a significant difference in the interpeduncular angle in patients with intracranial hypotension (mean, 25.3° ± 19.1°) and controls (mean, 56.3° ± 13.1°).

the control group was 49.6 years (range, 17–78 years). Thirteen patients in the intracranial hypotension group were women, significantly less than in the control group, of whom 22 were female ($P = .02$). Headache was the most frequent indication for imaging, comprising 87% of the study group and 73% of the control group. Nineteen of the 30 patients with intracranial hypotension received treatment with an epidural blood patch, 14 of whom experienced improvement in symptoms.

The average interpeduncular angle of the intracranial hypotension group was 25.3° ± 19.1° (95% CI, 18.2°–32.5°), while that of the control group was 56.3° ± 13.1° (95% CI, 51.4°–61.2°) (Fig 3). This difference was statistically significantly ($P < .001$). Comparison of representative images of the interpeduncular angle between a control patient and patients with intracranial hypotension can be found in Fig 4. Subgroup analysis in the controls revealed an average interpeduncular angle of 53.4° ± 12.6° in females and 64.4° ± 11.3° in males, a significant difference ($P = .04$). The interpeduncular angle demonstrated excellent interobserver reliability (intraclass correlation coefficient = 0.833).

With respect to classic features in the intracranial hypotension group, 1 patient had no qualitative findings and an interpeduncular angle of 39.3°, three patients had 1 finding with an average angle of 26.8°, seven patients had 2 findings with an average angle of 37.5°, twelve had 3 findings with an average angle of 25.1°, and 7 patients had all 4 analyzed features with an average angle of 10.8°. Twenty-six of 30 patients (86.7%) had pachymeningeal thickening or enhancement, with excellent interobserver reliability ($\kappa = 0.839$). Twenty (66.7%) had subdural collections with good interobserver reliability. Twenty (66.7%) had brain stem slumping with excellent interobserver reliability. Fifteen patients

(50.0%) had a positive venous distension sign with moderate interobserver reliability. The only feature with a significant correlation with the interpeduncular angle was brain stem slumping ($P < .001$). There was also a significant correlation between the interpeduncular angle and patients with ≥3 features of intracranial hypotension ($P = .01$).

With ROC curves, an optimal threshold of 40.5° yielded a sensitivity of 80.0% and specificity of 96.7%. The area under the curve was 0.920 (Fig 5).

DISCUSSION

Intracranial hypotension, whether spontaneous or from a secondary cause, can lead to high morbidity with serious delays in diagnosis because both clinical and imaging features can be non-specific. Classic findings on brain MR imaging, often the first-line investigation, have been previously reported to be variable and subjective.^{7–12} We found the interpeduncular angle to be an objective, reproducible diagnostic measure with high sensitivity and specificity for intracranial hypotension. Various other measurements have been previously investigated, including the mammillopontine distance, pontomesencephalic angle, distance from the diaphragmatic sella to the optic chiasm, and the height of the interpeduncular cistern at the plane of the cecum.^{11,12} A possible unifying mechanism explaining the changes in these measures is related to decreased basal cisternal volumes in intracranial hypotension, resulting in loss of buoyancy forces and subsequent central incisural herniation. These changes manifest as the classic brain stem slumping finding, with contributing pressure effects from supratentorial extra-axial collections. Supporting this theory, a smaller interpeduncular angle was found to be significantly correlated with the presence of brain stem slumping. Thus, a decrease in the interpeduncular angle likely represents an early manifestation of mass effect or even an objective proxy measurement for brain stem slumping, explaining both its increased sensitivity and specificity.

Although several alternative imaging measures also note good sensitivity and specificity, the greatest advantage of the interpeduncular angle is its practicality. While most reported measures rely on the sagittal plane, including traditional detection of brain stem slumping, the evaluation of the interpeduncular angle on a standard T2-weighted axial image means that it is easily incorporated into a routine search pattern. Once a mental data base of the normal range of the angle has been formed, the angle may not have to be explicitly measured. This would be highly valuable in cases in which intracranial hypotension may not be clinically suspected. Furthermore, unlike many of the proposed measures in the literature, the anatomic landmarks to make the measurement are well-known and the measurement does not require additional reference lines. Its simplicity likely contributes to its high reproducibility. In practice, we suggest measuring the interpeduncular angle with the posterior half of the cerebral peduncle because the anterior half often “flares out.” Additionally, some interpeduncular cisterns have a U-shaped apex, and we suggest measuring the linear portion of the cerebral peduncle. This may require an angle tool that can make 2 independent lines rather than a measurement that takes an apical point. In practice, the U-shaped cistern

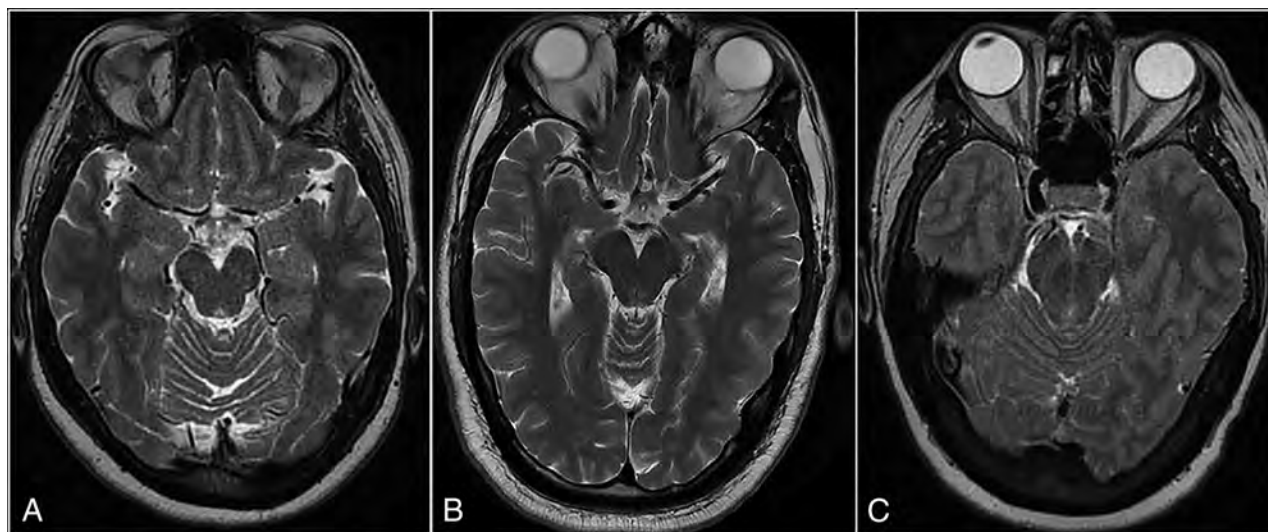


FIG 4. Axial T2-weighted MR images showing the difference in interpeduncular angles between a control subject (A) and 2 patients with intracranial hypotension (B and C). The angle in the control subject measures 52°. The first patient with intracranial hypotension (B) has mild narrowing in the angle (38°), while the second patient (C) has severe narrowing, with a completely closed angle (0°).

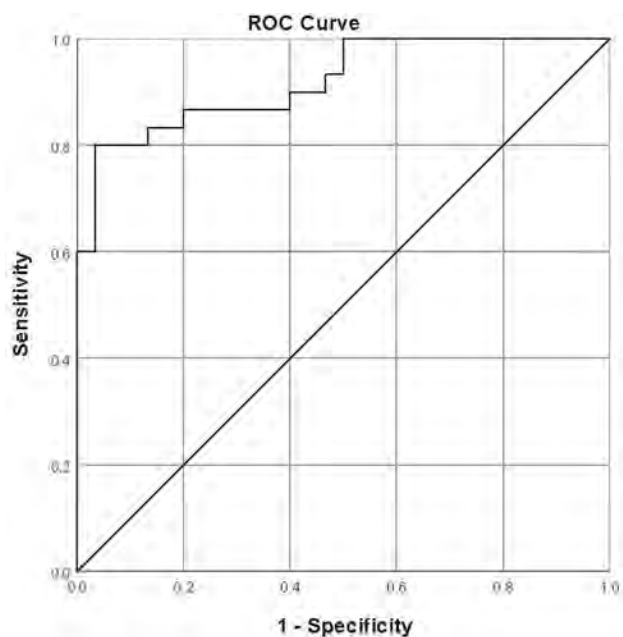


FIG 5. ROC curve for the interpeduncular angle. The optimal threshold was found to be 40.5°, yielding a sensitivity of 80% and specificity of 96.7%. The area under the curve was 0.92.

rarely affects the analysis because we have found that it is almost exclusively found in control subjects.

The other classic findings in intracranial hypotension are understood through the Monroe-Kellie doctrine, which describes a compensatory shift in volume of one intracranial compartment, most often the venous system, given its relatively increased compliance, in response to a change in the volume of another. We found pachymeningeal thickening/enhancement, essentially diffuse dilation of tiny dural-based venules, to be the most sensitive classic sign in intracranial hypotension, concordant with that reported in the literature (up to 80%).^{7,8} Unfortunately, the finding is not specific and is often present in patients postoperatively or after lumbar puncture. A more direct sign of venous engorgement

in intracranial hypotension is prominence of the epidural venous plexus at the craniocervical junction and pituitary gland. Farb et al¹³ reported the venous distention sign, described as a convex, inferior margin in the midportion of the dominant transverse sinus seen on a T1-weighted sagittal image, to be highly sensitive and specific, measuring 93% for both. We used this as the defining feature for venous engorgement but found this sign to be positive in only 50% of patients with intracranial hypotension and with only moderate interobserver agreement. This may be because a T1-weighted image was not readily available in many cases due to different protocolling depending on the clinical indication. Shifts in the extra-axial compartment in intracranial hypotension may also manifest as subdural hygromas or hematomas. We found these to be present in two-thirds of patients with intracranial hypotension, slightly higher than previously described (31%–50%).^{12,14} We did not find the interpeduncular angle to correlate significantly with any of these classic findings, likely because they represent different mechanisms in intracranial hypotension (ie, narrowing of the interpeduncular angle represents sequelae of mass effect, while these findings represent compensatory expansion following CSF loss). In our series, further narrowing of the interpeduncular angle was significantly correlated with patients with ≥ 3 classic features of intracranial hypotension, supporting the specificity of this marker. The number of features in patients with 0, 1, or 2 findings not significantly correlating with the interpeduncular angle is of doubtful clinical significance because there is no current evidence to suggest the correlation between disease severity and the number of MR imaging findings.

This study is limited by its retrospective nature. The lack of a criterion standard diagnostic tool for intracranial hypotension makes the entity challenging to study; it is difficult to draw definitive conclusions regarding MR imaging features of intracranial hypotension between study and control groups, given that MR imaging itself is an integral component of the diagnostic algorithm. Additionally, we found wide variation between the number

of classic findings and the perceived clinical severity of intracranial hypotension and the response to the epidural blood patch. Although the interpeduncular angle was narrowed in the most severe clinical cases of intracranial hypotension, its clinical utility in these cases is arguably less because the diagnosis has generally been elucidated. Development of a validated clinical grading scale could drastically improve the usefulness of objective imaging markers in populations in which the diagnosis is uncertain. A specific point to address in this study is the significantly higher number of females in the control group. This is likely due to the selection process and is consistent with the rate of use of MR imaging for neuroimaging in women in the literature.¹⁵ Reassuringly, we found that the average angle for female controls was significantly lower than that of male controls, which would have only decreased the average control angle overall. We also excluded pediatric patients, who may experience changes in anatomy during development. Establishing a normal reference range of the interpeduncular angle stratified by sex and age would be important for future research.

CONCLUSIONS

The interpeduncular angle is an objective, highly reproducible measure on brain MR imaging that is sensitive and specific for intracranial hypotension in adults. It is easily measured on axial T2-weighted sequences and can be practically incorporated into routine search patterns. This sign could serve as a useful adjunct marker in addition to classic findings and previously described measures in making the diagnosis.

Disclosures: Sachin K. Pandey—UNRELATED: Board Membership: London Health Sciences Center, Comments: Member of the Board of Directors of our local hospital center; Employment: London Health Sciences Center, London, Ontario, Canada, Comments: Academic neuroradiologist. Manas Sharma—UNRELATED: Employment: London Health Sciences Centre, London, Ontario, Canada, Comments: Academic neuroradiologist. Donald H. Lee—UNRELATED: Employment: London Health Sciences Center, London, Ontario, Canada, Comments: Academic neuroradiologist; Expert Testimony: medicolegal expert; Payment for Lectures Including Service on Speakers Bureaus: invited lecturer on multiple sclerosis for pharma companies.*
*Money paid to individual.

REFERENCES

- Schievink WI, Morreale VM, Atkinson JLD, et al. **Surgical treatment of spontaneous spinal cerebrospinal fluid leaks.** *J Neurosurg* 1998; 88:243–46 CrossRef Medline
- Berlit P, Berg-Dammer E, Kuehne D. **Abducens nerve palsy in spontaneous intracranial hypotension.** *Neurology* 1994;44:1552 CrossRef Medline
- Russo A, Tessitore A, Cirillo M, et al. **A transient third cranial nerve palsy as presenting sign of spontaneous intracranial hypotension.** *J Headache Pain* 2011;12:493–96 CrossRef Medline
- Schievink WI, Maya MM, Moser FG, et al. **Coma: a serious complication of spontaneous intracranial hypotension.** *Neurology* 2018;90:e1638–45 CrossRef Medline
- Schievink WI. **Misdiagnosis of spontaneous intracranial hypotension.** *Arch Neurol* 2003;60:1713–18 CrossRef Medline
- Headache Classification Committee of the International Headache Society (IHS): The International Classification of Headache Disorders, 3rd edition.** *Cephalalgia* 2018;38:1–211 CrossRef Medline
- Pannullo SC, Reich JB, Krol G, et al. **MRI changes in intracranial hypotension.** *Neurology* 1993;43:919 CrossRef Medline
- Mokri B, Piepgras DG, Miller GM. **Syndrome of orthostatic headaches and diffuse pachymeningeal gadolinium enhancement.** *Mayo Clin Proc* 1997;72:400–13 CrossRef Medline
- Fishman RA, Dillon WP. **Dural enhancement and cerebral displacement secondary to intracranial hypotension.** *Neurology* 1993;43(3 Part 1):609–11 CrossRef Medline
- Schievink WI, Maya MM, Louy C, et al. **Diagnostic criteria for spontaneous spinal CSF leaks and intracranial hypotension.** *AJNR Am J Neuroradiol* 2008;29:853–56 CrossRef Medline
- Young SJ, Quisling RG, Bidari S, et al. **An objective study of anatomic shifts in intracranial hypotension using four anatomic planes.** *Radiol Res Pract* 2018;2018:6862739 CrossRef Medline
- Shah LM, Mclean LA, Heilbrun ME, et al. **Intracranial hypotension: improved MRI detection with diagnostic intracranial angles.** *AJR Am J Roentgenol* 2013;200:400–07 CrossRef Medline
- Farb RI, Forghani R, Lee SK, et al. **The venous distension sign: a diagnostic sign of intracranial hypotension at MR imaging of the brain.** *AJNR Am J Neuroradiol* 2007;28:1489–93 CrossRef Medline
- Schievink WI, Maya MM, Moser FG, et al. **Spectrum of subdural fluid collections in spontaneous intracranial hypotension.** *J Neurosurg* 2005;103:608–13 CrossRef Medline
- Callaghan BC, Kerber KA, Pace RJ, et al. **Headaches and neuroimaging: high utilization and costs despite guidelines.** *JAMA Intern Med* 2014; 174:819–21 CrossRef Medline

Cytotoxic Lesions of the Corpus Callosum Caused by Thermogenic Dietary Supplements

J.A. Galnares-Olalde, A.J. Vázquez-Mézquita, G. Gómez-Garza, D. Reyes-Vázquez, V. Higuera-Ortiz, M.A. Alegría-Loyola, and A. Mendez-Domínguez

ABSTRACT

SUMMARY: Consumption of over-the-counter dietary supplements to reduce body weight is common among the population. Thermogenics are herbal combinations that claim to produce a fat-burning process through an increase in the cellular metabolic rate and greater cellular energy consumption, having a high risk for patients developing toxic leukoencephalopathy. We present a series of 6 patients with acute neurologic symptoms and MR imaging showing restricted diffusion and decreased apparent diffusion coefficient values (mean value, $400 \text{ mm}^2/\text{s} \times 10^{-6}$) in the entire corpus callosum compatible with a cytotoxic lesion of the corpus callosum. Although patients responded favorably to the product discontinuation with rapid recovery of neurologic symptoms, there was a more prolonged resolution on imaging alterations. Because of the widespread availability and unregulated nature of thermogenic dietary supplements, physicians must be aware of the clinical and radiologic characteristics of these potential complications of their use.

ABBREVIATION: CLOCC = cytotoxic lesion of the corpus callosum

Consumption of over-the-counter dietary supplements to reduce body weight is common among the population.¹ Thermogenics are natural herbal combinations that aim to augment fat-burning by producing an increase in the cellular metabolic rate and greater cellular energy consumption. These supplements are available in most countries and can be purchased over the Internet without a prescription. Although local drug-regulation agencies have warned against the indiscriminate use of these products, they are still widely available under various brand names.^{2,3}

Recently, there have been reports of severe-yet-reversible toxic leukoencephalopathy related to the intake of thermogenic supplements.³ Characteristic MR imaging findings reveal intramyelinic edema that has a predilection for the corpus callosum. These MR imaging changes have been recently termed “cytotoxic lesions of the corpus callosum” (CLOCCs).⁴ Previously, similar findings were described as mild encephalitis or encephalopathy with reversible splenic lesions and reversible splenic lesion syndrome

among others. However, not all cases are mild, reversible, or limited to the splenium.^{3,4}

It is believed that these lesions are a result of an inflammatory cascade of changes manifested as cytotoxic edema secondary to an increased influx of water molecules in astrocytes and neurons caused by the release of the inflammatory cytokines interleukin-1 and interleukin-6. These interactions create feedback loops that increase extracellular glutamate levels. The increased quantity of extracellular glutamate has an excitatory effect at membrane receptors such as the α -amino-3-hydroxy-5-methyl-4-isoxazole-propionic acid (AMPA) and N-methyl-D-aspartate (NMDA) receptors, as well as aquaporins and Na^+/K^+ pumps. The most affected region of the corpus callosum is the splenium due to its higher density of glutamate and cytokine receptors.⁴ The purpose of this research was to contribute to the understanding of toxic causes of CLOCCs, to describe the clinical and MR imaging findings of CLOCCs caused by thermogenic dietary supplements, and thus to expand the body of literature on the diagnosis of this condition.

Case Series

This case series report was performed under institutional review board approval. An observational, descriptive, retrospective study was conducted of both inpatient and outpatient subjects during a 3-year period. We searched the registry of the hospital for cases with clinical and brain MR imaging findings compatible with toxic leukoencephalopathy that reported previous use of thermogenic dietary supplements. As inclusion criteria, we considered

Received February 15, 2019; accepted after revision May 23.

From the Internal Medicine Service (J.A.G.-O.), Radiology Service (A.J.V.-M., G.G.-G., D.R.-V.), Department of Rheumatology (V.H.-O.), and Neurology Service (M.A.A.-L., A.M.-D.), The American British Cowdray Medical Center, Mexico City, Mexico.

J.S. Galnares-Olalde and A.J. Vázquez-Mézquita contributed equally to this work.

Please address correspondence to Gilberto Gómez-Garza, MD, The American British Cowdray Medical Center, Avenida Carlos Graef Fernández 154, Cuajimalpa, Tlalaxala Santa Fe, 05300 Mexico City, Mexico; e-mail: ggomezgarza@gmail.com

<http://dx.doi.org/10.3174/ajnr.A6116>

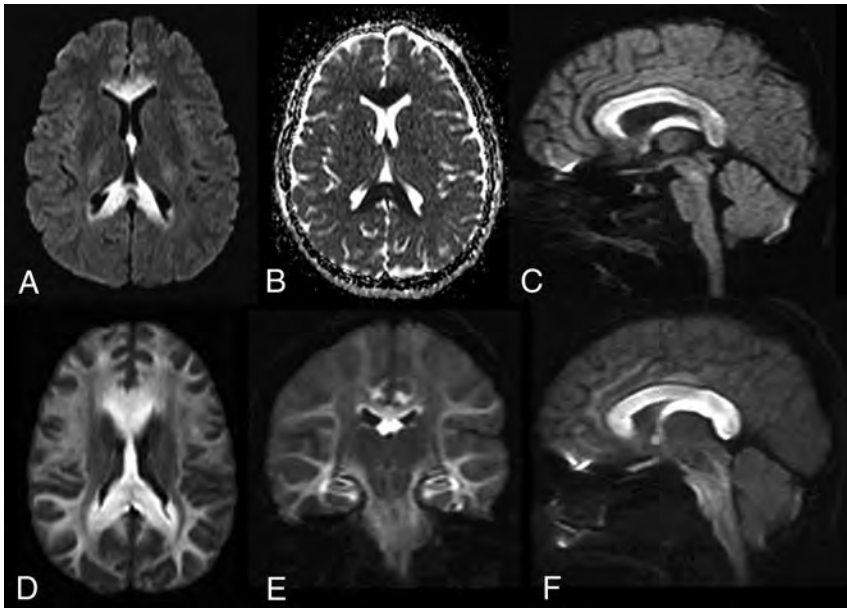


FIG 1. CLOCCs caused by thermogenic dietary supplements. Axial DWI (A) and corresponding ADC map (B) of case 1 show restricted diffusion representing cytotoxic edema at the corpus callosum. C, Sagittal DWI shows a hyperintense corpus callosum, cerebral commissures, and fornix in case 2. D and E, Axial DWI and corresponding ADC map from case 4 show more extensive cytototoxic edema that affects the entire corpus callosum and cerebral white matter. F, Sagittal DWI of case 5 reveals an enlarged and edematous corpus callosum, fornix, and cerebral commissures with involvement of the peripheral cerebral white matter, cerebral peduncles, and brain stem, along with the optic nerves.

those 18 years of age and older who had a history of thermogenic supplement intake during the previous 6 months, acute neurologic symptoms at presentation, and white matter brain alterations on MR imaging, characterized as diffusion-weighted imaging ($b=1000$) restriction with decreased apparent diffusion coefficient values. Six patients fulfilled the criteria and were included in this series; all of them were women. The mean age was 33 years (range, 23–43 years); all of the patients had normal body mass index values (mean, 21.01; range, 19.2–23.7) at the time of the examination. None were obese or significantly overweight before starting use of the dietary supplement.

Of the patients, one had a history of social alcohol consumption, 2 were active smokers, one was receiving an antiepileptic drug (phenytoin) and an anticoagulant (acenocumarol) for a previous ischemic stroke, and another was on antidepressant medication (amitriptyline). Regarding the dietary supplement intake, the median time of consumption for the 6 patients was 5.3 months (range, 1–18 months); all of them took the recommended dosage of the product.

At the time of the medical evaluation, headache was present in 5 patients; generalized weakness, in 4; distal paresthesia, in 3; blurred vision, in 3; photophobia, in 2; and phonophobia in 1. The clinical spectrum was nonspecific, ranging from normal examination findings to gait disturbances.

On MR imaging, restricted diffusion with low ADC values (mean, $400 \text{ mm}^2/\text{s} \times 10^{-6}$; range, $194\text{--}550 \text{ mm}^2/\text{s} \times 10^{-6}$) was present in the corpus callosum and cerebral commissures of all 6 patients (Fig 1), while the hemispheric cerebral white matter, brain stem, and dentate nucleus of the cerebellum were affected in 3 (Fig 2). The optic nerve was affected in 3 patients. The signal

alteration was less evident on the FLAIR sequence as a subtle hyperintensity in only 3 patients.

After suspending the dietary supplement intake, all neurologic symptoms resolved within a mean time of 2.8 days (range, 1–5 days). A total of 4 patients underwent control MR imaging studies. While 1 patient had complete resolution in the imaging findings at 6 weeks, 1 patient did not show improvement on imaging at 2 months. Only partial resolution of the MR imaging alterations showed in a 10-month control study for 1 patient, and 1 had complete resolution 22 months after the initial MR imaging. Demographic and MR imaging findings are listed in the Table.

Patient Presentation

Case 1. A 41-year-old woman with no relevant medical history presented with a progressive generalized headache, blurred vision, disorientation, gait disturbance, and difficulty concentrating. The physical examination revealed only diminished attention and anxiety with normal language fluency. The MR imaging

showed diffuse DWI hyperintensity of the entire corpus callosum with extension to the fornices with low ADC values ($461\text{--}550 \text{ mm}^2/\text{s} \times 10^{-6}$) in the structures mentioned above (Fig 1A, B). The patient had been consuming a thermogenic dietary supplement for 1 month. The supplement was suspended, and the patient was administered glucocorticoid therapy. Neurologic symptoms improved 5 days later. Meanwhile, the MR imaging alterations completely resolved on a control MR imaging after 6 weeks.

Case 2. A 30-year-old woman with no relevant medical history was admitted with 2-day distal ascending paresthesia associated with a generalized headache. The physical examination findings were normal. MR imaging showed a hyperintense DWI signal from the rostrum to the splenium of the corpus callosum with bilateral involvement of the cerebral commissures and the fornix columns (Fig 1C), with decreased ADC values ($351\text{--}475 \text{ mm}^2/\text{s} \times 10^{-6}$). The patient revealed a 1-month history of thermogenic intake. The supplement was suspended, and glucocorticoid was administered. All neurologic symptoms improved 3 days later. The patient was then discharged; she missed follow-up appointments.

Case 3. A 37-year-old woman with no relevant medical history presented with 7-month distal ascending paresthesia. The physical examination did not reveal any motor involvement, only mild hyporeflexia. A lumbar puncture was performed, which revealed high protein levels (125 mg/dL) with no leukocyte count. Intravenous immunoglobulin was administered on the basis of suspected Guillain-Barré syndrome; however, the patient's symptoms persisted after 2 months of treatment. The MR imaging

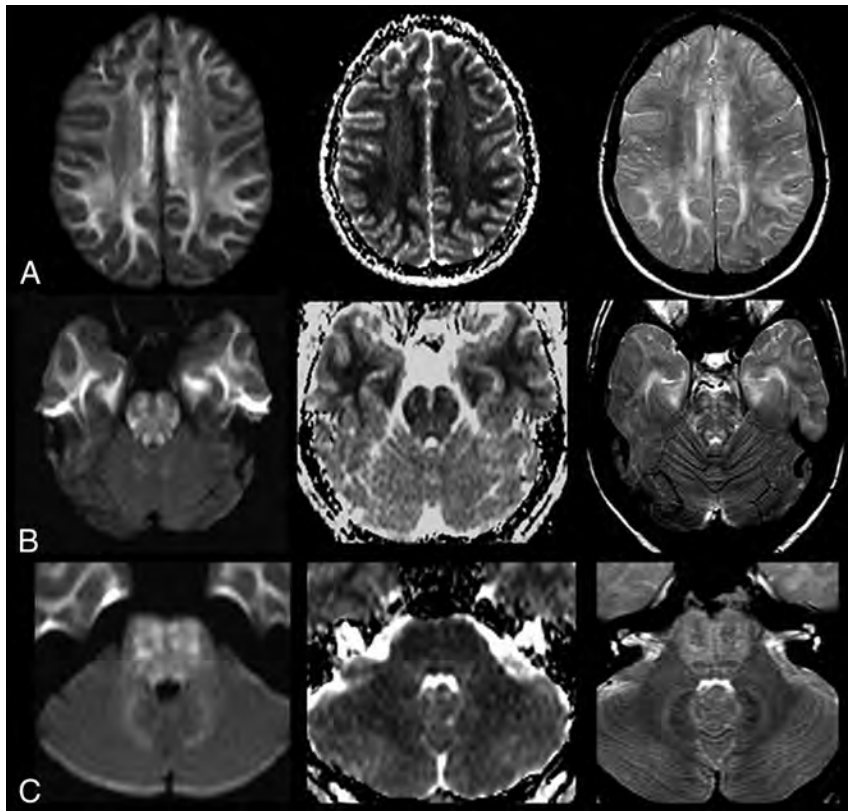


FIG 2. CLOCCs caused by thermogenic dietary supplements. Set of images from case 4 that show cytotoxic edema extending to the peripheral cerebral white matter (row A), brain stem (row B), and dentate nucleus of the cerebellum (row C). Left column, DWI trace images. Middle column, ADC map. Right column, T2WI.

Radiologic and demographic data for each patient

	Age (yr)	BMI	Duration of Thermogenic Use (mo)	Affected Brain Regions	ADC Values (Range) ($\text{mm}^2/\text{s} \times 10^{-6}$)
Case 1	41	20.1	1	CC, FR	461–550
Case 2	30	23.7	1	CC, FR, CO	351–475
Case 3	37	23.3	7	CC, FR, CO, WM	485–524
Case 4	23	19.2	3	CC, CO, BS, DN, ON	284–370
Case 5	43	19.5	18	CC, WM, DN, ON, CH, OT	405–440
Case 6	25	19.7	2	CC, WM, BS, DN, CH	194–275
	Mean = 33	Mean = 21.01	Mean = 5.3		Mean = 400

Note:—BMI indicates body mass index; CC, corpus callosum; FR, fornices; CO, cerebral commissures; BS, cerebral brain stem; DN, dentate nucleus of the cerebellum; ON, optic nerves; CH, chiasm; OT, optic tracts.

showed a hyperintense DWI signal of the corpus callosum, cerebral commissures, and fornices, with extension to the periventricular cerebral white matter, associated with discrete, low ADC values ($485\text{--}524 \text{ mm}^2/\text{s} \times 10^{-6}$). The patient then revealed a 7-month history of thermogenic supplement intake. Neurologic symptoms improved 3 days after supplement discontinuation. A control MR imaging performed after 2 months showed significant reduction of the DWI brain abnormalities, with only a mild bilateral symmetric edema on the hippocampi.

Case 4. A 23-year-old woman with no relevant medical history presented with a 7-day progressive generalized headache associated with blurred vision and left-arm weakness. The physical examination revealed left-arm paresis only. MR imaging showed extensive cytotoxic edema of the corpus callosum and cerebral

commissures, peripheral cerebral white matter (Fig 2A), brain stem (Fig 2B), and dentate nucleus of the cerebellum (Fig 2C), with enlargement and hyperintensity of the optic nerves on DWI, with low ADC values ($284\text{--}370 \text{ mm}^2/\text{s} \times 10^{-6}$). Loss of gyral cerebral morphology was also present with diminished convexity of the subarachnoid space. The patient had a 3-month history of thermogenic supplement intake. Intravenous glucocorticoid was administered, and notably, the neurologic symptoms improved the day after. The patient was discharged and had no follow-up imaging.

Case 5. A 43-year-old woman with a medical history of ischemic stroke 8 years before the onset of new symptoms presented with a 4-month history of blurred vision, intermittent frontal headache, and frequent falling. The physical examination revealed gait ataxia, bilateral dysmetria, and diminished pupillary light reflex. MR imaging showed increased volume and a hyperintense DWI signal of the corpus callosum with decreased ADC values ($405\text{--}440 \text{ mm}^2/\text{s} \times 10^{-6}$). Additionally, the hemispheric white matter showed increased signal in T2 and FLAIR sequences, with extension to the brain stem and dentate nucleus and compromised optic nerves, chiasm, and optic tracts. The patient received glucocorticoid therapy and then revealed continuous thermogenic supplement intake for 18 months. The neurologic symptoms improved 5 days after supplement discontinuation. Despite that, the MR imaging alterations were only partially resolved up to 10 months later in serial control studies (Fig 3A, -B).

Case 6. A 25-year-old woman with no relevant medical history presented with a 2-month progressive, generalized, oppressive headache associated with photophobia and phonophobia that did not improve with oral painkillers. The physical examination revealed papilledema and gait disturbances. The MR imaging showed a DWI hyperintense signal with decreased ADC values ($194\text{--}275 \text{ mm}^2/\text{s} \times 10^{-6}$) of the callosal commissure, brain stem, dentate nucleus of the cerebellum, optic chiasm, and bilateral frontal, parietal, and occipital white matter. The patient revealed a 2-month history of thermogenic supplement intake. She received supportive treatment with osmotic therapy, and neurologic symptoms improved 2 days after supplement discontinuation, whereas the MR imaging findings completely resolved after 22 months (Fig 3C, -D).

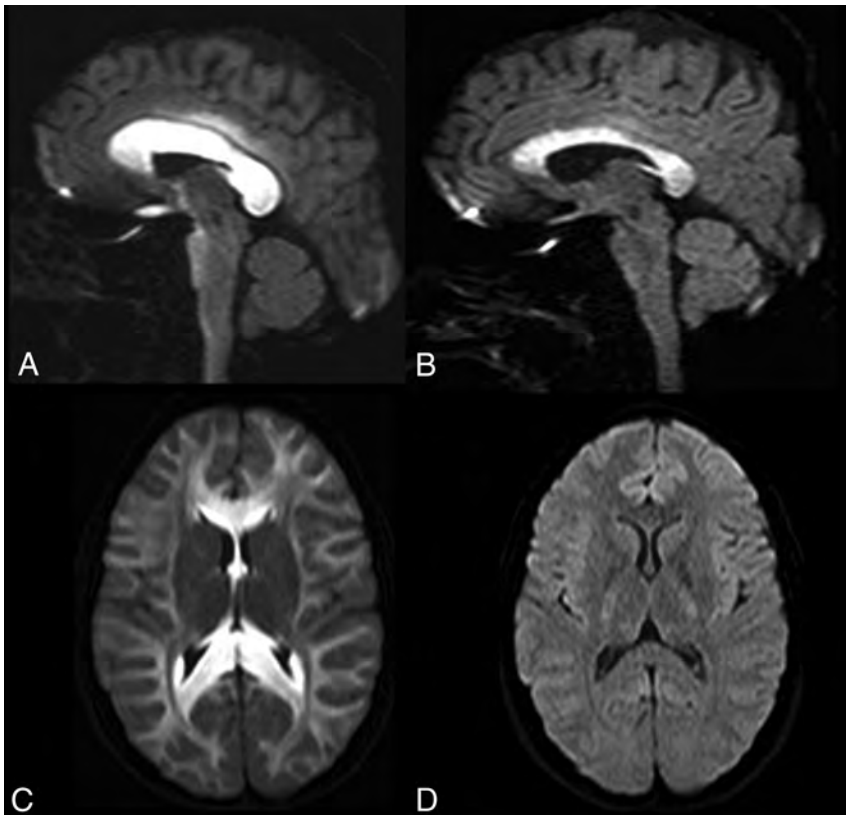


FIG 3. CLOCCs caused by thermogenic dietary supplements. *A*, Sagittal DWI shows an enlarged edematous corpus callosum with involvement of the optic chiasm in case 5. *B*, Sagittal DWI from an MR imaging control study of the same patient obtained 8 weeks after the discontinuation of the thermogenic dietary supplement shows a decrease in volume and signal hyperintensity of the corpus callosum and visual pathway, representing partial recovery. *C*, The initial MR imaging shows extensive cytotoxic edema of the corpus callosum and cerebral white matter in case 6. *D*, The MR imaging of the same patient obtained 22 months later shows complete recovery with normal brain findings on DWI.

DISCUSSION

Toxic leukoencephalopathy can be caused by different exogenous agents, and although the clinical and imaging presentation may be severe, it can be reversible. Some of these substances have a predilection for the corpus callosum.⁵ Thermogenics are readily available on the World Wide Web as over-the-counter dietary supplements. Herbal preparations consumed by this series of patients shared a combination of botanical and biochemical ingredients like bitter melon (*Momordica charantia*), green tea, horsetail herb (*Equisetum*), bearberry (*Arctostaphylos uva-ursi*), olive, juniper, ginger, yerba mate, grape, cempasuchil flower (*Tagetes erecta*) pigment, L-carnitine tartrate, and microcrystalline cellulose among unspecified others. Some substances found in these compounds, especially the combination of high doses of caffeine and ephedrine analogs, have an action mechanism that increases the rate of fat oxidation and lipolysis with reduced glycogen metabolism.^{6,7} Some of these plant molecules have other in vitro metabolic activities. For example, bitter melon is reported to be a bioactive insulin-like structure, which has exhibited a moderate effect on the reduction of blood glucose levels in clinical studies. Most interesting, CLOCCs in adult patients with acute hypoglycemia have a common predilection for the posterior corpus callosum and tracts of deep white matter.^{8,9} Thus, in

this series, the corpus callosum was more extensively affected in all patients. Bitter melon has also been associated with significant adverse effects, which include anxiety, insomnia, and cardiovascular disorders, caused by stimulation of the central nervous system.⁹

The term “leukoencephalopathy” encompasses a spectrum of diseases that predominantly involve the white matter structure as a result of exposure to a variety of exogenous agents; known causes are chemo- and immunotherapy, antibiotics, and environmental and infectious agents.¹⁰ In some cases, the cause is unknown.^{11,12} Although the central nervous system is naturally protected by the blood-brain barrier, some of these agents are known to interfere with or damage this barrier, allowing access of potentially threatening substances to neural tissue. Other agents are fat-soluble; this feature facilitates their distribution into the central nervous system.¹³ Acute toxic leukoencephalopathy may have a severe extension and may be reversible both clinically and radiologically.¹⁴ Clinical presentation is nonspecific, depending on the distribution of edema, often including neurologic decline, distal paresthesia, personality changes, memory alterations, headache, and other focal neurologic signs.¹⁵

Damage usually involves white matter tracts from the periventricular-to-subcortical areas, though other metabolically active areas may be susceptible to neurotoxicity, including the deep gray matter and the brain stem. Therefore, these structures may show changes in acute toxic leukoencephalopathy imaging. Regarding its pathophysiology, theories posit that cytotoxic edema is caused by the increased water molecule influx in neurons and astrocytes. The splenium is the most affected area of the corpus callosum because of its high density of glutamate, and cytokine and drug receptors.^{4,5,14,16,17}

Drug agencies around the world have issued health warnings against some of the thermogenic dietary supplements consumed by our series of patients, including the Comisión Federal para la Protección contra Riesgos Sanitarios (COFEPRIS) in Mexico and Agencia Española de Medicamentos y Productos Sanitarios (AEMPS) in Spain and this motivated a recall by the FDA in the United States.^{18,19} Nonetheless, these products can still be easily purchased on-line without a prescription under various brand names.^{3,18,19}

All the patients in our series had normal body weight with normal body mass index values at the time of examination. They did not indicate that previous obesity or being significantly overweight had motivated them to consume the dietary supplements,

which could be a risk factor for developing CLOCCs. However, due to the limited number of cases, we cannot make assumptions on this issue.

Two of our patients were on antiepileptic or antidepressant medication, both of which have been reported to cause drug-related CLOCCs.⁴ The fact that the other 4 patients lack this risk factor makes this association of a comorbid condition less plausible. Even so, there is a need for further analysis on a larger number of patients to determine whether there is any relationship. One patient had a history of social alcohol consumption but no chronic alcoholism that would raise the suspicion of Marchiafava-Bignami disease as an additional metabolic cause for developing CLOCCs.^{4,5,20}

As observed in our series, the clinical symptoms of CLOCCs caused by thermogenic dietary supplements are frequently subtle and may not always prompt subjects to seek medical attention, making it possible that a significant number of cases occur undetected.

Although the clinical neurologic signs and symptoms improved rapidly after the withdrawal of the supplement, the white matter lesions on MR imaging reduced gradually and progressively resolved in a highly variable fashion (6 weeks to 22 months), seemingly dependent on the extension of leukoencephalopathy. There may be signs of peripheral nerve involvement as in case 3, but there is not enough evidence to confirm this possibility. Additionally, we do not know if there is any potential long-term neurologic damage resulting from thermogenic consumption as in other toxic leukoencephalopathies.⁴

Given the lack of regulation in the manufacturing process of these herbal dietary supplements, it is difficult to know if the brain toxicity was caused by a single defective batch, though its widespread presentation for a long period suggests otherwise. Also, the information provided on the label of these products is often incomplete. For example, the labels do not state the specific parts of the plants used. Because the concentration of each active compound could be highly variable, this feature can result in possible toxic combinations not yet identified.²⁰ It is conceivable that incorrect handling of these ingredients or contamination due to inadequate supervision during fabrication could lead to potentially harmful products.

CONCLUSIONS

Thermogenics are widely available but potentially harmful dietary supplements that have prompted warnings and recalls by international drug regulation agencies; nonetheless, they can still be easily purchased on-line. These herbal preparations being labeled as natural does not mean that they are entirely safe. When used without medical supervision, they can produce toxic neurologic side effects such as CLOCCs. It is not known whether a normal body mass index before consumption could play a role in developing toxicity or if there could be any interactions between the dietary supplements and other substances, such as prescription drugs or over-the-counter medications. With this publication, we add 6 new cases to the 2 previously reported cases of toxic leukoencephalopathy caused by thermogenic dietary supplements and to the toxic etiologies of CLOCCs, making the medical community aware of the clinical and radiologic characteristics of this potential complication.

REFERENCES

1. Blanck HM, Serdula MK, Gillespie C, et al. **Use of nonprescription dietary supplements for weight loss is common among Americans.** *J Am Diet Assoc* 2007;107:441–47 CrossRef Medline
2. Hoffman JR, Kang J, Ratamess NA, et al. **Thermogenic effect of an acute ingestion of a weight loss supplement.** *J Int Soc Sports Nutr* 2009;6:1 CrossRef Medline
3. Olivas-Chacon C, Treviño-García M, Chua-Tuan J, et al. **Leukoencephalopathic changes on magnetic resonance imaging associated with a thermogenic dietary supplement (Thermatrim).** *Proc (Bayl Univ Med Cent)* 2015;28:389–91 CrossRef Medline
4. Starkey J, Kobayashi N, Numaguchi Y, et al. **Cytotoxic lesions of the corpus callosum that show restricted diffusion: mechanisms, causes, and manifestations.** *Radiographics* 2017;37:562–76 CrossRef Medline
5. Rimkus CM, Andrade CS, Leite C, et al. **Toxic leukoencephalopathies, including drug, medication, environmental, and radiation-induced encephalopathic syndromes.** *Semin Ultrasound CT MR* 2014;35:97–117 CrossRef Medline
6. Diepvens K, Westerterp KR, Westerterp-Plantenga MS. **Obesity and thermogenesis related to the consumption of caffeine, ephedrine, capsaicin, and green tea.** *Am J Physiol Regul Integr Comp Physiol* 2007;292:R77–85 CrossRef Medline
7. Liu AG, Smith SR, Fujioka K, et al. **The effect of leptin, caffeine/ephedrine, and their combination upon visceral fat mass and weight loss.** *Obesity (Silver Spring)* 2013;21:1991–96 CrossRef Medline
8. Evans JL. Diet, botanical and nutritional treatments for type 2 diabetes. 2003. <https://www.endotext.org/>. Accessed June 13, 2019
9. da Silva WV, de Andrade Gomes Silva MI, Tavares Toscano L, et al. **Supplementation prevalence and adverse effects in physical exercise practitioners.** *Nutr Hosp* 2014;29:158–65 CrossRef Medline
10. Sathananthasarma P, Weeratunga PN, Chang T. **Reversible splenic lesion syndrome associated with dengue fever: a case report.** *BMC Res Notes* 2018;11:9–12 CrossRef Medline
11. Singh P, Gogoi D, Vyas S, et al. **Transient splenic lesion: further experience with two cases.** *Indian J Radiol Imaging* 2010;20:254–57 CrossRef Medline
12. Cho JS, Ha SW, Han YS, et al. **Mild encephalopathy with reversible lesion in the splenium of the corpus callosum and bilateral frontal white matter.** *J Clin Neurol* 2007;3:53–56 CrossRef Medline
13. Zheng W. **Neurotoxicology of the brain barrier system: new implications.** *J Toxicol Clin Toxicol* 2001;39:711–19 CrossRef Medline
14. McKinney AM, Kieffer SA, Paylor RT, et al. **Acute toxic leukoencephalopathy: potential for reversibility clinically and on MRI with diffusion weighted and FLAIR imaging.** *AJR Am J Roentgenol* 2009;193:192–206 CrossRef Medline
15. Hagan IG, Burney K. **Radiology of recreational drug abuse.** *Radiographics* 2007;27:919–40 CrossRef Medline
16. Hassel B, Bolding KA, Narvesen C, et al. **Glutamate transport, glutamine synthetase and phosphate-activated glutaminase in rat CNS white matter: a quantitative study.** *J Neurochem* 2003;87:230–37 CrossRef Medline
17. Domercq M, Matute C. **Expression of glutamate transporters in the adult bovine corpus callosum.** *Brain Res Mol Brain Res* 1999;67:296–302 CrossRef Medline
18. Cofepris. LA COFEPRIS ALERTA SOBRE EL PRODUCTO THERMATRIM. Secretaría de Salud: Comunicado de prensa 2014. <https://www.gob.mx/salud/prensa/la-cofepris-alerta-sobre-el-producto-thermatrim>. Accessed June 13, 2019
19. Food Alert Network. Efectos adversos relacionados con el consumo del complemento alimenticio (Pura Alegría) procedente de México 2015. http://www.aecosan.mssi.gob.es/AECOSAN/web/seguridad_alimentaria/ampliacion/complemento_alimenticio_PURA_ALEGRIA.htm. Accessed June 13, 2019
20. Kakkar C, Prakashini K, Polnaya A. **Acute Marchiafava Bignami disease: clinical and serial MRI correlation.** *BMJ Case Rep* 2014;2014 CrossRef Medline

Manganese-Enhanced MRI of the Brain in Healthy Volunteers

 D.M. Sudarshana,  G. Nair,  J.T. Dwyer,  B. Dewey,  S.U. Steele,  D.J. Suto,  T. Wu,  B.A. Berkowitz,  A.P. Koretsky,  I.C.M. Cortese, and  D.S. Reich



ABSTRACT

BACKGROUND AND PURPOSE: The manganese ion is used as an intracellular MR imaging contrast agent to study neuronal function in animal models, but it remains unclear whether manganese-enhanced MR imaging can be similarly useful in humans. Using mangafodipir (Teslascan, a chelated manganese-based contrast agent that is FDA-approved), we evaluated the dynamics of manganese enhancement of the brain and glandular structures in the rostral head and neck in healthy volunteers.

MATERIALS AND METHODS: We administered mangafodipir intravenously at a rate of 1 mL/minute for a total dose of 5 μ mol/kg body weight. Nine healthy adult volunteers (6 men/3 women; median age, 43 years) completed baseline history and physical examination, 3T MR imaging, and blood work. MR imaging also followed mangafodipir administration at various time points from immediate to 7 days, with delayed scans at 1–3 months.

RESULTS: The choroid plexus and anterior pituitary gland enhanced within 10 minutes of infusion, with enhancement persisting up to 7 and 30 days, respectively. Exocrine (parotid, submandibular, sublingual, and lacrimal) glands also enhanced avidly as early as 1 hour postadministration, generally resolving by 1 month; 3 volunteers had residual exocrine gland enhancement, which resolved by 2 months in 1 and by 3 months in the other 2. Mangafodipir did not affect clinical parameters, laboratory values, or T1-weighted signal in the basal ganglia.

CONCLUSIONS: Manganese ions released from mangafodipir successfully enable noninvasive visualization of intra- and extracranial structures that lie outside the blood-brain barrier without adverse clinical effects, setting the stage for future neuroradiologic investigation in disease.

ABBREVIATIONS: FA = flip angle; GRE = gradient recalled-echo; MEMRI = manganese-enhanced MRI

Paramagnetic contrast agents play a key role in MR imaging by influencing local magnetic fields and widening tissue-specific differences to enhance intrinsic structural information. Functional contrast agents, an emerging field, provide an additional layer of molecular and cellular information through their ability to probe intracellular processes. In preclinical studies, the manganese ion (Mn^{2+}), a functional contrast agent, has garnered increasing attention due to its ability to accumulate within cells via

L-type calcium channels and induce a strong reduction in intracellular T1 relaxation time, as well as travel along neural circuits.¹ The application of manganese-enhanced MR imaging (MEMRI) has thus facilitated a greater understanding of brain laminar structure, neural activity, and neural connectivity.^{2–7}

The application of MEMRI in humans has been impeded by the cardiotoxicity and potential neurotoxicity of high doses of free Mn^{2+} ions.^{8,9} Mangafodipir trisodium is a chelated manganese-based contrast agent that is FDA-approved for liver and pancreas imaging.¹⁰ After intravenous administration, mangafodipir undergoes simultaneous dephosphorylation and transmetallation, resulting in a slow release of manganese ions; this is thought to curtail the hazardous effects seen with bolus doses of manganese chloride ($MnCl_2$).^{11,12}

Received January 18, 2019; accepted after revision June 13.

From the National Institute of Neurological Disorders and Stroke (D.M.S., G.N., J.T.D., B.D., S.U.S., D.J.S., T.W., A.P.K., I.C.M.C., D.S.R.), National Institutes of Health, Bethesda, Maryland; Cleveland Clinic Lerner College of Medicine of Case Western Reserve University (D.M.S.), Cleveland, Ohio; and Department of Ophthalmology (B.A.B.), Visual and Anatomical Sciences, Wayne State University School of Medicine, Detroit, Michigan.

This study was supported by the Intramural Research Program of National Institute of Neurological Disorders and Stroke (Z01NS003119), the National Institutes of Health Medical Research Scholars Program, and the National Institutes of Health (ROI EY026584, ROI AG058171 to B.A.B.).

Paper previously presented as an oral presentation at: Annual Meeting of American Society of Neuroradiology and the Foundation of the ASNR Symposium, June 2–7, 2018; Vancouver, British Columbia, Canada.

Please address correspondence to Daniel S. Reich, MD, PhD, Translational Neuro-radiology Section, National Institute of Neurological Disorders and Stroke/National Institutes of Health, 10 Center Dr MSC 1400, Building 10 Room 5C103, Bethesda, MD 20892; E-mail: daniel.reich@nih.gov

 Indicates open access to non-subscribers at www.ajnr.org

 Indicates article with supplemental on-line photos.

<http://dx.doi.org/10.3174/ajnr.A6152>

Healthy volunteer study protocol

	Screening	Baseline	Hours 0–2	Hour 4	Hour 6	Day 1	Day 2	Day 3	Day 4	Day 5	Day 6	Day 7	Month 1	Month 2	Month 3	Total Scans	
HV1			B				B	B				B	B			5	
HV2			B				B					B	B			4	
HV3				B	B				B	B	B		B			6	
HV4				B	B		B	B	B				B			6	
HV5	HP, BW, B	B + mangafodipir						B	B	B		B	BW	B	BW	B, BW	7
HV6						B							B				2
HV7								B				B	B		B, BW	B, BW	5
HV8									B			B	B		B, BW		4
HV9										B	B	B	B				4

Note:—HV indicates healthy volunteer; HP, history and physical; BW, blood work; B, brain MRI.

Preliminary studies in the human brain have demonstrated enhancement of structures outside the blood-brain barrier (choroid plexus and pituitary gland), with half-lives substantially longer than those of gadolinium chelates, which remain extracellular.¹³ However, detailed characterization of this enhancement has not been reported, to our knowledge.

The purpose of this study was to use MEMRI to evaluate the dynamics and pattern of manganese enhancement in the brain and rostral head-and-neck structures. Because of the limited availability of mangafodipir and of participants for repeat scans, temporal sampling was sparse for individuals but attenuated across the study population. We also performed quantitative T1 mapping to estimate contrast uptake and washout. Furthermore, we evaluated T1-weighted signal in the basal ganglia and cerebral cortex to assess retention of manganese ions.

MATERIALS AND METHODS

Participant Recruitment

Participants were enrolled in the National Institutes of Health institutional review board–approved study, “Manganese-Enhanced Magnetic Resonance Imaging in Healthy Volunteers and People with Multiple Sclerosis” (NCT01326715). Each participant provided written informed consent. Healthy volunteers were recruited between October 2013 and June 2017. Key inclusion criteria were the following: 18–70 years of age, normal complete blood count, normal findings of kidney function and liver function tests, and normal brain MR imaging findings within 1 year before enrollment. Key exclusion criteria were the following: hypertension (>160/100 mm Hg), previous or current alcohol or substance abuse, occupational exposure to manganese, family history of Parkinson disease, pregnancy/lactation, or treatment with calcium channel blockers.

Screening Visit and Mangafodipir Infusion

The screening visit consisted of a physical examination, medical history, laboratory testing, and routine clinical 3T MR imaging to ensure absence of structural abnormalities. Mangafodipir trisodium was infused intravenously (50 $\mu\text{mol}/\text{mL}$ at 1 mL/minute, for a total dose of 5 $\mu\text{mol}/\text{kg}$) after a baseline scan. Vital signs were monitored before, during, and after infusion.

MEMRI Protocol

Images were acquired on a Magnetom Skyra (Siemens, Erlangen, Germany) 3T scanner with a body-transmit and a 32-channel receiver head coil. Sequences acquired at each MEMRI time point (as detailed in the Table) included proton-density and T2-weighted (turbo spin-echo: TR = 5000 ms, TE = 18/82 ms,

FOV = 256 mm, 1-mm in-plane resolution, 54 slices of 3-mm thickness), multiple T1-weighted (gradient-recalled-echo [GRE]: TR = 7.8 ms, TE = 3 ms, FOV = 256 mm, 1-mm isotropic resolution, 192 slices, flip angles [FAs] of 3°, 6°, 9°, 12°, 15°, and 18°), T1-weighted MPRAGE (turbo flash: TR = 1900 ms, TE = 2.5 ms, TI = 900 ms, FOV = 256 mm, FA = 9°, 1-mm isotropic resolution, 176 slices), or MP2RAGE (turbo flash: TR = 5000 ms, TE = 3 ms, TI = 700 and 1400 ms, FA = 4°, FOV = 256 mm, 1-mm isotropic resolution, 176 slices), T2-weighted FLAIR (inversion recovery sampling perfection with application-optimized contrasts by using different flip angle evolutions [IR SPACE sequence; Siemens]: TR = 4800 ms, TE = 353 ms, TI = 1800 ms, FOV = 256 mm, 1-mm isotropic resolution, 176 slices), and T2*-weighted (multishot echo-planar imaging [EPI]: TR = 64 ms, TE = 35 ms, FA = 10°, FOV = 250 mm, 0.65-mm isotropic resolution, 256 slices, EPI factor = 15).

A B_1 map using a modified Bloch-Siegert method¹⁴ (turbo flash sequence: TR = 19 ms, TE = 9.8 ms, FOV = 256 mm, FA = 8°, 4-mm isotropic resolution, 48 slices) was acquired, and T1 maps were calculated using this and the multiple GRE scans in Medical Image Processing, Analysis and Visualization 8.0.2 (MIPAV, Version 8.0.2; <https://mipav.cit.nih.gov>).

Seven of the 9 participants received gadolinium as part of other National Institutes of Health MR imaging studies, and those scans were available for retrospective analysis. The gadolinium scan included here was from a T1-weighted GRE scan (TR = 8.1 ms, TE = 2 ms, FOV = 256 mm, FA = 18°, 1-mm isotropic resolution, 176 slices).

One participant (healthy volunteer 4) was excluded from analysis due to an incorrect sequence acquisition. Images were interpreted clinically by an experienced neuroradiologist (D.S.R.).

Blood Work

Laboratory testing consisted of complete blood count, comprehensive metabolic panel with liver function tests and studies of creatine kinase, prolactin, thyroid stimulating hormone, and urine pregnancy (when relevant). These tests were performed at screening, week 1, month 1, and subsequent scans.

Image Processing

Image analysis was conducted using the freely available image-analysis software MIPAV. For each participant, volumes of interest (VOIs) covering the anterior pituitary gland (entire gland) and choroid plexus (3 consecutive axial slices) were manually drawn on the baseline unenhanced T1-weighted GRE (FA = 18°) scan and transferred to registered postmangafodipir images (On-line

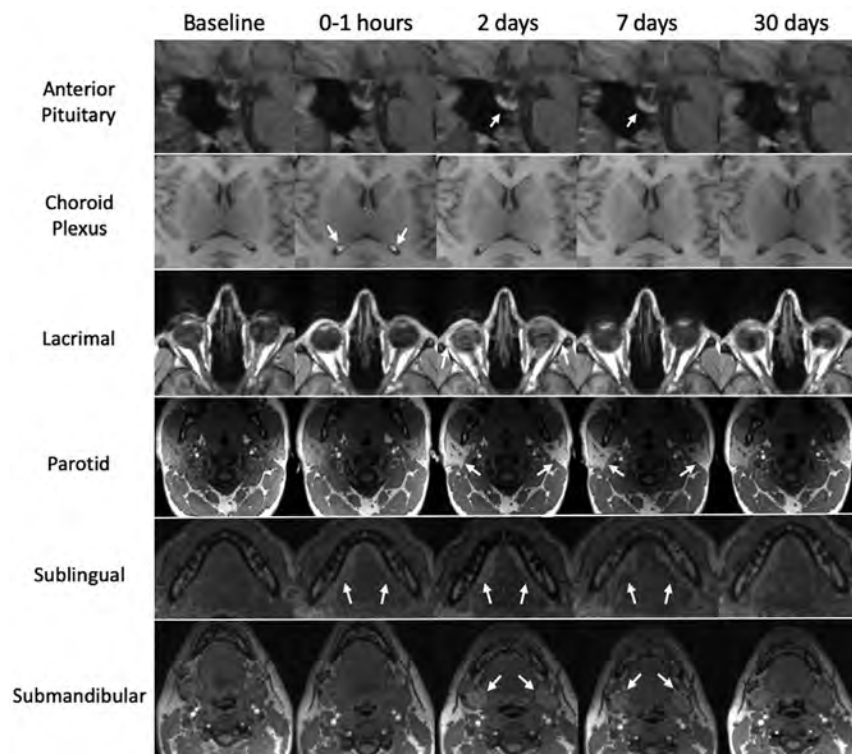


FIG 1. Manganese uptake in intracranial and extracranial structures. Images from healthy volunteer 1 and healthy volunteer 2 show manganese enhancement on T1-weighted images. Time points for the anterior pituitary, lacrimal, parotid, and submandibular glands were at 5 minutes, 2 days, 7 days, and 30 days after mangafodipir administration; for the choroid plexus and sublingual gland, postmangafodipir time points were at 1 hour, 2 days, 7 days, and 30 days.

Fig 1). Exocrine glands (lacrimal, ~3 slices; submandibular, ~14 slices; sublingual, ~16 slices; parotid, ~6 slices) were manually segmented in a similar manner at each postmangafodipir time point due to their variable configuration at each scan. The VOIs of basal ganglia structures (caudate, striatum, pallidum), thalamus, cerebral cortex, and whole brain were obtained through segmentation using the semiautomated segmentation pipeline FreeSurfer (Version 5.1.0; <http://surfer.nmr.mgh.harvard.edu>). The mean and SD of signal intensity from T1-weighted images and the median T1 relaxation time from T1 maps were calculated in each VOI. T1-weighted signal intensity was normalized to the signal intensity from the manually segmented corpus callosum (~11 slices) at each time point, and the fold change was calculated by dividing the normalized postmangafodipir intensity values by the normalized baseline intensity at each time point. The corpus callosum was selected for normalization due to the following: 1) prior animal and human data indicating that it does not enhance with manganese; and 2) the ease of segmentation due to its discrete borders on midline and paramedian sagittal slices.^{13,15}

T1 mapping was successful in 7 participants for quantification of the anterior pituitary gland, choroid plexus, exocrine glands, and corpus callosum; 5 participants had successful T1 mapping for quantification of basal ganglia substructures.

Statistical Analysis

Statistical analysis was conducted using SAS (Version 9.2; SAS Institute, Cary, North Carolina). For each structure variable (sig-

nal intensity and T1 times), the linear trapezoidal rule was used to calculate the area under the enhancement curve. The area under the curve used for analysis was the difference between the area under the enhancement curve and the area under the baseline (interval between baseline and screening scan) divided by the time length.

The enhancement was evaluated using both the Wilcoxon signed rank test and bootstrapping with 500 replicates. In addition, a piecewise linear mixed-effects model was applied to examine the pattern of manganese enhancement for each structure.

RESULTS

Nine healthy volunteers (median age, 43 years; range, 27–55 years; 3 women) participated in this study. MR imaging time points after mangafodipir administration are listed in the Table. As described in further detail below, we noted time-varying enhancement ($P < .05$) of several intracranial and extracranial structures, particularly the choroid plexus, anterior pituitary gland, and exocrine glands of the head and neck (parotid, sublingual,

submandibular, and lacrimal).

Choroid Plexus

On administration of mangafodipir, T1-weighted signal intensity of the choroid plexus increased within the first hour (Figs 1 and 2). In the 2 healthy volunteers scanned within the first 2 hours, enhancement was noted both quantitatively and qualitatively within the first 5 minutes after infusion (Fig 2), reaching maximum intensity in the 11- to 40-minute range. During the next 24 hours, the signal intensity decreased, achieving pre-infusion levels around 5–7 days (Figs 1 and 2). No further enhancement was noted for the remainder of the study period. Analysis of T1 maps did not show clear shortening of the T1 time (On-line Fig 2).

Anterior Pituitary Gland

In the 2 healthy volunteers scanned within the first 2 hours, enhancement was noted both quantitatively and qualitatively (Fig 2), but enhancement peaked in the 1- to 24-hour range (Figs 1 and 2). For most volunteers, this signal persisted for at least a week and resolved by the month 1 time point. In 2 volunteers, enhancement of the anterior pituitary gland resolved by the week 1 time point. No further enhancement of the anterior pituitary gland was observed for the remainder of the study period. Analysis of T1 values did not show a statistically significant decrease, in part because fewer data points were available for analysis (On-line Fig 2), but data suggest a possible nadir in the 1- to 24-hour range.

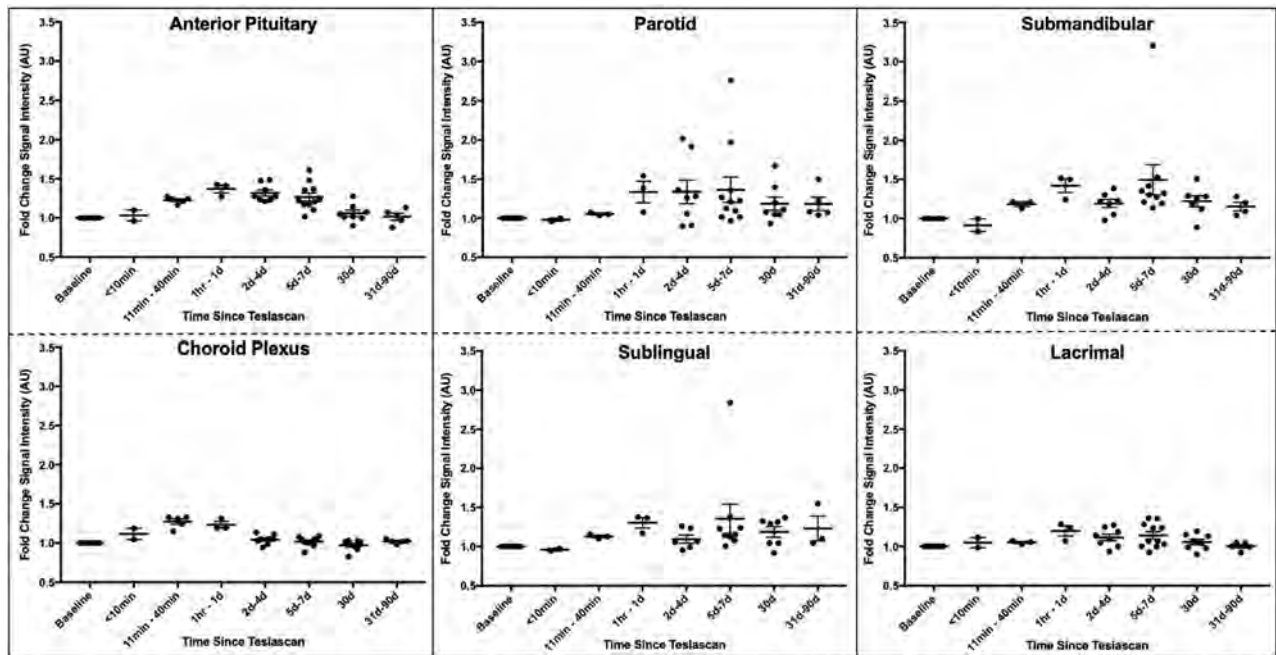


FIG 2. Kinetics of manganese enhancement in selected intracranial and extracranial structures. Quantification of T1-weighted signal intensity, normalized to the corpus callosum and measured as a fold change relative to baseline in healthy volunteers ($n = 8$). Each dot represents a scan at the specified time point; in some cases, a single individual had several scans within the same time window. The population mean and standard error are also shown. All structures enhanced at $P < .05$.

Exocrine Glands

The parotid, sublingual, submandibular, and lacrimal glands all demonstrated signal enhancement after mangafodipir infusion in the 1- to 24-hour range (Figs 1 and 2). The parotid and lacrimal glands had peak enhancement at approximately 5–7 days, whereas the sublingual and submandibular glands had peak enhancement in the 1- to 24-hour range (Fig 2). Probably due to their position at the edge of the head coil, T1-weighted signal in the exocrine glands was much more variable compared with enhancing intracranial structures. Whereas most volunteers had resolution of exocrine gland enhancement by month 1, two volunteers had resolution by month 2, and 1 volunteer had resolution by month 3. Quantitative T1 maps contained artifacts within several exocrine gland structures, which rendered analysis of T1 values highly variable (On-line Fig 2).

Brain

Relative to the corpus callosum, there was no evidence of manganese retention in the analyzed brain structures at various post-mangafodipir time points and at month 1 (Fig 3). In particular, signal intensities in the caudate, putamen, globus pallidus, thalamus, cerebral cortex, and whole brain showed no clear change during the entire study period. Similarly, T1 maps, which are not normalized to the corpus callosum, showed no change in any of these structures or in the corpus callosum itself (On-line Fig 3).

Adverse Reactions

There were no serious adverse reactions with mangafodipir administration. One volunteer reported a transient sensation of flushing and warmth, which did not require intervention. No additional symptoms were noted by the participants for the study period. Laboratory values did not significantly change after man-

gafodipir administration during the study period, at either week 1 or month 1.

Time Course of Manganese Enhancement

The time courses of manganese-induced signal enhancement and washout in the structures with significant changes with time are described in On-line Fig 4. For all 6 structures, the slopes before and after the knot were nonzero for the bootstrapped data. Although rates of enhancement were similar across structures, rates of washout were slowest in the exocrine glands.

DISCUSSION

Manganese has shown promise as a functional intracellular MR imaging contrast agent through its ability to evaluate cellular integrity, activity, and neural connectivity. Manganese ion has been used as an imaging biomarker for cellular viability and structural integrity, as a surrogate for the cellular calcium ion transport, and for neural tract visualization. In this study, manganese ions released from mangafodipir in healthy volunteers resulted in enhancement of several intracranial and extracranial structures: the choroid plexus, anterior pituitary gland, and exocrine glands of the head and neck. Structures covered with a blood-brain barrier did not exhibit visible manganese enhancement. Mangafodipir was well-tolerated, without serious adverse effects or changes in laboratory values.

Choroid Plexus

The choroid plexus is a collection of specialized ependymal cells that forms the blood-CSF barrier and is responsible for the accumulation and transport of several substrates and heavy metals, including manganese.¹⁶ In rats, manganese administration with a bolus dose of $MnCl_2$ revealed a specific time-dependent pattern of

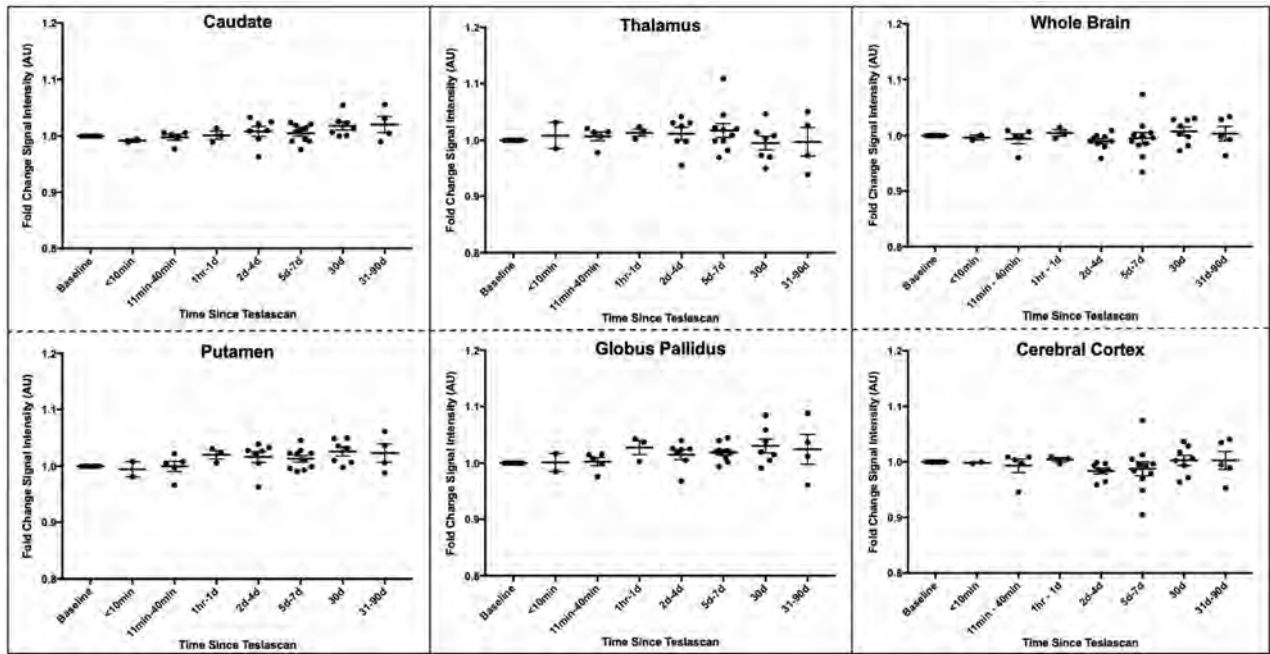


FIG 3. T1-weighted signal does not change in the basal ganglia, cerebral cortex, or whole brain after mangafodipir administration. Quantification of T1-weighted signal intensity, normalized to the corpus callosum and measured as a fold change relative to baseline in healthy volunteers ($n = 8$), in selected brain structures. Each *dot* represents a scan at the specified time point, summarized as mean \pm standard error.

enhancement of structures outside the blood-brain barrier: the choroid plexus within 10 minutes of administration, followed by CSF and periventricular brain structures.¹⁶ A similar distribution of manganese enhancement was observed in marmoset monkeys, with enhancement in the choroid plexus and later in the periventricular brain parenchyma, though no clear ventricular enhancement was seen.¹⁷ In a prior study in humans, bolus doses of mangafodipir provided enhancement of the choroid plexus, which peaked at 1.5 hours and resolved by 2 days.¹³ These findings correlate well with the enhancement dynamics of the choroid plexus that were noted in the current study. However, distinct from the findings in rats, no clear enhancement of the CSF or surrounding brain parenchyma has been demonstrated in human beings. This could potentially be explained by the much lower dose of manganese derived from mangafodipir compared with $MnCl_2$ delivered to animals. Furthermore, in this study, quantitative analysis of the choroid plexus did not show significant T1 shortening, even though there was clear signal enhancement on T1-weighted MR imaging. This is likely due to insufficient data at early time points and noise in the T1 measurements and to the small size of the choroid plexus, which results in partial volume effects from the long-T1 CSF.

The choroid plexus plays a significant biologic role in manganese ion homeostasis and transport. Whereas the blood-brain barrier and choroid plexus both transport the manganese ion at physiologic concentrations, when blood levels rise, the manganese ion preferentially accumulates in and is transported through the choroid plexus.¹⁸ Indeed, recent studies have provided evidence for active, unidirectional, blood-to-CSF transport in the choroid plexus with slow manganese ion efflux rates.¹⁹ Several transporters with varying levels of manganese ion affinity have been identified (eg, divalent metal transporter 1, ZIP8/14, calcium

ion $[Ca^{2+}]$ channels), but the specificity and presence of these channels in human choroidal tissue is yet to be determined.⁹ In our healthy volunteers, it is possible that manganese follows this established pathway with basolateral uptake, transcytoplasmic transfer, and release at the apical membrane into the CSF under the control of these transporters. While out of scope of this current study, characterization of manganese levels in the CSF could further provide evidence for this mechanism.

Anterior Pituitary Gland

The anterior pituitary gland lies outside the blood-brain barrier and has been known for several decades to be susceptible to manganese enhancement. Previous distribution studies in mice, rats, and monkeys identified liver, kidney, and endocrine glands as major sites of manganese accumulation after parenteral exposure.²⁰⁻²² Aoki et al¹⁶ demonstrated enhancement of the anterior pituitary gland within 2 hours of $MnCl_2$ infusion. In a different study, continuous $MnCl_2$ administration via mini-osmotic pumps led to a differential enhancement of manganese within the pituitary gland, with the anterior pituitary gland having a greater manganese-dependent increase in T1-weighted signal compared with the posterior pituitary gland.²³ In marmosets given $MnCl_2$, the greatest enhancement was in the anterior pituitary gland, with an approximate 3.5-fold increase in T1-weighted signal.¹⁵ Infusion of mangafodipir in healthy volunteers led to a dose-dependent stable enhancement of the anterior pituitary gland for >72 hours, with an approximately 1.5-fold increase from baseline signal.¹³ The same study noted a prolonged and slow recovery of manganese-associated enhancement, with 23% of initial signal still present at 4 weeks. Similarly, the findings from our own study show a peak signal intensity ~ 1.5 -fold greater than the baseline

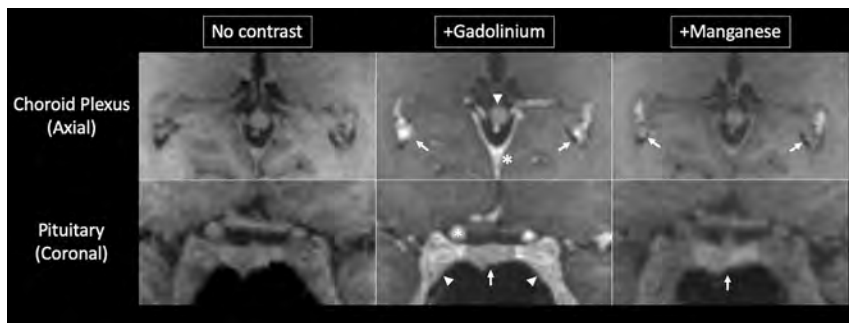


FIG 4. Manganese enhances brain structures in a different manner compared with gadolinium. *Upper row*, Gadolinium induces homogeneous enhancement of the choroid plexus (arrows), posterior falx cerebri (asterisk), and pineal gland (arrowhead). On the other hand, mangafodipir enhances the choroid glomus in a heterogeneous manner. *Lower row*, Gadolinium induces enhancement of the anterior pituitary gland (arrow), cavernous sinus (arrowheads), and internal carotid arteries (asterisks), whereas mangafodipir selectively enhances the pituitary gland. Note the enhancement of the vasculature with gadolinium but not with manganese. Images were obtained ~20 minutes after gadolinium administration and ~1 hour after mangafodipir administration. Gadolinium images were acquired before enrollment in this protocol as a part of other National Institutes of Health MR imaging studies.

scan in the anterior pituitary gland. However, resolution of enhancement was achieved quicker in the current study.

Exocrine Glands

There are reports of exocrine gland enhancement with manganese ions in various species. In mice given continuous $MnCl_2$ dosing, there was a several-fold increase in signal intensities of the submandibular and parotid glands.²³ Biodistribution studies with manganese-52 (^{52}Mn) PET imaging in mice demonstrated significant uptake and persistence in the salivary glands, with greater uptake noted through parenteral exposure as opposed to inhalation.²⁰ Similar findings have been observed in manganese distribution studies in rats and monkeys.^{21,24} Given this affinity of manganese for the salivary glands, Seshadri and Hoy²⁵ used MEMRI to evaluate manganese-dependent enhancement of salivary glands and head-and-neck tumors in nude mice. There was excellent visualization and delineation of both normal salivary glands and ectopic/orthotopic tumors with a strong T1-shortening effect.

Mechanisms of manganese ion entry and retention in exocrine glands have not been established, but 2 characteristics of the exocrine glands are likely to be at play: high mitochondrial density and extensive transport coupled to calcium signaling.²⁶ Synthesis of digestive enzymes by the salivary glands requires many mitochondria, which have been reported to accumulate intracellular manganese.⁹ Vesicular release of digestive enzymes occurs through calcium-mediated signaling and mobilization of intracellular stores of calcium from the endoplasmic reticulum into the cytoplasm, leading to exocytosis.²⁷ Also, it is thought that the calcium is stored in secretory vesicles, which occupy 30% and 55% of cytosolic space of the rat parotid and submandibular glands, respectively.²⁸ Manganese ions have also been seen to accumulate in the endoplasmic reticulum, and accumulation in secretory vesicles probably explains the ability of the manganese ion to cross synapses.²⁹ Therefore, it is not surprising that the salivary glands in our healthy volunteers had long-lasting enhancement due to manganese ions.

Quantification of exocrine gland enhancement showed high

variability of enhancement patterns across participants in the current study. Whereas all glands shared similar enhancement dynamics, fold change and T1 relaxation times were heterogeneous across glands (Fig 2). Although a biologic reason for these differences is possible, they are more likely explained by signal drop-out and inhomogeneities as a consequence of technical factors, including the larger distance between the exocrine glands and the radiofrequency receive coil used in this study. In addition, quantitative T1 maps contained numerous bright artifacts that interfered with accurate analysis of T1 values. The artifacts were likely derived from the presence of fluid and fat within exocrine glands, which can affect measurement of T1 relaxation times.³⁰ Further optimization

of MR imaging for salivary gland enhancement with manganese will likely provide a more accurate quantification of its enhancement dynamics and potential utility for detecting and discriminating glandular pathology.

Comparison of Manganese and Gadolinium

Retrospective comparison of contrast enhancement between manganese and gadolinium further highlights the distinct enhancement pattern of manganese (Fig 4). With manganese, there was selective enhancement of the anterior pituitary gland without appreciable signal change in neighboring structures. Gadolinium, on the other hand, induced broader enhancement in the region, increasing T1-weighted signal in the anterior pituitary gland, cavernous sinus, and intravascular spaces. Within the choroid plexus, the distribution of manganese-related enhancement was similar to that of gadolinium, with the exception of the choroid glomus regions. Additionally, enhancement of the posterior falx cerebri and pineal gland was demonstrated clearly with gadolinium, but not with manganese.

It has been shown that intracellularly, compared with an in vitro environment, manganese binds to macromolecules, which greatly enhances proton relaxation.³¹ Thus, it is likely that manganese enhancement reflects more specifically the cellular components of tissue. Conversely, intravascular spaces do not seem to enhance with manganese (at concentrations derived from mangafodipir). Together, these properties may aid in delineating tissue borders, providing useful information for clinical surveillance and surgical planning. Overall, this comparison highlights the ability of manganese to yield specific intracellular enhancement in regions not covered by the blood-brain barrier.

Mangafodipir Safety

Historically, the application of MEMRI in humans has been limited by the toxic effects of high bolus doses of free manganese ions. Mangafodipir is the only FDA-approved manganese-based contrast agent for intravenous use in humans and has an excellent safety record.³² The most common adverse effects observed in Phase III studies were flushing and nausea.³² Our findings further

strengthen the safety profile of mangafodipir. None of the healthy volunteers had serious adverse events during or after infusion. One healthy volunteer had mild transient flushing, likely due to vasodilatory effects of manganese, which self-resolved without further sequelae. We did not observe changes in prolactin, suggesting that the manganese ion did not impair anterior pituitary gland function. In addition, participants did not have changes in vital signs or clinical parameters postinfusion.³²

It has been observed that abnormal T1-weighted signal in the basal ganglia precedes development of neurologic symptoms related to manganese toxicity.³² Thus, monitoring T1-weighted signal changes in the basal ganglia provides a way to assess the development of manganese-related toxicity. In our study, postmanganese T1-weighted signal intensities did not change in the basal ganglia, whole brain, or cerebral cortex during the study period (On-line Fig 3). None of the participants reported additional neurologic or clinical changes within the study period.

Study Limitations

Given the exploratory nature of this study, there are key limitations that are important to address. The main objective of this study was to evaluate enhancement dynamics using MEMRI with mangafodipir in healthy volunteers. Thus, while this study has provided evidence of manganese enhancement in various structures at various time points as well as the lack of manganese retention in the brain, it was not powered for assessing safety. While we do not expect manganese-related adverse effects past our study window, we did not pursue long-term follow-up scans. Furthermore, this study was not designed to establish within-subject variability in manganese enhancement characteristics because we were primarily interested in obtaining a general trend of manganese enhancement.

The delivered dose of the manganese ion from mangafodipir also poses a limitation and probably explains why parenchymal structures behind the blood-brain barrier failed to enhance despite clear evidence of choroid plexus enhancement. Due to the potential neurotoxicity of repeat/chronic manganese exposure, mangafodipir is only FDA-approved for 1-time dosing. The manganese ion is released from mangafodipir and then likely binds, to some extent, to serum proteins, lowering the concentration of circulating manganese ions available for intracellular enhancement.¹¹ Reduced circulating free manganese ions could explain the differences seen in the enhancement patterns between human and animal studies, which use higher effective doses of manganese. Therefore, whether enhancement patterns seen in humans are due to differences in the manganese ion uptake in humans or to lower concentrations of the manganese ion is yet to be evaluated.

CONCLUSIONS

This study establishes MEMRI with mangafodipir as a viable neuroradiologic method in humans, especially for structures residing outside the blood-brain barrier (including the anterior pituitary gland, choroid plexus, and exocrine glands) and sets the stage for future exploration under normal and pathologic tissue states.

ACKNOWLEDGMENTS

We thank the staff of the National Institute of Neurological Disorders and Stroke Neuroimmunology Clinic and Clinical Trials Unit (in particular, Rosalind Hayden, Rosemarie Cuento, and Sandra Martin), the National Institutes of Health Pharmaceutical Development Section (especially Gopal Potti and Judith Starling), and the National Institute of Mental Health Functional MR imaging Facility for their assistance at various stages of this study.

Disclosures: Blake Dewey—UNRELATED: Grants/Grants Pending: Biogen, Comments: partially supported by a grant.* Bruce A. Berkowitz—UNRELATED: Employment: Wayne State University. *Money paid to the institution.

REFERENCES

1. Malheiros JM, Paiva FF, Longo BM, et al. **Manganese-enhanced MRI: biological applications in neuroscience.** *Front Neurol* 2015;6:161 CrossRef Medline
2. Silva AC, Lee JH, Wu CW, et al. **Detection of cortical laminar architecture using manganese-enhanced MRI.** *J Neurosci Methods* 2008;167:246–57 CrossRef Medline
3. Cloyd RA, Koren SA, Abisambra JF. **Manganese-enhanced magnetic resonance imaging: overview and central nervous system applications with a focus on neurodegeneration.** *Front Aging Neurosci* 2018;10:403 CrossRef Medline
4. Aoki I, Naruse S, Tanaka C. **Manganese-enhanced magnetic resonance imaging (MEMRI) of brain activity and applications to early detection of brain ischemia.** *NMR Biomed* 2004;17:569–80 CrossRef Medline
5. Saleem KS, Pauls JM, Augath M, et al. **Magnetic resonance imaging of neuronal connections in the macaque monkey.** *Neuron* 2002;34:685–700 CrossRef Medline
6. Bock NA, Kocharyan A, Silva AC. **Manganese-enhanced MRI visualizes V1 in the non-human primate visual cortex.** *NMR Biomed* 2009;22:730–36 CrossRef Medline
7. Pautler RG, Mongeau R, Jacobs RE. **In vivo trans-synaptic tract tracing from the murine striatum and amygdala utilizing manganese enhanced MRI (MEMRI).** *Magn Reson Med* 2003;50:33–39 CrossRef Medline
8. Wolf GL, Baum L. **Cardiovascular toxicity and tissue proton T1 response to manganese injection in the dog and rabbit.** *AJR Am J Roentgenol* 1983;141:193–97 CrossRef Medline
9. Tuschl K, Mills PB, Clayton PT. **Manganese and the brain.** *Int Rev Neurobiol* 2013;110:277–312 CrossRef Medline
10. Runge VM. **Safety of approved MR contrast media for intravenous injection.** *Magn Reson Med* 2000;12:205–13 Medline
11. Toft KG, Hustvedt SO, Grant D, et al. **Metabolism and pharmacokinetics of MnDPDP in man.** *Acta Radiol* 1997;38:677–89 CrossRef Medline
12. Schmidt PP, Toft KG, Skotland T, et al. **Stability and transmetallation of the magnetic resonance contrast agent MnDPDP measured by EPR.** *J Biol Inorg Chem* 2002;7:241–48 CrossRef Medline
13. Wang C, Gordon PB, Hustvedt SO, et al. **MR imaging properties and pharmacokinetics of MnDPDP in healthy volunteers.** *Acta Radiol* 1997;38:665–76 Medline
14. Duan Q, van Gelderen P, Duyn J. **Improved Bloch-Siegert based B1 mapping by reducing off-resonance shift.** *NMR Biomed* 2013;26:1070–78 CrossRef Medline
15. Takeda A. **Manganese action in brain function.** *Brain Res Brain Res Rev* 2003;41:79–87 CrossRef Medline
16. Aoki I, Wu YJ, Silva AC, et al. **In vivo detection of neuroarchitecture in the rodent brain using manganese-enhanced MRI.** *Neuroimage* 2004;22:1046–59 CrossRef Medline
17. Bock NA, Paiva FF, Nascimento GC, et al. **Cerebrospinal fluid to brain transport of manganese in a non-human primate revealed by MRI.** *Brain Res* 2008;1198:160–70 CrossRef Medline

18. Yokel RA. **Manganese flux across the blood-brain barrier.** *Neuro-molecular Med* 2009;11:297–310 CrossRef Medline
19. Schmitt C, Strazielle N, Richaud P, et al. **Active transport at the blood-CSF barrier contributes to manganese influx into the brain.** *J Neurochem* 2011;117:747–56 CrossRef Medline
20. Wooten AL, Aweda TA, Lewis BC, et al. **Biodistribution and PET imaging of pharmacokinetics of manganese in mice using manganese-52.** *PLoS One* 2017;12:e0174351 CrossRef Medline
21. Brunquell CL, Hernandez R, Graves SA, et al. **Uptake and retention of manganese contrast agents for PET and MRI in the rodent brain.** *Contrast Media Mol Imaging* 2016;11:371–80 CrossRef Medline
22. Dastur DK, Manghani DK, Raghavendran K. **Distribution and fate of ⁵⁴Mn in the monkey: studies of different parts of the central nervous system and other organs.** *J Clin Invest* 1971;50:9–20 CrossRef Medline
23. Sepúlveda MR, Dresselaers T, Vangheluwe P, et al. **Evaluation of manganese uptake and toxicity in mouse brain during continuous MnCl₂ administration using osmotic pumps.** *Contrast Media Mol Imaging* 2012;7:426–34 CrossRef Medline
24. Suzuki Y, Mouri T, Suzuki Y, et al. **Study of subacute toxicity of manganese dioxide in monkeys.** *Tokushima J Exp Med* 1975;22:5–10 Medline
25. Seshadri M, Hoy A. **Manganese-enhanced MRI of salivary glands and head and neck tumors in living subjects.** *Magn Reson Med* 2010; 64:902–06 CrossRef Medline
26. Terman BI, Gunter TE. **Characterization of the submandibular gland microsomal calcium transport system.** *Biochim Biophys Acta* 1983;730:151–60 CrossRef Medline
27. Won JH, Yule DI. **Measurement of Ca²⁺ signaling dynamics in exocrine cells with total internal reflection microscopy.** *Am J Physiol Gastrointest Liver Physiol* 2006;291:G146–55 CrossRef Medline
28. Martinez Jr, Willis S, Puente S, et al. **Evidence for a Ca²⁺ pool associated with secretory granules in rat submandibular acinar cells.** *Biochem J* 1996;320:627–34 CrossRef Medline
29. Pautler RG, Silva AC, Koretsky AP. **In vivo neuronal tract tracing using manganese-enhanced magnetic resonance imaging.** *Magn Reson Med* 1998;40:740–48 Medline
30. Kellman P, Bandettini WP, Mancini C, et al. **Characterization of myocardial T1-mapping bias caused by intramyocardial fat in inversion recovery and saturation recovery techniques.** *J Cardiovasc Magn Reson* 2015;17:33 CrossRef Medline
31. Federle M, Chezmar J, Rubin DL, et al. **Efficacy and safety of mangafodipir trisodium (MnDPDP) injection for hepatic MRI in adults: results of the U.S. Multicenter phase III clinical trials: efficacy of early imaging.** *J Magn Reson Imaging* 2000;12:689–701 CrossRef Medline
32. Zheng W, Fu SX, Dydak U, et al. **Biomarkers of manganese intoxication.** *Neurotoxicology* 2011;32:1–8 CrossRef Medline

The Association between FLAIR Vascular Hyperintensity and Stroke Outcome Varies with Time from Onset

W.J. Shang, H.B. Chen, L.M. Shu, H.Q. Liao, X.Y. Huang, S. Xiao, and H. Hong



ABSTRACT

BACKGROUND AND PURPOSE: FLAIR vascular hyperintensity has been recognized as a marker of collaterals in ischemic stroke, but the impact on outcome is still controversial. We hypothesized that the association between FLAIR vascular hyperintensity and outcome varies with time.

MATERIALS AND METHODS: We included 459 consecutive patients with middle cerebral artery stroke and divided them into 3 groups by symptom-to-MR imaging time (group 1, ≤ 7 days; group 2, 8–14 days; group 3, ≥ 15 days). The FLAIR vascular hyperintensity score, ranging from 0 to 3 points, was based on territory distributions of different MCA segments. The associations between FLAIR vascular hyperintensity and outcome with time were analyzed qualitatively and quantitatively.

RESULTS: No patients underwent MR imaging within 6 hours of onset. The proportion of FLAIR vascular hyperintensity (+) and severe stenosis or occlusion of MCA was not significantly dependent on time. In groups 1 and 2, FLAIR vascular hyperintensity (+) was significantly associated with larger lesions, the prevalence of flow injury, and unfavorable outcome ($mRS \geq 2$). There were no such associations in group 3. Multiple logistic regressions demonstrated that FLAIR vascular hyperintensity (+) was an independent risk factor for unfavorable outcome in group 2. Infarction volume tended to increase with the increase of the distal FLAIR vascular hyperintensity score in groups 1 and 2, while declining in group 3.

CONCLUSIONS: FLAIR vascular hyperintensity is associated with unfavorable outcome within 6 hours to 14 days of onset, while the wider distribution of distal FLAIR vascular hyperintensity may be favorable beyond 14 days of onset in MCA infarction. Symptom-to-MR imaging time should be considered when assessing the prognostic value of FLAIR vascular hyperintensity.

ABBREVIATION: FVH = FLAIR vascular hyperintensity

Cerebral ischemic damage depends on both the degree and duration of hypoperfusion. However, collaterals neither de-

velop rapidly nor remain invariant after arterial occlusion. Some collaterals such as leptomeningeal anastomoses may be anatomically present, though enhanced capacity for cerebral blood flow likely requires time to develop.^{1–5} Angiogenesis induced by hypoxia and increased fluid shear stress also requires several days to weeks.^{1,2} Furthermore, the incipient development of collaterals does not guarantee their persistence.¹ Therefore, the prognostic significance of an observation of the presence of collaterals after ischemic stroke varies with time.

FLAIR vascular hyperintensity (FVH), seen in some patients with ischemic stroke, is known to be associated with stenosis and occlusion of vessels and the attendant slow flow.^{6–9} FVH is also thought to be a marker of collaterals and a predictor of outcome.^{4,6–23} However, the relationship between these interpreta-

Received March 13, 2019; accepted after revision June 17.

From the Department of Neurology (W.J.S., H.B.C., L.M.S., S.X., H.H.), National Key Clinical Department and Key Discipline of Neurology, The First Affiliated Hospital, Sun Yat-sen University, Guangzhou, China; and Department of Neurology (L.M.S., H.Q.L., X.Y.H.), The Seventh Affiliated Hospital, Sun Yat-sen University, Shenzhen, China.

W.J. Shang and H.B. Chen contributed to the work equally.

The study was supported by grants from: National Natural Science Foundation of China (No. 81671134); Medical Scientific Research Foundation of Guangdong Province of China (No. A2017219); Guangzhou Science and Technology Programme (No. 2014Y2-00502); Guangdong Provincial Key Laboratory for Diagnosis and Treatment of Major Neurological Diseases (No. 2017B030314103); Southern China International Cooperation Base for Early Intervention and Functional Rehabilitation of Neurological Diseases (No. 2015B050501003); Guangdong Provincial Engineering Center for Major Neurological Disease Treatment; and Guangdong Provincial Translational Medicine Innovation Platform for Diagnosis and Treatment of Major Neurological Disease.

Please address correspondence to Hua Hong, Department of Neurology, National Key Clinical Department and Key Discipline of Neurology, The First Affiliated Hospital, Sun Yat-sen University, 58 Zhongshan 2nd Rd, Guangzhou, Guangdong Province, China, 510080; e-mail: hhsuns@126.com

Indicates open access to non-subscribers at www.ajnr.org

Indicates article with supplemental on-line tables.

Indicates article with supplemental on-line photos.

<http://dx.doi.org/10.3174/ajnr.A6142>

tions is confusing. FVH may represent slow collateral flow effective in maintaining perfusion to penumbral regions, restricting the progress of ischemic lesions and improving outcome.¹⁰⁻¹⁷ However, FVH can also seem to correspond to a perfusion deficit, larger lesions, and poor outcomes.^{6-8,18-23} The exact reason for such a huge discrepancy is still unclear. In addition to the differences in patient populations and FVH classifications, we found that many reported symptom-to-MR imaging times ranged from 3 hours to several days. Additionally, Maeda et al²⁴ showed that FVH decreased with time, indicating that differences in symptom-to-MR imaging time might account for the discrepancy.

Moreover, most studies^{6-8,10-18,21,22} were performed during the superacute or acute stages of ischemic stroke; however, many patients with subacute or even chronic ischemic strokes present to hospitals and undergo MR imaging. FVH has been observed in areas supplied by collateral blood flow in patients with symptom-to-MR imaging times that are several weeks in duration.²⁵ Given that FVH is easily obtained via MR imaging, it could serve as a helpful predictive measure in patients with ischemic stroke.

We hypothesized that the prognostic value of FVH in ischemic stroke might change with the MR imaging observation time relative to onset. Therefore, we here evaluate the dependence of the relationship between FVH and outcome on symptom-to-MR imaging time, in cases of middle cerebral artery ischemic stroke.

MATERIALS AND METHODS

Study Population

We retrospectively analyzed the records of patients with ischemic stroke treated in the First Affiliated Hospital of Sun Yat-sen University from April 2009 to February 2017. The inclusion criteria were the following: 1) patients with responsible lesions within the MCA distribution territory; 2) patients with FLAIR and 3D time-of-flight MRA images; 3) patients with ipsilateral M1-MCA stenosis or occlusion identified by 3D time-of-flight MRA; and 4) patients with a complete evaluation, which included a personal history, vascular risk factors (smoking, hypertension, diabetes mellitus, hyperlipidemia, previous stroke/transient ischemic attack, coronary artery disease, and atrial fibrillation), routine blood tests, and cardiologic work-up. Scores on the NIHSS at admission, mRS at discharge, and hospitalization days were also collected. We excluded the following: 1) patients with concomitant anterior cerebral artery or posterior circulation strokes; 2) patients with severe artifacts on FLAIR images; 3) patients with severe stenosis or occlusion of the ipsilateral internal carotid artery; and 4) patients having undergone endovascular therapy. Patients were divided into 3 groups according to symptom-to-MR imaging time: group 1, ≤ 7 days; group 2, 8-14 days; group 3, ≥ 15 days.

MR Imaging

MR imaging was performed on 3T scanners (Magnetom Trio and Magnetom Verio; Siemens, Erlangen, Germany) with a 12-channel head coil. The neuroimaging protocol comprised T1WI (TR, 500 ms; TE, 8.9 ms), T2WI (TR, 4000 ms; TE, 100 ms), FLAIR (TR, 9000 ms; TE, 111 ms; TI, 2500 ms), and DWI (TR, 5800 ms; TE, 100 ms; matrix number, 384×384 ; two b-values of 0 and 1000 s/mm^2). All patients' imaging data were independently reviewed by 2 readers who were blinded to the clinical data and

follow-up. Reader A had 18 years of neuroradiology experience, and reader B had 6 years of neuroradiology experience.

FVH

FVHs were defined as focal, tubular, or serpentine hyperintensities in the subarachnoid space relative to CSF and corresponding to the typical arterial course.¹¹ On the basis of the location and extent, FVHs were classified into proximal and distal FVHs. Proximal FVHs were defined as the presence of FVHs only within the territories of the MCA M1 and/or M2 segments. Distal FVHs were defined as the presence of FVHs in the MCA M3 and/or distal segments, which were further classified into anterior and posterior for the superior and inferior trunks of the MCA, respectively. The M3-segment FVHs, anterior FVHs, and posterior FVHs were all scored as 1 point.

Lesion Quantification

We used the ASPECTS on MR imaging.²⁶ The vascular territories were classified into perforator, pial, border zone, and large-territory infarct.²⁷

Angiography

The signal intensity of the MCA on the intracranial MRA was visually classified into the following 4 grades according to ability to visualize the MCA: All M3 branches of the MCA were visualizable to the cortical surface (grade A); ≥ 1 M3 branch could not be visualized on the cortical surface (grade B); the superior or inferior trunk of the MCA or ≥ 1 M2 branch could not be visualized along its course (grade C); and the M1 could not be visualized along its course (grade D) (On-line Fig 1).²⁸ Posterior cerebral artery laterality was considered to be present if ≥ 1 segmental extent of the ipsilateral posterior cerebral artery was observable on MRA.⁵

Statistical Analysis

The κ coefficient was used to assess interobserver agreement for FVH. Continuous variables with a normal distribution were described as mean \pm SD, and non-normally distributed variables were described as median and interquartile range. We compared variables between the patients with and without FVH in each group using a Mann-Whitney *U* test, Student *t* test, Pearson χ^2 test, or χ^2 test with continuity correction depending on the type of variable. We further compared FVH scores and baseline characteristics in all 3 groups using the Kruskal-Wallis-test or Pearson χ^2 test as appropriate. A multiple binary logistic regression analysis was applied to identify independent predictors of unfavorable scores on the modified Rankin Scale at discharge (mRS ≥ 2), signifying an unfavorable outcome. All covariates with a *P* value $\leq .1$ in a univariate analysis were entered into this logistic regression model. The results are presented as odds ratios and the 95% confidence intervals. A 2-tailed value of *P* $< .05$ indicated statistical significance (SPSS for Windows, Version 20.0; IBM, Armonk, New York).

RESULTS

In total, 579 consecutive patients met all the inclusion criteria, and 120 patients were excluded (concomitant anterior cerebral

Table 1: Clinical and demographic patient characteristics by symptom-to-MRI time and the presence of FVH^a

Characteristics	Group 1 (n = 191)			Group 2 (n = 164)			Group 3 (n = 104)		
	FVH (-) (n = 74)	FVH (+) (n = 117)	P Value	FVH (-) (n = 63)	FVH (+) (n = 101)	P Value	FVH (-) (n = 44)	FVH (+) (n = 60)	P Value
Women	27 (36.5)	37 (31.6)	.53	20 (31.7)	27 (26.7)	.60	10 (22.7)	20 (33.3)	.28
Age (yr)	60.7 ± 14.3	63.9 ± 12.5	.11	66 (46–73)	65.5 (54–74)	.88	55.1 ± 13.7	63.6 ± 11.0	.001 ^b
Symptom-to-admission time (days)	3 (2–4)	2 (1–4)	.05	5 (4–7)	4 (3–7)	.21	16.5 (12–31)	19.5 (12–30.75)	.79
Risk factors									
Hypertension	58 (78.4)	82 (70.1)	.24	35 (55.6)	70 (69.3)	.09	31 (70.5)	45 (75)	.66
Diabetes mellitus	29 (39.2)	28 (23.9)	.03 ^b	16 (25.4)	36 (35.6)	.23	12 (27.3)	13 (21.7)	.64
Hypercholesterolemia	24 (32.4)	43 (36.8)	.64	24 (38.1)	30 (29.7)	.31	8 (18.2)	8 (13.3)	.59
Smoker	24 (32.4)	52 (44.4)	.13	25 (39.7)	48 (47.5)	.34	19 (43.2)	26 (43.3)	1.00
Coronary heart disease	5 (6.8)	6 (5.1)	.88	1 (1.6)	6 (5.9)	.35	6 (13.6)	5 (8.3)	.59
Atrial fibrillation	4 (5.4)	8 (6.8)	.93	2 (3.2)	1 (1.0)	.88	1 (2.3)	2 (3.3)	1.00
Previous stroke	18 (24.3)	29 (24.8)	1.00	9 (14.3)	25 (24.8)	.12	9 (20.5)	19 (31.7)	.27
NIHSS score at admission	4 (2–7)	6 (3–10)	.02 ^b	4 (2–9)	5 (2–9)	.32	5 (2–10)	4.5 (2–9)	.56
Hospitalization (days)	10.5 (8–13)	13 (10–16)	.001 ^b	12 (9–15)	13 (9–15)	.95	13.5 (8–15)	12.5 (9.25–16)	.94
Outcome at discharge									
mRS	2 (1–3)	3 (2–4)	<.001 ^b	2 (1–3)	3 (2–4)	.10	2.5 (1–4)	3 (1.25–4)	.54
mRS ≥ 2	54 (73.0)	100 (85.5)	.04 ^b	43 (68.3)	85 (84.2)	.02 ^b	31 (70.5)	45 (75.0)	.66
mRS ≥ 3	31 (41.9)	70 (59.8)	.02 ^b	29 (46.0)	52 (51.5)	.52	22 (50.0)	34 (56.7)	.55

Note: (–) indicates negative; (+), positive.

^a Data are No. (%), mean ± SD, and median (interquartile range).

^b $P < .05$.

artery or posterior circulation strokes, $n = 27$; severe artifacts on FLAIR, $n = 18$; severe stenosis or occlusion of the ipsilateral internal carotid artery, $n = 47$; endovascular therapy, $n = 28$). We finally included 459 patients, and FVH was observed in 278 patients (60.6%). The interobserver agreement for FVH was $\kappa = 0.88$ (95% CI, 0.68–1.00). The proportion of observed FVH (+) was not significantly dependent on time (61.3%, 61.6%, and 57.7%; $P = .79$). Details of the clinical and demographic characteristics of patients by symptom-to-MR imaging time and the presence of FVH are presented in Table 1. In group 1, patients with FVH demonstrated a higher NIHSS score at admission ($P = .02$), a longer hospitalization ($P = .001$), a higher mRS at discharge ($P = .001$), and a higher prevalence of unfavorable outcome (mRS ≥ 2 ; $P = .04$) or poor outcome (mRS ≥ 3 ; $P = .02$) than those without FVH. In group 2, patients with FVH demonstrated a higher prevalence of unfavorable outcome (mRS ≥ 2 ; $P = .02$). However, in group 3, we found no significant difference in outcome between patients with and without FVH.

Details of the radiologic characteristics of patients by symptom-to-MR imaging time and FVH status are presented in On-line Table 1, Figs 1–3, and On-line Figs 2–4. No patients underwent MR imaging within 6 hours of onset. More patients with FVH demonstrated severe stenosis or occlusion of the MCA than those without it, independent of time (group 1, $P < .001$; group 2, $P < .001$; group 3, $P = .001$). In groups 1 and 2, patients with FVH demonstrated larger cortical extents of MCA and total lesion scores than those without it (group 1, $P < .001$, $P < .001$; group 2, $P = .003$, $P = .003$), and poorer MCA signal intensities (grades B–D; group 1, $P < .001$; group 2, $P < .001$). However, these differences were absent in group 3 ($P = .73$, $P = .45$, $P = .18$). We observed no significant differences in FVH scores ($P = 0.25$) across the 3 groups. The MCA cortical area and total lesion volume tended to increase with the distal FVH score in groups 1 and 2 and decrease in group 3 (Fig 3). Details of the baseline characteristics of the 3 groups are presented in On-line Table 2. There were no differences among the 3 groups, apart from hypercholesterolemia.

Variables associated with an unfavorable clinical outcome are shown in On-line Table 3. In group 1, sex ($P = .01$), NIHSS score on admission ($P < .001$), infarct volume ($P = .001$), and FVH ($P = .04$) were included in our analysis. After we adjusted for representative variables, FVH (+) did not appear as an independent predictor of unfavorable outcome ($P = .14$). In group 2, age ($P = .003$), NIHSS score on admission ($P < .001$), infarct volume ($P = .001$), FVH ($P = .002$), posterior cerebral artery laterality ($P = .008$), and MCA severe stenosis or occlusion ($P = .006$) were included in our analysis. After we adjusted for representative variables, FVH (+) appeared as an independent predictor of unfavorable outcome (odds ratio, 2.95; 95% CI, 1.06–8.18; $P = .04$). In group 3, FVH (+) was not included in our analysis ($P = .66$).

DISCUSSION

Our novel results demonstrate that the clinical value of FVH varies with time. Within 6 hours to 14 days of onset, FVH (+) is associated with greater lesion volume, poorer MCA signal intensity, and unfavorable outcome. These associations disappear beyond 14 days of onset. In addition, the lesion volume tended to increase with the distal FVH score within 6 hours to 14 days of onset and to decrease beyond 14 days of onset. Therefore, the symptom-to-MR imaging time, not just the presence or distribution of FVH, played an important role in predicting stroke outcomes in this study.

FVH is recognized as a marker of slow flow induced by severe stenosis or occlusion of vessels.^{6–9} The presence of FVH ranges from 44.1% to 100% in patients with stroke within 24 hours of onset,^{11,29} which increases to 75.9%–100% when accompanied by severe stenosis or occlusion of the MCA or ICA.^{11,12} Maeda et al²⁴ showed that the presence of FVH decreases from 100% within 24 hours of onset to 50% within 10–13 days of onset. In the present study, the proportion of severe stenosis or occlusion of the MCA was as high as 80.6%, and most of these patients did not undergo MR imaging a short time after onset, which could explain the median prevalence of FVH (60.6%). In addition, we saw no significant differences in the prevalence of FVH in our 3 groups,

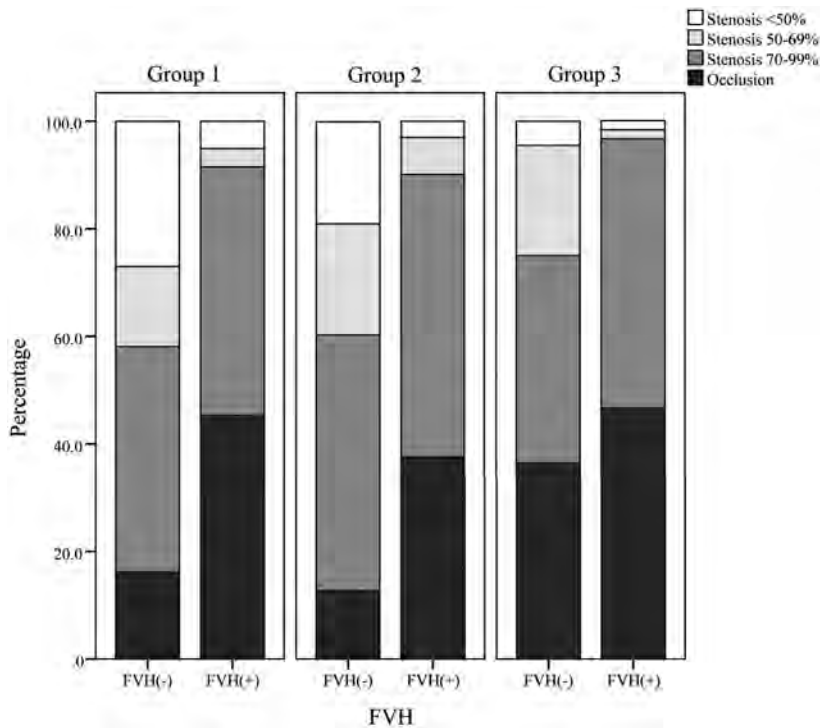


FIG 1. Detailed middle cerebral artery vascular status by symptom-to-MR imaging time, which increases with group number and the presence of FLAIR vascular hyperintensity.

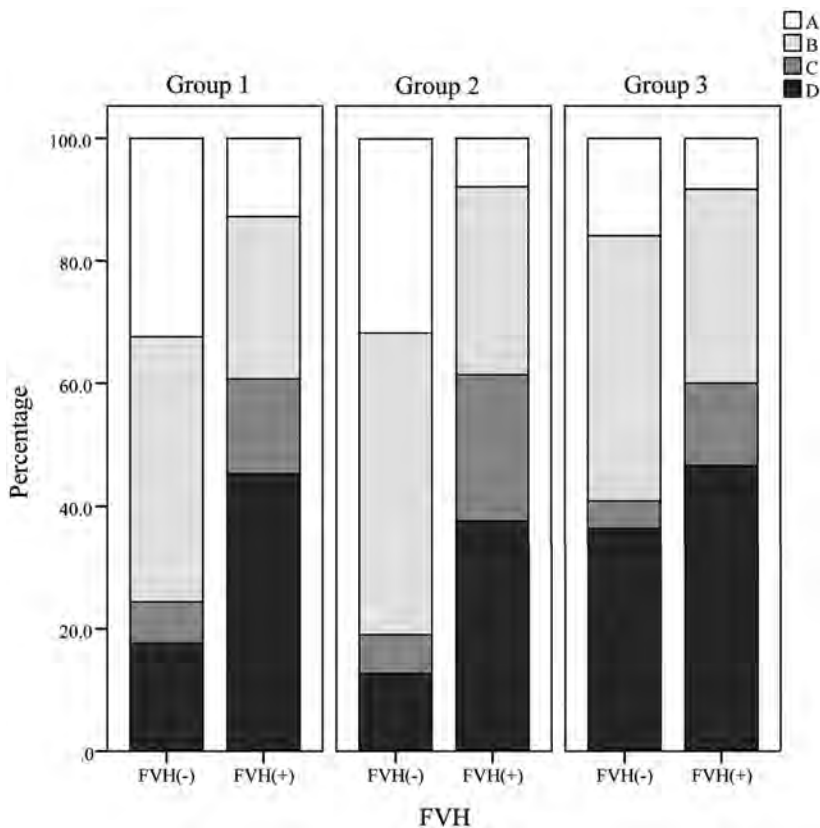


FIG 2. Detailed middle cerebral artery signal intensity by symptom-to-MR imaging time, which increases with group number and the presence of FLAIR vascular hyperintensity. A, All M3 branches of the MCA are visualized on the cortical surface. B, One or more M3 branches are not visualized on the cortical surface. C, The superior or inferior trunk of the MCA or ≥ 1 M2 branch is not visualized along its course. D, M1 branches are not visualized along the course of the MCA.

unlike Maeda et al.²⁴ One reason could be that the proportion of severe stenosis or occlusion and the signal intensity of MCA were not significantly different in our 3 groups, and the Maeda et al²⁴ study did not measure the degree of MCA lesion. Another possible reason is the much greater sample size in our study. The sample size in Maeda et al²⁴ was 27 patients, with only 2 patients imaged within 10–13 days of onset, which would have led to serious errors.

The prognostic value of FVH has been widely investigated,^{4,6-23} with greatly divergent results. Besides populations, end points, and FVH classifications, we think that the symptom-to-MR imaging time plays an important role in explaining the discrepancies in the literature. In our study, FVH (+) was associated with unfavorable clinical and radiographic outcomes within 6 hours to 14 days of onset, but these associations disappeared beyond 14 days of onset. On reviewing previous studies, we found that the symptom-to-MR imaging time was within 6 hours of onset or within the time window of reperfusion therapy in most of the studies that showed an association between FVH and good outcome.^{10,11,13-17} On the other hand, the symptom-to-MR imaging time was between 12 and 24 hours and several days in most of the studies showing an association between FVH and a poor outcome^{6-8,18-20}; these results are similar to ours for the group within 6 hours to 14 days of onset.

We assumed that the role of FVH would vary with time. Within 6 hours of onset or within the time window of reperfusion therapy, FVH might be a marker of leptomeningeal anastomoses that are anatomically present and develop dramatically and rapidly after the onset of acute ischemic stroke.^{2,5} The areas with FVH, especially those with FVH–DWI mismatch, represent the brain tissue at risk of infarction, which could be saved by reperfusion therapy to reduce the final lesion volume and improve outcome.^{6,9,16,29} This may explain why patients with FVH have better outcomes than those without FVH in this period.

Beyond the time window of reperfusion therapy, however, the observation of persistent FVH may represent persis-

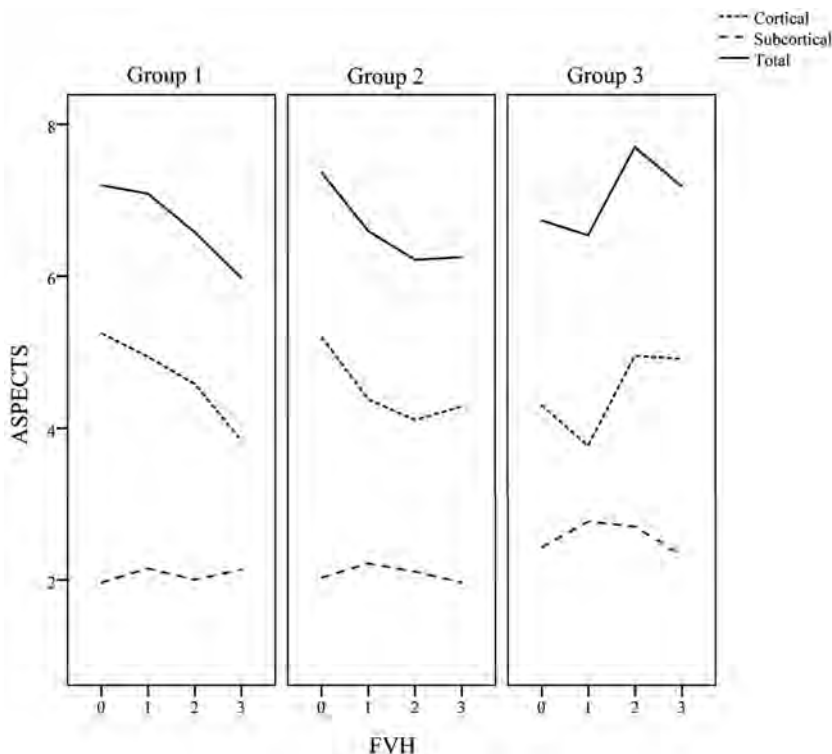


FIG 3. The ASPECTS lesion volume against the distal FLAIR vascular hyperintensity score.

tent vessel occlusion and impaired hemodynamics.^{4,14,29,30} Therefore, patients with FVH could be influenced much more by hemodynamic instability than patients without it.¹⁹ This difference might be correlated with a poor outcome in patients with FVH during this period. Some studies that re-examined MR imaging after the superacute period support this assumption.^{4,14,29} Sanossian et al¹⁴ found that a persistence of FVH on follow-up MR imaging was associated with a decreased or absent flow signal intensity on MRA, whereas the absence of FVH was seen in the setting of a return of the MR imaging flow signal intensity. This result is similar to our finding that patients with FVH had poorer MCA signal intensity. However, the observation of a decrease in FVH after reperfusion therapy predicted successful recanalization, smaller infarct volume, and good outcomes.^{4,29}

Here, FVH was not significantly associated with clinical or radiologic outcome in group 3, though we continued to see a preponderance of patients with FVH who had severe stenosis or occlusion of the MCA. In addition, the infarct volume tended to decrease with increases in the distal FVH score in group 3, which is the opposite of the results in groups 1 and 2. This outcome indicates that the wider distribution of distal FVH may be favorable when the symptom-to-MR imaging time extends beyond 14 days. We think that this possibility could be explained in the following 2 ways: First, new collaterals require time to develop significant capacity for cerebral blood flow.^{1,5} Second, achieving functional vessels through arteriogenesis requires several days to weeks.^{1,2} Therefore, these collaterals likely contribute more to alleviating the subacute or chronic stages of stroke than to mitigating acute ischemic events. The observation of no or little FVH in the subacute or chronic stages of stroke may represent an absence of effective collaterals. Future research should further refine

our knowledge of the importance of the symptom-to-MR imaging time beyond 14 days.

Unlike most studies that focused on the superacute stage of ischemic stroke, we used a much longer time span after ischemic stroke. Consequently, our study conditions more closely resembled “real world” clinical scenarios. Patients can undergo MR imaging any time after stroke onset, and using only FVH to evaluate the superacute ischemic stroke stage is insufficient for clinical work. However, FVH is relatively easy to detect on MR imaging and may therefore reflect collateral status and potentially act as a substitute for conventional angiography.³¹

This study has some limitations. First, this is a retrospective clinical study. However, it shows, by analysis, a clear time dependency of the prognostic value of FVH. Further prospective studies are needed to confirm our findings. Second, we excluded patients with endovascular therapy. Although this ex-

clusion ensures data homogeneity and avoids the influence of a diversity of treatments on outcome, it leads to no patients receiving MR imaging within 6 hours of onset in this study. However, many studies have focused on the superacute stage of stroke,^{10,11,13-17,21,22} while few²⁵ have focused on the subacute and chronic stages.

CONCLUSIONS

For patients with MCA infarctions, FVH (+) is associated with unfavorable outcomes within 6 hours to 14 days of onset, while the wider distribution of distal FVH may be favorable beyond 14 days of onset. Therefore, the symptom-to-MR imaging time should be taken into account when assessing the prognostic value of FVH.

Disclosures: Wenjin Shang—*RELATED: Grant:* National Natural Science Foundation of China (No. 81671134); Medical Scientific Research Foundation of Guangdong Province of China (No. A2017219); Guangzhou Science and Technology Programme (No. 2014Y2-00502). *Comments:* My institution is supported by the grants from Guangdong Provincial Key Laboratory for Diagnosis and Treatment of Major Neurological Diseases (No. 2017B030314103); Southern China International Cooperation Base for Early Intervention and Functional Rehabilitation of Neurological Diseases (No. 2015B050501003); Guangdong Provincial Engineering Center for Major Neurological Disease Treatment; Guangdong Provincial Translational Medicine Innovation Platform for Diagnosis and Treatment of Major Neurological Disease. Liming M. Shu—*RELATED: Grant:* National Natural Science Foundation of China (No. 81671134); Medical Scientific Research Foundation of Guangdong Province of China (No. A2017219); Guangzhou Science and Technology Programme (No. 2014Y2-00502).* Su Xiao—*RELATED: Grant:* Guangdong Provincial Key Laboratory for Diagnosis and Treatment of Major Neurological Diseases (No. 2017B030314103); Southern China International Cooperation Base for Early Intervention and Functional Rehabilitation of Neurological Diseases (No. 2015B050501003); Guangdong Provincial Engineering Center for Major Neurological Disease Treatment; Guangdong Provincial Translational Medicine Innovation Platform for Diagnosis and Treatment of Major Neurological Disease.* Hua Hong—*RELATED: Grant:* National Natural Science Foundation of China (No. 81671134); Medical Scientific Research Foundation of Guangdong Province of

China (No. A2017219); Guangzhou Science and Technology Programme (No. 2014Y2-00502). *Comments:* Our institution is supported by the grants from Guangdong Provincial Key Laboratory for Diagnosis and Treatment of Major Neurological Diseases (No. 2017B030314103); Southern China International Cooperation Base for Early Intervention and Functional Rehabilitation of Neurological Diseases (No. 2015B050501003); Guangdong Provincial Engineering Center for Major Neurological Disease Treatment; Guangdong Provincial Translational Medicine Innovation Platform for Diagnosis and Treatment of Major Neurological Disease; *Others:* We paid money to Editage, a division of Cactus Communications, for English editing to ensure that the language is clear and free of errors. The intent of our message was not altered in any way during the editing process. *Money paid to institution.

REFERENCES

- Liebesskind DS. **Collateral circulation.** *Stroke* 2003;34:2279–84 CrossRef Medline
- Iwasawa E, Ichijo M, Ishibashi S, et al. **Acute development of collateral circulation and therapeutic prospects in ischemic stroke.** *Neural Regen Res* 2016;11:368–71 CrossRef Medline
- Bang OY, Goyal M, Liebesskind DS. **Collateral circulation in ischemic stroke: assessment tools and therapeutic strategies.** *Stroke* 2015;46:3302–09 CrossRef Medline
- Ichijo M, Iwasawa E, Numasawa Y, et al. **Significance of development and reversion of collaterals on MRI in early neurologic improvement and long-term functional outcome after intravenous thrombolysis for ischemic stroke.** *AJNR Am J Neuroradiol* 2015;36:1839–45 CrossRef Medline
- Uemura A, O'Uchi T, Kikuchi Y, et al. **Prominent laterality of the posterior cerebral artery at three-dimensional time-of-flight MR angiography in M1-segment middle cerebral artery occlusion.** *AJNR Am J Neuroradiol* 2004;25:88–91 Medline
- Kamran S, Bates V, Bakshi R, et al. **Significance of hyperintense vessels on FLAIR MRI in acute stroke.** *Neurology* 2000;55:265–69 CrossRef Medline
- Kono T, Naka H, Nomura E, et al. **The association between hyperintense vessel sign and final ischemic lesion differ in its location.** *J Stroke Cerebrovasc Dis* 2014;23:1337–43 CrossRef Medline
- Cheng B, Ebinger M, Kufner A, et al; Stroke Imaging Repository (STIR) Investigators. **Hyperintense vessels on acute stroke fluid-attenuated inversion recovery imaging: associations with clinical and other MRI findings.** *Stroke* 2012;43:2957–61 CrossRef Medline
- Toyoda K, Ida M, Fukuda K. **Fluid-attenuated inversion recovery intraarterial signal: an early sign of hyperacute cerebral ischemia.** *AJNR Am J Neuroradiol* 2001;22:1021–29 Medline
- Mahdjoub E, Turc G, Legrand L, et al. **Do fluid-attenuated inversion recovery vascular hyperintensities represent good collaterals before reperfusion therapy?** *AJNR Am J Neuroradiol* 2018;39:77–83 CrossRef Medline
- Liu D, Scalzo F, Rao NM, et al. **Fluid-attenuated inversion recovery vascular hyperintensity topography: novel imaging marker for revascularization in middle cerebral artery occlusion.** *Stroke* 2016;47:2763–69 CrossRef Medline
- Huang X, Liu W, Zhu W, et al. **Distal hyperintense vessels on FLAIR: a prognostic indicator of acute ischemic stroke.** *Eur Neurol* 2012;68:214–20 CrossRef Medline
- Olindo S, Chausson N, Joux J, et al. **Fluid-attenuated inversion recovery vascular hyperintensity: an early predictor of clinical outcome in proximal middle cerebral artery occlusion.** *Arch Neurol* 2012;69:1462–68 CrossRef Medline
- Sanossian N, Saver JL, Alger JR, et al. **Angiography reveals that fluid-attenuated inversion recovery vascular hyperintensities are due to slow flow, not thrombus.** *AJNR Am J Neuroradiol* 2009;30:564–68 CrossRef Medline
- Lee KY, Latour LL, Luby M, et al. **Distal hyperintense vessels on FLAIR: an MRI marker for collateral circulation in acute stroke?** *Neurology* 2009;72:1134–39 CrossRef Medline
- Legrand L, Tisserand M, Turc G, et al. **Do FLAIR vascular hyperintensities beyond the DWI lesion represent the ischemic penumbra?** *AJNR Am J Neuroradiol* 2015;36:269–74 CrossRef Medline
- de la Ossa N, Hernandez- Pérez M, Domènech S, et al. **Hyperintensity of distal vessels on FLAIR is associated with slow progression of the infarction in acute ischemic stroke.** *Cerebrovasc Dis* 2012;34:376–84 CrossRef Medline
- Nam KW, Kwon HM, Park SW, et al. **Distal hyperintense vessel sign is associated with neurological deterioration in acute ischaemic stroke.** *Eur J Neurol* 2017;24:617–23 CrossRef Medline
- Kim SE, Lee BI, Kim SE, et al. **Clinical significance of fluid-attenuated inversion recovery vascular hyperintensities in borderzone infarcts.** *Stroke* 2016;47:1548–54 CrossRef Medline
- Gawlitza M, Gragert J, Quäsching U, et al. **FLAIR-hyperintense vessel sign, diffusion-perfusion mismatch and infarct growth in acute ischemic stroke without vascular recanalisation therapy.** *J Neuroradiol* 2014;41:227–33 CrossRef Medline
- Nave AH, Kufner A, Bücke P, et al. **Hyperintense vessels, collateralization, and functional outcome in patients with stroke receiving endovascular treatment.** *Stroke* 2018;49:675–81 CrossRef Medline
- Kufner A, Galinovic I, Ambrosi V, et al. **Hyperintense vessels on FLAIR: hemodynamic correlates and response to thrombolysis.** *AJNR Am J Neuroradiol* 2015;36:1426–30 CrossRef Medline
- Gawlitza M, Bohme J, Maros M, et al. **FLAIR vascular hyperintensities and 4D MR angiograms for the estimation of collateral blood flow in anterior cerebral artery ischemia.** *PLoS One* 2017;12:e0172570 CrossRef Medline
- Maeda M, Koshimoto Y, Uematsu H, et al. **Time course of arterial hyperintensity with fast fluid-attenuated inversion-recovery imaging in acute and subacute middle cerebral arterial infarction.** *J Magn Reson Imaging* 2001;13:987–90 CrossRef Medline
- Essig M, von Kummer R, Egelhof T, et al. **Vascular MR contrast enhancement in cerebrovascular disease.** *AJNR Am J Neuroradiol* 1996;17:887–94 Medline
- Barber PA, Demchuk AM, Zhang J, et al. **Validity and reliability of a quantitative computed tomography score in predicting outcome of hyperacute stroke before thrombolytic therapy: ASPECTS study group—Alberta Stroke Programme Early CT Score.** *Lancet* 2000;355:1670–74 CrossRef Medline
- Lee DK, Kim JS, Kwon SU, et al. **Lesion patterns and stroke mechanism in atherosclerotic middle cerebral artery disease: early diffusion-weighted imaging study.** *Stroke* 2005;36:2583–88 CrossRef Medline
- Hirooka R, Ogasawara K, Inoue T, et al. **Simple assessment of cerebral hemodynamics using single-slab 3D time-of-flight MR angiography in patients with cervical internal carotid artery stenocclusive diseases: comparison with quantitative perfusion single-photon emission CT.** *AJNR Am J Neuroradiol* 2009;30:559–63 CrossRef Medline
- Sakuta K, Saji N, Aoki J, et al. **Decrease of hyperintense vessels on fluid-attenuated inversion recovery predicts good outcome in t-PA patients.** *Cerebrovasc Dis* 2016;41:211–18 CrossRef Medline
- Liu W, Yin Q, Yao L, et al. **Decreased hyperintense vessels on FLAIR images after endovascular recanalization of symptomatic internal carotid artery occlusion.** *Eur J Radiol* 2012;81:1595–600 CrossRef Medline
- Kim SJ, Ha YS, Ryoo S, et al. **Sulcal effacement on fluid attenuation inversion recovery magnetic resonance imaging in hyperacute stroke: association with collateral flow and clinical outcomes.** *Stroke* 2012;43:386–92 CrossRef Medline

Leukoaraiosis May Confound the Interpretation of CT Perfusion in Patients Treated with Mechanical Thrombectomy for Acute Ischemic Stroke

S. Rudilosso, C. Laredo, C. Vivancos, X. Urra, L. Llull, A. Renú, V. Obach, Y. Zhao, J.L. Moreno, A. Lopez-Rueda, S. Amaro, and Á. Chamorro



ABSTRACT

BACKGROUND AND PURPOSE: Leukoaraiosis frequently coexists in patients with acute stroke. We studied whether leukoaraiosis could confound the interpretation of CTP findings in patients treated with mechanical thrombectomy.

MATERIALS AND METHODS: We analyzed 236 patients with stroke treated with mechanical thrombectomy and studied with CTP, of whom 127 (53.8%) achieved complete reperfusion. Periventricular white matter hyperintensities on MR imaging and hypodensities on NCCT were assessed through the Fazekas score. CTP-predicted nonviable tissue was defined as relative CBF <30%, and final infarct volume was quantified in DWI. We estimated mean MTT, CBV, and CBF in the asymptomatic hemisphere. In patients achieving complete reperfusion, we assessed the accuracy of nonviable tissue to predict final infarct volume using the intraclass correlation coefficient across periventricular hyperintensity/hypodensity Fazekas scores and variable relative CBF cutoffs.

RESULTS: MTT was longer (Spearman $\rho = 0.279$, $P < .001$) and CBF was lower ($\rho = -0.263$, $P < .001$) as the periventricular hyperintensity Fazekas score increased, while CBV was similar across groups ($\rho = -0.043$, $P = .513$). In the subgroup of patients achieving complete reperfusion, nonviable tissue–final infarct volume reliability was excellent in patients with periventricular hyperintensity Fazekas score grade 0 (intraclass correlation coefficient, 0.900; 95% CI, 0.805–0.950), fair in patients with periventricular hyperintensity Fazekas scores 1 (intraclass correlation coefficient, 0.569; 95% CI, 0.327–0.741) and 2 (intraclass correlation coefficient, 0.444; 95% CI, 0.165–0.657), and poor in patients with periventricular hyperintensity Fazekas score 3 (intraclass correlation coefficient, 0.310; 95% CI, –0.359–0.769). The most accurate cutoffs were relative CBF <30% for periventricular hyperintensity Fazekas score grades 0 and 1, relative CBF <25% for periventricular hyperintensity Fazekas score 2, and relative CBF <20% for periventricular hyperintensity Fazekas score 3. The reliability analysis according to periventricular hypodensity Fazekas score grades on NCCT was similar to that in follow-up MR imaging.

CONCLUSIONS: In patients with stroke, the presence of leukoaraiosis confounds the interpretation of CTP despite proper adjustment of CBF thresholds.

ABBREVIATIONS: FIV = final infarct volume; ICC = intraclass correlation coefficient; IQR = interquartile range; MT = mechanical thrombectomy; NVT = nonviable tissue; PVH = periventricular hyperintensity/hypodensity Fazekas score; rCBF = relative CBF

The main utility of perfusion images obtained from patients with acute ischemic stroke is the identification and quantifi-

cation of areas of nonviable tissue (NVT) and areas of ischemic penumbra that represent hypoperfused but still salvageable tissue.^{1,2} These focal alterations in patients eligible for acute stroke therapies can be evaluated by dynamic contrast-enhanced CT and MR imaging acquisitions,^{3,4} the former being the most commonly used technique worldwide for the assessment of cerebral perfusion in patients with acute stroke.⁵ However, a great variability

Received March 22, 2019; accepted after revision June 19.

From the Department of Neuroscience (S.R., C.L., X.U., L.L., A.R., V.O., Y.Z., S.A., Á.C.), Comprehensive Stroke Center, Hospital Clinic, University of Barcelona and August Pi i Sunyer Biomedical Research Institute (IDIBAPS), Barcelona, Spain; Neurosurgery Service (C.V.), University Hospital La Paz, Madrid, Spain; Medicine Department (Á.C.), School of Medicine, University of Barcelona, Barcelona, Spain; and Department of Radiology (J.L.M., A.L.-R.), Hospital Clínic, University of Barcelona, Barcelona, Spain.

Salvatore Rudilosso and Carlos Laredo contributed equally to this work.

Salvatore Rudilosso receives funding from Instituto de Salud Carlos III, with a Grant for Health Research (CM18/00116). Carlos Laredo receives funding from Instituto de Salud Carlos III, with a Predoctoral Grant for Health Research (PFIS, FI16/00231). Yashu Zhao received a scholarship from China Scholarship Council. This work was partially developed at the building Centro Esther Koplowitz, Barcelona, Research Centers of Catalonia (CERCA) Programme/Generalitat de Catalunya.

Please address correspondence to Ángel Chamorro and Sergio Amaro, Comprehensive Stroke Center, Department of Neuroscience, Hospital Clínic, Villarroel 170, 08036 Barcelona, Spain; e-mail: achamorro@clinic.ub.es and samaro@clinic.cat; @ictusclinic

Indicates open access to non-subscribers at www.ajnr.org

Indicates article with supplemental on-line tables.

Indicates article with supplemental on-line photo.

<http://dx.doi.org/10.3174/ajnr.A6139>

exists not only in image acquisition and postprocessing techniques but also in intrinsic features of cerebral perfusion.⁶ In fact, in physiologic conditions and in acute focal ischemia, brain perfusion is not the same in all its areas because it depends on the neuronal activity of different regions,^{7,8} where perfusion patterns may be different in patients with similar sites of occlusion and times from stroke onset to imaging acquisition.⁹ This variability in perfusion features may depend mostly on the efficiency of intrinsic compensatory mechanisms such as the collateral blood supply¹⁰ or vasodilation and oxygen extraction at capillary levels.¹¹ Moreover, brain perfusion might also depend on the extent of leukoaraiosis, which is an age-related pathologic process strongly associated with cardiovascular risk factors and stroke.¹² A recent study conducted on a large cohort of patients with acute stroke showed that hypoperfusion in the periventricular areas was related to the grade of leukoaraiosis, but a quantitative analysis was not assessed.¹³

Therefore, leukoaraiosis may be associated with hypoperfusion and may cause an overestimation of the NVT in ischemic stroke, confounding the interpretation of CTP in patients eligible for reperfusion therapy. In this study, we aimed to quantify the cerebral perfusion parameters according to the grade of leukoaraiosis in a cohort of patients with large-vessel stroke treated with mechanical thrombectomy (MT) and to assess the accuracy of the estimation of infarct core based on variable CBF thresholds.

MATERIALS AND METHODS

Patients

This is a retrospective single-center study of 236 patients with large-vessel ischemic stroke in the anterior circulation treated with MT within 3.9 hours (interquartile range [IQR], 2.6–6.0 hours) from stroke onset who had pretreatment multimodal CT imaging and brain MR imaging at follow-up from March 2010 to December 2017 (Fig 1). Reperfusion after MT was quantified with the modified TICI scale.¹⁴

The local Clinical Research Ethics Committee from the Hospital Clínic of Barcelona approved the study protocol (HCB/2019/0077) under the requirements of Spanish legislation in the field of biomedical research, the regulation (European Union) 2016/679 of the European Parliament and of the Council of April 27, 2016 on the protection of persons with regard to the processing of personal data and on the free movement of such data, the standards of Good Clinical Practice, as well as with the Helsinki Declaration of 1975 and 1983. Patient consent was not required due to the retrospective nature of the study design.

Neuroimaging Techniques

Multimodal imaging included, on admission, an NCCT, an angio-CT of the cervical and intracranial arteries, and a CTP. CTP was performed within a median of 166 minutes (IQR, 88–265 minutes) of stroke onset with a Somatom Definition Flash 128-section dual-source CT system (Siemens, Erlangen, Germany) with a 98-mm z-coverage and 31 time points (total acquisition time, 60 seconds); 50 mL of nonionic iodinated contrast was administered intravenously at 5 mL/s using a power injector. CTP imaging parameters were 80 kV(peak), 250 mAs, 1.5-second rotation, and 2-mm thickness. CTP maps were calculated with MIstar (Apollo Medical Imaging Technology, Melbourne, Australia), which uses singular-value decompo-

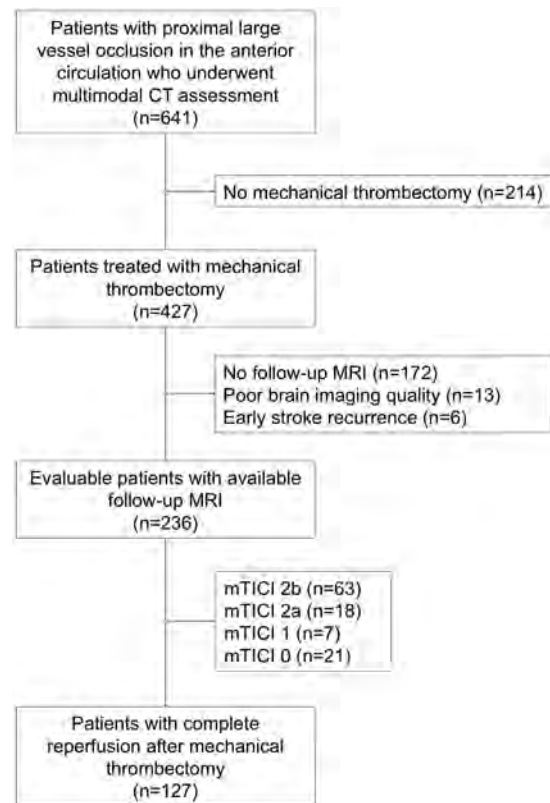


FIG 1. Flow chart of the study cohort.

sition without delay correction and automatically performs motion correction and selects an arterial input function from an unaffected artery and venous output function from a large draining vein. We generated the following perfusion maps: MTT, CBV, and CBF. The NVT was segmented automatically on the CBF maps and defined as a relative threshold of CBF (rCBF) <30% of the unaffected whole contralateral hemisphere.

MR imaging was performed at a median of 31 hours (IQR, 21–62 hours) after multimodal CT on a 1.5T scanner and included a DWI sequence obtained with b-values of 0 and 1000, 5-mm section thickness, and 128 × 128 matrix. FLAIR images were obtained with TR = 9000 ms, TE = 114 ms, FOV = 240 mm, and slice thickness = 5 mm. The final infarct volume (FIV) was calculated with a semiautomatic segmentation of the acute ischemic lesion on DWI sequences using Amira software (www.amira.com) as previously described.¹⁵

Neuroimaging Analysis in the Whole Cohort

Analyzing independently NCCT and FLAIR MR imaging sequences, 1 trained investigator (S.R.) used the Fazekas scale¹⁶ to calculate the extent of leukoaraiosis in the asymptomatic hemisphere only, thus avoiding the confounding effect of acute ischemic lesions. According to the neuroimaging technique, white matter changes were evaluated as periventricular hyperintensities on MR imaging and periventricular hypodensities on NCCT (periventricular hyperintensity/hypodensity Fazekas score [PVH]). In accordance with this scale, grade 0 defined the absence of white matter changes, grade 1 included caps or pencil-thin lining, grade 2 defined a smooth halo, and

Table 1: General clinical and radiologic characteristics of the whole population and in patients with complete reperfusion

	Whole Cohort (n = 236)	mTICI 3 Subgroup (n = 127)
Age (mean) (SD) (yr)	68.7 (14.6)	68.8 (14.2)
Female sex (No.) (%)	116 (49.2)	62 (49.2)
Baseline NIHSS score (median) (IQR)	11 (7–21)	16 (9–20)
Hypertension (No.) (%)	132 (55.9)	68 (53.5)
Diabetes mellitus (No.) (%)	34 (14.4)	21 (16.5)
Atrial fibrillation (No.) (%)	70 (29.7)	37 (29.1)
Previous stroke (No.) (%)	22 (9.3)	11 (8.7)
Time from symptom onset to CTP study (median) (IQR) (min)	167 (88–270)	150 (77–281)
Time from CTP to MRI study (median) (IQR) (hr)	34.9 (22.5–61.3)	30.9 (20.9–62.2)
TOAST (No.) (%) ³³		
Atherosclerotic	35 (14.8)	22 (12.7)
Cardioembolic	120 (50.8)	63 (49.6)
Undetermined	67 (28.4)	36 (28.3)
Infrequent	14 (6)	6 (4.7)
mTICI score (No.) (%)		
0	21 (8.9)	0 (0)
1	7 (3)	0 (0)
2a	18 (7.6)	0 (0)
2b	63 (26.7)	0 (0)
3	127 (53.8)	127 (100)
Collateral status (median) (IQR)	2 (1–3)	2 (2–3)
CBF (median) (IQR) (mL/100 g/min)	2.4 (2.2–2.6)	2.4 (2.2–2.6)
CBV (median) (IQR) (mL/100 g/min)	24.3 (20.5–26.9)	24.3 (20.5–26.5)
MTT (median) (IQR) (sec)	6.0 (5.5–6.5)	6.1 (5.5–6.6)
NVT (median) (IQR) (mL)	19.3 (8.0–34.5)	16.0 (7.4–33.0)
FIV (median) (IQR) (mL)	19.6 (7.4–51.0)	14.0 (3.6–58.4)

Note:—mTICI indicates modified TICI.

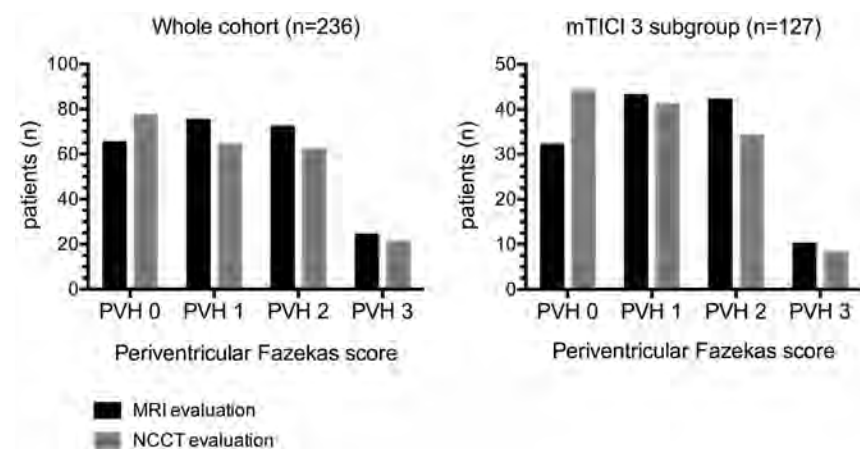


FIG 2. PVHs on MR imaging and noncontrast CT.

grade 3 defined irregular periventricular lesions extending into the deep white matter.

Neuroimaging Analysis in Patients with Complete Reperfusion

The relationship between the grade of leukoaraiosis and the FIV was analyzed only in patients with complete reperfusion after MT (modified TICI 3) to reduce the confounding effect of variable infarct growth in patients with incomplete reperfusion after MT. In this subgroup, we assessed the intraclass correlation coefficient (ICC) and the volumetric bias between the NVT and the FIV according to the PVH on MR imaging and also explored ICC values across

different rCBF thresholds (rCBF <30%, 25%, 20%, and 15%). Then, to assess the usefulness of evaluating the grade of leukoaraiosis on the pretreatment imaging, the same reliability analyses were conducted using the subgroups based on the NCCT-derived PVHs. Finally, to assess the internal validity of the study, we repeated the main imaging analysis in patients with complete reperfusion using a different software package (syngo.via CT Neuro Perfusion VB30; Siemens). We calculated the ICC and the volumetric bias according to the PVH on MR imaging and different rCBF thresholds (rCBF <30% and 20%).

Statistics

Categorical variables were compared using the χ^2 test if suitable, and alternatively using the Fisher exact test. Continuous variables with normal distribution were described by mean and SD, while continuous variables without normal distribution and ordinal variables were described by median and IQR. Means between 2 groups were compared using the Student *t* test, and medians between 2 groups were compared using the Mann-Whitney *U* or Kruskal-Wallis test as appropriate. The agreement between MR imaging and NCCT PVHs was evaluated with a linear-weighted κ statistic. The relationship between the MTT, CBV, and MTT values in the asymptomatic hemisphere with the Fazekas score was evaluated using the Spearman ρ correlation coefficient. The ICC was interpreted as previously described (ICC < 0.4, poor reliability; ICC, 0.4–0.75, from fair-to-good reliability; ICC > 0.75, excellent reliability).¹⁷ Volumetric bias was defined as the difference between the predicted and final infarct (NVT-FIV) across PVH groups. All statistical analyses were performed using

SPSS 23.0 (IBM, Armonk, New York). We considered as statistically significant *P* values < .05, and all hypotheses were 2-sided.

RESULTS

Leukoaraiosis and Hemodynamic Correlates in the Whole Population

The main demographic, clinical, and radiologic features of the whole study cohort (*n* = 236) and of patients with complete reperfusion at the end of MT (*n* = 127) are shown in Table 1. PVHs of the whole cohort evaluated on posttreatment MR imaging and pretreatment NCCT are shown in Fig 2. Overall, the agreement

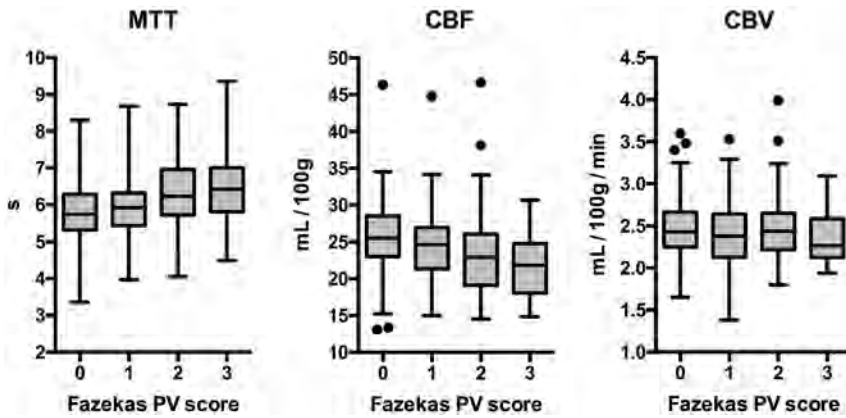


FIG 3. Boxplot analysis of CTP maps in the asymptomatic hemisphere according to the PVH score on MR imaging in the whole population ($N = 236$).

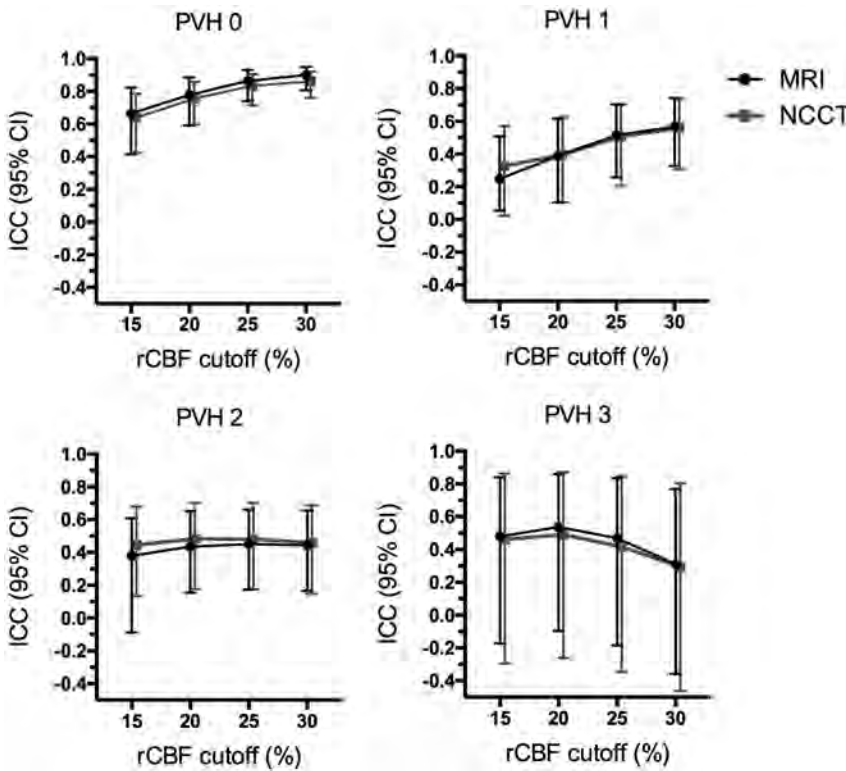


FIG 4. ICC analysis of the predicted final infarct volume on CTP according to different rCBF cutoffs and the grade of leukoaraiosis assessed by the PVH on follow-up MR imaging and on pretreatment NCCT in the subgroup of patients with complete reperfusion after mechanical thrombectomy ($n = 127$). Of note, the agreement in patients without leukoaraiosis was excellent for rCBF $<30\%$ and rCBF $<25\%$ cutoffs and remained good for rCBF $<20\%$ and rCBF $<15\%$. In patients with leukoaraiosis, across increasing PVHs, the overall reliability of CTP decreased and more restrictive thresholds (mostly rCBF $<25\%$ and rCBF $<20\%$) had better agreement than the commonly used rCBF $<30\%$.

between the evaluations on MR imaging and NCCT was good ($\kappa = 0.69$; 95% CI, 0.62–0.76). Higher PVHs were associated with longer MTT (Spearman $\rho = 0.279$, $P < .001$) and lower CBF ($\rho = -0.263$, $P < .001$) but were not correlated with CBV values ($\rho = -0.043$, $P = .513$), as shown in Fig 3 and On-line Table 1. There was no correlation between CBF, CBV, and MTT values in the asymptomatic hemisphere and NVT ($P = .573$, $P = .251$, and $P = .978$, respectively) or FIV ($P = .902$, $P = .207$, and $P = .522$, respectively). NVT was similar in patients with different grades of

reperfusion ($P = .657$), but the FIV was inversely related to TICI subgroups ($\rho = -0.450$, $P < .001$).

CTP Prediction of FIV in Relation to the Extent of Leukoaraiosis in Patients with Complete Reperfusion after MT

In patients with complete reperfusion at the end of MT ($n = 127$), the agreement between NVT and FIV using the rCBF $<30\%$ cutoff was inversely correlated with PVH ($\rho = -0.199$, $P < .001$): ICC was excellent (ICC, 0.900; 95% CI, 0.805–0.950) for patients with PVH 0 graded on MR imaging, remained fair for patients with PVH 1 (ICC, 0.569; 95% CI, 0.327–0.741) and PVH 2 (ICC, 0.444; 95% CI, 0.165–0.657), and was poor for patients with PVH 3 (ICC, 0.310; 95% CI, -0.359–0.769). The analysis of CTP prediction of the FIV based on the NCCT PVH evaluation showed results similar to those of the MR imaging–based analysis as shown in Fig 4 and in On-line Table 2. Median volumetric bias was similar among MR imaging–derived PVH subgroups regardless of the technique used to grade leukoaraiosis (Table 2). Two representative cases illustrating these observations are shown in Fig 5.

A comprehensive threshold-finding analysis across different CTP-derived rCBF cutoffs was implemented to evaluate whether the extent of leukoaraiosis affected the prediction of FIV. In this exploratory analysis, the rCBF $<30\%$ threshold showed the highest ICC between NVT and FIV in patients with PVHs 0 and 1, whereas the rCBF $<25\%$ and rCBF $<20\%$ thresholds had a higher ICC than rCBF $<30\%$ for patients with PVHs 2 and 3, regardless of the neuroimaging technique used for the evaluation of leukoaraiosis (Fig 4). The rCBF $<15\%$ cutoff was less reliable for each grade of leukoaraiosis. The correlation between NVT-FIV ICC and PVH was less strong for rCBF $<25\%$ ($\rho = -0.153$, $P = .002$) and rCBF $<20\%$ ($\rho = -0.129$, $P = .01$) thresholds compared with the rCBF $<30\%$ threshold, while no significant correlation was found for the rCBF 15% threshold ($\rho = -0.074$, $P = .139$). Complete data of this analysis are shown in the On-line Table 2. Of note, the distribution of collateral scores and time to recanalization was not different among PVH categories as shown in On-line Table 3.

In the comparative analysis of different commercial software

Table 2: Baseline traits and volumetric differences among PVH scores on MRI in patients achieving complete reperfusion after mechanical thrombectomy (n = 126)

	PVH 0	PVH 1	PVH 2	PVH 3	P Value
Age (mean) (SD) (yr)	59.0 (16.7)	68.0 (12.2)	76.6 (7.7)	72.9 (15.3)	<.001
Baseline NIHSS score (median) (IQR)	16 (11–19)	16 (11–20)	18 (8–20)	17 (13–21)	.921
Time from symptom onset to CTP study (median) (IQR) (min)	154 (89–233)	168 (92–296)	135 (64–263)	185 (73–385)	.871
CBF (median) (IQR) (mL/100 g/min)	2.4 (2.2–2.7)	2.4 (2.1–2.6)	2.5 (2.2–2.7)	2.4 (2.2–2.8)	.558
CBV (median) (IQR) (mL/100 g/min)	25.4 (22.9–28.1)	23.9 (21.0–26.1)	23.1 (19.4–26.9)	22.6 (18.0–28.0)	.205
MTT (median) (IQR) (sec)	5.7 (5.3–6.3)	6.0 (5.4–6.3)	6.2 (5.8–6.7)	6.4 (6.3–7.1)	.021
Collateral status (median) (IQR)	2 (2–3)	2 (2–3)	2 (2–3)	2 (1–2)	.174
NVT (median) (IQR) (mL)	15.4 (7.3–32.0)	16.0 (7.8–36.3)	15.4 (3.5–31.4)	23.1 (15.1–33.9)	.411
FIV (median) (IQR) (mL)	15.0 (3.5–32.4)	12.8 (5.3–19.8)	14.3 (2.8–40.0)	13.6 (1.3–25.8)	.826
Volumetric bias ^a (median) (IQR) (mL) using Fazekas score on MRI	4.2 (–18.5–9.8)	1.6 (–3.1–16.4)	0.0 (–18.7–16.0)	12.5 (0.9–30.4)	.205
Volumetric bias ^a (median) (IQR) (mL) using Fazekas score on NCCT	2.6 (–12.1–11.6)	2.3 (–3.5–13.2)	0.5 (–18.7–14.5)	11.4 (–1.1–31.4)	.557

^a Volumetric bias was defined as NVT (using the rCBF <30% cutoff)–FIV.

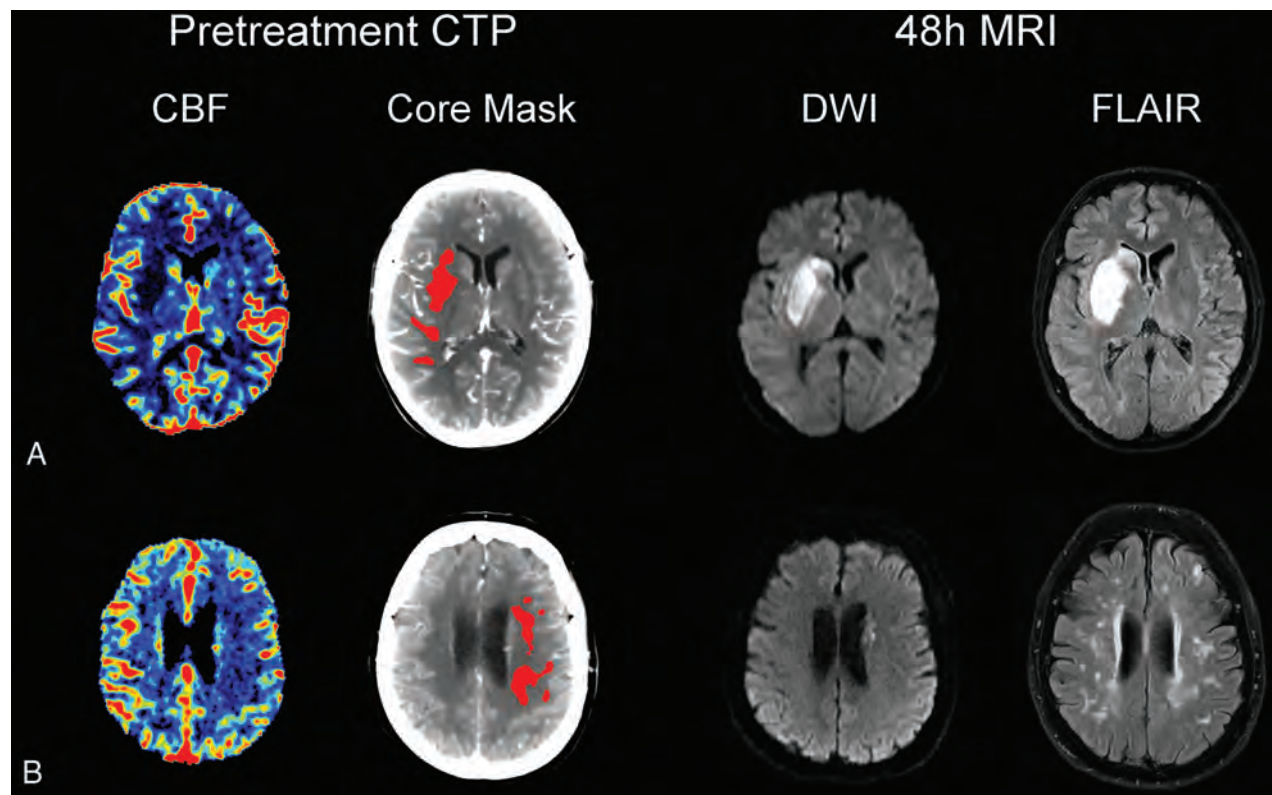


FIG 5. Representative cases of patients with acute ischemic stroke treated with mechanical thrombectomy. A, A 38-year-old patient with low-grade leukoaraiosis (PVH 0). B, A 79-year-old patient with high-grade leukoaraiosis (PVH 3). Both patients had a left middle cerebral artery stroke due to M1 occlusion and had complete reperfusion (modified TIC1 score of 3) after mechanical thrombectomy. The CTP-predicted NVT on CBF was similar to final infarct volume in patient A (NVT = 17.9 mL, FIV = 22.2 mL), while in patient B, CTP-predicted NVT overestimated the FIV (NVT = 11.2 mL, FIV = 0.8 mL).

packages, the agreement of NVT estimation using the rCBF <30% threshold between M1star and syngo.via software was good (ICC, 0.664; 95% CI, 0.469–0.782). A representative example is shown in the On-line Figure. With syngo.via, there was still an inverse correlation with PVHs for both rCBF <30% ($\rho = -0.275$, $P < .001$) and rCBF <20% ($\rho = -0.119$, $P = .018$). The rCBF <20% cutoff showed a higher ICC compared with rCBF <30% in patients with PVH >0 as shown in On-line Table 4.

DISCUSSION

In this study, we investigated whether the presence and severity of leukoaraiosis confounded the interpretation of CTP findings for the prediction of final infarct volume in patients with complete reperfusion following MT. The main result of the study was that

the extent of leukoaraiosis altered the prediction of final infarct volume following MT but was not correlated to overestimation of the final infarct volume. Although the use of more restrictive rCBF thresholds may improve the estimation of tissue viability in patients with a high grade of leukoaraiosis, the accuracy of CTP was reduced in these patients. Finally, the study also found that NCCT was a reliable imaging technique to identify those patients whose extent of leukoaraiosis could compromise the accuracy of CTP interpretation.

The estimation of infarct core by means of a relative CBF threshold lower than 30% (rCBF <30%) is broadly accepted to define NVT in acute stroke.^{18–20} In our study, the reliability of the rCBF <30% threshold decreased in relation to an increased

prominence of leukoaraiosis. Thus, the rCBF <30% threshold was only excellent for the prediction of FIV in patients without leukoaraiosis (PVH 0). Conversely, in patients with mild (PVH 1) and moderate (PVH 2) leukoaraiosis, the application of that threshold had a lower but still fair grade of agreement between CTP-derived NVT and the FIV on follow-up MR imaging, while tissue-viability prediction was only seriously hampered in patients with a severe grade of leukoaraiosis (PVH 3). According to these results, the rCBF <30% cutoff remained the most reliable in patients with PVHs 0 and 1. However, in patients with higher grades of leukoaraiosis, the prediction of tissue viability was only moderate, even after applying more restrictive thresholds (rCBF <25% or rCBF <20% cutoffs). Therefore, the burden of leukoaraiosis did not reflect overestimation of the infarct core despite an insignificant tendency for higher volumetric bias in the PVH 3 subgroup, and the worse FIV prediction might also depend on other factors that may affect hemodynamic measures in patients with small-vessel disease, such as blood-brain barrier permeability derangements,^{21,22} collateral circulation status,²³ and cerebrovascular reactivity.^{24,25}

In agreement with previous studies, the evaluation of periventricular leukoaraiosis on NCCT scans showed a good grade of agreement with the evaluation of the Fazekas scale on MR imaging.^{26,27} Accordingly, our study supports the use of NCCT to quantify the grade of leukoaraiosis and thus to improve the accuracy of the interpretation of CTP maps in potential candidates for endovascular therapy, especially in extended time windows in which the presence of severely hypoperfused areas might preclude the use of reperfusion therapy according to recent randomized clinical trials.²⁸⁻³⁰ Although perfusion imaging adds useful data about tissue viability in stroke assessment, our results highlighted the limitations of CTP in the prediction of final infarct, and support the current stroke guideline indications based on NCCT ASPECTS evaluation for endovascular therapies in the first 6-hour window, while perfusion imaging is required only in extended time windows. Further studies are warranted to assess the role of leukoaraiosis on the accuracy of CTP maps in patients with stroke imaged in late time windows.

The main results of this study were confirmed by using alternative commercial software packages. Despite small differences related to optimal thresholds according to the software used,³¹ the accuracy of final infarct prediction was still inversely related to the grade of leukoaraiosis, and the more restrictive rCBF <20% cutoffs were shown to be more suitable in patients with a high-grade of white matter hyperintensities as well.

This study has some limitations. First, the time from CTP to follow-up MR imaging may affect the accuracy of the FIV prediction due to possible dynamic alterations in the DWI intensity.³² However, our cohort was rather homogeneous because most patients had undergone MR imaging within 48 hours from MT. Second, the low prevalence of patients with PVH 3 in this cohort and the lack of a specific assessment of perfusion parameters in the white matter and the mirror region of the final infarct could have underpowered the analysis of CTP maps. Nevertheless, this cohort study represented faithfully the population eligible for stroke endovascular therapy at our center, and these findings may thus be valid for regular use in clinical practice.

CONCLUSIONS

The extent of leukoaraiosis in patients with acute stroke eligible for MT impairs the accuracy of CTP maps for the prediction of tissue viability, even despite appropriate adjustment of CBF cutoffs. Therefore, the variable prevalence of leukoaraiosis in this clinical setting should be accounted for at the time of the perfusion study evaluation. Further studies assessing the characteristics of white matter hemodynamics in acute stroke are required to provide further insight into the efficacy of reperfusion therapies in patients with this condition.

Disclosures: We thank the support of the Spanish Ministry of Economy and Competitiveness for grant to Sergio Amaro (project PII6/007II funded by Instituto de Salud Carlos III and co-funded by European Regional Development Fund [ERDF]).

REFERENCES

- Donnan GA, Davis SM. **Neuroimaging, the ischaemic penumbra, and selection of patients for acute stroke therapy.** *Lancet Neurol* 2002;1:417–25 CrossRef Medline
- Dani KA, Thomas RG, Chappell FM, et al; Translational Medicine Research Collaboration Multicentre Acute Stroke Imaging Study. **Computed tomography and magnetic resonance perfusion imaging in ischemic stroke: definitions and thresholds.** *Ann Neurol* 2011; 70:384–401 CrossRef Medline
- Etherton MR, Barreto AD, Schwamm LH, et al. **Neuroimaging paradigms to identify patients for reperfusion therapy in stroke of unknown onset.** *Front Neurol* 2018;9:327 CrossRef Medline
- Vilela P, Rowley HA. **Brain ischemia: CT and MRI techniques in acute ischemic stroke.** *Eur J Radiol* 2017;96:162–72 CrossRef Medline
- Donahue J, Wintermark M. **Perfusion CT and acute stroke imaging: foundations, applications, and literature review.** *J Neuroradiol* 2015;42:21–29 CrossRef Medline
- Heit JJ, Wintermark M. **Perfusion computed tomography for the evaluation of acute ischemic stroke: strengths and pitfalls.** *Stroke* 2016;47:1153–58 CrossRef Medline
- Ramli N, Ho K, Nawawi O, et al. **CT perfusion as a useful tool in the evaluation of leuko-araiosis.** *Biomed Imaging Interv J* 2006;2:e16 CrossRef Medline
- Chen C, Bivard A, Lin L, et al. **Thresholds for infarction vary between gray matter and white matter in acute ischemic stroke: a CT perfusion study.** *J Cereb Blood Flow Metab* 2019;39:536–46 CrossRef Medline
- Sakai Y, Delman BN, Fifi JT, et al. **Estimation of ischemic core volume using computed tomographic perfusion.** *Stroke* 2018;49: 2345–52 CrossRef Medline
- Vagal A, Aviv R, Sucharew H, et al. **Collateral clock is more important than time clock for tissue fate.** *Stroke* 2018;49:2102–07 CrossRef Medline
- Østergaard L, Jespersen SN, Mouridsen K, et al. **The role of the cerebral capillaries in acute ischemic stroke: the extended penumbra model.** *J Cereb Blood Flow Metab* 2013;33:635–48 CrossRef Medline
- Higashida RT, Furlan AJ, Roberts H, et al; Technology Assessment Committee of the American Society of Interventional and Therapeutic Neuroradiology, Technology Assessment Committee of the Society of Interventional Radiology. **Trial design and reporting standards for intra-arterial cerebral thrombolysis for acute ischemic stroke.** *Stroke* 2003;34:e109–37 Medline
- Arba F, Mair G, Carpenter T, et al; IST-3 Trial Collaborators. **Cerebral white matter hypoperfusion increases with small-vessel disease burden: data from the Third International Stroke Trial.** *J Stroke Cerebrovasc Dis* 2017;26:1506–13 CrossRef Medline
- Zaidat OO, Lazzaro MA, Liebeskind DS, et al. **Revascularization grading in endovascular acute ischemic stroke therapy.** *Neurology* 2012;79:S110–16 CrossRef Medline
- Rudilosso S, Urra X, San Román L, et al. **Perfusion deficits and mis-**

- match in patients with acute lacunar infarcts studied with whole-brain CT perfusion. *AJNR Am J Neuroradiol* 2015;36:1407–12 CrossRef Medline
16. Fazekas F, Chawluk JB, Alavi A, et al. MR signal abnormalities at 1.5 T in Alzheimer's dementia and normal aging. *AJR Am J Roentgenol* 1987;149:351–56 CrossRef Medline
 17. Rosner B. *Fundamentals of Biostatistics*. 6th ed. Thomson: Brooks/Cole; 2006
 18. Yu Y, Han Q, Ding X, et al. Defining core and penumbra in ischemic stroke: a voxel- and volume-based analysis of whole brain CT perfusion. *Sci Rep* 2016;6:20932 CrossRef Medline
 19. Lin L, Bivard A, Krishnamurthy V, et al. Whole-brain CT perfusion to quantify acute ischemic penumbra and core. *Radiology* 2016;279:876–87 CrossRef Medline
 20. Campbell BC, Christensen S, Levi CR, et al. Cerebral blood flow is the optimal CT perfusion parameter for assessing infarct core. *Stroke* 2011;42:3435–40 CrossRef Medline
 21. Wardlaw JM, Smith C, Dichgans M. Small vessel disease: mechanisms and clinical implications. *Lancet Neurol* 2019;18:684–96 CrossRef Medline
 22. Wardlaw JM, Doubal FN, Valdes-Hernandez M, et al. Blood-brain barrier permeability and long-term clinical and imaging outcomes in cerebral small vessel disease. *Stroke* 2013;44:525–27 CrossRef Medline
 23. Giurgiutiu DV, Yoo AJ, Fitzpatrick K, et al. Severity of leukoaraiosis, leptomeningeal collaterals, and clinical outcomes after intra-arterial therapy in patients with acute ischemic stroke. *J Neurointerv Surg* 2015;7:326–30 CrossRef Medline
 24. Shi Y, Thrippleton MJ, Blair GW, et al. Small vessel disease is associated with altered cerebrovascular pulsatility but not resting cerebral blood flow. *J Cereb Blood Flow Metab* 2018 Oct 8:271678X18803956. [Epub ahead of print] CrossRef Medline
 25. Østergaard L, Engedal TS, Moreton F, et al. Cerebral small vessel disease: capillary pathways to stroke and cognitive decline. *J Cereb Blood Flow Metab* 2016;36:302–25 CrossRef
 26. Rudilosso S, San Román L, Blasco J, et al. Evaluation of white matter hypodensities on computed tomography in stroke patients using the Fazekas score. *Clin Imaging* 2017;46:24–27 CrossRef Medline
 27. Ferguson KJ, Cvoro V, MacLulich AM, et al. Visual rating scales of white matter hyperintensities and atrophy: comparison of computed tomography and magnetic resonance imaging. *J Stroke Cerebrovasc Dis* 2018;27:1815–21 CrossRef Medline
 28. Albers GW, Marks MP, Kemp S, et al; DEFUSE 3 Investigators. Thrombectomy for stroke at 6 to 16 hours with selection by perfusion imaging. *N Engl J Med* 2018;378:708–18 CrossRef Medline
 29. Nogueira RG, Jadhav AP, Haussen DC, et al; DAWN Trial Investigators. Thrombectomy 6 to 24 hours after stroke with a mismatch between deficit and infarct. *N Engl J Med* 2018;378:11–21 CrossRef Medline
 30. Thomalla G, Simonsen CZ, Boutitie F, et al; WAKE-UP Investigators. MRI-guided thrombolysis for stroke with unknown time of onset. *N Engl J Med* 2018;379:611–22 CrossRef Medline
 31. Bathla G, Limaye K, Policeni B, et al. Achieving comparable perfusion results across vendors: the next step in standardizing stroke care: a technical report. *J Neurointerv Surg* 2019 May 22. [Epub ahead of print] CrossRef Medline
 32. Laredo C, Renú A, Tudela R, et al. The accuracy of ischemic core perfusion thresholds varies according to time to recanalization in stroke patients treated with mechanical thrombectomy: a comprehensive whole-brain computed tomography perfusion study. *J Cereb Blood Flow Metab* 2019 Jun 17:271678X19855885. [Epub ahead of print] CrossRef Medline
 33. Adams HP Jr, Bendixen BH, Kappelle LJ, et al. Classification of subtype of acute ischemic stroke. Definitions for use in a multicenter clinical trial. TOAST. Trial of Org 10172 in Acute Stroke Treatment. *Stroke* 1993;24:35–41 CrossRef Medline

One-Stop Management with Perfusion for Transfer Patients with Stroke due to a Large-Vessel Occlusion: Feasibility and Effects on In-Hospital Times

A. Brehm, I. Tsogkas, I.L. Maier, H.J. Eisenberger, P. Yang, J.-M. Liu, J. Liman, and M.-N. Psychogios



ABSTRACT

BACKGROUND AND PURPOSE: In-hospital time delays lead to a relevant deterioration of neurologic outcomes in patients with stroke with large-vessel occlusions. At the moment, CT perfusion is relevant in the triage of late-window patients with stroke. We conducted this study to determine whether one-stop management with perfusion is feasible and leads to a reduction of in-hospital times.

MATERIALS AND METHODS: In this observational study, we report the first 15 consecutive transfer patients with stroke with externally confirmed large-vessel occlusions who underwent flat panel detector CT perfusion and thrombectomy in the same room. Preinterventional imaging consisted of noncontrast flat panel detector CT and flat panel detector CT perfusion, acquired with a biplane angiography system. The flat panel detector CT perfusion was used to reconstruct a flat panel detector CT angiography to confirm the large-vessel occlusions. After confirmation of the large-vessel occlusion, the patient underwent mechanical thrombectomy. We recorded time metrics and safety parameters prospectively and compared them with those of transfer patients whom we treated before the introduction of one-stop management with perfusion.

RESULTS: Fifteen transfer patients underwent flat panel detector CT perfusion and were treated with mechanical thrombectomy from June 2017 to January 2019. The median time from symptom onset to admission was 241 minutes. Median door-to-groin time was 24 minutes. Compared with 23 transfer patients imaged with multidetector CT, it was reduced significantly (24 minutes; 95% CI, 19–37 minutes, versus 53 minutes; 95% CI, 44–66 minutes; $P < .001$). Safety parameters were comparable between groups.

CONCLUSIONS: In this small series, one-stop management with perfusion led to a significant reduction of in-hospital times compared with our previous workflow.

ABBREVIATIONS: FPDCT = flat panel detector CT; ICH = intracranial hemorrhage; IQR = interquartile range; LVO = large-vessel occlusion; MDCT = multidetector CT

After the publication of 5 landmark trials in 2015, thrombectomy became the criterion standard for the treatment of acute ischemic stroke due to a large-vessel occlusion (LVO) in the first 6 hours.¹ Although the treatment effect has been shown to be time-dependent,² door-to-groin times in the most recent studies remained >100 minutes.³ Therefore, we previously described a one-stop management⁴ for patients with acute stroke, which can

reduce door-to-groin times to 20–30 minutes by combining diagnostic work-up and endovascular treatment in 1 room.⁵ One drawback of the previously described setup, especially in patients with a late window,⁶ was that CT perfusion imaging was not available on flat panel detector CT (FPDCT). This made one-stop management for patients in the extended time window, who were often transfer patients, impractical. In this observational study, we report the time metrics and safety parameters of the first 15 consecutive transfer patients who were transported directly to the angiosuite and underwent FPDCT perfusion before their endovascular treatment as part of their diagnostic work-up.

MATERIALS AND METHODS

Patient Selection

This retrospective observational study includes all consecutive adults who were transfer patients and underwent FPDCT perfusion from June 2017 to January 2019. All patients underwent multidetector CT with angiography at the referring center before arrival at our center. In European stroke centers, it is common to

Received April 30, 2019; accepted after revision June 13.

From the Departments of Neuroradiology (A.B., I.T., H.J.E., M.-N.P.) and Neurology (I.L.M., H.J.E., J.L.), University Medical Center Goettingen, Goettingen, Germany; Department of Neurosurgery (P.Y., J.-M.L.), Changhai Hospital, Second Military Medical University, Changhai, China; and Department of Neuroradiology (A.B., I.T., M.-N.P.), Clinic of Radiology and Nuclear Medicine, University Hospital Basel, Basel, Switzerland.

Please address correspondence to Alex Brehm, MD, Department of Neuroradiology, University Medical Center Goettingen, Robert-Koch-Str 40, 37075, Goettingen, Germany; e-mail: Alex.brehm@med.uni-goettingen.de

 Indicates open access to non-subscribers at www.ajnr.org

 Indicates article with supplemental on-line photo.

<http://dx.doi.org/10.3174/ajnr.A6129>

repeat imaging (including CT perfusion) before thrombectomy in patients with an interhospital delay of >60 minutes, to ensure that they still meet the eligibility criteria. As part of our protocol after the introduction of FPDCT perfusion, transfer patients with an interhospital delay of >60 minutes and with a NIHSS score of >7 were triaged directly to the angiosuite. Data were extracted from a prospectively acquired institutional review board–approved data base. As a control group, we used transfer patients treated endovascularly between January 2016 and June 2017, before the introduction of FPDCT perfusion, presenting with an NIHSS score of >7 whom we triaged with multidetector CT (MDCT). In both groups, occupation of the angiosuite during arrival of the patients was an exclusion criterion. One experienced neuroradiologist (I.T. with >5 years of experience) rated FPDCT perfusion and FPDCT angiography regarding overall diagnostic quality, diagnostic quality of the FPDCT perfusion, motion artifacts, LVO detection, and evaluation of collaterals on a 5-point ordinal scale (0 = no diagnostic quality, 1 = poor diagnostic quality, 2 = fair diagnostic quality, 3 = good diagnostic quality, 4 = perfect diagnostic quality). The patient's consent for treatment was obtained according to institutional guidelines. The local ethics committee waived the need for a formal application or a separate consent concerning the inclusion in our observational data base.

Image Acquisition and Processing

All FPDCT/FPDCT perfusion images were acquired using an Artis Q angiography system (Siemens, Erlangen, Germany). First, we performed a noncontrast FPDCT to rule out hemorrhage. A commercially available 20-second rotational acquisition was used (20-second Dyna CT Head, 109 kV, 1.8 μ Gy/frame, 200° angle, 0.4°/frame angulation step, effective dose \sim 2.5 mSv). The raw data were automatically and instantly reconstructed in 5-mm multiplanar reconstructions on a commercially available workstation (syngo X Workplace). Second, we performed the FPDCT perfusion (multisweep FPDCT perfusion with 10 \times 5-second rotations, 77 kV, 0.36 μ Gy/frame, 200° angle, 0.5°/frame angulation step, effective dose \sim 5 mSv). The FPDCT perfusion protocol has been described in detail elsewhere.^{7,8}

Statistical Analysis

We used descriptive statistics to illustrate patient characteristics and time metrics. In case of time intervals, we opted for median and interquartile ranges (IQRs) to describe them in detail. For the comparison of continuous study parameters, the *t* test was used in the case of normal distribution, and the Mann-Whitney test, in the case of a non-normal or ordinal distribution. Categorical variables were compared with the 2 groups by Fischer exact test. The threshold for statistical significance was set at $P < .05$. We performed all analyses with MedCalc for Windows, Version 18, 2018 (MedCalc Software, Mariakerke, Belgium).

RESULTS

We included all 15 (mean age, 78 years; 7 women) transfer patients who underwent FPDCT perfusion after June 2017 in our study. The median NIHSS score at admission was 15, and the native ASPECTS was 8. Of the 15 patients, 7 arrived at our hospital within off-duty hours. The median symptom-to-door time was

Table 1: Baseline characteristics and time metrics of the patients with one-stop and MDCT perfusion^a

	One-Stop Perfusion (n = 15)	MDCT Perfusion (n = 23)	P Value
Baseline characteristics			
Female (No.)	7	9	1
Age (yr)	78 (68–88)	68 (61–78)	.048 ^b
NIHSS_a	15 (12–19)	18 (14–24)	.117
CCT-ASPECTS	8 (8–9)	7 (6–9)	.149
Symptom to door	241 (204–282)	248 (175–327)	.784
Other CT to in-house CT	133 (114–156)	170 (145–327)	.06
Time metrics			
Door to CT	11 (8–25)	15 (11–25)	.129
Door to groin	24 (19–34)	53 (41–69)	<.001 ^b
In-house CT to groin	14 (10–22)	34 (22–43)	<.001 ^b
Door to reperfusion	76 (59–95)	97 (81–122)	.078
Groin to reperfusion	41 (33–76)	54 (29–68)	.578
In-house CT to reperfusion	55 (47–85)	80 (63–106)	.083
Safety parameters			
sICH	1 (6.7%)	2 (8.7%)	1
Mortality	4 (26.7%)	4 (17.4%)	.114
SAH on follow-up scan	1 (6.7%)	3 (13%)	1

Note:—CCT indicates cranial CT; NIHSS_a, admission NIHSS; Other CT to in-house CT, external CT to our CT; sICH, symptomatic intracranial hemorrhage.

^a Data are median and IQR or No. (%).

^b Significant.

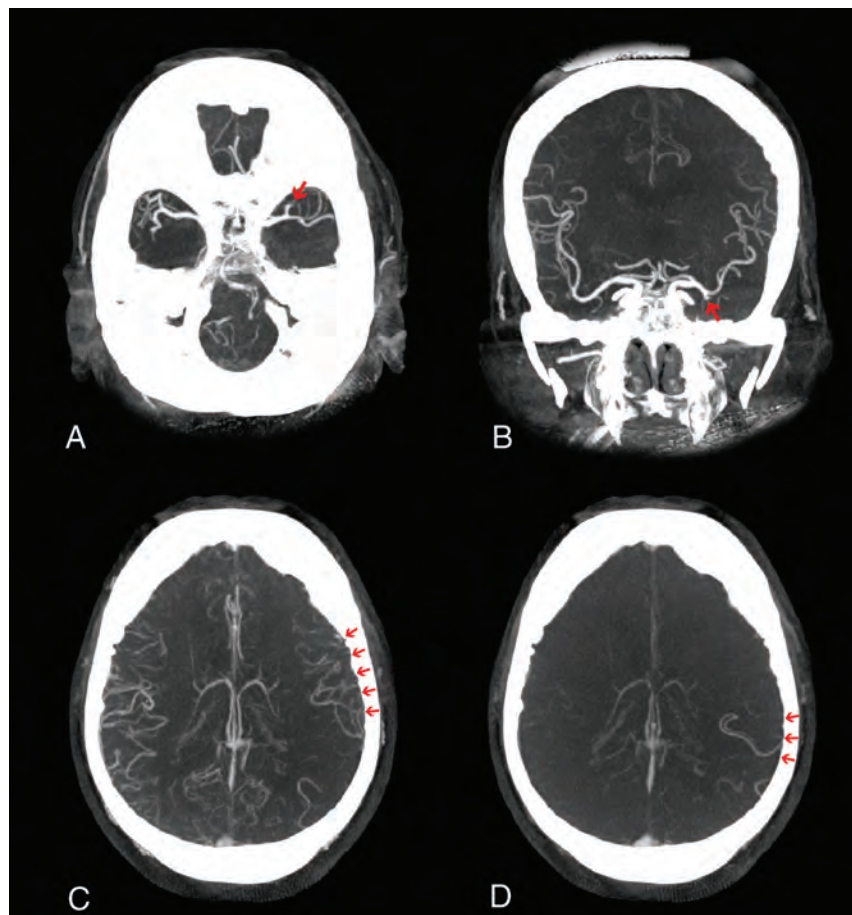
241 minutes (IQR, 204–282 minutes), while the median time from the external CT to our FPDCT was 133 minutes (IQR, 114–156 minutes) (Table 1). The median time between the registration in the hospital information system and the reconstruction of the first FPDCT slices was 11 minutes (IQR, 8–25 minutes). In all 15 cases, we confirmed the external diagnosis of an LVO. In 1 case, we detected an intracranial hemorrhage (ICH), which was not present on the external CT scan (On-line Figure). However, all 15 cases proceeded to endovascular treatment because the ICH was on the hemisphere contralateral to the LVO. We achieved successful reperfusion (defined as a modified TICI \geq 2b) in 11 of 15 cases, with median groin-to-reperfusion and door-to-reperfusion times of 41 minutes (IQR, 33–76 minutes) and 76 minutes (IQR, 59–95 minutes), respectively. Five of the reperfused patients presented with a tandem occlusion. We observed 1 symptomatic ICH and 1 SAH in this group. The mortality rate was 4 of 15 (26.7%).

The control group consisted of 23 transfer patients (mean age, 68 years; 9 women), with a median symptom-to-door time of 248 minutes (IQR, 175–327 minutes) and a median time from the external CT to our MDCT of 170 minutes (IQR, 145–327 minutes). All patients in the control group had an externally confirmed LVO. The median time between registration in the hospital information system and reconstruction of the first MDCT slide was 15 minutes (IQR, 11–25 minutes; $P = .129$) and therefore comparable. All other baseline parameters, excluding age, which was significantly higher in the one-stop management group (78 years; IQR, 68–88 years, versus 68 years; IQR, 61–78 years; $P = .048$), were comparable between groups.

In the one-stop management with perfusion group, 80% were treated with the Stent retriever Assisted Vacuum-locked Extraction⁹ (SAVE) technique (a primary combined approach of a stent retriever and an aspiration catheter), while the remaining 20% were treated with A Direct Aspiration first Pass Technique (ADAPT) as a first-pass strategy. In the control group, 65.2% were treated with SAVE, while

Table 2: Subjective evaluation of the quality of the FPDCT angiography and perfusion

Variable	No Diagnostic Quality/Severe	Poor Diagnostic Quality/Substantial	Fair Diagnostic Quality/Tolerable	Good Diagnostic Quality/Negligible	Perfect Diagnostic Quality/None
FPDCT angiography/perfusion overall	0	1	3	7	4
Detection of LVO	0	0	3	5	7
Evaluation of collaterals	0	0	4	5	6
FPDCT perfusion	1	1	3	6	4
Motion artifacts	1	2	4	5	3

**FIG 1.** FPDCT angiography for the identification of an LVO on a transversal FPDCT angiogram (A), a coronal FPDCT angiogram (B), and early-phase (C) and late-phase (D) collaterals.

the remaining 34.8% were treated with A Direct Aspiration first Pass Technique (ADAPT) as a first-pass strategy. There was no statistically significant difference between groups ($P = .333$). Of the control group, 52.2% received general anesthesia, while 46.7% of the one-stop management with perfusion group received general anesthesia ($P = 1.0$).

We were able to significantly reduce median door-to-groin times from 53 minutes (IQR, 41–69 minutes) in the MDCT group to 24 minutes (IQR, 19–34 minutes) in the one-stop management group ($P < .001$). In-house median CT-to-groin times were significantly reduced as well from 34 minutes (IQR, 22–43 minutes) to 14 minutes (IQR, 10–22 minutes) ($P < .001$). The impact on door-to-reperfusion times was also relevant; however, it was not statistically significant (76 minutes; IQR, 59–95 minutes, versus 97 minutes; IQR, 81–122 minutes; $P = .078$).

The frequencies of symptomatic ICH (6.7% versus 8.7%; $P = 1$), SAH observed on a follow-up scan (6.7% versus 13%; $P = 1$),

and mortality (26.7% versus 17.4%; $P = .114$) did not differ significantly between groups.

The diagnostic quality was sufficient for the delineation of the LVO and the evaluation of collaterals in all cases (Table 2). In 11 of 15 cases (73.3%), the overall diagnostic quality was at least good, while it was fair in 3 cases (20%) and poor in 1 case (7.7%), due to heavy motion artifacts. One of 15 FPDCT perfusions was not of diagnostic quality due to heavy motion artifacts.

DISCUSSION

In this small, observational study, one-stop management with perfusion for transfer patients with a confirmed LVO was safe and significantly shortened door-to-groin times compared with transfer patients imaged with an MDCT perfusion protocol. The reported door-to-groin times are comparable to the door-to-groin times, which we achieved with our original one-stop management with a biphasic FPDCT angiography protocol (20.5 minutes; 95% CI, 17–26 minutes).⁵ Acquisition and reconstruction of the FPDCT perfusion did not result in a relevant time loss. Besides, they are well below those times in recent randomized controlled trials

with median door-to-groin times of >60 minutes, even for transfer patients.^{2,3,10} The reduction of door-to-reperfusion times was relevant, but not statistically significant ($P = .078$). However, this has to be attributed to the small sample size and the high prevalence of carotid-terminus and tandem occlusion in this small sample. This argument is strengthened because imaging-to-reperfusion times were shorter as well with 55 minutes compared with 80 minutes ($P = .083$), which is well below the <90 minutes suggested by Goyal et al.¹¹ According to Guenego et al,¹² the main subgroup of transfer patients in which repeat perfusion imaging is necessary are those with fast-progressing strokes because they might miss the eligible criteria after transfer to the comprehensive stroke center. Saving 30 minutes of in-hospital time in this cohort of patients might result in significantly better clinical outcomes, strengthening the argument for a direct transfer to the angi suite for diagnostic work-up and mechanical thrombectomy.

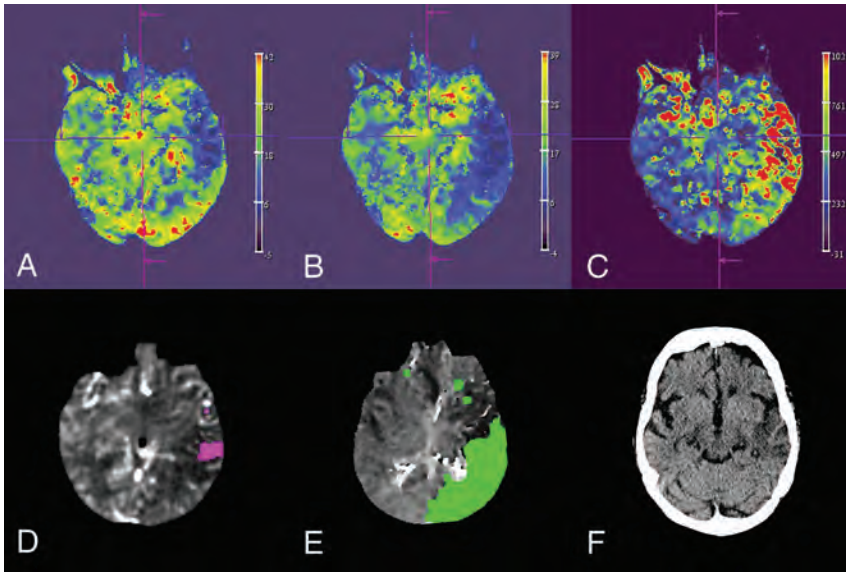


FIG 2. Reconstruction of the CBV (A), CBF (B), and MTT (C) map by the syngo X Workplace (Siemens). Visualization of the 10-mL infarct core (D), the 225-mL mismatch volume (E) by the RAPID ANGIO software solution, and the final infarction on a follow-up CT scan 2 days after the thrombectomy (F).

Regarding the differentiation between ischemic and hemorrhagic stroke, which is particularly important in “mothership” (direct admission) patients, previous work from our group showed that FPDCT detects ICH with a high sensitivity and specificity, comparable with MDCT.¹³ Furthermore the FPDCT perfusion dataset can be used to reconstruct FPDCT angiography as was pointed out by Yang et al¹⁴ in a prior publication. In our sample, the quality of the reconstructed FPDCT angiography was sufficient to delineate the LVO in all cases and evaluate collaterals (Fig 1 and Table 2). This confirms prior results of other work groups who used it successfully for evaluating collaterals and the clot-burden score.^{15,16} Collaterals can be used as an additional tool for patient selection as pointed out by Schregel et al,¹⁷ who compared the prognostic value of CBV-ASPECTS and collaterals. Although the time resolution of the FPDCT perfusion is 5 seconds lower than the time resolution of the MDCT Perfusion (1.5 seconds), motion artifacts were not a serious issue in our small cohort. Overall the diagnostic quality of the reconstructed FPDCT perfusion (Fig 2) was sufficient in 14 of 15 cases (93.3%). Furthermore, the next generation of FPDCT is reported to have faster acquisition times, which might improve the time resolution of the FPDCT perfusion protocol. Regarding automated evaluation of FPDCT perfusion, the RAPID ANGIO software solution (iSchemaView, Inc) was presented recently (Fig 2),¹⁸ providing swift and automated calculation of infarct core and mismatch. The reliability and accuracy of RAPID ANGIO for the exact depiction of core and penumbra are the subject of running studies. The effective dosage of the FPDCT perfusion protocol is comparable with the effective dosage of an MDCT perfusion protocol.^{19,20}

Another interesting aspect of our approach is that FPDCT angiography can be projected into the angiosuite, giving the treating physician important information about the vessel architecture, which can be particularly helpful in case of an occlusion of the terminus of the internal carotid artery because the down-

stream vessel architecture cannot be visualized with DSA. Even in case of an M1 occlusion, information about the downstream vessel architecture can be helpful to navigate the stent retriever into the more prominent truncus, which might improve angiographic outcomes.²¹

The primary limitations of our study are the observational design, which is prone to selection bias, and the small number of reported patients.

“Time is brain” is the mantra that was propagated by Saver et al,² who showed a tight correlation between door-to-reperfusion times and outcome. Even in our setting with the MDCT scanner only 20 meters away from the angiosuite, we were able to significantly reduce door-to-groin times compared with traditionally triaged patients, despite the fact that we had optimized the MDCT route with standardization and weekly training before introduction of the one-stop manage-

ment.²² Effects on door-to-groin times should be even more profound in other hospital settings, where the MDCT scanner is far away from the angiosuite or even located in another building. However, a prospective study is warranted to confirm the observed differences in a larger cohort and examine its effect on outcome. Furthermore, the equivalence of FPDCT and MDCT perfusion is still a topic of ongoing investigation.

CONCLUSIONS

One-stop management with perfusion for transfer patients with a confirmed LVO in a modern angiosuite is feasible and safe and leads to a significant reduction of door-to-groin times.

Disclosures: Alex Brehm—UNRELATED: Grant: research agreement with Siemens.* Hanna J. Eisenberger—OTHER RELATIONSHIPS: member of the Deutsche Gesellschaft für Neurologie. Jan Liman—UNRELATED: Expert Testimony: Pfizer; Payment for Lectures Including Service on Speakers Bureaus: Stryker, Bristol-Myers Squibb; Pfizer; Travel/Accommodations/Meeting Expenses Unrelated to Activities Listed: Bayer HealthCare Pharmaceuticals, Daiichi Sankyo. Marios-Nikos Psychogios—UNRELATED: Grant: Siemens, Comments: research grant with the Department of Neuro-radiology*; Consulting Fee or Honorarium: Siemens. *Money paid to the institution.

REFERENCES

- Goyal M, Menon BK, Van Zwam WH, et al; HERMES collaborators. Endovascular thrombectomy after large-vessel ischaemic stroke: a meta-analysis of individual patient data from five randomised trials. *Lancet* 2016;387:1723–31 CrossRef Medline
- Saver JL, Goyal M, Van Der Lugt A, et al; HERMES collaborators. Time to treatment with endovascular thrombectomy and outcomes from ischemic stroke: a meta-analysis. *JAMA* 2016;316:1279–88 CrossRef Medline
- Nogueira RG, Frei D, Kirmani JF, et al; Penumbra Separator 3D Investigators. Safety and efficacy of a 3-dimensional stent retriever with aspiration-based thrombectomy vs aspiration-based thrombectomy alone in acute ischemic stroke intervention: a randomized clinical trial. *JAMA Neurol* 2018;75:304–311 CrossRef Medline
- Psychogios MN, Bähr M, Liman J, et al. One stop management in acute

- stroke: first mothership patient transported directly to the angiography suite. *Clin Neuroradiol* 2017;27:389–91 CrossRef Medline
5. Psychogios MN, Behme D, Schregel K, et al. **One-stop management of acute stroke patients: minimizing door-to-reperfusion times.** *Stroke* 2017;48:3152–55 CrossRef Medline
 6. Nogueira RG, Jadhav AP, Haussen DC, et al; DAWN Trial Investigators. **Thrombectomy 6 to 24 hours after stroke with a mismatch between deficit and infarct.** *N Engl J Med* 2017;378:11–21 CrossRef Medline
 7. Struffert T, Deurling-Zheng Y, Kloska S, et al. **Dynamic angiography and perfusion imaging using flat detector CT in the angiography suite: a pilot study in patients with acute middle cerebral artery occlusions.** *AJNR Am J Neuroradiol* 2015;36:1964–70 CrossRef Medline
 8. Garcia M, Okell TW, Gloor M, et al. **Feasibility of flat panel detector CT in perfusion assessment of brain arteriovenous malformations: initial clinical experience.** *AJNR Am J Neuroradiol* 2017;38:735–39 CrossRef Medline
 9. Maus V, Behme D, Kabbasch C, et al. **Maximizing first-pass complete reperfusion with SAVE.** *Clin Neuroradiol* 2018;28:327–38 CrossRef Medline
 10. Lapergue B, Blanc R, Gory B, et al; ASTER Trial Investigators. **Effect of endovascular contact aspiration vs stent retriever on revascularization in patients with acute ischemic stroke and large vessel occlusion: the ASTER randomized clinical trial.** *JAMA* 2017;318:443–52 CrossRef Medline
 11. Goyal M, Menon BK, Hill MD, et al. **Consistently achieving computed tomography to endovascular recanalization <90 minutes: solutions and innovations.** *Stroke* 2014;45:e252–56 CrossRef Medline
 12. Guenego A, Mlynash M, Christensen S, et al. **Hypoperfusion ratio predicts infarct growth during transfer for thrombectomy.** *Ann Neurol* 2018;84:616–20 CrossRef Medline
 13. Leyhe JR, Tsogkas I, Hesse AC, et al. **Latest generation of flat detector CT as a peri-interventional diagnostic tool: a comparative study with multidetector CT.** *J Neurointerv Surg* 2017;9:1253–57 CrossRef Medline
 14. Yang P, Niu K, Wu Y, et al. **Time-resolved C-arm computed tomographic angiography derived from computed tomographic perfusion acquisition: new capability for one-stop-shop acute ischemic stroke treatment in the angiosuite.** *Stroke* 2015;46:3383–89 CrossRef Medline
 15. Hoelter P, Goelitz P, Lang S, et al. **Visualization of large vessel occlusion, clot extent, and collateral supply using volume perfusion flat detector computed tomography in acute stroke patients.** *Acta Radiol* 2019 Mar 12:284185119836220. [Epub ahead of print] CrossRef Medline
 16. Yang P, Niu K, Wu Y, et al. **Evaluation of collaterals and clot burden using time-resolved C-arm conebeam CT angiography in the angiography suite: a feasibility study.** *AJNR Am J Neuroradiol* 2017;38:747–52 CrossRef Medline
 17. Schregel K, Tsogkas I, Peter C, et al. **Outcome prediction using perfusion parameters and collateral scores of multi-phase and single-phase CT angiography in acute stroke: need for one, two, three, or thirty scans?** *J Stroke* 2018;20:362–72 CrossRef Medline
 18. Evers P. iSchemaView Launches RAPID™ ANGIO. *BusinessWire*. <https://www.businesswire.com/news/home/20190228005091/en/iSchemaView-Launches-RAPID%E2%84%A2-ANGIO>. Accessed April 2, 2019
 19. Psychogios M, Schramm P, Frölich AM, et al. **Alberta Stroke Program Early CT Scale evaluation of multimodal computed tomography in predicting clinical outcomes of stroke patients treated with aspiration thrombectomy.** *Stroke* 2013;44:2188–93 CrossRef Medline
 20. Struffert T, Hauer M, Banckwitz R, et al. **Effective dose to patient measurements in flat-detector and multislice computed tomography: a comparison of applications in neuroradiology.** *Eur Radiol* 2014;24:1257–65 CrossRef Medline
 21. Maus V, Brehm A, Tsogkas I, et al. **Stent retriever placement in embolectomy: the choice of the post-bifurcational trunk influences the first-pass reperfusion result in M1 occlusions.** *J Neurointerv Surg* 2019;11:237–40 CrossRef Medline
 22. Schregel K, Behme D, Tsogkas I, et al. **Optimized management of Endovascular Treatment for Acute Ischemic Stroke.** *J Vis Exp* 2018; 131:56397 Medline

A Standardized Aspiration-First Approach for Thrombectomy to Increase Speed and Improve Recanalization Rates

¹D. O'Neill, ²E. Griffin, ³K.M. Doyle, ⁴S. Power, ⁵P. Brennan, ⁶M. Sheehan, ⁷A. O'Hare, ⁸S. Looby, ⁹A.M. da Silva Santos, ¹⁰R. Rossi, and ¹¹J. Thornton

ABSTRACT

BACKGROUND AND PURPOSE: Direct aspiration is a recognized technique for revascularization in large-vessel ischemic strokes. There is ongoing debate regarding its efficacy compared with stent retrievers. Every delay in achieving revascularization and a decrease in reperfusion rates reduces the likelihood of patients achieving functional independence. We propose a standardized setup technique for aspiration-first for all anterior circulation thrombectomy procedures for increasing speed and recanalization rates.

MATERIALS AND METHODS: We analyzed 127 consecutive patients treated by a standardized approach to thrombectomy with an intention to perform aspiration-first compared with 127 consecutive patients treated with a stent retriever-first approach. Key time metrics evaluated included groin to first angiogram, first angiogram to reperfusion, groin to first reperfusion, and length of the procedure. The degree of successful recanalization (TICI 2b–3) and the number of passes were compared between the 2 groups.

RESULTS: In 127 patients who underwent the standardized technique, the median time from groin puncture to first reperfusion was 18 minutes compared with 26 minutes ($P < .001$). The duration of the procedure was shorter compared with the stent retriever group (26 minutes in the aspiration first group versus 47 minutes, $P < .001$) and required fewer passes (mean, 2.4 versus 3.1; $P < .05$). A higher proportion of patients had a TICI score of 2b–3 in the aspiration-first group compared with stent retriever group (96.1% versus 85.8%, $P < .005$).

CONCLUSIONS: Our study highlights the increasing speed and recanalization rates achieved with fewer passes in a standardized approach to thrombectomy with an intention to attempt aspiration-first. Any attempt to reduce revascularization time and increase successful recanalization should be used.

ABBREVIATIONS: ADAPT = A Direct Aspiration First Pass Technique; ENT = emboli to a new territory; IQR = interquartile range; RCT = randomized controlled trial

Every incremental delay in achieving vessel recanalization in patients with large-vessel ischemic stroke results in a reduced likelihood of achieving an independent functional outcome following thrombectomy.¹ Thrombectomy is the standard of care in acute ischemic stroke with large-vessel occlusion in selected patients presenting up to 24 hours after the onset of symptoms.² Most trials have primarily used second-generation stent retriever devices.³ However, aspiration techniques have also been described and demonstrated to be successful but appear to be less widespread in their use.^{4–6} The COMPASS Trial: A Direct Aspiration First Pass Technique (COMPASS) has shown noninferiority of direct aspiration compared with a primary stent retriever.⁷ The

likelihood of good clinical outcome depends on the speed and completeness of the recanalization achieved. We propose a technique that can be used as a standardized approach for all thrombectomy procedures, resulting in faster groin-to-recanalization times with an increased rate of successful recanalization and fewer passes than previously published.

MATERIALS AND METHODS

We maintain a prospective data base for ongoing audit and quality improvement with detailed analysis of all thrombectomy procedures in our institution in Beaumont Hospital. This is under the remit of ongoing service audit and is therefore excluded from the requirement for ethics approval. The ongoing audit of our service is registered with the Institutional Quality and Standards Department. Time metrics of each step in the process are gathered. We provide a 24-hour thrombectomy service for patients presenting to our comprehensive stroke center. We also accept referrals from 24 hospitals within the Republic of Ireland, using a drip and ship model and commonly also using a drip, ship, retrieve, and leave

Received February 25, 2019; accepted after revision May 31.

From the Interventional Neuroradiology Service (D.O., E.G., S.P., P.B., M.S., A.O., S.L., J.T.), Department of Radiology, Beaumont Hospital, Dublin, Ireland; Royal College of Surgeons (E.G., J.T.), Dublin, Ireland; and Department of Physiology (K.M.D., A.M.d.S.S., R.R.), School of Medicine, National University of Ireland, Galway, Ireland.

Please address correspondence to Emma Griffin, FAO, Department of Radiology, Beaumont Hospital, Dublin 9, Ireland; e-mail: emma.griffin.2@ucdconnect.ie

<http://dx.doi.org/10.3174/ajnr.A6117>

model with immediate repatriation to the hospital within a <1.5-hour transport distance. This model has previously been described in the literature.⁸ We perform endovascular thrombectomy in the anterior circulation with large-vessel occlusion within 24 hours of onset of symptoms, with ASPECTS of >5 and good (>50%) collateral circulation on triple-phase CTA.

Most patients come from outside institutions with stroke imaging work-up performed at the primary center. On arrival, they proceed directly to the Interventional Radiology suite or for a repeat CT in the same department if >2 hours have passed or if there has been clinical improvement or deterioration. For the cohort of patients in this study, CT perfusion was infrequently performed; however, the use of CTP is increasing in our department. Four interventional neuroradiologists perform the thrombectomy procedures. Three of our team have recently moved to a standardized approach to thrombectomy.

The standardized aspiration-first approach is as follows: An 8F short sheath is introduced to the common femoral artery with local anesthesia infiltrated in the overlying skin. Most patients are awake for the procedure. Conscious sedation and general anesthesia are infrequently used except in particularly agitated or unstable patients. A 6F Weinberg catheter (Balt Extrusion, Montmorency, France) inside an 8F MACH 1 Guide Catheter (Boston Scientific, Natick, Massachusetts) is advanced to the aortic arch with a 0.035-inch Glidewire (Terumo, Tokyo, Japan), and the relevant large vessel of the neck is catheterized. The 6–8F combination is then advanced in to the internal carotid artery with the 8F guide advanced over the 6F catheter for final tip placement in the proximal-to-mid-internal carotid artery. If there is a stenosis or occlusion of the ICA, an attempt is made to cross this first without angioplasty or stent placement. The wire and 6F Weinberg catheter are removed. Angiography confirms the site of vessel occlusion. Continuous heparinized saline flush is attached to the catheter through a pressure pump.

A 6F Sofia Plus 0.070-inch catheter (MicroVention, Tustin, California) is advanced through a rotating hemostatic Y-valve attached to a heparinized saline flush into the 8F guide catheter. A 20-mL syringe partially filled with saline is attached to the hub of the catheter, allowing back flow of blood in the absence of a wire within the catheter. Once the Sofia Plus catheter extends beyond the tip of the 8F guide catheter, the 20-mL syringe is switched, following aspiration of any blood, for a 10-mL contrast-filled syringe. Contrast is trickled forward as the Sofia Plus catheter advances. The Sofia Plus may be advanced through the distal internal carotid artery in this manner, with the operator being careful to avoid pushing against resistance. It is usually possible to push this catheter to the proximal end of the thrombus in the ICA or M1 segment. An inability to aspirate blood backwards through the Sofia Plus indicates engagement with the thrombus. A 50-mL Luer Lock lockable syringe is then attached to the catheter, and fixed suction is applied for approximately 30 seconds. It is usually necessary to withdraw the catheter a little into the proximal M1 or distal ICA, dislodging the thrombus before the thrombus is aspirated into the catheter and syringe and rapid back flow is obtained. Infrequently, back flow is not obtained, and the catheter has to be removed completely, usually due to thrombus at the tip of the catheter, and continuous aspiration is applied with the sy-

ringe, which is locked on suction. This appears more likely to happen with a “white clot.” Angiography will determine whether further aspiration is required or suitable.

Alternative steps are the following:

1) If the catheter will not advance distally in the internal carotid artery, a support wire may be used such as a 0.035-inch Glidewire, which is not advanced beyond the tip of the aspiration catheter.

2) If the aspiration catheter catches in the ophthalmic artery, which is a quite common occurrence, a 0.021- or 0.0027-inch microcatheter over a 0.014-inch wire may be advanced through the Sofia Plus into the distal ICA or MCA. This may be enough to allow the Sofia Plus to pass the ophthalmic artery. The inner microcatheter and wire may then be removed to allow the standard aspiration-first technique as described above.

3) If the Sofia catheter still does not go as far as the thrombus, the microcatheter-wire combination should be advanced beyond the thrombus as per standard stent retriever technique. Once beyond the thrombus, if the Sofia Plus has still not advanced, the stent retriever of choice may be deployed. Retrieval of the stent retriever to remove the clot usually allows advancement of the Sofia Plus catheter beyond the ophthalmic artery into the proximal end of the thrombus.⁹ The stent retriever may be retrieved entirely into the Sofia Plus catheter and removed. Ideally, the Sofia Plus catheter is maintained beyond the ophthalmic artery or in the M1 segment to avoid clot migration into anterior cerebral artery during clot extraction. Angiography determines whether there is a residual clot and whether it is suitable for aspiration now that the Sofia Plus catheter is beyond the ophthalmic artery. Alternatively, for smaller thrombi beyond the MCA bifurcation, further stent retrieval will be performed.

4) If necessary, the Sofia Plus catheter is also removed, capturing the thrombus between the stent and aspiration catheter. If angiography demonstrates a need for further thrombectomy, the process is repeated from the start.

5) Although we switched to intention to treat by aspiration-first, there had been no previous published benefit of aspiration over stent retriever. We therefore did not delay clot removal. If those steps did not work, we progressed quickly without delay to a stent retriever.

Before switching to this standardized approach, our regular approach consisted of using the same 6–8F access combination, an intermediate catheter in the distal ICA, crossing the occlusion with a microcatheter, and using a stent retriever. In general, we did not use balloon-guide catheters but rather used distal aspiration during clot retrieval through the intermediate catheter, which may have migrated into the M1 segment. There was some variation case to case of this nonstandardized approach.

Having switched to the standardized technique, we reviewed time metrics and recanalization rates to evaluate this approach. A consecutive cohort of thrombectomy procedures from our prospectively maintained stroke data base was analyzed. These were consecutive patients from 3 separate operators who have adopted this aspiration-first technique. Patients with any occlusion in the intracranial ICA and MCA M1 and M2 who were deemed suitable for thrombectomy were included, even if aspiration-first was not possible or unlikely (eg, due to M2 occlusion or tandem cervical

Table 1: Baseline characteristics

Variable/Sts	All (n = 254)	Aspiration (n = 127)	Stent Retriever (n = 127)	P Value
Age				
Mean	69.1 ± 15.6	70.4 ± 14.8	67.9 ± 16.4	.275
Median (IQR 25%–75%)	73.0 (62–80)	74.0 (63–80)	71.0 (58–79)	
NIHSS score				
Mean	15.7 ± 6.3	15.6 ± 6.7	15.7 ± 5.9	.844
Median (IQR 25%–75%)	16.0 (1–20)	15.0 (10–20)	16.0 (12–20)	
Thrombolysis (No.) (%)	132 (52.2%)	64 (50.4%)	68 (53.5%)	.662
Occlusion location (No.) (%)				
MCA, M1	176 (69%)	93 (73%)	83 (65%)	.292
MCA, M2	32 (12.6%)	12 (9%)	20 (15.7%)	
ICA, T/L	46 (18%)	22 (17%)	24 (18.8%)	
mRS 0–2 at 90 days (No.) (%)	121 (48%)	63 (50%)	58 (46%)	.53

Note:—Sts indicates statistics; T/L, carotid terminus.

ICA occlusions). The concept is to see the effect of this standardized approach in all patients. As a control, we included consecutive patients who underwent nonstandardized primary stent retrieval by the same operators during a similar time period before commencing this technique. We also analyzed specifically those cases when the aspiration technique was, in fact, the first technique used. Posterior circulation occlusions were excluded from the study. For evaluation of the success of revascularization, original TICI scores were re-evaluated by an independent neuroradiologist. If there was a disagreement from the original assessment, a third reviewer evaluated the angiograms to determine a final TICI score. We used the modified TICI score including 2c.

We compared 4 time parameters between our standardized technique and the stent retriever technique: 1) groin puncture to first angiogram, 2) groin puncture to first reperfusion, 3) time from first angiogram to first reperfusion, and 4) the duration of the procedure.

Time from groin puncture to first angiogram was used as a metric of ease/difficulty to attain a position in the ICA. This part of the procedure is unchanged from our prior technique. Time from first angiogram to first reperfusion was used to compare the speed of the techniques with achieving reperfusion, excluding any variation in difficulty in accessing the carotid artery. The overall duration of the procedure, from groin puncture to completion angiogram, was used as a metric of success of the techniques; those procedures with longer times were likely to be the more challenging cases, requiring multiple aspirations and/or multiple passes of stent retrievers. Sometimes with stent retrievers, flow is restored before pulling the stent but may be lost again, requiring further passes. This may give a false impression of the time to meaningful recanalization, which does not typically happen with aspiration.

SPSS-24 (IBM, Armonk, New York) was used for statistical analysis. Quantitative variables did not follow a standard normal distribution, as indicated by the Kolmogorov-Smirnov and Shapiro-Wilk tests. The nonparametric Mann-Whitney *U* or Kruskal-Wallis test was used to test the null hypothesis followed by the Dunn multiple comparison test to test the difference between groups. A level of significance for all analyses was $P < .05$.

RESULTS

A total of 127 consecutive patients with intracranial anterior circulation vessel occlusion underwent thrombectomy by a standardized aspiration-first technique from September 2017 to Sep-

tember 2018. This group was compared with 127 consecutive patients having undergone thrombectomies performed between April 2016 and May 2017, who were primarily treated with the stent retriever method. The baseline demographics, NIHSS score, those undergoing thrombolysis, and the TICI score are evaluated in Table 1. There was no significant difference in age, NIHSS score, and those undergoing thrombolysis between the 2 groups. In terms of vessel occlusion, there were more M2 occlusions in the stent retriever cohort; however, this was not statistically significant.

The aspiration-first technique had a median length from groin puncture to first angiogram of 6 minutes (interquartile range [IQR], 4–10 minutes) versus 5 minutes (IQR, 4–9 minutes) in the stent retriever group ($P = .234$). The aspiration-first technique had a shorter median time from the first angiogram to first reperfusion of 11 minutes (IQR, 7–20 minutes) versus 19 minutes 30 seconds (IQR, 12–32 minutes) in the stent retriever group ($P < .001$) and a shorter time from groin puncture to first reperfusion compared with the stent retriever group in the intention-to-treat group (18 versus 26 minutes, $P < .001$). The aspiration-first technique had a shorter overall procedural duration of 26 minutes (IQR, 15–41 minutes) versus 47 minutes (IQR, 32–80 minutes) in the stent retriever group ($P < .001$).

The aspiration-first technique necessitated fewer passes (mean, 2.4 versus 3.1; $P < .05$), which aided in the shorter procedural duration (Figure). Successful recanalization (TICI 2b–3) was observed in 90.9% of patients overall; 96.1% had successful recanalization (TICI 2b–3) in the aspiration-first group compared with 85.8% in the stent retriever group ($P < .005$). A higher proportion of patients had a TICI score of 2c–3 in the aspiration-first group compared with stent retriever group (78% versus 60.6%, $P < .005$). A TICI 3 result was achieved in 46% ($n = 59$) of the aspiration-first group compared with 39% ($n = 50$) in the stent retriever group ($P = .25$). There was a higher first-pass TICI 3 result in the aspiration group (25% versus 13%, $P = .01$) (Table 2).

In terms of functional outcome, 50% of those in the aspiration-first group achieved functional independence at 90 days (mRS 0–2) compared with 46% in the stent retriever–first group ($P = .53$).

In 36 patients, the aspiration catheter did not easily advance to the proximal end of the thrombus. Therefore, it was necessary to use a stent retriever first in these cases. The locations of these vessels were the MCA M1 ($n = 20$), MCA M2 ($n = 9$), MCA M3 ($n = 2$), carotid terminus ($n = 3$), and tandem cervical ICA and M2 ($n = 1$) and M1 ($n = 1$). For the remaining 91 patients, aspiration was used as the first technique. When aspiration was performed first, 18.8% of patients required rescue therapy with a stent retriever. For these patients with aspiration-first, the median time from first angiogram to reperfusion was 8 minutes, with a groin puncture to first reperfusion time of 17 minutes and overall procedural length of 22 minutes (IQR, 14–46 minutes).

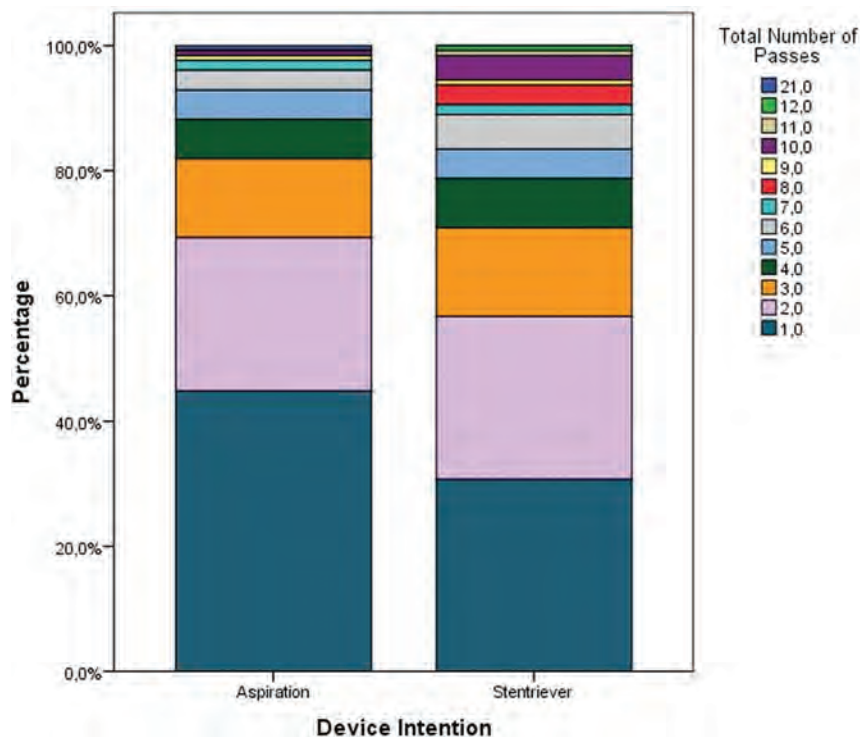


FIGURE. Type of device and the influence of total number of passes in percentages, $P < .05$

DISCUSSION

Previous randomized controlled trials showing the efficacy of thrombectomy have mainly involved the use of second-generation stent retrievers.³ However, newer technologies such as the use of aspiration devices have been developed at a greater rate than stent retriever technology through larger and more navigable catheters. The first-line aspiration technique is evolving as an established method of thrombectomy with noninferior results in terms of recanalization rates and patient outcomes compared with stent retrievers.^{7,10} Currently, there is an emphasis on reducing the time to revascularization, including the length of the procedure as well as improving the rate of recanalization, with the overall aim of improving patient outcomes.¹¹ There is continual development of novel techniques and optimization of techniques, some with very high rates of first-pass perfusion such as the Stent Retriever Assisted Vacuum-Locked Extraction (SAVE) and the Proximal Balloon Occlusion Together with Direct Thrombus Aspiration during Stent Retriever Thrombectomy (PROTECT^{Plus}) techniques.^{12,13}

There have been publications including the Contact Aspiration Versus Stent Retriever for Successful Revascularization (ASTER) randomized controlled trial (RCT), 2 meta-analyses, and the recently published COMPASS RCT evaluating the aspiration technique.^{7,10} Others report on case series of the aspiration technique but do not always define patient selection. They show varying impacts on speed and success rates with this technique. The A Direct Aspiration First Pass Technique (ADAPT) has been shown to have faster recanalization rates and reduced overall costs when used as the primary mechanism of thrombectomy compared with stent retrievers, though the results were not always statistically significant.^{4,7,14} A recently published meta-analysis has shown aspiration to have better success at

recanalization compared with stent retrievers but no benefit in terms of the number of passes or time to reperfusion.¹⁵

Our standardized approach as a technique for all anterior circulation occlusions, including tandem ICA/intracranial occlusions and occlusions beyond M1, results in shorter procedures and improved recanalization with fewer passes. We postulate that this is primarily due to the conversion to the aspiration-first technique. In our experience, it is a more streamlined and efficient process with fewer steps. Previously, we were placing an intermediate catheter distally in the ICA or even into the MCA for aspiration with a stent retriever. Changing to a method of advancing the newer, larger, and more flexible/trackable catheter as far as the clot when possible does not result in any significant delay. The clot may then be aspirated within minutes. If it does not advance to or remove the clot, a stent retriever can be easily deployed for clot retrieval without significant delay. In trial scenarios, physicians were required to try aspiration

on 3 occasions before switching to rescue therapy. In the real world, this is not required, resulting in shorter procedures. Our institution has significant experience in performing thrombectomy for acute stroke with >800 cases performed since 2010. Every procedure has a learning curve, and thrombectomy is no exception. With at least 500 cases performed prior to inclusion of any cases from the stent retriever cohort, this minimized the effect of the learning curve. Since September 2017, we have used a standardized method of setting up for attempting aspiration-first for all thrombectomy procedures. Although some improvement may be accounted for by standardization, we believe that the extensive experience before standardization would minimize this effect and that the true gain is in the use of fewer steps in most procedures.

Our median groin-to-reperfusion time in the standardized group was 18 minutes, with a mean of 26 minutes 30 seconds in comparison with 26 and 35 minutes, respectively, for the stent retriever cohort ($P < .001$) (Table 2). If we compare this to A Direct Aspiration First Pass Technique for Acute Stroke Thrombectomy (ADAPT FAST) (a multisite case series), the authors reported a mean time of 36 minutes 3 seconds.⁴ The ASTER trial was an RCT that compared revascularization rates (TICI 2b–3) as its primary outcome between the aspiration and stent retriever technique. The authors reported a median groin puncture-to-reperfusion time of 38 minutes for the aspiration group compared with 45 minutes for the stent retriever group ($P = .10$).¹⁰ The initial results from the COMPASS trial had the fastest times of any previous study, with a mean groin-to-reperfusion rate of 22 minutes for ADAPT versus 33 minutes for the stent retriever group ($P = .019$).⁷ The European Registry on the ACE Reperfusion Catheters and the Penumbra System in the Treatment of Acute

Table 2: Time variables—aspiration vs stent retriever

Variable/Sts	All (n = 254)	Aspiration (n = 127)	Stent Retriever (n = 127)	P Value
Length of procedure (min)				
Mean	47.7 ± 38.9	33.2 ± 25.1	62.2 ± 44.6	<.001
Median (IQR 25%–75%)	36.0 (22–62)	26.0 (15–41)	47.0 (32–80)	
Groin puncture to 1st angiogram (min)				
Mean	7.3 ± 5.9	7.7 ± 5.9	7.0 ± 5.8	.234
Median (IQR 25%–75%) (min)	6.0 (4–9)	6.0 (4–10)	5.0 (4–9)	
First angiogram to first 1st reperfusion (min)				
Mean	23.0 ± 25.8	18.2 ± 22.9	27.9 ± 27.6	<.001
Median (IQR 25%–75%)	15.0 (8–27)	11.0 (7–20)	19.5 (12–32)	
Groin puncture to 1st reperfusion (min)				
Mean	30.2 ± 27.1	25.6 ± 23.8	34.9 ± 29.4	<.001
Median (IQR 25%–75%)	22.0 (15–35)	18.0 (13–31)	26.0 (17–39)	
TICI (No.) (%)				
Y 2b–3	231 (90.9%)	122 (96.1%)	109 (85.8%)	<.005
2c–3	176 (69.3%)	99 (78%)	77 (60.6%)	<.005
3	109 (43%)	59 (46%)	50 (39%)	.25
First-pass 3	48 (19%)	32 (25%)	16 (13%)	.01

Note:—Y indicates TICI as standing for Thrombolysis in Cerebral Infarction Score; Sts, statistics; TICI, Thrombolysis in Cerebral Infarction Score.

Ischemic Stroke (PROMISE) observational study, which used the ADAPT technique with ACE68 and ACE64 catheters (Penumbra, Alameda, California), reported a median time to reperfusion of 31 minutes with a mean of 40 minutes.¹⁵ A meta-analysis of 17 aspiration studies versus the 5 RCTs included in the Highly Effective Reperfusion Evaluated in Multiple Endovascular Stroke (HERMES) meta-analysis recorded a trend toward a shorter procedural time with the aspiration group (44 minutes 42 seconds versus 61 minutes 28 seconds, $P = .088$).¹⁶

Observing groin puncture-to-reperfusion times is not the full story, however. For our described aspiration-first technique, the times from groin puncture to first angiogram are comparable with the conventional technique, without a statistically significant difference. This part of the procedure has not changed and has a similar patient cohort in terms of difficulty/ease of vascular access to the ICA. The main benefit of our technique comes after this stage, however, when the time from the first angiogram to the first restoration of flow is significantly shorter at 11 minutes (IQR, 7–20 minutes) versus 19 minutes 30 seconds (IQR, 12–32 minutes) in the stent retriever group, ($P < .001$) (8 minutes when aspiration is actually used first). Our overall procedure length is 26 minutes (22 minutes [IQR, 14–46 minutes] when aspiration is actually the first device used). These specific figures are not quoted in other studies; however, they highlight the speed of the aspiration technique once access is achieved, resulting in a much shorter procedural length.

In terms of reperfusion rates, 96% of the patients in the standardized aspiration-first group had a TICI of 2b–3 compared with 85.8% in the stent retriever cohort ($P < .005$) (Table 2). The ASTER and COMPASS trials reported rates of 85.4% and 83.2%, respectively, for the ADAPT technique.^{7,10} These trials did not show improved recanalization rates for ADAPT. If we examine the TICI 2c–3 rates alone, we report a rate of 78% for the aspiration approach versus 61% in the stent retriever cohort ($P < .005$). The ASTER trial separately evaluated TICI 2c–3 with rates of 56.3% and 56.6% for aspiration and stent retriever, respectively.¹⁰

The PROMISE study reported successful reperfusion rates (TICI 2b–3) of 93.1%.¹⁵ The ADAPT FAST study reported overall revascularization rates (TICI 2b–3) of 95%, and when aspiration was used alone, it was successful in achieving revascularization 78% of the time compared with our rate of 94.5% for this group.⁴ The meta-analysis of ADAPT versus the HERMES meta-analysis where stent retrievers were used by Phan et al¹⁶ showed significantly higher revascularization rates in the ADAPT group compared with stent retriever group (89.6% versus 71.7%, $P < .001$), though most groups appear to show improved recanalization rates now compared with HERMES.

In our study, when aspiration was performed first, 18.8% of cases required rescue therapy with a stent retriever, an outcome comparable with or lower than other reported studies. This may be due to operator-related factors and slight differences in occlusion location. In the ASTER trial, rescue treatment was required in 32.8% of patients in the aspiration group, 20.9% in the PROMISE study and 21% in COMPASS.^{7,10,15} The ASTER and PROMISE studies included 48 (27.6%) and 37 (18.1%) M2 branch occlusions, respectively, compared with our rate of 7.8% in the aspiration group and 14% in the stent retriever group.^{10,15} We believe that our higher rates of recanalization and lower use of rescue therapy following aspiration are likely due to using a larger bore catheter with excellent trackability. Larger bore catheters enable generation of greater aspiration pressure and presumably accommodate larger clots.

First restoration of flow does not necessarily equate with removal of the entire clot and further passes may be required. This is particularly the case with stent retrievers when you can get flow restoration without even removing the clot. Our aspiration-first group required fewer passes, and 45% ($n = 57$) needed only a single pass when aspiration was used first, compared with 35% ($n = 39$) in the stent retriever group, resulting in an overall shorter procedural time. The ASTER RCT reported no difference in the number of attempts between the 2 groups, with a median number of 2 passes.¹⁰ The PROMISE trial reported a median number of 2 passes before using adjunctive therapy.¹⁵ The authors of the ADAPT FAST study stated that they often only needed a single pass to achieve successful reperfusion; however, they did not quote exact figures.⁴

In terms of good functional outcome, our rates are comparable with those in both the ASTER and COMPASS RCT, yielding rates of 45.5% and 52%, respectively, for the aspiration-first technique group, while ADAPT FAST had slightly lower rates of 40% in this group.^{4,7,10} The PROMISE study had the highest rates of good functional outcome, with a rate of 60% compared with our rate of 50%; however, their inclusion criteria were limited to patients with onset of symptoms within 6 hours.¹⁵

A potential advantage of aspiration over stent retrievers is the

potential for fewer procedure-related complications resulting from direct trauma to the vessels caused by the stent retrievers. It is not fully understood where crossing a clot (MCA for example) results in any injury to the vessel wall, intima or media. It has been shown that using a microwire to cross a clot can result in vessel injury compared with using a microcatheter alone.¹⁷ Focal acceleration of blood flow velocities after mechanical thrombectomy is suggestive of residual stenosis or vasospasm, and this may be a sign of endothelial layer disruption/intimal injury.¹⁸ Intracranial arterial wall thickening and enhancement have been demonstrated postthrombectomy, indicating an arteritis.¹⁹ A study comparing vascular damage in ADAPT versus stent retrievers in animal models showed almost complete loss of the endothelium when stent retrievers were used. As we have described, our study showed fewer passes compared with stent retrievers. Furthermore, fewer passes will also lead to less disruption of clot, potentially leading to less risk of resulting emboli to a new territory (ENT).²⁰ The ADAPT FAST study reported no cases of ENT, while PROMISE reported a rate of 1.5%.^{4,15} Use of the ADAPT technique has been reported to increase the risk of ENT.²⁰ However, with newer, larger catheters such as the Sofia Plus, there is likely to be a higher rate of clot ingestion as opposed to pulling the clot through the circulation, preventing ENT. A recent meta-analysis published in September 2018 evaluated 9 studies comparing the efficacy and safety of the direct aspiration technique versus stent retrievers. This study showed fewer cases of symptomatic intracranial hemorrhage (4.8% versus 8.35%) and embolization to a new territory (5.1% versus 9.7%) with direct aspiration.²¹ Newer aspiration catheters, which are more flexible and atraumatic compared with stent retrievers, will arguably lead to less procedure-related complications.

The strengths of our study lie in the standardized approach used for consecutive patients, resulting in faster and better outcomes with no disadvantages for cases that need to be switched to stent retrievers, because this can be performed without a change in the setup. Furthermore, the consecutive nature of case selection and lack of difference between the groups, including similar groin puncture to first angiogram times, confirms the absence of selection bias or cherry-picking. While previous studies have shown comparable times and recanalization rates, we have been able to demonstrate significantly faster and better recanalization rates and fewer passes compared with stent retrievers.

A weakness in our study is that it is a single-center study that did not use a core laboratory in the assessment of TICI scores. However, final TICI scores required agreement by 2 independent neuroradiologists. Although the use of balloon-guide catheters is recommended by many, we have not developed this as a routine due to a preference for having larger bore intermediate catheters for distal aspiration in conjunction with a stent retriever. Nevertheless, our recanalization rates with our stent retriever cohort are comparable with those in other published series. We did not use the recently available Wedge device (MicroVention) designed to get the aspiration/Sofia catheter past the ophthalmic artery, which may help aspiration-first work in a higher percentage of patients. The effectiveness of this device is yet to be established. Furthermore, we did not use a smaller aspiration catheter that could have

reached more distal branches. It is likely that the rate of successful navigation of the aspiration catheter to the thrombus will improve with better technology and range of catheters.

CONCLUSIONS

In a procedure in which “time is brain,” any opportunity to improve times and success should be taken. This approach uses a standardized technique already possibly familiar to many neurovascular interventionalists and is potentially widely adaptable. By using this technique, we have demonstrated faster and better recanalization times with an overall reduced procedure length.

ACKNOWLEDGMENTS

The authors wish to express their gratitude to Dr Sean Fitzgerald for his contribution to this article.

Disclosures: Karen M. Doyle—RELATED: Grant: Science Foundation Ireland and Cerenovus.* John Thornton—UNRELATED: Board Membership: Neuravi, Comments: Scientific Advisory Board. *Money paid to the institution.

REFERENCES

1. Saver JL. **Time is brain—quantified.** *Stroke* 2005;37:263–66 Medline
2. Campbell BC, Donnan GA, Lees KR, et al. **Endovascular thrombectomy: the new standard of care for large vessel ischaemic stroke.** *Lancet Neurol* 2015;14:846–54 CrossRef Medline
3. Goyal M, Menon BK, van Zwam WH, et al; HERMES collaborators. **Endovascular thrombectomy after large-vessel ischaemic stroke: a meta-analysis of individual patient data from five randomised trials.** *Lancet* 2016;387:1723–31 CrossRef Medline
4. Turk AS, Frei D, Fiorella D, et al. **ADAPT FAST study: a direct aspiration first pass technique for acute stroke thrombectomy.** *J Neurointerv Surg* 2014;6:260–64 CrossRef Medline
5. Jankowitz B, Aghaebrahim A, Zirra A, et al. **Manual aspiration thrombectomy: adjunctive endovascular recanalisation technique in acute stroke interventions.** *Stroke* 2012;43:1408–11 CrossRef Medline
6. Massari F, Henninger N, Lozano JD, et al. **ARTS (Aspiration-Retriever Technique for Stroke): initial clinical experience.** *Interv Neuroradiol* 2016;22:325–32 CrossRef Medline
7. Turk AS 3rd, Siddiqui A, Fifi JT, et al. **Aspiration thrombectomy versus stent retriever thrombectomy as first-line approach for large vessel occlusion (COMPASS): a multicentre, randomised, open label, blinded outcome, non-inferiority trial.** *Lancet* 2019;393:998–1008 CrossRef Medline
8. Holodinsky JK, Patel AB, Thornton J, et al. **Drip and ship versus direct to endovascular thrombectomy: the impact of treatment times on transport decision-making.** *Eur Stroke J* 2018;3:126–35 CrossRef Medline
9. Singh J, Wolfe SQ, Janjua RM, et al. **Anchor technique: use of stent retrievers as an anchor to advance thrombectomy catheters in internal carotid artery occlusions.** *Interv Neuroradiol* 2015;21:707–09 CrossRef Medline
10. Lapergue B, Blanc R, Gory B, et al; ER Trial Investigators. **Effect of endovascular contact aspiration vs stent retriever on revascularization in patients with acute ischemic stroke and large vessel occlusion: the ASTER randomized clinical trial.** *JAMA* 2017;318:443–52 CrossRef Medline
11. Goyal M, Demchuk AM, Menon BK, et al; ESCAPE Trial Investigators. **Randomized assessment of rapid endovascular treatment of ischemic stroke.** *N Engl J Med* 2015;372:1019–30 CrossRef Medline
12. Maus V, Behme D, Kabbasch C, et al. **Maximizing first-pass complete reperfusion with SAVE.** *Clin Neuroradiol* 2018;28:327–38 CrossRef Medline
13. Maegerlein C, Berndt MT, Monch S, et al. **Development of combined**

- techniques using stent retrievers, aspiration catheters and BGC: the PROTECT^{PLUS} technique. 2018 Nov 9. [Epub ahead of print] CrossRef Medline
14. Turk AS, Turner R, Spiotta A, et al. **Comparison of endovascular treatment approaches for acute ischemic stroke: cost-effectiveness, technical success, and clinical outcomes.** *J Neurointerv Surg* 2015;7:666–70 CrossRef Medline
 15. Schramm P, Navia P, Papa R, et al. **ADAPT technique with ACE68 and ACE64 reperfusion catheters in ischemic stroke treatment: results from the PROMISE study.** *J Neurointerv Surg* 2019;11:226–31 CrossRef Medline
 16. Phan K, Dmytriw AA, Teng I, et al. **Direct aspiration first pass technique vs standard endovascular therapy for acute stroke: a systematic review and meta-analysis.** *Neurosurgery* 2018;83:19–28 CrossRef Medline
 17. Keulers A, Nikoubashman O, Mpotsaris A, et al. **Preventing vessel perforations in endovascular thrombectomy: feasibility and safety of passing the clot with a microcatheter without microwire: the wireless microcatheter technique.** *J Neurointerv Surg* 2018 Dec 7. [Epub ahead of print]. CrossRef Medline
 18. Perren F, Kargiotis O, Pignat JM, et al. **Hemodynamic changes may indicate vessel wall injury after stent retrieval thrombectomy for acute stroke.** *J Neuroimaging* 2018;28:412–15 CrossRef Medline
 19. Power S, Matouk C, Casaubon LK, et al. **Vessel wall magnetic resonance imaging in acute ischemic stroke: effects of embolism and mechanical thrombectomy on the arterial wall.** *Stroke* 2014;45:2330–34 CrossRef Medline
 20. Chueh J, Puri AS, Wakhloo AK, et al. **Risk of distal embolization with stent retriever thrombectomy and ADAPT.** *J Neurointerv Surg* 2016;8:197–202 CrossRef Medline
 21. Qin C, Shang K, Xu SB, et al. **Efficacy and safety of direct aspiration versus stent retriever for recanalization in acute cerebral infarction: A PRISMA-compliant systematic review and meta-analysis.** *Medicine (Baltimore)* 2018;97:e12770 CrossRef Medline

Distal Balloon Angioplasty of Cerebral Vasospasm Decreases the Risk of Delayed Cerebral Infarction

M.-A. Labeyrie, S. Gaugain, G. Boulouis, A. Zetchi, J. Brami, J.-P. Saint-Maurice, V. Civelli, S. Froelich, and E. Houdart



ABSTRACT

BACKGROUND AND PURPOSE: Conventional angioplasty of cerebral vasospasm combines proximal balloon angioplasty (up to the first segment of cerebral arteries) with chemical angioplasty for distal arteries. Distal balloon angioplasty (up to the second segment of cerebral arteries) has been used in our center instead of chemical angioplasty since January 2015. We aimed to assess the effect of this new approach in patients with aneurysmal SAH.

MATERIALS AND METHODS: The occurrence, date, territory, and cause of any cerebral infarction were retrospectively determined and correlated to angioplasty procedures. Delayed cerebral infarction, new angioplasty in the territory of a previous angioplasty, angioplasty complications, 1-month mortality, and 6- to 12-month modified Rankin Scale ≤ 2 were compared between 2 periods (before-versus-after January 2015, from 2012 to 2017) with adjustment for age, sex, World Federation of Neurosurgical Societies score, and the modified Fisher grade.

RESULTS: Three-hundred-ninety-two patients were analyzed (160 before versus 232 after January 2015). Distal balloon angioplasty was associated with the following: higher rates of angioplasty (43% versus 27%, $P < .001$) and intravenous milrinone (31% versus 9%, $P < .001$); lower rates of postangioplasty delayed cerebral infarction (2.2% versus 7.5%, $P = .01$) and new angioplasty (8% versus 19%, $P = .003$) independent of the rate of patients treated by angioplasty and milrinone; and the same rates of stroke related to angioplasty (3.6% versus 3.1%, $P = .78$), delayed cerebral infarction (7.7% versus 12.5%, $P = .12$), mortality (10% versus 11%, $P = .81$), and favorable outcome (79% versus 73%, $P = .21$).

CONCLUSIONS: Our study suggests that distal balloon angioplasty is safe and decreases the risk of delayed cerebral infarction and the recurrence of vasospasm compared with conventional angioplasty. It fails to show a clinical benefit possibly because of confounding changes in adjuvant therapies of vasospasm during the study period.

ABBREVIATIONS: aSAH = aneurysmal subarachnoid hemorrhage; DCIn = delayed cerebral infarction; WFNS = World Federation of Neurosurgical Societies

Angioplasty of cerebral vasospasm is broadly used in acute aneurysmal SAH (aSAH). Two main approaches to angioplasty are used alone or combined: the balloon angioplasty performed by most physicians up to the end of the first segment of cerebral arteries (ie, in the proximal and largest arterial segments)¹⁻³ and intra-arterial vasodilator infusion therapy (chemical angioplasty).^{4,5} Their efficacy to treat the arterial narrowing

has been demonstrated, but their benefit to prevent delayed cerebral infarction (DCIn) remains controversial.^{6,7} The feasibility of balloon angioplasty up to the end of the second segment of the cerebral arteries (distal balloon angioplasty) using an extracomppliant balloon has been recently reported.⁸ On the basis of this report, our experience of poor efficacy of chemical angioplasty, and our preliminary experience with distal balloon angioplasty, we decided to replace chemical angioplasty with distal balloon angioplasty for distal vasospasm. The aim of this study was to compare historically the safety and efficacy of this new approach with the conventional approach using proximal balloon angioplasty and chemical angioplasty.

MATERIALS AND METHODS

Patients

Consecutive patients hospitalized in our center (Lariboisière Hospital, France) between January 2012 and December 2017 within 15 days of aSAH with a modified Fisher grade of ≥ 1 were in-

Received February 6, 2019; accepted after revision June 5.

From the Departments of Interventional Neuroradiology (M.-A.L., A.Z., J.B., J.-P.S.-M., V.C., E.H.) and Neurosurgery (S.F.) and Emergency Care Unit (S.G.), Hôpital Lariboisière, Paris, France; EA 7334 REMES (M.-A.L., E.H.), L'Université Paris Diderot, Paris, France; and Department of Radiology (G.B.), Centre Hospitalier Sainte-Anne, Paris, France.

Please address correspondence to Marc-Antoine Labeyrie, MD, Service de Neuro-radiologie Interventionnelle, Hôpital Lariboisière, 2 rue Ambroise Paré, 75010 Paris, France; e-mail: marc-antoine.labeyrie@aphp.fr

 Indicates article with supplemental on-line appendix and table.

<http://dx.doi.org/10.3174/ajnr.A6124>

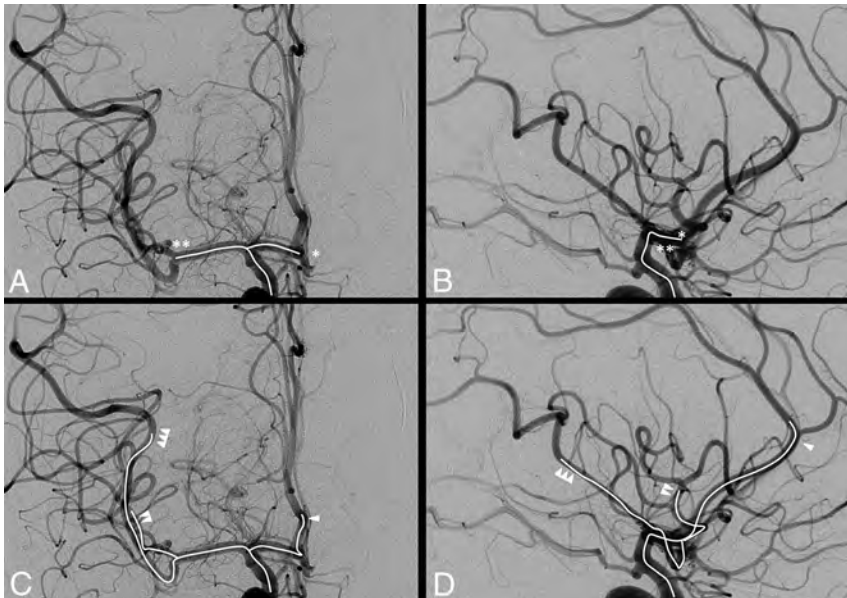


FIG 1. Anatomic definition of distal-versus-proximal balloon angioplasty. Frontal (A and C) and lateral (B and D) angiograms of the right internal carotid artery before cerebral vasospasm. Arterial segments treated using proximal balloon angioplasty are indicated in A and B (*intra-arterial white line*). They include the terminal internal carotid artery and the main segments of cerebral arteries up to the end of their first segment (*single star* for A1, *double star* for M1). Arterial segments treated using distal balloon angioplasty are shown in C and D (*intra-arterial white line*). They include the terminal internal carotid artery and the main segments of the cerebral arteries up to the end of their second segments (*single arrowhead* for pericallosal segment, *double arrowhead* for the anterior M2 branch, and *triple arrowhead* for the posterior M2 branch).

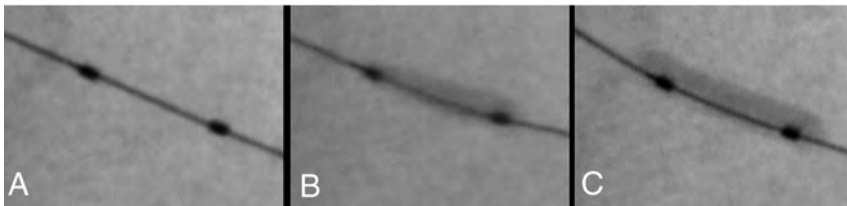


FIG 2. Distal balloon angioplasty in a 1.5-mm large M2 segment using an extracompliant 4-mm-large and 7-mm-long remodeling balloon. After we navigated in the distal M2 with a 0.010-inch guidewire, the balloon was positioned (A) and inflated progressively (B and C). The balloon has first a fusiform aspect (B) and then a tubular aspect and elongates (C) when it reaches the maximal diameter of the vessel. The balloon was immediately deflated. This maneuver was repeated within the entire segment from the proximal-to-distal M2.

cluded, except patients who died within the first 4 days after aSAH onset. All patients were hospitalized in an intensive care unit. Aneurysms were treated by embolization or clipping within 24 hours of admission. Acute hydrocephalus, neuroprotective measures, and primary prevention with oral nimodipine and detection of delayed cerebral ischemia were managed according to current guidelines.⁹ Clinical and imaging data were reviewed by consensus from 2 neuroradiologists, including 1 who was independent of the procedures. The mRS was retrospectively determined within 6–12 months after aSAH by an independent clinical research associate with mRS certification and blinded to the patient's care and the historical design of the study. Patients or their relatives were informed and provided their consent for all clinical care. The study was approved by our institution ethics committee.

Intensive Therapies of Vasospasm

Balloon angioplasty was performed using an extracompliant remodeling balloon, HyperForm 4–7 on an 0.010-inch Expedition

microwire (ev3, Irvine, California), or Scepter XC 412 (MicroVention, Tustin, California) on a 0.014-inch Transend microwire (Stryker, Kalamazoo, Michigan), inflated through a 3.5-mL syringe with a dilution of 50% Omnipaque (iohexol 300 mg I/mL; GE Healthcare, Piscataway, New Jersey). The anatomic definition of distal-versus-proximal balloon angioplasty is shown in Fig 1.

We performed balloon angioplasty using previously reported technique.⁸ A test inflation of the balloon was performed in the cervical artery to ensure that it was plainly visible. The balloon was inflated to the supposed normal diameter of the artery and until the lateral border of the balloon became parallel and the balloon elongated (Fig 2). Angulation and the diameter of the arterial segments were the most important safety variables considered before balloon angioplasty. Proximal balloon angioplasty was performed for arteries with a diameter ≥ 2.5 mm and located proximal to the first angulation of the cerebral arteries (up to the end of the first segments) (Fig 1A, -B). Distal balloon angioplasty was performed for arteries with a diameter of ≥ 1.5 mm and located proximal to the second angulation of the cerebral arteries (up to the end of the second segment), also including the pericallosal segment of the anterior cerebral artery or up to the end of the second segment of the 2 (or rarely 3) major division branches of the middle cerebral artery (Fig 1C, -D). Hypoplastic segments were excluded on the basis of prevasospasm vascular imaging.

Small anterior temporal branches from the middle cerebral arteries or anterior frontal branches from the anterior cerebral arteries were usually not dilated because of their small diameter and their excessive angulation. The posterior cerebral arteries were treated in a few selected cases and only proximally because DCIs in this territory were infrequent in our practice. Segments with obvious collateral supply through the circle of Willis were usually not treated. The parent vessel of an aneurysm was treated when necessary (except around a recent surgical clip) by taking care that the balloon did not bulge inside the aneurysm. Balloon angioplasty around a surgical clip was usually not performed because aneurysmal ruptures have been described during balloon angioplasty or navigation despite the clip. When a severe stenosis persisted after a first dilation, a second dilation was usually performed by taking care that the balloon did not overexpand on either side of the stenosis (giving a “dog bone” appearance).

Chemical angioplasty consisted of single or, when necessary,

repeat daily intra-arterial infusions for 30 minutes of 3 mg of nimodipine + 8 mg of milrinone + 40 mL of physiologic serum, or 1 single continuous infusion for 3 days of 4 mg/h of milrinone. Before January 2015, chemical angioplasty was performed for vasospasm of distal arterial segments when balloon angioplasty was not considered feasible. After January 2015, chemical angioplasty was replaced by distal balloon angioplasty.

All angioplasty procedures were performed with the patient under general anesthesia by keeping a mean arterial pressure of ≥ 90 mm Hg and normocapnia. Intravenous heparin (35–70 IU/kg) was administered before angioplasty. Since January 2013, continuous intravenous infusion of a high dose of intravenous milrinone (1.5mcg/kg/min, then adapted to clinical tolerance for at least 5 days) has been systematically considered after angioplasty.¹⁰ It was maintained when possible until the 14th day, and the patient was weaned as indicated.

Indications for Intensive Therapies for Vasospasm

Intensive therapies were considered in patients with a high suspicion or high risk of delayed cerebral ischemia. A high suspicion of delayed cerebral ischemia was defined by the following: 1) a vasospasm of $\geq 50\%$ on DSA, especially when it was associated with a delayed enhancement of distal cortical arteries; and 2) a decrease in the level of consciousness or deficit or cerebral infarction occurring between the fourth day and the 21st day unrelated to seizure, severe intracranial hypertension, hydrocephaly, hyponatremia, aneurysm occlusion complications, or severe sepsis with hypotension. In unconscious patients, a high risk of delayed cerebral ischemia was considered using only DSA criteria. The non-invasive screening for vasospasm of $\geq 50\%$ is detailed in the On-line Appendix. An induced hypertension was begun in patients with a high suspicion or a high risk of delayed cerebral ischemia. Angioplasty was then considered consensually between the interventional neuroradiologists and the intensive care physicians. It was performed only for arterial segments with vasospasms of $\geq 50\%$. It was contraindicated when a cerebral infarction extended to the major part of the territory because of the risk of reperfusion injury.

Safety of Angioplasty

Arterial embolism, dissection, perforation, and vasospasm worsening were retrospectively reviewed on postangioplasty DSA. Dissection was distinguished from embolism using previously reported criteria.¹¹ Vasospasm worsening was defined as worsening of arterial narrowing occurring after catheterization or balloon angioplasty, not related to embolism or dissection, which resolves spontaneously in most cases or after further angioplasty. Reperfusion syndromes after angioplasty including severe intracranial hypertension requiring a hypertonic solution and symptomatic intracerebral hematoma were also recorded. Chronic aneurysm formation or occlusions of the arteries treated with angioplasty were assessed on vascular imaging follow-up at 3–6 months.

Efficacy of Angioplasty

The efficacy of angioplasty was first determined by the rate of patients with DCIn occurring in the territory of a previous angioplasty (postangioplasty DCIn). The determination of DCIn is de-

tailed in the On-line Appendix. To summarize, DCIn was defined as any cerebral infarction occurring within 3–21 days of presentation, not related to an iatrogenic infarction or early low-flow infarction.¹² Only DCIn occurring after aneurysm treatment (in-hospital DCIn) was taken into account in the current study. The time and arterial territory of the DCIn were retrospectively determined using all available coregistered MR imaging and CT and clinical data. Then, the time and arterial territory of DCIn was compared with the timing and the territory of each angioplasty to determine whether the DCIn occurred or extended into the territory of a previous angioplasty (postangioplasty DCIn). DCIn and angioplasty were blinded. We also analyzed the occurrence of DCIn in a territory without angioplasty (ie, occurring in the parenchyma of nontreated vessels and including patients without any angioplasty or with angioplasty in another territory) and whether any new angioplasty was performed in the same territory of a previous angioplasty (in a different session).

Statistical Analysis

Continuous variables were described as medians and interquartile ranges and compared using the nonparametric Kruskal-Wallis test. Categorical variables were compared using the χ^2 or Fisher exact test (unilateral test) as appropriate (SPSS 19; IBM, Armonk, New York). A *P* value $\leq .05$ was considered significant. Baseline characteristics, intensive therapies of cerebral vasospasm, and outcome were univariately compared in historical analysis between the 2 periods (before-versus-after January 2015). DCIn, new angioplasty, 1-month death, and 6- to 12-month favorable outcome (mRS ≤ 2) were also compared between the 2 periods after adjustment for age, sex, and World Federation of Neurosurgical Societies (WFNS) score $\geq IV$ and a modified Fisher grade ≥ 3 using binary logistic regression. The main analysis included all patients with aSAH. Then, a sensitivity analysis was performed by including only patients treated with angioplasty and patients who did not receive intravenous milrinone or by comparing the angioplasty strategy used for each arterial territory rather than at the patient level.

RESULTS

Population

Four-hundred-eighteen consecutive patients were treated for acute aSAH in our center during the study period. We excluded 26 patients who died from early brain injury and before any angioplasty. A total of 392 patients were analyzed in the current study, including 232 patients treated after January 2015 (distal balloon angioplasty period) and 160 patients before that date (historical control). Clinical and imaging data were available for all patients. Follow-up MR imaging was available for 90% of them. Interobserver agreement for DCIn determination was 0.903. The baseline characteristics of the population are reported in Table 1.

Patients Treated by Distal Balloon Angioplasty

The intensive therapies used to treat cerebral vasospasm are detailed in Table 2. We observed a higher rate of patients treated by such therapies after January 2015 (*P* $\geq .001$). A total of 145 patients were treated by angioplasty including 109/145 (75%) by distal angioplasty in at least 1 arterial territory.

Table 1: Baseline characteristics of patients with aSAH

	Total (N = 392)	Period 1 (n = 160) ^a	Period 2 (n = 232) ^a	P Value
Age (range) (yr)	52 (44–61)	52 (44–62)	52 (46–61)	.9
Female (No.) (%)	254 (65%)	104 (65%)	150 (65%)	.5
Tobacco (No.) (%)	188 (48%)	75 (47%)	113 (49%)	.4
Chronic high blood pressure (No.) (%)	168 (43%)	76 (47%)	92 (40%)	.1
Dyslipidemia (No.) (%)	84 (21%)	36 (22%)	48 (21%)	.6
Diabetes mellitus (No.) (%)	19 (5%)	9 (6%)	10 (4%)	.3
Modified Fisher grade				
1, 2 (No.) (%)	73 (19%)	34 (21%)	39 (17%)	.3
3 (No.) (%)	103 (26%)	37 (23%)	66 (28%)	.2
4 (No.) (%)	216 (55%)	89 (56%)	127 (55%)	.8
WFNS				
I, II (No.) (%)	270 (69%)	105 (65%)	165 (71%)	.2
III (No.) (%)	22 (6%)	11 (7%)	13 (6%)	.6
IV (No.) (%)	56 (14%)	22 (14%)	32 (14%)	1
V (No.) (%)	44 (11%)	22 (14%)	22 (9%)	.2

^a Period 1/period 2 (before/after January 2015) means chemical/balloon angioplasty as a first-line treatment of distal vasospasm.

Table 2: Intensive therapies of vasospasm in patients with aSAH

	Total (N = 392)	Period 1 (n = 160) ^a	Period 2 (n = 232) ^a	P Value
Intensive treatment of vasospasm (No.) (%)	155 (40%)	47 (29%)	108 (46%)	<.001
Angioplasty (No.) (%)	145 (37%)	44 (27%)	101 (43%)	.001
Distal angioplasty (No.) (%) ^b	109 (28%)	35 (22%)	74 (32%)	.029
Distal balloon angioplasty (No.) (%) ^c	87 (22%)	13 (8%)	74 (32%)	<.001
Proximal balloon angioplasty (No.) (%) ^d	91 (23%)	26 (16%)	65 (28%)	.004
Chemical angioplasty (No.) (%) ^d	36 (9%)	31 (19%)	5 (2%)	<.001
Intravenous milrinone (No.) (%)	86 (22%)	15 (9%)	71 (31%)	<.001

^a Period 1/period 2 (see Table 1).

^b Distal angioplasty means distal balloon angioplasty or chemical angioplasty.

^c Distal balloon angioplasty was performed alone.

^d Chemical and proximal balloon angioplasties were performed alone or combined.

Distal balloon angioplasty was attempted in 187 arterial segments (90% of them in patients treated after January 2015). Catheterization failed in 21/187 (11%) because of an excess angulation between the first and second segments of cerebral arteries. For these segments or for those without distal vasospasm, only proximal balloon angioplasty was performed. Distal balloon angioplasty was performed in 166 arterial segments: M2 = 92, A2 = 69, posterior communicating artery P1 or P2 = 5. An example of distal balloon angioplasty is shown in Fig 3.

Safety of Distal Balloon Angioplasty

Complications of angioplasty are detailed in the On-line Table. Cerebral infarction related to embolism or arterial dissection or vasospasm worsening was observed in 5/87 (6%) patients after distal balloon angioplasty. This rate was similar after other angioplasty approaches ($P = .75$). Symptomatic intracranial hemorrhages were observed in 3/87 (3.4%) after distal balloon angioplasty. All had a large infarction on imaging before the procedure. This rate was similar to that in other approaches ($P = .32$). No malignant edema or arterial perforation was observed after distal balloon angioplasty. The historical comparison of the rate of complications after angioplasty is reported in Table 3. Whereas more patients had angioplasty in the second period, the rates of cerebral infarction or symptomatic intracranial hemorrhage related to angioplasty were similar between the 2 periods ($P \geq .64$).

Efficacy of Distal Balloon Angioplasty

Angioplasty efficacy and outcome are reported in Table 3. After adjustment for age, sex, and WFNS score \geq IV and a modified Fisher grade of \geq 3, the second period was associated with a lower rate of postangioplasty DCIn (OR= 0.26; 95% CI, .09–0.77; $P = .015$) and new angioplasty (OR= 0.39; 95% CI, 0.21–0.72; $P = .003$), without any significant association with DCIn ($P = .12$), 1-month mortality ($P = .81$), and 6- to 12-month favorable outcome ($P = .21$).

After adjustment with intravenous milrinone, the second period remained associated with a lower rate of postangioplasty DCIn and new angioplasty and became significantly associated with a lower rate of DCIn ($P \leq .001$).

By including only patients treated by angioplasty, the second period remained associated with a lower rate of postangioplasty DCIn and new angioplasty and became significantly associated with DCIn (OR= 0.25; 95% CI, 0.10–0.59; $P = .002$) and 6- to 12-month favorable outcome (OR= 2.5; 95% CI, 1.1–5.7; $P = .026$). Of note, in this population,

patients with a WFNS score \geq IV were less frequent in the second period (32% versus 50%, $P = .02$).

When we compared the angioplasty strategy used for each arterial territory rather than at the patient level, the rate of postangioplasty DCIn after distal balloon angioplasty was similar with or without intravenous milrinone (respectively, 1/56 versus 0/31, $P = 1$). It was lower than after other approaches (respectively, 41/87 versus 16/99, $P < .001$) even by including only patients who received intravenous milrinone (respectively, 1/56 versus 10/53, $P = .003$).

DISCUSSION

Our study suggests that distal balloon angioplasty is more effective than and has the same safety as conventional angioplasty to prevent DCIn and vasospasm. It failed to give evidence of a clinical benefit of this new angioplasty strategy in patients with aSAH.

Angioplasty for vasospasm is broadly used in many centers, but its benefit is still unproven.¹³ Conventional angioplasty combines balloon angioplasty for proximal vasospasm and chemical angioplasty for distal vasospasm.³ Chemical angioplasty is effective for treating distal vasospasm, but its effect is not lasting, even with daily sessions because vasospasm frequently reappears after a few hours.^{3–5,14} Continuous chemical angioplasty for several days may have a more lasting effect but is associated, in our experience, with a very high rate of cere-

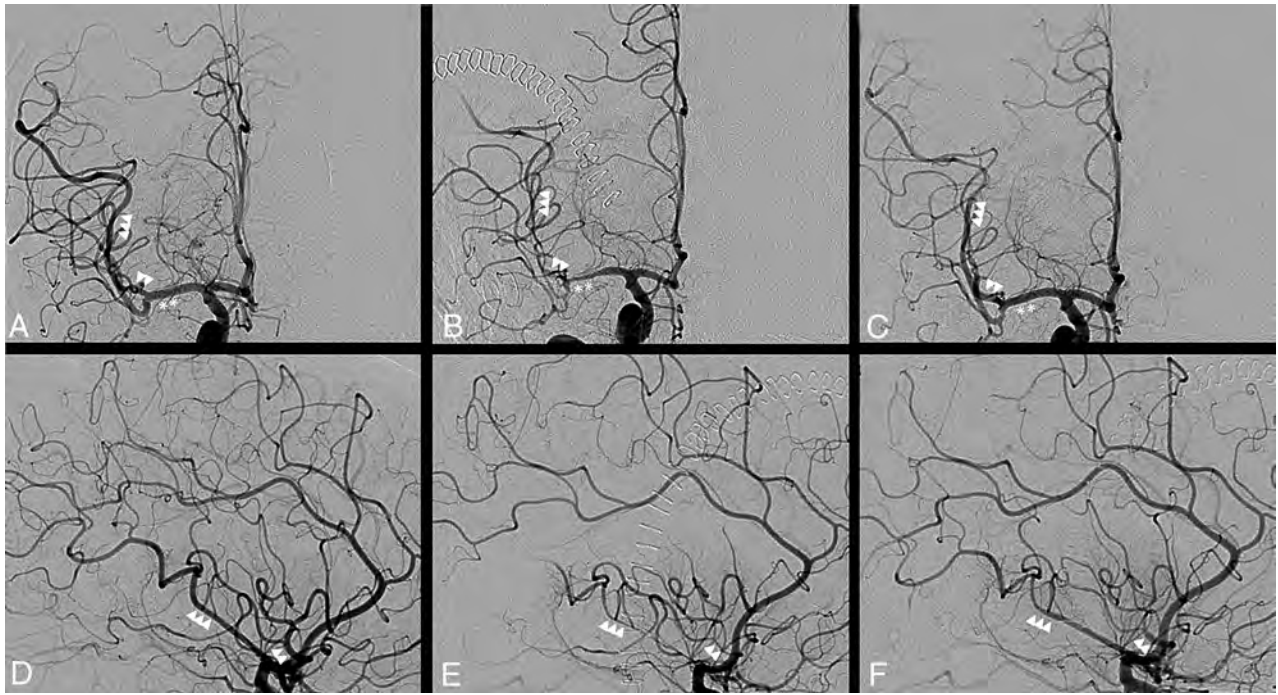


FIG 3. An example of distal transluminal balloon angioplasty of the anterior and posterior M2 branches of the right middle cerebral artery (same patient as in Fig 1). Front (A–C) and lateral (D–F) angiograms of the right internal carotid artery. DSA before angioplasty (B and E) shows a severe vasospasm (60%) of M1 (double star) and the anterior (double arrowhead) and posterior (triple arrowhead) M2 branches, with distal delayed enhancement compared with DSA before vasospasm (A and D), which is cured after a distal balloon angioplasty procedure (C and F).

Table 3: Outcome of patients with aSAH

	Total (N = 392)	Period 1 (n = 160) ^a	Period 2 (n = 232) ^a	P Value
Complications of angioplasty				
Cerebral infarction (No.) (%)	10 (2.5%)	4 (2.5%)	6 (2.6%)	.1
Intracranial hemorrhage (No.) (%)	4 (0.7%)	1 (0.6%)	3 (1.3%)	.64
Malignant edema (No.) (%)	4 (1%)	4 (2.5%)	0 (0)	.02
DCIn				
DCIn (No.) (%)	38 (9.6%)	20 (12.5%)	18 (7.7%)	.11
Postangioplasty DCIn (No.) (%)	17 (4.3%)	12 (7.5%)	5 (2.2%)	.01
DCIn without angioplasty (No.) (%)	26 (6.6%)	12 (7.5%)	14 (6.0%)	.27
New angioplasty (No.) (%)	49 (12%)	30 (19%)	19 (8%)	.002
1-Month death (No.) (%)	42 (11%)	18 (11%)	24 (10%)	.45
6- to 12-Month mRS ≤ 2 (No.) (%)	300 (76%)	117 (73%)	183 (79%)	.12

^aPeriod 1/period 2 (see Table 1).

bral embolism.⁴ However, arterial ruptures have been reported using a compliant balloon, especially in small and distal arteries.¹⁵ In that setting, most interventional neuroradiologists do not perform balloon angioplasty beyond the first segments of the cerebral arteries. Balloon angioplasty using noncompliant rather than compliant balloons has been suggested to prevent any overdistension and injury of the artery.¹⁶ However, in our experience, this technique was associated with a higher rate of recurrent vasospasm or failure of angioplasty or dissection because of the difficulty of choosing the right diameter of the balloon and navigating with a more rigid balloon catheter.

The feasibility of distal balloon angioplasty using an extracompliant balloon has been recently reported. Our study is the first, to our knowledge, to report a better efficacy with the same safety of this approach compared with conventional angioplasty to prevent DCIn. Its efficacy may be explained by both the lasting and distal effects of distal balloon angioplasty on vasospasm. Kohama et al¹⁷

showed that symptomatic vasospasm is due, in 30% of patients, to isolated vasospasm of the second segment of the cerebral arteries. The vasospasm of these segments cannot be treated by proximal balloon angioplasty. The recent use of an extracompliant balloon for distal balloon angioplasty probably explains the excellent safety of this approach in our series and that of Santillan et al.⁸ Extracompliant balloons navigate better than noncompliant balloons. When the balloon is inflated over the nominal diameter of the artery, it first tends to increase

its length rather than its diameter as shown in Fig 2. Thus, extracompliant balloons are commonly used for a remodeling technique to treat distal aneurysms.

Our study failed to prove the clinical benefit of distal balloon angioplasty in the aSAH population compared with the conventional approach, despite a lower rate of postangioplasty DCIn. We hypothesize that our study may have lacked power using the mRS scale, which underestimates cognitive impairment¹⁸ or by including, in the analysis, patients with aSAH rather than only those with angioplasty (see Limitations below). We also speculate that the higher rate of patients treated by intravenous milrinone in the second period may have had adverse confounding effects on clinical outcome.¹⁰ Comparison of our results with recent control groups of randomized trials is shown in Table 4.^{8,19,20} Our cohort of patients during the second period tended to have a lower rate of DCIn and a better rate of favorable outcome, with quite similar

Table 4: Comparative outcome with recent studies^a

	Fisher \geq 3	WFNS < IV	DCIn	Angioplasty/Approach	mRS \geq 4	Death
Our study (N = 232)	83%	77%	8%	42%/Distal balloon angioplasty	17%	10%
Matsuda et al 2016 ²⁰ (N = 74)	NA	92%	11%	18%/Conventional	18%	NA
Macdonald et al 2012 ¹⁹ (N = 189)	>85%	84%	13%	21%/Conventional	24%	6%
Santillan et al 2011 ⁸ (N = 32) ^b	65%	60%	NA	100%/Distal balloon angioplasty	17%	0%

Note:—NA indicates not applicable.

^a Our results during the second period (with distal balloon angioplasty) were compared with those in the series of Santillan et al⁸ and control groups of recent randomized aSAH trials.

^b Only patients who had an angioplasty of vasospasm were included.

baseline characteristics and a 2-times higher rate of angioplasty using a distal balloon rather than conventional angioplasty. Santillan et al⁸ reported a similar rate of new angioplasty (7.5%), a lower rate of procedure-related symptomatic complications (0%), and a higher rate of mRS < 2 outcome in a series of 32 patients treated by distal balloon angioplasty (82%). Better baseline characteristics may explain such differences in outcome compared with our series.

Our study reports complications with distal balloon angioplasty. The possible occurrence of arterial dissection, even if most are asymptomatic, underlines the importance of a careful technique of navigation and balloon inflation as described in the Materials and Methods. In our experience, arterial dissections occurred more often during catheterization of angulated arteries rather than during balloon inflation. No arterial rupture was observed in our study. Santillan et al⁸ reported 1 rupture of a remnant clipped communicating aneurysm during navigation. A full dose of heparin should be given during the procedure to prevent embolism (except in the presence of a large infarction). Angioplasty should not be performed in territories with an extensive infarct, given the high risk of reperfusion injury. Navigation may fail in angled or distal branches. Finally, our study shows that most of DCIn occur before any angioplasty. Further studies are needed to better determine indications of angioplasty as a preventive approach.

Limitations

Our study was retrospective and may have introduced interpretation biases. Safety and efficacy were assessed by 2 observers, including 1 independent of the treatment, to limit these biases. DCIn determination and angioplasty data were blinded, and clinical outcome was assessed by 1 independent observer.

The historical comparison may have introduced confounding factors. The higher rate of patients treated by intravenous vasodilators and angioplasty in the second period may have affected the DCIn rate (the higher the number of patients treated, the more likely it is that DCIn had been prevented). Some intravenous vasodilators such as clazosentan in the Conscious-3 (Clazosentan in Aneurysmal Subarachnoid Hemorrhage) trial are associated with a lower rate of DCIn.¹⁹ However, there is still no evidence of the efficacy effect of intravenous milrinone in the literature. Some authors even question intravenous vasodilators possibly being associated with a higher risk of adverse effects.^{10,20,21} We also analysed 'postangioplasty DCIn' and compared angioplasty strategy and subgroup of patient with and without intravenous milrinone. Actually, the rate of patient treated by angioplasty is more prone to have a bad confounding effect on 'postangioplasty DCIn' since

the higher the number of patients treated the more likely it is that DCIn had occurred rather after that without angioplasty.

The subgroup analysis of patients with high-grade vasospasm was not possible in the current study. Transcranial Doppler data were not available retrospectively for all the patients or for all the territories (including distal arteries). CTA and DSA data were available only in patients with high suspicion or high risk of delayed cerebral ischemia. By including only patients with angioplasty, we have shown a lower rate of DCIn and a higher rate of favorable outcome during the second period. However, these results are questionable because the higher rate of angioplasty during the second period, probably due to larger indication criteria, artificially decreases the ratio between DCIn or favorable outcome and angioplasty. Thus, all patients with aSAH (rather than only those with angioplasty or distal angioplasty) were included in the main analysis, even if this inclusion reduces the power of the study to show a benefit of distal balloon angioplasty.

CONCLUSIONS

Our study suggests that distal balloon angioplasty decreases the risk of DCIn and recurrence of vasospasm after angioplasty compared with the conventional approach of angioplasty. Randomization of distal balloon angioplasty versus no angioplasty in patients with a high risk of DCIn is warranted to provide evidence of its clinical benefit.

REFERENCES

1. Aburto-Murrieta Y, Marquez-Romero JM, Bonifacio-Delgadillo D, et al. **Endovascular treatment: balloon angioplasty versus nimodipine intra-arterial for medically refractory cerebral vasospasm following aneurysmal subarachnoid hemorrhage.** *Vasc Endovascular Surg* 2012;46:460–65 CrossRef Medline
2. Khatri R, Memon MZ, Zacharatos H, et al. **Impact of percutaneous transluminal angioplasty for treatment of cerebral vasospasm on subarachnoid hemorrhage patient outcomes.** *Neurocrit Care* 2011; 15:28–33 CrossRef Medline
3. Abruzzo T, Moran C, Blackham KA, et al. **Invasive interventional management of post-hemorrhagic cerebral vasospasm in patients with aneurysmal subarachnoid hemorrhage.** *J Neurointerv Surg* 2012;4:169–77 CrossRef Medline
4. Albanese E, Russo A, Quiroga M, et al. **Ultrahigh-dose intraarterial infusion of verapamil through an indwelling microcatheter for medically refractory severe vasospasm: initial experience—clinical article.** *J Neurosurg* 2010;113:913–22 CrossRef Medline
5. Anderegg L, Beck J, Z'Graggen WJ, et al. **Feasibility and safety of repeat instant endovascular interventions in patients with refractory cerebral vasospasms.** *AJNR Am J Neuroradiol* 2017;38:561–67 CrossRef Medline
6. Macdonald RL. **Delayed neurological deterioration after subarachnoid haemorrhage.** *Nat Rev Neurol* 2014;10:44–58 CrossRef Medline
7. Vergouwen MD. **Vasospasm versus delayed cerebral ischemia as an**

- outcome event in clinical trials and observational studies.** *Neurocrit Care* 2011;15:308–11 CrossRef Medline
8. Santillan A, Knopman J, Zink W, et al. **Transluminal balloon angioplasty for symptomatic distal vasospasm refractory to medical therapy in patients with aneurysmal subarachnoid hemorrhage.** *Neurosurgery* 2011;69:95–101; discussion 102 CrossRef Medline
 9. Connolly ES Jr, Rabinstein AA, Carhuapoma JR, et al; American Heart Association Stroke Council, Council on Cardiovascular Radiology and Intervention, Council on Cardiovascular Nursing, Council on Cardiovascular Surgery and Anesthesia, Council on Clinical Cardiology. **Guidelines for the management of aneurysmal subarachnoid hemorrhage: a guideline for healthcare professionals from the American Heart Association/American Stroke Association.** *Stroke* 2012;43:1711–37 CrossRef Medline
 10. Lannes M, Zeiler F, Guichon C, et al. **The use of milrinone in patients with delayed cerebral ischemia following subarachnoid hemorrhage: a systematic review.** *Can J Neurol Sci* 2017;44:152–60 CrossRef Medline
 11. Labeyrie MA, Civelli V, Reiner P, et al. **Prevalence and treatment of spontaneous intracranial artery dissections in patients with acute stroke due to intracranial large vessel occlusion.** *J Neurointerv Surg* 2018;10:761–64 CrossRef Medline
 12. Vergouwen MD, Vermeulen M, van Gijn J, et al. **Definition of delayed cerebral ischemia after aneurysmal subarachnoid hemorrhage as an outcome event in clinical trials and observational studies: proposal of a multidisciplinary research group.** *Stroke* 2010;41:2391–95 CrossRef Medline
 13. Boulouis G, Labeyrie MA, Raymond J, et al. **Treatment of cerebral vasospasm following aneurysmal subarachnoid haemorrhage: a systematic review and meta-analysis.** *Eur Radiol* 2017;27:3333–42 CrossRef Medline
 14. Linfante I, Delgado-Mederos R, Andreone V, et al. **Angiographic and hemodynamic effect of high concentration of intra-arterial nicardipine in cerebral vasospasm.** *Neurosurgery* 2008;63:1080–86; discussion 86–87 CrossRef Medline
 15. Zwienerberg-Lee M, Hartman J, Rudisill N, et al; Balloon Prophylaxis for Aneurysmal Vasospasm (BPAV) Study Group. **Effect of prophylactic transluminal balloon angioplasty on cerebral vasospasm and outcome in patients with Fisher grade III subarachnoid hemorrhage: results of a phase II multicenter, randomized, clinical trial.** *Stroke* 2008;39:1759–65 CrossRef Medline
 16. Eskridge JM, McAuliffe W, Song JK, et al. **Balloon angioplasty for the treatment of vasospasm: results of first 50 cases.** *Neurosurgery* 1998;42:510–16; discussion 16–17 CrossRef Medline
 17. Kohama M, Sugiyama S, Sato K, et al. **Difference in transcranial Doppler velocity and patient age between proximal and distal middle cerebral artery vasospasms after aneurysmal subarachnoid hemorrhage.** *Cerebrovasc Dis Extra* 2016;6:32–39 CrossRef Medline
 18. Eagles ME, Tso MK, Macdonald RL. **Cognitive impairment, functional outcome and delayed cerebral ischemia after aneurysmal subarachnoid hemorrhage.** *World Neurosurg* 2019 Jan 10. [Epub ahead of print] CrossRef Medline
 19. Macdonald RL, Higashida RT, Keller E, et al. **Randomized trial of clazosentan in patients with aneurysmal subarachnoid hemorrhage undergoing endovascular coiling.** *Stroke* 2012;43:1463–69 CrossRef Medline
 20. Matsuda N, Naraoka M, Ohkuma H, et al. **Effect of cilostazol on cerebral vasospasm and outcome in patients with aneurysmal subarachnoid hemorrhage: a randomized, double-blind, placebo-controlled trial.** *Cerebrovasc Dis* 2016;42:97–105 CrossRef Medline
 21. Shen J, Pan JW, Fan ZX, et al. **Dissociation of vasospasm-related morbidity and outcomes in patients with aneurysmal subarachnoid hemorrhage treated with clazosentan: a meta-analysis of randomized controlled trials.** *J Neurosurg* 2013;119:180–89 CrossRef Medline

Pretreatment Anterior Choroidal Artery Infarction Predicts Poor Outcome after Thrombectomy in Intracranial ICA Occlusion

 B.H. Baek,  Y.Y. Lee,  S.K. Kim, and  W. Yoon

ABSTRACT

BACKGROUND AND PURPOSE: Predictors of outcome after endovascular thrombectomy have not been investigated adequately in patients with intracranial ICA occlusions. This study aimed to assess the impact of anterior choroidal artery infarction in pretreatment DWI on the outcome of patients with acute intracranial ICA occlusion who underwent thrombectomy.

MATERIALS AND METHODS: This study included 113 patients with acute intracranial ICA occlusion who underwent DWI followed by thrombectomy between January 2011 and July 2016. Characteristics and outcomes were compared between the groups positive and negative for anterior choroidal artery infarction and patients with good outcomes (90-day mRS 0–2) and poor outcomes (mRS 3–6). Binary logistic regression analyses were performed to identify independent predictors of a good outcome.

RESULTS: On pretreatment DWI, anterior choroidal artery infarction was observed in 60 patients (53.1%). Good outcomes were significantly less frequent in the group positive for anterior choroidal artery infarction than in the group negative for it (25% versus 49.1%, $P = .008$). Parenchymal hemorrhage occurred only in the group positive for anterior choroidal artery infarction (13.3% versus 0%, $P = .007$). In the multivariate logistic regression analysis, independent predictors of good outcome were an absence of anterior choroidal artery infarction (OR, 0.333; 95% CI, 0.135–0.824; $P = .017$) and successful reperfusion (OR, 5.598; 95% CI, 1.135–27.604; $P = .034$).

CONCLUSIONS: Pretreatment anterior choroidal artery infarction is associated with parenchymal hemorrhage and poor outcome after thrombectomy in patients with acute intracranial ICA occlusion. In addition, the absence of anterior choroidal artery infarction and successful reperfusion were independent predictors of good outcome after thrombectomy in acute intracranial ICA occlusion.

Despite recent advances in endovascular therapy for occlusion of large intracranial vessels, occlusion of the intracranial ICA is still associated with poor clinical outcomes mainly due to a substantial clot burden and poor collateral circulation.^{1,2} Recent studies have reported that the rate of a good outcome is 34%–39% after endovascular thrombectomy in patients with intracranial ICA occlusions.^{1,2} Understanding the prognostic factors after endovascular thrombectomy may help refine patient-selection criteria and improve treatment outcomes in this specific group of patients. Although a few studies have investigated the predictors of outcomes following thrombectomy in patients with acute anterior circulation stroke,^{2,3} such predictors have not been in-

vestigated adequately in patients with acute intracranial ICA occlusions.

Occlusion of the intracranial ICA may compromise the origin of the anterior choroidal artery, causing anterior choroidal artery territory infarction. The anterior choroidal artery arises from the terminal segment of the ICA and supplies critical brain structures, including the uncus, amygdala, posterior limb of the internal capsule, lateral thalamus, tail of the caudate nucleus, rostral part of the hippocampus, and the lateral choroid plexus.^{4–8} Anterior choroidal artery territory infarction usually has a poor prognosis. Lee et al⁷ reported that 88% of patients with full anterior choroidal artery territory infarct or partial infarct involving the anterior choroidal artery territory other than the medial temporal lobe had a poor 90-day outcome (mRS 3–6). Anterior choroidal artery infarction can be found on imaging before endovascular thrombectomy in patients with acute intracranial ICA occlusion. However, the prognostic impact of anterior choroidal artery infarction observed on pretreatment imaging has not yet been investigated in patients with intracranial ICA occlusions, to our knowledge. Therefore, the purpose of this study was to investigate the prognostic

Received April 4, 2019; accepted after revision June 13.

From the Department of Radiology, Chonnam National University Medical School, Gwangju, Republic of Korea.

Please address correspondence to Woong Yoon, MD, PhD, Department of Radiology, Chonnam National University Medical School, Chonnam National University Hospital, 42 Jebong-ro, Dong-gu, Gwangju, 61469, Republic of Korea; e-mail: radyoon@jnu.ac.kr

<http://dx.doi.org/10.3174/ajnr.A6126>

factors of treatment outcomes following endovascular thrombectomy in patients with acute stroke due to intracranial ICA occlusion and the impact of anterior choroidal artery infarction on pretreatment DWI on treatment outcomes in these patients.

MATERIALS AND METHODS

Patients

From January 2011 to July 2016, a total of 380 patients presenting with acute anterior circulation stroke due to occlusion of the intracranial ICA ($n = 116$) or MCA ($n = 264$) were treated with endovascular thrombectomy at a comprehensive stroke center. Of 116 patients with ICA occlusion, 3 without pretreatment DWI data were excluded. Thus, a total of 113 patients with acute intracranial ICA occlusion who had pretreatment DWI before thrombectomy were enrolled in the study.

All patients underwent nonenhanced cranial CT and multimodal MR imaging, which included DWI, gradient-echo imaging, FLAIR, and 3D-TOF-MRA before endovascular therapy. Intravenous rtPA was administered to eligible patients. The inclusion criteria for endovascular therapy were the following: femoral artery puncture initiated within 6 hours of stroke onset, a baseline NIHSS score of ≥ 4 , no evidence of intracranial hemorrhage on pretreatment imaging, and infarct volume less than one-third of the MCA territory on pretreatment imaging. Clinical and radiologic data were collected prospectively in the stroke data base at our institution. This study was approved by our institutional ethics committee.

DWI Assessment

Pretreatment MR imaging examinations were performed using a 1.5T MR imaging scanner (Signa HDxt; GE Healthcare, Milwaukee, Wisconsin). DWI sequences were obtained in the axial plane using a single-shot, spin-echo EPI technique with the following parameters: TR = 9000 ms, TE = 80 ms, section thickness = 4 mm, intersection gap = 0 mm, FOV = 260×260 mm, and b-values = 0 and 1000 s/mm^2 . On DWI, anterior choroidal artery infarction was defined as an acute infarction located in the uncus, amygdala nucleus, posterior limb of the internal capsule, tail of the caudate nucleus, medial segment of the globus pallidus, lateral thalamus, optic radiation, cerebral peduncle, or hippocampus.⁴ DWI was evaluated retrospectively by 2 neuroradiologists who were blinded to the patients' clinical and angiographic information. Two readers also assessed the DWI-ASPECTS. Conclusions were reached by the consensus of 2 readers in the case of disagreement.

Endovascular Thrombectomy

Cerebral angiography and endovascular therapy were performed with the patient under local anesthesia. Intracranial ICA was defined as part of the ICA segment from the ophthalmic segment to the T-bifurcation. Intracranial ICA occlusion was confirmed by catheter DSA in all patients. Endovascular thrombectomy with either a Solitaire stent (Covidien, Irvine, California) or Trevo stent (Stryker, Kalamazoo, Michigan) was performed as the front-line thrombectomy technique. If the front-line thrombectomy was unsuccessful in achieving reperfusion, contact aspiration thrombectomy was performed using an intermediate catheter or a

Penumbra reperfusion catheter (Penumbra, Alameda, California).^{9,10} A balloon-guide catheter was not used in this study. When a patient had a simultaneous tandem occlusion at the proximal cervical segment of the ICA, carotid angioplasty and stent placement were performed before intracranial endovascular thrombectomy. Intracranial angioplasty with or without stent placement was also performed when underlying severe ($>70\%$) intracranial atherosclerotic stenosis was found at the occlusion site. Patients who underwent either intracranial angioplasty/stent placement or carotid stent placement received aspirin and clopidogrel immediately following the endovascular treatment. In these patients, dual-antiplatelet therapy was continued for at least 3 months after discharge. Intracranial reperfusion status was assessed on the final angiogram and classified according to the modified TICI scale.¹¹ Successful reperfusion was defined as a modified TICI grade of 2b or 3.

Outcome Measures

All patients underwent nonenhanced CT immediately and 24 hours following endovascular thrombectomy. Intracerebral hemorrhage was assessed on posttreatment CT scans and classified as either hemorrhagic infarction or parenchymal hemorrhage according to the European Cooperative Acute Stroke Study II (ECASS II) criteria.¹² Symptomatic hemorrhage was defined as any intracranial hemorrhage that caused neurologic deterioration (NIHSS score increase of ≥ 4 points). Stroke subtype was determined at the time of discharge by a stroke neurologist on the basis of the Trial of ORG 10172 in Acute Stroke Treatment (TOAST) classification.¹³ Clinical outcomes were assessed by a stroke neurologist using the mRS during an outpatient visit 3 months posttreatment. When patients were unable to visit, the mRS score was assessed via telephone interview. A good outcome was defined as mRS score of 0–2.

Statistical Analysis

Continuous variables were presented as medians and interquartile ranges, whereas discrete variables were presented as numbers and percentages. The χ^2 test or Fisher exact test was used for categorical variables, and the Mann-Whitney U test was used to compare continuous variables. We compared differences in patient characteristics and treatment outcomes between the groups positive and negative for anterior choroidal artery infarction and between patients with good and poor outcomes. Binary logistic regression analysis was performed to identify independent predictors of a good 90-day outcome. Finally, the associations between characteristics and good 90-day outcome were investigated only among patients with successful reperfusion. Variables with a P value of $< .05$ from the univariate analysis and those considered clinically relevant (age and baseline NIHSS) were included for the multivariate analysis. Statistical analysis was performed using SPSS software (Version 23.0; IBM, Armonk, New York) with $P < .05$ considered significant.

RESULTS

Data from 113 patients (53 men and 60 women; median age, 74 years) were analyzed. The median baseline NIHSS score was 14. Intravenous rtPA was administered in 53% of patients. The

Table 1: Comparison of characteristics according to the presence or absence of anterior choroidal artery infarction on pretreatment DWI^a

	All Patients (n = 113)	Positive for Anterior Choroidal Artery Infarction (n = 60)	Negative for Anterior Choroidal Artery Infarction (n = 53)	P
Age (yr)	74 (63–78)	73 (62.25–78)	74 (65–80.50)	.152
Sex, male	53 (46.9)	26 (43.3)	27 (50.9)	.419
Risk factors				
Hypertension	76 (67.3)	41 (68.3)	35 (66)	.795
Diabetes mellitus	31 (27.4)	20 (33.3)	11 (20.8)	.135
Dyslipidemia	31 (27.4)	16 (26.7)	15 (28.3)	.846
Smoking	25 (22.1)	8 (13.3)	17 (32.1)	.017
Atrial fibrillation	69 (61.1)	38 (63.3)	31 (58.5)	.598
Coronary artery disease	19 (16.8)	10 (16.7)	9 (16.9)	.964
Previous stroke or TIA	16 (14.2)	7 (11.7)	9 (16.9)	.419
Congestive heart failure	7 (6.2)	4 (6.7)	3 (5.7)	1.000
Intravenous thrombolysis	60 (53.1)	35 (58.3)	25 (47.2)	.235
DWI-ASPECTS	7 (5–8)	6 (4–8)	7 (5.5–8)	.059
Time to puncture (median) (IQR) (min)	220 (160–290)	205 (151.25–297.50)	240 (179–298)	.211
Procedure duration (min)	35 (25–50)	35 (25–50)	42 (23–53.5)	.490
Time to reperfusion (min)	253 (197–337)	236.50 (186.25–332.00)	282 (206.5–350)	.214
Baseline NIHSS score	14 (11–17)	14 (12–17)	15 (10–17)	.701
Underlying intracranial atherosclerotic stenosis	12 (10.6)	4 (6.7)	8 (15.1)	.221
Cervical ICA tandem occlusion	10 (8.8)	3 (5)	7 (13.2)	.185
Stroke subtype				.509
Cardioembolism	74 (65.5)	42 (70)	32 (60.4)	
Large-artery atherosclerosis	18 (15.9)	6 (10)	12 (22.6)	
Undetermined	19 (16.8)	12 (20)	7 (13.2)	
Other	2 (1.8)	0	2 (3.8)	

Note:—IQR indicates interquartile range.

^a Values are presented as No. (%) or median (IQR).

Table 2: Comparison of treatment outcomes between patients with and without anterior choroidal artery infarction^a

	All Patients (n = 113)	Positive for Anterior Choroidal Artery Infarction (n = 60)	Negative for Anterior Choroidal Artery Infarction (n = 53)	P
Successful reperfusion	89 (78.8)	45 (75)	44 (83.0)	.298
90-Day mRS 0–2	41 (37.2)	15 (25)	26 (49.1)	.008
Parenchymal hemorrhage	8 (7.1)	8 (13.3)	0	.007
Symptomatic hemorrhage	4 (3.5)	4 (6.7)	0	.121
90-Day mortality	12 (10.6)	6 (10)	6 (11.3)	.820

^a Values are presented as No. (%).

stroke subtype was cardioembolism in 74 patients (65.5%), large-artery atherosclerosis in 18 patients (15.9%), undetermined in 19 patients (16.8%), and other in 2 patients (1.8%). The median DWI-ASPECTS was 7. Twelve patients (10.6%) had underlying severe intracranial atherosclerotic stenosis, and 10 patients (8.8%) underwent carotid artery stent placement before endovascular thrombectomy. Overall, successful reperfusion was achieved in 79% of patients (89/113), and a good 90-day outcome, in 37% of patients (41/113). Parenchymal hemorrhage occurred in 7.1% of patients (8/113), and symptomatic hemorrhage, in 3.5% (4/113). The 90-day mortality rate was 10.6% (12/113).

Association between Anterior Choroidal Artery Territory Infarction and Treatment Outcomes

Anterior choroidal artery infarction was observed in 53.1% of patients (60/113) on pretreatment DWI, distributed as follows: the medial temporal lobe including the uncus and amygdala nucleus in 57 patients, the posterior limb of the internal capsule in 36

patients, tail of the caudate nucleus in 12 patients, optic radiation in 7 patients, lateral thalamus in 6 patients, medial pallidum in 5 patients, hippocampus in 2 patients, and cerebral peduncle in 1 patient. Among these, 21 patients (35%) had anterior choroidal artery infarction confined to the medial temporal lobe (uncus, amygdala, or both). Comparisons of the clinical and procedural characteristics between the groups positive and negative for anterior choroidal artery infarction are shown in Table 1.

Smoking history was less frequent in the group positive for anterior choroidal artery infarction than in the group negative for it. No significant differences were found between the 2 groups in other characteristics.

Comparisons of the treatment outcomes between the groups positive and negative for anterior choroidal artery infarction are shown in Table 2. A good 90-day outcome was significantly less frequent in the group positive for anterior choroidal artery infarction than the group negative for it (25% versus 49.1%, $P = .008$). Parenchymal hemorrhage occurred only in the group positive for anterior choroidal artery infarction (13.3% versus 0%, $P = .007$). Parenchymal hemorrhage occurred in the anterior choroidal artery territory in 3 patients (all in the uncus and amygdala) (Fig 1) and in other locations in 5 patients (basal ganglia in 5 patients, frontal lobe in 2 patients, and lateral temporal lobe in 1 patient). All 3 patients with parenchymal hemorrhage in the anterior choroidal artery territory had concomitant parenchymal hemor-

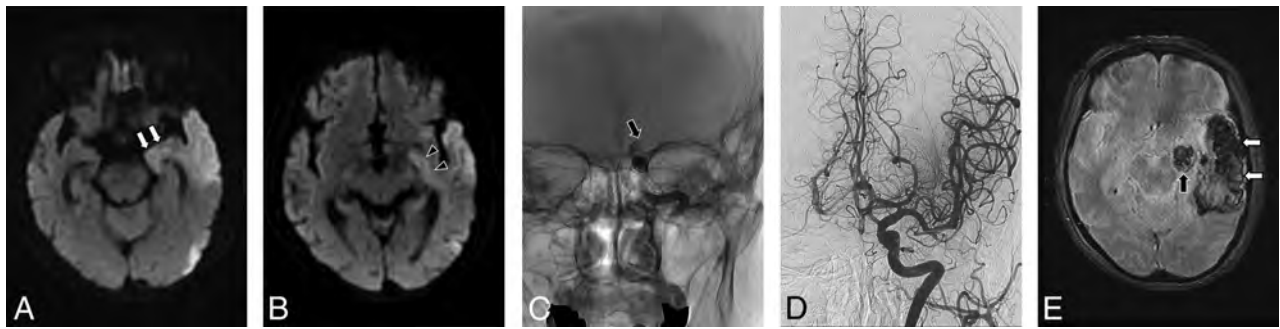


FIG 1. A 74-year-old female patient with acute stroke due to acute intracranial ICA occlusion. DWI (A and B) shows acute infarctions involving the left medial temporal lobe (arrows), left internal capsule (arrowheads), and other parts of left temporal lobe. C, A delayed-phase radiograph obtained after a left ICA angiographic run shows complete occlusion (arrow) at the distal intracranial portion of the left ICA. D, Left ICA angiogram obtained after stent-retriever thrombectomy shows complete recanalization of the left ICA with good distal perfusion. E, Gradient-echo MR image obtained 1 day after thrombectomy shows parenchymal hematomas in the left medial temporal lobe (black arrow) and other parts of the left temporal lobe (white arrows).

Table 3: Comparison of characteristics between patients with good and poor outcomes^a

	All Patients (n = 113)	Good Outcome (n = 41)	Poor Outcome (n = 72)	P
Age (yr)	74 (63–78)	70 (62–77.5)	74 (64–79.75)	.105
Sex, male	53 (46.9)	21 (51.2)	32 (44.4)	.488
Risk factors				
Hypertension	76 (67.3)	27 (65.9)	49 (68.1)	.810
Diabetes mellitus	31 (27.4)	8 (19.5)	23 (31.9)	.154
Dyslipidemia	31 (27.4)	13 (31.7)	18 (25)	.442
Smoking	25 (22.1)	12 (29.3)	13 (18.1)	.167
Atrial fibrillation	69 (61.1)	21 (51.2)	48 (66.7)	.105
Coronary artery disease	19 (16.8)	10 (24.4)	9 (12.5)	.104
Previous stroke or TIA	16 (14.2)	6 (14.6)	10 (13.9)	.913
Congestive heart failure	7 (6.2)	4 (9.8)	3 (4.2)	.253
Intravenous thrombolysis	60 (53.1)	21 (51.2)	39 (54.2)	.763
Anterior choroidal artery infarction on DWI	60 (53.1)	15 (36.6)	45 (62.5)	.008
DWI-ASPECTS	7 (5–8)	7 (5–9)	6 (5–8)	.044
Time to procedure (min)	220 (160–290)	225 (138.5–292.5)	220 (161.25–297.5)	.770
Procedural time (min)	35 (25–50)	30 (20–45)	43 (27.25–58.75)	.023
Time to reperfusion (min)	253 (197–337)	252 (173–338)	258 (200.75–358)	.429
Baseline NIHSS score	14 (11–17)	13 (10–17)	15 (12–17)	.182
Underlying severe intracranial stenosis	12 (10.6)	8 (19.5)	4 (5.6)	.028
Cervical ICA tandem occlusion	10 (8.8)	3 (7.3)	7 (9.7)	.745
Stroke etiology				.411
Cardioembolism	74 (65.5)	24 (58.5)	50 (69.4)	
Large-artery atherosclerosis	18 (15.9)	10 (24.4)	8 (11.1)	
Undetermined	19 (16.8)	5 (12.2)	14 (19.4)	
Other	2 (1.8)	2 (4.9)	0	
Successful reperfusion	89 (78.8)	39 (95.1)	50 (69.4)	.001
Parenchymal hemorrhage	8 (7.1)	0	8 (11.1)	.049
Symptomatic hemorrhage	4 (3.5)	0	4 (5.6)	.295

^a Values are presented as No. (%) or median (IQR).

rhage in the basal ganglia and lobar hemorrhages. Therefore, all 8 patients developed parenchymal hemorrhage in the basal ganglia. The epicenter of hematoma was the basal ganglia in 6 patients, the lateral temporal lobe in 1 patient, and the frontal lobe in 1 patient. We found no significant differences between the 2 groups in terms of successful reperfusion, symptomatic hemorrhage, and 90-day mortality. Of 21 patients with anterior choroidal artery infarction confined to the medial temporal lobe, 19.1% (4/21) had good outcomes. In the group positive for anterior choroidal artery infarction, there was no statistically significant difference in the rate of good outcome between patients with internal capsule involvement and those without it (20.8% versus 27.8%, $P = .543$).

Predictors of Clinical Outcomes

Comparisons of baseline characteristics and treatment outcomes according to 90-day functional outcome are shown in Table 3. In univariate analysis, the following baseline or procedural variables were associated with a good 90-day outcome: absence of anterior choroidal artery territory infarction ($P = .008$), higher DWI-ASPECTS ($P = .044$), shorter procedural time ($P = .023$), presence of underlying severe intracranial stenosis ($P = .028$), and successful reperfusion ($P = .001$).

In multivariate logistic regression analysis adjusted for potential confounders (age, baseline NIHSS score, anterior choroidal artery infarction, DWI-ASPECTS, procedural time, underlying severe intracranial stenosis, and successful reperfusion), anterior

choroidal artery infarction (OR, 0.333; 95% CI, 0.135–0.824; $P = .017$; Fig 2) and successful reperfusion (OR, 5.598; 95% CI, 1.135–27.604; $P = .034$; Fig 3) were independent predictors of a good outcome at 90 days (Table 4).

In subgroup analysis including only 89 patients with successful reperfusion, the following baseline or procedural variables were associated with a good 90-day outcome in the univariate analysis: absence of anterior choroidal artery territory infarction ($P = .004$) and higher DWI-ASPECTS ($P = .032$). In multivariate logistic regression analysis adjusted for potential confounders (age, baseline NIHSS score, anterior choroidal artery infarction, and DWI-ASPECTS), absence of anterior choroidal artery territory infarction was the only independent predictor of a good 90-day outcome (OR, 0.291; 95% CI, 0.114–0.742; $P = .010$) in this subgroup.

DISCUSSION

The present study found that anterior choroidal artery infarction commonly occurs in the early period of acute stroke (≤ 6 hours)

due to intracranial ICA occlusion at a rate of 53.1%. In addition, anterior choroidal artery infarction seen on pretreatment DWI was significantly associated with a poor 90-day functional outcome and the occurrence of parenchymal hemorrhage following endovascular thrombectomy in this patient group. Furthermore, an absence of anterior choroidal artery infarction and successful reperfusion were independent predictors of a good 90-day outcome following endovascular thrombectomy in patients with acute intracranial ICA occlusion.

The incidence and topography of anterior choroidal artery infarction in patients with intracranial ICA occlusion who undergo endovascular thrombectomy have not been reported previously, to our knowledge. Our study showed that anterior choroidal artery infarction might occur in approximately half of patients with acute occlusion of the intracranial ICA. Even when the origin of the anterior choroidal artery is occluded in patients with intracranial ICA occlusion, anterior choroidal artery territory infarction may be absent or minimized due to collateral flows from the ipsilateral posterior communicating artery, proximal posterior cerebral artery, temporal and hippocampal branches of the posterior cerebral artery, or the posterior choro-

idal artery.^{14,15} With regard to vascular topography, the medial temporal lobe, including the uncus and amygdala, was the most frequently affected region among patients with anterior choroidal artery infarction in our study, followed by the posterior limb of the internal capsule, tail of the caudate nucleus, optic radiation, lateral thalamus, medial pallidum, hippocampus, and cerebral peduncle. The infarct topography of anterior choroidal artery infarction may also vary according to the anatomic variation and degree of collateral flow. Our study suggests that the medial temporal lobe is the most consistent region supplied from the anterior choroidal artery (95% in our study) and is the region that may have the poorest collateral circulation.

Our study showed that anterior choroidal artery infarction on pretreatment DWI is associated with poor outcomes in patients with acute ICA occlusions even when successful reperfusion was achieved with endovascular thrombectomy. In the present study, good out-

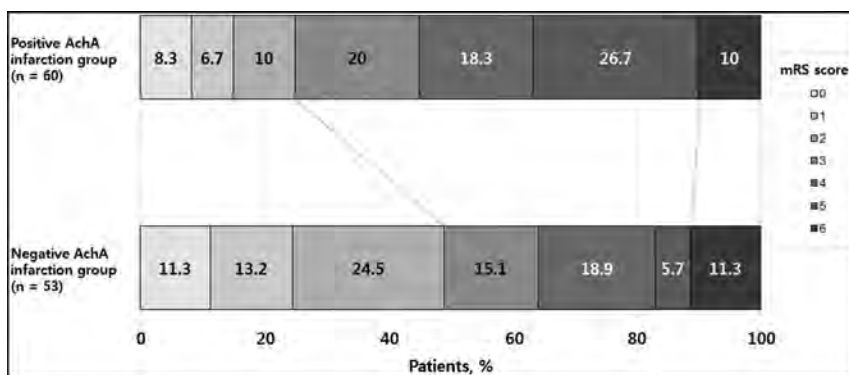


FIG 2. Distribution of mRS scores at 90 days according to the presence or absence of anterior choroidal artery infarction after thrombectomy in patients with acute intracranial ICA occlusion.

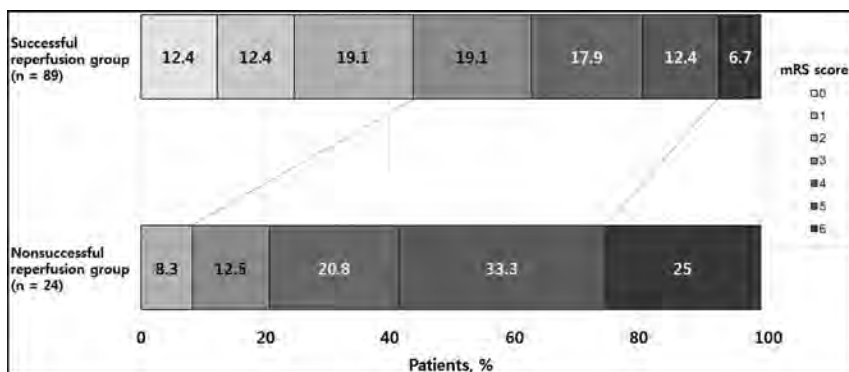


FIG 3. Distribution of mRS scores at 90 days, according to the reperfusion status after thrombectomy in patients with acute intracranial ICA occlusion.

Table 4: Univariate and multivariate binary logistic regression analysis for predictors of good 90-day outcome

Variable	Unadjusted OR (95% CI)	P	Adjusted OR (95% CI)	P
Age, per 1-year increase	0.975 (0.942–1.009)	.149	–	–
Baseline NIHSS score, per 1-point increase	0.922 (0.834–1.019)	.112	–	–
Anterior choroidal artery infarction	0.346 (0.156–0.766)	.009	0.333 (0.135–0.824)	.017
DWI-ASPECTS, per 1-point increase	1.232 (1.004–1.511)	.046	–	–
Procedure duration, per 1-min increase	0.980 (0.961–1.000)	.047	–	–
Underlying severe intracranial stenosis	4.121 (1.157–14.678)	.029	–	–
Successful reperfusion	8.580 (1.901–38.718)	.005	5.598 (1.135–27.604)	.034

comes were less frequent in the group positive for anterior choroidal artery infarction than in the group negative for it for the entire cohort (25% versus 49%, $P = .008$) and the subgroup of patients with successful reperfusion (28.9% versus 59.1%, $P = .004$). In addition, anterior choroidal artery infarction was an independent predictor of outcome on multivariate analyses performed in the entire cohort as well as in the subgroup with successful reperfusion. These findings may not be surprising because the anterior choroidal artery supplies deeply located eloquent areas, such as the internal capsule, amygdala, medial pallidum, thalamus, and hippocampus. Ois et al⁶ reported that 45.2% of patients with an isolated large (largest diameter, ≥ 2 cm) anterior choroidal artery territory infarction without hemispheric infarction had poor outcomes (mRS 3–6) at 3 months. Recently, Rosso et al¹⁶ also found that the involvement of the internal capsule was the strongest predictor of 90-day outcome among DWI-ASPECTS brain regions in patients with left-sided strokes. However, there was no statistically significant difference in the rate of good outcome between patients with internal capsule involvement and those without it ($P = .543$) among patients with pretreatment anterior choroidal artery infarction in our study. This finding may suggest that poor outcomes in the group positive for anterior choroidal artery infarction are mediated not only by the involvement of the internal capsule but also by other factors such as large baseline infarct extent, poor collateral circulation, or development of posttreatment hemorrhage in this group. In the current study, poor outcomes in patients with anterior choroidal artery infarction can be partly attributed to the occurrence of parenchymal hemorrhage, which is known to be a predictor of poor outcomes and mortality after endovascular thrombectomy in patients with anterior circulation large-vessel occlusion.^{2,17} This hemorrhage occurred only in patients with anterior choroidal artery infarction in our study, which may suggest that patients with anterior choroidal artery infarction have a severely hypoperfused lesion due to poor collateral status.¹⁸

To date, only 1 study has investigated the relationship between anterior choroidal artery infarction and functional outcome in patients with ICA occlusion. Lee et al⁷ reported that the absence of anterior choroidal artery infarction or infarction restricted to the medial temporal lobe, compared with other patterns of infarction, had a good discharge outcome (44.4% versus 12.1%) more frequently among 60 patients with ICA occlusions. In our study, only 19% of patients with anterior choroidal artery infarction confined to the medial temporal lobe had good outcomes at 90 days, which seems to be inconsistent with the results of the study of Lee et al. Apart from the inequality of the compared groups and endovascular treatment technique, this discrepancy may be due, in large part, to the differences in the timing of the outcome assessment (90-day versus discharge) and the proportions of stroke subtypes between the 2 studies. Anterior choroidal artery infarction tends to result in neurologic symptom progression,¹⁹ and cardioembolism was more common in our study than the study of Lee et al.

Yoon et al² reported that age, reperfusion status, parenchymal hemorrhage, and baseline NIHSS score were independent predictors of good outcome in 335 patients with acute anterior circulation stroke who underwent modern endovascular thrombec-

tomy. Among patients with acute anterior circulation stroke, those with ICA occlusions have a worse prognosis than those with MCA occlusions, even after endovascular thrombectomy. Therefore, the identification of more specific predictors directly related to ICA occlusions is needed to further improve patient management in acute anterior circulation stroke. However, such investigations have not been reported to date. Our study revealed that pretreatment anterior choroidal artery infarction independently predicts functional outcome after endovascular thrombectomy in acute ICA occlusions. Moreover, anterior choroidal artery infarction was independently associated with 90-day outcome regardless of reperfusion status. This finding suggests that performing DWI before thrombectomy is advantageous in the prognostication of patients with acute ICA occlusion because it is challenging to identify acute ischemic changes within the anterior choroidal artery territory with CT in the hyperacute stage. Our study also confirmed the strong association of successful reperfusion and good outcomes after endovascular thrombectomy in acute large-vessel occlusion, which has been observed in previous studies.^{2,3} In our study, a good outcome was achieved in 44% ($n = 39/89$) of patients with successful reperfusion, but only in 8.3% ($n = 2/24$) of patients without successful reperfusion in the entire cohort. Successful reperfusion was one of the independent predictors of good 90-day outcome (OR, 8.305). Although the rate of successful reperfusion was higher in our study than in previous reports (79% in our study versus 69% in a pooled analysis including 115 patients¹), this rate is unsatisfactory. Considering the importance of successful reperfusion, a more effective endovascular strategy is still needed for patients with acute ICA occlusions.

This study had some limitations. First, this was a retrospective study conducted in a single center. Second, we could not evaluate collateral circulation in this study because contralateral ICA and vertebral angiography were not performed according to our protocol for acute stroke intervention. In addition, the length of occlusion in the ICA, A1 segment of the anterior cerebral artery, and the M1 segment of the MCA could not be evaluated because microcatheter contrast injection was usually not recommended during an endovascular procedure to decrease hemorrhagic complications.²⁰

CONCLUSIONS

Our study suggests that anterior choroidal artery infarction is common during the early period after occlusion of the intracranial ICA, and pretreatment anterior choroidal artery infarction is associated with parenchymal hemorrhage and poor 90-day outcome after modern endovascular thrombectomy. In addition, this study revealed that an absence of anterior choroidal artery infarction and successful reperfusion are significant predictors of good outcomes after thrombectomy in acute intracranial ICA occlusions.

REFERENCES

1. Kappelhof M, Marquering HA, Berkhemer OA, et al. **Intra-arterial treatment of patients with acute ischemic stroke and internal carotid artery occlusion: a literature review.** *J Neurointerv Surg* 2015; 7:8–15 CrossRef Medline
2. Yoon W, Kim SK, Park MS, et al. **Predictive factors for good outcome and mortality after stent-retriever thrombectomy in patients**

- with acute anterior circulation stroke. *J Stroke* 2017;19:97–103 CrossRef Medline
3. Dekker L, Geraedts VJ, Hund H, et al. **Importance of reperfusion status after intra-arterial thrombectomy for prediction of outcome in anterior circulation large vessel stroke.** *Interv Neurol* 2018;7:137–47 CrossRef Medline
 4. Levy R, Duyckaerts C, Hauw JJ. **Massive infarcts involving the territory of the anterior choroidal artery and cardioembolism.** *Stroke* 1995;26:609–13 CrossRef Medline
 5. Palomeras E, Fossas P, Cano AT, et al. **Anterior choroidal artery infarction: a clinical, etiologic and prognostic study.** *Acta Neurol Scand* 2008;118:42–47 Medline
 6. Ois A, Cuadrado-Godia E, Solano A, et al. **Acute ischemic stroke in anterior choroidal artery territory.** *J Neurol Sci* 2009;281:80–84 CrossRef Medline
 7. Lee M, Saver JL, Hao Q, et al; UCLA Stroke Investigators. **Anterior choroidal artery ischaemic patterns predict outcome of carotid occlusion.** *J Neurol Neurosurg Psychiatry* 2012;83:586–90 CrossRef Medline
 8. Sohn H, Kang DW, Kwon SU, et al. **Anterior choroidal artery territory infarction: lesions confined to versus beyond the internal capsule.** *Cerebrovasc Dis* 2013;35:228–34 CrossRef Medline
 9. Yoon W, Jung MY, Jung SH, et al. **Subarachnoid hemorrhage in a multimodal approach heavily weighted toward mechanical thrombectomy with Solitaire stent in acute stroke.** *Stroke* 2013;44:414–19 CrossRef Medline
 10. Kim SK, Yoon W, Moon SM, et al. **Outcomes of manual aspiration thrombectomy for acute ischemic stroke refractory to stent-based thrombectomy.** *J Neurointerv Surg* 2015;7:473–77 CrossRef Medline
 11. Zaidat OO, Yoo AJ, Khatri P, et al; Cerebral Angiographic Revascularization Grading (CARG) Collaborators, STIR Revascularization Working Group, STIR Thrombolysis in Cerebral Infarction (TICI) Task Force. **Recommendations on angiographic revascularization grading standards for acute ischemic stroke: a consensus statement.** *Stroke* 2013;44:2650–63 CrossRef Medline
 12. Larrue V, von Kummer R, Müller A, et al. **Risk factors for severe hemorrhagic transformation in ischemic stroke patients treated with recombinant tissue plasminogen activator: a secondary analysis of the European-Australasian Acute Stroke Study (ECASS II).** *Stroke* 2001;32:438–41 CrossRef Medline
 13. Adams HP Jr, Bendixen BH, Kappelle LJ, et al. **Classification of subtype of acute ischemic stroke: definitions for use in a multicenter clinical trial—TOAST. Trial of Org 10172 in Acute Stroke Treatment.** *Stroke* 1993;24:35–41 CrossRef Medline
 14. Takahashi S, Suga T, Kawata Y, et al. **Anterior choroidal artery: angiographic analysis of variations and anomalies.** *AJNR Am J Neuroradiol* 1990;11:719–29 Medline
 15. Takahashi S, Tobita M, Takahashi A, et al. **Retrograde filling of the anterior choroidal artery: vertebral angiographic sign of obstruction in the carotid system.** *Neuroradiology* 1992;34:504–07 CrossRef Medline
 16. Rosso C, Blanc R, Ly J, et al; ASTER Trial and Pitié-Salpêtrière Investigators. **Impact of infarct location on functional outcome following endovascular therapy for stroke.** *J Neurol Neurosurg Psychiatry* 2019;90:313–19 CrossRef Medline
 17. Nogueira RG, Gupta R, Jovin TG, et al. **Predictors and clinical relevance of hemorrhagic transformation after endovascular therapy for anterior circulation large vessel occlusion strokes: a multicenter retrospective analysis of 1122 patients.** *J Neurointerv Surg* 2015;7:16–21 CrossRef Medline
 18. Mishra NK, Christensen S, Wouters A, et al; DEFUSE 2 Investigators. **Reperfusion of very low cerebral blood volume lesion predicts parenchymal hematoma after endovascular therapy.** *Stroke* 2015;46:1245–49 CrossRef Medline
 19. Derflinger S, Fiebach JB, Böttger S, et al. **The progressive course of neurological symptoms in anterior choroidal artery infarcts.** *Int J Stroke* 2015;10:134–37 CrossRef Medline
 20. Khatri R, Khatri P, Khoury J, et al. **Microcatheter contrast injections during intra-arterial thrombolysis increase intracranial hemorrhage risk.** *J Neurointerv Surg* 2010;2:115–19 CrossRef Medline

GUide sheath Advancement and aspiRation in the Distal petrocavernous internal carotid artery (GUARD) Technique during Thrombectomy Improves Reperfusion and Clinical Outcomes

 S.A. Ansari,  M. Darwish,  R.N. Abdalla,  D.R. Cantrell,  A. Shaibani,  M.C. Hurley,  B.S. Jahromi, and  M.B. Potts

ABSTRACT

BACKGROUND AND PURPOSE: Adjunctive techniques to stent retriever thrombectomy include balloon-guide catheters and/or distal access catheters for aspiration. We describe a novel technique using a flexible, 6 French 088 distal guide sheath advanced past the skull base to augment mechanical thrombectomy. We studied the relative safety and efficacy of this technique in the setting of a combined stent retriever–distal access catheter aspiration thrombectomy protocol.

MATERIALS AND METHODS: We performed a retrospective case-control study of intracranial internal carotid artery or M1–M2 middle cerebral artery occlusions requiring mechanical thrombectomy. Patients were divided into 2 groups based on thrombectomy techniques: conventional stent retriever with distal access catheter aspiration without (standard) and with adjunctive GUide sheath Advancement and aspiRation in the Distal petrocavernous internal carotid artery (GUARD). Using propensity score matching, we compared procedural safety, reperfusion efficacy using the modified Thrombolysis in Cerebral Infarction scale and clinical outcomes with the modified Rankin Scale.

RESULTS: In comparing the GUARD (45 patients) versus standard (45 matched case controls) groups, there were no significant differences in demographics, NIHSS presentations, IV rtPA use, median onset-to-groin puncture times, procedural complications, symptomatic intracranial hemorrhage, or mortality. The GUARD group demonstrated significantly higher successful mTICI $\geq 2b$ reperfusion rates (98% versus 80%, $P = .015$) and improved functional mRS ≤ 2 outcomes (67% versus 43%, $P = .04$), with independent effects of the GUARD technique confirmed in a multivariable logistic regression model.

CONCLUSIONS: The GUARD technique during mechanical thrombectomy with combined stent retrieval–distal access catheter aspiration is safe and effective in improving reperfusion and clinical outcomes.

ABBREVIATIONS: BGC = balloon-guide catheter; DAC = distal access catheter; DGS = distal guide sheath; GUARD = GUide sheath Advancement and aspiRation in the Distal petrocavernous internal carotid artery; F = French; mTICI = modified Thrombolysis in Cerebral Infarction; mRS = modified Rankin Scale; NIHSS = National Institutes of Health Stroke Scale; ASPECTS = Alberta Stroke Program Early CT Score; ICA = internal carotid artery; MCA = middle cerebral artery; IV rtPA = intravenous recombinant tissue plasminogen activator; SICH = symptomatic intracranial hemorrhage; ELVO = emergent large-vessel occlusions

Endovascular mechanical thrombectomy for emergent large-vessel occlusions (ELVO) is the standard of care in acute ischemic stroke treatment as confirmed by multiple randomized controlled trials.^{1,2} The rate of successful recanalization and effective reperfusion (TICI $\geq 2b$) was attributed to modern stent-retriever technology and was estimated to be 71% in the pooled Highly Effective Reperfusion evaluated in Multiple Endovascular Stroke

Trials (HERMES)² meta-analysis, corresponding to better functional outcomes for treatment-versus-control groups (46% versus 26.5%, mRS ≤ 2), respectively. Subsequently, several thrombectomy devices and protocols were developed to optimize angiographic and clinical outcomes.

Early adaptations in thrombectomy techniques can be classified into 3 groups: traditional stent retriever thrombectomy, a distal access catheter (DAC) aspiration technique (A Direct Aspiration First Pass Technique [ADAPT] or Forced Aspiration Suction Thrombectomy [FAST]),^{3,4} and a combined stent retriever with DAC aspiration approach (SOLUMBRA, Continuous Aspiration Prior To Intracranial Vascular Embolectomy [CAPTIVE], or Stent retriever Assisted Vacuum-locked Extraction [SAVE]).⁵⁻⁷ Although the Contact Aspiration vs Stent Retriever for Successful Revascularization (ASTER) and Aspiration thrombectomy versus stent retriever thrombectomy as first-line approach for large ves-

Received March 26, 2019; accepted after revision June 17.

From the Departments of Radiology (S.A.A., M.D., R.N.A., D.R.C., A.S., M.C.H., B.S.J., M.B.P.), Neurology (S.A.A.), and Neurological Surgery (S.A.A., D.R.C., A.S., M.C.H., B.S.J., M.B.P.), Feinberg School of Medicine, Northwestern University, Chicago, Illinois; Department of Neurology (M.D.), Assiut University, Assiut, Egypt; and Department of Radiology (R.N.A.), Ain Shams University, Cairo, Egypt.

Please address correspondence to Sameer A. Ansari, MD, PhD, Departments of Radiology, Neurology, and Neurological Surgery, Northwestern University, Feinberg School of Medicine, 676 N St. Clair St, Suite 800, Chicago, IL 60611-2927; e-mail: s-ansari@northwestern.edu

<http://dx.doi.org/10.3174/ajnr.A6132>

sel occlusion (COMPASS) randomized controlled trials demonstrated equivalency of stent retriever versus contact aspiration thrombectomy, these trials did not study combined techniques or control for adjunctive aspiration through a proximal guide-catheter/sheath or balloon guide catheter (BGC).^{8,9} Compared with stent retriever thrombectomy alone, the combination of stent retrievers with DAC aspiration reported higher rates of successful (>80%) and first-pass (37%–72%) reperfusion, indicating lower rates of thrombus fragmentation.^{5–7}

BGCs have also been extensively employed to minimize the risk of thrombus fragmentation and embolization via flow modification or flow arrest in the proximal parent artery. A meta-analysis by Brinjikji et al¹⁰ showed BGC utilization to be more effective in successful TIC1 2b/3 reperfusion (78.9% versus 67%), single-pass recanalization (63.1% versus 45.2%), reduced procedure times (70.5 versus 90.9 minutes), and improved functional outcomes (59.7% versus 43.8%, mRS 0–2).¹¹ Further complementary techniques were described by Massari et al¹² (Aspiration Retriever Technique for Stroke [ARTS]) and Stampfl et al¹³ that combined stent retriever thrombectomy with both BGC and DAC aspiration. Maegerlein et al¹⁴ directly compared this type of PROximal balloon Occlusion TOgEther with direCt Thrombus aspiration during stent retriever thrombectomy (PROTECT) technique against stent retriever thrombectomy with DAC aspiration alone; the PROTECT technique achieved higher rates of successful TIC1 \geq 2b (100% versus 78%) and complete TIC1 3 (70% versus 39%) reperfusion, as well as shorter procedure times (29 versus 40 minutes).

We investigated a novel method of flow modification via coaxial advancement and aspiration of a flexible 6F 088 distal guide sheath (DGS) past the skull base during mechanical thrombectomy, analogous to BGC and DAC adjunctive techniques. We hypothesized that this Guide sheath Advancement and aspiRation in the Distal petrocavernous internal carotid artery (GUARD) technique could reduce antegrade flow as well as clot-retrieval distance, allowing more efficient and complete reperfusion. We examined the safety, technical and clinical efficacy of the adjunctive GUARD technique compared with our standard combined stent retriever with DAC aspiration thrombectomy protocol in a propensity score–matched patient cohort.

MATERIALS AND METHODS

Institutional review board approval was obtained for a retrospective case-control study of all patients with acute ischemic stroke secondary to anterior circulation ELVO who underwent mechanical thrombectomy at 3 comprehensive stroke centers by 5 neurointerventionalists, using a standardized thrombectomy protocol from November 2016 to August 2018. Patient and imaging criteria for mechanical thrombectomy included severe acute ischemic stroke symptoms (NIHSS \geq 5), presentation <24 hours from last known well, CT ASPECTS \geq 6, CT angiography confirmed ELVO (intracranial ICA or M1–M2 MCA), and CT perfusion (CTP) profile consistent with the Endovascular Therapy Following Imaging Evaluation for Ischemic Stroke (DEFUSE 3)¹⁵ or Clinical Mismatch in the Triage of Wake-Up and Late Presenting Strokes Undergoing Neuro-

intervention with Trevo (DAWN)¹⁶ trial inclusion criteria if presenting >6 hours from last known well.

Cases were separated by thrombectomy technique into a standard group versus a novel GUARD group with technical adaptation as detailed below. Use of the adjunctive GUARD technique was first introduced by a single neurointerventionalist and subsequently adopted by the remaining practitioners during the study period. After initial data analysis of both groups, a propensity score–matched analysis to control for confounding variables provided equivalent case controls in the standard group for comparison against the GUARD group.

Interventions: Standard-versus-GUARD Thrombectomy Techniques

All procedures were initiated via transfemoral puncture using 6F \times 80–100 cm guide sheaths (Flexor Shuttle, Cook; Neuron MAX, Penumbra; or AXS Infinity, Stryker), which were initially placed in the cervical ICA. All procedures used a triaxial system with coaxial advancement of large-bore DACs (ACE 60, ACE 64, or ACE 68; Penumbra) and 021/027 microcatheters using 0.014-/0.016-inch microwires to cross the thromboembolus. Stent retrievers (Trepo XP ProVue Retriever, Stryker; Solitaire/Solitaire 2, Medtronic) were deployed with >50% of the stent construct distal to the clot followed by immediate DAC advancement under continuous vacuum aspiration (MAX/Engine Pump, Penumbra) to the proximal aspect of the clot until cessation of flow indicated engagement of the thromboembolus and stent retriever. Next, the internal 021/027 stent delivery microcatheter was removed to maximize the DAC aspiration force. In the standard thrombectomy protocol, after >5 minutes to optimize clot integration, the combined stent retriever–DAC aspiration complex was removed from the cervical guide sheath under manual (>30 mL) syringe aspiration.

In the modified GUARD technique, only flexible 6F 088 \times 90–100 cm guide sheaths (Neuron MAX, Penumbra; or AXS Infinity, Stryker) were used. Following stent retriever deployment and DAC advancement under vacuum aspiration to engage the proximal aspect of the thromboembolus, the flexible 6F 088 DGS was further triaxially advanced across the skull base (horizontal petrous to posterior genu cavernous segment of the ICA) over the large-bore (6F) DAC, deployed stent retriever, and 021/027 stent-delivery microcatheter. After removal of the internal 021/027 stent-delivery microcatheter to maximize the DAC aspiration force and ~5 minutes to optimize clot integration with the stent retriever, the combined stent retriever–DAC aspiration complex was removed from the flexible 6F 088 DGS within the petrocavernous ICA, while continuous aspiration was applied to both the DAC (vacuum) and DGS (manual). Finally, the 6F 088 DGS was continuously aspirated and retracted into the cervical or proximal petrous segments of the ICA until blood return confirmed guide-sheath clearance and no residual flow limitation (Fig 1).

Data and Outcome Analysis

All patient and imaging data were extracted from a prospectively maintained stroke intervention data base integrated across all comprehensive stroke centers, the electronic medical record, and/or PACS. We analyzed patient demographics (age, sex), presentations (NIHSS, IV rtPA), imaging selection (CT

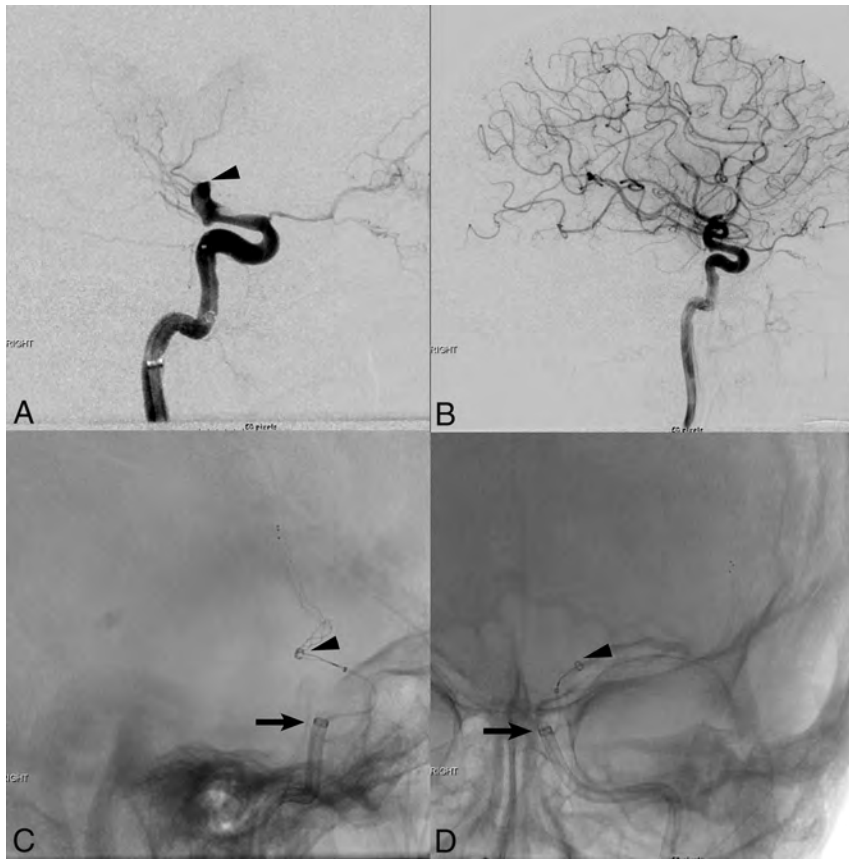


FIG 1. Lateral pre- (A) and post- (B) thrombectomy DSA images demonstrate complete TIC1 3 reperfusion of a left ICA terminus (arrowhead) occlusion using the GUARD technique with distal guide sheath placement and combined stent retriever–distal access catheter aspiration thrombectomy. Fluoroscopic intraoperative images in the lateral (C) and antero-posterior (D) projections show stent retriever deployment across the supraclinoid ICA/M1 MCA occlusion with advancement of a large-bore ACE 68 distal access catheter (arrowheads) to the proximal aspect of the clot under vacuum aspiration, and triaxial advancement of the Neuron Max 088 guide sheath (arrows) distally into the posterior genu cavernous segment of the left ICA.

ASPECTS/CTP), vessel occlusion locations, times to treatment (symptom onset to groin puncture or successful reperfusion), procedure times, angiographic outcomes (thrombectomy passes, mTICI scores), major (neurovascular) and minor (access site) procedural complications, SICH per the European Cooperative Acute Stroke Study (ECASS-3) criteria,¹⁷ clinical outcomes (mRS), and mortality. We adjudicated 2 study outcomes: angiographic and clinical outcomes. Angiographic outcomes were determined by measuring the mTICI score on post-thrombectomy cerebral angiography; each score reported during the procedure was graded and confirmed by a blinded neurointerventionalist who did not perform the procedure. Successful revascularization or reperfusion efficacy was defined as mTICI $\geq 2b$, and complete reperfusion was defined as mTICI 2c/3.¹⁸ Clinical success was defined as a good functional neurological outcome measured by mRS ≤ 2 , requiring concordance of separate assessments by both stroke neurology and neurointerventional surgery practitioners at 90-day follow-up. In cases of disagreement, the lower TICI and higher mRS scores were used for analysis of angiographic and clinical outcomes, respectively. Safety was assessed by comparing major procedural complications, SICH, and mortality at 90 days in the GUARD relative to standard control groups.

Statistical Analysis

A propensity score–matched analysis was performed to compare patients who underwent thrombectomy treated by the GUARD-versus-standard techniques with a ratio of 1:1 using confounding variables on the initial data analysis: age, IV rtPA use, CTP selection, and previous stroke/TIA as predictors with a greedy Euclidian matching algorithm and matching tolerance of 0.2 (XLSTAT-Premium 2018.6; Addinsoft, Long Island City, New York). Baseline characteristics along with procedural and clinical outcomes were compared between the GUARD and standard groups using Mann-Whitney and Fisher exact tests for continuous and categorical variables, respectively, with statistical significance set at a P value $< .05$ (SPSS 24; IBM, Armonk, New York).

A multivariable logistic regression analysis was performed to assess the independent effects of the GUARD technique by adjusting for outcome confounders. Prespecified dependent variables were set to either a good functional outcome (mRS ≤ 2), successful or complete reperfusion; the independent variables included age, onset to groin puncture, IV rtPA use, occlusion location, and CTP selection. Results of the logistic regression analysis were reported as an adjusted odds ratio (aOR) with 95% confidence intervals (CI). All data were reported as percentages or median (range), except for the number of thrombectomy passes reported as a mean \pm standard deviation (SD).

RESULTS

We identified 112 consecutive patients with acute ischemic stroke with anterior circulation ELVO who underwent mechanical thrombectomy with a standard stent retriever–DAC aspiration protocol during the study period, including 45 patients with an adjunctive DGS in the petrocavernous ICA composing the GUARD group. After propensity score 1:1 ratio matching, we identified 45/67 patients in the standard group (clot retrieval into a cervical ICA guide sheath) as case controls for direct comparison.

There were no significant differences in baseline age, sex, stroke risk factors (atrial fibrillation, hypertension, hyperlipidemia, diabetes mellitus, smoking, or prior TIA/stroke), initial NIHSS presentation, CT ASPECTS and/or CTP imaging selection, IV rtPA use, vessel occlusion location (including tandem ICA/MCA occlusions), or symptom onset-to-groin puncture time between the GUARD and standard groups (Table 1). Although there remained a trend toward younger patients being

Table 1: Comparison of baseline demographics, presentations, procedural efficacy, and safety between the GUARD and standard thrombectomy techniques

	GUARD (n = 45)	Standard (n = 45)	P Value
Sex (% male)	42	51	.53
Median age (range/yr)	69 (21–92)	74 (39–92)	.09
Median NIHSS score (range)	17 (6–30)	17 (5–32)	.68
Median CT ASPECTS (range)	9 (6–10)	9 (6–10)	.89
CTP (%)	44	56	.40
IV rtPA (%)	36	49	.29
Vessel occlusion (%)			.88
ICA terminus	25	22	
Cervical ICA + MCA	4	7	
MCA (M1–M2)	71	71	
Risk factors (%)			
AF	44	53	.53
HTN	76	80	.80
DM	20	27	.62
Smoker	9	9	.99
HLD	49	49	.99
Previous stroke/TIA	7	11	.71
Median symptom onset-to-groin puncture time (range/min)	192 (78–1193)	219 (27–1097)	.241
Median symptom onset to reperfusion time (range/min)	254 (107–1245)	279 (108–1226)	.21
Median groin puncture to reperfusion time (range/min)	52 (29–225)	61 (23–184)	.20
Mean No. of passes ± SD	2.3 ± 1.3	2.8 ± 1.5	.09
First-pass reperfusion (%)	39	23	.17
Final mTICI score (%)			.046 ^a
3	51	40	
2c	16	7	
2b	31	33	
2a	2	16	
1	0	2	
0	0	2	
Successful reperfusion mTICI ≥ 2b (%)	98	80	.015 ^a
Complete reperfusion mTICI 2c/3 (%)	67	47	.09
mTICI 3 (%)	51	40	.40
Adjunctive stenting/angioplasty (%)	20	11	.26
SICH (%)	2	9	.36
Neurovascular complications (%)	4	9	.68
Median mRS at 90 days (range)	2 (0–6)	4 (0–6)	.01 ^a
mRS ≤ 2 at 90 days (%)	67	43	.04 ^a
Mortality at 90 days (%)	13	30	.10

Note:—AF indicates atrial fibrillation; HTN, hypertension; DM, diabetes mellitus; HLD, hyperlipidemia.

^a Significant.

treated with the GUARD technique (median, 69 versus 74 years; $P = .09$), this was not statistically significant.

The GUARD technique demonstrated significantly higher successful TICI ≥ 2b reperfusion rates (98% versus 80%, $P = .015$) compared with the standard thrombectomy protocol (Fig 2A). Additionally, there were trends toward complete TICI 2c/3 reperfusion (67% versus 47%, $P = .09$), first-pass recanalization (39% versus 23%, $P = .17$), fewer thrombectomy passes (2.3 versus 2.8, $P = .09$), and faster groin-to-final reperfusion times (52 versus 61 minutes, $P = .2$) in the GUARD group, but these did not reach statistical significance (Table 1). Endovascular angioplasty and/or stent placement were required for vessel salvage after revascularization in cases deemed refractory to thrombectomy from underlying vessel wall pathology (atherosclerosis or dissections). There was no difference in the frequency of extracranial carotid angioplasty/stent placement (5 versus 3 interventions) and intracranial stent placement (5 versus 3 interventions)

performed in the GUARD (9/45 patients) versus standard (5/45 patients) group (20% versus 11% respectively, $P = .26$).

Safety was assessed with respect to major neurovascular complications, and no difference was noted with GUARD (2/45 patients) versus standard (4/45 patients) thrombectomy techniques (4% versus 9% respectively, $P = .68$). A non-flow-limiting petrocavernous ICA dissection ($n = 1$) was related to aggressive DGS advancement across the posterior genu segment of the cavernous ICA, which was medically treated with aspirin and without neurologic sequelae. Three suspected iatrogenic, non-flow-limiting intracranial MCA dissections (GUARD $n = 1$ versus standard $n = 2$) were managed medically with IV eptifibatid and postprocedural antiplatelets. Other major iatrogenic complications in the standard thrombectomy group included new territory emboli ($n = 2$) in the fetal posterior cerebral artery distribution and a secondary intraprocedural occlusion of the contralateral ICA. Minor access-site complications included a groin pseudoaneurysm requiring percutaneous thrombin injection in the GUARD group, a carotid puncture-related pseudoaneurysm treated with sonography-guided compression, and 3 minor groin hematomas managed conservatively in the standard group. Furthermore, there were nonsignificant trends toward lower SICH rates (2% versus 9%, $P = .36$) and decreased mortality at 90 days (13% versus 30%, $P = .10$) in the GUARD cohort (Table 1).

We found significantly improved clinical outcomes with GUARD thrombectomy, measured by either a median mRS (2 versus 4, $P = .01$) or mRS ≤ 2 (67% versus 43%; $P = .04$) at 90 days (Fig 2B). After adjusting for confounding variables in a multivariable logistic regression model (Table 2), the GUARD technique was independently associated with successful TICI ≥ 2b reperfusion (aOR, 13.7; 95% CI, 1.2–150.9; $P = .03$) and good functional mRS ≤ 2 outcomes (aOR = 3.77; 95% CI, 1.15–12.34; $P = .03$). The GUARD technique also demonstrated a strong trend toward complete TICI 2c/3 reperfusion (aOR, 2.45; 95% CI, 0.93–6.42; $P = .07$), but this did not reach statistical significance.

DISCUSSION

Mechanical thrombectomy via stent retriever and/or large-bore DAC aspiration technology has revolutionized the treatment of acute ischemic stroke secondary to ELVO.^{2–8} The success of multiple stroke thrombectomy randomized controlled trials has been attributed in large part to higher reper-

fusion rates than prior failed intra-arterial thrombolysis/thrombectomy trials using first- and second-generation devices.¹⁹ Further work since then has focused on improving stroke processes and thrombectomy techniques to optimize the efficiency and effectiveness of vessel recanalization by reducing times to revascularization, number of required thrombectomy passes, thrombus fragmentation, and distal or new territory embolization.

Large-bore DAC aspiration alone via the ADAPT technique has shown promise as an equivalent alternative to stent retriever-based thrombectomy,^{3,8,9} but several recent studies

have suggested enhanced performance when combining both approaches.⁵⁻⁷ A meta-analysis from large-registry data also demonstrated the adjunctive value of proximal flow-arrest techniques using BGCs in embolic protection.^{10,11} Finally, proximal aspiration techniques via BGC (ARTS, PROTECT)^{12,14} or cervical guide catheter/sheath (SAVE)⁷ in conjunction with stent retriever-DAC aspiration thrombectomy have yielded the most impressive results, nearly 100% successful TIC1 2b and 70%–80% complete TIC1 2c/3 reperfusion rates, corresponding to excellent 50%–60% mRS ≤2 clinical outcomes. However, BGCs are typically large-profile devices limited to 8F/9F femoral sheath access, poor trackability in difficult aortic arch or great vessel anatomy, and cervical ICA placement requiring clot retrieval across the tortuous petrocavernous segments.

In addition, the rate of clinically significant groin complications in patients treated with IV rtPA and mechanical thrombectomy using a BGC has been estimated to be 0.4%–0.8%,²⁰ and larger sheath sizes of >8F have been shown to be an independent predictor of retroperitoneal hematomas associated with longer hospital stays and higher mortality rates.^{21,22}

In our GUARD technique, we safely advanced a 6F 088 DGS past the skull base into the petrocavernous ICA for flow modification and aspiration during thrombus retrieval. Although we were initially concerned that a 6F profile sheath could be associated with risks of vessel injury or severe vasospasm in smaller, tortuous, and distal ICA segments, we encountered only a single (2%) iatrogenic petrocavernous non-flow-limiting dissection. We attributed this success to both flexible DGS technology and methodical triaxial advancement of the 6F 088 DGS over a large-bore 6F DAC (1:1 profile) with internal support of a deployed stent retriever and

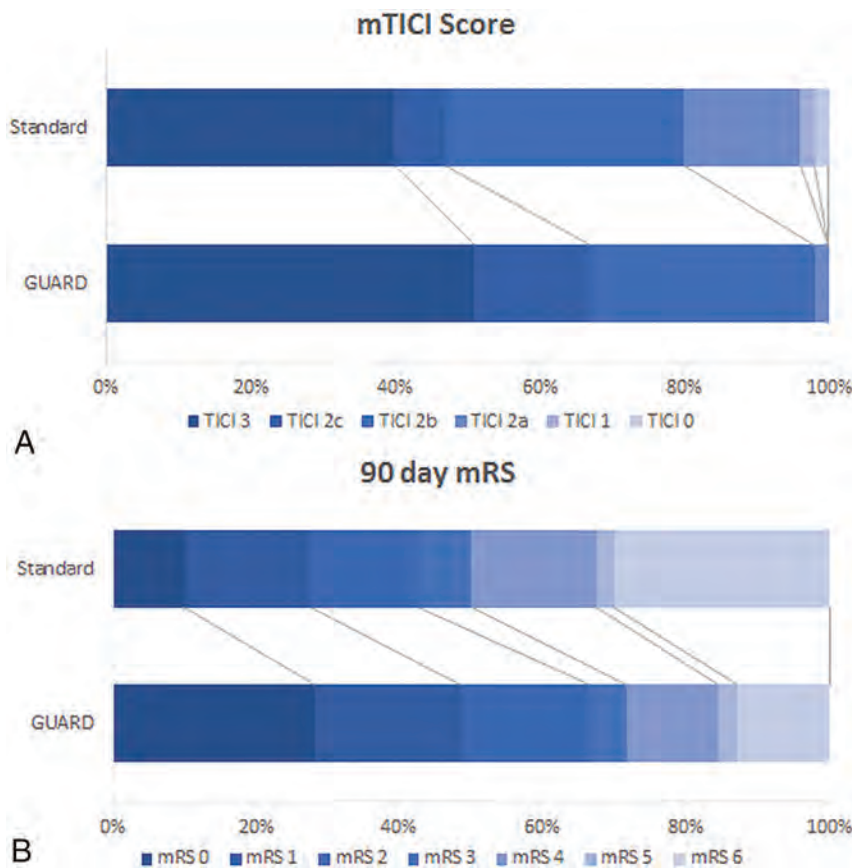


FIG 2. A, Comparison of recanalization results measured with a modified TIC1 score between the GUARD and standard techniques ($P = .046$). B, Comparison of functional clinical outcomes by an mRS at 90 days between the GUARD and standard techniques ($P = .01$).

Table 2: Multivariable logistic regression analysis with dependent variables for successful reperfusion, complete reperfusion, and independent functional clinical outcomes

	Successful Reperfusion TIC1 ≥2b		Complete Reperfusion TIC1 2c/3		Clinical Outcomes mRS ≤2	
	aOR	P Value	aOR	P Value	aOR	P Value
GUARD	13.7 (1.24–150.85)	.03 ^a	2.45 (0.93–6.42)	.07	3.77 (1.15–12.34)	.03 ^a
Age	1	.42	0.98	.25	1.03	.19
Sex (male)	4.2	.17	1.28	.6	2.68	.09
Onset to groin time	1.0	.49	1.0	.18	1.0	.11
IV rtPA	0.72	.75	0.72	.54	2.71	.15
Location						
MCA	9.0	.14	0.78	.80	8.82	.08
ICA terminus	4.7	.35	1.06	.96	4.71	.24
Cervical ICA + MCA	1	.286	1	.84	1	.15
CTP	1.5	.69	1.68	.32	2.82	.11

Note:—Data reported as adjusted odds ratio (aOR) including 95% confidence intervals (CI) for the GUARD technique.

^a Significant.

a 021/027 stent-deployment microcatheter under gentle traction to overcome vascular tortuosity. Furthermore, placement of a 6F (8F outer diameter) DGS in 4- to 5-mm diameter ICA segments combined with large-bore DAC aspiration may have sufficiently reduced both antegrade flow and clot-retrieval distance for more effective and efficient thrombectomy.

Failure or incomplete thrombectomy due to distal and new territory embolization has been attributed to limited clot integration during device retrieval across the length and tortuosity of the intracranial vasculature. Combined stent retriever–DAC aspiration techniques increase the retrieval force (F_R) and reduce antegrade flow or the impaction force (F_I) by using a large-bore (diameter) DAC, but this may be further modified with proximal flow arrest and/or aspiration techniques using a BGC or DGS. While GUARD does not accomplish complete flow arrest akin to a BGC, coaxial DGS placement into the distal petrocavernous segment improves F_R vectors in tortuous vasculature and reduces the distance (work = $F_R \times d$) and time (momentum = $F_R \times t$) required for successful clot retrieval.²³ New flexible DGS technology with larger inner diameters (6F 091) is being introduced into the market that will allow safe trackability and access into the distal and smaller ICA segments, but with improved proximal aspiration capacity during retrieval of large-bore DAC-stent retriever complexes to further diminish the F_I .

In our study, we achieved higher rates of successful $\text{TICI} \geq 2b$ (98% versus 80%) and complete $\text{TICI} 2c/3$ reperfusion (67% versus 47%) with an adjunctive GUARD technique compared with propensity score–matched controls using stent retriever–DAC aspiration thrombectomy alone. Indeed with GUARD, we achieved equivalence with the most favorable published results that similarly combined adjunctive BGC aspiration with stent retriever–DAC aspiration thrombectomy (ARTS/PROTECT), reporting successful and complete reperfusion in 98%–100% and 70% of patients, respectively.¹⁴ In contrast, BGC-mediated stent retriever thrombectomy alone without concomitant DAC aspiration has demonstrated relatively lower successful (76%–79%) and complete (54%–58%) reperfusion rates in the North American Solitaire Stent-Retriever Acute Stroke (NASA) registry and a large BGC meta-analysis.^{10,11} Although statistical trends toward higher single-pass recanalization (39% versus 23%) and shorter procedure times with the GUARD technique did not reach statistical significance, first-pass recanalization was comparable with both the ARTS (43%) and PROTECT (48%) techniques. Higher rates of successful and complete reperfusion with GUARD or similarly effective ARTS/PROTECT techniques suggest that adjunctive DGS or BGC devices confer similar benefits. In addition, the SAVE and CAPTIVE techniques using proximal aspiration from a cervical guide sheath and/or continuous DAC aspiration during stent retriever deployment instead of a BGC also yielded excellent complete $\text{TICI} 2c/3$ (78%–80%) and first-pass (59%–72%) reperfusion rates, superior to stent retriever–DAC aspiration alone techniques (SOLUMBRA).^{5–7} Interestingly, most cases using SAVE used 8F guide catheters with diameters equivalent to those in the 6F 088 DGS used in our GUARD technique.

Studies yielding the highest reperfusion rates combined

stent retriever thrombectomy with both DAC and proximal BGC/DGS aspiration and resulted in the best clinical outcomes (ARTS, SAVE, PROTECT, GUARD). Our improved reperfusion rates in the GUARD cohort correlated with significantly higher rates of functional independence (67% versus 43%, $\text{mRS} \leq 2$ at 90 days, $P = .01$), equivalent to previously published studies using BGCs and/or proximal aspiration in either the large BGC meta-analysis (60%)¹⁰ or the single-arm SAVE (59%) and ARTS (66%) studies. Although the PROTECT technique failed to report 90-day clinical outcomes, prior description of this combined stent retriever with DAC and proximal BGC aspiration approach by Stampfl et al¹³ noted 52% $\text{mRS} 0–2$ at 90 days.^{13,14} Further larger cohort comparative studies of our GUARD technique using DGS aspiration against similarly effective and adjunctive BGC aspiration techniques are warranted and planned in a multicenter setting.

Several limitations in our study include a retrospective, non-randomized study design. We attempted to mitigate this risk with propensity score matching to provide case controls without statistically significant differences in baseline parameters. In addition, a multivariate logistic regression analysis was performed to investigate the independent effect of the GUARD technique on reperfusion and good functional outcomes, while adjusting for possible confounders. However, despite propensity score matching, a nonstatistical trend toward a younger age bias in the GUARD group persisted. Our study may have been prone to patient-selection bias as DGS advancement could have been hindered in challenging aortic arch anatomy or 360° cervical vascular loops. We identified 7 cases in which we failed to advance a DGS into the petrocavernous ICA segments to initiate the GUARD technique, and 4 of these cases had a 360° loop in the proximal ICA. Despite traversing the vascular loops with the DGS, inadequate catheter length prevented further distal access into the petrocavernous ICA, which may have been mitigated if longer (100 cm) DGSs were used or available. The remaining 3 cases presented with extremely tortuous aortic and/or great vessel anatomy preventing either distal DGS placement ($n = 1$) or requiring direct carotid access ($n = 2$), with short introducer sheaths limited to the cervical ICA. However, there were no cases in which the GUARD technique was possible and then abandoned for another technique to achieve successful recanalization. In contrast, we reverted to the GUARD technique from our standard technique in 3 patients after several failed thrombectomy attempts; these patients were analyzed within the GUARD cohort, potentially negatively impacting procedure times, number of passes, and percentage of first-pass recanalizations.

Finally, caution is warranted in comparing studies on adjunctive thrombectomy techniques, especially when combining stent retrieval, DAC aspiration, and/or proximal BGC/DGS aspiration. It may be difficult to control for the various types and sizes of thrombectomy devices or other uncontrolled techniques such as positioning or deployment of devices, time for thrombus integration/engagement, and retrieval techniques. Furthermore, most studies to date have been nonrandomized, single-arm, and small-sample-size studies without control populations. Nevertheless, the only comparative studies with internal control groups remain CAPTIVE, PROTECT, and the current GUARD study, all dem-

onstrating relatively higher reperfusion rates and better clinical outcomes.

CONCLUSIONS

We describe a novel GUARD technique using a flexible 6F 088 DGS that is advanced into the petrocavernous segment of the ICA during combined stent retriever–DAC aspiration thrombectomy. In comparison with a propensity score–matched patient cohort, the adjunctive GUARD technique was shown to be safe and independently effective in improving both reperfusion and functional clinical outcomes. Our results using GUARD appear equivalent to the most optimum techniques published to date, including proximal BGC aspiration in combination with stent retriever–DAC aspiration thrombectomy.

REFERENCES

1. Powers WJ, Rabinstein AA, Ackerson T, et al; American Heart Association Stroke Council. **2018 Guidelines for the Early Management of Patients with Acute Ischemic Stroke: a Guideline for Healthcare Professionals from the American Heart Association/American Stroke Association.** *Stroke* 2018;49:e46–110 CrossRef Medline
2. Goyal M, Menon BK, van Zwam WH, et al; HERMES collaborators. **Endovascular thrombectomy after large-vessel ischaemic stroke: a meta-analysis of individual patient data from five randomised trials.** *Lancet* 2016;387:1723–31 CrossRef Medline
3. Turk AS, Frei D, Fiorella D, et al. **ADAPT FAST study: a direct aspiration first pass technique for acute stroke thrombectomy.** *J Neurointerv Surg* 2014;6:260–64 CrossRef Medline
4. Lee HC, Kang DH, Hwang YH, et al. **Forced arterial suction thrombectomy using distal access catheter in acute ischemic stroke.** *Neurointervention* 2017;12:45–49 CrossRef Medline
5. Humphries W, Hoyt D, Doss VT, et al. **Distal aspiration with retrievable stent assisted thrombectomy for the treatment of acute ischemic stroke.** *J Neurointerv Surg* 2015;7:90–94 CrossRef Medline
6. McTaggart RA, Tung EL, Yaghi S, et al. **Continuous aspiration prior to intracranial vascular embolectomy (CAPTIVE): a technique which improves outcomes.** *J Neurointerv Surg* 2017;9:1154–59 CrossRef Medline
7. Maus V, Behme D, Kabbasch C, et al. **Maximizing first-pass complete reperfusion with SAVE.** *Clin Neuroradiol* 2018;28:327–33 CrossRef Medline
8. Lapergue B, Blanc R, Gory B, et al; ASTER Trial Investigators. **Effect of endovascular contact aspiration vs stent retriever on revascularization in patients with acute ischemic stroke and large vessel occlusion: the ASTER Randomized Clinical Trial.** *JAMA* 2017;318:443–52 CrossRef Medline
9. Turk AS 3rd, Siddiqui A, Fifi JT, et al. **Aspiration thrombectomy versus stent retriever thrombectomy as first-line approach for large vessel occlusion (COMPASS): a multicentre, randomised, open label, blinded outcome, non-inferiority trial.** *Lancet* 2019;393:998–1008 CrossRef Medline
10. Brinjikji W, Starke RM, Murad MH, et al. **Impact of balloon guide catheter on technical and clinical outcomes: a systematic review and meta-analysis.** *J Neurointerv Surg* 2018;10:335–39 CrossRef Medline
11. Nguyen TN, Malisch T, Castonguay AC, et al. **Balloon guide catheter improves revascularization and clinical outcomes with the Solitaire device: analysis of the North American Solitaire Acute Stroke Registry.** *Stroke* 2014;45:141–45 CrossRef Medline
12. Massari F, Henninger N, Lozano JD, et al. **ARTS (Aspiration-Retriever Technique for Stroke): initial clinical experience.** *Interv Neuroradiol* 2016;22:325–32 CrossRef Medline
13. Stampfl S, Pfaff J, Herweh C, et al. **Combined proximal balloon occlusion and distal aspiration: a new approach to prevent distal embolization during neurothrombectomy.** *J Neurointerv Surg* 2017;9:346–51 CrossRef Medline
14. Maegerlein C, Monch S, Boeckh-Behrens T, et al. **PROTECT: PROximal balloon Occlusion TOgether with direCt Thrombus aspiration during stent retriever thrombectomy: evaluation of a double embolic protection approach in endovascular stroke treatment.** *J Neurointerv Surg* 2018;10:751–55 CrossRef Medline
15. Albers GW, Marks MP, Kemp S, et al; DEFUSE 3 Investigators. **Thrombectomy for stroke at 6 to 16 hours with selection by perfusion imaging.** *N Engl J Med* 2018;378:708–18 CrossRef Medline
16. Nogueira RG, Jadhav AP, Haussen DC, et al; DAWN Trial Investigators. **Thrombectomy 6 to 24 hours after stroke with a mismatch between deficit and infarct.** *N Engl J Med* 2018;378:11–21 CrossRef Medline
17. Hacke W, Kaste M, Bluhmki E, et al. **Thrombolysis with alteplase 3 to 4.5 hours after acute ischemic stroke.** *N Engl J Med* 2008;359:1317–29 CrossRef Medline
18. Goyal M, Fargen KM, Turk AS, et al. **2C or not 2C: defining an improved revascularization grading scale and the need for standardization of angiography outcomes in stroke trials.** *J Neurointerv Surg* 2014;6:83–86 CrossRef Medline
19. Broderick JP, Palesch YY, Demchuk AM, et al; Interventional Management of Stroke (IMS) III Investigators. **Endovascular therapy after intravenous t-PA versus t-PA alone for stroke.** *N Engl J Med* 2013;368:893–903 CrossRef Medline
20. Shah VA, Martin CO, Hawkins AM, et al. **Groin complications in endovascular mechanical thrombectomy for acute ischemic stroke: a 10-year single center experience.** *J Neurointerv Surg* 2016;8:568–70 CrossRef Medline
21. Frank JJ, Kamalakannan D, Kodenchery M, et al. **Retroperitoneal hematoma in patients undergoing cardiac catheterization.** *J Interv Cardiol* 2010;23:569–74 CrossRef Medline
22. Trimarchi S, Smith DE, Share D, et al; BMC2 Registry. **Retroperitoneal hematoma after percutaneous coronary intervention: prevalence, risk factors, management, outcomes, and predictors of mortality—a report from the BMC2 (Blue Cross Blue Shield of Michigan Cardiovascular Consortium) registry.** *JACC Cardiovasc Interv* 2010;3:845–50 CrossRef Medline
23. Yoo AJ, Andersson T. **Thrombectomy in acute ischemic stroke: challenges to procedural success.** *J Stroke* 2017;19:121–30 CrossRef Medline

Posterior Fossa Dural Arteriovenous Fistulas with Subarachnoid Venous Drainage: Outcomes of Endovascular Treatment

L. Détraz, K. Orlov, V. Berestov, V. Borodetsky, A. Rouchaud, L.G. de Abreu Mattos, and C. Mounayer



ABSTRACT

BACKGROUND AND PURPOSE: Dural AVFs located in the posterior fossa are a rare entity. The objectives of the study were to analyze the anatomy of dural AVFs, their endovascular treatment strategies, and clinical outcomes.

MATERIALS AND METHODS: Two centers retrospectively selected patients treated between January 2009 and June 2018 having posterior fossa dural AVFs. We collected patient demographics, clinical presentation, arterial and venous outflow anatomy of the dural AVFs, and treatment outcomes.

RESULTS: Twenty-six patients treated endovascularly for posterior fossa dural AVFs, type III, IV, or V, were included. One hundred percent of the dural AVFs were occluded. A transarterial approach was performed in 23 dural AVFs (88.5%); a combined transarterial and transvenous approach, for 2 dural AVFs (7.7%); and a transvenous approach alone, for 1 dural AVF (3.8%). The middle meningeal artery was the most common artery chosen to inject embolic liquid (46%, 12/26). Procedure-related morbidity was 15.4% at 24 hours, 7.7% at discharge, and 0% at 6 months. Procedure-related mortality was 0%.

CONCLUSIONS: Endovascular treatment offers high occlusion rates for posterior fossa dural AVFs with low morbidity and mortality rates. The arterial approach is the first-line preferred approach, even if a transvenous or combined approach would be a safe and effective option for patients with favorable anatomy.

ABBREVIATIONS: APA = ascending pharyngeal artery; dAVF = dural AVF; MHT = meningohypophyseal trunk; MMA = middle meningeal artery; NAEL = nonadhesive embolic liquid; PMA = posterior meningeal artery

Dural AVFs (dAVFs) are a rare pathology, accounting for 10%–15% of all intracranial vascular shunts.¹ dAVFs of the posterior fossa are defined as intracranial direct shunts involving the tentorium and the dura that covers the remainder of the posterior fossa.²

On the basis of their drainage, dAVFs of the posterior fossa can be divided into 2 entities: benign fistulas,³ draining into a sinus, and those with a high risk of bleeding, with a subarachnoid venous drainage. If one excluded shunts of the transverse and sigmoid

sinuses, posterior fossa fistulas are the most dangerous fistulas due to their cortical drainage at risk of rupture and their eloquent location.^{3,4}

Due to their rarity, only a few studies^{2–4} have described the anatomic settings, clinical presentation, and endovascular management of posterior fossa dAVFs. Hence, we reviewed dAVFs located in the posterior fossa with subarachnoid venous drainage from 2 centers (University Hospital of Limoges, France and National Medical Research, Center of the Ministry of Health of the Russian Federation, Novosibirsk, Russia), all treated by an endovascular approach. We analyzed their anatomy and clinical presentation and discussed their endovascular treatment.

MATERIALS AND METHODS

Data Collection

Data regarding patient demographics, baseline clinical presentations, embolization techniques, and follow-up outcomes were collected in prospective data bases of dural arteriovenous shunts treated by an endovascular approach at 2 interventional neuroradiology centers from January 2009 to June 2018. During this period, every patient presenting at the hospital with a posterior fossa

Received April 19, 2019; accepted after revision June 19.

From the Service de Neuroradiologie Interventionnelle et Diagnostique (L.D.), Centre Hospitalier Universitaire de Nantes-Hopital Laennec, Saint-Herblain, France; Department of Neurosurgery (K.O., V. Berestov), E. Meshalkin National Medical Research Center of the Ministry of Health of the Russian Federation, Novosibirsk, Russia; Service de Radiologie (V. Borodetsky, A.R., L.G.d.A.M., C.M.), Neuroradiologie Interventionnelle, Centre Hospitalier Universitaire de Limoges, Limoges, France; and CNRS (A.R., C.M.), XLIM, UMR 7252, University of Limoges, Limoges, France.

Please address correspondence to Lili Détraz, MD, Service de Neuroradiologie interventionnelle et Diagnostique, HGRL, CHU de Nantes, 44000 Nantes; e-mail: lili.detrax@gmail.com

Indicates article with supplemental on-line tables.

<http://dx.doi.org/10.3174/ajnr.A6140>

dAVF with subarachnoid venous drainage, ruptured or not, was treated by a multidisciplinary neurovascular staff (neurosurgeons and neuroradiologist). Cases of posterior fossa dAVFs with subarachnoid venous drainage have been retrospectively identified from those data bases for this specific study. A retrospective analysis of the patient record, neuroimaging, and follow-up was performed by 2 investigators in each center. At least 1 of the 2 investigators was not involved into the patient's treatment. Investigators had at least 2 years of experience in interventional neuro-radiology. In case of discrepancy, the investigators reviewed the cases together to reach consensus.

Patient Selection

All cases were diagnosed with initial MR imaging or CT angiography and further confirmed and analyzed by selective DSA. Initial DSA included a complete angiography (bilateral internal and external carotid arteries, and bilateral vertebral artery).

Inclusion criteria were endovascularly treated patients with ruptured and unruptured dAVFs, with a dural shunt located in the posterior fossa and subarachnoid venous drainage. Exclusion criteria were dAVFs directly draining into the sinus.

Endovascular Treatment Protocol

In each center, the therapeutic strategy was defined by a multidisciplinary neurovascular team. All the selected patients had been treated endovascularly, under general anesthesia. Procedures were performed in a biplane, flat panel angiographic suite (Allura Xper FD20; Philips Healthcare, Best, the Netherlands). Arterial vascular access was achieved by a transfemoral approach using a 6F catheter. When venous access was needed, a transjugular or transfemoral approach was used. For each patient, 3000–5000 IU of heparin was administered intravenously at the beginning of the intracranial catheterization.

Nonadhesive embolic liquid (NAEL) and adhesive embolic liquid agents were used. NAELs used were the following: Onyx (Covidien, Irvine, California), SQUID (<http://medcinpharma.com/products-solutions/emboflu/>), or Precipitating Hydrophobic Injectable Liquid (PHIL; MicroVention, Tustin, California). The adhesive embolic liquid used was Glubran Tiss (Glubran®, GEM, Viareggio, Italy).

Clinical and Imaging Follow-Up

Every patient underwent full clinical and neurologic evaluation by the senior neuroradiologist in charge, before the treatment, at awakening, at discharge, and 6 months after the endovascular procedure. The 6-months evaluation was usually followed by DSA. If DSA was not performed, patients underwent MR imaging. The mRS was assessed before the treatment, at discharge, and at 6 months. A stable or improved mRS between pretreatment and 6-month follow-up was considered a good clinical outcome.

RESULTS

Patient Baseline Characteristics

Of the 198 dAVFs treated in the 2 centers, 26 patients (13.1%) presented with posterior fossa dAVFs with subarachnoid venous drainage and were included in this study. The mean age was 54 ± 15 years (range, 23–80 years) with 80.7% men (21/26).

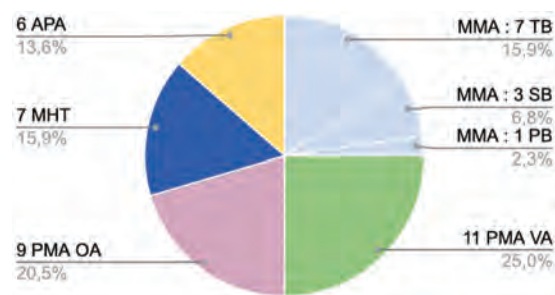


FIG 1. Arterial feeders of the dAVFs and number of dAVF fed by a given artery. Twenty-two of 26 dAVFs had multiple feeders. OA indicates occipital artery; PB, petrous branch; TB, tentorial branch; SB, squamous branch; VA, vertebral artery.

Eight patients (30.7%) presented with intracranial hemorrhage (On-line Table 1).

According to the Cognard classification,⁵ 10 dAVFs (38.5%) were type III, 10 were type IV (38.5%), and 6 were type V (23.1%).

Clinical symptoms leading to the diagnosis were headache (9 cases, 34.6%), cerebellar syndrome (4 cases, 15.4%), hemiparesis (2 cases, 7.7%), myelopathy (4 cases, 15.4%), acute cervical pain (1 case, 3.8%), and pulsatile tinnitus (1 case, 3.8%). Five cases (19.2%) were incidental findings.

Location and Angioarchitecture

All dAVFs were fed by a meningeal branch of the external carotid artery. Multiple arterial feeders were observed in 84.4% (22/26) of cases, with a bilateral supply in 61.5% (16/26). The most common feeding artery was the middle meningeal artery (MMA) (11 cases, 42.3%; 7 from a tentorial branch, 3 from a squamous branch, 1 from a petrosal branch); then, the posterior meningeal artery (PMA) arising from the vertebral artery (11 cases, 42.3%); the PMA from occipital artery (9 cases, 34.6%); the medial tentorial branch of the meningohypophyseal trunk (MHT) (7 cases, 26.7%); and the ascending pharyngeal artery (APA) (6 cases, 23.1%; 3 from the hypoglossal branch and 3 from the jugular branch) (Fig 1 and On-line Table 1).

Seven dAVFs with a petrosal location presented with a shunt into the superior petrosal vein: Five dAVFs had a venous outflow into the basal vein, 1 dAVF had an outflow into the tentorial lateral sinus, and 1 dAVF, into the perimedullary veins (On-line Tables 1 and 2).

Four dAVFs located on the free edge of the tentorium presented with a shunt into the tectal vein with a venous outflow into the torcular. All were supplied by a meningeal branch of the superior cerebellar artery with different secondary supplies, with branches arising from the internal carotid artery or from the PMA (On-line Tables 1 and 2).

Eight dAVFs with a posterior tentorial location presented with a shunt into the declival vein with an outflow into the cerebellar veins (On-line Tables 1 and 2).

Two dAVFs also presented with a posterior tentorial location but with a shunt into the inferior cerebellar vein and a lateral tentorial sinus outflow (On-line Tables 1 and 2).

Six dAVFs had a perimedullary outflow: Five dAVFs were located on the foramen magnum with a shunt into the lateral medullary vein and without any MMA feeding, whereas 1 dAVF, de-

Endovascular treatment strategy

	Arterial Approach					Combined Approach	Venous Approach
	Onyx 18 +				SQUID		
	PHIL	Glubran	Glubran	SQUID			
No. of dAVFs treated						2	1
No. of sessions	17	3	2	2	2	3	1
Complications (No. of cases)	3	0	0	1	0	0	0

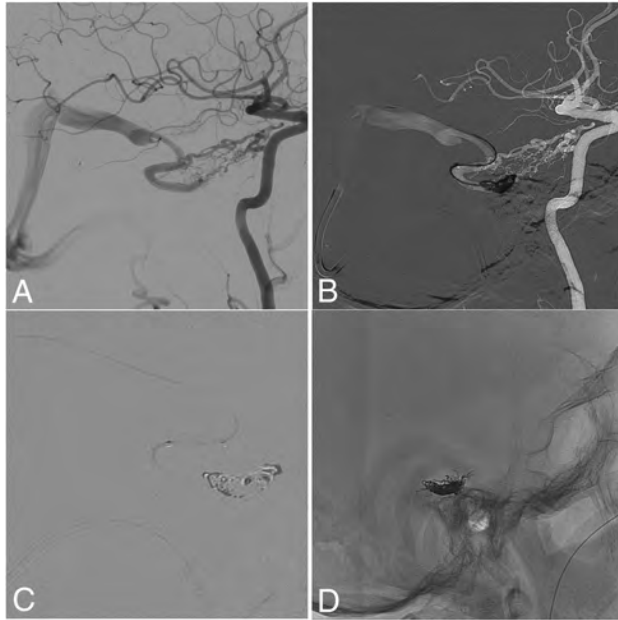


FIG 2. Transvenous approach. Arteriography of a petrosal dAVF with petrosal outflow, fed by the recurrent tentorial branch of the infero-lateral trunk and a posterior meningeal branch, draining into the internal temporal vein. Retrograde catheterization of the straight sinus via the jugular golf and lateral sinus. Two Echelon 10 microcatheters (Covidien) were navigated to the foot vein located on the internal temporal vein. By means of 1 microcatheter, platinum coils were rolled; then Onyx 18 was injected through the second microcatheter. The dAVF was totally cured at the end of the intervention. A, Lateral initial angiogram. B, Transvenous coiling. C, Transvenous Onyx injection. D, Cast of Onyx and coils.

scribed above, had a petrosal location with a shunt into the superior petrosal vein, fed by the tentorial branch of MMA (On-line Tables 1 and 2).

Endovascular Treatment Strategies

A transarterial approach was performed in 23 dAVFs (88.5%); a combined transarterial and transvenous approach, in 2 patients (7.7%); and a transvenous approach alone, in 1 patient (3.8%) (On-line Tables 1 and 2 and Table). During the selected period, 100% of the dAVFs were totally occluded. Twenty-two (84.6%) dAVFs were totally occluded with a single session; 3 dAVFs, (7.7%) after 2 sessions; and 1 (3.8%), after 3 sessions. Details are provided in the Table. No patients had an operation.

Regarding dAVFs draining into the basal vein, MMA embolization was the first option in 80.0% of cases, even if the MHT/infero-lateral trunk was the principal feeder. One dAVF was occluded using a single transvenous approach due to the narrowed caliber of the main feeding artery and the risk of reflux into the ICA. Details are provided in Fig 2.

dAVFs with a tectal shunt and a torcular outflow were fed by

the meningeal branch of the SCA and by different accessory supplies from the PMA or the MHT. Hence, embolization through the meningeal branch of the SCA was the first option (50.0% of the cases) when the navigation and Onyx reflux were acceptable. For 1 case, due to

incomplete occlusion and arterial navigation difficulties, embolization was completed by a transvenous approach with a pressure cooker technique using coils and NAEL to increase the ability to push more NAEL and control the flow.

Concerning dAVFs draining into the cerebellar cortical veins, the MMA was the most frequent feeder (75.0%), and the embolization via the MMA was the first option when possible (5 cases, 62.5%) (Fig 3). The PMA (3 cases, 37.5%) and transosseous branches (1 case, 12.5%) were the second option due to the risk of ischemia in case of reflux into the vertebral artery and navigation difficulties.

For dAVFs draining into the lateral tentorial sinus, a transarterial approach via the MMA was the first option when possible. In 1 case, a complementary transvenous approach through the tentorial sinus was also performed because of the partial occlusion via injection of embolic liquid through a narrow MMA. Occlusion was total.

For dAVFs draining into the perimedullary veins, a venous approach was not possible. Regarding the foramen magnum fistulas, despite the frequency of anastomosis in this area, 3 cases (60.0%) of dAVFs were treated via the PMA. For the petrosal location, the MMA was chosen (Fig 4).

Clinical and Angiographic Outcomes

Treatment-related morbidity was observed in 4 patients (15.4%), including 2 with complete recovery in <24 hours. The 2 other patients had a full recovery at 6-month follow-up. Transient symptoms presented were a fourth cranial nerve palsy after NAEL embolization and hemiparesis after reflux of NAEL into the vertebral artery. The 2 major complications were hydrocephaly due to mass effect after a venous thrombosis and superior cerebellar ischemia due to a NAEL arterial reflux (On-line Table 1). We report no complications with transvenous or combined procedures. Thus, procedure-related morbidity at 24 hours was 15.5%; at discharge, it was 7.7%; and at 6 months, it was 0%. Procedure-related mortality was 0%.

Four patients were lost to follow-up, for whom the mRS at discharge was zero. Compared with the clinical situation at the time of diagnosis, every patient had a stable or improved clinical situation at 6 months (Fig 5). All of them achieved independence (mRS < 2) at 6 months or at discharge versus 80.0% at the time of the diagnosis.

Twenty-two patients (84.6%) underwent a control angiography at 6 months, which showed permanent occlusion for each of them.

DISCUSSION

Treatment Considerations and Classification

When intervention is indicated, the cornerstone of dAVF treatment is the disconnection of the vein foot. Proximal draining

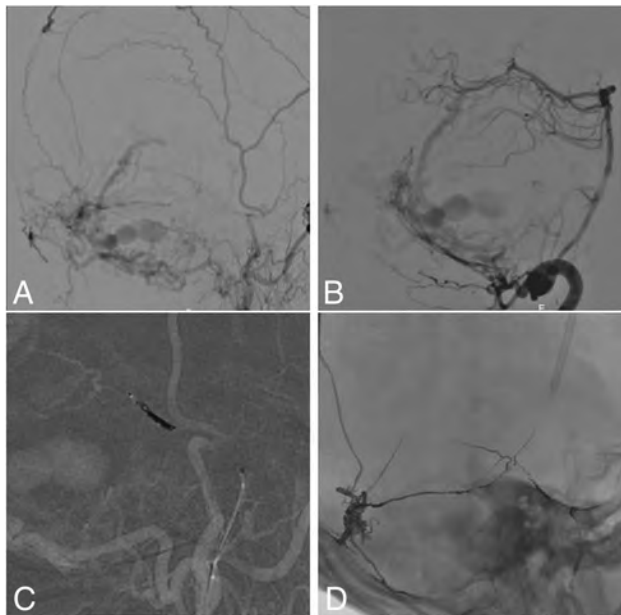


FIG 3. Transarterial approach. Arteriography of a ruptured dAVF with a shunt located in the declival vein and venous outflow into the cerebellar veins, fed by the PMA of the vertebral artery, transosseous branches of the occipital artery and squamous branch of the MMA. The MMA was catheterized; platinum coils were rolled into the MMA to improve NAEL penetration, and then, NAEL was injected. *A*, Lateral initial angiogram via the external carotid artery. *B*, Lateral initial angiogram via the vertebral artery. *C*, Coils with the pressure cooker technique in the MMA. *D*, Final cast of Onyx and coils.

veins must be occluded at the end of the treatment.⁶ Due to their rarity, endovascular treatment of posterior fossa dAVFs has been less often described. Nevertheless, the arterial approach is the most common one even if a transvenous or combined approach can be a safe and effective option.^{7,8} As described in the literature,⁷ in our series the transarterial route was the first-line approach. However, regarding the 3 patients treated by a transvenous approach, alone or combined, we detected no clinical complications, and the mRS was stable or improved at 6 months for those patients. Hence, even if we cannot support any conclusion with such a small number of patients, the transvenous approach could be an option for some selective cases.

Furthermore, in agreement with the literature,^{6,9,10} the MMA was the most commonly selected artery to navigate to the shunt, even if it was not the main feeding artery, because of the less tortuous route and the lower rate of dangerous anastomosis. We report 2 main complications: extended venous thrombosis causing hydrocephaly and cerebellar ischemia unrelated to the MMA navigation.

In the present series, complication rates linked to the procedure were low. However, the complication rates reported in the literature were even lower. Indeed, Maimon et al⁶ reported a complication rate of 5.8%, and Cognard et al,¹¹ a rate of 6.7%. However, those rates do not specifically concern posterior fossa dAVFs but all dAVFs with cortical venous drainage, including dAVFs that are considered safer to treat. Besides, Zhou et al,⁴ in a series of 5 tentorial dAVFs, reported 1 complication (20%) due to a cerebellar infarctus, whereas Motebajane and Choi,¹² in a series of 12

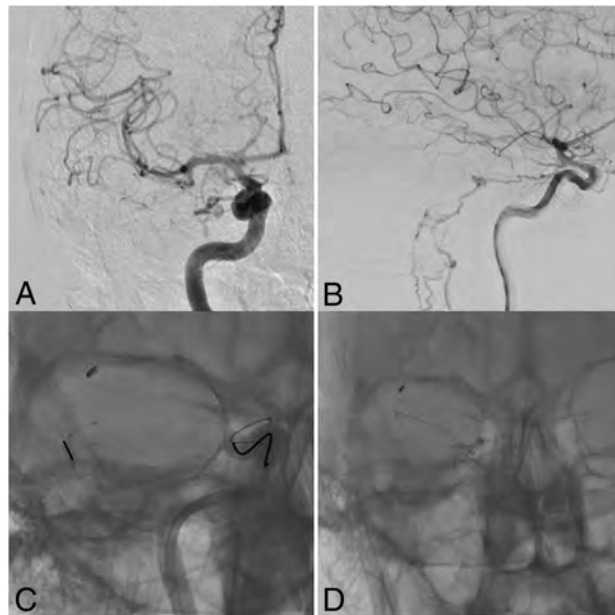


FIG 4. Double balloons with a pressure cooker technique. Arteriography of an unruptured petrosal dAVF, fed by the medial tentorial branch of the MHT and a tentorial branch of the MMA, draining into superior petrosal vein with an outflow into the perimedullary veins. A balloon pressure cooker technique was used. A Scepter XC 4 × 11 balloon (MicroVention, Tustin, California) was inflated in the MMA to improve the Onyx injection, while protecting the carotid siphon with a Copernic balloon (Balt Extrusion, Montmorency, France). While both balloons were inflated, Onyx 18 was injected in a single session using a Marathon microcatheter (Covidien). Total occlusion of the shunt was noted on the final angiography. *A*, Antero-posterior initial angiogram. *B*, Lateral initial angiogram. *C*, Balloon pressure cooker technique in the MMA with the balloon-protecting device in the ICA. *D*, Final cast of Onyx.

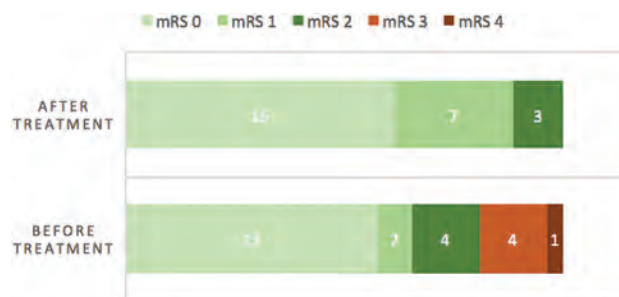


FIG 5. mRS before treatment at the time of the diagnosis and 6 months after treatment when available, or at discharge if not.

dAVFs of the foramen magnum treated with *n*-BCA, reported no complications as Liang et al¹³ in a series of 5 dAVFs of the foramen magnum treated with Onyx. Besides, tentorial fistulas are more challenging because there is usually a dural supply from both the internal and external carotid arteries, increasing the procedural risk of intracranial embolic events.⁹ Furthermore, because the venous drainage pattern is linked to the clinical symptoms,^{14,15} this slightly higher complication rate regarding fossa posterior fistulas might be linked to the specificity of posterior fossa drainage. Likewise, posterior fossa fistulas are located in a very eloquent zone.

Finally, the complication rate of the present series might also be linked to a more intensive endovascular treatment because

100% of the dAVFs were occluded, whereas Maimon et al⁶ reported a rate of 88.3%, and Cognard et al,¹¹ a rate of 80% of total occlusion.

Anatomic Considerations and Classification

We analyzed 26 dAVFs of the posterior fossa with infratentorial venous drainage. Because of the importance of venous drainage in the clinical presentation,¹⁵ special attention should be given to the venous outflow to improve the understanding of the shunt and the flow. Venous outflow can be defined according to the main draining vein at the level of the shunt. Thus, based on their venous outflow, cases have been classified into 5 groups, considering the shunt, the arterial feeders, and the treatment strategy.

The 5 groups noted were the following: group 1, vein outflow into the basal vein; group 2, vein outflow into the torcular; group 3, vein outflow into the cerebellar cortical vein; group 4, vein outflow into the lateral tentorial sinus; and group 5, vein outflow into the perimedullary venous plexus.

Other classifications exist but are not adapted to the endovascular approach because they are not specifically based on the outflow. Indeed, Lawton et al¹⁶ established a very detailed classification dividing 31 tentorial dAVFs into 6 groups. Nevertheless, this classification is anatomic and does not examine the venous outflow pattern. It is mainly to prepare the surgical access but is not adapted for an endovascular approach. There is another classification based on the location of the shunt and not on the outflow, thus including a posterior fossa shunt with occasionally supratentorial drainage.¹⁷ Hence, the proposed classification is more adapted to the endovascular approach and based on venous outflow, which is the most clinically impactful.¹⁵ However, due to the rarity of the cases, this classification has to be strengthened by further studies including more patients.

All of the dAVFs draining into the basal vein were petrosal and had a venous shunt into the superior petrosal vein. One other petrosal dAVF drained into the tentorial sinus, and another petrosal dAVF drained into perimedullary veins. Hence, for petrosal dAVFs, the anatomic location of the shunt did not predict the outflow and thus the symptoms, enhancing the need for a classification considering the venous outflow. In fact, our results were consistent with the pattern of drainage of the petrosal dAVF, which was described by Li et al¹⁸ and Matsushima et al.¹⁹ They classified petrosal dAVFs into 4 groups based on the draining area: the posterior mesencephalic group, anterior pontomesencephalic group, petrosal group, and tentorial group. They showed that all patients from the posterior mesencephalic group and some patients from the pontomesencephalic group had supratentorial drainage via a connection to the basilar vein. However, in the present series, we focused only on infratentorial drainage, so we do not present any pontomesencephalic dAVFs in our series.

Regarding the perimedullary drainage, the 5 dAVFs with a shunt into the lateral medullary vein were located on the foramen magnum and fed by the PMA of the vertebral artery or the APA as classically described in the literature.^{3,12}

Limitations

Limitations should be noted in the present series. First, it is a retrospective analysis with inherent bias due to this method. Second, the cohort is relatively small because posterior fossa dAVFs are rare, and patients were not randomized into transarterial, transvenous, or combined approaches, which does not allow comparison among the different endovascular approaches.

Finally, due to their rarity, not many studies focusing on dAVFs of the posterior fossa can be found in the literature. To our knowledge, our series is the largest in the literature specifically concerning dAVFs of the posterior fossa.

CONCLUSIONS

dAVFs of the posterior fossa with subarachnoid venous drainage are rare and difficult to treat. Special attention should be given to the venous outflow to understand the pathology and analyze the therapeutic procedure. An arterial approach was the most common. A venous approach, isolated or combined, could also be safe and successful in some selected cases; additional data are needed regarding this approach.

ACKNOWLEDGMENTS

We acknowledge Suzana Saleme and Vladimir Boretsky for their support.

REFERENCES

1. Newton TH, Cronqvist S. **Involvement of dural arteries in intracranial arteriovenous malformations.** *Radiology* 1969;93:1071–78 [CrossRef](#) [Medline](#)
2. Newton TH, Weidner W, Greitz T. **Dural arteriovenous malformation in the posterior fossa.** *Radiology* 1968;90:27–35 [CrossRef](#) [Medline](#)
3. Pierot L, Chiras J, Meder JF, et al. **Dural arteriovenous fistulas of the posterior fossa draining into subarachnoid veins.** *AJNR Am J Neuroradiol* 1992;13:315–23 [Medline](#)
4. Zhou LF, Chen L, Song DL, et al. **Tentorial dural arteriovenous fistulas.** *Surg Neurol* 2007;67:472–81; discussion 481–82 [CrossRef](#) [Medline](#)
5. Cognard C, Gobin YP, Pierot L, et al. **Cerebral dural arteriovenous fistulas: clinical and angiographic correlation with a revised classification of venous drainage.** *Radiology* 1995;194:671–80 [CrossRef](#) [Medline](#)
6. Maimon S, Nossek E, Strauss I, et al. **Transarterial treatment with Onyx of intracranial dural arteriovenous fistula with cortical drainage in 17 patients.** *AJNR Am J Neuroradiol* 2011;32:2180–84 [CrossRef](#) [Medline](#)
7. Lee SK, Hetts SW, Halbach V, et al; Standard and Guidelines Committee for the Society of Neurointerventional Surgery. **Standard and guidelines: intracranial dural arteriovenous shunts.** *J Neurointerv Surg* 2017;9:516–23 [CrossRef](#) [Medline](#)
8. Wong GK, Poon WS, Yu SC, et al. **Transvenous embolization for dural transverse sinus fistulas with occluded sigmoid sinus.** *Acta Neurochir (Wien)* 2007;149:929–35; discussion 935–36 [CrossRef](#) [Medline](#)
9. Kortman H, Bloemsmas G, Boukrab I, et al. **Treatment of cranial dural arteriovenous fistulas with exclusive cortical venous drainage: a single-center cohort of 35 patients.** *Interv Neuroradiol* 2017;23:661–65 [CrossRef](#) [Medline](#)
10. Stiefel MF, Albuquerque FC, Park MS, et al. **Endovascular treatment of intracranial dural arteriovenous fistulae using Onyx: a case series.** *Neurosurgery* 2009;65(6 Suppl):132–39; discussion 139–40 [CrossRef](#) [Medline](#)
11. Cognard C, Januel AC, Silva NA Jr, et al. **Endovascular treatment of intracranial dural arteriovenous fistulas with cortical venous**

- drainage: new management using Onyx.** *AJNR Am J Neuroradiol* 2008;29:235–41 CrossRef Medline
12. Motebejane MS, Choi IS. **Foramen magnum dural arteriovenous fistulas: clinical presentations and treatment outcomes: a case-series of 12 patients.** *Oper Neurosurg (Hagerstown)* 2018;15:262–69 CrossRef Medline
 13. Liang G, Gao X, Li Z, et al. **Endovascular treatment for dural arteriovenous fistula at the foramen magnum: report of five consecutive patients and experience with balloon-augmented transarterial Onyx injection.** *J Neuroradiol* 2013;40:134–39 CrossRef Medline
 14. Houser OW, Baker HL Jr, Rhoton AL Jr, et al. **Intracranial dural arteriovenous malformations.** *Radiology* 1972;105:55–64 CrossRef Medline
 15. Lasjaunias P, Chiu M, ter Brugge K, et al. **Neurological manifestations of intracranial dural arteriovenous malformations.** *J Neurosurg* 1986;64:724–30 CrossRef Medline
 16. Lawton MT, Sanchez-Mejia RO, Pham D, et al. **Tentorial dural arteriovenous fistulae: operative strategies and microsurgical results for six types.** *Neurosurgery* 2008;62(3 Suppl 1):110–24; discussion 124–25 CrossRef Medline
 17. Byrne JV, Garcia M. **Tentorial dural fistulas: endovascular management and description of the medial dural-tentorial branch of the superior cerebellar artery.** *AJNR Am J Neuroradiol* 2013;34:1798–804 CrossRef Medline
 18. Li J, Ren J, Du S, et al. **Dural arteriovenous fistulas at the petrous apex.** *World Neurosurg.* 2018;119:e968–76 CrossRef Medline
 19. Matsushima K, Matsushima T, Kuga Y, et al. **Classification of the superior petrosal veins and sinus based on drainage pattern.** *Neurosurgery* 2014;10(Suppl 2):357–67; discussion 367 CrossRef Medline

Carotid Artery Stiffness Accurately Predicts White Matter Hyperintensity Volume 20 Years Later: A Secondary Analysis of the Atherosclerosis Risk in the Community Study

A. de Havenon, K.-H. Wong, A. Elkhetafi, J.S. McNally, J.J. Majersik, and N.S. Rost

ABSTRACT

BACKGROUND AND PURPOSE: Arterial stiffness is a biomarker of cerebrovascular disease and dementia risk. Studies have shown an association between carotid artery stiffness and increased white matter hyperintensity volume and, as a result, reduced total brain volume on MR imaging, but none have had prolonged follow-up to fully evaluate the slow change seen in white matter hyperintensity volume and total brain volume with time. Our objective was to determine whether common carotid artery stiffness on sonography accurately predicts white matter hyperintensity volume and total brain volume on MR imaging more than 20 years later.

MATERIALS AND METHODS: We performed a secondary analysis of the Atherosclerosis Risk in the Community study to compare 5 measurements of carotid artery stiffness, including strain, distensibility, compliance, Stiffness index, and pressure-strain elastic modulus, with the white matter hyperintensity volume and total brain volume on a follow-up MR imaging using linear regression.

RESULTS: We included 1402 patients enrolled in the Atherosclerosis Risk in the Community study. There was a significant relationship between increasing carotid artery stiffness and both higher white matter hyperintensity volume and lower total brain volume on MR imaging, measured at a mean of 21.5 years later. In multivariable linear regression models, the carotid strain, distensibility, Stiffness index, and pressure-strain elastic modulus were associated with white matter hyperintensity volume. Only compliance was associated with total brain volume in the multivariate models.

CONCLUSIONS: Sonography measurements of carotid artery stiffness are predictive of white matter hyperintensity volume and total brain volume on MR imaging more than 20 years later. The association is more robust for white matter hyperintensity volume than total brain volume. These findings support the role of arterial stiffness as a method for identifying patients at risk of developing white matter hyperintensity volume and as a potential mechanism leading to small-artery disease of the brain.

ABBREVIATIONS: CS = carotid artery stiffness; TBV = total brain volume; WMH = white matter hyperintensity; WMHv = white matter hyperintensity volume

White matter hyperintensity (WMH), a radiographic signature of diffuse small cerebral vasculopathy, and brain atrophy on MR imaging are associated with impaired cognitive function and poor neurologic outcomes.¹⁻³ Arterial stiffness is a marker of cerebrovascular disease, which is caused by advanced

age, hypertension, smoking, and diabetes.^{4,5} Carotid artery stiffness (CS), measured with sonography, is an independent risk factor for cerebrovascular disease, cognitive impairment, and mortality.^{4,6} Carotid wall stiffness is postulated to transmit the increase in blood pressure during systole to the brain, where it can harm the sensitive microvasculature, whose dysfunction is implicated in the pathogenesis of WMH and, as a result, brain atrophy.⁷ Most studies that examined the association of CS with WMH or brain atrophy have been cross-sectional with concurrent sonography and brain MR imaging or relied on aortic or peripheral arterial stiffness measurements rather than those of the carotid artery.^{4,8,9} Two longitudinal studies failed to show an association between CS and WMH or total brain volume (TBV) with time, but both had significantly shorter periods of follow-up.^{10,11} Given the slow pace of WMH and brain atrophy development, we sought to explore their association with CS during a more physiologically plausible time interval spanning 2 decades.

Received December 27, 2018; accepted after revision May 28, 2019.

From the Department of Neurology (A.d.H., K.-H.W., A.E., J.S.M., J.J.M.), University of Utah, Salt Lake City, Utah; and Harvard Medical School (N.S.R.), Boston, Massachusetts.

Research reported in this publication was supported by an American Heart Association Scientist Development Grant 17SDG33670114 (Dr de Havenon).

The content of this work is solely the responsibility of the authors and does not represent the official views of the American Heart Association.

Please address correspondence to Adam de Havenon, MD, University of Utah, Department of Neurology, 175 N Medical Dr, Salt Lake City, UT 84132; e-mail: adam.dehavenon@hsc.utah.edu

<http://dx.doi.org/10.3174/ajnr.A6115>

Table 1: Baseline demographics at visit 2 and P values for association with concurrent carotid distensibility measurement^a

Variable	Full Cohort (n = 1402)	P Value for Association with Carotid Distensibility
Age (mean)	55.6 ± 5.3	<.001 ^d
Male (No.) (%)	571, 40.7	.214
Caucasian (No.) (%)	1,023, 73.0	.007 ^d
Hypertension (No.) (%) (n = 1396)	280, 20.1	<.001 ^d
Diabetes (No.) (%) (n = 1398)	71, 5.1	.265
History of myocardial infarction (No.) (%)	26, 1.9	.898
History of stroke (No.) (%)	10, 0.7	.602
Prevalent coronary heart disease (No.) (%)	16, 1.2	.297
Current cigarette smoking (No.) (%) (n = 1400)	206, 14.7	<.001 ^d
Current alcohol consumption (No.) (%) (n = 1400)	846, 60.4	.009 ^d
Body mass index (mean)	27.1 ± 4.6	<.001 ^d
LDL cholesterol (mean) (mg/dL) (n = 1376)	131.2 ± 35.0	.493
HDL cholesterol (mean) (mg/dL) (n = 1328)	49.3 ± 16.7	.067
Fasting blood glucose (mean) (mmol/L)	5.9 ± 1.6	.077
Antihypertensive in last 2 weeks (No.) (%) (n = 1397)	248, 17.8	<.001 ^d
Aspirin in last 2 weeks (No.) (%) (n = 1400)	632, 45.1	.369
Statin in last 2 weeks (No.) (%) (n = 1400)	29, 2.1	.651
Plaque in either carotid on ultrasound (No.) (%) (n = 1392)	310, 22.3	.270
Voltage of left ventricular leads on ECG (mean) (n = 1391)	1174.2 ± 525.4	<.001 ^d
WMH volume (mean) (mL)	17.5 ± 17.4	
Total brain volume (mean) (mL) (n = 1397) ^b	1015.8 ± 109.4	
Ratio of WMH/TBV (mean) (%) (n = 1397) ^b	1.7 ± 1.7	
Mean systolic blood pressure (mm Hg) ^c	135.0 ± 12.4	
Mean systolic SD (mm Hg) ^c	15.8 ± 4.2	
Mean number of blood pressure readings ^c	23.3 ± 3.1	
Years between carotid ultrasound and MRI (mean)	21.5 ± 0.9	

Note:—ECG indicates electrocardiography; HDL, high-density lipoprotein; LDL, low-density lipoprotein.

^a Association tested with linear regression for continuous variables and Student *t* test for categorical variables.

^b Derived from visit 5 MRI.

^c Derived from all available blood pressure readings from visit 2 through visit 5.

^d Significant.

MATERIALS AND METHODS

This is a secondary analysis of the Atherosclerosis Risk in the Community (ARIC) study,¹² a large prospective epidemiologic study conducted in 4 communities in the United States. Participants were 45–64 years of age at enrollment in 1987–1989, and they continue to be followed periodically for vascular health status. No study-based intervention was provided. With a local institutional review board waiver from the University of Utah, we obtained the anonymized ARIC dataset from the National Heart, Lung, and Blood Institute Biologic Specimen and Data Repository Information Coordinating Center. We included patients who had both a carotid sonography at visit 2 (1990–1992) and a brain MR imaging at visit 5 (2011–2013). No brain MR imaging was performed at visit 2. The methods of carotid sonography measurements have been previously described,¹³ as have the methods of the white matter hyperintensity volume (WMHv) and TBV measurement on MR imaging.¹⁴ In short, the MR imaging was performed at a 3T field strength with a standardized protocol for all study sites. The ARIC MR imaging reading center (Mayo Clinic, Rochester, Minnesota) was responsible for quality control and interpretation of the scans. TBV was measured on a sagittal T1-weighted 3D volumetric MPRAGE pulse sequence using FreeSurfer (Version 5.1; (<http://surfer.nmr.mgh.harvard.edu>)) and an

ARIC-specific algorithm. WMHv was measured using similar methodology on an axial T2 FLAIR pulse sequence.

We included 5 measures of CS of the common carotid artery, which take into account the peak systolic diameter (PSD) of the carotid artery, end diastolic diameter (EDD), systolic blood pressure (SBP), diastolic blood pressure (DBP), and pulse pressure (PP). The 5 CS measures are the following: strain [(PSD-EDD) / EDD], distensibility [$100 \times (\text{PSD}^2 - \text{EDD}^2) / (\text{PP} \times \text{EDD}^2)$], compliance [$\pi \times (\text{PSD}^2 - \text{EDD}^2) / (4 \times \text{PP})$], Stiffness index [$\log(\text{SBP} / \text{DBP}) / \text{strain}$], and pressure-strain elastic modulus [$\text{PP} / \text{strain}$]. For strain, distensibility, and compliance, higher values reflect less CS. For the Stiffness index and pressure-strain elastic modulus, higher values reflect more CS. All measures of CS were treated as continuous variables in statistical analyses, unless otherwise specified.

We report the association between visit 2 baseline demographics and carotid distensibility as a surrogate for CS, using linear regression and the Student *t* test. We further divided the 5 CS measurements into quintiles and tested for differences in the mean WMHv and TBV with ANOVA. We fit multivariate linear regression models to the outcomes of WMHv and TBV. Model 1 was adjusted for all available systolic blood pressure measurements between visits 2 and 5 because chronic hypertension has shown the best correlation with WMHv. For the subsequent models, we tested candidate covariates from the demographic data in Table 1 with stepwise backward selection fit to the outcomes and set to a threshold of a *P* < 0.1 for inclusion. Using this methodology, we adjusted model 2 for selected visit 2 demographics (the WMH model adjusted for patient age, sex, body mass index, high-density lipoprotein cholesterol level, current smoking, history of hypertension; the TBV model adjusted for patient age, sex, black race, fasting glucose level, and current smoking), and model 3 was adjusted for selected visit 3 demographics (1993–1995) (the WMH model adjusted for patient age, current cigarette smoking, history of hypertension, and voltage of left ventricular leads on electrocardiography; the TBV model adjusted for patient age, sex, black race, diabetes, and high-density lipoprotein cholesterol level). Sensitivity analyses were conducted adjusted for demographics from visit 4 and with the WMHv standardized to TBV (WMHv:TBV).

RESULTS

The final cohort included 1402 patients with a mean of 21.5 years between carotid sonography and MR imaging. The mean age at

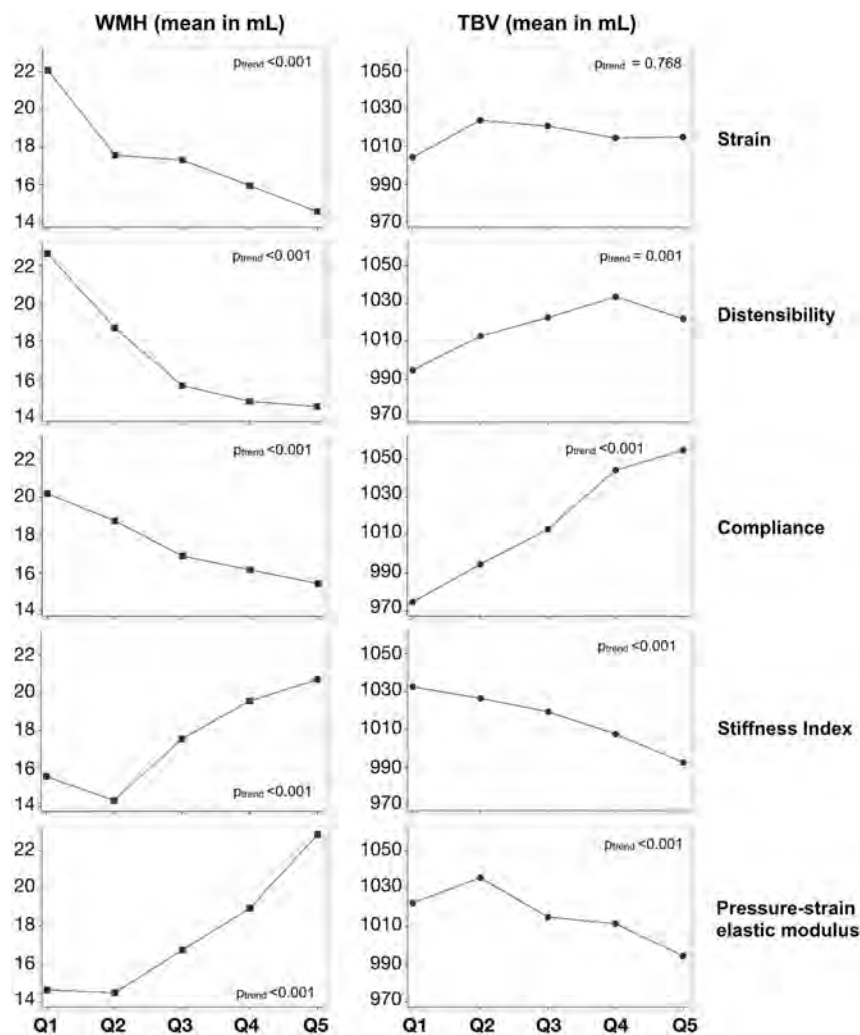


FIGURE. Mean values of WMH and TBV in the quintiles of carotid sonography measurements. For strain, distensibility, and compliance, the higher quintiles reflect less carotid stiffness. For the Stiffness index and pressure-strain elastic modulus, the higher quintiles reflect more carotid stiffness.

sonography was 57 years, and at MR imaging, it was 76 years. Baseline demographics from visit 2, when the carotid sonography was performed, are shown in Table 1. Although cerebrovascular risk factors were modestly prevalent (hypertension = 20.1%, smoking = 14.7%, diabetes = 5.1%, plaque in either carotid artery on sonography = 22.3%), only 0.7% had a history of prior stroke. The mean values for CS were the following: strain = $5.4\% \pm 1.9\%$, distensibility = $1.8\% \pm 0.8\%/kPa$, compliance = $8.0 \pm 3.1 \text{ mm}^3/kPa$, Stiffness index = 0.11 ± 0.04 (unitless), pressure-strain elastic modulus = $131.1 \pm 56.1 \text{ kPa}$. We found that the following visit 2 variables were significantly associated with increased CS: advanced patient age, black race, hypertension, smoking, not consuming alcohol, higher body weight, and evidence of left ventricular hypertrophy (LVH) on electrocardiography (Table 1).

The mean WMHv increased linearly with higher CS (Figure). In the linear regression models fit to WMHv, carotid strain, distensibility, Stiffness index, and the pressure-strain elastic modulus were consistently associated with WMHv, while compliance failed to maintain significance (Table 2). The relationship be-

tween CS and TBV was less consistent than WMHv, and strain was not significantly predictive. Only compliance had an association with TBV in the multivariate models. These results were not changed in our sensitivity analyses (data not shown).

DISCUSSION

CS is associated with WMHv, and, to a lesser extent, with TBV on MR imaging obtained >2 decades later. The association with WMHv is more robust than for TBV, which is a multifactorial outcome that combines vascular injury and neurodegeneration. The percentage difference in WMHv between the least stiff to most stiff quintile of CS was on the order of 30%, while for TBV, it was on the order of 2%. These represent clinically meaningful differences that may translate to divergent outcome rates. Arterial stiffness has a direct pathophysiologic link to WMH, which is caused by dysfunction of cerebral microvasculature that is hypothesized to be uniquely sensitive to the hypertension transmitted by stiffer arteries.⁷ In addition, our findings may be explained by shared long-term WMHv and CS risk-factor exposure, including hypertension, diabetes, smoking, and hyperlipidemia.

Our study is consistent with prior studies that were either cross-sectional or used peripheral measures of arterial stiffness,^{4,8,9} but the findings conflict with 2 prior longitudinal studies. The Second Manifestations of ARterial disease-MR (SMART-MR) study looked at the change in WMHv and TBV and failed to find an association with CS, but it had only 4 years of follow-up.¹⁰ Likewise, in the Framingham Offspring Cohort, the carotid-femoral pulse wave velocity was not associated with change in WMHv and TBV, but the follow-up period was 6 years.¹¹ While baseline MR imaging scans are not available for this analysis to account for temporal change in WMHv or TBV, these patients were relatively young at baseline, making the large volumes of WMH and brain atrophy seen on MR imaging at visit 5, when the mean age was 76 years, an effective, though imperfect, proxy for change in WMHv or TBV. We posit that our findings reflect the more biologically meaningful interval between the measurements of CS and WMHv or TBV, which would allow the gradual progression of disease and accumulation of damage from increased arterial stiffness.

This analysis has the unique strength of a prolonged exposure period, a larger cohort than prior longitudinal studies, and validated measurements of the exposures and outcomes in a landmark epidemiologic study. Limitations include the lack of a base-

Table 2: Linear regression fit to WMHv and TBV on the visit 5 MRI

Ultrasound Variable	Model 1 ^a	Model 2 ^b	Model 3 ^c
WMHv (mL)			
Strain			
β	-1.2	-0.7	-0.9
95% CI	(-1.7 to -0.8)	(-1.2 to -0.2)	(-1.4 to -0.4)
P value	<.001	.007	.001
Distensibility			
β	-1.9	-1.6	-1.7
95% CI	(-3.2 to -0.6)	(-2.9 to -0.3)	(-3.0 to -0.4)
P value	.003	.019	.009
Compliance			
β	-0.1	-0.3	-0.2
95% CI	(-0.4-0.2)	(-0.6-0.1)	(-0.5-0.1)
P value	.355	.115	.127
Stiffness index			
β	45.1	30.6	35.9
95% CI	(23.1-67.2)	(6.6-54.6)	(12.5-59.3)
P value	<.001	.012	.003
Pressure-strain elastic modulus			
β	0.03	0.03	0.04
95% CI	(0.02-0.05)	(0.02-0.05)	(0.02-0.05)
P value	.001	<.001	<.001
TBV (mL)			
Strain			
β	0.1	0.7	0.3
95% CI	(-2.9-3.2)	(-1.7-3.1)	(-2.2-2.8)
P value	.940	.581	.820
Distensibility			
β	4.1	4.4	2.8
95% CI	(-4.0-12.3)	(-1.7-10.4)	(-3.4-9.0)
P value	.319	.158	.382
Compliance			
β	7.7	2.5	2.1
95% CI	(5.9-9.6)	(1.0-3.9)	(0.6-3.6)
P value	<.001	.001	.007
Stiffness index			
β	-276.3	-72.7	-55.1
95% CI	(-417.7 to -135.9)	(-183.7-38.3)	(-170.6-60.3)
P value	<.001	.199	.349
Pressure-strain elastic modulus			
β	-0.1	-0.1	-0.1
95% CI	(-0.2 to -0.01)	(-0.2-0.01)	(-0.1-0.03)
P value	.030	.070	.183

^a Model 1: adjusted for systolic blood pressure mean between visit 2 and visit 5 ($n = 1402$ for WMH and $n = 1397$ for total brain volume).

^b Model 2: WMH model adjusted for visit 2, patient age, sex, body mass index, HDL cholesterol, current smoking, history of hypertension ($n = 1320$). TBV model adjusted for patient age, sex, black race, fasting glucose, and current smoking ($n = 1393$).

^c Model 3: WMH model adjusted for visit 3, patient age, current cigarette smoking, history of hypertension, and voltage of left ventricular leads on ECG ($n = 1289$). TBV model adjusted for patient age, sex, black race, diabetes, and HDL cholesterol level ($n = 1296$).

line MR imaging, inability to adjust with more granularity for potential confounders such as medication use or blood pressure, and the absence of data on cerebrovascular stenosis or perfusion during the exposure period.

CONCLUSIONS

We report a strong association between CS and WMHv on MR imaging performed >20 years later and a less consistent association between CS and TBV. A larger WMHv is independently associated with impaired cognitive function, higher risk of both ischemic and hemorrhagic stroke, and worse outcomes after stroke. The Systolic Blood Pressure Intervention Trial-Memory and Cognition in Decreased Hypertension (SPRINT-MIND) trial

recently reported that intensive blood pressure control attenuates WMH progression,¹⁵ and several other ongoing studies are being planned to evaluate interventions that could reduce WMH. Against this backdrop, our data suggest the importance of CS as an intermediate step in the WMH development pathway, which could be informative for clinical trials of WMH reduction.

Disclosures: Adam de Havenon—RELATED: Grant: American Heart Association, Comments: Research reported in this publication was supported by an American Heart Association Scientist Development Grant 17SDG33670114.* Jennifer J. Majersik—UNRELATED: Grants/Grants Pending: National Institutes of Health/ National Institute of Neurological Disorders and Stroke 5U10NS08660*; Travel/Accommodations/Meeting Expenses Unrelated to Activities Listed: American Academy of Neurology, Comments: Transforming Leaders Program.* Natalia S. Rost—UNRELATED: Consultancy: Sanofi Genzyme, Broadview Ventures, Omniox; Grants/Grants Pending: National Institutes of Health*; Royalties: Up-To-Date, J. Scott McNally—UNRELATED: Grants/Grants Pending: American Heart Association and National Institutes of Health, Comments: amyloid deposition and pre-existing vulnerable carotid plaque features predicting cognitive improvement after surgery, Principal Investigator: J. Scott McNally; National Institutes of Health R01, High-Resolution, Motion-Corrected 3D Cine MRI of carotid plaque, role: Co-I.* Money paid to institution.

REFERENCES

1. Au R, Massaro JM, Wolf PA, et al. Association of white matter hyperintensity volume with decreased cognitive functioning: the Framingham Heart Study. *Arch Neurol* 2006;63:246-50 CrossRef Medline
2. Kuller LH, Longstreth WT Jr, Arnold AM, et al; Cardiovascular Health Study Collaborative Research Group. White matter hyperintensity on cranial magnetic resonance imaging: a predictor of stroke. *Stroke* 2004;35:1821-25 CrossRef Medline
3. Appelman AP, Exalto LG, van der Graaf Y, et al. White matter lesions and brain atrophy: more than shared risk factors? A systematic review. *Cerebrovasc Dis* 2009;28:227-42 CrossRef Medline
4. Singer J, Trollor JN, Baune BT, et al. Arterial stiffness, the brain and cognition: a systematic review. *Ageing Res Rev* 2014;15:16-27 CrossRef Medline
5. Mitchell GF, Guo CY, Benjamin EJ, et al. Cross-sectional correlates of increased aortic stiffness in the community: the Framingham Heart Study. *Circulation* 2007;115:2628-36 CrossRef Medline
6. van Sloten TT, Protogerou AD, Henry RM, et al. Association between arterial stiffness, cerebral small vessel disease and cognitive impairment: a systematic review and meta-analysis. *Neurosci Biobehav Rev* 2015;53:121-30 CrossRef Medline
7. Mitchell GF, van Buchem MA, Sigurdsson S, et al. Arterial stiffness, pressure and flow pulsatility and brain structure and function: the Age, Gene/Environment Susceptibility-Reykjavik study. *Brain* 2011;134:3398-407 CrossRef Medline
8. van Sloten TT, Mitchell GF, Sigurdsson S, et al. Associations be-

- tween arterial stiffness, depressive symptoms and cerebral small vessel disease: cross-sectional findings from the AGES-Reykjavik Study. *J Psychiatry Neurosci* 2016;41:162–68 CrossRef Medline
9. Yuan C, Wang J, Ying M. Predictive value of carotid distensibility coefficient for cardiovascular diseases and all-cause mortality: a meta-analysis. *PLoS One* 2016;11:e0152799 CrossRef Medline
 10. Jochemsen HM, Muller M, Bots ML, et al; SMART Study Group. Arterial stiffness and progression of structural brain changes: the SMART-MR study. *Neurology* 2015;84:448–55 CrossRef Medline
 11. Tsao CW, Himali JJ, Beiser AS, et al. Association of arterial stiffness with progression of subclinical brain and cognitive disease. *Neurology* 2016;86:619–26 CrossRef Medline
 12. The Atherosclerosis Risk in Community (ARIC) study: design and objectives—the ARIC investigators. *Am J Epidemiol* 1989;129:687–702 CrossRef Medline
 13. Yang EY, Chambless L, Sharrett AR, et al. Carotid arterial wall characteristics are associated with incident ischemic stroke but not coronary heart disease in the Atherosclerosis Risk in Communities (ARIC) study. *Stroke* 2012;43:103–08 CrossRef Medline
 14. Power MC, Lamichhane AP, Liao D, et al. The association of long-term exposure to particulate matter air pollution with brain MRI findings: the ARIC study. *Environ Health Perspect* 2018;126:027009 CrossRef Medline
 15. SPRINT MIND Trial Finds Lower Risk of MCI and Dementia with Lower BP. American College of Cardiology. <https://www.acc.org/latest-in-cardiology/articles/2018/07/26/16/36/sprint-mind-trial-finds-lower-risk-of-mci-and-dementia-with-lower-bp>. Accessed June 15, 2019

Carotid CTA at the Lowest Tube Voltage (70 kV) in Comparison with Automated Tube Voltage Adaption

A. Eller, M. Wiesmüller, W. Wüst, R. Heiss, M. Kopp, M. Saake, M. Brand, M. Uder, and M.M. May

ABSTRACT

BACKGROUND AND PURPOSE: CTA is the imaging modality of choice in many institutions for the evaluation of the supraaortic vessels, but radiation exposure remains a matter of concern. Our aim was to evaluate a 70-kV protocol for CT angiography of the carotid arteries with respect to image quality and radiation exposure compared with automated tube voltage adaption.

MATERIALS AND METHODS: A total of 90 consecutive patients were included in this prospective study and randomized to the study group ($n = 45$, 70 kV) or control group ($n = 45$, automated tube voltage adaptation). Volume CT dose indices and dose-length products were recorded in the examination protocol. Image quality was assessed as arterial vessel contrast, signal-to-noise ratio, contrast-to-noise ratio, and contrast-to-noise ratio in reference to the radiation dose. Subjective overall image-quality analysis, image-artifact analysis, and diagnostic evaluation were performed by 2 observers by using a 4-point Likert scale.

RESULTS: Radiation exposure was significantly lower in the study group (volume CT dose index reduced by 22%, dose-length product reduction by 20%; each $P < .001$). Contrast ($P = .15$), SNR ($P = .4$), and contrast-to-noise ratio ($P = .5$) did not show significant differences between the groups. The contrast-to-noise ratio in reference to the radiation dose was not significantly increased using the study protocol ($P = .2$). Subjective image quality and visualization of pathologic findings did not differ significantly between the groups.

CONCLUSIONS: Carotid CTA using the lowest available voltage (70 kV) is feasible at very-low-dose levels, while overall image quality is comparable with protocols using automated tube voltage selection.

ABBREVIATIONS: A = relative attenuation; BMI = body mass index; C = contrast; CNR = contrast-to-noise ratio; CNRD = contrast-to-noise ratio in reference to the radiation dose; CTDI_{vol} = volume CT dose index; DLP = dose-length product

Besides screening with Doppler sonography, CT angiography is an established second-line technique in imaging of extracranial carotid artery disease.¹ Following its technologic evolution and the increasing availability, the number of CT examinations has been steadily rising in the past years, though CT is the main factor accounting for medical x-ray exposure. Increasing knowledge of the potential risks of even relatively low radiation doses has led to increased concern about CT as a screening tool, as well as in serial use.²⁻⁵ Biologic experiments have demonstrated that the number of DNA double-strand breaks is closely related to the applied radiation dose, and according to the as low as reasonably achievable (ALARA) prin-

ciple, the applied radiation dose should be as low as reasonably achievable.³ To lower radiation exposure, automated attenuation-based tube current modulation or automatic exposure control protocols are widely established.^{6,7}

In addition to minimizing tube current, lowering the tube voltage is a good option for reducing the overall radiation dose. A drawback of low-kilovolt scanning is increased image noise, which needs to be partially compensated for by raising the milliampere-second setting. In examinations with contrast media, a low kilovolt enables scanning closer to the k-edge of iodine. This feature strongly increases the image contrast so that despite the increased image noise, the contrast-to-noise ratio can be kept constant or even increased compared with conventional imaging protocols. Therefore, the radiation dose efficiency is increased. This effect has already been described earlier in phantom studies and has also been used in several clinical studies to reduce contrast agent or radiation dosages compared with conventional tube voltage settings.⁸⁻¹¹ The need for complex manual adaption of tube voltage and tube current to individual patient anatomy has precluded its widespread use in the past.

Received September 18, 2018; accepted after revision May 26, 2019.

From the Department of Radiology (A.E., M.W., W.W., R.H., M.K., M.S., M.B., M.U., M.M.M.), University Hospital Erlangen, Erlangen, Germany; and Imaging Science Institute (M.U., M.M.M.), Erlangen, Germany.

Please address correspondence to Matthias M. May, MD, Department of Radiology, University Hospital Erlangen, Maximiliansplatz 1, 91054 Erlangen, Germany; e-mail: Matthias.May@uk-erlangen.de

<http://dx.doi.org/10.3174/ajnr.A6108>

Recently, fully automatic algorithms adapting the setting of tube potential (kilovolt) and the tube current time product (milliamperere-second) by attenuation information from a scout scan have made low-kilovolt scanning popular for various indications.¹²⁻¹⁶ For the carotid arteries, an automated, attenuation profile-based kilovolt-selection algorithm has been established as being beneficial for reducing radiation exposure while maintaining a high image quality.¹⁷ Spearman et al¹⁸ reported an average radiation dose reduction of 36.4% for this state-of-the-art technique in a worldwide meta-analysis. Study protocols for carotid or cerebral CT angiographies used 100 kV (19% of all cases), 120 kV (79%), or 140 kV (2%) before the use of automated tube voltage selection, which was considerably reduced to 80 kV (9%), 100 kV (74%), 120 kV (16%), or 140 (1%) after its implementation. However, it remains unclear whether this positive effect could be further exploited by aggressively using the lowest available tube voltage for all patients, regardless of their anatomy. Recent x-ray tubes are especially tuned into this low-kilovolt range for high-tube-current supply.

Therefore, our aim was to evaluate the effects on radiation exposure and image quality in CTA of the carotid arteries using a fixed 70-kV protocol in comparison with the established protocol with automated kilovolt selection.

MATERIALS AND METHODS

A total of 90 consecutive patients scheduled for CTA of the carotid arteries were enrolled in this prospective study and randomized for examination following either the study or the reference protocol. Body mass index (BMI) was calculated for all patients using the following formula: Weight (kg) / [Height (m)]². Indications included stenosis of the carotid arteries as well as cervical CTA in patients undergoing reconstructive operations due to head and neck malignancies. The study protocol was approved by the institutional review board (University Hospital Erlangen) and complies with the Declaration of Helsinki. All examinations were performed on a third-generation dual-source CT scanner in a single-source mode (Somatom Force; Siemens, Erlangen, Germany).

A total of 45 patients were enrolled in the study group. CTA was performed using a protocol with a fixed 70-kV setting and activated automated exposure control (167 reference milliamperere-second), corresponding to an image quality of 120 reference kilovolts with 85 reference milliamperere-seconds. The full detector collimation was used (192 × 0.6 mm by a z-flying focal spot), the pitch factor was set to 0.85, and the rotation time was 0.25 seconds.

Another 45 patients were assigned to the control group and examined with activated automated tube voltage selection (CARE kV; Siemens) using the same reference values. All other parameters were identical to those in the study protocol.

Circulation time was individually calculated for both groups using a test-bolus injection with 10 mL of iodinated contrast medium (iopamidol, Imeron 350; Bracco, Milan, Italy) at a flow rate of 5 mL/s chased by a 50-mL saline bolus at the same flow rate using a power injector (Accutron CT-D; Medtronic, Saarbrücken, Germany). The ROI to measure the time to peak was placed in the aortic arch. Two seconds were added as a start delay of the diag-

nostic scan after injecting 50 mL of iodinated contrast medium and 50 mL of saline chaser, both at a flow rate of 5 mL/s.

Image reconstruction was performed in the axial plane using filtered back-projection with a smooth vascular kernel (Bv 36) and 3-mm slice thickness for basic image-quality evaluation in this study. Thin slices (Bv 36, 0.6 mm) were reconstructed for 3D evaluations.

Radiation Exposure

Values for effective milliamperere-second, volumetric CT dose index (CTDI_{vol}), and the dose-length product (DLP) were recorded in the patient protocol, allowing a direct comparison of radiation dose exposure in the study and the control groups. The effective dose was calculated using the published conversion factor for neck CT at 80 kV, which is usually indicated as the most appropriate value in the literature for this type of imaging (effective dose = DLP × 0.0052 mSv / mGy × cm).¹⁹ BMI-dependent subgroups below and above 27 kg/m² were used to evaluate the previously reported effect of body size on low-tube-voltage protocols.²⁰

Objective Image Quality

Objective assessment of the image quality was performed on a standard PACS workstation on 3-mm images in the axial plane. For each examination, 2 ROIs were manually placed in the carotid arteries on both sides, in the muscles of the neck, and in the air right and left anterior to the neck. Calcifications of the carotid walls were carefully excluded to avoid false iodine relative attenuation values. ROIs were not placed in slices with severe artifacts (ie, due to dental hardware or motion).

Mean relative attenuation (A) and its SD were obtained for each measurement in Hounsfield units. The SD was considered as a measure of image noise. Vessel contrast (C) was defined as the difference between the attenuation of the carotid artery and the muscle (C = A_{carotid} - A_{muscle}). Signal-to-noise ratio (SNR = A_{carotid} / SD_{carotid}), and contrast-to-noise ratio [CNR = (A_{carotid} - A_{muscle}) / SD_{muscle}] were calculated for the carotid artery. CNR in reference to the radiation dose exposure (CNRD) was calculated using the following formula: CNRD = CNR × √CTDI_{vol}^{-1/2}.

Subjective Image Quality

Subjective image quality of all examinations was assessed on a 4-point Likert scale (4, excellent; 3, good; 2, moderate; 1, not diagnostic). Artifacts were grouped into 4 categories of strength (4, no artifacts; 3, mild artifacts, not affecting diagnostic value; 2, artifacts, affecting diagnostic value; 1, strong artifacts, nondiagnostic) and assessed in 3 locations: 1) in the environment of the highly concentrated inflowing contrast media in the subclavian vein, 2) at the level of the shoulder girdle, and 3) at the level of the skull base. Regions affected by metal artifacts (eg, due to dental implants) were not considered due to strong interindividual differences. Artifacts of dental implants were assessed using a 4-point scale (4, no dental hardware; 3, dental implants, not affecting vessel evaluation; 2, dental hardware, mildly affecting vessel imaging, not affecting diagnostic confidence; 1, dental hardware with severe artifacts affecting diagnostic accuracy in the affected slices). Image quality and the presence of artifacts were indepen-

Table 1: Results of measurements and dose exposure^a

	Study			Control			
	Complete	Subgroups		Complete	Subgroups		
		BMI <27	BMI >27		70 kV	80 kV	90 kV
No.	45	29	16	45	19	20	6
BMI (kg/m ²)	25 ± 4.7	22 ± 2.7	30.4 ± 2	25.9 ± 4.1	23.6 ± 3.5	26.4 ± 3.2	31.4 ± 2.6
Ref. mAs	167	167	167	NA	167	125	104
Eff. mAs	235 ± 52	213 ± 35	274 ± 57 ^{bc}	NA	225 ± 26	200 ± 23	182 ± 16
CTDI _{vol} (mGy)	2.9 ± 1	2.7 ± 0.4	3.4 ± 0.7 ^{bc}	3.7 ± 1 ^{bd}	2.8 ± 0.3	4.1 ± 0.4 ^{bd}	5.6 ± 0.6 ^{bd}
DLP (mGy × cm)	107 ± 25	95 ± 15	127 ± 28 ^{bc}	133 ± 47 ^{bd}	96 ± 13 ^{bc}	150 ± 41 ^{bd}	200 ± 26 ^{bd}
ED (mSv)	0.56 ± 0.13	0.5 ± 0.08	0.66 ± 0.15	0.70 ± 0.24 ^{bd}	0.50 ± 0.06 ^{bc}	0.78 ± 0.21 ^{bd}	1.04 ± 0.13 ^{bd}
ROI carotid							
A (HU)	482 ± 173	496 ± 183	457 ± 155	515 ± 172	644 ± 131 ^{bd}	460 ± 115	287 ± 107 ^{bc}
SD (HU)	10 ± 3	10 ± 4	10 ± 2	11 ± 4 ^{bc}	12 ± 4 ^{bc}	11 ± 3	11 ± 3
C (HU)	419 ± 171	434 ± 183	391 ± 150	456 ± 169	581 ± 128 ^{bd}	407 ± 115	224 ± 105 ^{bc}
SNR	52 ± 25	55 ± 27	47 ± 21	50 ± 30	64 ± 13	45 ± 15	27 ± 12 ^{bc}
CNR	45 ± 24	48 ± 26	40 ± 20	44 ± 28	56 ± 36	40 ± 14	21 ± 10 ^{bc}
CNRD (mGy ^{-1/2})	26.9 ± 15	29.9 ± 16	22.1 ± 12	22.4 ± 17	29.7 ± 12	19.8 ± 7 ^{bc}	8.8 ± 4 ^{bd}
ROI muscle							
A (HU)	63 ± 12	61 ± 12	67 ± 14	69 ± 56	64 ± 13	58 ± 11 ^{bc}	63 ± 4
SD (HU)	8 ± 3	7 ± 3	10 ± 3 ^{bc}	8 ± 3	8 ± 3	8 ± 3	9 ± 3
ROI air							
A (HU)	-998 ± 7	-998 ± 5	-998 ± 4	-999 ± 5	-998 ± 5	-1000 ± 5	-1000 ± 6
SD (HU)	4 ± 2	4 ± 1	5 ± 1 ^{bc}	5 ± 1	4 ± 1	4 ± 1	5 ± 1

Note:—No. indicates sample size; ED, effective dose; NA, not applicable; Ref., reference; Eff. mAs, effective mAs; A, relative attenuation.

^a BMI-related subgroups from the study group are compared with each other; tube voltage-related subgroups of the control group are compared with the study group.

^b Significant difference.

^c $P < .05$.

^d $P < .001$.

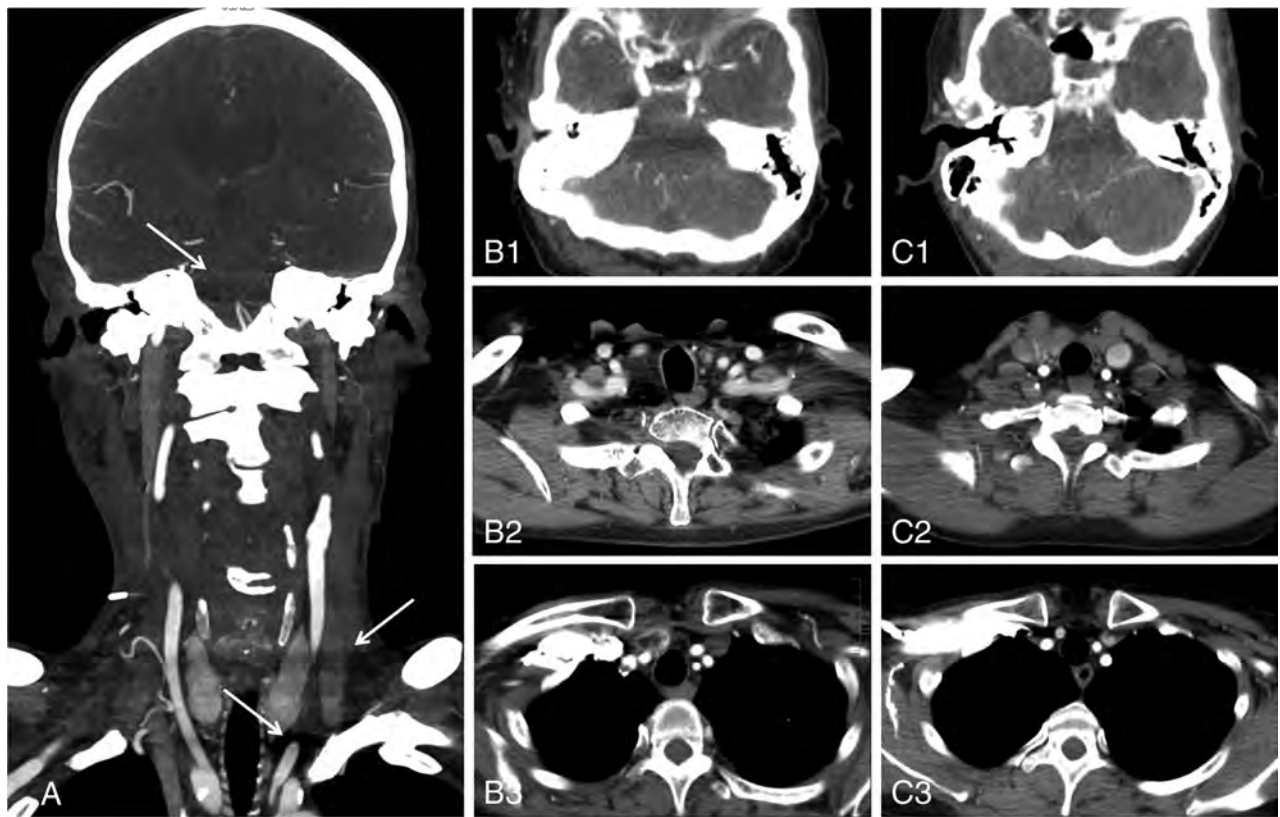


FIG 1. Coronal maximum intensity projection (5 mm) of a patient with obesity from the study group (BMI, 30.4 kg/m²; 70 kV) provides an overview of the evaluated artifacts (arrows) at the level of the skull base, shoulders, and venous contrast agent inflow (A). Axial examples of mild artifacts not affecting the diagnosis (Likert 3) in patients from the study (70 kV, B1–B3) and the control group (80 kV, C1–C3). Note the distinct increase at the lowest tube voltages that did not affect the rating.

Table 2: Grading numbers in the subjective image analysis^a

Grade	Image Quality		Artifacts (CM-Influx)		Artifacts (Shoulder)		Artifacts (Skull)		Artifacts (Dental Hardware)	
	Study	Control	Study	Control	Study	Control	Study	Control	Study	Control
	4	38	36	11	15	0	0	0	0	14
3	7	8	22	23	43	45	42	43	3	5
2	0	1	12	7	2	0	3	2	27	25
1	0	0	0	0	0	0	0	0	1	2

Note:—CM indicates contrast medium; meant are the artifacts by highly-concentrated inflowing contrast medium in the subclavian vein.

^a Each group ($n = 45$).

Table 3: Results of the diagnostic evaluation

Group	Study			Control			
	Complete	Subgroups		Complete	Subgroups		
		BMI <27	BMI >27		70 kV	80 kV	90 kV
No.	45	29	16	45	19	20	6
Right superior thyroid artery	3.6	3.6	3.7	3.4	3.3	3.6	3.2
Right lingual artery	3.7	3.6	3.8	3.7	3.6	3.9	3.5
Right facial artery	3.2	3.1	3.5	3.2	3.1	3.3	3
Left superior thyroid artery	3.4	3.2	3.8	3.5	3.5	3.6	3.2
Left lingual artery	3.7	3.7	3.8	3.7	3.8	3.8	3.3
Left facial artery	3.2	3.1	3.4	3.2	3.3	3.2	3.2
Calcification, right carotid artery	2.2	2.1	2.3	2.3	2.2	2.2	2.7
Calcification, left carotid artery	2.1	2.0	2.3	2.0	1.9	2.0	2.7
Stenotic disease, right carotid artery	0.6	0.5	0.8	0.5	0.5	1.1	0.7
Stenotic disease, left carotid artery	0.4	0.3	0.6	0.8	0.1	0.8	1.2

dently evaluated by 2 observers (both with >8 years of experience in carotid CTA).

Diagnostic Evaluation

All examinations were independently evaluated by the same 2 experienced radiologists with respect to image quality of the surgically important branches of the external carotid artery (lingual, facial, and superior thyroid arteries) as well as with respect to calcification and stenotic disease of the common and internal carotid arteries on a 3D postprocessing console (syngo.via VB20; Siemens). Visualization of the branches of the external carotid artery was assessed on a 4-point Likert scale as following: 4, complete visualization; 3, slightly suboptimal visualization; 2, only segmental visualization; 1, not visible. Calcification of the carotids was assessed as follows: 1, no calcification; 2, mild calcification; 3, moderate calcification; 4, severe calcification.

Stenotic disease was evaluated according to the NASCET style and grouped as follows: 0, no stenosis; 1, mild (0%–49%); 2, moderate (50%–69%); 3, severe (70%–99%); 4, obstruction.²¹

Diagnostic confidence was assessed independently by both observers as follows: 4, excellent; 3, substantial; 2, limited; 1, poor.

Statistical Analysis

All statistical analyses were performed using a dedicated software package (SPSS 15.0; IBM, Armonk, New York). The presence of normally distributed data was tested using the Kolmogorov-Smirnov test. The Student *t* test was used for radiation-dose comparisons, and the Mann-Whitney *U* test was used to evaluate the subjective image-quality scores as well as the diagnostic evaluation. Subgroup analysis of the different kilovolt settings of the

control group and BMI subgroups of the study group was performed using Kruskal-Wallis analysis. A *P* value < .05 was considered statistically significant. The Cohen κ was used to assess interobserver agreement in rating image quality, diagnostic confidence, and artifacts. κ values above 0.41 were interpreted as moderate; above 0.61, as substantial; and above 0.81, as almost perfect agreement.

RESULTS

Patient Characteristics

In the study group, the mean age was 64 ± 12 years, the range was 35–84 years, and 28 patients were men and 17 were women. The mean age in the control group was 65 ± 13 years with a range of 24–87 years, and 29 patients were men and 16 were women. There was no significant difference in the BMI between the study and the control groups. The BMI in the kilovolt subgroups of the reference differed statistically significantly ($P < .001$).

Radiation Exposure

Radiation exposure was significantly lower in the study group, with a CTDI_{vol} reduction of 22% ($P < .001$) and a DLP and effective dose reduction of 20% ($P = .001$). Subgroup analyses showed significant differences between the study group and the 70-kV examinations of the control group, with a significantly lower dose exposure in the 70-kV subgroup of the control group ($P = .03$). In the 80- and 90-kV subgroups, all radiation dose parameters were significantly higher compared with the study group (each, $P < .001$). The radiation dose for patients of the study group below 27 kg/m^2 was significantly lower than that for patients above it ($P = .001$). Both BMI-related subgroups of the study group had significantly lower radiation dose values than the corresponding BMI-related subgroups of the control group ($P =$

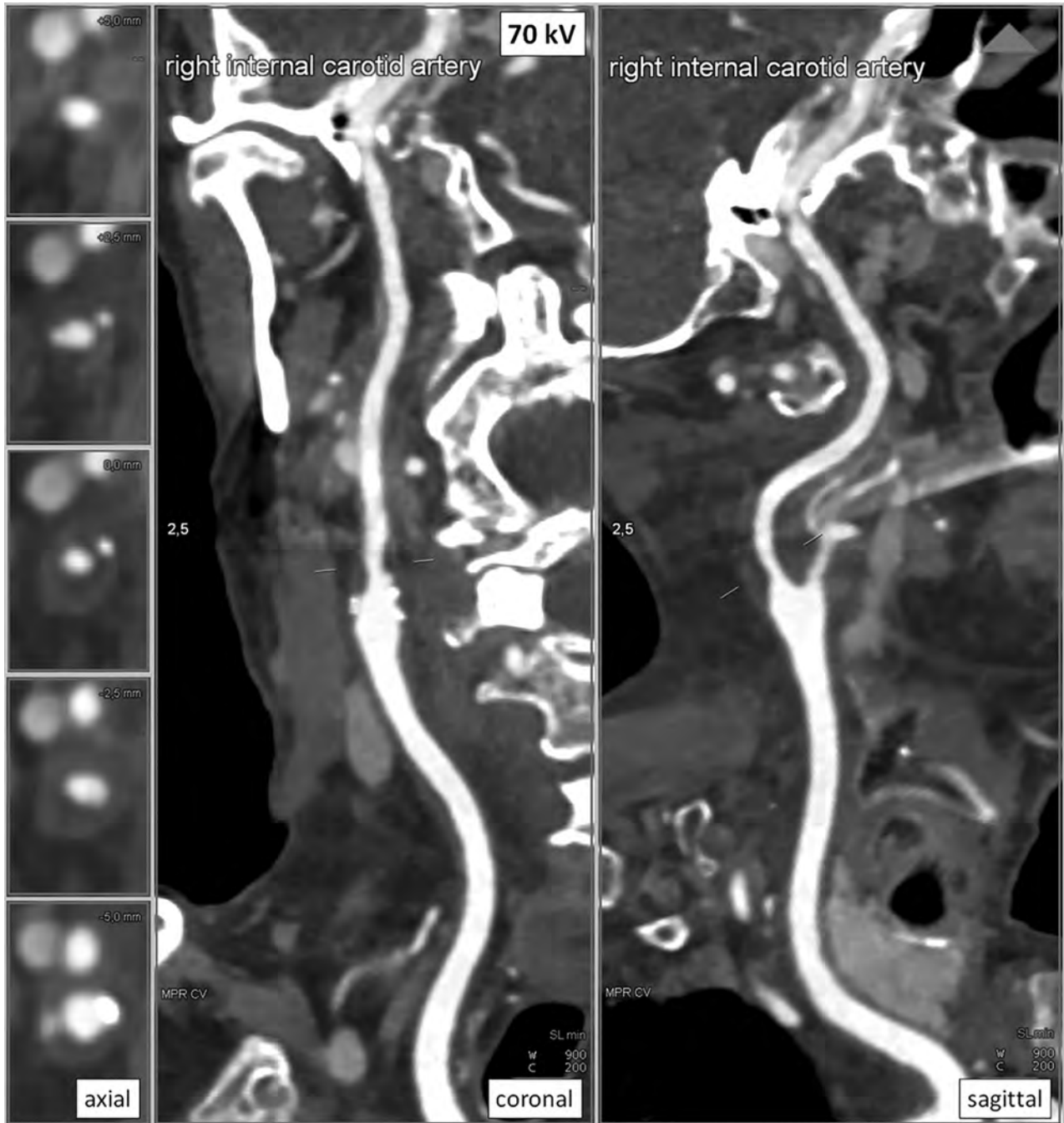


FIG 2. CT of a 51-year-old female patient of the study group (BMI, 25.4 kg/m²): curved MPR of the right side in 3 planes; 2.5-mm slice thickness; window level, 900 HU, and center, 200 HU. High vessel contrast with excellent overall image quality (Likert 4), moderate stenosis of the internal carotid artery (NASCET 2), and artifacts from dental implants not affecting the diagnosis (Likert 2). CTDI_{vol} was 2.92 mGy, and DLP was 108 mGy × cm.

.007 for BMI < 27 kg/m² and $P = .01$ in BMI > 27 kg/m². Detailed results are shown in Table 1.

Objective Image Quality

Attenuation of the carotids was comparable in the study and the control groups. Differences in image noise was discrete but statistically significant in ROI measurements of the vessels, with higher values in the study group ($P = .02$). No significant differences were found in contrast, SNR, and CNR. The CNRD was not significantly increased using the 70-kV protocol (26.9 ± 15.2 mGy^{-1/2} versus 22.4 ± 17 mGy^{-1/2}, $P = .2$). A ($P < .001$), SD

($P = .01$), and C ($P < .001$) were significantly higher in the 70-kV subgroup of the control group compared with the 70-kV examinations of all patients of the study group, but differences in SNR and CNR were nonsignificant. CNRD values were highest in the 70-kV subgroup of the control group (29.7 ± 12 mGy^{-1/2}), but not significantly higher than the CNRD in the study group ($P = .24$). A, SD, C, SNR, and CNR in the 80-kV subgroup were comparable with those of the study group, but at the expense of significantly decreased CNRD (19.8 ± 6.7 mGy^{-1/2}, $P = .03$). Results of the 90-kV subgroup were significantly lower compared with those of the study group, with an intensive drop in CNRD

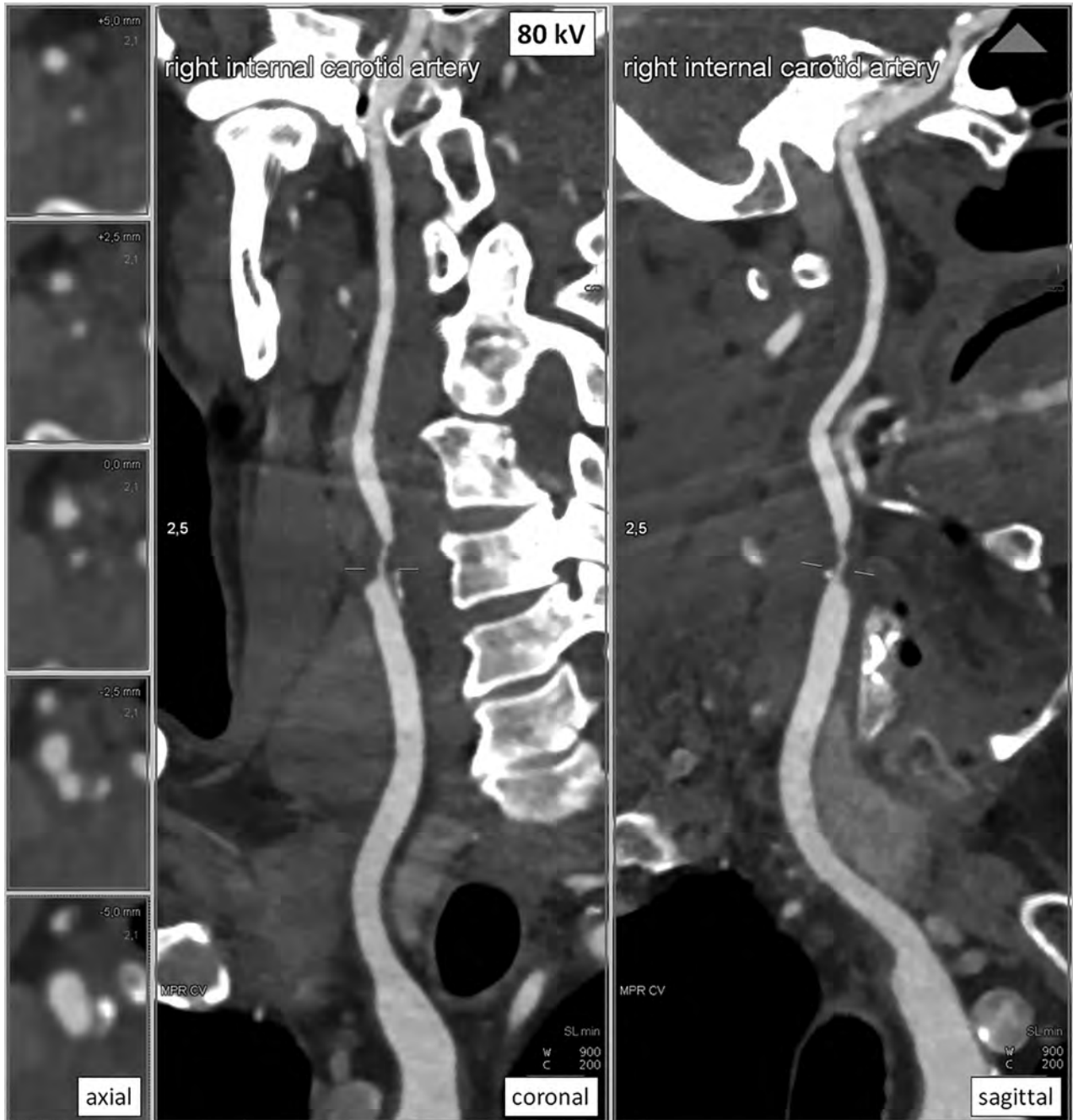


FIG 3. CT imaging of a 60-year-old male patient of the control group (BMI 25.7 kg/m²) curved MPR of the right side in 3 planes; 2.5-mm slice thickness; window level, 900 HU, and center, 200 HU. Intermediate vessel contrast with excellent overall image quality (Likert 4), severe stenosis of the internal carotid artery (NASCET 3), and artifacts from dental implants not affecting the diagnosis (Likert 2). CTDI_{vol} was 4.01 mGy, and DLP was 146 mGy × cm.

($8.8 \pm 4.2 \text{ mGy}^{-1/2}$, $P = .003$). A and SD in the muscles and air were comparable between both groups, with a significant drop in A_{muscle} in the 80-kV subgroup in comparison with the study group ($P = .02$). No significant differences in SNR, CNR, and CNRD were found for the BMI subgroups of the study group (all, $P > .1$). Detailed results are shown in Table 1.

Subjective Image Quality

Subjective overall image quality was without significant differences between the 2 groups ($P = .56$). Also, artifacts were evalu-

ated with no significant differences between the study and control groups (Fig 1), but slightly higher ratings of artifacts that might affect the image quality were found in the study group. Mean ranks of artifacts around the highly concentrated contrast influx in the height of the subclavian vein were 3.00 in the study group and 3.18 in the control group ($P = .23$); at the shoulder girdle, they were 2.98 in the study group and 3.00 in the control group ($P = .36$); and at the level of the skull base, they were 2.93 in the study and 2.96 in the control group ($P = .65$). No significant differences were found for artifacts in the BMI-related subgroup

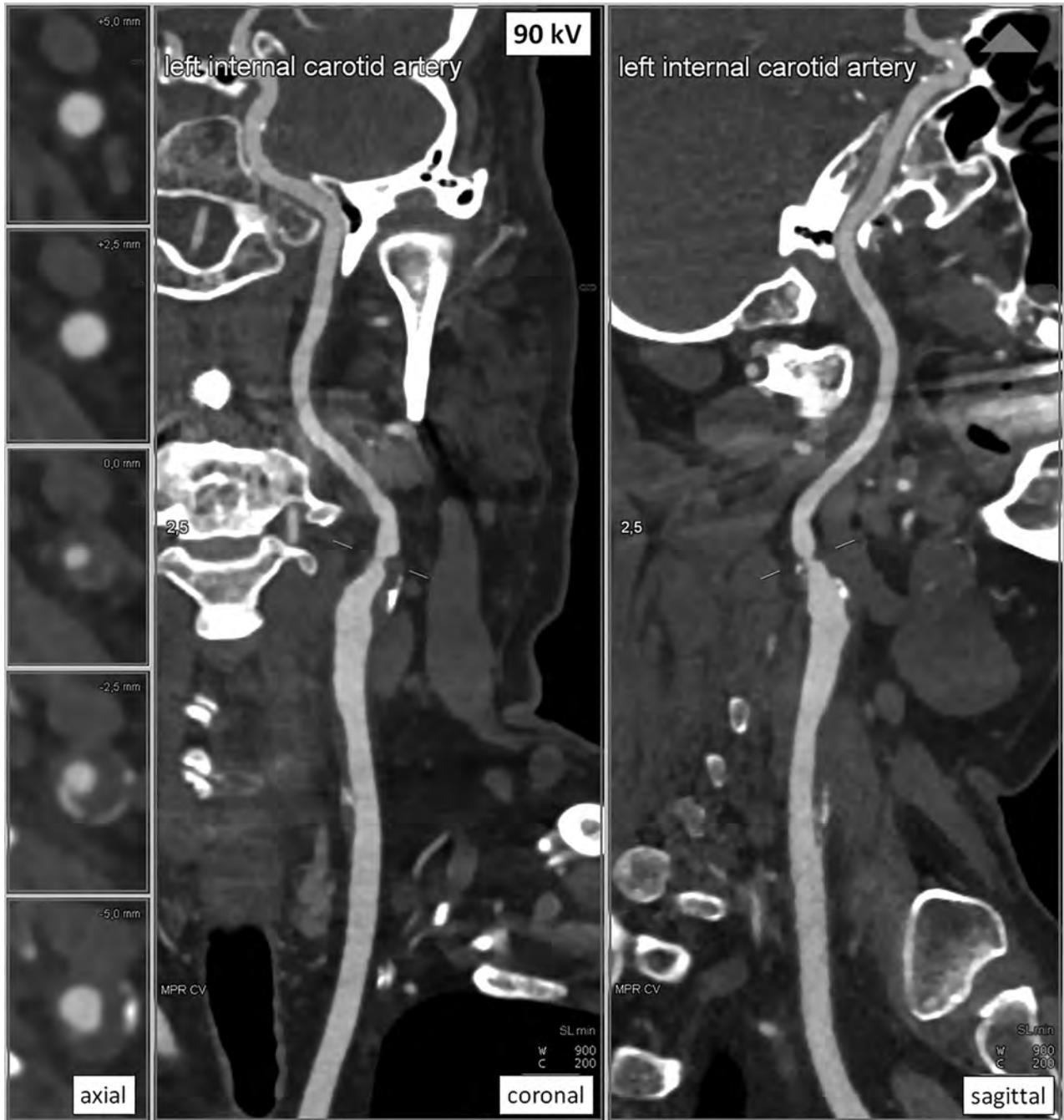


FIG 4. CT of a 69-year-old male patient of the control group (BMI, 31.6 kg/m²): curved MPR of the left side in 3 planes; 2.5-mm slice thickness; window level, 900 HU, and center, 200 HU. Low vessel contrast with excellent overall image quality (Likert 4), moderate stenosis of the internal carotid artery (NASCET 2), and artifacts from dental implants not affecting the diagnosis (Likert 2). The CTDI_{vol} was 5.74 mGy, and the DLP was 202 mGy × cm.

analysis of the study and control groups. Interobserver agreement was 0.93 in evaluating image quality and 0.87 for artifact analysis. Detailed results are shown in Table 2.

Metal artifacts due to dental implants were found in 31 (69%) subjects in the study group and were rated as follows: 3 ($n = 3$; 7%), 2 ($n = 27$; 60%), and 1 ($n = 1$; 2%). In the control group, dental implants occurred in 32 (71%) subjects, and they were rated as 3 ($n = 5$, 11%), 2 ($n = 25$, 56%), and 1 ($n = 2$, 4%).

Diagnostic Findings

The mean values of the diagnostic evaluation are given in Table 3; image examples are given in Figs 2–4. The ratings for pathologic findings were not significantly different between the study and reference groups (all, $P > .308$). Mean subjective confidence was 3.89 (observer 1) and 3.86 (observer 2) in the study group and 3.91 (observer 1) and 3.89 (observer 2) in the control group, with an overall κ value of 0.66. No significant differences were found.

DISCUSSION

The lowest tube voltages provided a consistent overall image quality with very high dose efficiency in CTA of the carotids. The slight increase of image artifacts (example in Fig 1) compared with a protocol with automated individual tube voltage selection was nonsignificant and did not disturb the vessel reproduction.

Especially in CTA of the carotids, the lowest kilovolt approach seems promising, and adaptation of the tube voltage to the scout information may not be necessary in all cases. First, the examined volume of the head and neck usually does not have the volume and interindividual differences of, for example, examinations of the abdomen, where habitus and obesity are more likely to limit the extent of tube voltage reduction possible.²²

Because of the relatively high iodine concentration in angiographic examinations, approaching the mean energy of the radiation spectrum to the k-absorption edge of iodine seems especially advantageous. Providing a strong increase of image contrast (Figs 2–4) alleviates the disadvantages of potential elevations in image noise on the representation of the vessels, especially compared with soft-tissue examinations. Furthermore, radiation-sensitive organs like the thyroid gland and the ocular lenses are included in the exposed volume, so dose optimization should be of special interest.

In previous studies, higher image-noise levels in low-kilovolt protocols were described, compensated for by higher attenuation resulting in constant or even improved SNR/CNR in comparison with conservative protocols with fixed kilovolt levels for various body regions.^{12,17,20} Our study results showed, however, that the 70-kV study protocol provided comparable or even slightly lower image noise than the reference protocol. The latest high-end scanners are equipped with x-ray tubes that are optimized for high tube currents, especially at low tube voltages. The balanced image noise in this study might, therefore, be explained by these technical advantages, compared with previous studies. Different explanations could be the interindividual differences between the 2 randomized groups or the rather small ROI measurements due to the small vessel size, which are more prone to be biased.

The high tube current capacity of the system is also reflected by the decreased median tube voltage using the automated tube voltage selection algorithm in the reference group (80 kV), compared with the results of previous scanner generations seen in the literature (100 kV).¹⁷ Hence, modern scanners can boost the dose at very low tube voltages compared with earlier models. CNRD, which served as a figure of merit for radiation dose effectiveness in this study, was increased by 20% using the lowest tube voltage approach. However, these differences were statistically nonsignificant. The highest A, C, and also CNRD values were found in the 70-kV subgroup of the control group, which could be explained by the automated selection of smaller or thinner patients. This might also be reflected by the shorter mean volume coverage in the z-axis (34 cm) compared with the study group (37 cm).

Our results contradict Beitzke et al,²⁰ who found a significant reduction of image quality at the level of the shoulder girdle for patients with a BMI above 27 kg/m² using 80 kV on a different CT system. Artifacts in that region did not affect the diagnosis in the control group and had little impact in the study group. The most

limiting artifacts were reported around the contrast inflow in the venous system, which was not evaluated in particular in previous studies. The overall subjective image evaluation and evaluation of pathologic findings were of comparably high quality in both groups, without statistically significant differences (Figs 2–4).

Some limitations have to be considered while interpreting our results. First, optimal timing of the contrast bolus is in direct relation to the vessel contrast, but the patient's physiology can strongly vary interindividually. Therefore, we sought to standardize the bolus timing using a test-bolus technique. The high intensity of artifacts around the contrast inflow could probably be reduced by further optimization of the injection protocols. Second, a transfer of these results to CTAs of other parts of the body (eg, aortic imaging) is difficult. The larger soft-tissue diameter of the chest and abdomen could overstrain the capacities of the x-ray tubes, resulting in increased image noise and artifacts. Third, our findings can only represent the evaluated CT system. A transfer to other tube-detector systems is strongly limited by the dedicated specifications. Fourth, we were only able to report diagnostic information about stenotic disease and assessment of the side branches of the external carotid artery. Other pathologies, for example dissections or aneurysms, should be systematically evaluated in future studies, especially if pooling of the contrast agent is likely to alter the visualization.

CONCLUSIONS

We demonstrate that the best radiation-dose efficiency in CTA of the carotids is provided by modern scanners using the lowest available tube voltage in a broad range of patients. The radiation dose can be reduced by about 20% in comparison with the state-of-the-art protocols with automated tube voltage adaptation, while the image quality is comparable.

Disclosures: Wolfgang Wüst—UNRELATED: Payment for Lectures Including Service on Speakers Bureaus: Siemens Speakers Bureau. Marc Saake—UNRELATED: Payment for Lectures Including Service on Speakers Bureaus: Siemens. Matthias M. May—UNRELATED: Consultancy: Siemens. Comments: coordination of educational courses; Payment for Lectures Including Service on Speakers Bureaus: Siemens. Comments: lectures and classroom courses. Rafael Heiss—UNRELATED: Payment for Lectures Including Service on Speakers Bureaus: member of Siemens Speakers Bureau. Michael Uder—UNRELATED: Grants/Grants Pending: Bayer Schering Pharma, Siemens.* *Money paid to the institution.

REFERENCES

1. Brott TG, Halperin JL, Abbara S, et al. 2011 ASA/ACCF/AHA/AANN/AANS/ACR/ASNR/CNS/SAIP/SCAI/SIR/SNIS/SVM/SVS guideline on the management of patients with extracranial carotid and vertebral artery disease: a report of the American College of Cardiology Foundation/American Heart Association Task Force on Practice Guidelines, and the American Stroke Association, American Association of Neuroscience Nurses, American Association of Neurological Surgeons, American College of Radiology, American Society of Neuroradiology, Congress of Neurological Surgeons, Society of Atherosclerosis Imaging and Prevention, Society for Cardiovascular Angiography and Interventions, Society of Interventional Radiology, Society of NeuroInterventional Surgery, Society for Vascular Medicine, and Society for Vascular Surgery. *J Am Coll Cardiol* 2011;57:e16–94 CrossRef Medline
2. Berrington de Gonzalez A, Mahesh M, Kim KP, et al. Projected cancer risks from computed tomographic scans performed in the United States in 2007. *Arch Intern Med* 2009;169:2071–77 CrossRef Medline

3. Kuefner MA, Grudzinski S, Schwab SA, et al. **DNA double-strand breaks and their repair in blood lymphocytes of patients undergoing angiographic procedures.** *Invest Radiol* 2009;44:440–46 CrossRef Medline
4. van Gils MJ, Vukadinovic D, van Dijk AC, et al. **Carotid atherosclerotic plaque progression and change in plaque composition over time: a 5-year follow-up study using serial CT angiography.** *AJNR Am J Neuroradiol* 2012;33:1267–73 CrossRef Medline
5. Narvid J, Do HM, Blevins NH, et al. **CT angiography as a screening tool for dural arteriovenous fistula in patients with pulsatile tinnitus: feasibility and test characteristics.** *AJNR Am J Neuroradiol* 2011;32:446–53 CrossRef Medline
6. Söderberg M, Gunnarsson M. **Automatic exposure control in computed tomography—an evaluation of systems from different manufacturers.** *Acta Radiol* 2010;51:625–34 CrossRef Medline
7. Coakley FV, Gould R, Yeh BM, et al. **CT radiation dose: what can you do right now in your practice?** *AJR Am J Roentgenol* 2011;196:619–25 CrossRef Medline
8. Kalender WA, Deak P, Kellermeier M, et al. **Application- and patient size-dependent optimization of x-ray spectra for CT.** *Med Phys* 2009;36:993–1007 CrossRef Medline
9. Chen GZ, Fang XK, Zhou CS, et al. **Cerebral CT angiography with iterative reconstruction at 70kVp and 30mL iodinated contrast agent: initial experience.** *Eur J Radiol* 2017;88:102–08 CrossRef Medline
10. Kayan M, Demirtas H, Türker Y, et al. **Carotid and cerebral CT angiography using low volume of iodinated contrast material and low tube voltage.** *Diagn Interv Imaging* 2016;97:1173–79 CrossRef Medline
11. Chen GZ, Zhang LJ, Schoepf UJ, et al. **Radiation dose and image quality of 70 kVp cerebral CT angiography with optimized sinogram-affirmed iterative reconstruction: comparison with 120 kVp cerebral CT angiography.** *Eur Radiol* 2015;25:1453–63 CrossRef Medline
12. Eller A, May MS, Scharf M, et al. **Attenuation-based automatic kilovolt selection in abdominal computed tomography: effects on radiation exposure and image quality.** *Invest Radiol* 2012;47:559–65 CrossRef Medline
13. Andreini D, Mushtaq S, Conte E, et al. **Coronary CT angiography with 80 kV tube voltage and low iodine concentration contrast agent in patients with low body weight.** *J Cardiovasc Comput Tomogr* 2016;10:322–26 CrossRef Medline
14. Wei L, Li S, Gao Q, et al. **Use of low tube voltage and low contrast agent concentration yields good image quality for aortic CT angiography.** *Clin Radiol* 2016;71:1313.e5–10 CrossRef Medline
15. Eller A, Wuest W, Scharf M, et al. **Attenuation-based automatic kilovolt (kV)-selection in computed tomography of the chest: effects on radiation exposure and image quality.** *Eur J Radiol* 2013;82:2386–91 CrossRef Medline
16. Winklehner A, Goetti R, Baummueller S, et al. **Automated attenuation-based tube potential selection for thoracoabdominal computed tomography angiography: improved dose effectiveness.** *Invest Radiol* 2011;46:767–73 CrossRef Medline
17. Eller A, Wuest W, Kramer M, et al. **Carotid CTA: radiation exposure and image quality with the use of attenuation-based, automated kilovolt selection.** *AJNR Am J Neuroradiol* 2014;35:237–41 CrossRef Medline
18. Spearman JV, Schoepf UJ, Rottenkolber M, et al. **Effect of automated attenuation-based tube voltage selection on radiation dose at CT: an observational study on a global scale.** *Radiology* 2016;279:167–74 CrossRef Medline
19. Deak PD, Smal Y, Kalender WA. **Multisection CT protocols: sex- and age-specific conversion factors used to determine effective dose from dose-length product.** *Radiology* 2010;257:158–66 CrossRef Medline
20. Beitzke D, Wolf F, Edelhauser G, et al. **Computed tomography angiography of the carotid arteries at low kV settings: a prospective randomised trial assessing radiation dose and diagnostic confidence.** *Eur Radiol* 2011;21:2434–44 CrossRef Medline
21. Bartlett ES, Walters TD, Symons SP, et al. **Quantification of carotid stenosis on CT angiography.** *AJNR Am J Neuroradiol* 2006;27:13–19 Medline
22. Lurz M, Lell MM, Wuest W, et al. **Automated tube voltage selection in thoracoabdominal computed tomography at high pitch using a third-generation dual-source scanner: image quality and radiation dose performance.** *Invest Radiol* 2015;50:352–60 CrossRef Medline

Standardization of Temporal Bone CT Planes across a Multisite Academic Institution

J.P. Guenette, L. Hsu, B. Czajkowski, and D.B. Nunez



ABSTRACT

BACKGROUND AND PURPOSE: Variable head positioning in the CT gantry results in variable and inconsistent temporal bone imaging planes. Our aim was to evaluate whether an automated postprocessing algorithm or an educational intervention with postprocessing by a technologist could result in consistent temporal bone image reformations into planes referenced to the lateral semicircular canal.

MATERIALS AND METHODS: Instructions to reformat small-FOV images in planes referenced to the lateral semicircular canal were posted at 12 CT scanner consoles and e-mailed to 65 CT technologists at a single multisite institution. Automated reformatted images were also produced. The angles between the technologist- and automated-reformatted axial image planes and lateral semicircular canal planes were measured. Group differences were calculated with Mann-Whitney–Wilcoxon tests. Differences in homogeneity of variances were calculated with Fligner-Killeen tests.

RESULTS: Two hundred ten temporal bones were imaged in 4 months following the intervention. Reformats by technologists were accurate in 87% of the axial and 81% of the coronal planes, with a trend toward improvement with time. Eighty percent of incorrectly reformatted images occurred at off-site, inpatient, and emergency department scanners. The error angle was significantly lower for technologist-reformatted images (median, 4.9°) than for acquisition plane images (median, 14.6°; $P = 3 \times 10^{-14}$) or automated-reformatted images (median, 13.8°; $P = 9 \times 10^{-13}$). The angle error variance was significantly more homogeneous for technologist-reformatted images ($P = 3 \times 10^{-8}$) and automated-reformatted images ($P = 1 \times 10^{-5}$) than for acquisition plane images.

CONCLUSIONS: Both technologist and automated reformatting of temporal bone images resulted in significantly less imaging plane variance compared with images reformatted in the acquisition plane, but reformatting by technologists remains necessary at our institution given our preference for standardized planes referencing the lateral semicircular canals.

Patient postural constraints, patient comfort, and technologist's preference all result in variable head positioning in the CT gantry. Differences in head positioning result in associated alterations in temporal bone imaging planes when the imaging planes are based on the acquisition plane. In our practice, imaging plane variability has made it difficult to directly compare sequential temporal bone CT examinations. Moreover, imaging plane variability may interfere with pattern recognition and the ability to distinguish normal from subtle abnormal findings. However, standardization of temporal bone imaging planes can be challeng-

ing in our system of 12 CT scanners, 65 CT technologists, and a small volume of temporal bone examinations relative to other CT examinations.

Prior studies have shown that 80% of diagnostic radiology errors are perceptual: Findings are either missed or not identified as abnormal.¹ For the following reasons, consistency of imaging planes through the small structures of the temporal bone is likely important in minimizing perceptual diagnostic errors. The search patterns of radiologists evolve through training.² However, search pattern evolution may be inhibited when the imaging scene varies from examination to examination. Moreover, expert radiologists evaluate groups of features rather than individual features.³ This type of evaluation may be compromised when feature groups are inconsistently spread across a variable number of images. Finally, context and structure constrain where we search.^{4,5} Altering the scene and context in each imaging examination can potentially negate normal search constraints and result in a more scattered search pattern. Similarly, just as chess masters have impairment of recall when normal chess piece positions are distorted,⁶ it is rea-

Received February 5, 2019; accepted after revision May 27.

From the Division of Neuroradiology, Brigham & Women's Hospital, Boston, Massachusetts.

Please address correspondence to Jeffrey P. Guenette, MD, Brigham & Women's Hospital, Division of Neuroradiology, 75 Francis St, Boston, MA 02115; e-mail: jpguenette@bwh.harvard.edu; @gunetty

Indicates article with supplemental on-line appendix.

<http://dx.doi.org/10.3174/ajnr.A6111>

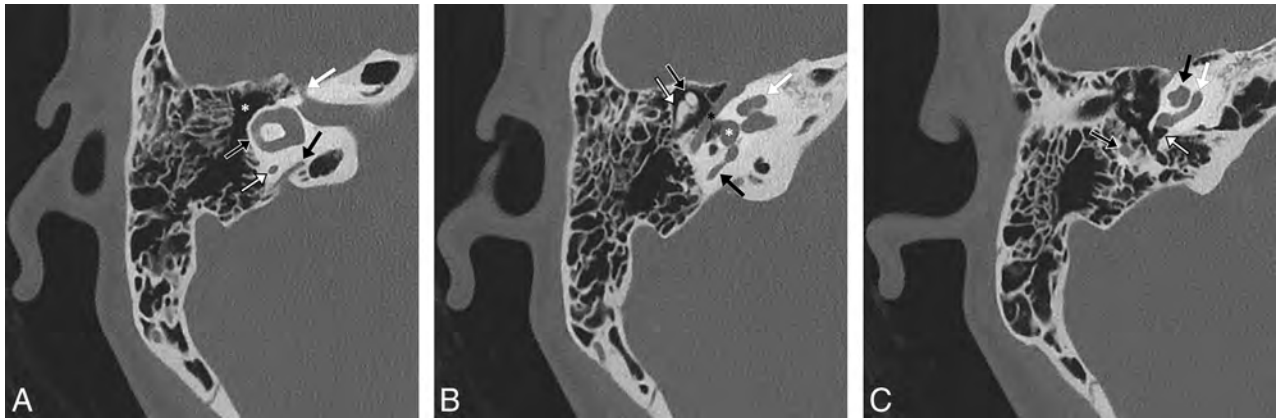


FIG 1. A 23-year-old woman with a normal right temporal bone. Noncontrast 0.6-mm-thick CT images in bone windows reformatted into an axial plane through the lateral semicircular canal. Major structures as seen in this plane include the following. *A*, at the level of the lateral semicircular canal: lateral semicircular canal (black arrow with white outline), posterior limb of the posterior semicircular canal (white arrow with black outline), vestibular aqueduct (black arrow), canal of the facial nerve labyrinthine segment (white arrow), and epitympanum/attic (asterisk). *B*, slightly inferior to *A*: the classic ice cream cone appearance of the malleus head (black arrow with white outline) and incus body (white arrow with black outline), entire length of the facial nerve tympanic segment (black asterisk), vestibule (white asterisk) at the upper aspect of the oval window, middle turn of the cochlea (white arrow), and upper limb of the posterior semicircular canal (black arrow). *C*, slightly inferior to *B*: the proximal aspect of the facial nerve mastoid segment (black arrow with white outline), round window niche (white arrow with black outline), basal turn of the cochlea (white arrow), and lower portions of the apical and middle turns of the cochlea (black arrow).

sonable to suspect that radiologists have impairment of normal anatomy recognition when imaging planes are distorted. If one assumes that radiologists do not have inherently better visual skills than nonradiologists,⁷ each of these search limitations may render an experienced neuroradiologist not much better than a novice trainee at rapidly identifying subtle temporal bone abnormalities when the imaging planes are inconsistent.

The optimal planes for temporal bone imaging have been described in one of the primary head and neck imaging textbooks: an axial plane parallel to the lateral semicircular canal and a coronal plane orthogonal to the lateral semicircular canal.⁸ This plane has also been described and used in research studies.⁹

The specific aim of this intervention and study was to evaluate whether a new automated postprocessing algorithm or a minor educational intervention with manual postprocessing procedures could result in consistent reformatting of temporal bone images into the previously published optimal planes, even across a large multisite institution.

MATERIALS AND METHODS

This quality-improvement study was performed and is reported following the Revised Standards for Quality Improvement Reporting Excellence 2.0 guidelines.¹⁰

Context

Before February 13, 2018, all temporal bone helical CT examinations at our institution were manually reformatted at the CT scanner console by the CT technologist into small-FOV images of the right and left temporal bones. Axial images were reformatted in the acquisition plane, while coronal images were reformatted perpendicular to the acquisition plane. Sagittal, Stenvers, and Poschl planes were not part of our routine protocol. The axial and coronal images were, therefore, created in essentially random planes dependent on patient head positioning, not in the published optimal preferred axial plane of the lateral semicircular canal (Fig 1)

or the coronal plane orthogonal to the lateral semicircular canal, as described by Curtin et al.⁸

Intervention

On February 13, 2018, an instruction form (Temporal Bone Basic Multiplanar Reformation Guides, On-line Appendix) was posted at all CT scanner consoles and e-mailed to all 65 CT technologists at our institution. The instruction form described the following process for reformatting small-FOV axial images in the plane of the lateral semicircular canal, performed separately for the right and left temporal bones: 1) Locate the sagittal reformatted images on the console; 2) optimize windowing on the console so that the bony structures can be visualized; 3) identify the anterior and posterior limbs of the lateral semicircular canal on the sagittal images; 4) set the plane for the reformatted axial images so that it intersects both the anterior and posterior limbs of the lateral semicircular canal; and 5) reformat the axial images. The form then instructs the technologist to create coronal images in the same FOV in a plane orthogonal to the axial images.

In collaboration with 2 senior neuroradiologists who have >50 years of combined experience and in collaboration with a lead CT technologist with >15 years of experience, the reformatting process and instruction form were developed by a neuroradiology trainee. All temporal bone CT examinations were reviewed for adequacy of the reformatted image planes on a biweekly basis. Any errors by the technologist in choosing the reformat planes were reviewed with the performing technologist. Any technologist who did not attempt to follow the process was instructed to follow the process for all future examinations.

Measures

Each CT examination was reviewed to evaluate the CT technologist's compliance with the process and the CT technologist's success in generating the appropriate imaging planes. Axial plane images were verified to be in the plane of the lateral semicircular

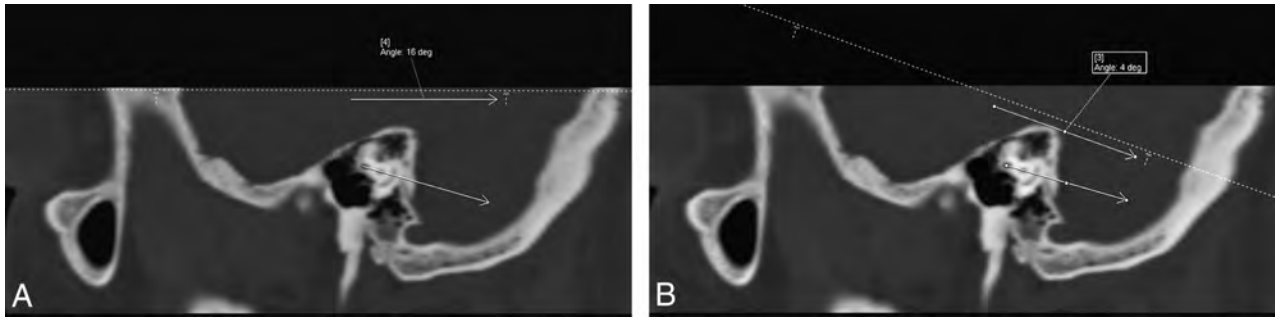


FIG 2. A 55-year-old woman with a normal left temporal bone. Sagittal noncontrast CT images in bone windows at the same location demonstrate the method of measuring the axial plane error angle. *A*, The angle between a line drawn by a radiologist at a PACS workstation through the anterior and posterior limbs of the lateral semicircular canal and a line drawn parallel to the plane chosen by the automation software (*dotted line*), which, in this case, is very close to the acquisition plane, is 16°. *B*, The angle between a line drawn by a radiologist at a PACS workstation through the anterior and posterior limbs of the lateral semicircular canal and a line drawn parallel to the plane selected by the technologist (*dotted line*) at the CT console is 4°.

canal. Coronal plane images were verified by a radiologist to be perpendicular to the axial plane using electronic cross-reference lines on the PACS workstation. The lead technologist reviewed with the performing technologist any examination that was not performed correctly to ensure improvement with time.

The difference in the angle between the axial reformat plane and the plane of the lateral semicircular canal was measured by the neuroradiology trainee and confirmed as accurate by the senior neuroradiologist. This angle difference is hereafter termed the “error angle.” The error angle was measured by generating sagittal images and then using an electronic angle-measurement tool, drawing a first line along the dashed axial image cross-reference line followed by a second line through the anterior and posterior limbs of the lateral semicircular canal (Fig 2). Sagittal images were generated and angles were measured with the postprocessing software of our department (syngo.via; Siemens, Erlangen, Germany).

Analysis

To determine an appropriate sample size, we measured the error angle for each of the 20 consecutive temporal bones (10 CT examinations) imaged immediately before the intervention. To enable a power calculation, we assumed that an error angle of up to 5° would result in a reasonable viewing plane. The sample size needed to detect an angle of at least 6° difference, with a known SD of 8.96° in the 20 temporal bones imaged before the intervention, a significance level of .05, and a power of 0.80, was calculated to be 36 in each group for a 2-sample *t* test. Because nonparametric analyses were planned due to potential between-group differences in variance, the estimated necessary sample size was increased to 40.

The error angle was thus measured for the 40 consecutive postintervention CT examinations (80 temporal bones) for which axial reformats were correctly performed and for which postprocessing could be performed. In addition, reformatted images of these 80 temporal bones were created with the automated temporal bone multiplanar reformatting module available with the postprocessing software of our department (syngo.via), and the error angle was separately measured for these reformatted images. The error angle was also measured for the 40 consecutive temporal bone CT examinations (80 temporal bones) performed immediately before the intervention. The preintervention and postintervention groups had no overlapping subjects. The right and left

temporal bones of a single subject were considered independently because the head is often not positioned straight within the gantry, which would inherently result in different angle errors and because the right and left sides were processed independently to achieve the optimal imaging plane for each temporal bone.

Statistical significance was set at .05. Median angle error measurements were compared between the set of subjects in the preintervention group and the separate set of subjects in the postintervention group with Mann-Whitney *U* tests. Postintervention technologist-reformatted and automated-reformatted median angle error measurements were compared between the same set of subjects in the postintervention group with paired Wilcoxon signed rank tests. Differences in angle error homogeneity of variances between the preintervention and postintervention angle error and between the postintervention technologist-reformatted and automated-reformatted angle error were calculated with Fligner-Killeen tests. Boxplots were created to provide visual comparison of the angle errors by group. All statistics were performed with R statistical and computing software, Version 3.5.0 (<http://www.r-project.org/>).

Ethical Considerations

The retrospective review of medical records, including imaging examinations, was approved by our institutional review board with a waiver of informed consent and was performed in compliance with the Health Insurance Portability and Accountability Act.

RESULTS

During the 16 weeks (4 months) immediately following the intervention, a total of 105 temporal bone CT examinations were performed, for a total of 210 temporal bones imaged at our institution. A total of 183 (87%) axial reformats were correctly created in the plane of the lateral semicircular canal, and a total of 171 (81%) coronal reformats were correctly created in the plane perpendicular to the lateral semicircular canal. The percentage of reformats correctly generated trended higher across time (Table). Fifty-three of the 66 (80%) incorrectly reformatted images occurred at off-site, inpatient, and emergency department scanners as opposed to hospital-based outpatient scanners.

The mean error angle for the 80 temporal bones imaged immediately before the intervention was $14.6^\circ \pm 8.7^\circ$ with a median

Results of reformatting by a technologist

	Total No. of Exams	Total No. of Temporal Bones	Axial Reformat Plane Correct (No.) (%)	Coronal Reformat Plane Correct (No.) (%)
Weeks 1–2	9	18	15 (83)	13 (72)
Weeks 3–4	12	24	18 (75)	16 (67)
Weeks 5–6	16	32	26 (81)	22 (69)
Weeks 7–8	21	42	42 (100)	41 (98)
Weeks 9–10	13	26	23 (88)	20 (77)
Weeks 11–12	14	28	22 (79)	22 (79)
Weeks 13–14	13	26	24 (92)	24 (92)
Weeks 15–16	7	14	13 (93)	13 (93)
Total	105	210	183 (87)	171 (81)

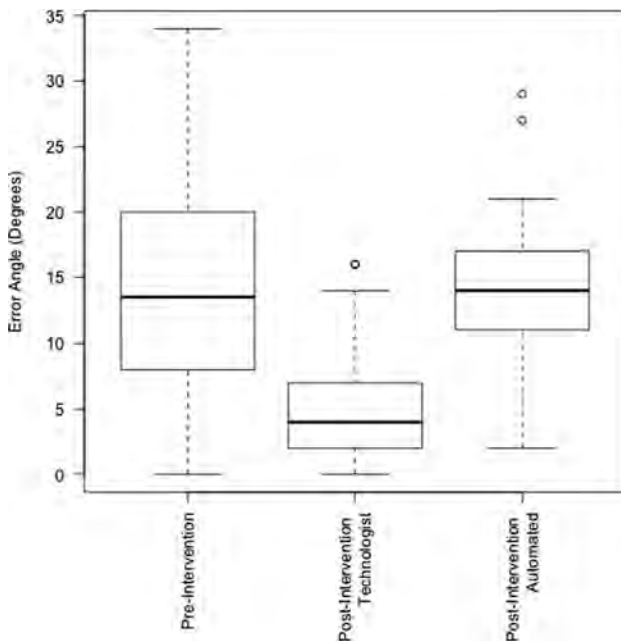


FIG 3. Boxplots depicting the difference in angles between the plane of the lateral semicircular canal and the plane of the temporal bone images in the preintervention group (image plane = acquisition plane), postintervention technologist group (image plane = plane as reformatted by a technologist in the clinical setting), and postintervention automated group (image plane = reformatted by commercially available syngo.via software).

of 13.5°. The mean error angle for the 80 temporal bones imaged immediately following the intervention and reformatted by the CT technologists was 4.9° ± 3.8°, with a median of 4°. The mean error angle for the 80 temporal bones imaged immediately following the intervention and reformatted with the automated tool was 13.8° ± 4.9°, with a median of 14°. Boxplots are provided in Fig 3 for visual comparison of these results.

The angle error was significantly lower for technologist-reformatted axial images than for axial images in the acquisition plane ($W = 5419.5, P = 3 \times 10^{-14}$). The angle error was also significantly lower for technologist-reformatted axial images than for images reformatted with the automation software ($V = 118, P = 9 \times 10^{-13}$).

The angle error variance was significantly more homogeneous for technologist-reformatted axial images than for axial images in the acquisition plane ($\chi^2 = 31, df = 1, P = 3 \times 10^{-8}$) as well as for automated-reformatted axial images than for axial images in the

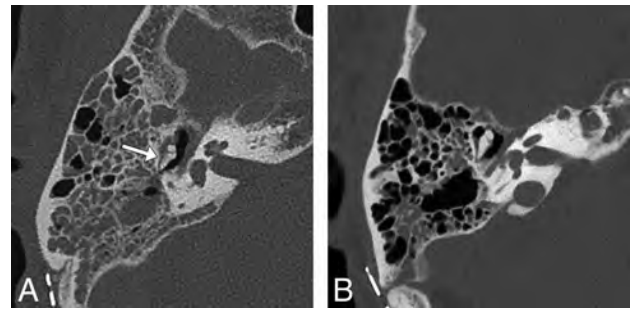


FIG 4. A 64-year-old man status post resection of a right vestibular schwannoma. Right temporal bone noncontrast CT images in bone windows demonstrate a possible perception error when images are reconstructed in random planes. *A*, Axial image in the acquisition plane obtained before the study intervention with a 29° error angle shows soft tissue in the Prussak space with a hazy appearance of the adjacent incus, suggesting possible erosion of the incus (arrow). *B*, Axial image in the plane of the lateral semicircular canal as reformatted by a CT technologist 3 months later following the study intervention shows the normal ice cream cone configuration of the malleus and incus with soft tissue in the Prussak space but no evident erosion of the incus, consistent with expected postoperative fluid in the middle ear cavity. The fluid had increased between the 2 examinations (not shown), so the finding is not a result of decreased fluid but a result of volume averaging with the incus body projected in an oblique plane.

acquisition plane ($\chi^2 = 19.2, df = 1, P = 1 \times 10^{-5}$). However, the angle error homogeneity of variance was not significantly different for technologist-reformatted axial images versus images reformatted with the automation software ($\chi^2 = 2.7, df = 1, P = .099$).

There were no unexpected benefits, problems, or failures.

DISCUSSION

This study demonstrates that there is significantly more variance in temporal bone imaging planes when those planes are based on the acquisition scan plane as opposed to when those planes are reformatted either by a technologist or with automation software. In addition, this study demonstrates that it is currently necessary to manually reformat axial and coronal images to obtain consistent and reproducible images in the preferred temporal bone imaging planes referenced to the lateral semicircular canals, as they have been previously described by Curtin et al.⁸

A search of MEDLINE demonstrated no prior study designed to evaluate temporal bone imaging planes, either from a standardization/efficiency standpoint or from the standpoint of which plane is optimal. The planes chosen for this intervention and study are based on the planes as standardized and used at one of the world's leading head and neck imaging centers.^{8,9} Although this study demonstrates a reduction in image plane variability with both manual and automated procedures and provides a standardized plane for performing clinical and research measurements, and although this intervention now allows our neuroradiologists to directly compare findings on sequential temporal bone CT examinations, further research is needed to clarify whether the reduced variability does, in fact, improve the expert radiologist search pattern and whether it reduces perceptual diagnostic errors (Fig 4). Similarly, comparison of the planes used in this study with other described planes, such as those referenced to the cochlea, may be helpful.

This intervention has been favorably viewed by the neuroa-

diologists in our group, specifically because they anecdotally report now being more able to compare sequential examinations. However, the intervention has resulted in slightly more work for the CT technologists. Some CT technologists have responded favorably, appreciating the opportunity to improve their craft in generating high-value images, while some others have responded unfavorably, finding the process an unwelcome additional task.

Ideally, the reformatted images produced by the automated software system would have produced images in a plane similar to those produced by a technologist, referenced to the lateral semicircular canal. Unfortunately, the automation algorithm available to us was based on a plane referenced to the cochlea, and this plane is, on average, approximately 9° to 10° farther out of plane from the lateral semicircular canal than the planes manually produced in this study. Given that the variance of the manual technologist planes and automated planes was not significantly different, an automated algorithm that references the lateral semicircular canals should be a feasible option in the near future.

The primary limitation of this study is that it was performed at a single institution. However, the intervention was applied across multiple models of CT scanners from 2 different vendors. Additionally, the study was limited by the algorithm of the available automated postprocessing software, which generates imaging planes that reference the cochlea. Ideally, the automated software would have generated images in the plane of the lateral semicircular canal. In that case, a direct comparison of technologist-reformatted and automated image error angles could have been performed with a goal of adopting automated reformats to reduce the need for training of technologists and the time the technologists spend on reformatting images. It is very likely that automated postprocessing software will generate similar or better results than a technologist reformatting the images into the described favored image planes in the near future.

CONCLUSIONS

Both technologist and automated reformatting of temporal bone images results in significantly less imaging plane variance compared with images reformatted in the acquisition plane, but manual reformatting remains necessary at our institution, given the preference for standardized planes referencing the lateral semicir-

cular canals. This method of image reformatting is sustainable within our system but will require continued quality assurance due to reasonable expectations of personnel changes across time and to prevent perpetuation of technologists' errors. Further study is suggested to evaluate the effects of standardization of the temporal bone image plane on neuroradiologists' efficiency and perceptual errors. Further work is also suggested to automate image reformatting into planes referencing the lateral semicircular canals.

Disclosures: Jeffrey P. Guenette—UNRELATED: Grants/Grants Pending: American Society of Head and Neck Radiology, Comments: William N. Hanafee 2017 Research Grant.* *Money paid to institution.

REFERENCES

1. Donald JJ, Barnard SA. **Common patterns in 558 diagnostic radiology errors.** *J Med Imaging Radiat Oncol* 2012;56:173–78 CrossRef Medline
2. Kundel HL, La Follette PS. **Visual search patterns and experience with radiological images.** *Radiology* 1972;103:523–28 CrossRef Medline
3. Kundel HL, Nodine CF. **Interpreting chest radiographs without visual search.** *Radiology* 1975;116:527–32 CrossRef Medline
4. Foulsham T, Alan R, Kingstone A. **Scrambled eyes? Disrupting scene structure impedes focal processing and increases bottom-up guidance.** *Atten Percept Psychophys* 2011;73:2008–25 CrossRef Medline
5. Drew T, Evans K, Vö ML, et al. **Informatics in radiology: what can you see in a single glance and how might this guide visual search in medical images?** *Radiographics* 2013;33:263–74 CrossRef Medline
6. Gobet F, Simon HA. **Recall of random and distorted chess positions: implications for the theory of expertise.** *Mem Cognit* 1996;24:493–503 CrossRef Medline
7. Nodine CF, Krupinski EA. **Perceptual skill, radiology expertise, and visual test performance with NINA and WALDO.** *Acad Radiol* 1998; 5:603–12 CrossRef Medline
8. Curtin HD, Gupta R, Bergeron RT. **Embryology, anatomy, and imaging of the temporal bone.** In: Som PM, Curtin HD. *Head and Neck Imaging*. 5th ed. St. Louis: Mosby Elsevier; 2011:1053–96
9. Reinshagen KL, Curtin HD, Quesnel AM, et al. **Measurement for detection of incomplete partition type II anomalies on MR imaging.** *AJNR Am J Neuroradiol* 2017;38:2003–07 CrossRef Medline
10. Ogrinc G, Davies L, Goodman D, et al. **SQUIRE 2.0 (Standards for Quality Improvement Reporting Excellence): revised publication guidelines from a detailed consensus process.** *BMJ Qual Saf* 2016; 25:986–92 CrossRef Medline

Prolapse of Orbital Fat through the Inferior Orbital Fissure: Description, Prevalence, and Assessment of Possible Pathologic Associations

P.M. Bunch, K. Buch, and H.R. Kelly

ABSTRACT

BACKGROUND AND PURPOSE: A few patterns of orbital fat prolapse have been described. Some are associated with disease, and others may mimic a neoplasm. We have observed prolapse of orbital fat into the infratemporal fossa via the inferior orbital fissure on MR imaging. The clinical relevance of this finding, if any, is unknown. The purposes of this study were to describe the MR imaging appearance of orbital fat prolapse through the inferior orbital fissure, to estimate the prevalence of this finding, and to assess possible pathologic associations.

MATERIALS AND METHODS: For this retrospective study of 228 orbital MR imaging examinations, 3 neuroradiologists independently assessed the presence of prolapse on high-resolution T1-weighted images. Discrepancies were resolved by consensus, and interobserver agreement was calculated. Patient demographics, indications for imaging, and pertinent clinical history were recorded. One-way analysis of variance and the Fisher exact test were used to assess possible associations between prolapse and specific patient characteristics.

RESULTS: Orbital fat prolapse through the inferior orbital fissure was observed in 20/228 patients (9%). This finding was unilateral in 11 patients (55%) and bilateral in 9 patients (45%). There was no significant association with age, sex, obesity, Graves disease, hypercortisolism, prior orbital trauma, proptosis, or enophthalmos. Interobserver agreement was 90%.

CONCLUSIONS: Prolapse of orbital fat into the infratemporal fossa via the inferior orbital fissure is a relatively common finding on orbital MR imaging that has no identified pathologic association. Neuroradiologists should recognize this finding so as not to report it as pathologic.

Several patterns of orbital fat prolapse have been previously described,¹⁻⁴ some of which are clinically relevant. Intracranial fat prolapse has been associated with optic nerve compression in thyroid eye disease.¹ Subconjunctival fat prolapse can mimic a neoplasm²; conversely, orbital lymphoma may mimic subconjunctival fat prolapse.⁵ Also, some data suggest an association between subconjunctival fat prolapse and thyroid eye disease.⁶

Not infrequently, orbital fat prolapse may be posttraumatic.^{3,4} Orbital fat prolapse may but does not necessarily occur in the setting of proptosis. In a small study of patients with proptosis with excess orbital fat,⁷ obesity, Graves disease, and Cushing syndrome were found to represent the underlying disease processes.

We have observed prolapse of the orbital fat into the infratemporal fossa via the inferior orbital fissure on MR imaging. The prevalence of this finding and the clinical relevance, if any, are unknown. We hypothesized that this finding falls within the range of normal anatomic variations and is not associated with orbital disorders or systemic diseases with orbital manifestations.

The purposes of this study were to describe the MR imaging appearance of orbital fat prolapse through the inferior orbital fissure, to estimate the prevalence of this finding, and to test our hypothesis that this finding represents a normal variant by assessing possible pathologic associations with aging, obesity, Graves disease, hypercortisolism (eg, Cushing disease, exogenous steroids), prior orbital trauma, proptosis, and enophthalmos.

Received March 20, 2019; accepted after revision May 27.

From the Department of Radiology (P.M.B.), Wake Forest School of Medicine, Winston Salem, North Carolina; Department of Radiology (K.B., H.R.K.), Massachusetts General Hospital, Harvard Medical School, Boston, Massachusetts; and Department of Radiology (H.R.K.), Massachusetts Eye and Ear, Harvard Medical School, Boston, Massachusetts.

A previous and more primitive version of this work was presented as an electronic scientific poster at: Annual Meeting of the American Society of Head and Neck Radiology, September 26–30, 2018; Savannah, Georgia. This article contains additional data and analyses not included in the previous electronic scientific presentation.

Please address correspondence to Paul M. Bunch, MD, Department of Radiology, Wake Forest School of Medicine, Medical Center Blvd, Winston Salem, NC 27157; e-mail: paul.m.bunch@gmail.com; @pbunchmd

<http://dx.doi.org/10.3174/ajnr.A6113>

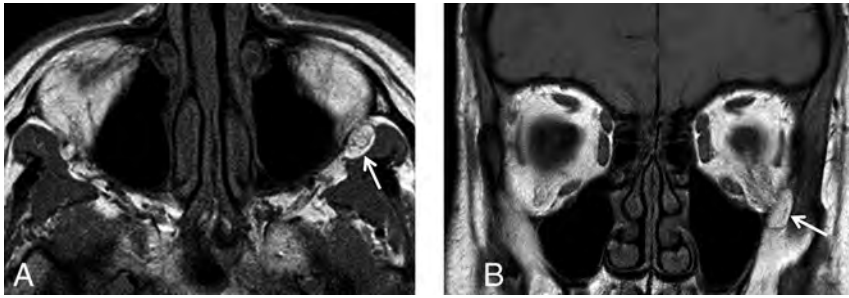


FIG 1. Axial (A) and coronal (B) T1-weighted images demonstrate prolapse of the left orbital fat (white arrows) into the left infratemporal fossa via the left inferior orbital fissure.



FIG 2. Axial T1-weighted image (A) demonstrates septa within the prolapsed orbital fat (circle). Coronal STIR image (B) demonstrates faintly increased fluid signal associated with the prolapsed orbital fat (circle). Axial gadolinium-enhanced T1-weighted image with fat suppression (C) demonstrates faint enhancement associated with the prolapsed orbital fat (circle).

MATERIALS AND METHODS

Subjects

For this retrospective, Health Insurance Portability and Accountability Act–compliant, institutional review board–approved study, all orbital MR imaging examinations performed at Massachusetts Eye and Ear between January 1, 2017, and August 1, 2017, were reviewed ($n = 324$) by 3 neuroradiologists. Inclusion criteria were the following: 1) a high-resolution axial T1-weighted sequence through the orbits without gadolinium contrast, and 2) no prior orbital operation. Examinations were excluded if an orbital MR imaging examination had already been included in the study cohort for the same patient or the diagnostic assessment was precluded by severe motion artifacts or other artifact degradation. A total of 228 orbital MR imaging examinations satisfied these criteria and formed the study cohort.

Medical Record Review

Basic patient characteristics including age, sex, and body mass index were recorded. Pertinent medical history was also recorded, including a history of orbital trauma and endocrinopathies, including Graves disease and Cushing syndrome. A targeted review of patient medications was also performed, including the use of oral steroid medications.

Image Acquisition

All orbital MR imaging examinations were performed on a 3T scanner (Achieva; Philips Healthcare, Best, the Netherlands) using an 8-channel head coil (SENSE Flex M coil; Philips Healthcare). Although there was some variability in the individual sequences included in each orbital MR imaging examination related to the retro-

spective nature of this study, the typical examination included sagittal T1, axial DWI, axial T2, and axial T1 gadolinium-enhanced images of the brain as well as high-resolution axial T1, coronal T1, coronal STIR, and coronal fat-suppressed T1 gadolinium-enhanced images of the orbits. For high-resolution sequences, the slice thickness was 3-mm and the acquisition matrix ranged from 300×300 to 415×415 .

Reader Assessment

After a training session based on 10 orbital MR imaging examinations that were not included in this study cohort, 3 fellowship-trained neuroradiologists (8, 3, and 2 years' subspecialty expertise) independently reviewed the high-resolution axial T1-weighted images from the 228 included orbital MR imaging examinations using the PACS of our institution. When present, the high-resolution coronal T1-weighted images were also reviewed.

Each neuroradiologist recorded the presence or absence of orbital fat prolapse for each eye in all patients. The recorded results were compared, and discrepancies were resolved by a consensus review.

discrepancies were resolved by a consensus review.

Prolapse was defined as present when a discrete, rounded focus of fat signal intensity could be identified as both distinguishable from the normal infratemporal fossa fat and contiguous with the normal orbital fat via the inferior orbital fissure (Fig 1). When prolapse was present, 1 fellowship-trained neuroradiologist performed a long-axis measurement of the prolapsed fat on high-resolution T1 images. The same neuroradiologist also evaluated the prolapsed fat for associated septa on T1-weighted images, fluid signal on STIR images, and enhancement on gadolinium-enhanced T1-weighted images with fat suppression (Fig 2). Additionally, a different neuroradiologist measured the perpendicular distance from the anterior margin of each globe to the interzygomatic line with the upper limit of normal defined as 21 mm⁷ and the lower limit of normal defined as 12 mm.⁸

Statistical Analysis

Absolute and relative frequencies are reported for categorical variables and interobserver agreement. The Fisher exact test was used to compare proportions, and 1-way analysis of variance was used to compare continuous variables. The Light κ coefficient was calculated to assess interrater reliability. All analyses were performed with JMP, Version 14 (SAS Institute, Cary, North Carolina), and a P value $< .05$ indicated a statistically significant difference.

RESULTS

Subjects

A total of 324 orbital MR imaging examinations were reviewed with 72 examinations excluded for lack of a high-resolution axial

Characteristics of the study group^a

Study Group Characteristics	
Sex	
Male	85 (37%)
Female	143 (63%)
Age (mean) (SD) (yr)	51.2 (19.9)
BMI (mean) (SD)	27.2 (6.2)
Obese	
Yes	51 (28%)
No	133 (72%)
Graves	
Yes	8 (4%)
No	220 (96%)
Hypercortisolism	
Yes	12 (5%)
No	216 (95%)
Prior orbital trauma	
Documented	3 (1%)
None documented	225 (99%)
Globe position	
Normal	397 (87%)
Proptosis	37 (8%)
Enophthalmos	22 (5%)
Indication (No.)	
Diplopia	41
Vision changes/loss/field cut	32
Mass	28
Optic neuropathy	14
Papilledema	11
Optic neuritis	10
Various other	92

Note:—BMI indicates body mass index.

^aBMI information was not available for $n = 44$.

T1-weighted sequence through the orbits without gadolinium contrast, 22 examinations excluded because of a prior orbital operation, and 2 examinations excluded because an orbital MR imaging examination from the same patient was already included in the study cohort. This yielded 228 patients who met the inclusion criteria of this study.

Patient age, sex, body mass index, Graves disease, hypercortisolism, prior orbital trauma, globe position, and study indication data are provided in the Table.

Reader Assessment

Interobserver agreement was 90.4% among the 3 readers for the presence or absence of orbital fat prolapse (206 patients without discrepancy, 22 patients with discrepancy). The Light κ coefficient was 0.65, indicating “good” agreement.

Prolapse of orbital fat into the infratemporal fossa via the inferior orbital fissure was observed in 20 patients (9%) ranging in age from 25 to 79 years. This finding was unilateral in 11 patients (55%) and bilateral in 9 patients (45%). The measured long axis of prolapsed fat ranged from 2 to 14 mm (mean, 7 ± 3 mm).

Among instances of prolapsed orbital fat, associated septa were present in 69%, faintly increased fluid signal was present in 26%, and faint enhancement was seen in 8%. There was no statistically significant association between orbital fat prolapse and age ($P = .44$), sex ($P = 1.00$), obesity ($P = .52$), Graves disease ($P = 1.00$), hypercortisolism ($P = .07$), prior orbital trauma ($P = 1.00$), proptosis ($P = .61$ for both right and left globes), or enophthalmos ($P = .26$ for the right globe, $P = 1.00$ for the left globe).

DISCUSSION

Radiologists' responsibilities include confidently differentiating normal anatomy and normal variants from disease. Although the distinction between normal anatomy and pathology is often relatively straightforward, determining that a finding represents a normal variant rather than disease can be more problematic. Misdiagnosis of normal variation as pathology can lead to unnecessary additional tests and subject the patient to potentially harmful procedures. Accordingly, textbooks^{9,10} and articles¹¹⁻¹⁵ have been devoted to normal variants that may simulate disease. However, not infrequently, the evidence underlying the supposition that a particular finding represents a normal variant rather than pathology is anecdotal or, in some cases, altogether lacking. Because differentiating normal variants from disease is central to the work of the radiologist, we believe an evidence-based approach is worthwhile.

Numerous patterns of orbital fat prolapse have been previously described, many of which are clinically relevant. This study describes an additional pattern of orbital fat prolapse involving the inferior orbital fissure with an estimated prevalence of 9%, which is more commonly unilateral. This study provides evidence in support of our hypothesis that this finding falls within the range of normal anatomic variations and is unlikely to be of clinical significance.

It is unknown whether this pattern of prolapse results from a structural anomaly of the orbit. A recent case report¹⁶ describes herniation of buccal fat into the orbit through an abnormally enlarged inferior orbital fissure and postulates that herniation was possible because of the inferior orbital fissure configuration. It remains an open question whether prolapse of orbital fat into the infratemporal fossa via the inferior orbital fissure is associated with variations in the dimensions of the inferior orbital fissure from reported norms,¹⁷⁻¹⁹ and this question would likely best be addressed with a future CT-based investigation.

An important limitation of this study is that a restricted number of possible pathologic associations were tested. An additional limitation is that the electronic medical record was used to determine the presence or absence of the diseases of interest. Relevant documentation could be incomplete or inaccurate, and it is also possible that relevant information was overlooked during our search. Although the literature informed the tested pathologic associations in this study, it is possible that a pathologic association that was not tested exists. Statistical testing for additional associations outside those supported by the literature could be performed but would also increase the risk of a type I error in this relatively small cohort. Future studies of larger cohorts testing additional possible associations could mitigate the theoretic risk of a true pathologic association not detected by the current study.

CONCLUSIONS

Prolapse of orbital fat into the infratemporal fossa via the inferior orbital fissure is a relatively common finding on orbital MR imaging that is likely a normal anatomic variant of no clinical significance. It is important for practicing neuroradiologists to recognize this finding so as not to mistake it for a pathologic entity, such as a mass.

Disclosures: Hillary R. Kelly—UNRELATED: Royalties: Elsevier. Comments: Book royalties were earned as editor of textbook on neuroradiology and head and neck radiology.

REFERENCES

1. Birchall D, Goodall KL, Noble JL, et al. **Graves ophthalmopathy: intracranial fat prolapse on CT images as an indicator of optic nerve compression.** *Radiology* 1996;200:123–27 CrossRef Medline
2. Lin CC, Liao SL, Liou SW, et al. **Subconjunctival herniated orbital fat mimicking adipocytic neoplasm.** *Optom Vis Sci* 2015;92:1021–26 CrossRef Medline
3. Cellina M, Floridi C, Panzeri M, et al. **The role of computed tomography (CT) in predicting diplopia in orbital blowout fractures (BOFs).** *Emerg Radiol* 2018;25:13–19 CrossRef Medline
4. Takahashi Y, Nishimura K, Kakizaki H. **Orbital fat prolapse into the nasal cavity in orbital blowout fracture.** *J Craniofac Surg* 2016;27:e615–17 CrossRef Medline
5. Tong L, Qian J, Adam R. **Bilateral orbital lymphoma presenting as recurrence of orbital fat pad after blepharoplasty.** *Can J Ophthalmol* 2017;52:e9–11 CrossRef Medline
6. Chatzistefanou KI, Samara C, Asproudis I, et al. **Subconjunctival orbital fat prolapse and thyroid associated orbitopathy: a clinical association.** *Clin Interv Aging* 2017;12:359–66 CrossRef Medline
7. Peyster RG, Ginsberg F, Silber JH, et al. **Exophthalmos caused by excessive fat: CT volumetric analysis and differential diagnosis.** *AJR Am J Roentgenol* 1986;146:459–64 CrossRef Medline
8. Forrest C. **Secondary management of posttraumatic craniofacial deformities.** In: Weinzwieg J, ed. *Plastic Surgery Secrets*. 2nd ed. Philadelphia: Mosby/Elsevier;2010:330–39
9. Keats TE, Anderson MW. *Atlas of Normal Roentgen Variants That May Simulate Disease*. Philadelphia: Elsevier/Saunders; 2013
10. Bancroft LW, Bridges MD, eds. *MRI Normal Variants and Pitfalls*. Philadelphia: Wolters Kluwer Health/Lippincott Williams and Wilkins; 2009
11. Helms CA, Sims R. **Foraminal spurs: a normal variant in the lumbar spine.** *Radiology* 1986;160:153–54 CrossRef Medline
12. Shpilberg KA, Daniel SC, Doshi AH, et al. **CT of anatomic variants of the paranasal sinuses and nasal cavity: poor correlation with radiologically significant rhinosinusitis but importance in surgical planning.** *AJR Am J Roentgenol* 2015;204:1255–60 CrossRef Medline
13. Motamedi D, Everist BM, Mahanty SR, et al. **Pitfalls in shoulder MRI: Part 1, normal anatomy and anatomic variants.** *AJR Am J Roentgenol* 2014;203:501–07 CrossRef Medline
14. Earwaker J. **Anatomic variants in sinonasal CT.** *Radiographics* 1993;13:381–415 CrossRef Medline
15. Welker KM, DeLone DR, Lane JI, et al. **Arrested pneumatization of the skull base: imaging characteristics.** *AJR Am J Roentgenol* 2008;190:1691–96 CrossRef Medline
16. Aldridge T, Thomson A, Ilankovan V. **Abnormal anatomy of inferior orbital fissure and herniation of buccal fat pad.** *Br J Oral Maxillofac Surg* 2015;53:92–93 CrossRef Medline
17. De Battista JC, Zimmer LA, Theodosopoulos PV, et al. **Anatomy of the inferior orbital fissure: implications for endoscopic cranial base surgery.** *J Neurol Surg B Skull Base* 2012;73:132–38 CrossRef Medline
18. Turvey TA, Golden BA. **Orbital anatomy for the surgeon.** *Oral Maxillofac Surg Clin N Am* 2012;24:525–36 CrossRef Medline
19. Ozer MA, Celik S, Govsa F. **A morphometric study of the inferior orbital fissure using three-dimensional anatomical landmarks: application to orbital surgery.** *Clin Anat* 2009;22:649–54 CrossRef Medline

Detection of Local Recurrence in Patients with Head and Neck Squamous Cell Carcinoma Using Voxel-Based Color Maps of Initial and Final Area under the Curve Values Derived from DCE-MRI

J.Y. Lee, K.L. Cheng, J.H. Lee, Y.J. Choi, H.W. Kim, Y.S. Sung, S.R. Chung, K.H. Ryu, M.S. Chung, S.Y. Kim, S.-W. Lee, and J.H. Baek



ABSTRACT

BACKGROUND AND PURPOSE: Early detection of local recurrence is important to increase the chance of cure because local recurrence is the main cause of treatment failure in head and neck squamous cell carcinoma. We evaluated the added value of voxel-based color maps of dynamic contrast-enhanced MR imaging compared with conventional MR imaging alone for detecting local recurrence of head and neck squamous cell carcinoma.

MATERIALS AND METHODS: We retrospectively enrolled 63 consecutive patients with head and neck squamous cell carcinoma after definitive treatment and posttreatment surveillance MR imaging studies that demonstrated focal enhancement at the primary site. Three independent readers assessed conventional MR imaging and a pair of color maps of initial and final 90-second time-signal intensity areas under the curve from dynamic contrast-enhanced MR imaging. The sensitivities, specificities, and accuracies of both conventional MR imaging alone and combined interpretation of conventional and dynamic contrast-enhanced MR imaging were assessed using the clinicopathologic diagnosis as the criterion standard. κ statistics were used to evaluate interreader agreement.

RESULTS: There were 28 patients with subsequently documented local recurrence and 35 with posttreatment change. Adding dynamic contrast-enhanced MR imaging to conventional MR imaging significantly increased the diagnostic accuracies for detecting local recurrence (48%–54% versus 87%–91%; $P < .05$), with excellent interreader agreement ($\kappa = 0.8$; 95% CI, 0.67–0.92 to $\kappa = 0.81$; 95% CI, 0.69–0.93). By all 3 readers, the specificities were also significantly improved by adding dynamic contrast-enhanced MR imaging to conventional MR imaging (22%–43% versus 87%–91%; $P < .001$) without sacrificing the sensitivities (68%–82% versus 86%–89%; $P > .05$).

CONCLUSIONS: Adding voxel-based color maps of initial and final 90-second time-signal intensity areas under the curve from dynamic contrast-enhanced MR imaging to conventional MR imaging increases the diagnostic accuracy to detect local recurrence in head and neck squamous cell carcinoma by improving the specificity without sacrificing the sensitivity.

ABBREVIATIONS: CI = confidence interval; CE = contrast-enhanced; HNSCC = head and neck squamous cell carcinoma; DCE = dynamic contrast-enhanced; FAUC₉₀ = final 90-second time-signal intensity area under the curve; IAUC₉₀ = initial 90-second time-signal intensity area under the curve; SI = signal intensity; TSI = time-signal intensity

Local tumor recurrence is the main cause (25.0%–54.9%) of treatment failures in head and neck squamous cell carcinoma

(HNSCC).^{1–4} Because distant metastasis occurs less frequently than local recurrence, it is reasonable that posttreatment surveillance should focus on detecting local tumor recurrence to increase the chance of cure.⁵ Biopsies can be a dilemma in heavily irradiated tissue because biopsy procedure may increase the risk of superimposed infection, failure to heal, and increased edema.⁶ Therefore, diagnostic techniques should provide a better estimate

Received January 4, 2018; accepted after revision June 17, 2019.

From the Department of Radiology (J.Y.L.), Eulji Medical Center, Eulji University College of Medicine, Seoul, Korea; Department of Medical Imaging (K.L.C.) and School of Medical Imaging and Radiological Sciences (K.L.C.), Chung Shan Medical University, Taichung, Taiwan; Department of Veterinary Medicine (K.L.C.), National Chung Hsing University, Taichung, Taiwan; Department of Radiology and Research Institute of Radiology (J.Y.L., K.L.C., J.H.L., Y.J.C., H.W.K., Y.S.S., S.R.C., J.H.B.), and Departments of Otolaryngology (S.Y.K.) and Radiation Oncology (S.-W.L.), University of Ulsan College of Medicine, Asan Medical Center, Seoul, Korea; Department of Radiology (K.H.R.), Gyeongsang National University School of Medicine and Gyeongsang National University Changwon Hospital, Changwon, Korea; and Department of Radiology (M.S.C.), Chung-Ang University Hospital, Chung-Ang University College of Medicine, Seoul, Korea.

Ji Ye Lee and Kai Lun Cheng contributed equally to this work.

Please address correspondence to Jeong Hyun Lee, MD, PhD, Department of Radiology and Research Institute of Radiology, University of Ulsan College of Medicine, Asan Medical Center, 86 Asanbyeongwon-Gil, Songpa-Gu, Seoul 05505, Republic of Korea; e-mail: jeonghlee@amc.seoul.kr

 Indicates article with supplemental on-line appendix.

 Indicates article with supplemental on-line photos.

<http://dx.doi.org/10.3174/ajnr.A6130>

of the likelihood of a recurrence and thus enable a more reliable selection of patients who should undergo pathologic examination.

Conventional and advanced imaging techniques, including diffusion-weighted MR imaging and FDG-PET, have shown variable results in distinguishing posttreatment change from recurrent or persistent disease.⁷ Dynamic contrast-enhanced (DCE)-MR imaging has emerged as a complementary technique for the posttreatment surveillance of patients with HNSCC and has shown promising results for distinguishing benign lesions from malignancies and predicting future treatment response.⁸⁻¹¹ A quantitative DCE-MR imaging study by Ishiyama et al¹² demonstrated that posttreatment changes had significantly higher permeability surface area than newly diagnosed or previously treated recurrent tumor. In addition to quantitative analysis, semiquantitative analysis of DCE-MR imaging can also be performed, offering the advantage of easier implementation, because it does not require the acquisition of baseline T1 mapping or arterial input function and does not rely on the assumptions of pharmacokinetic modeling. Regarding semiquantitative analysis, another previous study showed that benign postradiation changes had significantly longer time-to-peak and a lower relative wash-out ratio than recurrent tumors.¹³ A recent study showed that K_{ep} (flux rate constant) and area under the gadolinium concentration-time curve were significantly higher in residual tumor, showing the potential of DCE-MR imaging to distinguish benign posttreatment change from residual HNSCC.¹⁴ Our recent studies using semiquantitative analysis of DCE-MR imaging have shown a significant difference in time-signal intensity (TSI) curve patterns between recurrence and posttreatment change¹⁵ and that histogram analysis of the ratios between the initial and final 90-second area under the TSI curve from DCE-MR imaging improves the sensitivity of MR imaging with 11% more recurrent tumors detected compared with conventional MR imaging without compromising diagnostic specificity.¹⁶ However, there are limitations in using both techniques in clinical practice. Considering that most recurrent tumors are mixed with posttreatment change, TSI curve analysis averaging dynamic characteristics of the individual voxels of the entire volume of interest cannot detect early tumor recurrence or select a proper biopsy site for pathologic confirmation due to loss of anatomic information. Histogram analysis might detect early recurrent tumors mixed with posttreatment change but cannot provide a visual guide to select a proper biopsy site either.

To overcome those limitations, we obtained voxel-based color maps of area under the curve (AUC) values extracted from TSI curves during the initial and final 90 seconds, to assess the voxel-by-voxel difference in signal intensity change according to the time lag. The study aimed to evaluate the feasibility and added value of visual assessment of voxel-based color maps using the initial and final AUC values of TSI curves derived from DCE-MR imaging to detect local tumor recurrence in patients with HNSCC after definitive treatment.

MATERIALS AND METHODS

This case-controlled, retrospective cohort was approved by the institutional review board of Asan Medical Center, and acquisi-

tion of informed consent from patients was waived due to the retrospective nature of the study.

Study Patients

A review of the data base of our institution revealed 192 consecutive patients with pathologically confirmed HNSCC and surveillance MR imaging after definitive treatment between March 2014 and May 2015. Definitive treatment included curative resection, an operation and adjuvant radiation therapy, or concurrent chemoradiation. Among these, we found 135 patients with a focal moderate to intensely contrast-enhancing lesion at the primary site on fat-suppressed contrast-enhanced (CE) T1-weighted MR images and, finally, recruited 68 patients with a final diagnosis made by pathology or clinicoradiologic follow-up of >12 months. Subsequently, an independent neuroradiologist (J.Y.L., with 5 years of experience in head and neck imaging) who was not involved in the following image interpretation and data processing checked the image quality of DCE-MR imaging and excluded 5 patients with significant metallic artifacts, leaving 63 patients as a test patient group. Three of 63 patients have been previously reported.¹⁶ This prior article dealt with histogram analysis of DCE-MR imaging to evaluate local tumor recurrence in HNSCC, whereas in the current article, we investigated the feasibility of voxel-based color maps of DCE-MR imaging. Twenty patients were randomly selected as a separate patient group for a training session to distinguish among those with an enhancing lesion at the primary site but not confirmed as either recurrence or posttreatment change, to train readers and to minimize interreader variability (Fig 1).

MR Imaging Acquisition and Generation of Voxel-Based Color Maps from DCE-MR Imaging

MR imaging examinations were performed with a 3T MR imaging scanner (Magnetom Skyra; Siemens, Erlangen, Germany) using a 64-channel head and neck coil. Our MR imaging protocol for head and neck tumors consists of axial and coronal T1- and T2-weighted turbo spin-echo sequences with DCE-MR images. All of the axial T1- (TR/TE = 790/11 ms) and T2-weighted images (TR/TE = 5470/85 ms) were acquired with an FOV = 190 × 190 mm², matrix size = 448 × 291, and slice thickness = 3 mm without gap. DCE-MR imaging was performed in an axial plane with 3D controlled aliasing in parallel imaging results in higher acceleration (CAIPIRINHA) technique before, during, and after administration of a standard single-bolus administration of 0.1 mmol of gadoterate meglumine (Dotarem; Guerbet, Aulnay-sous-Bois, France) per kilogram of patient body weight dose with a rate of 4 mL/s. Dynamic acquisition was performed with a temporal resolution of 3.2 seconds, and contrast was administered after 11 baseline dynamics (total = 144 dynamics). Axial (TR/TE = 650/12 ms) and coronal (TR/TE = 540/11 ms) CE-T1WIs with fat suppression were obtained after DCE-MR imaging. Detailed imaging parameters for DCE-MR imaging are as follows: slice thickness = 3 mm without gap; 20 slices; z-axis coverage = 60 mm; spatial in-plane resolution = 184 × 160; TR/TE = 6.3/3.1 ms; flip angle = 15°; FOV = 19 cm; total acquisition time = 7 minutes 24 seconds.

The DCE-MR imaging data were transferred to a personal

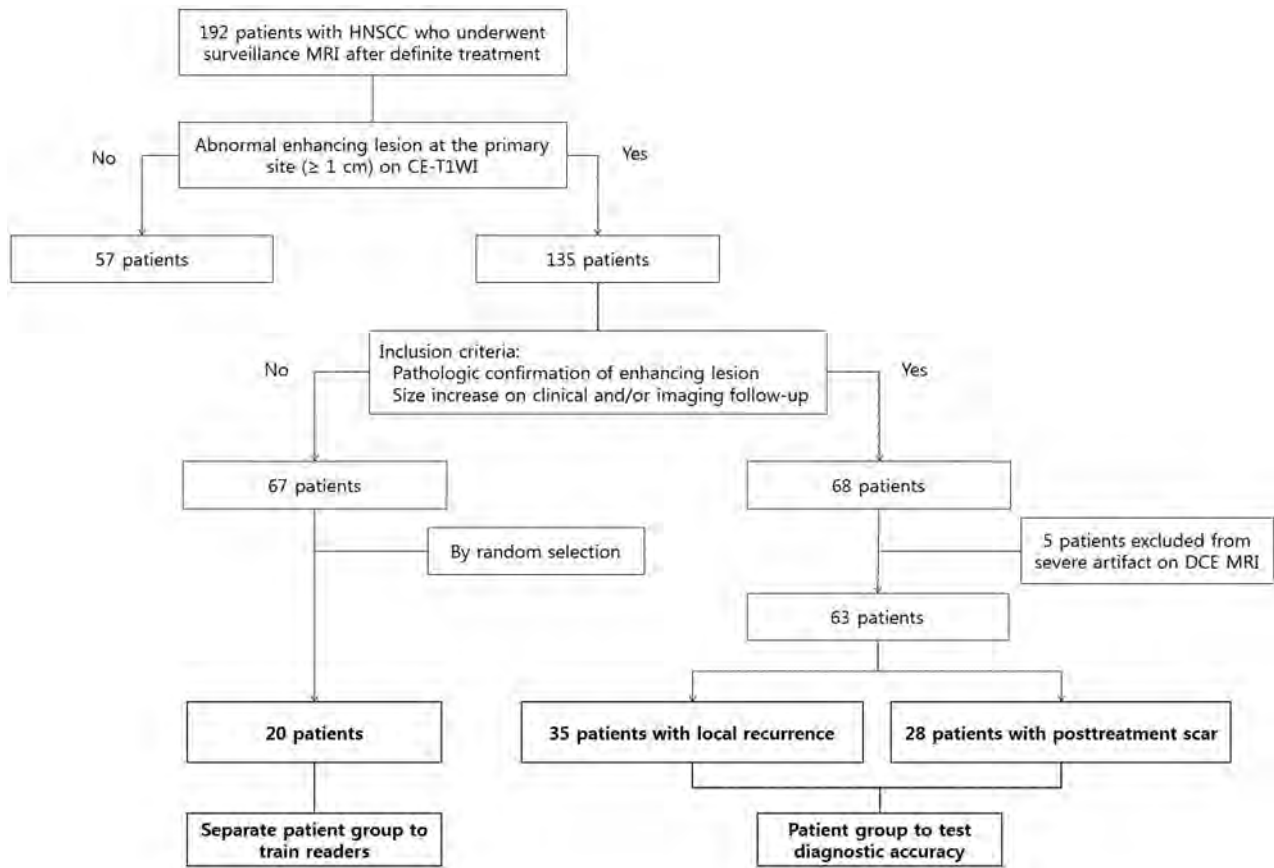


FIG 1. Diagram of study population enrollment.

computer to process perfusion parametric maps with an in-house plug-in program, which was developed for DCE-MR imaging data processing by calculating the trapezoidal integration of normalized signal intensity (SI)¹⁷ using ImageJ software (National Institutes of Health, Bethesda, Maryland). The contrast index was calculated for the voxels on each DCE-MR image using the following formula: Contrast Index = [SI (Postcontrast) – SI (Precontrast)] / SI (Precontrast).¹⁶ The time course of the contrast index was plotted to obtain a TSI curve and the initial and final 90-second AUC TSI values (IAUC₉₀ and FAUC₉₀) for each voxel. IAUC₉₀ was defined as the trapezoidal integration of the normalized TSI curve during the initial 90 seconds from the onset of contrast enhancement in the contrast-enhancing voxel, indicating a measurement of the initial arrival of contrast agent in the tissue of interest after intravenous bolus administration that reflects blood flow, vascular permeability, and the fraction of interstitial space.¹⁸ FAUC₉₀ was defined as the trapezoidal integration of the normalized TSI curve during the last 90 seconds in the same contrast-enhancing voxel, with IAUC₉₀, indicating the amount of contrast agent leakage within the extravascular extracellular space.¹⁹ The IAUC₉₀ and FAUC₉₀ values were then constructed to generate voxel-based color maps, which ranged from blue, green, yellow, to red (Fig 2). The SI of the enhanced tissue was displayed after normalization, relative to the unaffected prevertebral muscles on baseline images. The signal intensity of skeletal muscles was coded blue, and the vascular signal intensity exhibiting maximal enhancement was coded red. The av-

erage time for generating a pair of color maps in 1 DCE study was <2 minutes. Details for the postprocessing of the DCE-MR imaging data using the in-house-developed plug-in are described in the On-line Appendix and On-line Figs 1 and 2.

Analysis of Conventional and DCE-MR Imaging Examinations

After reviewing axial CE-T1WI of 20 patients in the separate patient group to train readers, a neuroradiologist (K.L.C., with 7 years of experience), who was aware of the location of the primary tumor, constructed a TSI curve of DCE-MR imaging for the focal masslike enhancing lesion at the primary site using a hand-drawn ROI with ImageJ software. The ROIs were double-checked and supervised by another experienced neuroradiologist (J.H.B., with 20 years of experience). All ROIs were free from areas of necrosis or nontumor macrovessels depicted on structural images. The TSI curve was interpreted by the neuroradiologist as progressive increment (type 1), plateau (type 2), or washout (type 3). The same neuroradiologist drew a rectangular ROI on axial CE-T1WIs of the separate patient group used to train readers and the patient group to assess the diagnostic accuracy as a guide for visual assessment of voxel-based color maps by different readers.

Three neuroradiologists (J.H.L., Y.J.C., and H.W.K. with 16, 9, and 5 years of experience in head and neck imaging, respectively) conducted a visual assessment of voxel-based color maps of the

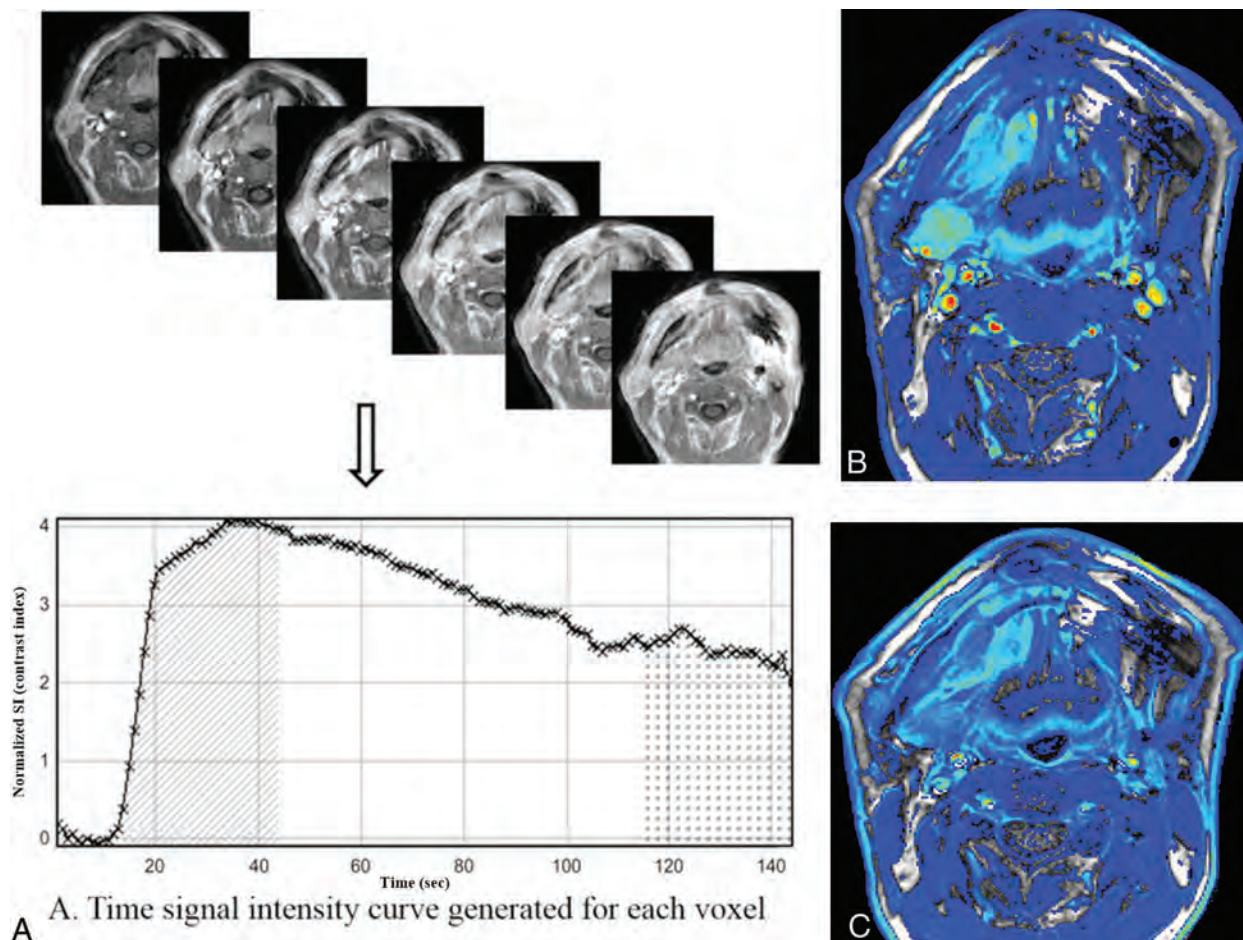


FIG 2. Illustration of the steps for generating color maps of initial and final 90-second AUC values using the TSI curve. **A**, The time course of the contrast index was plotted to obtain a TSI curve and the initial and final 90-second AUC values for each voxel. $IAUC_{90}$ (*diagonal pattern*) and $FAUC_{90}$ (*dotted pattern*) were defined as the trapezoidal integration of the normalized TSI curve during the initial and final 90 seconds from the onset of contrast enhancement in the voxel. **B** and **C**, Voxel-based color maps corresponding to $IAUC_{90}$ and $FAUC_{90}$ values were constructed in blue, green, yellow, and red.

separate patient group used to train readers to minimize inter-reader variability in their interpretation. For each patient, they assessed each pair of $IAUC_{90}$ and $FAUC_{90}$ images and then determined the patterns of the color change as progressive increment (type 1), plateau (type 2), and washout (type 3). The results were then correlated with those of the TSI curve-pattern analysis, and discrepancies were discussed to assess agreement. After the training session, they performed an independent analysis of the patient group to assess the diagnostic accuracy blinded to the final diagnosis using the same methods. They regarded type 2 (plateau) or type 3 (washout) as a recurrent tumor and type 1 (progressive increment) as a posttreatment change.^{10,15,20,21}

All 3 neuroradiologists performed a blinded review of conventional MR images of the patient group to test the diagnostic accuracy to detect recurrent tumor or posttreatment change, and those results were used to investigate the added value of voxel-based color maps over conventional MR imaging. Image sets included axial T2-weighted images, T1WIs, fat-suppressed CE-T1WIs, and coronal fat-suppressed CE-T1WIs. The interpretation of conventional MR imaging was performed according to the following criteria²²⁻²⁴: Recurrent tumors were defined as a focal mass discriminated by the surrounding tissue, with intermediate

to slightly high signal intensity on T2WI, low signal on T1WI, and moderate-to-strong enhancement after gadolinium administration. Degree of enhancement was defined as “moderate” when enhancement was weaker than mucosal enhancement but greater than skeletal muscles. “Strong enhancement” was defined when the degree of enhancement was similar to or stronger than mucosal enhancement. “Posttreatment change” was defined as a fibrous scar on any focal linear or triangular enhancing lesion with very low signal intensity on T2WIs and low signal intensity on T1WIs, and “posttreatment inflammation,” as a diffuse hyperintense abnormality on T2WIs with strong contrast enhancement. Results of conventional MR imaging analysis for the detection of recurrent tumor were classified into very probable = 1, somewhat probable = 2, somewhat unlikely = 3, and unlikely = 4.

Interpretation of both conventional and DCE-MRIs was conducted with a 1-month interval from the interpretation session for conventional MR imaging alone. To assess the added value of DCE-MR imaging, we accepted the result on DCE-MR imaging with only score 2 or 3 on conventional MR imaging. Score 1 or 4 on conventional MR imaging was accepted as a final interpretation result regardless of the pattern on DCE-MR imaging.

Table 1: Clinical characteristics of patients in training and test groups^a

Clinical Characteristics	Separate Patient Group to Train Readers (n = 20)	Patient Group to Test Diagnostic Accuracy		P Value
		Recurrent Tumor (n = 28)	Posttreatment Change (n = 35)	
Male/female ratio	12:8	18:10	29:6	.105
Age (mean) (yr)	55 ± 10	60 ± 11	58 ± 12	.452
Primary site				
Nasopharynx	5 (25)	6 (21)	9 (26)	
Oral cavity	6 (30)	11 (39)	11 (31)	
Oropharynx	4 (20)	5 (18)	5 (14)	
Larynx/hypopharynx	2 (10)	3 (11)	4 (11)	
PNS	3 (15)	3 (11)	6 (17)	
Treatment modality				.183
OP	10 (50)	13 (46)	12 (34)	
CCRT	8 (45)	13 (46)	16 (45)	
OP + RT	2 (10)	2 (7)	7 (20)	
Mean time interval (range) ^b	28 (12–35)	27 (12–60)	24 (10–41)	.518
Final diagnosis				
Pathologic exam		18	7	
Clinical follow-up		10	28	

Note:—CCRT indicates concurrent chemoradiation therapy; NA, not applicable; OP, operation; PNS, paranasal sinus; RT, radiation therapy.

^a Numbers in parentheses are percentages except where noted.

^b Mean time interval is expressed as months and the period between the end of treatment and MR imaging.

Table 2: Results of analysis of conventional MRI alone and combined interpretation of conventional and DCE-MRI for detecting local tumor recurrence

	Recurrent Tumor			Posttreatment Change		
	TP	FN	FNR (%)	TN	FP	FPR (%)
Reader 1						
Conventional MRI	21	7	25	8	27	77
Conventional and DCE-MRI	25	3	11	32	3	9
Reader 2						
Conventional MRI	19	9	32	15	20	57
Conventional and DCE-MRI	23	5	18	32	3	9
Reader 3						
Conventional MRI	23	5	18	10	25	71
Conventional and DCE-MRI	24	4	14	32	3	9

Note:—FN indicates false-negative; FNR, false-negative rate; FP, false-positive; FPR, false-positive rate; TN, true-negative; TP, true-positive.

Statistical Analysis

Pathology or clinicoradiologic follow-up for at least 12 months was the diagnostic reference standard for interpretation of conventional MR imaging and voxel-based color maps of DCE-MR imaging. To compare clinical characteristics between groups, we conducted the χ^2 or Fisher exact test for categorical variables. Student *t* and the Mann-Whitney *U* test were performed for the comparison of continuous variables after checking the normality with the Kolmogorov-Smirnov test. The sensitivity, specificity, positive and negative predictive values, and accuracies of the conventional MR imaging alone and the combined interpretation of conventional and DCE-MRIs were calculated for differentiation of recurrent tumor and posttreatment change, with score 1 on conventional MR imaging or score 2 on conventional MR imaging with either type 2 or 3 on DCE-MR imaging being considered recurrence. Comparison of the sensitivity, specificity, positive predictive value, negative predictive value, and accuracy of conventional MR imaging alone and the combined interpretation of conventional MR imaging and color maps of DCE-MR imaging was performed using a generalized estimating equation model.

The Cohen κ coefficient was used to measure interreader agreement of the results of DCE-MR imaging voxel-based color maps among 3 readers and agreement of the results between the TSI curve pattern and voxel-based color maps in the training session. All statistical analyses were performed using MedCalc for Windows, Version 13.0 (MedCalc Software, Mariakerke, Belgium) and SAS 9.4 software (SAS Institute, Cary, North Carolina). The significance threshold for the differences was set at a *P* value < .05.

RESULTS

The patient group to test the diagnostic accuracy included 47 men (mean age, 59 years; range, 25–84 years) and 16 women (mean age, 59 years; range, 33–79 years) with a mean age of 59 years (range, 25–84 years). There were 35 patients (male/female ratio = 29:6) with posttreatment change and 28 (male/female ratio = 18:10) with local tumor recurrence. All cases with local recurrence were located at the area of the primary site. Local tumor recurrence was confirmed by pathologic examination (*n* = 18, 64%) or size increase during follow-up (*n* = 10, 36%). Posttreatment change was confirmed by pathologic examination (*n* = 7, 20%) or a decrease or no growth of the abnormal enhancing lesion without any treatment by at least 12-month follow-up imaging (*n* = 28, 80%). The median time interval between the end of definitive treatment and the detection of an enhancing lesion

in the primary site was 26.3 months (range, 12–60 months) for all patients in the test group, 27.0 months (range, 12–60 months) for the posttreatment-change group, and 24.0 months (range, 10–41 months) for the recurrence group, respectively. All enhancing lesions were detected during routine imaging surveillance in asymptomatic patients. There was no significant difference in demographic data or treatment modalities between the 2 subgroups. Descriptive statistics regarding the demographic and clinical data obtained in both test and training groups are summarized in Table 1.

Among the separate patient group to train readers, TSI curve patterns were classified into type 1 in 12 (60%), type 2 in 5 (25%), and type 3 in 3 (15%) patients. Voxel-based color maps were classified into type 1 in 11 (55%), type 2 in 6 (30%), and type 3 in 3 (15%) patients by visual assessment. Agreement between the TSI curve pattern and visual assessment of voxel-based color maps was excellent (κ = 0.96; 95% CI, 0.89–0.98; *P* < .001).

Table 2 shows the detailed results of analysis of conventional MR imaging and the combined approach of conventional MR

Table 3: Diagnostic accuracies of conventional MRI alone and combined interpretation of conventional and DCE-MRI for detecting local tumor recurrence^a

	PPV	NPV	Sensitivity	Specificity	Accuracy
Reader 1					
Conventional MRI	45 (39–51) ^b	57 (32–80) ^b	79 (66–90)	22 (11–32) ^b	48 (35–61) ^b
Conventional and DCE-MRI	89 (74–96) ^b	91 (79–97) ^b	89 (72–98)	91 (77–98) ^b	91 (80–96) ^b
Reader 2					
Conventional MRI	49 (39–58) ^b	63 (38–75) ^b	68 (54–81)	43 (25–49) ^b	54 (41–67) ^b
Conventional and DCE-MRI	82 (67–91) ^b	91 (79–97) ^b	88 (70–98)	87 (71–96) ^b	87 (77–91) ^b
Reader 3					
Conventional MRI	48 (40–54) ^b	67 (42–86) ^b	82 (69–93)	29 (18–37) ^b	52 (39–65) ^b
Conventional and DCE-MRI	89 (73–96) ^b	89 (76–95) ^b	86 (67–96)	91 (77–98) ^b	89 (78–95) ^b

Note:—NPV indicates negative predictive value; PPV, positive predictive value.

^a Numbers in parentheses are 95% confidence intervals.

^b Statistical difference between conventional MRI and combined interpretation of conventional and DCE-MRI ($P < .05$).

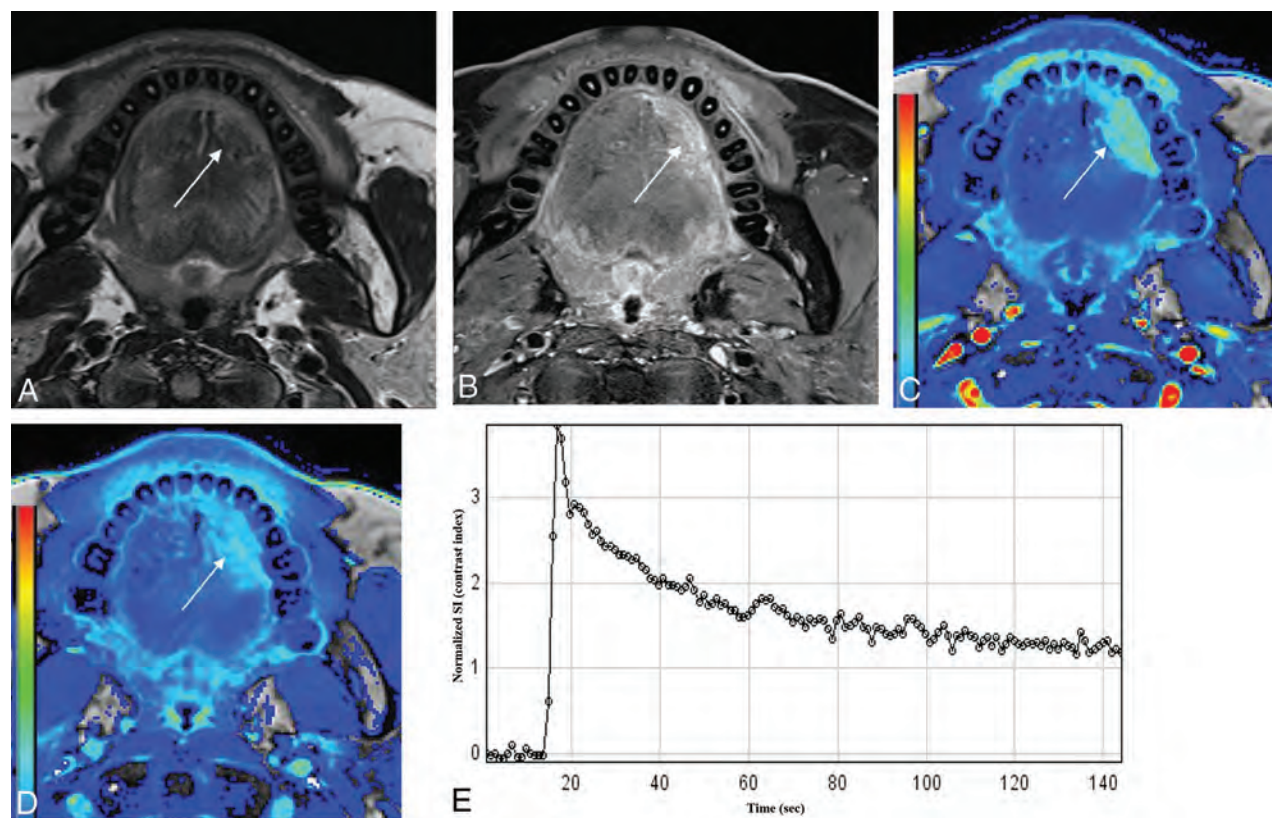


FIG 3. A 53-year-old man after hemiglossectomy for squamous cell carcinoma of the oral tongue 12 months previously (T2N0M0; depth of invasion, 10 mm). A and B, T2-weighted and contrast-enhanced fat-suppressed T1-weighted images show an ill-defined enhancing lesion at the operative bed of the oral tongue (arrows). C and D, IAUC₉₀ and FAUC₉₀ images of DCE-MR imaging show contrast washout at the corresponding area. E, The time-signal intensity curve obtained from the enhancing area using a hand-drawn ROI also shows contrast washout. This lesion was confirmed as recurrent tumor on subsequent surgical excision.

imaging and DCE-MRI for detection of local tumor recurrence after evaluation of the patient group to test diagnostic accuracy. False-positive and false-negative rates from Table 2 were 57%–77% and 18%–32% for conventional MR imaging and 9% and 11%–18% for the combined interpretation of conventional and DCE-MRI by 3 readers, respectively. There was a 48–68 percentage point and 4–14 percentage point reduction in both false-positive and false-negative rates by combined interpretation compared with conventional MR imaging alone. Agreement between the TSI curve pattern and visual assessment of voxel-based color maps was excellent among 3 readers in the patient group to test diagnostic accuracy ($\kappa = 0.86$; 95% CI, 0.75–0.96 to $\kappa = 0.87$; 95% CI, 0.77–0.97). Interreader

agreement for interpretation of voxel-based color maps of DCE-MR imaging was also excellent ($\kappa = 0.80$; 95% CI, 0.67–0.92 to $\kappa = 0.81$; 95% CI, 0.69–0.93).

Table 3 summarizes diagnostic accuracies of conventional MR imaging alone and combined interpretation of conventional and DCE-MRIs. Diagnostic accuracies of conventional MR imaging by all 3 readers were significantly increased from 48%–54% to 87%–91% by adding DCE-MR imaging to conventional MR imaging in all patients ($P < .05$). The specificities were also significantly improved by adding DCE-MR imaging to conventional MR imaging (22%–43% versus 87%–91%; $P < .001$) without sacrificing the sensitivities (68%–82% versus 86%–89%; $P > .05$). Figures 3–5 are representative cases.

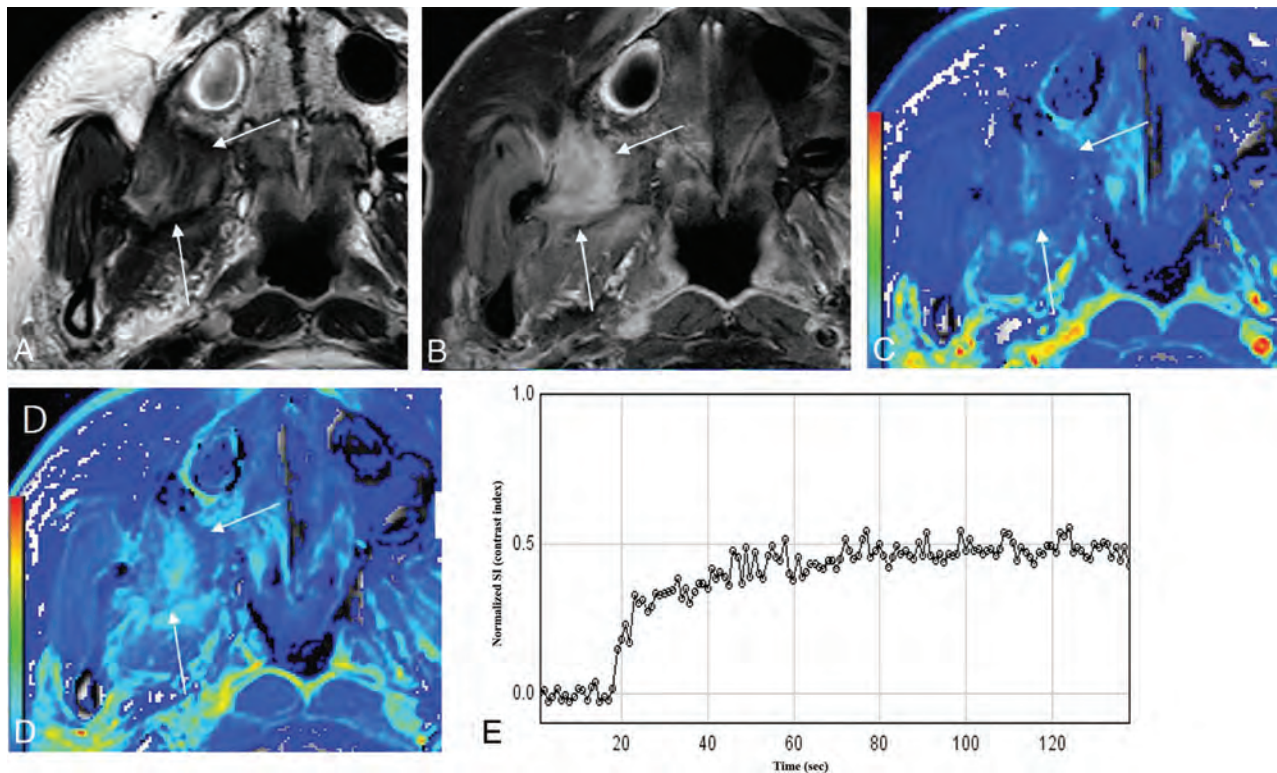


FIG 4. A 40-year-old female patient after wide excision for buccal cancer 36 months previously (T1N0M0). T2-weighted image shows a low signal intensity lesion in the right retroantral region (A) with heterogeneous contrast enhancement on contrast-enhanced fat-suppressed T1-weighted imaging (B) (arrows). IAUC₉₀ (C) and FAUC₉₀ (D) images of DCE-MR imaging show a progressive increment pattern. Time-signal intensity curve obtained at the enhancing portion also shows a progressive increment pattern (E). This lesion was confirmed as fibrosis at excisional biopsy.

DISCUSSION

Differentiating residual or recurrent tumor from posttreatment change is a clinically challenging decision, resulting in high false-positive rates (26%–46%) using conventional MR imaging criteria.^{25,26} FDG-PET has also been widely used to detect recurrent tumor due to its low false-negative rates and high negative predictive values for local tumor recurrence.²⁷ However, low specificity might be a problem of PET/CT due to posttreatment granulation tissue and inflammatory changes.²⁷

In this study, we demonstrated that visual assessment of voxel-based color maps of DCE-MR imaging is both feasible and technically valid for detecting local tumor recurrence at the primary site in patients with HNSCC during surveillance. When conventional MR imaging showed low specificity for distinguishing recurrence from posttreatment change, there was significant improvement of the specificity and accuracy without sacrificing sensitivity when conventional and DCE-MRIs were interpreted together. Hence, we conclude that voxel-based color maps of DCE-MR imaging might be useful to rule out the probability of local tumor recurrence as a complementary tool to conventional MR imaging during posttreatment surveillance. We believe that this technique has the potential to reduce unnecessary biopsy or imaging studies and to lead to a more targeted diagnostic and therapeutic approach with reduced complications by improving the diagnostic accuracy of conventional MR imaging.

Previous studies on the diagnostic performance of conventional MR imaging for local tumor recurrence showed a wide variation in the diagnostic sensitivity (84%; 95% CI, 72%–92%)

and specificity (82%; 95% CI, 72%–89%), according to a recent meta-analysis.²⁸ In our study, the specificity of conventional MR imaging was relatively low, which might be attributable to our strict interpretation criteria: We considered any focal enhancement inconsistent with posttreatment scar or inflammatory change as recurrent tumor. In contrast, DCE-MR imaging has the potential of low sensitivity compared with conventional MR imaging due to the relatively low signal-to-noise ratio and the spatial resolution of the color maps and the variable degree of enhancement from posttreatment change. However, our results demonstrated that morphologic information with conventional MR imaging and functional information with color maps of DCE are complementary and might contribute in different ways to improvement of overall diagnostic performance. Therefore, combined interpretation of conventional and DCE-MRIs might be more practical and accurate during posttreatment surveillance of patients with HNSCC.

DCE-MR imaging has been useful in differentiating recurrent tumor from posttreatment change in head and neck cancer as well as in other anatomic areas. Previous studies revealed that enhancement patterns after gadolinium contrast injection differed between malignant and benign lesions: Early enhancement and washout corresponded to recurrence, while a progressive enhancement pattern corresponded to benign lesions, including fibrosis.^{10,29,30} Our study used the same methodology as the previous studies and revealed the feasibility and repeatability of using voxel-based color maps of IAUC₉₀ and FAUC₉₀ values from DCE-MR imaging in differentiating recurrent tumor from post-

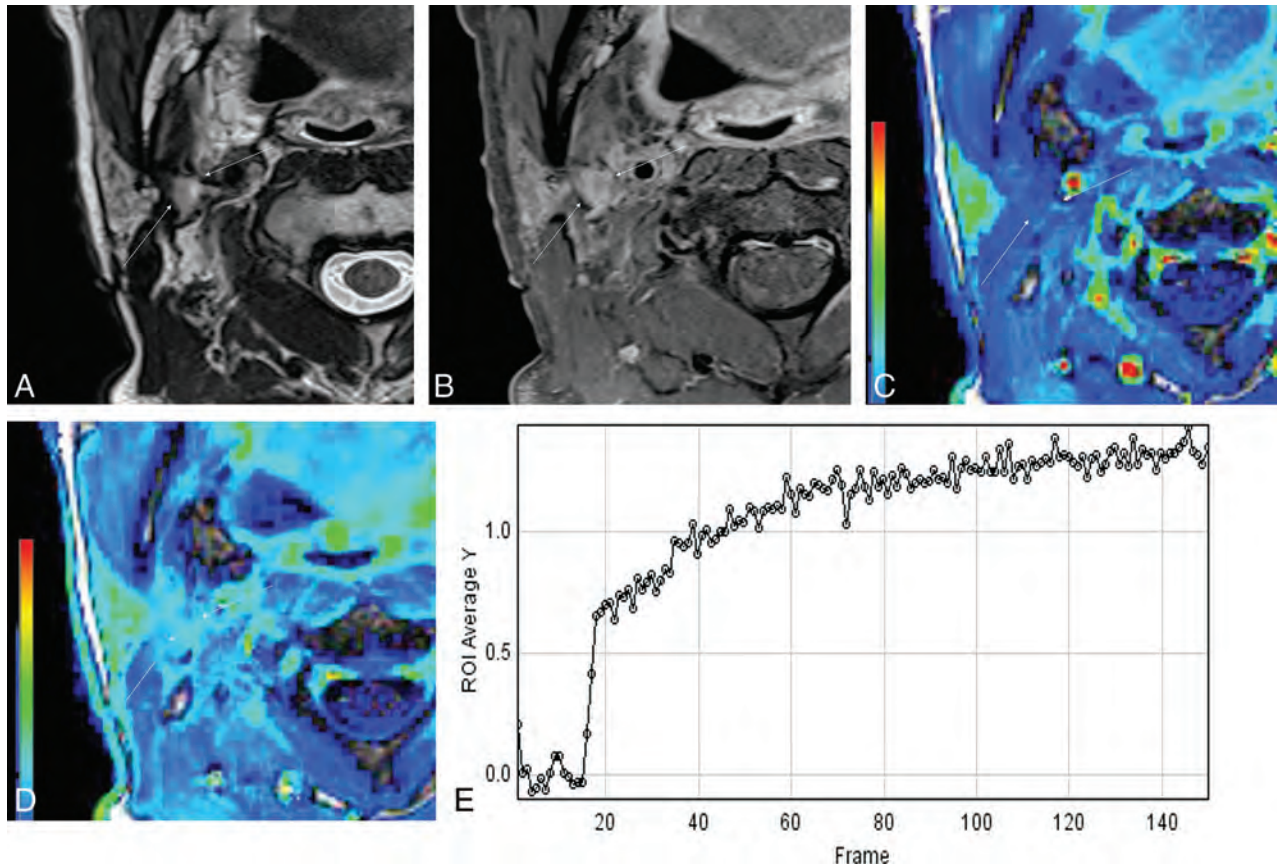


FIG 5. A 48-year-old female patient after wide excision and flap reconstruction for right-tongue cancer 13 months previously (T1N0M0). T2-weighted image (A) shows a slightly high signal intensity lesion posterolateral to the reconstructed flap with moderate contrast enhancement on the T1-weighted image (B, arrows). IAUC₉₀ (C) and FAUC₉₀ (D) images of DCE-MR imaging show a prolonged enhancement pattern. The time-signal intensity curve obtained at the enhancing portion also shows a prolonged enhancement pattern (E). This lesion was confirmed as dense fibrosis at excisional biopsy.

treatment change in HNSCC. Increased IAUC₉₀ values in recurrent tumors are a reflection of increased blood flow and contrast agent leakage to the extravascular extracellular space, related to the hypervascularity and neoangiogenesis of malignant tumor. A progressive increase in FAUC₉₀ in posttreatment change is due to increased retention of contrast agent in the extravascular extracellular space due to low cellularity.¹⁹

On DCE-MR imaging, model-based pharmacokinetic DCE parameters are quantitative, having the potential to measure “true” physiologic mechanisms such as blood flow and permeability. However, model-based DCE parameters is difficult to apply in clinical practice for several reasons, including arterial input function measurement and model fit instability.³¹ AUC during a given time is a model-free parameter that describes the uptake of the contrast agent in a tissue of interest. It has advantages over the model-based approach because it does not require arterial input function measurement and does not need complex postprocessing pharmacokinetic modeling.¹⁸ In addition, the model-free technique is more robust, is unlikely to be influenced by scan sequence variation, and is easier and more reproducible compared with the model-based method.³²

The current study emphasizes the usefulness of visual assessment of voxel-based color maps. Many recurrent tumors occur intermixed with posttreatment changes. Because the TSI curve itself has averaged hemodynamic characteristics of the entirety of

voxels in the ROI, the TSI curve has inherent limitations. If there is only a small focal area of recurrent tumor showing washout or a plateau pattern within the entire enhancing lesion, TSI curve analysis may overlook a small focus of viable tumor. To overcome this limitation, histogram-based assessment can be an alternative method because it allows comprehensive evaluation of an entire lesion volume. However, both time and effort to obtain the histogram parameters are required for all patients during daily practice. Voxel-based color maps may compensate for the drawbacks of TSI curve-pattern analysis and histogram analysis. While TSI curve analysis and histogram analysis need an ROI segmentation to extract a TSI curve or AUC-derived parameters, voxel-based color maps can provide simple and visually intuitive images and can help radiologists differentiate recurrent tumor from post-treatment change.

Our study has several limitations. In addition to the retrospective nature, the small sample size may diminish the statistical validity of the results. Future research with a large prospective cohort could further validate the methodology. Second, our study did not investigate any difference in the TSI curve pattern according to the status of human papillomavirus or Epstein-Barr virus, histologic tumor grade, or lesion volume. Given that these factors might affect the TSI curve pattern on DCE-MR imaging, the use of a fixed time interval on the TSI curve for voxel-based color maps can be another limitation. Again, additional investigation

with a larger sample size may be necessary to verify the preliminary results of the study. Third, our study included patients with various tumor locations, which could present different natural histories. However, we believe that the coherent results of our study reflect the histologic consequences of an operation or chemoradiation that are common (granulation tissue and fibrosis), irrespective of the tumor location. Further studies might be necessary to evaluate any difference in the dynamic features of DCE-MR imaging according to a specific tumor subsite.

CONCLUSIONS

We demonstrated that adding visual assessment of voxel-based color maps of IAUC₉₀ and FAUC₉₀ derived from DCE-MR imaging is both a technically valid and reliable method for detecting local tumor recurrence at the primary site in patients with HNSCC during surveillance. Combined interpretation of both conventional and DCE-MRIs can be useful in ruling out the probability of a locally recurrent tumor by improved diagnostic specificity without sacrificing sensitivity.

Disclosures: Jung Hwan Baek—UNRELATED: Consultancy: RF Medical and StarMed since 2017.

REFERENCES

- Agra IM, Carvalho AL, Ulbrich FS, et al. Prognostic factors in salvage surgery for recurrent oral and oropharyngeal cancer. *Head Neck* 2006;28:107–13 CrossRef Medline
- Goodwin WJ Jr. Salvage surgery for patients with recurrent squamous cell carcinoma of the upper aerodigestive tract: when do the ends justify the means? *Laryngoscope* 2000;110(3 Pt 2 Suppl 93):1–18 Medline
- Kowalski LP, Bagietto R, Lara JR, et al. Prognostic significance of the distribution of neck node metastasis from oral carcinoma. *Head Neck* 2000;22:207–14 CrossRef Medline
- Carvalho AL, Magrin J, Kowalski LP. Sites of recurrence in oral and oropharyngeal cancers according to the treatment approach. *Oral Dis* 2003;9:112–18 CrossRef Medline
- Yom SS, Machtay M, Biel MA, et al. Survival impact of planned restaging and early surgical salvage following definitive chemoradiation for locally advanced squamous cell carcinomas of the oropharynx and hypopharynx. *Am J Clin Oncol* 2005;28:385–92 CrossRef Medline
- Bahadur S, Amatya RC, Kacker SK. The enigma of post-radiation oedema and residual or recurrent carcinoma of the larynx and pyriform fossa. *J Laryngol Otol* 1985;99:763–65 CrossRef Medline
- Cheung PK, Chin RY, Eslick GD. Detecting residual/recurrent head neck squamous cell carcinomas using PET or PET/CT: systematic review and meta-analysis. *Otolaryngol Head Neck Surg* 2016;154:421–32 CrossRef Medline
- Cao Y, Popovtzer A, Li D, et al. Early prediction of outcome in advanced head-and-neck cancer based on tumor blood volume alterations during therapy: a prospective study. *Int J Radiat Oncol Biol Phys* 2008;72:1287–90 CrossRef Medline
- Chikui T, Kitamoto S, Kawano S, et al. Pharmacokinetic analysis based on dynamic contrast-enhanced MRI for evaluating tumor response to preoperative therapy for oral cancer. *J Magn Reson Imaging* 2012;36:589–97 CrossRef Medline
- Semiz Oysu A, Ayanoglu E, Kodalli N, et al. Dynamic contrast-enhanced MRI in the differentiation of posttreatment fibrosis from recurrent carcinoma of the head and neck. *Clin Imaging* 2005;29:307–12 CrossRef Medline
- Tomura N, Omachi K, Sakuma I, et al. Dynamic contrast-enhanced magnetic resonance imaging in radiotherapeutic efficacy in the head and neck tumors. *Am J Otolaryngol* 2005;26:163–67 CrossRef Medline
- Ishiyama M, Richards T, Parvathaneni U, et al. Dynamic contrast-enhanced magnetic resonance imaging in head and neck cancer: differentiation of new H&N cancer, recurrent disease, and benign post-treatment changes. *Clin Imaging* 2015;39:566–70 CrossRef Medline
- Furukawa M, Parvathaneni U, Maravilla K, et al. Dynamic contrast-enhanced MR perfusion imaging of head and neck tumors at 3 Tesla. *Head Neck* 2013;35:923–29 CrossRef Medline
- King AD, Chow SK, Yu KH, et al. DCE-MRI for pre-treatment prediction and post-treatment assessment of treatment response in sites of squamous cell carcinoma in the head and neck. *PLoS One* 2015;10:e0144770 CrossRef Medline
- Choi YJ, Lee JH, Sung YS, et al. Value of dynamic contrast-enhanced MRI to detect local tumor recurrence in primary head and neck cancer patients. *Medicine (Baltimore)* 2016;95:e3698 CrossRef Medline
- Choi SH, Lee JH, Choi YJ, et al. Detection of local tumor recurrence after definitive treatment of head and neck squamous cell carcinoma: histogram analysis of dynamic contrast-enhanced T1-weighted perfusion MRI. *AJR Am J Roentgenol* 2017;208:42–47 CrossRef Medline
- Chung WJ, Kim HS, Kim N, et al. Recurrent glioblastoma: optimum area under the curve method derived from dynamic contrast-enhanced T1-weighted perfusion MR imaging. *Radiology* 2013;269:561–68 CrossRef Medline
- Evelhoch JL, LoRusso PM, He Z, et al. Magnetic resonance imaging measurements of the response of murine and human tumors to the vascular-targeting agent ZD6126. *Clin Cancer Res* 2004;10:3650–57 CrossRef Medline
- Suh CH, Kim HS, Choi YJ, et al. Prediction of pseudoprogression in patients with glioblastomas using the initial and final area under the curves ratio derived from dynamic contrast-enhanced T1-weighted perfusion MR imaging. *AJNR Am J Neuroradiol* 2013;34:2278–86 CrossRef Medline
- Yabuuchi H, Fukuya T, Tajima T, et al. Salivary gland tumors: diagnostic value of gadolinium-enhanced dynamic MR imaging with histopathologic correlation. *Radiology* 2003;226:345–54 CrossRef Medline
- Yuan J, Chow SK, Yeung DK, et al. A five-colour colour-coded mapping method for DCE-MRI analysis of head and neck tumours. *Clin Radiol* 2012;67:216–23 CrossRef Medline
- Ailianou A, Mundada P, De Perrot T, et al. MRI with DWI for the detection of posttreatment head and neck squamous cell carcinoma: why morphologic MRI criteria matter. *AJNR Am J Neuroradiol* 2018;39:748–55 CrossRef Medline
- Becker M, Varoquaux AD, Combescure C, et al. Local recurrence of squamous cell carcinoma of the head and neck after radio(chemo)therapy: diagnostic performance of FDG-PET/MRI with diffusion-weighted sequences. *Eur Radiol* 2018;28:651–63 CrossRef Medline
- King AD, Keung CK, Yu KH, et al. T2-weighted MR imaging early after chemoradiotherapy to evaluate treatment response in head and neck squamous cell carcinoma. *AJNR Am J Neuroradiol* 2013;34:1237–41 CrossRef Medline
- Gong QY, Zheng GL, Zhu HY. MRI differentiation of recurrent nasopharyngeal carcinoma from postradiation fibrosis. *Comput Med Imaging Graph* 1991;15:423–29 CrossRef Medline
- Lell M, Baum U, Greess H, et al. Head and neck tumors: imaging recurrent tumor and post-therapeutic changes with CT and MRI. *Eur J Radiol* 2000;33:239–47 CrossRef Medline
- Mukherji SK, Wolf GT. Evaluation of head and neck squamous cell carcinoma after treatment. *AJNR Am J Neuroradiol* 2003;24:1743–46 Medline
- van der Hoorn A, van Laar PJ, Holtman GA, et al. Diagnostic accuracy of magnetic resonance imaging techniques for treatment response evaluation in patients with head and neck tumors: a systematic review and meta-analysis. *PLoS One* 2017;12:e0177986 CrossRef Medline

29. Dao TH, Rahmouni A, Campana F, et al. **Tumor recurrence versus fibrosis in the irradiated breast: differentiation with dynamic gadolinium-enhanced MR imaging.** *Radiology* 1993;187:751–55 CrossRef Medline
30. Kinkel K, Ariche M, Tardivon AA, et al. **Differentiation between recurrent tumor and benign conditions after treatment of gynecologic pelvic carcinoma: value of dynamic contrast-enhanced subtraction MR imaging.** *Radiology* 1997;204:55–63 CrossRef Medline
31. Cheng HL. **Improved correlation to quantitative DCE-MRI pharmacokinetic parameters using a modified initial area under the uptake curve (mIAUC) approach.** *J Magn Reson Imaging* 2009;30:864–72 CrossRef Medline
32. Galbraith SM, Lodge MA, Taylor NJ, et al. **Reproducibility of dynamic contrast-enhanced MRI in human muscle and tumours: comparison of quantitative and semi-quantitative analysis.** *NMR Biomed* 2002;15:132–42 CrossRef Medline

Prevalence of Spontaneous Asymptomatic Facial Nerve Canal Meningoceles: A Retrospective Review

J.C. Benson, K. Krecke, J.R. Geske, J. Dey, M.L. Carlson, J. Van Gompel, and J.I. Lane

ABSTRACT

BACKGROUND AND PURPOSE: The prevalence of patent facial nerve canals and meningoceles along the facial nerve course is unknown. This study aimed to assess the frequency of such findings in asymptomatic patients.

MATERIALS AND METHODS: A retrospective review was completed of patients with high-resolution MR imaging of the temporal bone whose clinical presentations were unrelated to facial nerve pathology. Facial nerve canals were assessed for the presence of fluid along each segment and meningoceles within either the labyrinthine segment (fluid-filled distention, ≥ 1.0 -mm diameter) or geniculate ganglion fossa (fluid-filled distention, ≥ 2.0 -mm diameter). If a meningocele was noted, images were assessed for signs of CSF leak.

RESULTS: Of 204 patients, 36 (17.6%) had fluid in the labyrinthine segment of the facial nerve canal and 40 (19.6%) had fluid in the geniculate ganglion fossa. Five (2.5%) had meningoceles of the geniculate ganglion fossa; no meningoceles of the labyrinthine segment of the canal were observed. No significant difference was observed in the ages of patients with fluid in the labyrinthine segment of the canal or geniculate ganglion compared with those without fluid ($P = .177$ and $P = .896$, respectively). Of the patients with a meningocele, one had a partially empty sella and none had imaging evidence of CSF leak or intracranial hypotension.

CONCLUSIONS: Fluid within the labyrinthine and geniculate segments of the facial nerve canal is relatively common. Geniculate ganglion meningoceles are also observed, though less frequently. Such findings should be considered of little clinical importance without radiologic evidence of CSF otorrhea, meningitis, or facial nerve palsy.

Meningocele of the facial nerve canal is a rare cause of CSF leak, with 15 reported cases in the literature.¹⁻⁴ CSF leak in the context of facial nerve canal meningocele occurs when the bony remodeling leads to dehiscence into the middle ear.^{5,6} Patients may present with symptomatic unilateral conductive hearing loss, middle ear fluid, otorrhea, rhinorrhea (from CSF flow through the Eustachian tube), or facial nerve paresis.^{7,8} Commonly, patients are misdiagnosed with a middle ear effusion and are ultimately found to have a CSF leak when persistent clear otorrhea is noted after myringotomy.¹ If otorrhea is present, preoperative meningitis has been reported in approximately half of patients.¹ Imaging of facial nerve canal meningoceles typically demonstrates smooth bony enlargement of the geniculate gan-

gion fossa with internal signal that is isointense to CSF on all sequences; bony dehiscence may or may not be present.^{5,9}

Observation of fluid or a meningocele within the facial nerve canal is a potential source of consternation to radiologists. No prior studies, to our knowledge, have described the incidence of such findings within the facial nerve canal in asymptomatic patients; the existing literature has focused on either microscopic analyses or meningoceles with bony dehiscence leading to symptomatic CSF leakage. Hence, this retrospective study sought to establish the prevalence of fluid or meningocele in the facial nerve canal in a cohort of patients asymptomatic for CSF leak, meningitis, or facial nerve palsy.

MATERIALS AND METHODS

Patient Selection

Institutional review board approval was obtained for this study. A retrospective review was completed of all patients at our institution who underwent internal auditory canal protocol MR imaging between January 1, 2017, and June 30, 2018. Only patients with thin-slice (0.5-mm thickness with differing in-plane resolutions) T2-weighted axial images were included. Such thin-slice T2 images were completed using sampling perfection with application-

Received March 19, 2019; accepted after revision June 17.

From the Department of Neuroradiology (J.C.B., K.K., J.I.L.), Division of Biomedical Statistics and Informatics (J.R.G.), and Departments of Otorhinolaryngology (J.D., M.L.C.) and Neurosurgery (J.V.G.), Mayo Clinic, Rochester, Minnesota.

Please address correspondence to John C. Benson, MD, 723 6th St SW, Rochester, MN 55902; e-mail: benso905@umn.edu

<http://dx.doi.org/10.3174/ajnr.A6133>

optimized contrasts by using different flip angle evolutions (SPACE; Siemens, Erlangen, Germany), (CISS; Siemens), or FIESTA sequences. Patients were excluded for the following reasons: 1) the images were judged to be prohibitively degraded by artifacts (eg, motion), 2) imaging was obtained as part of a work-up for symptomatic otorrhea, or 3) imaging was performed to assess clinically suspected abnormalities of the seventh cranial nerve.

Imaging and Electronic Medical Record Review

Two neuroradiologists and a neuroradiology fellow reviewed MR images for the presence or absence of fluid within the labyrinthine, geniculate, and tympanic segments of the facial nerve canal and the presence or absence of meningoceles within the same locations. Meningocele was defined as CSF-intensity fluid within a portion of the facial nerve canal that was widened on the basis of size criteria: ≥ 1.0 -mm diameter of the labyrinthine segment of the facial nerve canal and ≥ 2.0 -mm diameter of the geniculate ganglion fossa.¹⁰⁻¹² Size criteria were based on mean \pm 2 SDs of normal labyrinthine size based on a study by Shin et al¹⁰ and on analyses of the geniculate ganglion fossa by Gacek¹¹ and Mu et al.¹² In patients determined to have meningoceles, images were secondarily assessed for imaging evidence of dehiscence and/or CSF (eg, middle ear effusion). If ≥ 1 meningocele was detected, images were also assessed for the following: 1) secondary signs of CSF leak (eg, middle ear effusion, obvious bony dehiscence), 2) evidence of prior trauma or an operation, and 3) intracranial pathology that may have caused or suggested elevated intracranial pressure (eg, empty or partially empty sella, abnormal fluid within the optic nerve sheaths, tortuosity of the optic nerves, or slit-like ventricles). The body mass index of all patients was obtained via a retrospective review of the electronic medical record.

Statistical Analysis

Proportions of men and women with fluid in the specific anatomic compartments were compared using χ^2 tests. Association of both age and body mass index with the presence or absence of fluid was tested using *t* tests. Experiment-wide α was set at .05. Statistical analyses were performed using SAS (Version 9.4; SAS Institute, Cary, North Carolina).

RESULTS

Patient Characteristics and Presence of Fluid in the Facial Nerve Canal

Two hundred four patients (408 temporal bones) were included in the study cohort with 107 women (52.5%). The mean age was 53.3 ± 10.1 years (1 SD). CSF was present in the labyrinthine segment of the facial nerve canal in 36/204 patients (17.6%) and was present in the geniculate ganglion fossa in 40/204 patients (19.6%). No patients had CSF or meningoceles in the tympanic segment of the facial nerve canal. There was no significant difference in the ages of patients with fluid in the labyrinthine segment of the canal compared with those without fluid (55.4 ± 10.3 versus 52.9 ± 10.1 years, respectively; $P = .177$), nor was there a significant difference in the ages of patients with fluid in the geniculate ganglion fossa compared with those without (53.1 ± 10.5 versus 53.4 ± 10.1 years, respectively; $P = .896$).

Incidence of facial nerve canal fluid/meningocele^a

	None (No.)	Unilateral (No.)	Bilateral (No.)
Labyrinthine segment fluid	168 (82.4%)	22 (10.8%)	14 (6.9%)
Geniculate ganglion fossa fluid	164 (80.4%)	21 (10.3%)	19 (9.3%)
Geniculate ganglion fossa meningocele	199 (97.5%)	5 (2.5%)	0 (0.0%)

^a Incidence of fluid signal in the facial nerve canal on 3D fast spin-echo T2 sequences in 204 patients. Meningocele was defined on the basis of size criteria: ≥ 1.0 -mm diameter of the labyrinthine segment of the facial nerve canal, and ≥ 2.0 -mm diameter of the geniculate ganglion fossa. No meningoceles were observed within the labyrinthine segment.

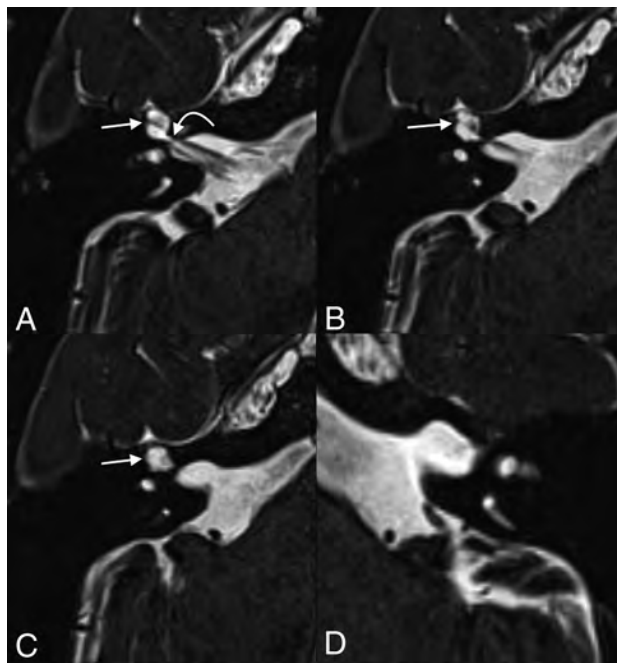


FIG 1. A 55-year-old woman who presented with persistent dizziness. From inferior to superior, axial T2 SPACE images demonstrate fluid-filled remodeling/expansion of the right geniculate ganglion fossa (straight arrows), compatible with a meningocele (A–C). The labyrinthine segment of the facial nerve canal (curved arrow) is 0.9 mm in diameter, which is at the upper limit of normal but does not meet the defined size criteria for a meningocele. The normal left side is shown for comparison (D).

Facial Nerve Canal Fluid Location, Laterality, and Meningocele

Location and laterality of fluid within the facial nerve canal are presented in the Table. Labyrinthine segment fluid was unilateral in 22/36 (61.1%) patients and on the right in 12/22 (54.5%). Geniculate ganglion fossa fluid was unilateral in 21/40 (52.5%) patients and on the left in 11/21 (52.4%). In 21/40 (52.5%) patients with fluid in the geniculate ganglion fossa, the finding was isolated, with no fluid in the labyrinthine segment or meningocele observed. No significant difference was observed between the rate of patients with fluid in the labyrinthine segment of the facial nerve canal based on sex ($P = .681$). However, females were significantly more likely to have fluid in the geniculate ganglion fossa segment of the facial nerve canal than men (26.2% versus 12.4%, respectively; $P = .013$).

Five patients within the cohort (2.5%) had meningoceles, all of which were located in the geniculate ganglion fossa (Figs 1–3). Four of 5 (80%) meningoceles were located on the right side. All

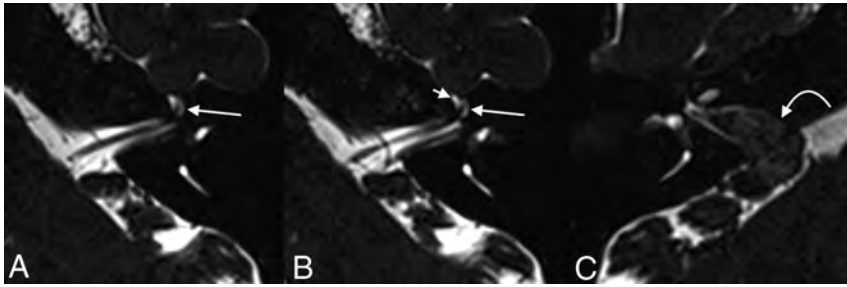


FIG 2. A 45-year-old woman who underwent imaging to follow up a known right vestibular schwannoma. Axial T2 SPACE images demonstrate fluid within the geniculate ganglion of the left facial nerve canal, with dilation measuring up to 2.7 mm, compatible with a meningocele (long arrows, A and B). Fluid is also seen tracking along the expected course of the proximal left greater superficial petrosal nerve (short arrow, B). The known vestibular schwannoma is seen in the contralateral right internal auditory canal, extending through the porus acusticus (curved arrow, C).

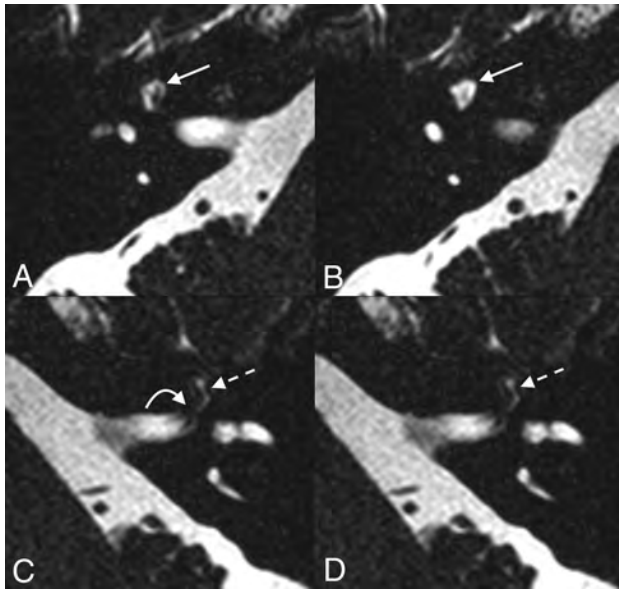


FIG 3. A 64-year-old woman who presented with bilateral sensorineural hearing loss. Axial T2 SPACE imaging demonstrates fluid-filled dilation of the right geniculate ganglion fossa, compatible with a meningocele (solid straight arrow, A and B). Fluid is seen in the left labyrinthine (curved arrow, C) and geniculate (dashed straight arrow, C and D) segments of the left facial nerve canal without remodeling/dilation of the osseous canal.

(100.0%) patients with meningoceles had fluid within the ipsilateral labyrinthine segments and geniculate ganglion fossa. None of the patients with meningoceles had evidence of bony dehiscence. No patients had meningoceles of the labyrinthine or tympanic segments of the facial nerve canal. None of the patients with meningoceles had secondary intracranial findings to suggest clinically occult CSF leak or intracranial hypotension, nor did these patients have imaging evidence of prior trauma or an operation. Of the patients with meningoceles, one had a contralateral vestibular schwannoma. One patient with a meningocele had a partially empty sella. There was no significant difference in the body mass indexes among patients with fluid in the facial nerve canal or geniculate ganglion fossa versus those without fluid ($P = .584$ and $P = .688$, respectively), nor was there a difference between patients with meningoceles and those without ($P = .566$).

DISCUSSION

This study set out to describe the prevalence of asymptomatic fluid and meningoceles within the facial nerve canal. We found that fluid is commonly present in the facial nerve canal in asymptomatic patients, occurring with near-equal incidence in the labyrinthine segment and geniculate ganglion fossa. To our knowledge, this is the first report of the incidental presence of fluid or meningocele in the facial nerve canal on MR imaging. Our results suggest that these are normal variants and should not be considered an unexpected or actionable finding.

According to multiple authors, CSF is prevented from flowing into the facial nerve canal in healthy patients by 2 anatomic barriers: An arachnoid sheath at the meatal foramen (the anatomic proximal end of the facial nerve canal) seals the facial nerve in the canal, and the facial nerve nearly fills the entire diameter of the relatively small osseous canal, thereby excluding CSF flow.^{1,13-15} However, a large histologic study of temporal bones by Gacek¹¹ found at least some extension of the subarachnoid space along the labyrinthine segment of the facial nerve canal in 88% of patients. Most of the remaining patients who had subarachnoid space extension to, or past, the geniculate ganglion in that study had intracranial pathology that may have been associated with intracranial hypertension.¹¹ In our study, the incidence of fluid within the labyrinthine segment of the facial nerve canal is much lower than that observed by Gacek. Although the disparity between the study by Gacek and the current study is unknown, it is likely that the spatial and contrast resolution of MR imaging is less sensitive to fluid than histologic analysis. In the current study, only 1 patient had a partially empty sella without clinical evidence of pseudotumor cerebri; there was otherwise no imaging evidence of intracranial hypertension among patients with meningoceles. Furthermore, it is possible that both fluid and meningoceles within the facial nerve canal represent sequelae of mild or compensated intracranial hypertension, similar to petrous apex cephaloceles and arachnoid granulations.^{5,16}

Although it is unknown why fluid along the labyrinthine and/or geniculate segments of the facial nerve was observed in spontaneous cases, it is possible that either congenital enlargement of the facial nerve canal or increased intracranial pressure contributed to the findings.¹⁷ Even slight congenital enlargement of the facial nerve canal could allow the subarachnoid space, and thereby CSF, to extend along the course of the facial nerve. Pressure and repetitive pulsations related to CSF could lead to remodeling of the osseous canal and dehiscence/fistulization into adjacent structures such as the middle ear.¹³ It is notable that while meningoceles were observed in the geniculate ganglion fossa, none were seen in the labyrinthine segment of the facial nerve canal. It is possible that the architecture of the geniculate fossa is more susceptible to bony remodeling related to high-pressure environments in accordance with Bernoulli's principle: Fluid within a system is at higher pressure as the diameter of the canal increases, and the geniculate ganglion fossa is larger than the laby-

rinthine segment of the facial nerve canal. It is also possible that geniculate ganglion dehiscence plays a role; a prior study by Isaacson and Vrabec¹⁸ found geniculate ganglion dehiscence to be a common radiographic finding, present in 14.5% of all patients.

This study has limitations shared by any retrospective review. Determination of CSF within the facial nerve canal was based on imaging tools with intrinsic (spatial and contrast resolution) and situational (bone-air interface artifacts) shortcomings compared with the histologic standard; laboratory analysis would be required to confirm that the observed fluid was CSF. Next, although the differentiation between CSF within the facial nerve canal and meningocele was sharply defined in this study based on canal diameter, the 2 entities likely exist on a spectrum; a patent facial nerve canal allows CSF flow, which may cause bony remodeling and hence meningocele formation across time—again, in accordance with Bernoulli's principle. Also, the opening CSF pressure was not available for review, limiting the ability of this study to correlate any findings with intracranial hyper- or hypotension. Finally, as stated above, the patient population of the study had dedicated internal auditory canal protocol MR imaging, limiting the ability to assess evidence of or pathology potentially related to intracranial hypertension.

CONCLUSIONS

Fluid in the labyrinthine and geniculate segments of the facial nerve canal is a relatively common incidental finding on temporal bone MRIs and presumably represents CSF. Meningoceles of the geniculate ganglion fossa, too, are observed in asymptomatic patients, though less frequently. In the absence of clinical or radiologic evidence of associated CSF otorrhea, these findings should be considered incidental variants.

REFERENCES

1. Dey J, Van Gompel JJ, Lane JL, et al. **Fallopian canal meningocele with spontaneous cerebrospinal fluid otorrhea: case report and systematic review of the literature.** *World Neurosurg* 2019;122:e285–90 CrossRef Medline
2. Mong S, Goldberg AN, Lustig LR. **Fallopian canal meningocele: report of two cases.** *Otol Neurotol* 2009;30:525–28 CrossRef Medline
3. Kong WK, Lee CH, Eunhye Y, et al. **Unruptured translabyrinthine**

- meningocele without CSF otorrhea.** *Int J Pediatr Otorhinolaryngol* 2014;78:556–59 CrossRef Medline
4. Franco-Vidal V, Baretto GP, Vignes JR, et al. **Spontaneous cerebrospinal fluid fistula through a congenitally patent facial nerve canal: incrimination of idiopathic intracranial hypertension.** *Otol Neurotol* 2009;30:123–24 CrossRef Medline
5. Petrus LV, Lo WW. **Spontaneous CSF otorrhea caused by abnormal development of the facial nerve canal.** *AJNR Am J Neuroradiol* 1999;20:275–77 Medline
6. Truesdale CM, Peterson RB, Hudgins PA, et al. **Internal auditory canal meningocele-perilabyrinthine/translabyrinthine fistula: case report and imaging.** *Laryngoscope* 2016;126:1931–34 CrossRef Medline
7. Alonso RC, de la Peña MJ, Caicoya AG, et al. **Spontaneous skull base meningoencephaloceles and cerebrospinal fluid fistulas.** *Radiographics* 2013;33:553–70 CrossRef Medline
8. Remenschneider AK, Kozin ED, Curtin H, et al. **Histopathology of idiopathic lateral skull base defects.** *Laryngoscope* 2015;125:1798–806 CrossRef Medline
9. Gray BG, Willinsky RA, Rutka JA, et al. **Spontaneous meningocele, a rare middle ear mass.** *AJNR Am J Neuroradiol* 1995;16:203–07 Medline
10. Shin KJ, Gil YC, Lee JY, et al. **Three-dimensional study of the facial canal using microcomputed tomography for improved anatomical comprehension.** *Anat Rec (Hoboken)* 2014;297:1808–16 CrossRef Medline
11. Gacek RR. **Anatomy and significance of the subarachnoid space in the fallopian canal.** *Am J Otol* 1998;19:358–65 Medline
12. Mu X, Quan Y, Shao J, et al. **Enlarged geniculate ganglion fossa: CT sign of facial nerve canal fracture.** *Acad Radiol* 2012;19:971–76 CrossRef Medline
13. Foyt D, Brackmann DE. **Cerebrospinal fluid otorrhea through a congenitally patent fallopian canal.** *Arch Otolaryngol Head Neck Surg* 2000;126:540–42 CrossRef Medline
14. Mortazavi MM, Latif B, Verma K, et al. **The fallopian canal: a comprehensive review and proposal of a new classification.** *Childs Nerv Syst* 2014;30:387–95 CrossRef Medline
15. Cavusoglu M, Duran S, Hatipoglu HG, et al. **Petrous apex cephalocele: contribution of coexisting intracranial pathologies to aetiopathogenesis.** *Br J Radiol* 2015;88:20140721 CrossRef Medline
16. Watane GV, Patel B, Brown D, et al. **The significance of arachnoid granulation in patients with idiopathic hypertension.** *J Comput Assist Tomogr* 2018;42:282–85 CrossRef Medline
17. Brainard L, Chen DA, Aziz KM, et al. **Association of benign intracranial hypertension and spontaneous encephalocele with cerebrospinal fluid leak.** *Otol Neurotol* 2012;33:1621–24 CrossRef Medline
18. Isaacson B, Vrabec JT. **The radiographic prevalence of geniculate ganglion dehiscence in normal and congenitally thin temporal bones.** *Otology Neurotol* 2007;28:107–10 CrossRef Medline

Evaluating Tissue Contrast and Detecting White Matter Injury in the Infant Brain: A Comparison Study of Synthetic Phase-Sensitive Inversion Recovery

D.Y. Kim, W.S. Jung, J.W. Choi, J. Choung, and H.G. Kim



ABSTRACT

BACKGROUND AND PURPOSE: Synthetic MR imaging enables the acquisition of phase-sensitive inversion recovery images. The aim of this study was to compare the image quality of synthetic phase-sensitive inversion recovery with that of other sequences in infants.

MATERIALS AND METHODS: Brain MR imaging with 3D T1-weighted fast-spoiled gradient recalled, synthetic TIWI, and synthetic phase-sensitive inversion recovery of 91 infants was compared. Contrast between unmyelinated WM and myelinated WM and between unmyelinated WM and cortical GM was calculated. Qualitative evaluation of image quality and myelination degree was performed. In infants with punctate white matter injuries, the number of lesions was compared.

RESULTS: The contrast between unmyelinated WM and myelinated WM was higher in synthetic phase-sensitive inversion recovery compared with fast-spoiled gradient recalled or synthetic TIWI ($P < .001$). Compared with synthetic TIWI, synthetic phase-sensitive inversion recovery showed higher gray-white matter differentiation ($P < .001$) and myelination degree in the cerebellar peduncle ($P < .001$). The number of detected punctate white matter injuries decreased with synthetic phase-sensitive inversion recovery compared with fast-spoiled gradient recalled sequences (1.2 ± 3.2 versus 3.4 ± 3.6 , $P = .001$).

CONCLUSIONS: Synthetic phase-sensitive inversion recovery has the potential to improve tissue contrast and image quality in the brain MR imaging of infants. However, we have to be aware that synthetic phase-sensitive inversion recovery has limited value when assessing punctate white matter injuries compared with 3D fast-spoiled gradient recalled imaging.

ABBREVIATIONS: CP = cerebellar peduncle; FSPGR = fast-spoiled gradient recalled; GM-WM = gray-white matter differentiation; mWM = myelinated white matter; PSIR = phase-sensitive inversion recovery; uWM = unmyelinated white matter

Numerous biologic changes occur in the brain tissue of infants. The brain continues myelination and vascularization before and after birth and eventually develops neurons and dendritic connections.¹ Various imaging modalities have been used to depict this brain maturation in infants. MR imaging has been

recognized as the most practical technique to do so by means of T1WI and T2WI.^{2,3} Several quantitative markers are widely accepted for this assessment, including T1 and T2 relaxation times⁴ and diffusion anisotropy.⁵ Yet, qualitative assessment of brain maturation is just as important as quantitative assessment in clinical practice.

One of the MR imaging sequences used for myelination assessment is phase-sensitive inversion recovery (PSIR). PSIR image reconstruction provides higher resolution by increasing gray-white matter differentiation (GM-WM) and the overall signal-to-noise ratio.^{6,7} In past studies, PSIR also enabled superior detection of focal lesions in adult patients with progressive multiple sclerosis or with cerebral autosomal-dominant arteriopathy with subcortical infarcts and leukoencephalopathy.^{8,9} In infants, another study concluded that PSIR images correlated well with the chronology of brain maturation and provided adequate information about brain injuries.¹

There has been much effort to make MR imaging clinically more feasible for children and especially to resolve issues with its long acquisition time.^{2,10} The recently developed synthetic MR

Received March 23, 2019; accepted after revision June 17.

From the Department of Radiology (D.Y.K., W.S.J., J.W.C., H.G.K.) and Biomedical Informatics (J.C.), Ajou University School of Medicine, Suwon, Republic of Korea; Office of Biostatistics (J.C.), Ajou Research Institute for Innovative Medicine, Ajou University Medical Center, Suwon, Republic of Korea; and Department of Radiology (H.G.K.), Eunpyeong St. Mary's Hospital, College of Medicine, The Catholic University of Korea, Seoul, Republic of Korea.

This work was funded by the National Research Foundation of Korea (NRF-2017RID1A1B03034768).

Paper previously presented at: 74th Korean Congress of Radiology, September 2018, Seoul, Republic of Korea.

Please address correspondence to Hyun Gi Kim, MD, PhD, Department of Radiology, Eunpyeong St. Mary's Hospital, College of Medicine, The Catholic University of Korea, 1021, Tongil-ro, Eunpyeong-gu, Seoul, Republic of Korea, 03312; e-mail: catharina@catholic.ac.kr; @hgkim315

Indicates open access to non-subscribers at www.ajnr.org

<http://dx.doi.org/10.3174/ajnr.A6135>

imaging is a multiparametric quantitative MR imaging that can generate multiple sequences by manipulating TR, TE, and TI.^{2,11} This technique has reduced scanning times in pediatric brain MR imaging.² With synthetic MR imaging, we are able to obtain not only synthetic T1WI, T2WI, and proton-density images but also synthetic PSIR images.⁹

To the best of our knowledge, there has been no study conducted on synthetic PSIR in the assessment of brain maturation in infants. In previous studies, synthetic T1WI or T2WI showed lower or equivalent image quality compared with conventional T1WI or T2WI.^{2,10,12} However, the brain MR imaging protocol of infants frequently includes 3D-T1WI instead of 2D.¹³ The role of thin-slice images from 3D acquisition is important because it allows detection and quantification of WM injuries from perinatal insult, which predict the outcome in infants.¹⁴ Thus, the image quality of synthetic images and conventional 3D-T1WI needs to be compared before synthetic MR imaging can be implemented in infants. Therefore, the aim of our study was to compare tissue contrast, image quality, myelination degree, and the number of punctate white matter lesions assessed with synthetic PSIR in infants with those assessed with synthetic T1WI, conventional 3D-T1WI, and conventional T2WI.

MATERIALS AND METHODS

Patients

The institutional review board of Ajou University Hospital approved this retrospective study. We reviewed the brain MR imaging of infants obtained from July 2016 to October 2017 using a 3T scanner (Discovery 750W; GE Healthcare, Milwaukee, Wisconsin). During the study period, the routine MR imaging protocols of infants included 3D-T1WI fast-spoiled gradient recalled (FSPGR) and multiparametric quantitative MR imaging, with or without the axial T2WI fast spin-echo sequence. With multiparametric quantitative MR imaging, synthetic T1WI and synthetic PSIR images were generated and automatically loaded on a PACS system. Demographic information and indications for MR imaging were collected through a review of the medical records. We also further classified a subgroup of infants with punctate white matter injuries.

Image Acquisition

The parameters for FSPGR were the following: TR = 9 ms, TE = 3 ms, slice thickness = 1 mm, NEX = 1, and FOV = 22 × 22 cm (scanning time = 3 minutes 6 seconds). Multiparametric quantitative MR imaging was performed using 4 saturation delays of 130, 500, 1370, and 2970 ms, and the TR was 4452 ms. The TR included 2 TEs of 22 and 128 ms. Each acquisition created 8 images per section (scanning time = 5 minutes). Slice thickness was 3 mm, and the FOV was 20 × 20 cm.³ For synthetic T1WI, the parameters were TR = 550 ms and TE = 10 ms. For synthetic PSIR, the parameters were TR = 6000 ms, TE = 10 ms, and TI = 500 ms. The parameters for synthetic PSIR were the default setting of the MR imaging scanner. The parameters for T2WI were the following: TR = 6000 ms, TE = 151 ms, slice thickness = 3 mm, NEX = 2, and FOV = 18 × 18 cm (scanning time = 3 minutes 18 seconds). Synthetic T1WI and PSIR were automatically generated

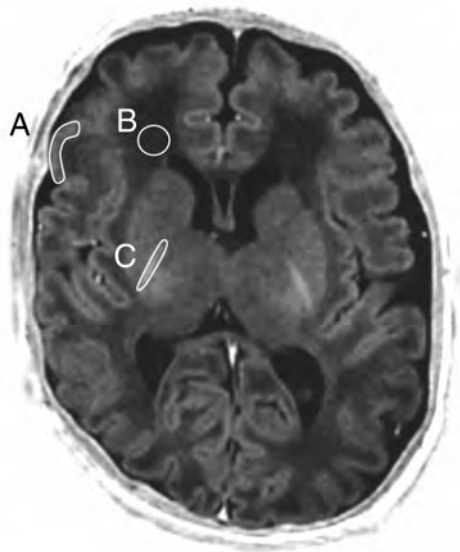


FIG 1. Representative synthetic PSIR image showing the drawn ROI along with cortical GM (A), uWM (B), and mWM (C).

after multiparametric quantitative MR imaging and were displayed on the PACS.

Image Analysis

For quantitative analysis, ROIs were manually drawn and the mean signal intensities of unmyelinated white matter (uWM), myelinated white matter (mWM), and cortical GM were measured on the images (Fig 1). The ROIs were drawn using PACS of our hospital. The contrast between uWM and mWM and between uWM and GM was measured using the Michelson contrast equation. In this equation, the contrast is the difference between the maximal and minimal intensities divided by the sum of the maximal and minimal intensities.²

For qualitative analysis, 2 radiologists with 8 years of experience in pediatric neuroradiology (radiologist 1) and 6 years of experience in neuroradiology (radiologist 2) performed the visual assessment. Images of 26 infants without visual abnormalities were analyzed blindly and independently in random order. The qualitative analysis was composed of 2 assessments, 1 for image quality and 1 for myelination degree. Image quality was evaluated by diagnostic quality and GM-WM. Both parameters were graded as follows: 1 = poor, 2 = moderate, and 3 = good. Myelination degree was evaluated in the cerebellar peduncle (CP), posterior limb of internal capsule, anterior limb of the internal capsule, and frontal and occipital WM. The myelination degree of each anatomic region was scored as follows: 1 = unmyelinated, 2 = intermediate, and 3 = fully myelinated.

For the subgroup with punctate white matter injuries, the injuries were shown as focal lesions with increased T1 signal intensity.¹⁵ The total number of lesions in each sequence was counted by the radiologist with 8 years of experience in pediatric neuroradiology. Then, using the coronal images of 3D-FSPGR, we measured the cranial-to-caudal diameters of lesions that were not detectable with synthetic PSIR.

Table 1: Contrast comparison of the FSPGR, synthetic T1WI, and synthetic PSIR sequences (n = 91)^a

	FSPGR	T1WI ^b	PSIR ^b	P Value	FSPGR vs T1WI ^b (P Values)	T1WI ^b vs PSIR ^b (P Values)	FSPGR vs PSIR ^b (P Values)
uWM-mWM	0.249 (0.101)	0.182 (0.062)	0.506 (0.211)	<.001	<.001	<.001	<.001
uWM-GM	0.124 (0.117)	0.099 (0.067)	0.393 (0.309)	<.001	.454	<.001	<.001

^a Data are median (interquartile range) unless otherwise indicated.

^b Synthetic images.

Statistical Analysis

In quantitative analysis, the Friedman test was used to compare the first 3 sequences, which were FSPGR, synthetic T1WI, and synthetic PSIR. Two of the 3 sequences were compared using the Wilcoxon signed rank test, and Bonferroni correction was applied to reduce errors associated with multiple comparison. The Wilcoxon signed rank test was also used to compare tissue contrast between synthetic PSIR and T2WI. In qualitative analysis, Cochran-Mantel-Haenszel statistics were used to compare the image quality and myelination degree of the 3 sequences. To compare 2 among the 3 sequences, we performed the χ^2 test after reclassifying image quality and myelination degree into 2 categories (1 or 2 versus 3). To compare the number of punctate WM lesions detected on the 3 sequences, we used the Friedman test. The mean relative comparison for synthetic PSIR versus FSPGR and synthetic PSIR versus synthetic T1WI was expressed as a percentage of FSPGR and T1WI, respectively. A positive relative comparison value means a gain in the number of lesions detected using PSIR, and a negative value indicated a loss. Statistical analyses were performed with SAS, Version 4.9 (SAS Institute, Cary, North Carolina) and R statistical and computing software, Version 3.5.0 (<http://www.r-project.org/>), and *P* values < .05 were considered statistically significant.

RESULTS

Patient Information

A total of 91 infants (58 boys and 33 girls) were included in this study. The age range of the infants was from 1 to 180 days, and the mean corrected gestational age at MR imaging was 42.1 ± 11.1 weeks. The infants underwent brain MR imaging for various indications, with prematurity and intracranial hemorrhage being the most common. Other indications included an apnea event, seizure, suspicion of hydrocephalus, minor head trauma, and history of meningitis. The T2WI sequence was performed in 86 of 91 infants. The age range of infants with T2WI was from 1 to 175 days, and the mean corrected gestational age of these infants was 42.9 ± 10.4 weeks. There were 10 infants with punctate white matter injuries.

Contrast Comparison of the FSPGR, Synthetic T1WI, and Synthetic PSIR Sequences

Contrast observed with FSPGR, synthetic T1WI, and synthetic PSIR was compared, and the comparison results are summarized in Table 1. For the contrast between uWM and mWM, there were significant differences among the 3 sequences. When 2 of the 3 sequences were compared, PSIR (0.506) showed higher contrast compared with FSPGR (0.249, *P* < .001) and synthetic T1WI (0.182, *P* < .001). FSPGR showed significantly higher contrast compared with synthetic T1WI (*P* < .001). For the contrast between uWM and GM, there were also significant differences

Table 2: Contrast comparison between the T2WI and synthetic PSIR sequences (n = 86)^a

	T2WI	PSIR ^b	P Value
uWM-mWM	0.226 (0.106)	0.516 (0.214)	<.001
uWM-GM	0.176 (0.081)	0.386 (0.327)	<.001

^a Data are median (interquartile range) unless otherwise indicated.

^b Synthetic image.

among the 3 sequences. Again, synthetic PSIR (0.393) showed the highest contrast compared with FSPGR (0.124, *P* < .001) and synthetic T1WI (0.099, *P* < .001). There was no significant difference between FSPGR and synthetic T1WI (*P* = .454).

Contrast Comparison between the T2WI and PSIR Sequences

Contrast observed with T2WI and synthetic PSIR was compared, and the comparison results are summarized in Table 2. Compared with T2WI, synthetic PSIR showed significantly higher contrast between uWM and mWM (0.516 versus 0.226, *P* < .001). For the contrast between uWM and GM, synthetic PSIR showed significantly higher contrast compared with T2WI (0.386 versus 0.176, *P* < .001).

Assessment of Image Quality and Myelination Degree

The qualitative comparison of the 3 sequences is summarized in Table 3, and representative images are shown in Fig 2. For image quality, diagnostic quality and GM-WM assessed by radiologist 1 and GM-WM assessed by radiologist 2 showed significant differences among the 3 sequences. When 2 of the 3 sequences were compared by radiologist 1, synthetic PSIR showed significantly higher diagnostic quality (synthetic PSIR versus FSPGR, *P* = .023; synthetic PSIR versus synthetic T1WI, *P* = .002) and GM-WM (synthetic PSIR versus FSPGR, *P* = .002; synthetic PSIR versus synthetic T1WI, *P* < .001) compared with the other 2 sequences. When 2 of the 3 sequences were compared by radiologist 2, synthetic PSIR showed significantly higher GM-WM compared with synthetic T1WI (*P* < .001) but not compared with FSPGR (*P* > .999).

Myelination degree in the CP assessed by radiologist 1 and that in the CP and posterior limb of the internal capsule assessed by radiologist 2 showed significant differences among the 3 sequences. When 2 of the 3 sequences were compared by radiologist 1, the CP showed a significantly higher myelination degree with synthetic PSIR compared with FSPGR (*P* = .023) and synthetic T1WI (*P* < .001). When 2 of the 3 sequences were compared by radiologist 2, synthetic PSIR showed a significantly higher myelination degree in the CP compared with synthetic T1WI (*P* < .001), but not compared with FSPGR (*P* > .999). The posterior limb of the internal capsule showed significantly higher myelination degree with synthetic PSIR compared with FSPGR (*P* = .049) and synthetic T1WI (*P* < .001) by radiologist 2. Myelination de-

Table 3: Image quality and myelination degree assessment by the 2 radiologists^a

	Radiologist 1				Radiologist 2			
	FSPGR	T1WI ^b	PSIR ^b	P Value	FSPGR	T1WI ^b	PSIR ^b	P Value
Image quality								
Diagnostic quality	0/6/20	0/9/17	0/0/26	.006	0/1/25	0/0/26	0/1/25	.603
GM-WM	0/9/17	0/16/10	0/0/26	<.001	0/3/23	1/23/2	0/2/24	<.001
Myelination								
CP	0/6/20	0/20/6	0/0/26	<.001	0/1/25	2/21/3	0/0/26	<.001
PLIC	2/16/8	3/18/5	2/15/9	.452	1/22/3	1/22/3	0/1/25	<.001
ALIC	21/0/5	21/5/0	21/0/5	.513	22/4/0	22/4/0	21/1/4	.460
Frontal WM	22/4/0	26/0/0	22/4/0	.111	24/2/0	24/2/0	21/4/1	.421
Occipital WM	21/5/0	22/4/0	21/5/0	.918	21/5/0	21/5/0	21/0/5	.549

Note:—ALIC indicates anterior limb of the internal capsule; PLIC, posterior limb of the internal capsule.

^a Number of cases graded in 3-point scale are presented in order: Image quality, 1 = poor, 2 = moderate, and 3 = good; myelination, 1 = unmyelinated, 2 = intermediate, and 3 = fully myelinated.

^b Synthetic image.

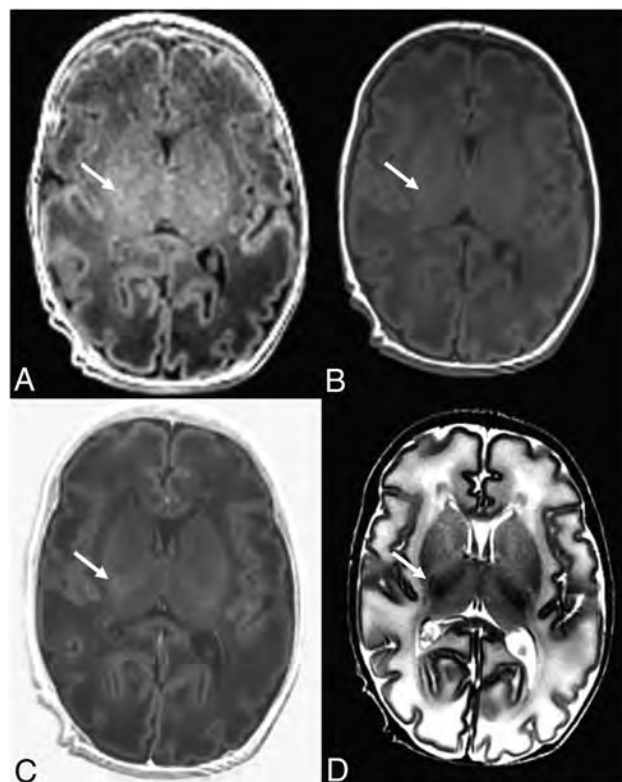


FIG 2. A 30-day-old neonate. There is limited myelination at the posterior limb of the internal capsule (arrow), showing higher signal intensity on the FSPGR (A), synthetic T1WI (B), and synthetic PSIR (C) images compared with the uWM regions. D, On the T2WI, the myelinated posterior limb of internal capsule (arrow) shows lower signal intensity compared with the uWM regions.

degrees in other regions (anterior limb of the internal capsule, frontal WM, and occipital WM) were not significantly different.

Punctate WM Lesions

The number and location of the WM lesions found in the 10 infants using the 3 sequences are summarized in Table 4. Several lesions that appeared on FSPGR were not detectable on the synthetic PSIR images (Fig 3). Among the 10 infants with punctate WM injuries, FSPGR revealed a total of 67 lesions, whereas both synthetic T1WI and PSIR revealed 24 lesions. The number of lesions detected using FSPGR (3.35 ± 3.62) was significantly higher than the number of lesions detected using synthetic T1WI ($1.2 \pm$

2.89 , $P = .002$) and synthetic PSIR (1.2 ± 3.24 , $P = .001$). The mean relative differences in the numbers of lesions for synthetic PSIR versus FSPGR and synthetic PSIR versus T1WI were -67.2% and 0% , respectively. The mean of the cranial-to-caudal diameters of punctate WM lesions that were not detectable on synthetic PSIR was 1.57 ± 0.27 mm.

DISCUSSION

In this study, we found that synthetic PSIR could be a practical imaging sequence for assessing brain maturation both quantitatively and qualitatively in infants. Synthetic PSIR showed significantly higher tissue contrast compared with conventional 3D-T1WI, synthetic T1WI, and T2WI. In our qualitative assessment, synthetic PSIR showed comparable or higher image quality or myelination degree than 3D-T1WI or synthetic T1WI. On the other hand, punctate WM injuries were better detected with 3D-T1WI than with synthetic PSIR.

Synthetic MR imaging is a time-efficient imaging technique that can generate multiple synthesized images at a single acquisition.^{2,16,17} A few studies have shown that synthetic MR imaging can be used in children^{2,10,18} as well as in adults.^{12,19} However, while one of these previous studies did compare the value of synthetic T1WI, T2WI, and FLAIR with conventional sequences,² the value of synthetic PSIR has not been evaluated in any study that we know of.

In our study, tissue contrast was superior with synthetic PSIR compared with synthetic T1 or FSPGR, and this result is consistent with those of a previous study using conventional PSIR.²⁰ The previous study compared contrast between GM and WM but did not compare contrast between uWM and mWM. PSIR provides a greater range of signal intensity compared with FSPGR and T1WI with conventional magnitude reconstruction, resulting in higher tissue contrast.²¹ This is possible by additively combining positive and negative longitudinal magnetization in PSIR images, in contrast to magnitude images without any directional component of magnetization.

According to our results, synthetic PSIR showed higher tissue contrast than conventional T2WI. This is in line with the previous qualitative comparison study that showed higher contrast with the PSIR sequence compared with the T2 spin-echo sequence.²⁰ With a decrease in water content and an increase in lipids and protein levels, mWM appears to be hyperintense compared with

Table 4: Number of punctate WM lesions detected on FSPGR, synthetic TIWI, and synthetic PSIR in the 10 patients

	FSPGR		TIWI ^a		PSIR ^a	
	Rt Lobe	Lt Lobe	Rt Lobe	Lt Lobe	Rt Lobe	Lt Lobe
Patients						
1	12	13	12	6	12	9
2	2	1	0	0	0	0
3	1	0	0	0	0	0
4	2	0	0	0	0	0
5	2	3	0	0	0	0
6	4	6	0	1	0	0
7	5	5	1	2	0	1
8	3	0	0	0	0	0
9	4	3	1	1	1	1
10	0	1	0	0	0	0
Total	67		24		24	
Mean No. of lesions detected (SD)	3.35 (3.62)		1.20 (2.89)		1.20 (3.24)	
	P Values					
FSPGR vs TIWI ^a	.002					
FSPGR vs PSIR ^a	.001					
TIWI ^a vs PSIR ^a	>.999					

Note:—Rt indicates right; Lt, left; SD, standard deviation.
^a Synthetic image.

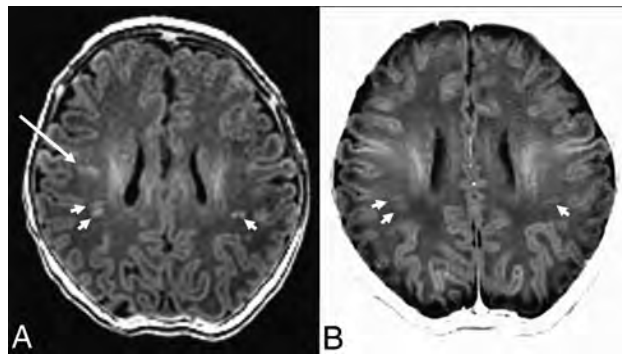


FIG 3. A 7-day-old neonate who underwent brain imaging due to an apnea event. There are multifocal high signal intensity lesions in the WM, which are readily detectable on both the FSPGR (A) and synthetic PSIR (B) images (*short arrows*). However, some of the lesions only appear on the FSPGR (*long arrow*) and not on the synthetic PSIR image.

uWM or GM on T1WI, while mWM on T2WI shows decreased signal intensities.^{1,22,23} In addition, the milestones of normal maturation are different between T1WI and T2WI.²³ Therefore, a direct comparison of contrast between T2WI and PSIR images has limited value.

We also showed that for image quality, synthetic PSIR showed the highest level of qualitative GM-WM among the 3 sequences. Recently, conventional and synthetic PSIR were compared for the detection of cortical lesions in patients with multiple sclerosis.¹⁶ In that study, synthetic PSIR showed similar sensitivity to conventional PSIR.¹⁶ We did not acquire conventional PSIR, so we could not compare its performance with that of synthetic PSIR in the infant brain. A prospective study on this subject is needed in the future.

Assessing myelin development can be crucial in infants. This is because many disorders are associated with delayed or abnormal myelination, and early detection is essential for early treatment and better prognostication.²⁴ Myelination assessment has been

facilitated by the introduction of MR imaging, and there have been many attempts to evaluate myelination in infants more noninvasively and accurately. The high signal intensity observed on PSIR with neural development reflects the shorter longitudinal relaxation times of water protons in mWM. Water content decreases in mWM, and this may induce a decrease in the relaxation times of the water protons.²⁵ Conversely, lipid and protein levels increase in mWM. These changes in the developing brain result in signal intensity changes on MR imaging.²²

Therefore, the assessment of myelination degree in our study reflects the ability to find clinically relevant features using different sequences. In a past study with children, myelination patterns observed with synthetic T1WI were compared with those observed with conventional T1WI, and the estimated age

based on myelination degree was found to be similar between both sequences.¹⁰ Our qualitative results regarding myelination degree were superior with synthetic PSIR in the CP or posterior limb of the internal capsule. There was no significant difference in myelination degree in the anterior limb of the internal capsule, frontal WM, and occipital WM. This is probably because myelination was limited in those regions as our subjects were young, with a mean corrected gestational age of 42 weeks. If a larger group of subjects with older ages were included, there might have been significant differences in the above-mentioned regions as well. Synthetic MR imaging may not only allow quantitative assessment³ but also enhance the qualitative assessment of myelination degree in children.

As a subgroup analysis, we evaluated the potential of synthetic PSIR to detect punctate WM injuries. Reports have shown that most preterm neonates have abnormal neuroimaging findings such as parenchymal volume loss, cystic change, or enlargement of ventricles.^{13,14} Among such abnormal findings in preterm neonates, WM signal abnormalities are referred to as “periventricular white matter injuries of prematurity.” Because tissue contrast comparisons showed higher contrast with synthetic PSIR images, we expected the periventricular WM lesions to appear more prominently on synthetic PSIR than on FSPGR images. However, periventricular WM lesions were more readily and sensitively detected using FSPGR rather than synthetic PSIR imaging. We speculate that this finding is most likely due to higher spatial resolution in 3D-FSPGR compared with 2D synthetic PSIR sequences. This is because the mean cranial-to-caudal diameter of lesions that were not detectable with synthetic PSIR (1.57 mm) was smaller than the slice thickness of 2D synthetic images (3 mm) but larger than that of 3D FSPGR (1 mm). In addition, the number of lesions detected with synthetic T1WI and PSIR imaging were the same. Another possible reason is the pathologic characteristics of punctate WM lesions, which are different from normal brain tissue. The high T1 signal intensities of punctate WM lesions in-

dicating focal necrosis with macrophages and foci of activated microglia.²⁶ In addition, hemorrhagic components commonly accompany punctate WM injuries.^{27,28} Because the lesions have shorter T1 values than surrounding normal WM, if we applied an optimal null point of normal WM (ie, optimal TI value), a higher sensitivity for detecting WM lesions might be possible. Future studies comparing the contrast of WM lesions and surrounding normal WM lesions between synthetic PSIR and other sequences would also be helpful. Because neonatal MR imaging plays a role in predicting neurodevelopmental outcomes and the detection of periventricular WM lesions is one such marker, radiologists have to be aware that 2D synthetic PSIR imaging has limited value when detecting punctate WM lesions.

This study has some limitations. First, the study group included infants and neonates with brain abnormalities. Although we included subjects without visual abnormalities for qualitative comparison, these subjects cannot reflect a healthy population. Myelination degree of the abnormal brain such as in hydrocephalus is noticeably different from that of the normal brain.²⁹ Therefore, the 4 sequences we compared in this study do not reflect the myelination of the healthy population. Second, 2 radiologists with different degrees of experience in pediatric neuroradiology performed the qualitative assessment. Inter- and intraobserver variability was not evaluated, and differing experience levels in pediatric neuroradiology may have caused the discordant results between the 2 radiologists. Third, we did not optimize TR, TE, and TI for infants when generating synthetic PSIR from synthetic MR imaging. With synthetic MR imaging, we can create multiple different contrast images combining distinctive TR, TE, and TI.³⁰ Future studies with optimized TR, TE, and TI could further improve the image quality of synthetic PSIR in the infant population.

CONCLUSIONS

Synthetic PSIR has the potential to improve tissue contrast, image quality, and myelination degree assessment when evaluating the brains of infants compared with conventional sequences and other synthetic images, despite being of limited value when evaluating punctate WM injuries.

ACKNOWLEDGMENTS

The authors thank Sung-Min Gho of GE Healthcare Korea for technical assistance.

Disclosures: Hyun Gi Kim—RELATED: Grant: National Research Foundation of Korea grant.

REFERENCES

1. Christophe C, Muller MF, Balériaux D, et al. **Mapping of normal brain maturation in infants on phase-sensitive inversion-recovery MR images.** *Neuroradiology* 1990;32:173–78 CrossRef Medline
2. Lee SM, Choi YH, Cheon JE, et al. **Image quality at synthetic brain magnetic resonance imaging in children.** *Pediatr Radiol* 2017;47:1638–47 CrossRef Medline
3. Kim HG, Moon WJ, Han J, et al. **Quantification of myelin in children using multiparametric quantitative MRI: a pilot study.** *Neuroradiology* 2017;59:1043–51 CrossRef Medline
4. Paus T, Collins DL, Evans AC, et al. **Maturation of white matter in the human brain: a review of magnetic resonance studies.** *Brain Res Bull* 2001;54:255–66 CrossRef Medline
5. Neil J, Miller J, Mukherjee P, et al. **Diffusion tensor imaging of normal and injured developing human brain: a technical review.** *NMR Biomed* 2002;15:543–52 CrossRef Medline
6. Favaretto A, Poggiali D, Lazzarotto A, et al. **The parallel analysis of phase sensitive inversion recovery (PSIR) and double inversion recovery (DIR) images significantly improves the detection of cortical lesions in multiple sclerosis (MS) since clinical onset.** *PLoS One* 2015;10:e0127805 CrossRef Medline
7. Nelson F, Poonawalla AH, Hou P, et al. **Improved identification of intracortical lesions in multiple sclerosis with phase-sensitive inversion recovery in combination with fast double inversion recovery MR imaging.** *AJNR Am J Neuroradiol* 2007;28:1645–49 CrossRef Medline
8. Harel A, Ceccarelli A, Farrell C, et al. **Phase-sensitive inversion-recovery MRI improves longitudinal cortical lesion detection in progressive MS.** *PLoS One* 2016;11:e0152180 CrossRef Medline
9. Wallaert L, Hagiwara A, Andica C, et al. **The advantage of synthetic MRI for the visualization of anterior temporal pole lesions on double inversion recovery (DIR), phase-sensitive inversion recovery (PSIR), and myelin images in a patient with CADASIL.** *Magn Reson Med Sci* 2017;17:275–76 CrossRef Medline
10. Betts AM, Leach JL, Jones BV, et al. **Brain imaging with synthetic MR in children: clinical quality assessment.** *Neuroradiology* 2016;58:1017–26 CrossRef Medline
11. Riederer SJ, Suddarth SA, Bobman SA, et al. **Automated MR image synthesis: feasibility studies.** *Radiology* 1984;153:203–06 CrossRef Medline
12. Krauss W, Gunnarsson M, Nilsson M, et al. **Conventional and synthetic MRI in multiple sclerosis: a comparative study.** *Eur Radiol* 2018;28:1692–700 CrossRef Medline
13. Rutherford M, Biarge MM, Allsop J, et al. **MRI of perinatal brain injury.** *Pediatr Radiol* 2010;40:819–33 CrossRef Medline
14. Woodward LJ, Anderson PJ, Austin NC, et al. **Neonatal MRI to predict neurodevelopmental outcomes in preterm infants.** *N Engl J Med* 2006;355:685–94 CrossRef Medline
15. Ramenghi LA, Fumagalli M, Righini A, et al. **Magnetic resonance imaging assessment of brain maturation in preterm neonates with punctate white matter lesions.** *Neuroradiology* 2007;49:161–67 CrossRef Medline
16. Forslin Y, Bergendal Å, Hashim F, et al. **Detection of leukocortical lesions in multiple sclerosis and their association with physical and cognitive impairment: a comparison of conventional and synthetic phase-sensitive inversion recovery MRI.** *AJNR Am J Neuroradiol* 2018;39:1995–2000 CrossRef Medline
17. Warntjes JB, Leinhard OD, West J, et al. **Rapid magnetic resonance quantification on the brain: optimization for clinical usage.** *Magn Reson Med* 2008;60:320–29 CrossRef Medline
18. Andica C, Hagiwara A, Nakazawa M, et al. **The advantage of synthetic MRI for the visualization of early white matter change in an infant with Sturge-Weber syndrome.** *Magn Reson Med Sci* 2016;15:347–48 CrossRef Medline
19. Granberg T, Uppman M, Hashim F, et al. **Clinical feasibility of synthetic MRI in multiple sclerosis: a diagnostic and volumetric validation study.** *AJNR Am J Neuroradiol* 2016;37:1023–29 CrossRef Medline
20. Hou P, Hasan KM, Sitton CW, et al. **Phase-sensitive T1 inversion recovery imaging: a time-efficient interleaved technique for improved tissue contrast in neuroimaging.** *AJNR Am J Neuroradiol* 2005;26:1432–38 Medline
21. Rinaldi F, Calabrese M, Grossi P, et al. **Cortical lesions and cognitive impairment in multiple sclerosis.** *Neurol Sci* 2010;31:S235–37 CrossRef Medline
22. Laule C, Vavasour IM, Kolind SH, et al. **Magnetic resonance imaging of myelin.** *Neurotherapeutics* 2007;4:460–84 CrossRef Medline
23. Barkovich AJ, Kjos BO, Jackson DE Jr, et al. **Normal maturation of the neonatal and infant brain: MR imaging at 1.5 T.** *Radiology* 1988;166:173–80 CrossRef Medline
24. Welker KM, Patton A. **Assessment of normal myelination with magnetic resonance imaging.** *Semin Neurol* 2012;32:15–28 CrossRef Medline

25. Mansfield P, Morris PG. *NMR Imaging in Biomedicine*. New York: Academic Press; 1982:ix, 10–30
26. Wisnowski JL, Schmithorst VJ, Rosser T, et al. **Magnetic resonance spectroscopy markers of axons and astrogliosis in relation to specific features of white matter injury in preterm infants.** *Neuroradiology* 2014;56:771–79 CrossRef Medline
27. Niwa T, de Vries LS, Benders MJ, et al. **Punctate white matter lesions in infants: new insights using susceptibility-weighted imaging.** *Neuroradiology* 2011;53:669–79 CrossRef Medline
28. Kersbergen KJ, Benders MJ, Groenendaal F, et al. **Different patterns of punctate white matter lesions in serially scanned preterm infants.** *PLoS One* 2014;9:e108904 CrossRef Medline
29. Hanlo PW, Gooskens RJ, van Schooneveld M, et al. **The effect of intracranial pressure on myelination and the relationship with neurodevelopment in infantile hydrocephalus.** *Dev Med Child Neurol* 1997;39:286–91 Medline
30. Bobman SA, Riederer SJ, Lee JN, et al. **Cerebral magnetic resonance image synthesis.** *AJNR Am J Neuroradiol* 1985;6:265–69 Medline

Comparison of CSF and MRI Findings among Neonates and Infants with *E coli* or Group B Streptococcal Meningitis

S.F. Kralik, M.K. Kukreja, M.J. Paldino, N.K. Desai, and J.G. Vallejo

ABSTRACT

BACKGROUND AND PURPOSE: Group B *Streptococcus* and *Escherichia coli* (*E coli*) are the 2 most common causes of bacterial meningitis in neonates. The purpose of this study was to determine whether CSF and/or MR imaging findings differ between infants with group B streptococcal or *E coli* meningitis.

MATERIALS AND METHODS: A retrospective review was performed among neonates (younger than 28 days) and infants (younger than 120 days) with proved group B streptococcal ($n = 57$) or *E coli* meningitis ($n = 50$). A CSF or blood culture positive for *Streptococcus* or *E coli* and an elevated CSF white blood cell count were used as the criterion standard. Independent, blinded review of brain MRIs obtained within 21 days of presentation were performed by 2 board-certified neuroradiologists. CSF laboratory values and MR imaging findings were compared between the groups.

RESULTS: There was no statistically significant difference between the mean age at presentation for patients with group B streptococcal (40 days; range, 2–111 days) versus patients with *E coli* meningitis (31 days; range, 12–115 days) ($P = .18$). There was no statistically significant difference in the CSF white blood cell count, glucose, or protein. There was a significant difference between group B streptococcal and *E coli* meningitis in the frequency of hydrocephalus (0% versus 22%, $P = .001$) and infarct (40% versus 14%; $P = .038$), respectively. There was no statistically significant difference in leptomeningeal enhancement, cerebritis, ventriculitis, abscess/granuloma, subdural effusion, extra-axial purulent material, intraventricular purulent material, hemorrhage, and sinus thrombosis.

CONCLUSIONS: Although neonates and infants with group B streptococcal or *E coli* meningitis had similar age and CSF laboratory values, patients with group B streptococcal meningitis more frequently demonstrated infarcts, while those with *E coli* meningitis more frequently had early onset of hydrocephalus.

ABBREVIATIONS: GBS = group B *Streptococcus*; WBC = white blood cell

Bacterial meningitis is an inflammation of the meninges affecting the pia, arachnoid, and subarachnoid space in response to bacteria and bacterial products. Despite an array of antibiotics, neonatal meningitis remains a devastating disease. In developed countries, the incidence of culture-proved neonatal meningitis is estimated at 0.3 per 1000 live births.¹ In the modern era, the mortality is approximately 10%, and survivors remain at high risk for neurologic sequelae.^{2,3} In neonates, the most common pathogens are group B *Streptococcus* (GBS) and *Escherichia coli* (*E coli*).^{2,4,5}

Although early-onset GBS meningitis has decreased by two-thirds following the institution of intrapartum antibiotic prophylaxis, late-onset GBS remains a major cause of bacterial meningitis in infants.⁶

Neonates and infants may present with a wide range of non-specific clinical symptoms of meningitis, including fever, hypothermia, irritability, poor feeding, bulging fontanelle, and seizure. A lumbar puncture is necessary for definitive diagnosis of bacterial meningitis. Typical CSF findings in bacterial meningitis include elevated white blood cell (WBC) count, predominance of polymorphonuclear leukocytes, reduced glucose levels, and elevated protein levels.⁷

Neonates with bacterial meningitis will routinely have an MR imaging of the brain to assess complications, which can include abscess, empyema, infarct, and hydrocephalus. Detection of complications from meningitis is necessary in the management of these patients to assess the need for abscess or empyema

Received March 20, 2019; accepted after revision June 17.

From the Department of Radiology (S.F.K., M.K.K., M.J.P., N.K.D.), Texas Children's Hospital, Houston, Texas; Indiana University Riley Children's Hospital (S.F.K.), Indianapolis, Indiana; and Department of Pediatrics (J.G.V.), Baylor College of Medicine, Houston, Texas.

Please address correspondence to Stephen F. Kralik, MD, Department of Radiology, Texas Children's Hospital, 6701 Fannin St, Suite 470, Houston, TX, 77030; e-mail: steve.kralik@gmail.com

<http://dx.doi.org/10.3174/ajnr.A6134>

drainage and ventricular shunting as well as for assessment of parenchymal injury.

A previous report on infants with meningitis indicated a potential trend for different complications depending on the pathogen.⁸ The purpose of this research was to determine whether CSF and/or MR imaging findings differ between neonates and infants with GBS or *E coli* meningitis.

MATERIALS AND METHODS

Following institutional review board approval from Texas Children's Hospital and Indiana University Riley Children's Hospital, a multicenter retrospective review was performed from 2011 to 2018 among neonates (younger than 28 days) and infants (younger than 120 days) with culture-confirmed GBS ($n = 57$) or *E coli* meningitis ($n = 50$). Diagnosis of GBS or *E coli* meningitis was determined by a CSF culture positive for either *Streptococcus* or *E coli*, or a blood culture positive for *Streptococcus* or *E coli* combined with an elevated CSF WBC count (>20 WBC/ μ L for neonates younger than 30 days of age, >9 WBC/ μ L for 30–90 days of age, and >6 WBC/ μ L for older than 90 days of age).⁹

The CSF WBC count per μ L, corrected WBC count per μ L, red blood cell (RBC) count per μ L, glucose (mg/dL), and total protein (mg/dL) obtained within 7 days of presentation were recorded. Corrected WBC count was obtained by dividing the red blood cell count by 500 and subtracting this value from the WBC count. Patients with immunodeficiency, malignancy, or intracranial shunt were excluded. The electronic medical record was reviewed to determine patient age at presentation, duration from presentation to initial CSF obtained by lumbar puncture, duration from presentation to initial MR imaging, prematurity (<37 weeks' gestation), and history of a ventriculoperitoneal shunt procedure.

MR imaging of the brain was performed in all patients on 1.5 T and 3T MR imaging scanners using precontrast axial and sagittal T1-weighted turbo spin-echo, axial FLAIR, axial and coronal T2-weighted, axial gradient-echo, axial diffusion-weighted, and post-contrast axial and coronal T1-weighted turbo spin-echo imaging.

Retrospective independent blinded reviews of brain MRIs were performed within 21 days of presentation by 2 board-certified neuroradiologists (S.F.K., M.K.K.) with 7 and 9 years of experience, respectively, for the presence of the following: leptomeningeal enhancement, cerebritis, ependymal enhancement, hydrocephalus, abscess/granuloma, subdural effusion, infarct, hemorrhage, extra-axial purulent material, intraventricular purulent material, and sinus thrombosis. The neuroradiologist reviewed the MRIs of the brain with the clinical indications of possible meningitis but was blinded to the CSF laboratory results and pathogen diagnosis.

Leptomeningeal enhancement was defined as abnormal contrast enhancement of the leptomeninges on postcontrast T1-weighted imaging. Ependymal enhancement was defined as enhancement of the ependymal surface of the ventricles on postcontrast T1-weighted imaging. Abscess was defined as a peripherally enhancing intraparenchymal lesion on postcontrast T1-weighted imaging with or without associated diffusion restriction. Granuloma was defined as a homogeneously enhancing parenchymal lesion on postcontrast T1-weighted imaging. Cere-

britis was defined as superficial brain parenchymal diffusion restriction, enhancement on postcontrast T1-weighted imaging, or T2-weighted/FLAIR hyperintense signal. Infarct was defined as diffusion restriction or T2-weighted hyperintense signal in either a wedge-shaped cortical distribution or a lacunar type distribution. Hemorrhage was defined as abnormal hypointense signal on gradient-echo or T1-weighted hyperintense signal. Subdural effusion was defined as a subdural fluid collection without diffusion restriction or hemorrhage indicated by a lack of susceptibility artifacts or T1-weighted shortening. Extra-axial purulent material was defined as extra-axial (subarachnoid, subdural, or epidural space) diffusion restriction not caused by hemorrhage. Intraventricular purulent material was defined as diffusion restriction within the ventricles not caused by hemorrhage. Sinus thrombosis was defined as abnormal loss of T2-weighted flow void and loss of venous sinus contrast enhancement. Hydrocephalus was defined subjectively as disproportionate enlargement of the ventricles relative to cerebral sulci with reduced subarachnoid spaces in the sulci or cisterns.

Following determination of a statistically significant difference in hydrocephalus between groups, the reviewers subsequently reviewed all sonography, CT, and MRIs of the brain performed in the clinical care of the patients in inpatient and outpatient settings in all patients to determine the time from presentation to development of hydrocephalus on imaging.

For all patients in whom there was a discordant MR imaging finding, the reviewers performed a combined review and reached a consensus on the MR imaging finding, and this consensus was used as the final diagnosis. Interobserver agreement for individual MR imaging findings was calculated using the κ statistic. A κ value of 0.81–1.0 indicated excellent agreement, 0.61–0.80 indicated good agreement, 0.41–0.60 indicated moderate agreement, 0.21–0.40 indicated fair agreement, and 0–0.20 indicated slight agreement.

A Fisher exact test and an unpaired t test were used when appropriate to compare differences between patients with GBS meningitis and those with *E coli* meningitis for patient age at presentation, prematurity, duration from presentation to initial CSF collection, duration from presentation to MR imaging, duration from presentation to development of hydrocephalus on imaging, ventriculoperitoneal shunt procedure, CSF laboratory values (corrected WBC count, glucose and protein levels), and MR imaging findings (leptomeningeal enhancement, cerebritis, ependymal enhancement, hydrocephalus, abscess/granuloma, subdural effusion, infarct, hemorrhage, extra-axial purulent material, intraventricular purulent material, and sinus thrombosis). A Bonferroni correction was used to adjust for multiple comparisons for CSF and MR imaging findings between groups ($n = 14$), and a final P value $< .05$ was considered statistically significant.

RESULTS

A total of 57 patients with GBS meningitis and 50 with *E coli* meningitis were included. There was no significant difference for positive CSF culture detection of meningitis for GBS meningitis patients (46/57; 81%) compared to *E Coli* meningitis patients (35/50; 70%) ($P = .26$). There was no significant difference in the frequency of positive blood cultures between patients with GBS

Comparison of CSF and MRI findings in patients with GBS and *E coli* meningitis^a

Finding	GBS (n = 57)	<i>E coli</i> (n = 50)	P Value ^b
CSF corrected WBC count (cells/ μ L)	3116 \pm 5058	4770 \pm 12684	1.00
CSF glucose (mg/dL)	35.2 \pm 21.8	34.0 \pm 24.6	1.00
CSF total protein (mg/dL)	517.8 \pm 867.0	910.7 \pm 1414.2	1.00
Leptomeningeal enhancement	49%	46%	1.00
Cerebritis	21%	7%	.77
Ependymal enhancement	7%	28%	.063
Abscess/granuloma	2%	2%	1.00
Subdural effusion	49%	26%	.24
Hemorrhage	33%	46%	1.00
Extra-axial purulent material	37%	38%	1.00
Intraventricular purulent material	9%	22%	.84
Sinus thrombosis	11%	4%	1.00
Hydrocephalus	0%	22%	.0014
Infarct	40%	14%	.038

^a CSF values are listed as mean \pm SD.

^b P value is adjusted for multiple comparisons (n = 14).

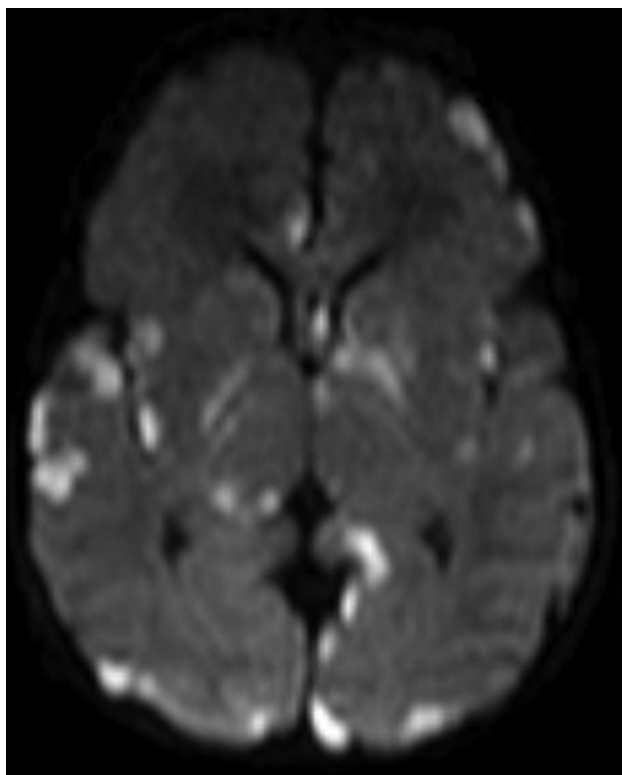


FIG 1. A 12-day-old neonate with GBS meningitis. Axial DWI demonstrates multifocal areas of diffusion restriction (ADC not shown) in the parenchyma, consistent with infarcts and cerebritis.

meningitis (46/57; 81%) and those with *E coli* meningitis (44/50; 88%) ($P = .43$).

There was no statistically significant difference between the mean age at presentation for patients with GBS meningitis (40 days; median interquartile range, 38.3 days) versus the mean age for those with *E coli* meningitis (31 days; median interquartile range, 34.0 days) ($P = .18$). There was no significant difference in the history of prematurity in patients with GBS meningitis (10/57; 18%) compared with those with *E coli* meningitis (15/50; 30%) ($P = .17$).

There was excellent interobserver agreement for all MR imaging findings as follows: leptomeningeal enhancement 0.84 (95%

CI, 0.74–0.95); cerebritis 0.87 (95% CI, 0.74–0.99); ependymal enhancement 0.93 (95% CI, 0.83–1.0); hydrocephalus 0.95 (95% CI, 0.84–1.0); abscess 1.0 (95% CI, 1.0–1.0); effusion 0.83 (95% CI, 0.71–0.94); infarct 0.93 (95% CI, 0.84–1.0); hemorrhage 0.92 (95% CI, 0.84–1.0); extra-axial purulent material 0.92 (95% CI, 0.84–1.0); intraventricular purulent material 0.96 (95% CI, 0.89–1.0); and sinus thrombosis 0.93 (95% CI, 0.79–1.0).

Comparison of CSF and MR imaging findings between groups is found in the Table. There was no statistically significant difference between patients with GBS and *E coli* meningitis in the mean

duration from presentation to the date of the initial CSF laboratory study (0.65 versus 1.57 days; $P = .06$). There was no statistically significant difference in the CSF corrected WBC count and glucose levels or total protein levels between groups.

There was no statistically significant difference between groups for the duration from presentation to the date of MR imaging (10.1 versus 12.8 days, $P = .08$). There was a significant difference between GBS and *E coli* meningitis for acute development of hydrocephalus (0% versus 22%, $P = .001$). Ultimately, 7% (4/57) of patients with GBS meningitis required ventriculoperitoneal shunting compared with 18% (9/50) of patients with *E coli* meningitis ($P = .14$). There was a shorter mean time to development of hydrocephalus among patients with *E coli* meningitis compared with those with GBS meningitis (18 versus 92 days; $P = .006$). There was a significant difference between GBS and *E coli* meningitis for the development of infarct (40% versus 14%; $P = .038$). There was no statistically significant difference between GBS and *E coli* groups for leptomeningeal enhancement, cerebritis, ependymal enhancement, abscess/granuloma, subdural effusion, hemorrhage, extra-axial purulent material, intraventricular purulent material restriction, or sinus thrombosis. Representative examples of patients with GBS and *E coli* meningitis are seen in Figs 1 and 2.

DISCUSSION

The results of this study demonstrate that neonates and infants with GBS meningitis more frequently develop infarcts, while patients with *E coli* meningitis more frequently develop early onset of hydrocephalus. Some patients with GBS meningitis may ultimately develop hydrocephalus requiring shunting, but there was a shorter duration from presentation to the development of hydrocephalus in patients with *E coli* meningitis. While CSF remains necessary to obtain a definitive pathogen, no differences in corrected CSF WBC count and protein or glucose levels were detectable between groups. These findings suggest that neurologic complications of meningitis may differ by causative pathogen.

Cerebral infarcts and hydrocephalus are common complications of bacterial meningitis in neonates and infants, found in 28%–43% and 20%–25%, respectively, which is similar to our results.^{2,5} Despite both of these complications being relatively

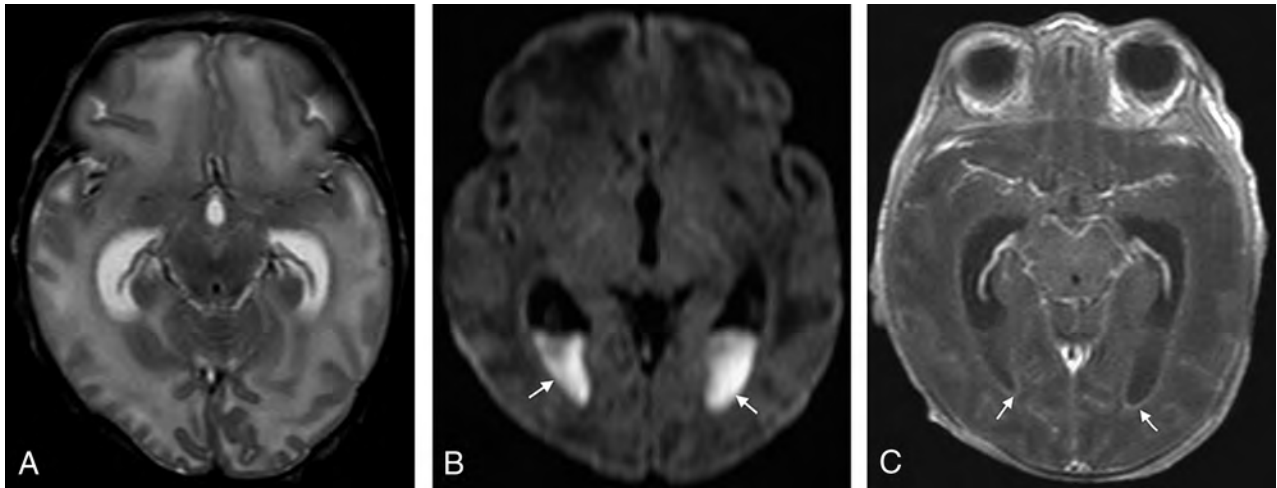


FIG 2. A 19-day-old neonate with *E coli* meningitis. *A*, Axial T2-weighted image demonstrates disproportionate enlargement of the lateral ventricles relative to the sulci, consistent with hydrocephalus. *B*, Axial DWI demonstrates areas of diffusion restriction (ADC not shown) in the ventricles (arrows), consistent with intraventricular purulent material. *C*, Axial T1-weighted postcontrast image demonstrates abnormal ependymal enhancement along the lateral ventricles (arrows).

common, it is interesting that a significant difference in these complications in the acute setting was detected between GBS and *E coli* meningitis. Our results are similar to those of Jaremko et al,⁸ who, in a smaller series of neonates and infants with meningitis, compared all streptococcal pathogens with *E coli* pathogens and found that infarcts were more common with streptococcal pathogens compared with *E coli* meningitis (59% versus 27%), while hydrocephalus was more common with *E coli* compared with streptococcal pathogens (64% versus 22%). These results are different from the results of Chang et al,¹⁰ who demonstrated no difference in GBS compared with *E coli* meningitis for the presence of infarcts. This discrepancy may reflect methodologic differences in Chang et al, including a different definition for the diagnosis of bacterial meningitis, a different patient population (Taiwanese), patient collection during a 16-year period, and the use of CT or MR imaging to detect infarcts. The results of our study were obtained during a shorter timeframe and used the gold standard of MR imaging for the diagnosis of infarcts. A longer timeframe in the study of Chang et al may also introduce unknown factors of patient management affecting patient care.

Neonates with bacterial meningitis who develop infarcts have poor outcomes.^{10,11} Infarcts can occur with other pathogens, particularly *Streptococcus pneumoniae* so that detection of infarcts on MR imaging is not specific for GBS meningitis.¹¹ The pathogenesis of infarcts from bacterial meningitis is likely related to vasculopathy induced by bacterial products and host inflammatory response.¹² Among the bacterial factors, GBS β -hemolysin/cytolysin is directly cytotoxic to the brain endothelium, triggers the endothelium to generate an inflammatory response, and induces macrophage production of inducible nitric oxide synthase and generation of nitric oxide.^{13,14} Nitric oxide plays a major role in regulating cerebral blood flow and autoregulation and plays a role in neurotoxicity in the developing brain.¹⁵ In addition to infarcts being more frequently identified with GBS compared with *E coli*, the frequency of cerebritis in patients with GBS meningitis was 3 times greater than in those with *E coli* meningitis, a finding that could reflect cytotoxicity on a microvascular level.

Conversely, *E coli* is capable of entering the central nervous system through the cerebral vasculature without altering the microvascular endothelium or permeability; this feature may partially explain differences in development of infarcts between GBS and *E coli*.¹⁶

Hydrocephalus may result from purulent exudates in the subarachnoid spaces and/or ependymal surface, resulting in impaired CSF flow or impaired absorption of CSF by the arachnoid villi. Hydrocephalus has been associated with motor disability in neonates with bacterial meningitis.⁷ In addition to early hydrocephalus being more frequently identified with *E coli*, our results indicated a 4-fold increase in the frequency of ependymal enhancement and a greater than 2-fold increase in the frequency of intraventricular purulent material with *E coli* meningitis. These factors may account for the more rapid development of hydrocephalus with *E coli* compared with GBS. Therefore, differences in the inflammatory response may partially explain the differences in hydrocephalus observed in these patients. These results also provide the clinically important information that patients with GBS meningitis may develop hydrocephalus at a much longer time duration from presentation. Finally, because both infarcts and hydrocephalus can result in injury to the brain parenchyma, these findings are important for patient prognosis and indicate the need for imaging to detect these complications.

Limitations of this study include the retrospective nature of the study and the low number of patients. The small sample size may limit our ability to confirm statistically significant differences in the longer term requirement for intracranial shunt. Although there was greater than twice the frequency of patients with *E coli* meningitis than with GBS meningitis who ultimately required an intracranial shunt, this determination may require an even larger sample size. Despite the low number of patients, this remains the largest series comparing CSF and MR imaging findings in infants with GBS and *E coli* meningitis. This study was limited to patients who had MR imaging. At our institution, it has become the standard of care for these patients to undergo MR imaging of the brain, so it is unlikely to result in a selection bias. We acknowledge

that CT and sonography can also be used for detection of complications of meningitis such as hydrocephalus, but they are less sensitive and specific for the other findings used in this study.¹⁷

Another potential limitation of this study is the subjectivity in the determination of individual MR imaging findings. This subjectivity was mitigated by independent imaging reviews by 2 neuroradiologists, consensus diagnosis in discordant findings, and calculation of interobserver agreement. We observed excellent interobserver agreement for all MR imaging findings. Although there are various ventricular measurements that can be performed to assess hydrocephalus, these are uncommonly required in clinical practice. Lastly, this study used a gold standard diagnosis of meningitis to be either a positive CSF culture or positive blood culture with elevated CSF WBC count. Patients with a positive blood culture and normal CSF WBC count were therefore excluded from this study.

CONCLUSIONS

Although infants with GBS and *E coli* meningitis may have similar ages and CSF laboratory values, MR imaging findings may differ between the groups. Patients with GBS meningitis more frequently demonstrate infarcts, while those with *E coli* meningitis more frequently have early onset of hydrocephalus. These findings suggest that neurologic complications of meningitis may reflect the specific causative pathogen.

Disclosures: Nilesh K. Desai—UNRELATED: Expert Testimony: multiple legal firms, Comments: expert review of cases. Jesus G. Vallejo—UNRELATED: Royalties: Wolters Kluwer, Comments: UptoDate chapters.

REFERENCES

1. Ku LC, Boggess KA, Cohen-Wolkowicz M. **Bacterial meningitis in infants.** *Clin Perinatol* 2015;42:29–45, vii–viii CrossRef Medline
2. Ouchenir L, Renaud C, Khan S, et al. **The epidemiology, management, and outcomes of bacterial meningitis in infants.** *Pediatrics* 2017;140 CrossRef Medline
3. de Louvois J, Halket S, Harvey D. **Neonatal meningitis in England and Wales: sequelae at 5 years of age.** *Eur J Pediatr* 2005;164:730–34 CrossRef Medline
4. Chávez-Bueno S, McCracken GH. **Bacterial meningitis in children.** *Pediatr Clin North Am* 2005;52:795–810, vii CrossRef Medline
5. Oliveira CR, Morriss MC, Mistrot JG, et al. **Brain magnetic resonance imaging of infants with bacterial meningitis.** *J Pediatr* 2014; 165:134–39 CrossRef Medline
6. Baker CJ, Byington CL, Polin RA; Committee on Infectious Diseases, Committee on Fetus and Newborn. **Policy statement: recommendations for the prevention of perinatal group B streptococcal (GBS) disease.** *Pediatrics* 2011;128:611–16 CrossRef Medline
7. Lin WL, Chi H, Huang FY, et al. **Analysis of clinical outcomes in pediatric bacterial meningitis focusing on patients without cerebrospinal fluid pleocytosis.** *J Microbiol Immunol Infect* 2016;49: 723–28 CrossRef Medline
8. Jaremko JL, Moon AS, Kumbala S. **Patterns of complications of neonatal and infant meningitis on MRI by organism: a 10-year review.** *Eur J Radiol* 2011;80:821–27 CrossRef Medline
9. Kestenbaum LA, Ebberson J, Zorc JJ, et al. **Defining cerebrospinal fluid white blood cell count reference values in neonates and young infants.** *Pediatrics* 2010;125:257–64 CrossRef Medline
10. Chang CJ, Chang WN, Huang LT, et al. **Cerebral infarction in perinatal and childhood bacterial meningitis.** *QJM* 2003;96:755–62 CrossRef Medline
11. Katchanov J, Heuschmann PU, Endres M, et al. **Cerebral infarction in bacterial meningitis: predictive factors and outcome.** *J Neurol* 2010;257:716–20 CrossRef Medline
12. Iijma S, Shirai M, Ohzeki T. **Severe, widespread vasculopathy in late-onset group B streptococcal meningitis.** *Pediatr Int* 2007;49: 1000–03 CrossRef Medline
13. Doran KS, Liu GY, Nizet V. **Group B streptococcal beta-hemolysin/cytolysin activates neutrophil signaling pathways in brain endothelium and contributes to development of meningitis.** *J Clin Invest* 2003;112:736–44 CrossRef Medline
14. Doran KS, Nizet V. **Molecular pathogenesis of neonatal group B streptococcal infection: no longer in its infancy.** *Mol Microbiol* 2004; 54:23–31 CrossRef Medline
15. Garry PS, Ezra M, Rowland MJ, et al. **The role of the nitric oxide pathway in brain injury and its treatment: from bench to bedside.** *Exp Neurol* 2015;263:235–43 CrossRef Medline
16. Kim KS. **Current concepts on the pathogenesis of Escherichia coli meningitis: implications for therapy and prevention.** *Curr Opin Infect Dis* 2012;25:273–78 CrossRef Medline
17. Littwin B, Pomiećko A, Stępień-Roman M, et al. **Bacterial meningitis in neonates and infants: the sonographic picture.** *J Ultrason* 2018; 18:63–70 CrossRef Medline

Human Parechovirus Meningoencephalitis: Neuroimaging in the Era of Polymerase Chain Reaction–Based Testing

A. Sarma, E. Hanzlik, R. Krishnasarma, L. Pagano, and S. Pruthi



ABSTRACT

SUMMARY: Human parechovirus infection is an increasingly recognized cause of neonatal meningoencephalitis. We describe characteristic clinical features and brain MR imaging abnormalities of human parechovirus meningoencephalitis in 6 infants. When corroborated by increasingly available polymerase chain reaction–based testing of the CSF, the distinctive MR imaging appearance may yield a specific diagnosis that obviates costly and time-consuming further clinical evaluation. In our study, infants with human parechovirus presented in the first 35 days of life with seizures, irritability, and sepsis. MR imaging consistently demonstrated low diffusivity within the thalami, corpus callosum, and subcortical white matter with a frontoparietal predominance. T1 and T2 shortening connoting white matter injury along the deep medullary veins suggests venous ischemia as an alternative potential pathogenetic mechanism to direct neuroaxonal injury.

ABBREVIATIONS: HPeV = human parechovirus; PCR = polymerase chain reaction

Historically, many cases of neonatal meningoencephalitis have had no specific identifiable cause.^{1–10} Human parechovirus (HPeV) is an increasingly recognized cause of neonatal meningoencephalitis in the era of rapid polymerase chain reaction (PCR)-based assays for CSF.⁷ HPeV is a single-stranded ribonucleic acid virus from the family *Picornaviridae*. Among 19 identified genotypes, HPeV-3 is most commonly identified in severe infection of young infants and CNS infection.^{10,11} Infection occurs via a respiratory or gastrointestinal route with hematogenous dissemination.¹⁰ Cases usually occur with seasonal outbreaks in summer and autumn with biannual cycles.¹⁰ Common reported clinical manifestations in minor infection include gastroenteritis and respiratory symptoms. Similar to enterovirus, typical clinical presentation in young infants with severe CNS infection includes fever, rash, irritability, and features of sepsis with rare CSF pleocytosis. Children younger than 2 years of age are at greatest

risk, and illness is especially severe in children younger than 6 months.¹⁰

Because of its noninflammatory CSF profile, HPeV meningoencephalitis has likely been under-recognized. Indeed, since the recent advent of PCR-based assays, HPeV has been identified as the second most common causative pathogen after enterovirus in infants younger than 2 months of age.¹⁰ Multiple case reports and small case series suggest a distinctive clinical and imaging presentation.^{12–15} However, few descriptions exist within the radiology literature.¹² This report provides detailed clinical and radiologic description of 6 infants with HPeV meningoencephalitis with a current literature review.

Case Series

No institutional review board approval was required for this retrospective series. Six cases were identified between October 2016 and September 2018 at Monroe Carell Jr. Children's Hospital at Vanderbilt and Boston Children's Hospital.

Electronic medical record review yielded birth history and gestational age, age at presentation, presenting symptoms, length of hospital and intensive care unit stay, CSF analysis (cell count, glucose, protein, viral PCR analysis, FilmArray meningoencephalitis panel, BioFire Diagnostics, Salt Lake City, Utah; and qualitative PCR assay for HPeV, ARUP Laboratories, Salt Lake City, Utah), electroencephalography reports and descriptions of seizures, and the status of the patient at discharge and follow-up.

All patients underwent brain MR imaging. Two of 6 underwent sonography, and 2 underwent CT before MR imaging. The MR imaging technique varied by institution. All patients at Mon-

Received March 29, 2019; accepted after revision June 2.

From the University Medical Center (A.S., E.H., L.P., S.P.), Vanderbilt University, Nashville, Tennessee; and Boston Children's Hospital (R.K.), Harvard Medical School, Boston, Massachusetts.

Data previously presented in a different format for oral presentation at: Society for Pediatric Radiology Annual Meeting and Categorical Course, April 30 to May 4, 2019; San Francisco, California.

Please address correspondence to Sumit Pruthi, MD, Vanderbilt University Medical Center, Vanderbilt University, Department of Radiology & Radiological Sciences, Monroe Carell Jr. Children's Hospital, 2200 Children's Way, Nashville, TN 37232; e-mail: sumit.pruthi@vumc.org; @sumsnet

Indicates article with supplemental on-line table.

<http://dx.doi.org/10.3174/ajnr.A6118>

roe Carell Jr. Children's Hospital at Vanderbilt were scanned on a 1.5T MR imaging unit (Phillips Achieva 3T, Phillips Healthcare, Best, the Netherlands), and all patients at Boston Children's Hospital were scanned on a 3T MR imaging unit (Siemens Skyra 3T, Siemens, Erlangen, Germany). Sequences included 3D T1-weighted MPRAGE, T2-weighted DWI, gradient recalled-echo (3/6), SWI (3/6), postgadolinium T1-weighted (1/6), time-of-flight MRA (1/6), time-of-flight MRV (2/6), and multivoxel MR spectroscopy (3/6). Three-month follow-up MR imaging was performed in 1/6. All MR imaging studies were retrospectively reviewed by 2 fellowship-trained pediatric neuroradiologists.

Clinical data are summarized in the On-line Table. Six patients presented from 6 to 35 days of life with irritability ($n = 4$), poor feeding ($n = 5/6$), and fever ($n = 6/6$). Multifocal seizures were

present in 5/6. Four full-term neonates presented in the first 10 days of life, and 2 premature neonates (33 and 35 weeks' gestational age) presented on days of life 20 and 35. CSF showed no pleocytosis and was culture negative for bacterial pathogens and HSV with PCR-based testing positive for HPeV in 5/6. In 1 case, HPeV was detected in serum and stool samples.

Head sonography in 2/6 and head CT in 1/6 had normal findings. Head CT in 1/6 showed parieto-occipital hypoattenuation and loss of gray-white differentiation.

The most characteristic finding in all cases was diffuse/multifocal frontal-predominant subcortical white matter and callosal involvement with associated low diffusivity (Fig 1). The thalami were involved in all cases to varying degrees. The 2/6 with striking occipital involvement were also the only cases with cortical signal abnormality (also in the occipital lobe). No cases exhibited signal abnormality within the basal ganglia, hippocampi, brain stem, and cerebellum. Branching T1 and T2 shortening along the distribution of the deep medullary veins was noted in 4/6 (Fig 2). In 2/6, these foci were identified on either T1- or T2-weighted imaging but not both. One patient (patient 4, Fig 2) had mild diffuse white matter T2 prolongation, even considering the premature myelination pattern. Scant susceptibility foci consistent with hemorrhage or mineralization were noted in the peritrial white matter in 1/6. Of the 3/6 who underwent MR spectroscopy, only one had elevated lactate in the basal ganglia. Postcontrast, MRA, and MRV results were normal.

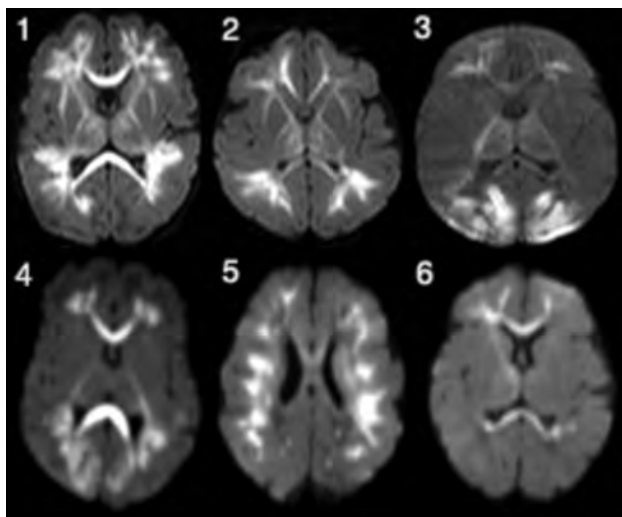


FIG 1. Axial diffusion-weighted images in patients 1–6 (infants with HPeV infection) demonstrate low diffusivity variably involving the periventricular white matter with frontoparietal predominance and also involving the corpus callosum, thalami, and internal and external capsules. Patients 3 and 4 exhibit greater involvement of the occipital white matter and the occipital cortex. Patient 5 shows more confluent involvement of the subcortical white matter.

DISCUSSION

This series describes 6 infants with HPeV meningoencephalitis and characteristic MR imaging findings that rapidly yielded a diagnosis in conjunction with PCR testing of the CSF.

Distinctive supratentorial white matter and callosal diffusion abnormality on MR imaging is shared between ours and other published series.^{3,12,13,15–17} Thalamic involvement and sparing of the posterior fossa structures have been reported variably but were universally present in our cases.^{12,18} T1- and T2-shortening foci branching along the distribution of the deep medullary veins

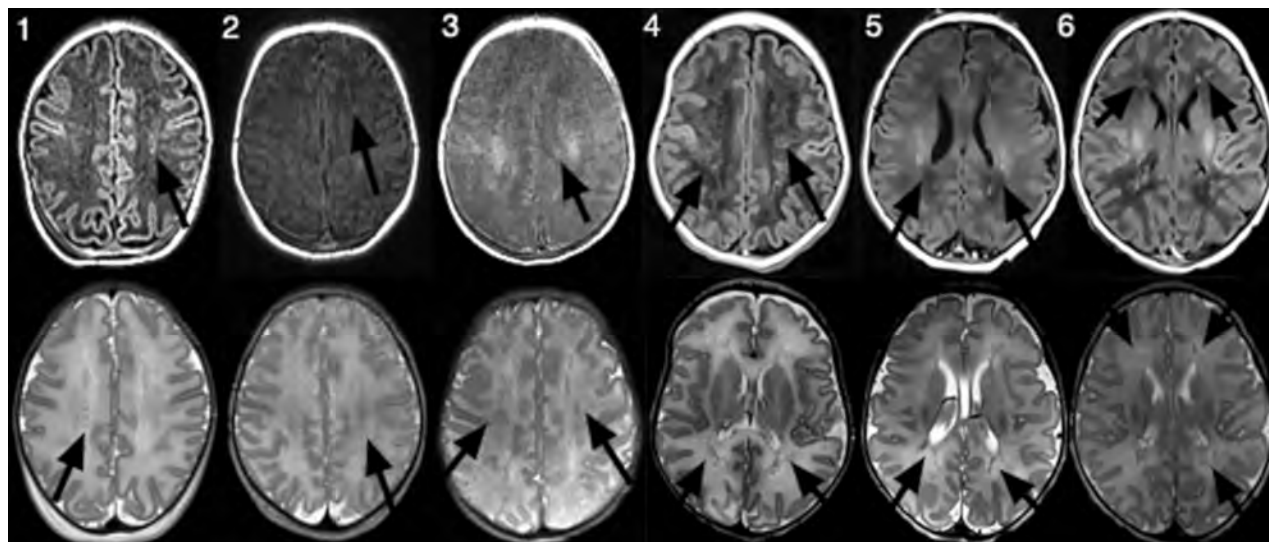


FIG 2. Axial 3D T1-weighted MPRAGE images (*upper row*) and axial T2-weighted images (*lower row*) in patients 1–6 (infants with HPeV infection) demonstrate foci of T1 and/or T2 shortening following the distribution of the deep medullary veins (*arrows*).

is consistent with examples presented by Belcastro et al¹³ and Verboon-Macielek et al⁹ but has not been consistent across studies. Occipital white matter and cortical involvement in 2/6 cases is also dissimilar to previous descriptions and may be explained by hypoglycemia in one and transient hypoglycemia or, alternatively, a seizure-related or vascular phenomenon such as posterior reversible encephalopathy syndrome in the other.

The pathophysiology of CNS injury in HPeV infection is not well-understood. The pattern of MR imaging signal abnormality preferentially affecting the supratentorial white matter tracts in our cases could suggest neuroaxonal tropism; however, signal abnormality along the course of the deep medullary veins on T1- and T2-weighted imaging in 5/6 cases suggests perivenular invasion or venous ischemia as a potential alternative etiology. Supporting the first hypothesis, a study of patients with clinical CNS infection and stool samples positive for HPeV-3 showed faster replication in a cultured neural cell line.¹⁹ Verboon-Macielek et al⁹ and Volpe²⁰ reported that the HPeV RNA activates toll-like receptors in microglia, resulting in the release of inflammatory substances that injure preoligodendrocytes and axons as part of an innate immune response, as well as toll-like receptors in neurons and growing axons, resulting in direct injury. Alternatively, supporting the venous ischemia hypothesis, a postmortem examination study of 2 premature neonates (33 and 34 weeks gestational age) with fatal HPeV infection by Bissel et al¹¹ demonstrated severe inflammatory changes of the periventricular white matter with macrophage infiltration and astrogliosis. While HPeV-3 RNA probes hybridized with abundant viral particles within brain meningeal cells and blood vessel walls, they did not reveal the presence of HPeV within parenchymal cells. The authors therefore hypothesized that parenchymal injury is a consequence of vascular compromise rather than direct infection. Low diffusivity of the corpus callosum may result from seizure activity and/or Wallerian degeneration, given the relative resistance of the corpus callosum to ischemic insults. Low diffusivity in the thalamus may be due to some combination of venous ischemia and seizure activity.

While the clinical and imaging characteristics of HPeV meningoencephalitis are characteristic in a neonate with sepsis and seizures, there is a differential diagnosis. Distinction from enterovirus, rotavirus, and chikungunya infection may not be possible.^{21,22} In contradistinction to neonates with hypoxic-ischemic injury, neonates with HPeV infection lack a history of a sentinel event. Frontoparietal white matter–predominant low diffusivity and sparing of the basal ganglia favor HPeV encephalitis over hypoxic-ischemic injury.¹² Isolated sulfite oxidase deficiency and molybdenum cofactor deficiency can present in the neonatal period; however, the basal ganglia are usually affected.

Reported long-term outcomes are variable, with limited available data, but overall suggest adverse developmental outcomes in patients with encephalitis and abnormal MR imaging findings. In a study comparing longitudinal gross motor development between infants with HPeV infection and those with no pathogen found, a statistically significant difference was noted at 6 months, but not at 24 months.²³ In a study in which 6 patients with clinically diagnosed HPeV encephalitis underwent MR imaging during both acute illness and follow-up developmental assessment at

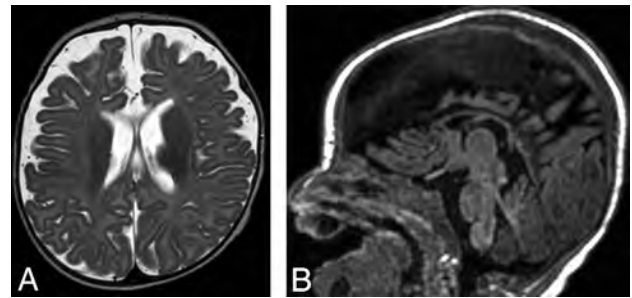


FIG 3. Axial T2-weighted image (A) and sagittal T1-weighted image (B) obtained in patient 1 approximately 3 months after acute HPeV infection show new diffuse enlargement of the extra-axial spaces and thinning of the corpus callosum, suggesting volume loss.

12 months, Britton et al¹⁵ reported concern for abnormal development in all 6. Verboon-Macielek et al⁹ found that in the 50% (5/10) of patients in their cohort who had a developmental disability, the severity of imaging abnormalities correlated with neurodevelopmental outcome. Two patients in our cohort have been noted to be clinically well at 6- to 8-week follow-up; however, long-term follow-up data are not yet available.

A few reports have described long-term imaging follow-up, with mixed results. Pariani et al²⁴ and Amarnath et al¹² had resolution of imaging abnormalities at 2-month and 1-year follow-up, respectively. In 3 patients, Verboon-Macielek et al⁹ reported variable degrees of visible white matter injury at 3-month-to-7-year follow-up, with abnormalities ranging from mild periventricular gliosis to extensive white matter volume loss and cystic leukomalacia. Brownell et al¹⁶ described a patient with severe white matter injury at day 3, with only mild white matter signal abnormality and callosal thinning at 1 year. On the contrary, Belcastro et al¹³ described the development of extensive cystic leukomalacia at 4-month follow-up in 1 patient. Some data suggest that preterm infants are at higher risk for severe cystic leukoencephalomalacia.⁹⁻¹¹ One patient in our study had a 3-month follow-up MR imaging showing diffuse parenchymal volume loss (Fig 3). Further study will help to correlate the severity of clinical and imaging findings with long-term outcomes.

Current study limitations include the retrospective design and small number of cases. Viral genotyping was not performed, and this study did not determine imaging characteristics that distinguish among viral genotypes. Furthermore, imaging techniques varied. Referral to imaging may not be performed in less severe cases, biasing MR imaging requests toward patients with severe clinical presentation. An additional limitation is limited clinical and imaging follow-up, which warrants further study. Finally, findings in patients with less severe disease are currently not well-established and could also be determined by future study.

The stereotypical MR imaging appearance correlated with molecular testing in our patients yielded a specific diagnosis of HPeV meningoencephalitis, resulting in a less extensive metabolic and genetic work-up than would have been undertaken otherwise. Knowledge of the distinctive imaging findings in young infants with HPeV meningoencephalitis thus has potential for substantial cost- and time-savings.

CONCLUSIONS

HPeV infection is an increasingly recognized cause of neonatal sepsis or meningoencephalitis, often presenting with seizures, and MR imaging is an essential component of the clinical evaluation of seizures in neonates. DWI is of paramount importance in making the diagnosis and shows distinctive low diffusivity of the supratentorial white matter with frontoparietal predominance, with involvement of the corpus callosum and thalami and sparing of the basal ganglia, brain stem, and cerebellum.

Disclosures: Asha Sarma—UNRELATED: Royalties: Cambridge University Press, Comments: textbook previously published on a different topic.

REFERENCES

1. Leber AL, Everhart K, Balada-Llasat JM, et al. **Multicenter evaluation of BioFire FilmArray Meningitis/Encephalitis Panel for detection of bacteria, viruses, and yeast in cerebrospinal fluid specimens.** *J Clin Microbiol* 2016;54:2251–61 CrossRef Medline
2. Midgley CM, Jackson MA, Selvarangan R, et al. **Severe parechovirus 3 infections in young infants: Kansas and Missouri, 2014.** *J Pediatric Infect Dis Soc* 2018;7:104–12 CrossRef Medline
3. Khatami A, McMullan BJ, Webber M, et al. **Sepsis-like disease in infants due to human parechovirus type 3 during an outbreak in Australia.** *Clin Infect Dis* 2015;60:228–36 CrossRef Medline
4. Ferreras Antolín L, Kadambari S, Braccio S, et al. **Increased detection of human parechovirus infection in infants in England during 2016: epidemiology and clinical characteristics.** *Arch Dis Child* 2018;103:1061–66 CrossRef Medline
5. Vergnano S, Kadambari S, Whalley K, et al. **Characteristics and outcomes of human parechovirus infection in infants (2008–2012).** *Eur J Pediatr* 2015;174:919–24 CrossRef Medline
6. Sharp J, Harrison CJ, Puckett K, et al. **Characteristics of young infants in whom human parechovirus, enterovirus or neither were detected in cerebrospinal fluid during sepsis evaluations.** *Pediatr Infect Dis J* 2013;32:213–16 CrossRef Medline
7. Aizawa Y, Izumita R, Saitoh A. **Human parechovirus type 3 infection: an emerging infection in neonates and young infants.** *J Infect Chemother* 2017;23:419–26 CrossRef Medline
8. Joseph L, May M, Thomas M, et al. **Human parechovirus 3 in infants: expanding our knowledge of adverse outcomes.** *Pediatr Infect Dis J* 2019;38:1–5 CrossRef Medline
9. Verboon-Maciolek MA, Groenendaal F, Hahn CD, et al. **Human parechovirus causes encephalitis with white matter injury in neonates.** *Ann Neurol* 2008;64:266–73 CrossRef Medline
10. Olijve L, Jennings L, Walls T. **Human parechovirus: an increasingly recognized cause of sepsis-like illness in young infants.** *Clin Microbiol Rev* 2018;31 CrossRef Medline
11. Bissel SJ, Auer RN, Chiang CH, et al. **Human parechovirus 3 meningitis and fatal leukoencephalopathy.** *J Neuropathol Exp Neurol* 2015; 74:767–77 CrossRef Medline
12. Amarnath C, Helen Mary T, Periakarupan A, et al. **Neonatal parechovirus leucoencephalitis: radiological pattern mimicking hypoxic-ischemic encephalopathy.** *Eur J Radiol* 2016;85:428–34 CrossRef Medline
13. Belcastro V, Bini P, Barachetti R, et al. **Teaching neuro images: neonatal parechovirus encephalitis: typical MRI findings.** *Neurology* 2014;82:e23 CrossRef Medline
14. de Jong EP, Holscher HC, Steggerda SJ, et al. **Cerebral imaging and neurodevelopmental outcome after entero- and human parechovirus sepsis in young infants.** *Eur J Pediatr* 2017;176:1595–602 CrossRef Medline
15. Britton PN, Dale RC, Nissen MD, et al; PAEDS-ACE Investigators. **Parechovirus encephalitis and neurodevelopmental outcomes.** *Pediatrics* 2016;137:e20152848 CrossRef Medline
16. Brownell AD, Reynolds TQ, Livingston B, et al. **Human parechovirus-3 encephalitis in two neonates: acute and follow-up magnetic resonance imaging and evaluation of central nervous system markers of inflammation.** *Pediatr Neurol* 2015;52:245–49 CrossRef Medline
17. Leow JY, Gupta R, Sohal AP. **Human parechovirus central nervous system infection: a rare cause of neonatal encephalitis.** *J Paediatr Child Health* 2015;51:1244 CrossRef Medline
18. Van Zwol AL, Lequin M, Aarts-Tesselaar C, et al. **Fatal neonatal parechovirus encephalitis.** *BMJ Case Rep* 2009;2009 CrossRef Medline
19. Westerhuis BM, Koen G, Wildenbeest JG, et al. **Specific cell tropism and neutralization of human parechovirus types 1 and 3: implications for pathogenesis and therapy development.** *J Gen Virol* 2012; 93(Pt 11):2363–70 CrossRef Medline
20. Volpe JJ. **Neonatal encephalitis and white matter injury: more than just inflammation?** *Ann Neurol* 2008;64:232–36 CrossRef Medline
21. Verboon-Maciolek MA, Truttmann AC, Groenendaal F, et al. **Development of cystic periventricular leukomalacia in newborn infants after rotavirus infection.** *J Pediatr* 2012;160:165–68.e1 CrossRef Medline
22. Ganesan K, Diwan A, Shankar SK, et al. **Chikungunya encephalomyelorradiculitis: report of 2 cases with neuroimaging and 1 case with autopsy findings.** *AJNR Am J Neuroradiol* 2008;29:1636–37 CrossRef Medline
23. van Hinsbergh TM, Elbers RG, van Furth MA, et al. **Longitudinal association between human parechovirus central nervous system infection and gross-motor neurodevelopment in young children.** *Pediatr Infect Dis J* 2019;38:110–14 CrossRef Medline
24. Pariani E, Pellegrinelli L, Pugni L, et al. **Two cases of neonatal human parechovirus 3 encephalitis.** *Pediatr Infect Dis J* 2014;33:1191–93 CrossRef Medline

The Complex Spine in Children with Spinal Muscular Atrophy: The Transforaminal Approach—A Transformative Technique

 R. Towbin,  C. Schaefer,  R. Kaye,  T. Abruzzo, and  D.J. Aria

ABSTRACT

BACKGROUND AND PURPOSE: Spinal muscular atrophy, a genetic disease resulting in loss of motor function, presents from in utero to adulthood. Depending on progression and secondary scoliosis, spinal stabilization may be necessary. When planning intrathecal access in these patients, spinal anatomy is the most important factor. Therefore, when planning intrathecal nusinersen injections, we subdivided patients with spinal muscular atrophy into simple-versus-complex spine subgroups. Our purpose was to present our experience with our first 42 transforaminal intrathecal nusinersen injections.

MATERIALS AND METHODS: We reviewed 31 consecutive patients with spinal muscular atrophy types 1–3 who presented for intrathecal nusinersen injections from March 2017 to September 2018. Nine children had complex spines (ie, spinal instrumentation and/or fusion) and required preprocedural imaging for route planning for subarachnoid space access via transforaminal or cervical approaches.

RESULTS: A total of 164 intrathecal nusinersen injections were performed in 31 children 4–226 months of age, with 100% technical success in accessing the subarachnoid space. Nine patients with complex spinal anatomy underwent 45 intrathecal nusinersen injections; 42 of 45 procedures were performed via a transforaminal approach with the remaining 3 via cervical techniques. There were no complications.

CONCLUSIONS: Our initial experience has resulted in a protocol-driven approach based on simple or complex spinal anatomy. Patients with simple spines do not need preprocedural imaging or imaging-guided intrathecal nusinersen injections. In contrast, the complex spine subgroup requires preprocedural imaging for route planning and imaging guidance for therapy, with the primary approach being the transforaminal approach for intrathecal nusinersen injections.

ABBREVIATIONS: ITNI = intrathecal nusinersen injection; SMA = spinal muscular atrophy; TF = transforaminal

Spinal muscular atrophy (SMA) is the result of a deletion at exon 7 on the short arm of chromosome 5 and may present from in utero (type 0) to adulthood (type 4). Across time, there is a loss of motor neurons in the anterior horn of the spinal cord, resulting in weakness and muscular imbalance. These patients often develop progressive scoliosis. The spinal deformity may further stress individuals with respiratory challenges due to their underlying muscular weakness. Depending on the rapidity of the progression of the spinal curvature and its severity, spinal stabilization with rods and spinal fusion may be necessary. Nusinersen is currently the only FDA-approved drug for the treatment of SMA and is administered intrathecally. The dosing protocol for

nusinersen administration is divided into induction and maintenance phases. The induction phase consists of 3 doses administered 14 days apart followed by a fourth dose given 30 days later. The maintenance phase lasts indefinitely, with dose administration at 4-month intervals. Children with types 1 and 2 SMA may not require spine instrumentation until they are about 6 years of age.¹ However, older individuals often require rods and/or spinal fusion.

When planning the route to the intrathecal space in patients with SMA, it seems that the status of the spine is the most important factor. Therefore, instead of using the SMA typing system (types 0–4) to plan the procedure, we subdivide patients into simple and complex spine subgroups to plan their therapeutic approach. Clinical history, physical examination findings, and radiographs, if available, are reviewed. For procedural planning, spines of individuals, regardless of age or SMA type, who do not have rods or spinal fusion have been termed “simple spines.” Spines of those with instrumentation (ie, spinal rods) and/or fusion are deemed “complex spines.”²

Received February 20, 2019; accepted after revision June 17.

From the Department of Radiology (R.T., C.S., R.K., T.A., D.J.A.), Phoenix Children's Hospital, Phoenix, Arizona; and University of Arizona College of Medicine, Phoenix (R.T., C.S., R.K., D.J.A.), Phoenix, Arizona.

Please address correspondence to David J. Aria, MD, MBA, Phoenix Children's Hospital, 1919 E Thomas Rd, Department of Radiology, Phoenix, AZ 85016; e-mail: daria@phoenixchildrens.com

<http://dx.doi.org/10.3174/ajnr.A6131>

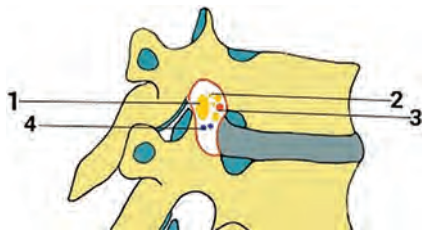


FIG 1. A view illustrating some of the components of the thoracic intervertebral foramina including the following: 1) segmental spinal nerve/dorsal root ganglion, 2) sinuvertebral nerves and rami communicantes, 3) spinal branch of segmental arteries, and 4) intervertebral veins.³

The purpose of this article was to present our experience with our 42 transforaminal (TF) intrathecal nusinersen injections (ITNIs). To our knowledge, this is the largest reported series of TF nusinersen therapy for SMA.

MATERIALS AND METHODS

Our entire patient population from the initiation of intrathecal therapy with nusinersen was examined. We reviewed all patients with SMA who were referred for ITNIs between March 2017 and September 2018 at Phoenix Children's Hospital. Thirty-one children with SMA were treated. Of these, 9 children had complex spines and were the focus of this presentation. Patients with complex spines required preprocedural spinal radiographs and lumbar spine CT and imaging-guided ITNIs. 3D reformatting was performed as needed. All ITNIs were performed in an interventional radiology suite equipped with an AlluraClarity FD Biplane Angiography System (Philips Healthcare, Best, the Netherlands), regardless of whether fluoroscopic or conebeam CT guidance (Allura Xper FD system; Philips Healthcare) was used. Four pediatric interventionalists, with experience ranging from 4 to 38 years (4, 10, 26, and 38 years, respectively) performed all procedures. Fluoroscopy times were recorded when fluoroscopic guidance was used.

All procedures were performed using a sterile technique with needle selection dependent on patient body habitus and operator preference. The needles of choice were 22-ga, ranging from 3.5 to 7 inches and, in almost all instances, were the Quincke type. On occasion, Whitacre needles (Becton, Dickinson, and Company) were used, particularly if there was a history of a spinal headache. In obese patients, a coaxial technique may be used to minimize needle tracking. Coaxial needle insertion consisted of an 18-ga 10-cm Chiba Biopsy needle (Cook Medical, Bloomington, Indiana) as a guide with an inner 22-ga 7-inch lumbar puncture needle. Needle tip position was confirmed by the acquisition of CSF. All children who received ITNIs were followed clinically by their referring neurologist and physical medicine and rehabilitation teams. All untoward effects were identified and reviewed.

Transforaminal Puncture Technique

Before considering the TF approach, one must understand the anatomy of the neural foramina. The neurovascular bundle is located within the upper half of the neural foramina. Therefore, the lower half of the neural foramina is targeted, with the posterior-inferior quadrant the ideal location (Fig 1).³ The lumbar entry level and sidedness are selected after reviewing

the lumbar spine CT. When needed, a 3D reconstruction is used to better understand the pathologic anatomy and anticipated needle course.

In all cases, the procedure was performed with the patient under general anesthesia. The child is placed in the decubitus position with the convex side of the scoliotic curvature at the planned lumbar entry level directed toward the ceiling. This positioning allows the ostial plane of the neural foramina to be perpendicular to the radiation beam, optimizing visualization of the neural foramina. In children with complex spines, it is commonly not feasible to position the entire spine in an ideal position visualizing multiple neural foramina levels. Therefore, we focus on positioning only the previously determined target level in the projection maximizing the visibility of the target neural foramina. Also, many of these children have severe osteopenia, making it challenging to distinguish the vertebral body from superimposed bowel gas. The needle tip is positioned over the posterior-inferior quadrant of the neural foramina. When the operator is looking down the hub of the puncture needle, he or she can be confident that the needle angle is appropriate. A 5- or 7-inch needle is used due to the longer distance to the intrathecal space from a paraspinous approach. In our early experience, conebeam CT and XperCT navigation (Philips Healthcare) and guidance (Allura Xper FD System) were used to assist needle placement (Fig 2).⁴ As we became more comfortable and experienced with the TF approach, we substituted fluoroscopic guidance as our first option (Fig 3).

Cervical Puncture Technique

When a cervical approach is considered, additional preprocedural imaging is performed. In this subgroup, limited cervical MR imaging is obtained for assessing the CSF space posterior to the spinal cord. Depending on operator preference, the patient may be positioned in the prone, supine, or decubitus position. It is our preference to use the decubitus position because it maximizes access to the craniocervical junction region, especially in smaller children. The preferred skin-entry site is at C1–2 with the needle positioned about midway between the flare point⁵ anteriorly that approximates the posterior border or the spinal cord and the spinal lamina line posteriorly that approximates the margin of the subarachnoid space (Fig 4). A 3.5-inch needle is used, and under continuous biplane fluoroscopic guidance, the needle tip is positioned in the midline, confirmed on the frontal projection. If C1–2 access cannot be achieved, alternative approaches include the C1 cisterna magna and suboccipital approaches. Successful needle position is confirmed by acquisition of CSF or contrast injection.

All technical details, including fluoroscopy time, anesthetic type, procedural details, and untoward events, were documented.

RESULTS

A total of 164 ITNIs were performed in 31 children with simple and complex spines, 4–226 months of age, with a mean age of 97.9 months at the time of initial therapy. Of these, 9 children had complex spines and underwent a total of 45 ITNIs. There was 100% technical success in accessing the subarachnoid space in a single session.

Each child had 4–6 procedures with a mean of 5.0 injections. Of these 9 patients, there were 5 girls and 4 boys who ranged in age from 119 to 216 months, with a mean age of 173.8 months. The subgroup

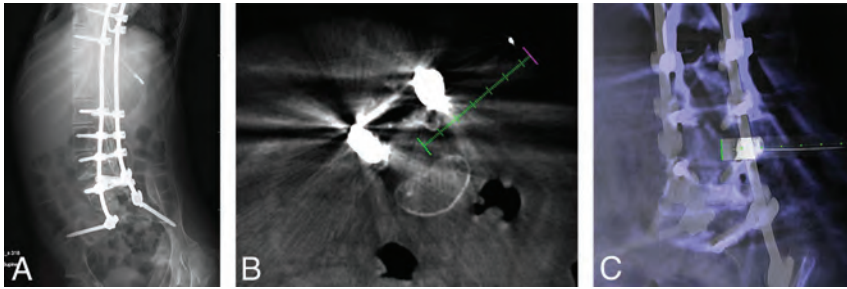


FIG 2. A, A 14-year-old girl with SMA type 2 and an abdominal radiograph demonstrating thoracolumbar spinal rods extending to the sacrum with posterior spinal osseous fusion. B, Conebeam CT using XperCT guidance software (Philips Healthcare) (green dashed line) to access the thecal sac via a right L3–L4 transforaminal approach. C, XperCT fluoroscopic overlay “progress” view used to determine needle tip position depth in the thecal sac.

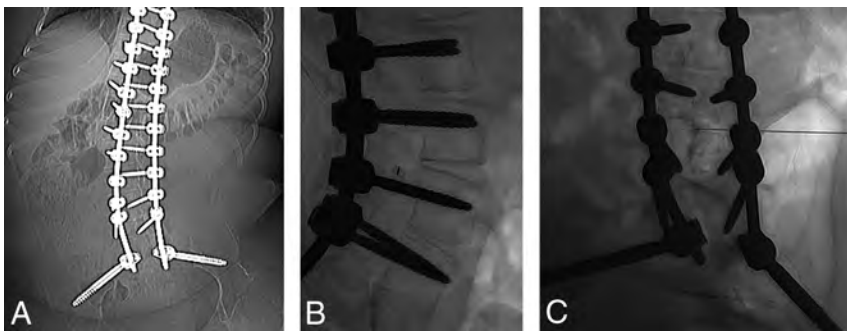


FIG 3. A, A 15-year-old boy with SMA type 3. Frontal abdominal radiograph demonstrates diffuse spinal fusion extending to the sacrum. B, With the patient in the left lateral decubitus position, a true-lateral radiograph at the L3–L4 level demonstrates the spinal needle positioned over the posteroinferior aspect of the right neural foramina. C, With the orthogonal view, the spinal needle tip is centered in the thecal sac.

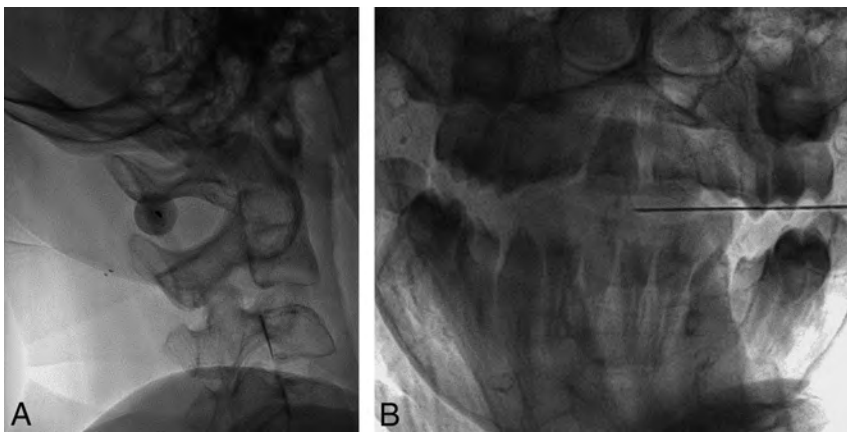


FIG 4. A, A 14-year-old boy with SMA type 3 and diffuse osseous spinal fusion. With the patient in lateral decubitus position, lateral fluoroscopic image demonstrates the spinal needle superimposed over the C1–C2 interspace. B, The orthogonal view is used for monitoring progress of the needle tip position to midline.

was composed of 6 children with type 2 SMAs who had an age range of 119–201 months and a mean age of 175.2 months, and 3 children with type 3 SMA with an age range of 168–226 months and a mean of 193.1 months. All 9 patients had both spinal rods and long-segment spinal fusion.

All 45 procedures were performed with the patient under general anesthesia, though the anesthesiologist’s method of ventilation varied. Of the 45 ITNIs, a laryngeal mask airway was used in 40 cases; endotracheal intubation, in 2; and mask ventilation, in 3.

Almost all children had their ITNIs performed in the decubitus position. Fourteen procedures were performed with the patient in the right lateral decubitus position; 28, in left lateral decubitus; and 3, with the patient prone for navigation and XperCT guidance. Cervical spine puncture was used in 3 procedures, all performed with the patient in the left decubitus position. The skin-entry site levels varied minimally with 1 at the C1 cisterna magna, 2 at C1–2, one at L2–3, thirty-seven at L3–4, and 4 at L4–5. As experience was gained with the TF approach, the cervical approach was abandoned. In our practice, the first option is the TF approach with cervical approaches considered if the TF approach fails.

Forty-one of the 45 procedures used a 5- or 7-inch needle. The remaining 4 injections used a 3.5-inch needle, of which 3 were for cervical approaches. For fluoroscopically guided TF access, fluoroscopy times ranged from 48 seconds to 4 minutes 54 seconds with a mean of 2.0 minutes. Conebeam CT–guided TF injections averaged 4 minutes 6 seconds, with the C1–2 puncture taking 4 minutes 54 seconds and the C1 cisterna magna puncture taking 14 minutes 30 seconds, for a mean of 8 minutes 6 seconds for both cervical routes. Room times varied, with a range of 27–89 minutes, with a mean time of 50 minutes 18 seconds. There were no immediate or reported short-term complications.

DISCUSSION

In reviewing our data, we strongly believe that our 100% technical success rate in obtaining intrathecal access was aided by preprocedural imaging. Because all children with complex spinal anatomy underwent lumbar CT for route planning of ITNIs, we were able to identify patent access routes to the intrathecal space before procedural scheduling. In our experience, the diagnostic

technique of choice is lumbar CT, with 3D reconstructions as needed, because it allows assessment of TF (and even interspinous) approaches at all lumbar levels. Once the intrathecal access route is identified, patient positioning needs can be relayed to the anesthesiologist involved in the procedure, thereby reducing the need for repositioning and extended room and general anesthesia times. Also, if needed, the lumbar CT data can be transferred to the CT navigation system in the interventional radiology suite for imaging guidance.

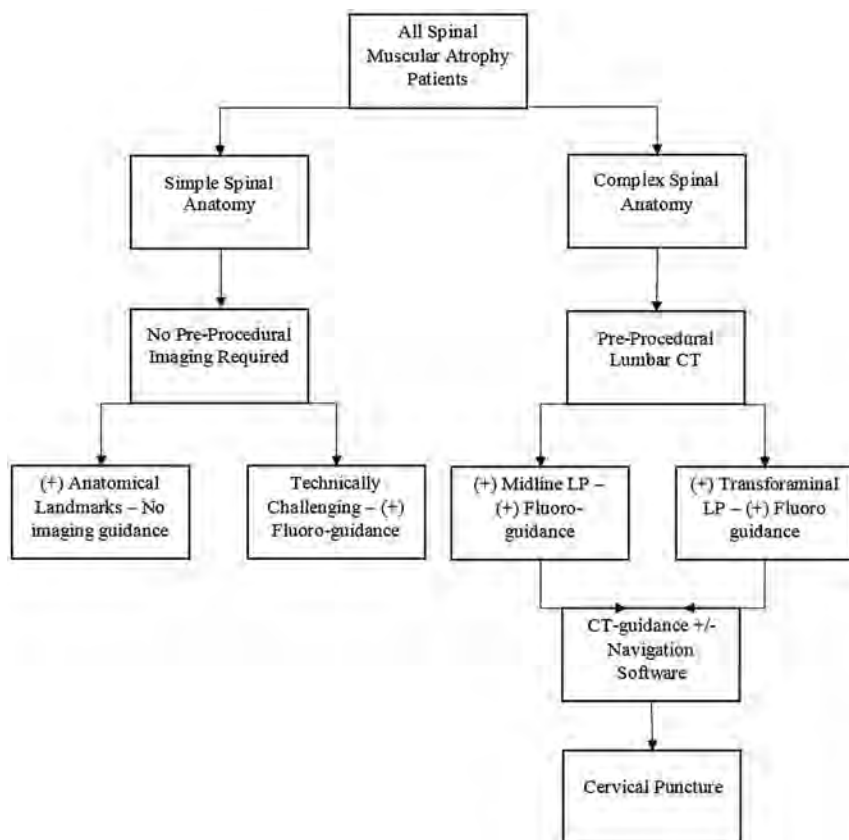


FIG 5. An algorithmic approach to ITNIs in patients with spinal muscular atrophy.

Although all of our TF ITNIs were performed with the patient under general anesthesia, the method of ventilation varied. Children with SMA commonly have compromised pulmonary function due to scoliosis, spinal fusion, and weakened chest wall musculature. Therefore, minimizing respiratory strain on the patient with SMA is important in their management. Because our preferred position for the TF approach is left- or right-sided lateral decubitus, there is a reduced need for endotracheal intubation compared with the prone position. In our population, general anesthesia via an endotracheal tube was used in only 2 of 42 TF procedures. The avoidance of endotracheal intubation leads to a shorter postprocedural recovery time compared with the laryngeal mask airway or mask ventilation approaches and a decreased risk of prolonged intubation, which is significantly higher in patients with SMA than in the general population.

As our experience with the TF approach to ITNIs evolved, the use of CT-guided navigation ceased. In fact, the use of CT guidance was limited to 3 early TF ITNIs compared with 39 subsequent fluoroscopically guided TF ITNIs. Previously, the literature almost exclusively reported using CT guidance for the TF approach.^{4,6} Despite our transition to a rotating fluoroscopic C-arm for guidance, given the advanced technology in our interventional radiology suite with both fluoroscopic and CT navigation guidance available, we suggest the interventional radiology suite as the ideal setting for the procedure. At practices or institutions where CT guidance is not available in the interventional radiology suite, a diagnostic CT scanner is a viable second option for imaging guidance and should be reserved before beginning the procedure

in case fluoroscopic guidance should fail. However, an interventional radiology suite with conebeam CT navigational guidance available is helpful in 2 ways: First, the interventional radiology suite serves as a central location where all necessary guidance tools are available, avoiding patient transportation and traveling concerns; and second, it offers the most sophisticated setting for maximizing the likelihood for technical success.

Historically, the TF approach has been used for epidural steroid injections⁷ and for myelography, with an excellent safety and technical success history, specifically when image guidance is used.⁶ The primary risks of the TF approach include nerve and vascular injury, potential bleeding, and spinal cord injury. Transgression of the kidney is possible, but preprocedural lumbar CT helps plan a route that avoids the kidney, as does patient positioning with the convex side of the spinal curvature toward the ceiling. Targeting the lower half of the neural foramina is key to avoiding neurovascular injury. In our experience, no complications occurred, while prior

reports indicated occasional minor complications.^{4,6} Collectively, all TF ITNIs were technically successful.

When caring for pediatric patients specifically, being aware and considerate of fluoroscopy time and radiation exposure is a high priority. Most interesting, our experience with the fluoroscopically guided TF approach revealed an unexpected observation. Although we anticipated that our fluoroscopically guided TF fluoroscopy times (mean, 2 minutes) would compare favorably with the cervical (mean, 8 minutes 6 seconds) and CT-guided TF (mean, 4 minutes 6 seconds) approaches, we did not expect the times to be similar to those that we commonly see with the midline interspinous lumbar approach (mean, 2 minutes). Given the longer trajectory to the intrathecal space via the TF approach, as confirmed with the predominant use of 5- or 7-inch spinal needles, the probability of needle deflection increases and may increase fluoroscopy time or decrease the success of intrathecal access. These untoward effects may have been minimized with the use of a coaxial needle technique as discussed previously.

Last, in 2 children with SMA with complex spines, 3 cervical punctures were performed because we were not yet using the TF approach. Although cervical approaches were successful without complications, the TF approach is preferred because of the lower risk profile and the extended fluoroscopy times encountered with the cervical routes. In both patients, the TF approach was subsequently used for future ITNIs.

The limitations of this study include its small number of transforaminal injections and its lack of comparison with other methods and techniques. A variety of alternative needle approaches to

the subarachnoid space has been described, including transforaminal, interlaminar, cervical, and suboccipital into the cisterna magna, sacral canal, and sacral foramina. In addition, there are other considerations such as surgical or percutaneous access with device implantation and/or creation of bone windows. In our series, we explored the cervical and TF approaches but did not use implanted devices or bone windows.

CONCLUSIONS

Our initial experience has led us to create a protocol-driven approach to guide our technical choices based on the patient's spinal anatomy, whether simple or complex. Patients with simple spines without instrumentation generally do not need preprocedural imaging to assess spinal anatomy, and most do not need imaging guidance. In contrast, the complex spine group requires preprocedural imaging and imaging guidance with the primary approach being the TF approach. With the evolution of the interventionalists' experience, fluoroscopically guided transforaminal ITNIs should be the preferred method. Figure 5 presents our algorithmic approach to these patients.

Disclosures: Richard Towbin—*UNRELATED: Expert Testimony: medicolegal, primarily pediatric brain injury; Royalties: Halyard Health.*

REFERENCES

1. Lenhart RL, Youlo A, Schroth Mk, et al. **Radiographic and respiratory effects of growing rods in children with spinal muscular atrophy.** *J Pediatr Orthop* 2017;37:e500–04 CrossRef Medline
2. Mousa M, Aria D, Schaefer C, et al. **A comprehensive institutional overview of intrathecal nusinersen injections for spinal muscular atrophy.** *Pediatr Radiol* 2018;48:1797–1805 CrossRef Medline
3. Gkasdaris G, Tripsianis G, Kotopoulos K, et al. **Clinical anatomy and significance of the thoracic intervertebral foramen: a cadaveric study and review of the literature.** *J Craniovertebr Junction Spine* 2016;7:228–35 CrossRef Medline
4. Weaver JJ, Natarajan N, Shaw DW, et al. **Transforaminal intrathecal delivery of nusinersen using conebeam computed tomography for children with spinal muscular atrophy and extensive surgical instrumentation: early results of technical success and safety.** *Pediatr Radiol* 2018;48:392–97 CrossRef Medline
5. Peckham ME, Shah LM, Tsai AC, et al. **C1 posterior arch flare point: a useful landmark for fluoroscopically guided C1–2 puncture.** *AJNR Am J Neuroradiol* 2018;39:1562–67 CrossRef Medline
6. Nascene DR, Ozutemiz C, Estby H, et al. **Transforaminal lumbar puncture: an alternative technique in patients with challenging access.** *AJNR Am J Neuroradiol* 2018;39:986–91 CrossRef Medline
7. Botwin KP, Gruber RD, Bouchlas CG, et al. **Complications of fluoroscopically guided transforaminal lumbar epidural injections.** *Arch Phys Med Rehabil* 2000;81:1045–50 CrossRef Medline

MRI Predictors of Recurrence and Outcome after Acute Transverse Myelitis of Unidentified Etiology

 E. Bulut,  T. Shoemaker,  J. Karakaya,  D.M. Ray,  M.A. Mealy,  M. Levy, and  I. Izbudak



ABSTRACT

BACKGROUND AND PURPOSE: The early prediction of recurrence after an initial event of transverse myelitis helps to guide preventive treatment and optimize outcomes. Our aim was to identify MR imaging findings predictive of relapse and poor outcome in patients with acute transverse myelitis of unidentified etiology.

MATERIALS AND METHODS: Spinal MRIs of 77 patients (mean age, 36.3 ± 20 years) diagnosed with acute transverse myelitis were evaluated retrospectively. Only the patients for whom an underlying cause of myelitis could not be identified within 3 months of symptom onset were included. Initial spinal MR images of patients were examined in terms of lesion extent, location and distribution, brain stem extension, cord expansion, T1 signal, contrast enhancement, and the presence of bright spotty lesions and the owl's eyes sign. The relapse rates and Kurtzke Expanded Disability Status Scale scores at least 1 year (range, 1–14 years) after a myelitis attack were also recorded. Associations of MR imaging findings with clinical variables were studied with univariate associations and binary log-linear regression. Differences were considered significant for P values $< .05$.

RESULTS: Twenty-seven patients (35.1%) eventually developed recurrent disease. Binary logistic regression revealed 3 main significant predictors of recurrence: cord expansion (OR, 5.30; 95% CI, 1.33–21.1), contrast enhancement (OR, 5.05; 95% CI, 1.25–20.34), and bright spotty lesions (OR, 3.63; 95% CI, 1.06–12.43). None of the imaging variables showed significant correlation with the disability scores.

CONCLUSIONS: Cord expansion, contrast enhancement, and the presence of bright spotty lesions could be used as early MR imaging predictors of relapse in patients with acute transverse myelitis of unidentified etiology. Collaborative studies with a larger number of patients are required to validate these findings.

ABBREVIATIONS: BSL = bright spotty lesion; EDSS = Expanded Disability Status Scale; LETM = longitudinally extensive transverse myelitis; NMOSD = neuromyelitis optica spectrum disorder

In the initial evaluation of acute transverse myelitis, a specific underlying cause of the immunologic attack cannot be determined in many circumstances. The early prediction of recurrence in such cases helps to guide preventive treatment, which, in turn, may improve long-term prognosis. Alternatively, features that favor monophasic disease may save the patients from unnecessary

long-term immunosuppression. Accordingly, several independent demographic and laboratory risk factors for recurrent disease after acute transverse myelitis have been determined, including female sex, African American race, vitamin D insufficiency, and serum antibodies such as anti-aquaporin 4 antibodies, anti-Ro/SS-A antibodies, and a high ($\geq 1:160$) antinuclear antibody titer.¹ Previous studies also suggested clinical factors associated with poor functional recovery, such as symmetric motor dysfunction at onset, sphincter dysfunction, and spinal cord shock-like symptoms.^{2,3}

Unlike previously established clinical variables, imaging predictors of relapse and poor outcome after acute transverse myelitis of unidentified etiology have not been comprehen-

Received April 6, 2019; accepted after revision June 6.

From the Departments of Radiology (E.B.) and Statistics (J.K.), Hacettepe University Faculty of Medicine, Ankara, Turkey; Department of Neurology (T.S., M.A.M., M.L.) and Division of Neuroradiology (D.M.R., I.I.), The Russell H. Morgan Department of Radiology and Radiological Science, Johns Hopkins University School of Medicine, Baltimore, Maryland; Department of Neurological Sciences (T.S.), Rush University Medical Center, Chicago, Illinois; and Department of Neurology (M.L.), Massachusetts General Hospital and Harvard Medical School, Boston, Massachusetts.

This study was funded by a Research Project Grant from the National Institute of Allergy and Infectious Diseases, grant A1130548, ML.

Paper previously presented, in part, as an oral presentation at: American Society of Neuroradiology Annual Meeting and the Foundation of the ASNR Symposium, June 2–7, 2018; Vancouver, British Columbia, Canada. The presentation number was O-257.

Please address correspondence to Elif Bulut, MD, Hacettepe University Faculty of Medicine, Department of Radiology, Sıhhiye Ankara, Turkey; e-mail: drelifbulut@yahoo.com

 Indicates open access to non-subscribers at www.ajnr.org

<http://dx.doi.org/10.3174/ajnr.A6121>

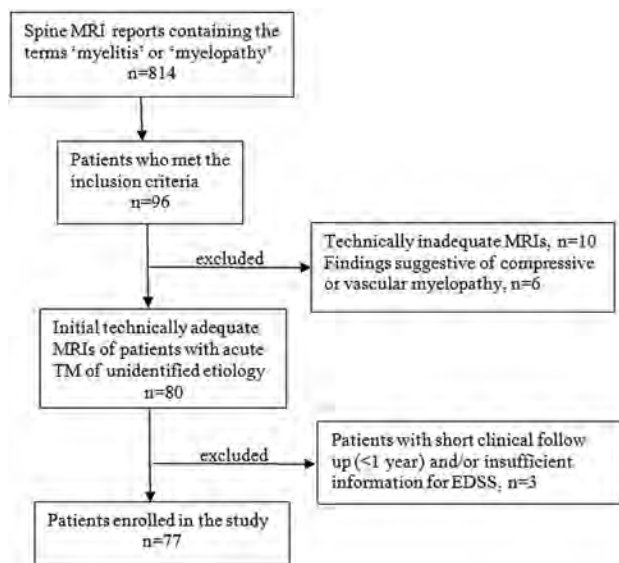


FIG 1. Flow chart of patients who met the inclusion/exclusion criteria for the study population.

sively studied to date. Longitudinally extensive lesions extending ≥ 3 vertebral lengths have been associated with the relapsing myelitis diseases, neuromyelitis optica, and myelin oligodendrocyte glycoprotein antibody disease.¹ In addition, there are other MR imaging features that could be used to predict relapse or outcome, including contrast enhancement, expansion, bright spotty lesions, and T1 hypointensity, that have not been assessed in this patient population. Therefore, we aimed to identify spinal MR imaging findings at onset that are associated with an increased risk of recurrence and poor outcome.

MATERIALS AND METHODS

An institutional review board–approved data base search was performed using the keywords “myelitis” and “myelopathy” in spine MR imaging reports dictated at Johns Hopkins Hospital from January 1, 2005, to January 1, 2017. The acquired MR imaging reports were reviewed with clinical data to identify patients referred for the diagnosis of acute transverse myelitis. The inclusion criteria were as follows: 1) fulfillment of diagnostic criteria established by the Transverse Myelitis Consortium Working Group 2002 for acute transverse myelitis⁴; 2) patients whose initial evaluation (within 3 months of symptom onset) could not yield sufficient information to identify a specific underlying disorder (eg, aquaporin-4 antibody testing negative for neuromyelitis optica); and 3) patients whose spinal MR imaging studies were obtained within 1 month of symptom onset.⁵ The patients with technically inadequate scans or having MR imaging findings of a compressive etiology or abnormal flow voids on the cord surface, consistent with vascular myelopathy, were excluded (Fig 1).

Patient demographics, serologies, and relapse rates were recorded. The Kurtzke Expanded Disability Status Scale (EDSS) scores⁶ at least 1 year (range, 1–14 years) after the first attack were assigned retrospectively using clinical documentation. Relapsing disease was defined as a clinical relapse with a change on neurologic examination and a report of a new lesion on spine MR imaging. Patients with short clinical follow-up

(<1 year) and/or insufficient information for calculating the EDSS were further excluded from the study (Fig 1).

Spinal cord MR imaging studies were performed at presentation, before treatment (mean, 10 days after symptom onset; range, 1–30 days) either on 1.5T or 3T magnets from different manufacturers: Achieva (Philips Medical Systems, Best, the Netherlands), Signa Excite (GE Healthcare, Milwaukee, Wisconsin), and Aera, Avanto, Verio, Skyra and Trio (Siemens, Erlangen, Germany). For some patients, the initial MR imaging study was performed at an outside institution before the transfer to our medical center. Spinal MR imaging protocol included sagittal T1-weighted, sagittal and axial T2-weighted, sagittal STIR, and contrast-enhanced sagittal and axial T1-weighted imaging ($n = 76$). The details of the acquisition parameters are provided in Table 1.

Image analysis was performed in consensus by 2 neuroradiologists (E.B. and I.I.) blinded to the clinical outcome. T2-hyperintense spinal cord lesions were evaluated in terms of the following: 1) extent, 2) location, 3) distribution, 4) brain stem extension, 5) cord expansion (ie, swelling), 6) T1 signal, and 7) contrast enhancement.

The extent of involvement, lesion distribution, and cord expansion were evaluated from sagittal T2-weighted images. The lesions were grouped as either longitudinally extensive or short-segment lesions according to the number of the vertebral bodies spanned. The lesions extending at least 3 vertebral levels were considered longitudinally extensive lesions. According to the cord segments involved, lesion distribution was grouped as cervical, cervicothoracic, thoracic, or confined to the conus. Lesion location was determined from axial T2-weighted images and classified as lesions confined to gray matter, confined to white matter, or involving both gray and white matter. Lesions involving $\geq 50\%$ of the spinal cord area were also noted, as were multiple lesions with no radiologically detectable continuity. The presence of bright spotty lesions (lesions similar to or higher in signal intensity than CSF) and the owl’s eyes sign (Fig 2)⁷ were also assessed from axial T2-weighted images. The presence and pattern of contrast enhancement were assessed on both axial and sagittal postcontrast images of available examinations.

When available, brain MR imaging examinations performed at the same time or within 1 month of the spine MR imaging were also reviewed. The brain MR imaging protocol included T1-weighted images, fast spin-echo T2-weighted images, FLAIR images, diffusion-weighted images, and postcontrast T1-weighted images. The brain MR imaging findings were classified as either normal/insignificant or abnormal. The findings were classified as “abnormal” in the following circumstances: multiple (≥ 2) non-specific lesions not fulfilling the 2017 McDonald MR imaging criteria; extensive cerebral lesions with or without contrast enhancement; findings suggestive of neuromyelitis optica spectrum disorder (NMOSD) but not sufficient to fulfill the diagnostic criteria, such as lesions located in the hypothalamus or area postrema; and leptomeningeal enhancement.

Statistical Analysis

Demographic data, serologies, and MR imaging findings were analyzed for associations with recurrence and EDSS. EDSS scores of patients with longitudinally extensive transverse myelitis (LETM)

Table 1: Imaging parameters used in spinal MRI

Sequence	TR/TI (ms)	TE (ms)	Matrix Size	FOV (mm)	Section Thickness/Spacing (mm)
T1WI sagittal	397–562	8.7–11	256–384 × 256–288	25–32 × 35.3–45.2	3–3.5/3.3–4.3
T2WI sagittal	2340–4070	96–109	256–384 × 256–288	25–32 × 35.3–45.2	3–3.5/3.3–4.3
STIR sagittal	3210–4610/150–220	42–79	256–384 × 256–288	25–32 × 35.3–45.2	3–3.5/3.3–4.3
T2WI axial	2874–4100	98–109	256–320 × 192–280	18–20 × 25.4–28.3	3–4/3.3–5
T1WI axial	400–654	8.4–9.7	256–320 × 192–280	18–20 × 25.4–28.3	3–4/3.3–5

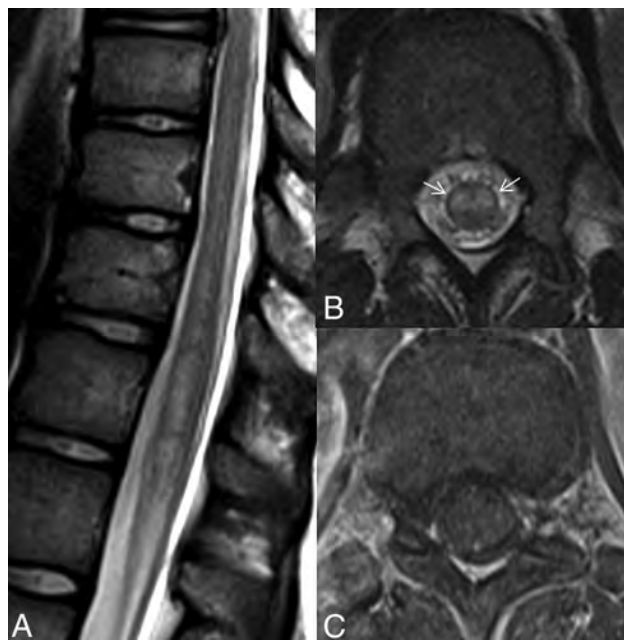


FIG 2. Spine MR images of a 13-year-old female patient with monophasic idiopathic transverse myelitis. The sagittal T2-weighted image (A) shows a longitudinally extensive, minimally expansile hyperintense lesion at the distal spinal cord. The axial T2-weighted (B) and postcontrast T1-weighted (C) images show central involvement with the owl's eyes sign (arrows in B) and no discernible contrast enhancement of the lesion.

were also compared with those having short-segment lesions involving $\leq 50\%$ of the transectional area of the cord and with those of patients having short-segment lesions confined to the white matter. All analyses were performed with the SPSS (Version 23.0; IBM, Armonk, New York) statistical package program. Numeric variables were evaluated for normality of data distribution using the Kolmogorov-Smirnov test. Descriptive statistics were expressed as mean \pm SD or median (minimum-maximum), according to the assumption of normal distribution for quantitative variables. Qualitative variables were given as proportions (percentages). An independent-samples *t* test was performed to compare the means of 2 independent groups. For non-normally distributed data, the Mann-Whitney *U* test was used to compare the 2 groups. The χ^2 (continuity correction or Fisher exact test) was used to compare differences among groups for categorical variables. A *P* value $< .05$ was accepted as statistically significant.

Logistic regression analysis was performed to determine important risk factors for developing recurrent myelitis. Binary logistic regression with a backward stepwise method was used to evaluate which independent imaging variables were statistically significant predictors of the binary dependent variable (relapse).

Using the logistic models, we calculated ORs and their respective 95% confidence intervals.

RESULTS

Initial inquiry of spine MR imaging reports containing the terms “myelitis” or “myelopathy” yielded 814 MR imaging scans. After we applied inclusion and exclusion criteria, 77 patients (female/male ratio, 46:31; mean age, 36.4 ± 20 years) were enrolled in the study. The clinical characteristics of the patients are provided in Table 2. Twenty-seven patients (35.1%) eventually developed recurrent disease. The mean time to relapse was 17.3 months (range, 3–117 months). Time to relapse was ≤ 1 year in 21 patients (77%). Eighteen (66.6%) patients had > 1 relapse (mean, 3.05; range, 2–5 relapses). Age at presentation did not differ between patients with monophasic and recurrent disease (*P* = .2). There were higher ratios of female (*P* = .03) and African American patients (*P* = .02) in the recurrent group, as expected. Among the 27 patients who relapsed, 8 patients (29.6%) eventually seroconverted for the anti-aquaporin 4 antibody after initially testing negative, all of whom presented with LETM at onset. Four patients with relapse were ultimately diagnosed with aquaporin 4 seronegative NMOSD, 3 with multiple sclerosis, 1 with acute disseminated encephalomyelitis, 1 with neurosarcoidosis, 1 with systemic lupus erythematosus, and the other 9 (33%) were diagnosed with recurrent transverse myelitis of unknown etiology. The mean time to diagnosis was 23.2 months (range, 3.2–108 months) for the 18 patients with recurrence and specific diagnoses. For the 9 patients with recurrent transverse myelitis of unknown etiology, the mean follow-up time was 45.2 months (range, 13.5–169 months), which was much longer than the mean time to diagnosis in patients with specific diagnoses.

The frequencies of spinal cord MR imaging findings and associations with monophasic/relapsing disease are outlined in Table 3. Imaging findings of LETM, brain stem extension, cord expansion, bright spotty lesions (BSLs), and contrast enhancement were higher among patients who relapsed (Fig 3). When binary logistic regression with the backward stepwise method was used, findings of cord expansion, BSLs, and contrast enhancement were calculated to be significant predictors of recurrent disease (Table 4).

Thirteen (48%) of the patients having BSLs on their spinal MR imaging were ultimately diagnosed with NMOSD. Multiple sclerosis (*n* = 1), acute disseminated encephalomyelitis (*n* = 1), and neurosarcoidosis (*n* = 1) were other entities with BSLs. Additional MR imaging features of the NMOSD cohort included cord expansion and brain stem extension.

Brain MR imaging was available in 63 patients, of whom 17 had abnormal findings not necessarily suggestive of a specific diagnosis, except for 1 patient with NMOSD who had a lesion in the area postrema. Two patients had cerebral leptomeningeal enhancement without a discernible parenchymal lesion.

Table 2: The clinical characteristics of 77 patients who presented with acute transverse myelitis

Characteristics	Monophasic (n = 50)	Recurrent (n = 27)	P Values
Age at initial manifestation (mean) (yr)	34.2 ± 20.6	40.4 ± 18.5	.196
Female (n) (%)	25 (50%)	21 (77.8%)	.033
Ethnicity			.020
African American (n) (%)	10 (20%)	10 (37%)	
Caucasian (n) (%)	38 (76%)	12 (44.4%)	
Asian American (n) (%)	1 (2%)	3 (11%)	
Hispanic (n) (%)	1 (2%)	2 (7.4%)	
Seropositivity for anti-AQP4 Ab	1 (2%)	8 (29.6%)	.003
Mean follow-up time (yr)	2.4 ± 1.7	3.8 ± 3.8	.023
Mean EDSS score	4.2 ± 2.1	3.3 ± 1.8	.064
Patients with follow-up spine MRIs (n) (%)	16 (32%)	27 (100%)	<.001
Use of immunosuppressive/immunomodulatory treatment (n) (%)	9 (18%)	18 (66.7%)	<.001

Note:—AQP4 Ab indicates aquaporin 4 antibody.

Table 3: The frequencies of spinal MRI findings and associations with monophasic/relapsing disease

MRI Findings	Monophasic Disease (n = 50) (n) (%)	Recurrent Disease (n = 27) (n) (%)	P Value	Unadjusted OR (95% CI)
LETM (n = 42) (54.5%)	22 (44%)	20 (74.1%)	.022 ^a	3.63 (1.30–10.14)
Multifocal lesions (n = 16) (22.5%)	9/44 (20.5%)	7 (25.9%)	.808	1.36 (0.44–4.21)
Distribution			.304	
Cervical (n = 21) (27.3%)	14 (28%)	7 (25.9%)		
Cervicothoracic (n = 14) (18.2%)	6 (12%)	8 (29.6%)		
Thoracic (n = 35) (45.5%)	25 (50%)	10 (37%)		
Holocord (n = 7) (9.1%)	5 (10%)	2 (7.4%)		
Brain stem extension (n = 5) (6.5%)	1/46 (2.2%)	4/25 (16%)	.049 ^a	8.57 (0.90–81.46)
Location			.521	
Gray matter (n = 3) (3.9%)	3 (6%)	0		
Gray + white matter (n = 65) (84.4%)	42 (84%)	23 (85.2%)		
White matter (n = 9) (11.7%)	5 (10%)	4 (14.8%)		
>1/2 of the cord area (n = 55) (71.4%)	33 (66%)	22 (81.5%)	.242	2.26 (0.73–7.04)
Cord expansion (n = 48) (62.3%)	26 (52%)	22 (81.5%)	.021 ^a	4.06 (1.32–12.42)
TI hypointensity (n = 23) (30.3%)	11/49 (22.4%)	12 (44.4%)	.089	2.76 (1.01–7.61)
BSLs (n = 27) (35.1%)	12 (24%)	15 (55.6%)	.012 ^a	3.95 (1.45–10.74)
Owl's eyes sign (n = 2) (2.6%)	2 (4%)	0	.539	0.58 (0.06–5.88)
Enhancement (n = 48) (62.3%)	26 (52%)	22/26 (84.6%)	.011 ^a	5.07 (1.52–16.87)
Brain involvement (n = 17) (27%)	11/43 (25.6%)	6/20 (30%)	.950	1.24 (0.38–4.04)

^a Significant.

There was no significant correlation between recurrent disease and EDSS scores of the patients ($P = .14$), though there was an unexpected trend for recurrent cases to end up with better EDSS scores, at least early in their disease course. Also, none of the imaging variables analyzed for association with recurrent disease showed significant correlation with EDSS scores. We could not find a significant difference between EDSS scores of the patients with LETM and scores of patients having short-segment lesions involving $\leq 50\%$ of the transectional area of the cord or confined to white matter.

DISCUSSION

Spinal cord MR imaging is essential in the evaluation of acute transverse myelitis because MR imaging features, including location, distribution and extent of the lesions, and enhancement pattern could narrow the differential diagnosis considerably. Identification of MR imaging features predictive of relapsing disease may also prompt clinical decision-making in favor of empiric treatment with immunosuppression. These patients also could be considered candidates for more frequent follow-up within the first year of the initial attack with repeat serologic testing. This

consideration is because titers of specific antibodies, such as the anti-aquaporin 4 antibody, may fluctuate and retesting may reveal sufficient levels to confirm a diagnosis of NMOSD.

There was a significantly higher rate of recurrent myelitis in female and African American patients in our cohort. This finding was similar to findings in the previous report of Kimbrough et al,¹ and most likely reflects a higher incidence of NMOSD in these demographic groups. Although it is often associated with NMOSD, LETM has a wide range of differential diagnoses, including parainfectious myelitis, systemic autoimmune disease-related myelitis, and idiopathic transverse myelitis.⁸ A significantly higher proportion of patients with recurrent disease in our cohort had LETM, which was compatible with the previous reports noting the increased risk of developing recurrent disease in LETM.^{1,9}

As distinctive features of our study, cord expansion, BSLs, and enhancement were also found promising for predicting relapse after acute transverse myelitis at initial evaluation. Cord expansion was previously suggested to be specific to NMOSD and useful in differentiating it from longitudinally extensive lesions of MS.^{10–12} On the other hand, cord expansion did not significantly

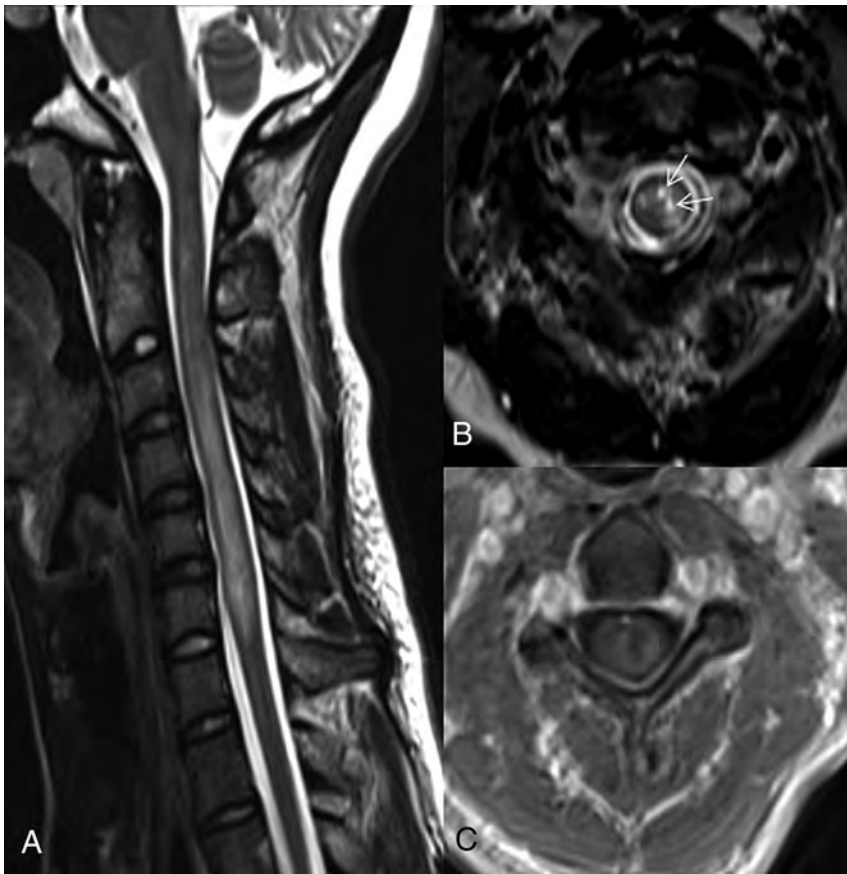


FIG 3. Spine MR images of a 29-year-old female patient with recurrent transverse myelitis. The sagittal T2-weighted image (A) shows a longitudinally extensive, expansile hyperintense lesion at the cervical spine. The axial T2-weighted (B) and postcontrast T1-weighted (C) images show gray and white matter involvement with bright spotty lesions (arrows in B) and ring enhancement of the lesion. The patient was diagnosed with NMOSD later at follow-up.

Table 4: Adjusted ORs for associations of imaging variables/age

Variable	Adjusted ORs	P Value	95% CI
Cord expansion	5.30	.018	1.33–21.11
BSLs	3.63	.040	1.06–12.43
Enhancement	5.05	.023	1.25–20.34
Age	1.03	.084	0.99–1.061
Constant	0.01	.00	

distinguish neuromyelitis optica from other causes of LETM in another recent study.⁵ Most cases showing cord expansion were non-NMOSD in our cohort. This could be explained by the low number of previously diagnosed cases of acute NMOSD in our study, which were excluded.

BSLs are defined as hyperintense small lesions on T2-weighted images, similar to or higher in signal intensity than CSF.¹³ They have been previously suggested as a highly distinctive feature of NMOSD and infrequently noted in multiple sclerosis and other causes of LETM.^{5,13} Similarly, a large number of our patients with BSLs (48%) were later diagnosed with NMOSD, though cases that remained idiopathic were also represented. The predictive value of both bright spotty lesions and cord expansion is likely driven by their association with NMOSD.

Brain stem extension was an infrequent finding ($n = 5$) in our cohort. Although infrequent, brain stem extension has been re-

ported as specific to NMOSD.^{10,12} Similarly, most of our patients (75%) with brain stem extension had a final diagnosis of NMOSD. Although it was found to increase the risk of recurrence in univariate analysis, adjusted odds ratios were not significant. This is probably due to its low frequency, which could affect the statistical analysis.

Although it partially defines acute attacks of inflammatory myelitis, contrast enhancement on MR imaging could also occur in other etiologies, including dural arteriovenous fistula and spondylotic myelopathy.⁸ It was reported to be more frequent in multiple sclerosis and other autoimmune etiologies compared with idiopathic myelitis in a previous study.¹⁴ Contrast enhancement, regardless of its pattern, was also found to be significantly higher in NMOSD compared with the other causes of LETM.⁵ It was a frequent finding in our cohort, with a wide range of patterns, from patchy or nodular to ring enhancement. We found a significant correlation between contrast enhancement and the risk of developing relapse, reflecting the greater incidence of contrast enhancement in disease entities associated with increased relapse rates. Our result is different from those in previous reports that could not find a significant association between enhancement and recurrence.

This difference could be explained by small cohort size⁹ and differences in case selection³ in those studies.

Brain MR imaging features could give a clue to recognize a specific etiology in an acute transverse myelitis attack. For example, brain lesions localized at sites rich in aquaporin 4 expression such as the area postrema are highly suggestive of NMOSD. Brain MR imaging findings either nonspecific or suggestive of a specific etiology were not frequent in our cohort, probably due to preclusion of patients who could be diagnosed at initial evaluation. The low frequency of brain lesions could negatively affect the statistical power of its association with recurrence or outcome.

Recurrent disease was not associated with poor outcome in our study, similar to a previous study that analyzed prognostic factors in LETM.⁹ This finding is probably due to the relatively short mean follow-up in both studies, because in another study³ with longer follow up (mean, 6.2 years), relapsing disease was found to be a predictor of worse outcome.

Previous studies yielded conflicting results regarding the association of LETM and functional outcome.^{2,9,14,15} Contrary to the studies of Carnero Contentti et al,^{2,15} LETM did not predispose to poor functional outcome in our cohort. This variation may be due to differences in patient groups. The partial lesions defined in the study of Carnero Contentti et al,¹⁵ which are frequently associated with multiple sclerosis, were uncommon ($n = 8$) in our study.

Additionally, the mean follow-up period of our study is much longer than those in 2 previous studies (3 and 3–6 months). Our results were similar to those in prior studies with longer follow-up periods.^{9,14}

Other spinal MR imaging features that we analyzed (distribution, T1 signal, extension in a transverse section, multiplicity, and contrast enhancement) were also evaluated in a previous study in which no association could be found with clinical outcome after acute transverse myelitis.¹⁶ Our study supports these findings, though more studies with large numbers of cases are needed for confirmation.

This retrospective study has several limitations. Most important, the follow-up periods varied widely, and we cannot rule out a future relapse in all of the patients who are currently monophasic.

Additionally, most patients with monophasic disease in our cohort did not receive preventive immunosuppression treatment during follow-up; therefore, the effects of those therapies on outcome could not be estimated. Other limitations were related to image acquisition. As a retrospective study, MR images were obtained from scanners with different magnet strengths and different sequence parameters. Also, postcontrast images were not acquired in a patient. All of these limitations could affect the sensitivity of image evaluation.

CONCLUSIONS

MR imaging findings of cord expansion, BSLs, and contrast enhancement could be used as early imaging predictors of relapse in acute transverse myelitis of unidentified etiology. Collaborative studies with larger number of patients are required to validate these findings.

Disclosures: Michael Levy—*RELATED: Grant:* Transverse Myelitis Association, *Comments:* grant to study genetics of transverse myelitis*; *UNRELATED: Board Membership:* Genentech, Alexion Pharmaceuticals, and Viela Bio; *Consultancy:* Genentech, Alexion Pharmaceuticals, and Viela Bio, Gerson Lehrman Group; *Expert Testimony:* various legal firms; *Grants/Grants Pending:* National Institutes of Health, Alexion Pharmaceuticals, Alnylam Pharmaceuticals, Viela Bio*; *Travel/Accommodations/Meeting Expenses Unrelated to Activities Listed:* Alexion Pharmaceuticals, Genentech, Union Chimique Belge Pharma. Izlem Izbudak—*UNRELATED: Consultancy:* Alexion Pharmaceuticals, *Comments:* MRI reads for neuromyelitis optica recurrence adjudication; *Grants/Grants Pending:* Biogen, *Comments:* MSPATHS study.*
*Money paid to the institution.

REFERENCES

1. Kimbrough DJ, Mealy MA, Simpson A, et al. **Predictors of recurrence following an initial episode of transverse myelitis.** *Neurol Neuroimmunol Neuroinflamm* 2014;1:e4 CrossRef Medline
2. Carnero Contentti E, Hryb JP, Leguizamón F, et al. **Differential diagnosis and prognosis for longitudinally extensive myelitis in Buenos Aires, Argentina** [in Spanish, English]. *Neurologia* 2017;32:99–105 CrossRef Medline
3. Gajofatto A, Monaco S, Fiorini M, et al. **Assessment of outcome predictors in first-episode acute myelitis: a retrospective study of 53 cases.** *Arch Neurol* 2010;67:724–30 CrossRef Medline
4. Transverse Myelitis Consortium Working Group. **Proposed diagnostic criteria and nosology of acute transverse myelitis.** *Neurology* 2002;59:499–505 CrossRef Medline
5. Pekcevik Y, Mitchell CH, Mealy MA, et al. **Differentiating neuromyelitis optica from other causes of longitudinally extensive transverse myelitis on spinal magnetic resonance imaging.** *Mult Scler* 2016;22:302–11 CrossRef Medline
6. Kurtzke JF. **Rating neurologic impairment in multiple sclerosis: an expanded disability status scale (EDSS).** *Neurology* 1983;33:1444–52 CrossRef Medline
7. Leboutoux MV, Franques J, Guillemin R, et al. **Revisiting the spectrum of lower motor neuron diseases with snake eyes appearance on magnetic resonance imaging.** *Eur J Neurol* 2014;21:1233–41 CrossRef Medline
8. Flanagan EP. **Autoimmune myelopathies.** *Handb Clin Neurol* 2016; 133:327–51 CrossRef Medline
9. Sepúlveda M, Blanco Y, Rovira A, et al. **Analysis of prognostic factors associated with longitudinally extensive transverse myelitis.** *Mult Scler* 2013;19:742–48 CrossRef Medline
10. Cassinotto C, Deramond H, Olindo S, et al. **MRI of the spinal cord in neuromyelitis optica and recurrent longitudinal extensive myelitis.** *J Neuroradiol* 2009;36:199–205 CrossRef Medline
11. Qiu W, Wu JS, Zhang MN, et al. **Longitudinally extensive myelopathy in Caucasians: a West Australian study of 26 cases from the Perth Demyelinating Diseases Database.** *J Neurol Neurosurg Psychiatry* 2010;81:209–12 CrossRef Medline
12. Kitley JL, Leite MI, George JS, et al. **The differential diagnosis of longitudinally extensive transverse myelitis.** *Mult Scler* 2012;18: 271–85 CrossRef Medline
13. Yonezu T, Ito S, Mori M, et al. **“Bright spotty lesions” on spinal magnetic resonance imaging differentiate neuromyelitis optica from multiple sclerosis.** *Mult Scler* 2014;20:331–37 CrossRef Medline
14. Cobo-Calvo A, Alentorn A, Mañé Martínez MA, et al. **Etiologic spectrum and prognosis of longitudinally extensive transverse myelopathies.** *Eur Neurol* 2014;72:86–94 CrossRef Medline
15. Carnero Contentti E, Hryb JP, Diego A, et al. **Etiologic spectrum and functional outcome of the acute inflammatory myelitis.** *Acta Neurol Belg* 2017;117:507–13 CrossRef Medline
16. Gupta A, Kumar SN, Taly AB. **Neurological and functional recovery in acute transverse myelitis patients with inpatient rehabilitation and magnetic resonance imaging correlates.** *Spinal Cord* 2016;54: 804–08 CrossRef Medline

CT-Guided Block and Radiofrequency Ablation of the C2 Dorsal Root Ganglion for Cervicogenic Headache

J.L. Chazen, E.J. Ebani, M. Virk, J.F. Talbott, and V. Shah



ABSTRACT

SUMMARY: The purpose of this report is to describe the technical aspects of CT-guided C2 dorsal root ganglion diagnostic block and radiofrequency ablation for refractory cervicogenic headache. CT guidance allows precise and safe positioning of a needle adjacent to the C2 dorsal root ganglion. At-risk neural and vascular structures can be avoided with CT, and it can provide a thorough understanding of upper cervical neuroanatomy.

ABBREVIATIONS: DRG = dorsal root ganglion; RF = radiofrequency

Cervicogenic headache is defined as pain referred to the head from the cervical spine or nerve roots. Clinical features are inadequate to isolate the cervical spine as a source of headache, and imaging in conjunction with diagnostic injections is required for a definitive diagnosis.¹ Osteoarthritis of the lateral atlantoaxial joints is an important consideration in refractory cases resulting from irritation of the C2 dorsal root ganglion (DRG). Unlike the lower cervical roots, the C2 nerve root has only sensory components and arborizes to both the greater and lesser occipital nerves.² Patients presenting with pain in the posterior scalp radiating to the vertex may be incorrectly diagnosed with primary occipital nerve entrapment.³ Clinical and imaging work-up may reveal irritation of the C2, C3, or C4 nerve roots, resulting in occipital distribution pain. Herein, we describe the technical considerations of a C2 dorsal root ganglion nerve block and radiofrequency (RF) ablation using CT guidance. Image-guided pulsed or thermal RF ablation of the C2 DRG has been described with high response rates^{4,5}; however, the CT-guided technique has not been previously reported, to our knowledge.

Patient Selection

Complete patient selection criteria are beyond the scope of this technical report; suggested indications and contraindications are outlined in the Table. Briefly, patients should be considered for C2 DRG RF ablation if they present with occipital-distribution pain of a cervicogenic origin and have failed conservative therapy, including medication and physical therapy. An occipital nerve block is often performed initially to exclude a peripheral occipital nerve entrapment. CT and/or MR imaging of the cervical spine should be performed to evaluate the upper cervical nerve roots and facet joints. Classically, an asymmetric pattern of C1–C2 facet osteoarthritis is seen with loss of cartilage and subchondral sclerosis (Fig 1). Posterior osteophyte formation may narrow the C1–C2 foramen and impinge on the C2 DRG, resulting in occipital neuralgia. Corresponding subarticular bone marrow edema may further suggest the C1–C2 joint as the pain generator (Fig 1).

Technique

Patients should be placed head first on the CT gantry table in the supine or prone position with the head in neutral alignment facing the ceiling or in slight rotation away from the painful side. Moderate sedation may be offered for patient comfort; however, it is important that the patient remain awake for RF ablation sensory testing. Scout topograms of the craniocervical junction are acquired in the frontal and lateral planes. An axial CT stack can then be prescribed from the skull base through C3. The C2 dorsal root ganglion can be visualized in the axial plane just dorsal to the C2 lateral mass (Fig 2). An adequate CT dose is necessary for visualization, and the authors recommend 120 kV and 100–200 mA (diagnostic dose) at 2.5 mm (reconstructed to 0.625-mm bone and standard algorithms) for the initial preprocedural planning scan. The dose may be reduced to 10–50 mA for subsequent

Received April 17, 2019; accepted after revision June 13.

From the Departments of Radiology (J.L.C., E.J.E.) and Neurosurgery (M.V.), Weill Cornell Medicine, NewYork-Presbyterian Hospital, New York, New York; Department of Neurosurgery, (M.V.), Center for Comprehensive Spine Care, New York, New York; Department of Radiology & Biomedical Imaging (J.F.T.), University of California, San Francisco and Zuckerberg San Francisco General Hospital, San Francisco, California; and Department of Radiology & Biomedical Imaging (V.S.), University of California, San Francisco, San Francisco, California.

Please address correspondence to J. Levi Chazen, MD, Weill Cornell Medicine, NewYork-Presbyterian Hospital, Department of Radiology, 525 East 68th St, Starr 631, New York, NY 10065, 212-746-2578; e-mail: jlc2008@med.cornell.edu; @levichazen



Indicates article with supplemental on-line video.

<http://dx.doi.org/10.3174/ajnr.A6127>

Suggested indications and contraindications for the C2 nerve block and RFA procedure

Indications	Contraindications
Occipital neuralgia for >6 weeks Ipsilateral arthrosis of the lateral C1–C2 facet joint on CT and/or MR imaging with C1–C2 foraminal stenosis Lack of response to conservative management (medication and/or occipital nerve block)	Coagulopathy (INR > 1.5, platelets <50) Known vertebral artery variant crossing at C1–C2 along the needle trajectory Contrast allergy ^a

Note:—RFA indicates radiofrequency ablation; INR, international normalized ratio.

^aRelative contraindication because preoperative noncontrast MRA may be performed.

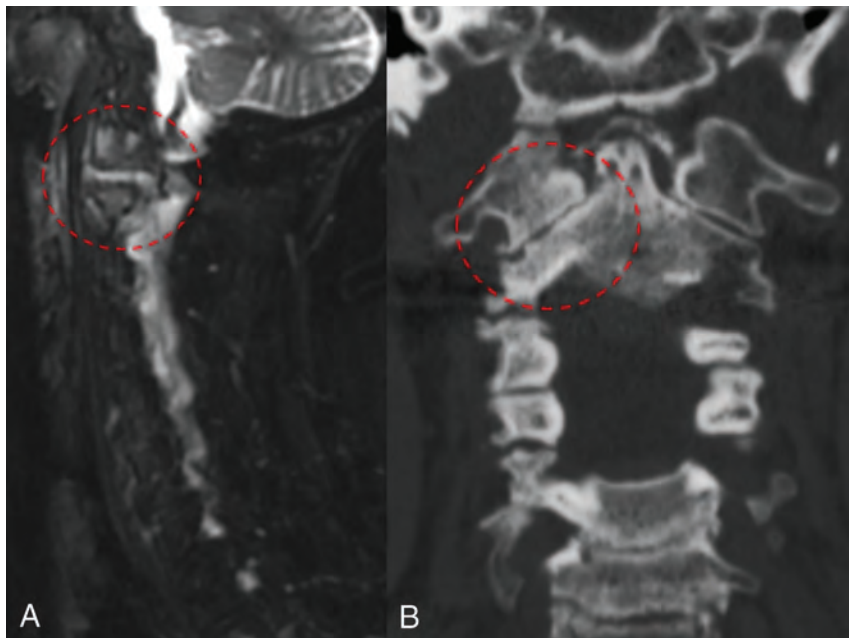


FIG 1. A, Sagittal STIR sequence reveals increased T2-hyperintense signal in the right C1–C2 joint and periarticular bone marrow edema (*circle*). B, Coronal CT scan shows asymmetric marked osteoarthrosis of the right C1–C2 articulation, with loss of joint height, cortical irregularity, and subchondral sclerosis (*circle*).

procedural scans acquired for needle localization. Serial CT or CT fluoroscopy can be used on the basis of the interventionalist's preference. If preoperative angiography or MR imaging is not available, a targeted CT angiogram may be performed with intravenous contrast. It is important to identify relevant vertebral artery variants that may be present in up to 31% of patients at the C1–C2 level.⁶ Due to the transient nature of intravenous CT contrast, the authors recommend that if performed, a procedural CTA scan be obtained once the needle entry site has been selected and the patient's head immobilized because the CTA may be of limited utility if the patient is significantly repositioned (On-line Video).

C2 Nerve Block

In preparation for needle insertion, the skin is sterilized and buffered 1% lidocaine is instilled subcutaneously for local anesthesia. A 22-ga, 2.5- to 3.5-inch Quincke-type spinal needle is then inserted. By means of intermittent CT guidance, the needle is advanced to approximate the C2 dorsal root ganglion. Care should be taken to avoid advancing the needle medial to the DRG, given the close proximity to the dura. If blood is seen in the hub, the needle may be carefully repositioned. There is a rich venous

plexus surrounding the C2 DRG; a small volume (0.2–0.3 mL) of iohexol (Omnipaque 180; GE Healthcare, Piscataway, New Jersey) 180 or 240 contrast diluted with normal saline should be injected to ensure appropriate positioning and exclude inadvertent arterial or dural puncture. Once the appropriate position is confirmed, a 1- to 2-mL 1:1 mixture of preservative-free dexamethasone, 10 mg/mL, and 0.5% or 0.75% of bupivacaine is prepared and slowly instilled through the needle. The needle is then removed with the stylet in place.

Radiofrequency Ablation

For RF ablation, the authors recommend a 22-ga, 5- or 10-cm-length cannula with a 5-mm uninsulated tip. A grounding pad is placed on the upper thigh. Following the steps described above, an RF ablation cannula is substituted for the spinal needle. Once the appropriate position is confirmed on CT, the stylet is removed and the radiofrequency probe is inserted (Fig 3). Impedance levels should be checked and are typically <300 Ω . Sensory testing is then performed at 50 Hz up to 2 V. Pain should be elicited in the distribution of the ipsilateral occipital nerve. Motor testing at 2 Hz may then be performed, which may evoke mild local contraction of the paraspinous musculature. Then, 0.5 mL of unbuffered 1% lidocaine is instilled in the RF cannula, and a CT scan

is obtained with the RF probe in place for final confirmation of positioning. Thermal RF ablation is then performed at 80°C for 90 seconds. The patient may experience local discomfort during the thermal ablation and should be encouraged to hold still for the duration of the ablation. Discomfort during the ablation typically improves as the ablation continues. If the pain is severe and/or persistent, the ablation should be stopped and the needle withdrawn slightly before re-ablating, or alternatively, pulsed radiofrequency ablation may be considered. If pulsed RF ablation is desired, identical treatment steps may be followed, but the RF generator should be set to pulsed RF at 42°C for 120 seconds.

Following RF ablation, the probe is removed and a nerve block can be performed through the cannula with dexamethasone and bupivacaine as described above to decrease postprocedural inflammation and discomfort. The cannula is then removed with the stylet in place, and a sterile bandage is applied. Patients may experience a flare of symptoms for 24–72 hours following thermal RF ablation; oral nonsteroidal anti-inflammatory drugs are generally adequate for pain control. In cases of severe postoperative pain inadequately controlled with nonsteroidal anti-inflammatory drugs, a methylprednisolone

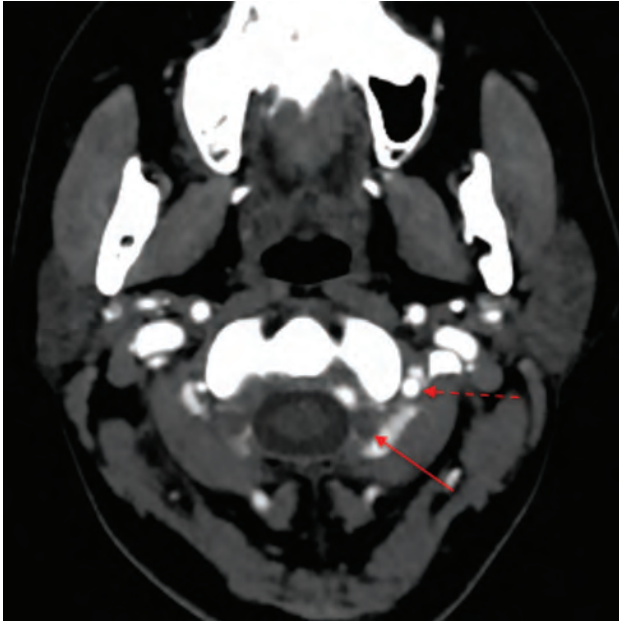


FIG 2. Axial CT angiogram showing the left C2 dorsal root ganglion (arrow) positioned behind the left C2 lateral mass. The left proximal V3-segment vertebral artery is highlighted (dashed arrow) anterolateral to the target.

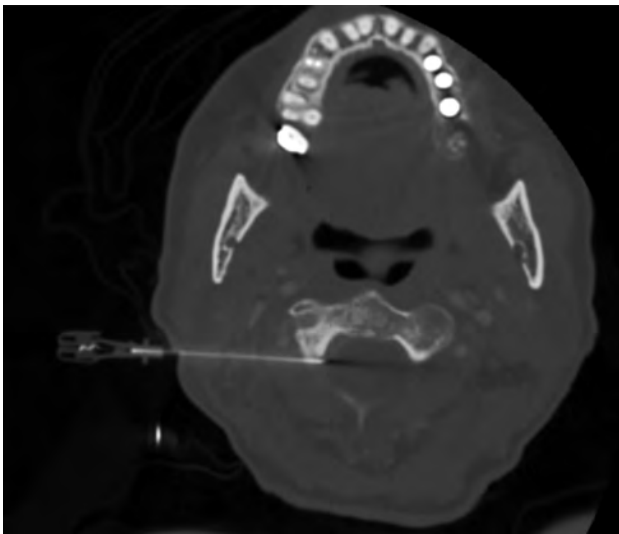


FIG 3. Intraprocedural axial CT scan showing appropriate placement of a 5-cm RF cannula targeting the right C2 DRG.

(Medrol) dose pack may be helpful to decrease inflammation and discomfort.

DISCUSSION

Cervicogenic headache has an estimated prevalence of up to 4.1% of the general population and up to 20% in patients with chronic headache.⁷⁻⁹ Image-guided injection of the upper cervical spine has been described for treatment of cervicogenic headache, including the atlanto-occipital, atlantoaxial, C2–C3, and C3–C4 facet joints and nerve blocks of C1 through C4. The C2 DRG is the principal nerve root supplying the greater and lesser occipital nerves and provides an ideal target for direct neurolysis. The corridor for needle insertion is generally safe, lying at the axial level of

the proximal V3-segment vertebral artery where it traverses anterolateral to the C2 DRG (Fig 2). Vascular variants such as an inferior course of the PICA may be problematic in cases of dural puncture at the C1–C2 level but should not affect the epidural C2 DRG injection.¹⁰ However, intraprocedural CT angiography can be performed to ensure a safe procedural approach because head positioning may alter expected axial anatomy.

Pulsed RF can be considered in place of thermal RF and has advantages including a decreased potential for local thermal injury and a decreased incidence of postprocedural inflammation. However, the pulsed RF procedure is potentially less efficacious than thermal RF. Patients may experience a shorter duration of pain relief compared with thermal RF, necessitating repeat procedures.

Complications from C2 RF ablation are uncommon and usually present as numbness and dysesthesia following neurotomy. However, in the largest described case series of thermal C2 RF ablation, >90% of patients reported that they would undergo the procedure again if pain returned.⁴ Some authors advocate sacrificing the C2 DRG during surgical C1–C2 fusion because numbness often has no effect on health-related quality of life, unlike neuralgia.² A meta-analysis of radiofrequency ablation for cervicogenic headache yielded mixed results but covered a heterogeneous population with a variety of targets, image-guidance modalities, and RF techniques.⁸ Potential risks of the procedure include intra-arterial or intrathecal puncture and injection of medication. The risks of intrathecal puncture include spinal fluid leak or spinal cord puncture. The implications of intrathecal injection include nontarget injection (false-negative response from the nerve block), high spinal block, and arachnoiditis. Implications of an intra-arterial injection include a nontarget injection and spinal cord or posterior fossa infarct from intra-arterial injection of steroids. Although ischemic complications of intra-arterial injection have not been reported with nonparticulate steroids in the cervical spine, the authors recommend using preservative-free dexamethasone in all cases. Anecdotally, the thermal RF procedure has excellent sustained results and may obviate morbid upper cervical fusion, but further prospective study is needed to confirm these observations.

CONCLUSIONS

CT provides excellent guidance for C2 DRG injection and radiofrequency ablation and can be combined with procedural CT angiography to highlight vascular anatomy.

Disclosures: Michael Virk—UNRELATED: Consultancy: Globus Medical, Depuy Synthes, Brainlab.

REFERENCES

1. Bogduk N. **The neck and headaches.** *Neurol Clin* 2014;32:471–87 CrossRef Medline
2. Janjua MB, Zhou PL, Greenfield JP, et al. **C2 and greater occipital nerve: the anatomic and functional implications in spinal surgery.** *Cureus* 2017;9:e1074 CrossRef Medline
3. Bogduk N, Govind J. **Cervicogenic headache: an assessment of the evidence on clinical diagnosis, invasive tests, and treatment.** *Lancet Neurol* 2009;8:959–68 CrossRef Medline
4. Hamer JF, Purath TA. **Response of cervicogenic headaches and occipital neuralgia to radiofrequency ablation of the C2 dorsal root**

- ganglion and/or third occipital nerve. *Headache* 2014;54:500–10 CrossRef Medline
5. Zhang J, Shi DS, Wang R. Pulsed radiofrequency of the second cervical ganglion (C2) for the treatment of cervicogenic headache. *J Headache Pain* 2011;12:569–71 CrossRef Medline
 6. Katoh Y, Itoh T, Tsuji H, et al. Complications of lateral C1–2 puncture myelography. *Spine (Phila Pa 1976)* 1990;15:1085–87 CrossRef Medline
 7. Haldeman S, Dagenais S. Cervicogenic headaches: a critical review. *Spine J* 2001;1:31–46 CrossRef Medline
 8. Nagar VR, Birthi P, Grider JS, et al. Systematic review of radiofrequency ablation and pulsed radiofrequency for management of cervicogenic headache. *Pain Physician* 2015;18:109–30 Medline
 9. Grandhi RK, Kaye AD, Abd-Elsayed A. Systematic review of radiofrequency ablation and pulsed radiofrequency for management of cervicogenic headaches. *Curr Pain Headache Rep* 2018;22:18 CrossRef Medline
 10. Brinjikji W, Cloft H, Kallmes DF. Anatomy of the posterior inferior cerebellar artery: relevance for C1–C2 puncture procedures. *Clin Anat* 2009;22:319–23 CrossRef Medline

Epidural Spinal Injections in Spinal Stenosis due to Lipomatosis: With or without Steroids?

Spinal epidural lipomatosis (SEL) is characterized by the overgrowth of epidural adipose tissue inside the spinal canal and may present with symptoms of spinal stenosis or nerve root compression.¹ In a recent study, it has been reported that 6.26% of patients presenting with clinical signs of spinal stenosis showed symptomatic SEL.² Spinal epidural infiltrations under imaging guidance are a safe treatment for symptomatic spinal stenosis and are frequently performed by interventional radiologists. Usually, a mixture of local anesthetics and corticosteroids is used. Botwin and Sakalkale³ reported a good clinical response (pain relief of 80%–85%) after epidural injections with steroids in 2 patients with SEL and symptoms of spinal stenosis. On the other hand, repeat epidural infiltrations with corticosteroids have been discussed as an etiologic factor in the development of SEL. The study by Jaimes and Rocco⁴ reported that >1 epidural steroid injection was linked to the occurrence of SEL in a logistic regression model.

Because larger studies and prospective investigations are missing, the interventional radiologist is in a dilemma whether steroids should be used in symptomatic SEL. In these cases, we suggest a pragmatic approach. According to the data of Jaimes and Rocco,³ the first epidural injection can be performed with the use of steroids. In their study, a single epidural steroid injection was not associated with SEL; it seems that a single dose of epidurally administered steroids is not enough to aggravate epidural fat accumulation.

In the case of a symptomatic spinal stenosis, we usually perform a single epidural injection using CT guidance and an interlaminar approach with the use of steroids and local anesthetics (4 mL of mepivacaine/1 mL of dexamethasone). If there is a marked improvement after this first injection, other treatment components such as physiotherapy and medication are adjusted to maintain the improvement. Only in the case of persistent or immediately relapsing pain is treatment with epidural injection repeated. The safe time interval between 2 epidural injections with steroids in patients with good clinical SEL is unknown. If there is no significant improvement after the first injection with steroids in symptomatic SEL, we think further injections in the short term should be performed with local anesthetics only.

In a recent meta-analysis, no significant difference between epidural injections with steroids and local anesthetics or local anesthetics alone has been found⁵—that is, an epidural injection with local anesthetics only is also an evidence-based approach. This sequential use of an injection with steroids followed by infiltrations without steroids may limit the risk of worsening SEL. In the treatment of patients with symptomatic SEL, the underlying etiology should also be considered. For example, in patients with SEL due to obesity, weight reduction has been shown to reduce SEL.⁶

In conclusion, evidence in the treatment of spinal stenosis due to SEL with epidural infiltrations is very limited. We propose a sequential approach using an epidural infiltration with steroids for the first injection followed, if needed, by further epidural infiltrations with local anesthetics only. This procedure may reduce deleterious effects on the progression of SEL. Further studies on this topic are needed.

REFERENCES

1. Kim K, Mendelis J, Cho W. **Spinal epidural lipomatosis: a review of pathogenesis, characteristics, clinical presentation, and management.** *Global Spine Journal* 2018 Aug 13. [Epub ahead of print] CrossRef
2. Malone JB, Bevan PJ, Levis TJ, et al. **Incidence of spinal epidural lipomatosis in patients with spinal stenosis.** *J Orthop* 2018;15:36–39 CrossRef Medline
3. Botwin KP, Sakalkale DP. **Epidural steroid injections in the treatment of symptomatic lumbar spinal stenosis associated with epidural lipomatosis.** *Am J Phys Med Rehabil* 2004;83:926–30 CrossRef Medline
4. Jaimes R 3rd, Rocco AG. **Multiple epidural steroid injections and body mass index linked with occurrence of epidural lipomatosis: a case series.** *BMC Anesthesiol* 2014;14:70 CrossRef Medline
5. Meng H, Fei Q, Wang B, et al. **Epidural injections with or without steroids in managing chronic low back pain secondary to lumbar spinal stenosis: a meta-analysis of 13 randomized controlled trials.** *Drug Des Devel Ther* 2015;9:4657–67 CrossRef Medline
6. Borstlap AC, van Rooij WJ, Sluzewski M, et al. **Reversibility of lumbar epidural lipomatosis in obese patients after weight-reduction diet.** *Neuroradiology* 1995;37:670–73 CrossRef Medline

J. Gossner

Department of Diagnostic and Interventional Radiology
Evangelisches Krankenhaus Göttingen-Weende
Göttingen, Germany

Blood-Brain Barrier Permeability in Patients with Systemic Lupus Erythematosus

We read with much interest the article by Chi et al¹ in the March 2019 issue of the *American Journal of Neuroradiology*, “Alterations in Blood-Brain Barrier Permeability in Patients with Systemic Lupus Erythematosus.”

Reportedly, dynamic contrast-enhanced (DCE) imaging supports the hypothesis that patients with systemic lupus erythematosus have increased blood-brain barrier (BBB) permeability, specifically in the hippocampus, compared with other brain regions.¹ However, some technical issues in the current study may limit its conclusions.

First, the authors stated that the pharmacokinetic 2-compartment exchange model used to calculate BBB leakage was the Tofts extended permeability model, but they provided only 2 derived parameters: the transfer constant (K^{trans}) and the extravascular extracellular volume fraction (V_e), despite the fact that the Tofts extended model is supposed to provide the blood volume fraction (V_b) in addition. V_b corresponds to the volume of vessels per volume of tissue (in milliliters/100 mL of tissue or in percentages). Thus, it is likely that the model used was a Tofts-Kety model or the Tofts and Kermode model using the Olea Sphere software (Olea Medical, La Ciotat, France), which provides only V_e and K^{trans} .^{2,3} The more complex extended Tofts model was developed to overcome some important limitations of the Tofts-Kety model, which imperfectly models DCE data and loses a significant amount of information and might not be suitable to detect subtle changes, as is the case with BBB leakage.

Second, the K^{trans} parameter is a combination of tissue blood flow (F_t), corresponding to the blood flow entering and exiting a volume of tissue, and of permeability surface-area product (PS), corresponding to the flow of molecules through the capillary membranes per volume of tissue, in varying proportions. Therefore, the K^{trans} method of calculation includes both perfusion- and permeability-related phenomena, leading to a possible misinterpretation of the parameters, even when accurately fitting the data. As a result, its use should be avoided when exploring permeability. Using a more complex and robust pharmacokinetic model like the 2CX, which provides 4 distinct parameters, including 2

perfusion-related parameters (F_t and V_b) and 2 permeability-related parameters (PS and V_e), would be more suitable.^{3,4}

Third, the authors did not provide the exact duration of their DCE sequence, though this should have been a critical part of their method. Indeed, the leakage process occurs late after contrast injection, and pharmacokinetic models calculate permeability-derived parameters on the basis of a long acquisition time. A minimal duration of 10 minutes for DCE acquisitions is therefore recommended to provide accurate data, especially when observing subtle changes, as is the case in BBB leakage.³

In conclusion, one should remain cautious when interpreting these results, especially given the very low number of patients. Using a more complex and robust model such as the 2CX, as well as optimized DCE acquisitions, might substantially improve detection and understanding of BBB leakage in patients with systemic lupus erythematosus.

Disclosures: Julien Savatovsky—UNRELATED: Payment for Lectures Including Service on Speakers Bureaus: Medtronic, Biogen, Philips Healthcare, Sanofi, Novartis; Travel/Accommodations/Meeting Expenses Unrelated to Activities Listed: Bayer Healthcare.

REFERENCES

1. Chi JM, Mackay M, Hoang A, et al. **Alterations in blood-brain barrier permeability in patients with systemic lupus erythematosus.** *AJNR Am J Neuroradiol* 2019;40:470–77 CrossRef Medline
2. Tofts PS, Brix G, Buckley DL, et al. **Estimating kinetic parameters from dynamic contrast-enhanced T(1)-weighted MRI of a diffusable tracer: standardized quantities and symbols.** *J Magn Reson Imaging* 1999;10:223–32 CrossRef Medline
3. Sourbron SP, Buckley DL. **Classic models for dynamic contrast-enhanced MRI.** *NMR Biomed* 2013;26:1004–27 CrossRef Medline
4. Brix G, Zwick S, Kiessling F, et al. **Pharmacokinetic analysis of tissue microcirculation using nested models: multimodel inference and parameter identifiability.** *Med Phys* 2009;36:2923–33 CrossRef Medline

● A. Lecler

● J.C. Sadik

● J. Savatovsky

Department of Neuroradiology
Fondation Ophtalmologique Adolphe de Rothschild
Paris, France

<http://dx.doi.org/10.3174/ajnr.A6137>

REPLY:

We appreciate the comments from Drs Lecler, Sadik, and Savatovsky on our article, "Alterations in Blood-Brain Barrier Permeability in Patients with Systemic Lupus Erythematosus." The comments are mainly focused on the permeability model used in dynamic contrast-enhanced (DCE)-MR imaging postprocessing. In our study, we used a commercially available software, Olea Sphere (Olea Medical, La Ciotat, France), using the Tofts and Kermode (TK) permeability model, to postprocess the acquired DCE-MR imaging data into blood-brain barrier permeability (BBBP) parameters of the volume transfer constant (K^{trans}) and V_e . The authors suggest the use of a more complex pharmacokinetic model, the 2-compartment exchange model (2CX), which they state may overcome important limitations of our current model, to detect subtle changes in BBBP.

Different theoretic models have been proposed for DCE-MR imaging data analysis, including the TK and extended TK models, the adiabatic tissue homogeneity model, the 2CX model, the distributed capillary adiabatic tissue homogeneity model, and the γ capillary transit time model.¹ The TK model used in our study, while less robust as indicated by the authors, is readily integrated into the clinical setting and is thus more practical from a clinical standpoint compared with the other aforementioned models. The TK model has previously been shown to overestimate K^{trans} ; however, marked variability in K^{trans} values across different models is a known issue affecting all models.² Most important, even if absolute K^{trans} values may have been overestimated in our study, all patients and controls were analyzed with the same model conditions; therefore, our conclusions regarding relative region-based and disease-based changes in K^{trans} remain valid.

The 2CX model is a complex and robust pharmacokinetic model, as discussed by the authors, and provides 4 distinct parameters including 2 perfusion-related parameters and 2 permeability-related parameters. The authors have recently published a study on the application of the 2CX model in differentiating benign from malignant orbital tumors.³ This is a valuable contribution to the large body of literature comparing different DCE-MR imaging models, in which the authors state that regardless of the permeability model used, there were no differences in their conclusions.

The TK model used in our study has previously been applied in the detection of subtle permeability changes.⁴ While there are certain inherent disadvantages to the TK model, our study, nevertheless, revealed statistically significant BBBP differences in patients with systemic lupus erythematosus (SLE) compared with healthy controls. We would, in fact, expect similar results with any of the aforementioned models, including the 2CX. If anything, the 2CX model may augment the differences observed between the SLE and healthy control groups.

Furthermore, the purpose of our study was not to compare permeability models or parameters. We used a commonly used commercial software and found statistically significant results comparing patients with SLE with healthy controls. One of the points of this exercise was to expand the usefulness of these complex models so that their clinical efficacy could be tested.

Therefore, we are in substantial agreement with the authors' recently published study.³ However, we acknowledge that the application of the 2CX model to assess BBBP across different disease or stress states of patients with SLE remains to be fully evaluated.

Although we described 80 cine phases being performed in our imaging protocol, we take this opportunity to add that the total acquisition time for the DCE-MR imaging sequence was 11 minutes 14 seconds. While we agree with the authors that a minimal duration of 10 minutes for DCE acquisitions will increase the detectability of BBBP changes, these benefits to the physics of the protocol must be weighed against the biology we are attempting to understand and the risk to that biology (for example, patient tolerability and renal clearance of gadolinium).⁵

As in almost all past work with brain imaging, larger studies are needed to validate the findings in our study. We stated in our Conclusion: "These *initial data are proof-of-concept* which support our hypothesis that the BBB is selectively compromised, particularly in the hippocampus region in SLE subjects with little to no disease activity and no history of CNS insult who demonstrate impaired performance on cognitive testing. The significance of these findings may advance our understanding of the underlying pathophysiologic mechanisms affecting the brain in autoimmune diseases. Importantly, larger studies are necessary to validate these results and confirm the value of DCE-MR imaging methodology as a potential biomarker for blood-brain barrier permeability imaging."

We appreciate the authors' interest in our study. We hope our reply clarifies that the purpose of our study was not to determine the optimal pharmacokinetic model, BBBP parameters, or imaging protocol to use in assessing BBBP in patients with SLE. While our study used a debatably less sensitive permeability model, its clinical effectiveness and usefulness have detected BBBP alterations in patients with SLE, a clinically important addition to the literature in this disease. We would like to emphasize, and think the authors would agree, that more robust permeability models would not necessarily alter this conclusion. We acknowledge that our study reveals initial proof-of-concept findings that warrant further investigations.

REFERENCES

1. Sourbron SP, Buckley DL. **On the scope and interpretation of the Tofts models for DCE-MRI.** *Magn Reson Med* 2011;66:735–45 CrossRef Medline
2. Bergamino M, Saitta L, Barletta L, et al. **Measurement of blood-brain barrier permeability with T1-weighted dynamic contrast-enhanced MRI in brain tumors: a comparative study with two different algorithms.** *ISRN Neurosci* 2013;2013:905279 CrossRef Medline
3. Lecler A, Balvay D, Cuenod CA, et al. **Quality-based pharmacokinetic model selection on DCE-MRI for characterizing orbital lesions.** *J Magn Reson Imaging*. 2019 Apr 15. [Epub ahead of print] CrossRef Medline
4. Heye AK, Thrippleton MJ, Armitage PA, et al. **Tracer kinetic modelling for DCE-MRI quantification of subtle blood-brain barrier permeability.** *Neuroimage* 2016;125:446–55 CrossRef Medline
5. Thrippleton MJ, Backes WH, Sourbron S, et al. **Quantifying blood-brain barrier leakage in small vessel disease: review and consensus recommendations.** *Alzheimers Dement* 2019;15:840–58 CrossRef Medline

• **J.M. Chi**
Department of Radiology

• **M. Mackay**
Feinstein Institute for Medical Research
The Center for Autoimmune, Musculoskeletal and Hematopoietic Diseases
Donald and Barbara Zucker School of Medicine at Hofstra/Northwell
Hempstead, New York

• **A. Hoang**
Department of Radiology
Northwell Health
New York, York

• **K. Cheng**
Department of Radiology

• **C. Aranow**
Feinstein Institute for Medical Research
The Center for Autoimmune, Musculoskeletal and Hematopoietic Diseases
Donald and Barbara Zucker School of Medicine at Hofstra/Northwell
Hempstead, New York

• **J. Ivanidze**
Department of Radiology
Weill Cornell Medical College
New York, New York

• **B. Volpe**
Feinstein Institute for Medical Research
The Center for Biomedical Science

• **B. Diamond**
Feinstein Institute for Medical Research
The Center for Health Innovations and Outcomes Research

• **P.C. Sanelli**
Feinstein Institute for Medical Research
The Center for Health Innovations and Outcomes Research
Donald and Barbara Zucker School of Medicine at Hofstra/Northwell
Hempstead, New York
Department of Radiology
Imaging Clinical Effectiveness and Outcomes Research Program
Northwell Health
New York, New York